U.S. DEPARTMENT OF ENERGY

Office of ENERGY EFFICIENCY & RENEWABLE ENERGY

Consortium for Production of Affordable Carbon Fibers in the United States

Final Report (Phase 1 and Phase 2 Topical Reports)

Federal Grant Number DE-EE0008203

FOA: Fiscal Year 2017 Vehicles Technologies Program Wide Funding Opportunity Announcement, # DE-FOA-0001629

Jeramie J. Adams, Ph.D., Program Manager for Hydrocarbons,
Jeramie.adams@uwyo.edu
Western Research Institute (DUNS # 10-849-0236)
3474 North 3rd Street
Laramie, WY 82072-9571
www.westernresearch.org

Reporting Period: October 1, 2017-July 30, 2021

Submission Date: October 29, 2021

Table of Contents

List of Tables

List of Figures

Disclaimer

Acknowledgments

Although this effort was led and managed by the WRI, this work was performed as a consortium with cooperation between several different industrial and academic institutions. The work put forth in this study must be acknowledge from these primary important and key contributors:

- Nicola Ferralis at MIT: micro-scale modeling, ML, data management
- Logan Kearny and Amit Naskar at ORNL: CF spinning, precursor thermal and rheological characterization, CF characterization, model integration
- Ray Fertig III and Carl Frick at UW: FEA modeling, tow-level composite fabrication, tow-level composite characterization
- Brett Johnston, Stacey McKinney, Billy Cairns, Carl Muller at Koppers: Production and donation of decant oil, PP, PPM and CTP
- Amit Goyal at SRI: production of bio-ACN and bio-ACN techno economic analysis
- Charlie Atkins, Jim Dietz, Charlie Hill, Chris Yurchick at Ramaco: techno economic analysis for pitch and bio-ACN CF production
- Khalid Baig at WRI: for pitch preparation, mesophase production and pitch characterization
- Chris Boyer and Don Malone: for providing PP and PPM samples
- Billy Harmon, Girish Deshpande and Desmond Cook at Solvay: for providing technical insight and guidance to the project
- John Terneus and Felix Wu at DOE: for project management and assistance

Executive Summary

This Final Report is an in series combination of the Phase 1 and Phase 2 Topical Reports.

PHASE 1 (BUDGET PERIOD 1 AND 2) TOPICAL REPORT

Executive Summary

Various feedstocks from coal, petroleum and bio-based acrylonitrile were investigated for their ability to produce carbon fiber within DOE strength (250 ksi), modulus (25 Msi), elongation (>1%) and cost (≤$5/lb) goals for wider utilization in light-weight vehicles for the automotive industry. The overarching approach was to chemically identify and map the various feedstocks, understand the molecular transformation to produce carbon fiber precursors (mesophase for pitch materials of polyacrylonitrile polymer) and how these impact carbon fiber quality. Predictive models were built to relate the feedstocks and precursors to carbon fiber properties using atomistic and micro-scale modeling within ±15%. Using tow-level carbon fiber epoxy composites, carbon fibers tow-level predictions of elastic components of the carbon fibers were also successfully modeled within ±15%, using finite element analysis to confirm single filament carbon fiber properties. These models were validated with tow-level epoxy composite experiments from carbon fibers produced in this study.

New approaches to machine learning were developed which can provide some chemical and physical insight behind correlations while also minimizing the risks of overfitting. This was accomplished by selectively including data from correlative heat maps, as opposed to using all collected data indiscriminately. The optimization of essential parameters feeding into the machine learning algorithms were tested and successfully validated against experimental data.

High temperature coal tar pitch, petroleum pitch and bio-based acrylonitrile were down selected for further study and scale up. The scaled up materials continued to meet DOE mechanical property targets. A more detailed cost analysis showed that all three feedstocks were capable of being produced at less than $5/lb within given assumptions of the various models.

Introduction

Significant weight reduction for vehicles would have several economic and environmental advantages; most notably, reduced fuel consumption and greenhouse gas emissions. Additional cascading benefits would include reductions in infrastructure costs and maintenance by virtue of less stress applied to vehicles, roads, and other transportation infrastructure, as well as far-reaching geopolitical impacts, such as improved national security, by reducing the dependency of the United States (U.S.) on foreign crude oil. Another key aspect is that electric vehicles are becoming more widely accepted and that these vehicles are significantly heavier than their petrol-powered equivalents leading to increased energy utilization and safety issues. The U.S. Drive (Driving Research and Innovation for Vehicle Efficiency and Energy sustainability)

Partnership Plan was launched through the Department of Energy's (DOE) Office of Energy Efficiency and Renewable Energy (EERE) and the Vehicle Technologies Office (VTO) to advance and encourage development of automotive and related energy infrastructure technology research and development (U.S. Drive, 2021).

One such way to reduce the weight of vehicles, while not sacrificing strength and crashworthiness, is to replace traditional stress bearing metal components with lightweight advanced materials and composites, such as those made from comprising carbon fiber (CF). These advanced materials can be engineered to have physical strength properties greater than steel at a fraction of the weight. By properly selecting materials and manufacturing protocols, very strong and flexible materials can be produced. Therefore, CFs are used to produce materials as diverse as the spaceship nosecones to shafts of fly-fishing rods. This gives validity to pursuing CFs for future development of lightweight vehicles.

One difficulty in the large-scale deployment of CF for the commercial vehicle industry is the availability of large quantities of CF with appropriate physical properties at a reasonable cost (Das, Warren, & West, 2016). To address these limitations the Consortium for Affordable CFs in the U.S. was created through funding from EERE award number DE-EE0008203. The consortium including academic, government, non-profit, and commercial entities was assembled to study the feasibility of using large-volume, low-cost natural resources to produce CFs of the appropriate quality and cost for use in the vehicle industry. Some of the most abundant natural resources are those from current biomass, such as sugars derived from agricultural sources, or those from ancient biomass, such as coal and petroleum. The results of a study including several different types of feedstocks, and blends of these feedstocks, will provide for a robust roadmap for potential materials, while also reducing economic risks that can arise by becoming too dependent on any one material, which may itself be subject to climatic, environmental, geopolitical, and, ultimately, market variations. Therefore, within this program, no preference was given to any one feedstock or CFs are being produced from coal-, petroleum-, and biomass-based feedstocks.

The objective of this research is to investigate the current landscape of appropriate raw starting materials from petroleum-, coal-, and biomass-based feedstocks to derive precursors to produce low-cost CF materials for lightweight vehicles in the U.S. This objective is divided into two complementary parts:

1. Develop, integrate, and demonstrate a suite of Integrated Computational Materials Engineering (ICME) modeling tools that predict CF properties within 15% of measured properties. This will enable the design, development, and optimization of precursor chemistry and molecular structure associated with conversion into CF and evaluate alternative precursors for their suitability to manufacture low-cost CF. The ICME models will also include methodologies to simulate the manufacturing processes, including variability from both process and material. All non-proprietary and non-business-sensitive public data and code—such as technical data used to support published journal articles or research code used for simulations—has been provided to the LightMat Consortium for curation and hosting.

2. Develop, manufacture, and demonstrate CF precursor technology and processing techniques where CF is a material consisting of thin, strong, multi-crystalline filaments of carbon used as a reinforcement material especially in resins, capable of achieving the requirements in Table 1. A representation of the strength and modulus requirements for this project are shown relative to other types of CF in Figure 1.

Table 1: DOE CF project parameter requirements.

Parameter	Requirement
Cost	≤ $5/pound
Strength	≥ 250 Ksi
Modulus	≥ 25 Msi
Strain	≥ 1%

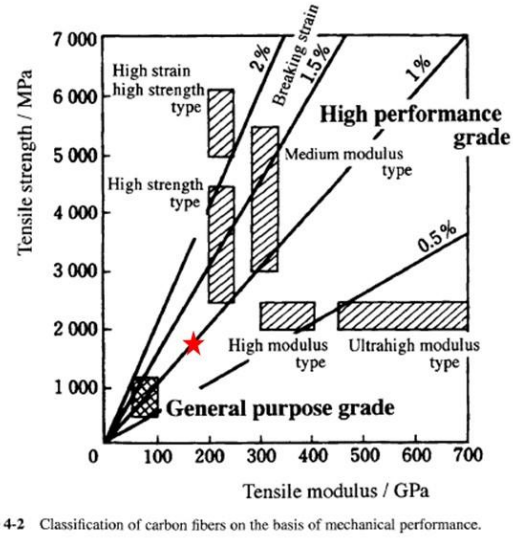

Figure 4-2 Classification of carbon fibers on the basis of mechanical performance.

Figure 1: Plot showing the relationship between strength and modulus for various types of CF. The red star shows the properties that are being targeted for this project (Ingaki, 2000).

The approach will be to study readily available, large-volume, feedstocks from biomass, coal, and petroleum to produce precursors of appropriate qualities that lend themselves to the production of CF with the appropriate physical properties and cost to be used in the commercial vehicle industry. The project will remove risk from this process by developing predictive models that can be used to guide the development of CF materials from new or blended feedstocks. To achieve this goal, a project team consortium was assembled including partners that have significant experience working with these different feedstocks, as well as experts in CF production, mechanical testing, and modeling from the molecular-, micro-, and macro-levels. The team chosen for this project comprises:

- Western Research Institute (WRI): Prime recipient
- Oak Ridge National Laboratory (ORNL): Subrecipient, funded by a field-work proposal (FWP)
- Grossman Group at Massachusetts Institute of Technology (GG-MIT): Subrecipient
- Southern Research Institute (SRI): Subrecipient
- University of Wyoming (UW): Subrecipient
- Advanced Carbon Products (ACP): Subrecipient
- Ramaco Carbon, LLC (RAMACO): Subrecipient
- Solvay Composites (Solvay): Industrial advisor
- Koppers: Industrial advisor

Each member of the consortium brings a unique and complementary aspect necessary to buildup fundamental scientific, and yet industrially relevant understanding between the chemistry and molecular structure of different organic feedstocks and subsequent precursor formation, while following the production chain up through CF tow-level fabrication, mechanical characterization, and modeling. These individual aptitudes have been integrated using a database exploited by high-level data mining. Model inputs include density function theory–assisted molecular dynamics, chemical and compositional characterization, morphology and mechanical CF data, CF processing parameters, tow-level epoxy mechanical information, ML, and computational methods to deliver state-of-the-art, holistic, and robust models. The strengths of each consortium member are necessary for the wide scope set forth in the project, while producing minimum overlap and duplication of efforts. Figure 2 shows a high-level depiction of the consortium organization and primary strengths and responsibilities for each consortium member.

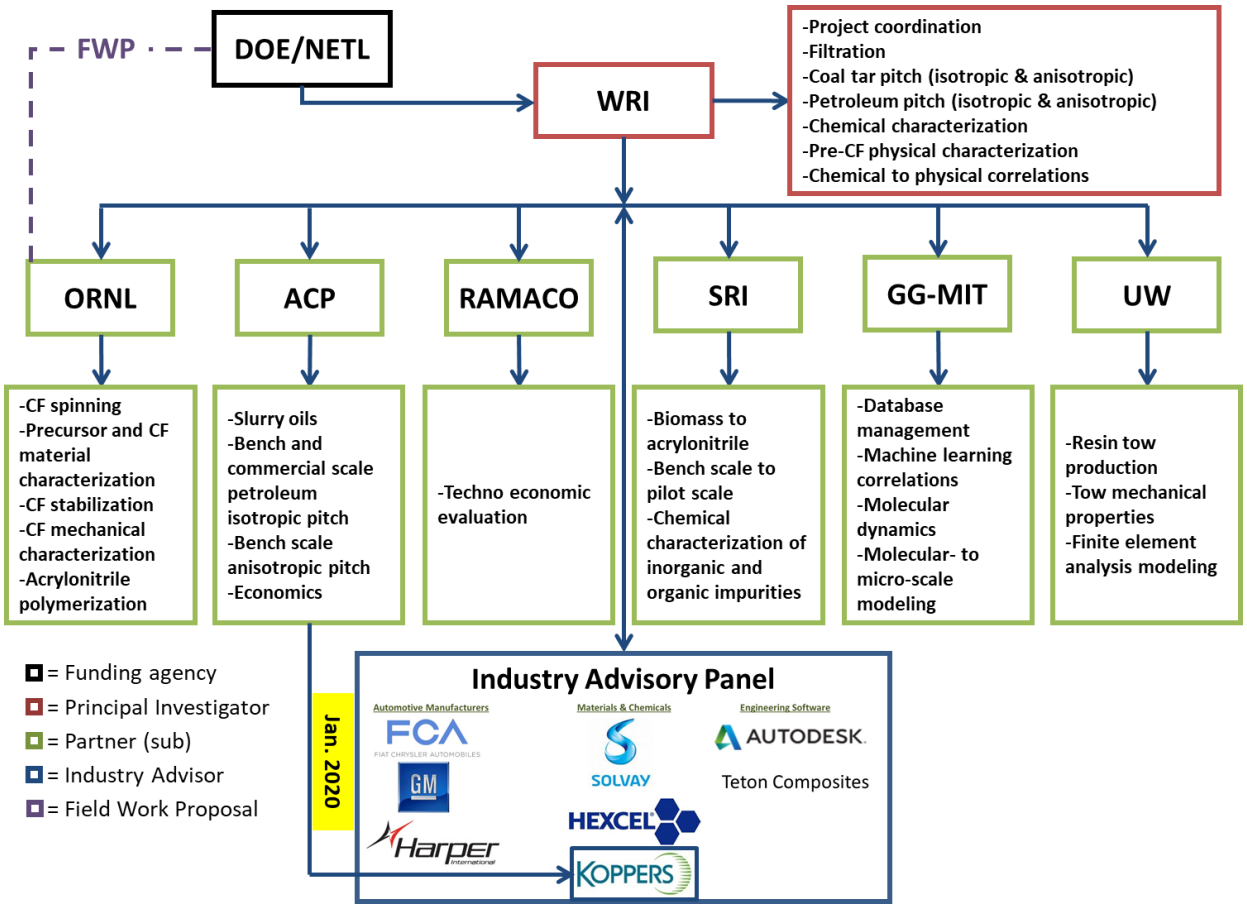

Figure 2: Organization for the Consortium for Production of Affordable Carbon Fibers in the United States.

The project was conducted in three budget periods (BPs). This Final report combines the Phase 1 Topical Report which covers the findings from BP1 and BP2 and how this relates to CF ICME with the Phase 2 Topical Report. A high-level summary of the three BPs are as follows:

BP1 (October 2017 – December 2018): Carbon Fiber Precursor Screening and Down-selection

Carbon Fiber feedstocks and precursors were studied to down-select precursors capable of achieving the physical property goals at less than $5/lb. The project entered a no-cost extension from October 2018-December 2019 and all milestones were achieved by the end of the no-cost extension. Carbon Fiber produced from coal tar pitch (CTP), petroleum pitch (PP), and bio-based polyacrylonitrile (bio-PAN) met the DOE's targets for BP1 for both mechanical properties and cost from the preliminary techno-economic analysis.

BP2 (January 2019 – July 2020): Carbon Fiber Tow-level Material System Properties and Analyses

Scale-up of acceptable candidates from BP1 was accomplished to produce larger batches of CF so that composite macro-level models will be created, and CF tow-level composites will be fabricated and tested at extreme temperatures for light-duty vehicle components to update micro-

level and cost estimate models. Micro-level models are being developed to optimize CF properties and production-engineering cost trade-off studies.

BP3 (August 2020 – July 2021): Validation and Transfer of Models and Data to DOE ICME Program

The most promising CF materials will be further evaluated for producibility and to improve macro-level models while building a comprehensive performance database up to the tow-level. Macro- and micro-level models will be integrated and validated for industry use. Models and data will be transferred to the DOE ICME program, and a final cost estimate will be produced.

In this program, pitch-based materials and bio-PAN were extensively studied as CF precursors. Carbon Fiber production is fundamentally different for pitch-based (isotropic or mesophase) and PAN-based materials. Pitch-based CF is generally produced through melt spinning of a mesophase pitch which is simpler and cheaper than methods used to produce PAN-based CF. Mesophase is produced by thermal oligomerization of smaller aromatic molecules from CTP or PP to produce larger aromatic molecules that will align to form liquid crystalline material. Melt spinning requires extruding molten pitch through a spinneret dye. This process aligns the molecules parallel to the axis of the fiber. After final processing of the spun fibers into CF this alignment is retained yielding stacked sheets of molecules along the fiber axis providing great strength. Polyacrylonitrile (PAN) CF production requires solution spinning of a formulated multicomponent copolymer of acrylonitrile (ACN) to produce fibers. The other component units are added to accelerate stabilization and provide other benefits. Solution spinning of PAN is more complex as it requires a solution at controlled temperatures, proper stretching of the fibers during spinning to align the molecules and careful thermal and stress control during oxidation to prevent thermal runaway while producing adequate condensation and structuring of the molecules. Directly after spinning, both pitch-based and PAN-based fibers are referred to as green fibers, or as spun fibers, and they require additional processing to crosslink the molecules and increase the graphitic structure to produce CF. These additional processing methods consist of oxidative stabilization, carbonization, and graphitization. Oxidative stabilization uses oxygen to thermally crosslink the various aromatic-like domains so that the material can then undergo higher temperature treatments without deforming or melting. These higher temperature treatments fall into a lower-temperature regime, carbonization (800-1200 °C for pitch, 1200-1400 °C for PAN) and graphitization (1500-3000 °C for pitch and 2000-3000 °C for PAN) (Ingaki, 2000). Figure 3 shows a generalized schema for the melt spinning process used to produce pitch-based CF and Figure 4 shows a generalized schema for PAN solution spinning.

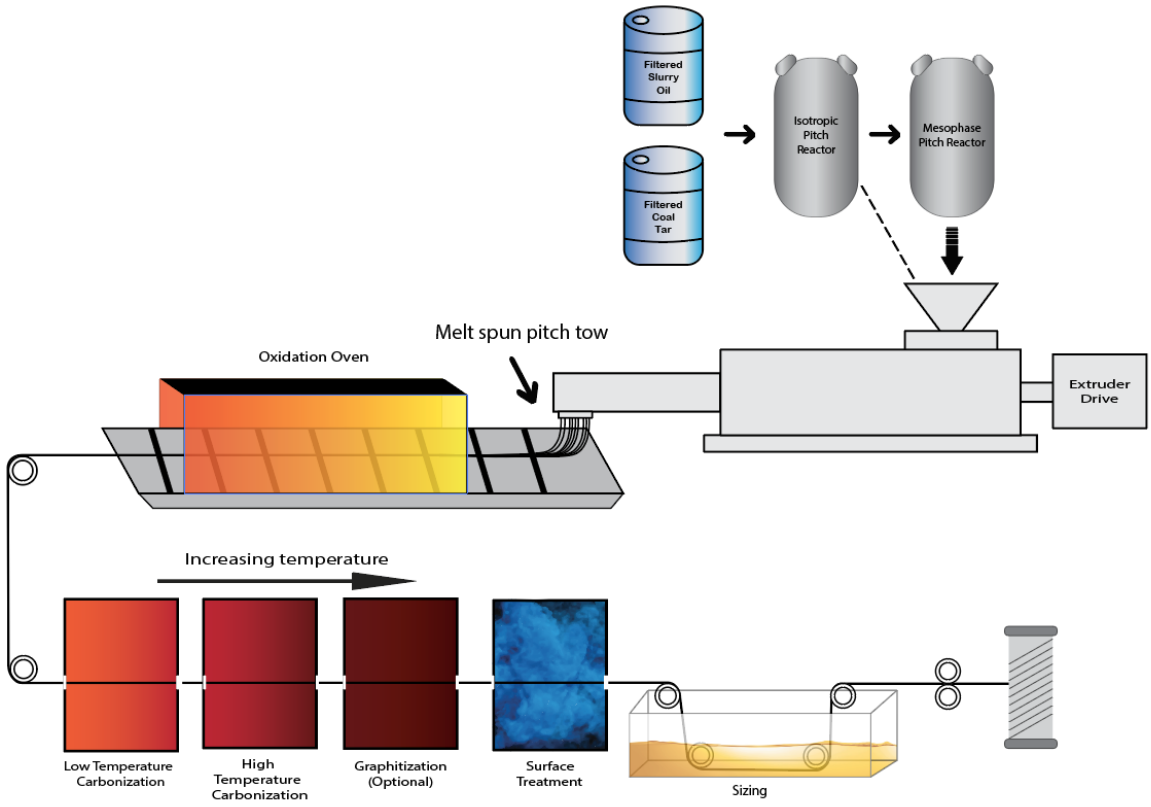

Figure 3: Generic illustration for the production of melt spun pitch-based Carbon Fiber.

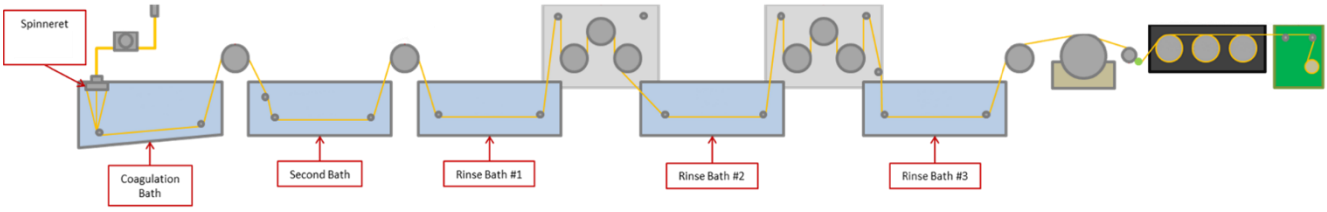

Figure 4: Generic illustration for the production of solution spun PAN Carbon Fiber. Note that thermal processing is not shown.

Modeling Effort

A key effort of this work, within the ICME effort, is modeling the CF synthesis from precursors. Modeling was used to understand the molecules that were present in various feedstocks, how these molecules changed to produce CF precursors which are spun into CF, the various CF processing conditions, CF single filament properties, and tow-level CF properties. There are other various relationships that can be understood, such as the impact of processing parameters on the feedstocks to produce better or worse precursors, and the effect of the various other processing parameters on single filament CF properties. During BP3 the integration of the micro-scale modeling to the macro-scale modeling was performed, this process is provided later in the Phase 2 Topical Report. Figure 5 shows a high level of the modeling efforts that were performed

during this study, and which properties were linked using either machine learning (ML) or artificial neural networks.

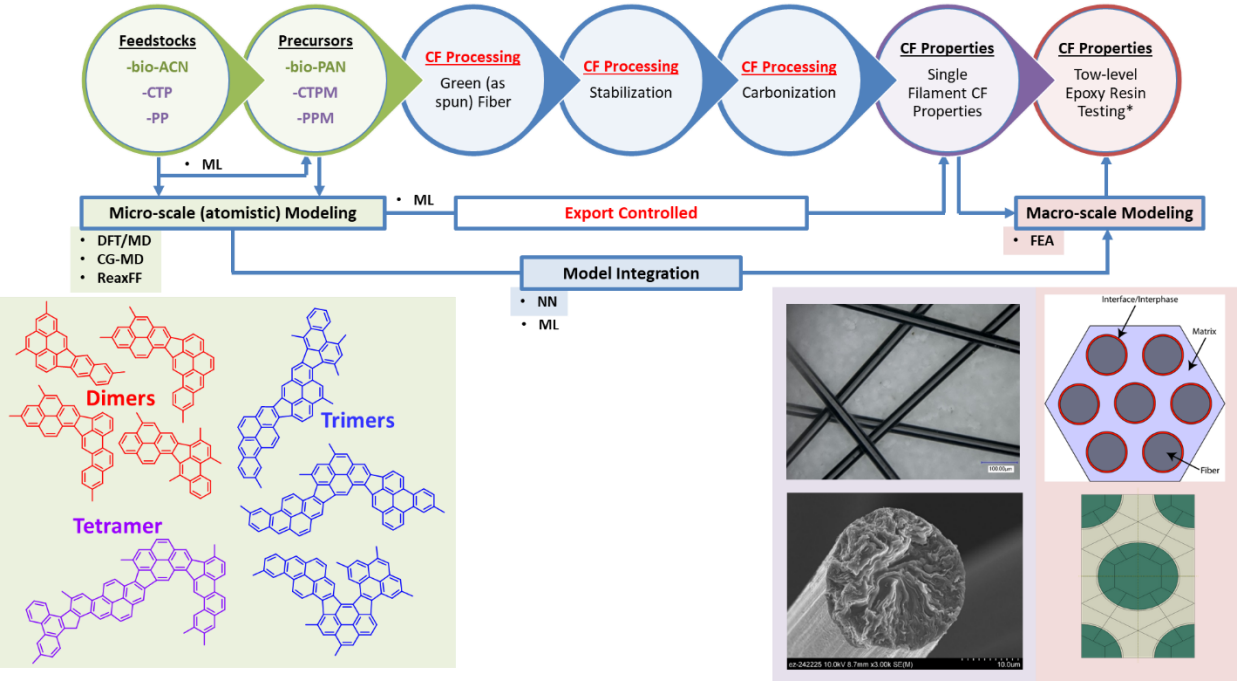

Figure 5: A diagram showing the modeling efforts that were performed during this study. The model integration was performed during BP3 and will be presented in a separate Topical report. DFT = density functional theory, MD = molecular dynamics, CG-MD = coarse grain molecular dynamics, ReaxFF = reactive force field, ML = machine learning, NN = artificial neural networks, FEA = finite element analysis.

Feedstock and Precursor Materials Investigated

Isotropic Pitch

During BP1, several feedstocks were screened for their ability to produce CF as isotropic or mesophase pitch. These included high-temperature CTP (HTCTP), a low-temperature CTP, gilsonite, hydrocracker bottoms (HCB), and reclaimed asphalt shingle (RAS) asphalt. Appendix A provides the source of these materials and characterization data.

Typically, isotropic fibers do not produce CF of the properties required for this project, however with decreasing CF diameters it is possible to increase the strength of isotropic pitch-based CF significantly (Diez, et al., 2012), and in general for most fibers including PAN CF (Tagawa & Miyata, 1997). Gilsonite of three different grades were used. The grades were the whole gilsonite (SEL347), the heptane-soluble resins fraction (ER 125) and the heptane-insoluble fraction (IR200) were spun into fibers. The ER 125 was too soft (lowest SP) to produce CF with sufficient integrity to do low temperature stabilization without the fibers deforming and undergoing inter-filament fusing. SEL347 was able to produce fibers that could be stabilized at

low temperatures for very long times to produce CF. IR200 had the highest softening point and was relatively easy to spin into fibers and could be stabilized at low temperatures, however it did not produce fibers with a homogenous surface. Figure 6 shows the CF surface for the gilsonite samples.

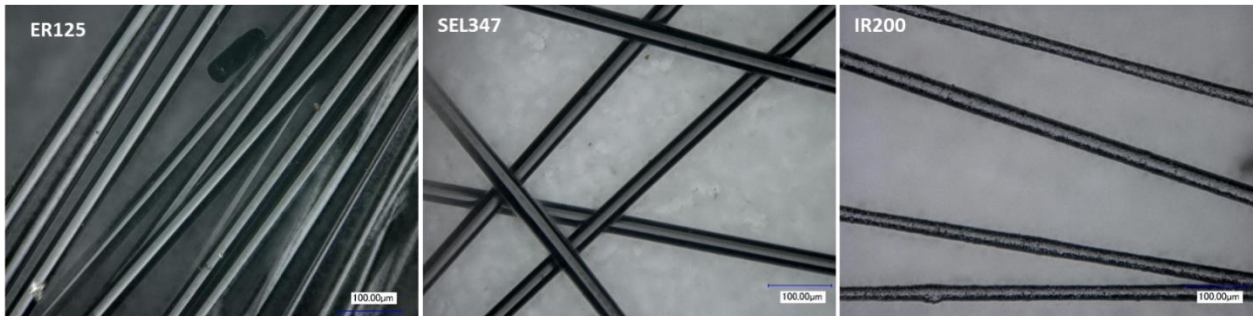

Figure 6: As spun gilsonite fibers for ER125, SEL347 and IR200.

RAS and hydrocracker bottoms were not spun into isotropic CF because their softening point was too low to form stable fibers at ambient temperature.

Low-temperature CTP contained significantly different chemical composition than HTCTP (García, Crespo, Snape, & Moinelo, 2003). Low-temperature CTP has more oxygen, more carbon residue content, more insoluble species, and less unsubstituted aromatic species than HTCTP (see Characterization section). This material could be spun into fibers with low surface defects by removing the primary quinoline solubles, but it produced general purpose quality CF.

HTCTP was filtered to remove primary quinoline-insolubles (QI), and when small diameter fibers (<12 microns) were spun these could be converted in CF with qualities (strength of 205 Ksi, modulus of 17 Msi, and 1.02 strain) that almost meet specifications for this project, and are higher quality than general purpose CF. These properties are very similar to several low temperature carbonization mesophase pitch CF samples. This result challenges the widely accepted notation that it is not possible to produce higher performance CF from isotropic pitch. If it were possible to produce higher performance CF directly from isotropic pitch, this would save on the cost and need to do mesophase conversion. However, the tradeoff is that spun isotropic fibers initially need to be stabilized at very low temperatures and over a much longer time, preventing deforming the fibers or undergoing inter-filament fusing. The difficulty in handling, and lack of commercially available and economic stabilization methods for large production of CF from isotropic fibers, was a deciding factor for abandoning the further study of isotropic pitch-based CF for this study. Figure 7 shows as spun fibers produced from a low-temperature CTP (CTP3) and a HTCTP (CTP7) after removal of primary QI by dissolving the samples in n-methyl-2-pyrrolidone (NMP) and filtering.

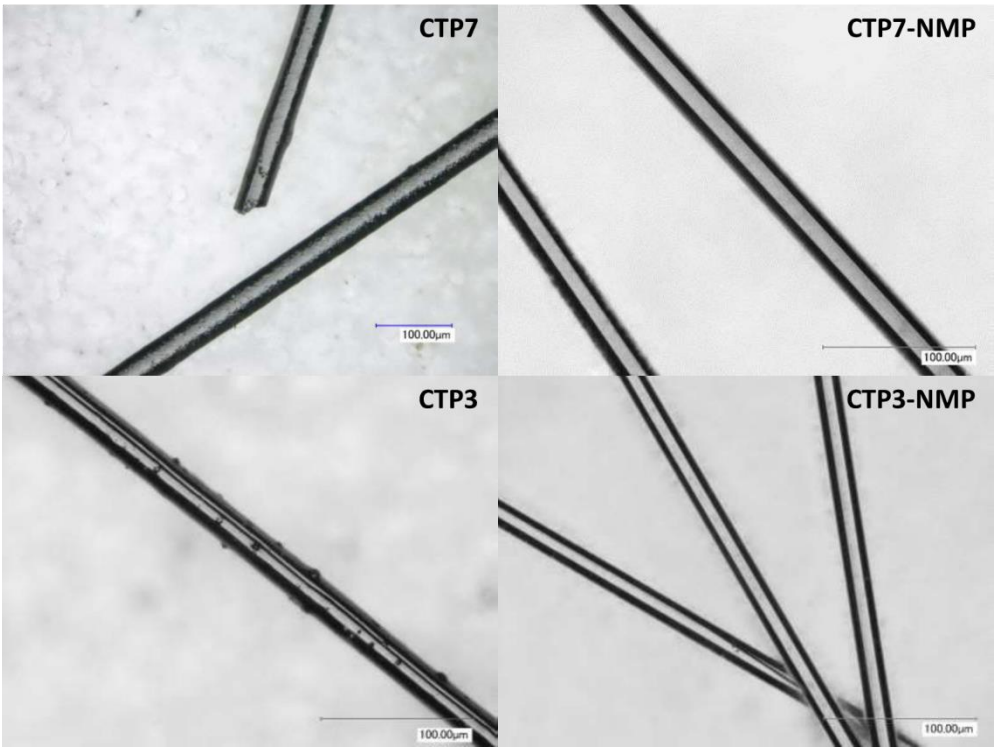

Figure 7: Surface texture of as spun Carbon Fiber produced from low-temperature CTP before (CTP3) and after removal of primary QI (CTP3-NMP) and from a HTCTP before (CTP7) and after removal of primary QI (CTP7-NMP).

Mesophase Pitch

It is widely accepted that it is necessary to convert pitch-based materials, such as CTP and PP, into mesophase to induce high ordering of the aromatic molecules in the pitch, which is then ordered along the fiber axis during spinning, leading to higher performance CF (Diefendorf, 2000; Bermudez, Lukubira, & Ogale, 2018; Inagaki & Kang, 2014). Mesophase is the ordering of the aromatic domains to a point where liquid crystalline behavior is observed. Typical pitches capable of forming mesophase can be derived from ethylene cracker bottoms, PVC, petroleum or coal. Petroleum and coal are two of the largest and most widely available feedstocks. Coal tar is produced from the high temperature destructive distillation of coal during the production of metallurgical grade coke. Distillation of the tar to about a 350 °C to remove lighter volatiles produces the CTP. PP can be produced form a variety of sources including the bottoms of catalytic crackers, steam cracking and residues from various processes (Morgan, 2005). The materials from these sources are then processed by different methods to produce the pitch. These methods include mild pyrolysis under pressure, air blowing, steam stripping with vacuum, and simply by distillation. Of these methods mild pyrolysis under pressure is often used because it creates a high yield when recycle of the effluent streams included. General considerations for a mesophase pitch with good properties for producing HPCF are (Rebouillat, Donnet, & Wang, 1998; Diefendorf, 2000; Morgan, 2005):

- Low ash (physical defects) and metallic ion content (defects during carbonization and graphitization)
- Low heteroatom content (can interfere with mesophase, impact viscosity, and cause defects from puffing during carbonization and graphitization)
- Very low insolubles of inorganic (typically catalyst fines in cracker bottoms) or organic insolubles (coke-like materials in PP and particularly North American CTP)
- Softening point range 230-340 °C
- Thermal stability against further cross-linking reaction so that the viscosity changes little during spinning
- No significant chemical reactions that liberate volatiles (effects spinning and causes fiber defects)
- Low amount of volatiles at the spinning temperatures
- Low viscosity at the appropriate spinning temperature
- Mesophase that can orient during spinning
- As spun fibers should be sensitive enough towards oxidative stabilization at temperatures low enough to prevent fiber deformation and inter-filament fusing
- High carbon yield

Mesophase pitches produced from naphthalene, smaller polycyclic aromatic hydrocarbons (PAH) (5 or less rings) and anthracene oil are generally produced through strong Lewis Acid catalyzed reactions using $AlCl_3$ or HF/BF_3. These pitches have low levels of contaminants from metals and heteroatoms which lead to defects in CF, especially during carbonization and graphtitization (Diefendorf, 2000). Pitches produced from smaller PAHs generally have a lower softening point than non-hydrogenated PP and CTP mesophase pitches with the same relative amount of anisotropic material. The draw back to PAH "synthetic" pitches is that their starting materials are more costly, and corrosion can be an issue.

Early in the program, RAS, Gilsonite, CTP (low-temperature and high-temperature) and PP were converted to mesophase. RAS did produce some mesophase spheres but also some coarse coke-like mesophase domains, gilsonite produced coarse mesophase more like coke and low-temperature CTP produced non-spherical anisotropic domains. The non-spherical nature of anisotropic material in low-temperature CTP indicates that the high oxygen content was interfering with normal mesophase sphere formation. This doesn't mean that these materials may not be successful in producing mesophase by solvent fractionation or other treatment methods. Additional treatment of the materials would have added processing cost, thus likely causing the resulting CF to be >$5/lb. Due to this limitation these materials were not studied further. Figure

8 shows cross-polarized light optical microscopy of the materials produced after attempted mesophase conversion.

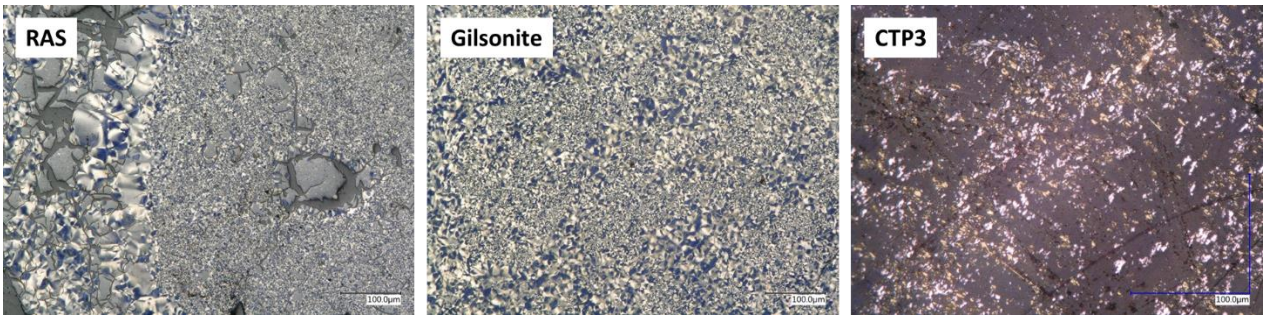

Figure 8: Cross-polarized light optical microscopy images of material produced using mesophase conditions for RAS, SEL347 Gilsonite and low-temperature CTP (CTP3).

As most pitch-based mesophase has been traditional produced from high volume, readily available, fluidized catalytic cracker (FCC) PP and HTCTP feedstocks, these two materials became the focus for further study. CTP and PP mesophases were successfully produced according to standard methods, heating at above ~400 °C with an inert gas sparge (U.S. Patent No. 4,026,788, 1977). Several different mesophase samples with various mesophase contents and softening points were prepared from CTP (CTPM). Figure 9 shows cross-polarized light optical microscopy for the progress of mesophase formation from CTP6-NMP (CTP6M) under different conditions showing smaller mesophase spheres increasing in number and size until phase inversion and coalesce of the mesophase until +95% mesophase is obtained. The mesophase sample with a SP of 320°C was used to produce CF that met DOE targets with 361 Ksi strength, 26 Msi modulus and 1.17% strain to failure.

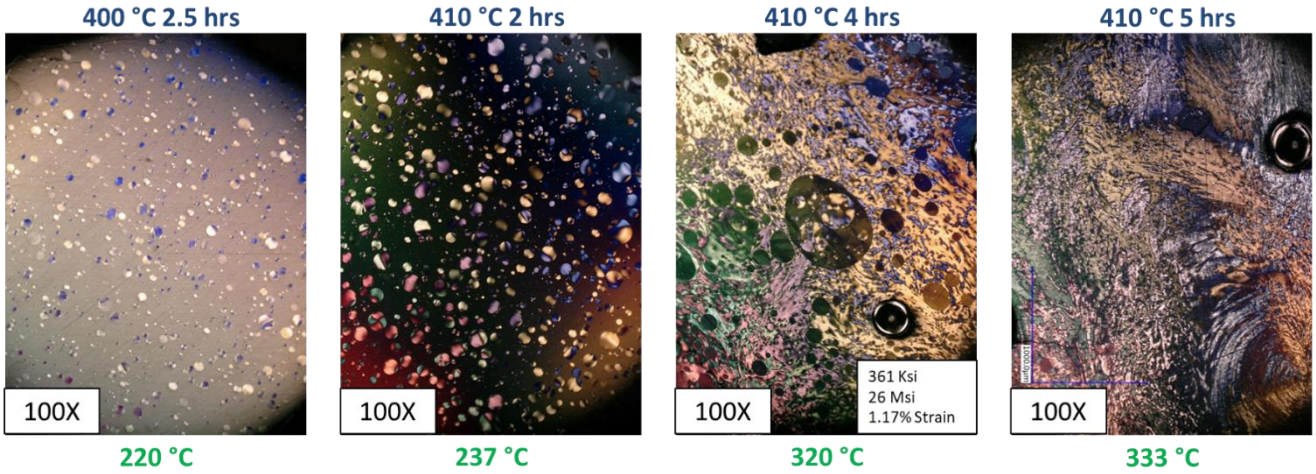

Figure 9: Cross-polarized light optical microscopy of CTP6M at various stages of mesophase conversion. Conditions are given above each image and the softening point is given below each image.

Scaled up batches, in a 1 L reactor, of CTP6M were produced with a SP around 315-320 °C. Scaled up batches for CTP6M SP 320 for single filament test had a strength of 333.6 Ksi, a

modulus of 34 Msi and a strain of 0.95%. Combined batches of CTP6 SP315 and 317 produced 21 filament tows with a strength of 260 Ksi, 24 Msi and a strain of 1.0%. In some cases, some of the CF properties we slightly shy of DOE targets. However, slight changes to the spinning in CF diameter, stabilization procedure, and carbonization procedure changed the properties of the CF. For instance, decreasing the CF diameter will increase the strength and make stabilization more efficient (Chung, 1994), and increases in carbonization temperature will typically lower the strength and strain but increase the modulus (Manocha, 2007). Other types of trends have been documented. Large scale up would be further useful for understanding all the parameters of mesophase quality and spinning and processing.

A sample of petroleum pitch mesophase (PPM) was produced by ACP (ACP-M1) from their proprietary technology from their ACP-10 isotropic pitch. The ACP-10 PP is produced from FCC oil and is similar to previously commercially available M-50 pitch. ACP-M1 was hot filtered to remove any residual inorganic contaminants. The sample was 95+% mesophase with a SP of 329.7 °C. Figure 10 shows cross light optical microscopy for ACP-M1. Filtered ACP-M1 produced CF that met DOE specifications with a strength of 347.9 Ksi, a modulus of 25.2 Msi and a strain of 1.18%. Further heat treatment of the sample to graphitization temperatures decreased the strength (243.3 Ksi) and strain (0.57%) but increased the modulus (36.6 Msi).

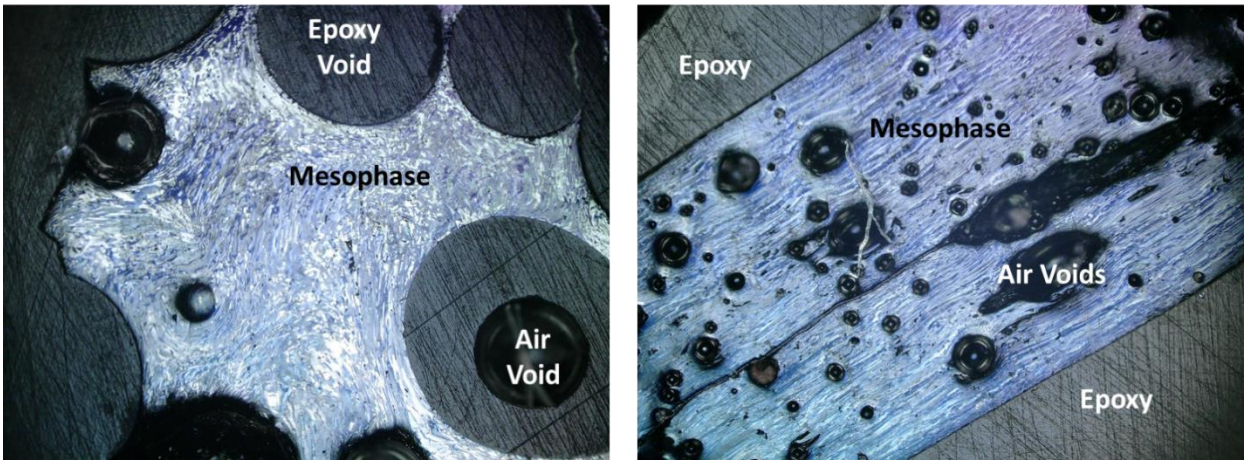

Figure 10: Cross-polarized light optical microscopy of as received ACP-M1 at 500X magnification (left) and the same material after it had melted and flowed after a softening point test at 100X magnification (right).

Additional samples of ACP-M1 were not able to be obtained and Koppers joined this effort in January of 2020 to provide additional samples of PPM for testing during the end of BP2. Koppers provided a PPM SP298 (KOP MP 1) and single filament CF that were 21 µm gave a strength of 263 Ksi, a modulus of 56 Msi and a strain of 0.57%. Despite several attempts it was not possible to get a strain above 1% with this material. The underlying reason for this low strain is detailed later in the Phase 2 Topical Report section. Additional Koppers samples KP-MP-19 and KP-MP-20 were received and found suitable to produce CF.

CTPM experimental conditions and yields are given in Appendix A.

Bio-ACN and Bio-PAN

Bio-ACN was produced from sugars using a proprietary process developed by SRI. It was determined that producing bio-ACN—that contained ≥ 99.26% bio-ACN, ≤0.38% acetonitrile and ≤0.36% water—was sufficient in quality to produce bio-ACN that polymerized sufficiently to produce a concentrate capable of being spun and processed into CF that meet DOE targets. Bio-PAN was produced from bio-ACN by ORNL using standard procedures as summarized in Figure 11. The polymerization reaction was carefully controlled so that the bio-ACN methyl acrylate copolymer had a molecular weight above about 136 KDa. CF that met DOE targets was successfully solution spun from the bio-PAN as 1512 filament tows with a diameter of 7.7 µm and a strength of 328.9 ± 0.53 Ksi, a modulus of 30.0 ± 1.0 Msi and a strain of 1.11 ± 0.15%.

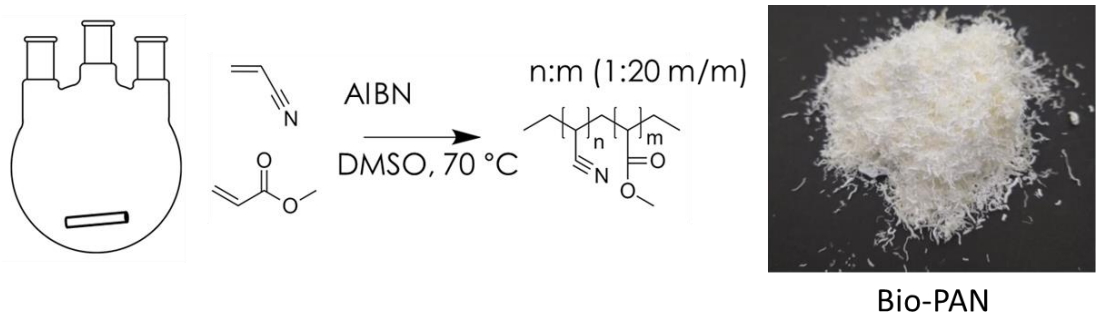

Figure 11: Schematic representation of the bio-PAN polymerization process and a photograph of the produced bio-PAN.

Feedstock and Precursor Characterization Data

Pitch

Sources of the isotropic pitch feedstocks and their CI (carbon content/carbon residue) and SP are provided in Table 2. Low-temperature and high-temperature CTP (LTCTP and HTCTP, respectively) samples were obtained from China, and one typical high-temperature North American CTP was obtained from Koppers. M-50 pitch was provided by ACP and the gilsonite samples were provided by American Gilsonite. RAS and HCB were provided by WRI.

Table 2: Source of the various isotropic feedstocks evaluated during BP1 and BP2.

Sample Name	Sample Description	Source	Origin	Coking Index	Softening Point, °C
W-CTP 3	Low Temperature	Handan Jinghao Chemical Co., Ltd	China	28.04	126.2
W-CTP 4	High Temperature	Handan Jinghao Chemical Co., Ltd	China	36.00	108.4
W-CTP 5	High Temperature	Handan Jinghao Chemical Co., Ltd	China	37.71	99.4
W-CTP 6	High Temperature	Koppers (US)	China	37.82	109.5
W-CTP 7	High Temperature	Koppers (China)	North America	37.91	114.2
SEL 347	Whole	American Gilsonite	US, Utah	21.07	178.7
ER 125	C7-Soluble	American Gilsonite	US, Utah	21.54	141.9
IR 200	C7-Insoluble	American Gilsonite	US, Utah	34.74	287.8
HCB	Hydrocraker Bottoms	Major Oil Company (WRI)	Canada	15.18	too soft
M-50	Slurry Oil Pitch	ACP	US	35.39	121.6
RAS	Air Blown Asphalt	North America (WRI)	US	-	-

Insolubles in pitch play a critical role in the quality of pitch-based CF. Organic-based insolubles, that do not melt to become a part of the molecularly aligned CF structure, introduce heterogeneities and boundaries where stress can accumulate leading to breaks. Inorganic-based insolubles, typically present in FCC decant oil feeds, are typically present in low levels (<0.1 wt%); however, these can cause significant defects during chemical changes and gas evolution during carbonization and graphitization.

HTCTP typically contains a high amount (7-20 wt%) of primary QI which are produced during the coking process of swelling bituminous coal to produce metallurgical grade coke. CTP primary QI is ~1-3 microns and consists of about half coal/coke fines and the other half consisting of carbon black produced during the process. This material must be filtered from the isotropic pitch prior to mesophase conversion as it will accumulate at the surface of the mesophase spheres. This prevents coalescences of the spheres thus inhibiting formation of a homogenous continuous mesophase. During this study it was determined that NMP could be substituted for quinoline and that the amount of insolubles was less than about 3% between the two solvents using a method similar to ASTM D2318. NMP is desirable because it has a low odor, a lower viscosity to facilitate filtration, and a lower boiling point making it easier to remove by distillation. Other solvents such as acetone, THF, and pyridine were tested as alternative solvents; however they were unable to dissolve as much CTP. Table 3 shows the

amount of NMP-insolubles (NMPI), pyridine-insolubles and quinoline-insolubles in the various CTP samples.

Table 3: Weight percent of solvent-insoluble material collected on filters of different pore sizes. QI = quinoline-insolubles, PI = pyridine insolubles, NMPI = NMP-insolubles, 1.5 = 1.5 micron glass fiber filter, 0.7 = 0.7 micron glass fiber filter, 0.22 = 0.22 PTFE filter.

Trial #1						Trial #2					
Sample	**W-CTP 3**	**W-CTP 4**	**W-CTP 5**	**W-CTP 6**	**W-CTP 7**	**Sample**	**W-CTP 3**	**W-CTP 4**	**W-CTP 5**	**W-CTP 6**	**W-CTP 7**
$\%QI_{1.5}$	1.83	9.70	7.20	12.23	7.63	$\%QI_{1.5}$	1.83	9.86	7.24	12.25	7.72
$\%QI_{0.7}$	0.09	0.10	0.04	0.01	0.12	$\%QI_{0.7}$	0.04	0.05	0.04	0.10	0.08
$\%QI_{0.22}$	0.08	1.57	0.12	0.22	0.06	$\%QI_{0.22}$	0.19	0.00	0.09	0.24	0.14
Total %QI	**2.00**	**11.76**	**7.36**	**12.46**	**7.82**	**Total %QI**	**2.06**	**9.91**	**7.37**	**12.58**	**7.94**
Sample	**W-CTP 3**	**W-CTP 4**	**W-CTP 5**	**W-CTP 6**	**W-CTP 7**	**Sample**	**W-CTP 3**	**W-CTP 4**	**W-CTP 5**	**W-CTP 6**	**W-CTP 7**
$\%PI_{1.5}$	2.09	16.33	12.67	17.88	10.79	$\%PI_{1.5}$	1.82	10.90	10.61	16.53	14.03
$\%PI_{0.7}$	0.05	0.63	7.70	4.75	6.67	$\%PI_{0.7}$	0.02	6.49	8.08	6.78	3.18
$\%PI_{0.22}$	0.06	0.22	0.02	0.01	0.00	$\%PI_{0.22}$	0.14	0.04	0.00	0.03	0.14
Total %PI	**2.19**	**17.18**	**20.39**	**22.63**	**17.46**	**Total %PI**	**1.98**	**17.43**	**18.69**	**23.34**	**17.35**
Sample	**W-CTP 3**	**W-CTP 4**	**W-CTP 5**	**W-CTP 6**	**W-CTP 7**	**Sample**	**W-CTP 3**	**W-CTP 4**	**W-CTP 5**	**W-CTP 6**	**W-CTP 7**
$\%NMPI_{1.5}$	1.73	10.00	7.81	14.88	8.68	$\%NMPI_{1.5}$	0	0	0	13.40	8.02
$\%NMPI_{0.7}$	0.14	0.20	0.19	0.10	0.17	$\%NMPI_{0.7}$	0	0	0	0.09	0.10
$\%NMPI_{0.22}$	0.00	0.00	0.00	0.20	0.00	$\%NMPI_{0.22}$	0	0	0	0.00	0.00
Total %NMPI	**1.86**	**10.21**	**8.00**	**15.18**	**8.85**	**Total %NMPI**	**0**	**0**	**0**	**13.49**	**8.12**

Gilsonite is a naturally occurring asphaltite material mined in Utah. Its solubility is typically determined in carbon disulfide and is marketed as having less than 0.1 wt% of insolubles. Solubility tests in chlorobenzene showed that the ER125 and SEL347 were completely soluble however 20 wt% of the IR200 was insoluble.

Petroleum pitch form M-50 and the feed for the Koppers mesophase sample KP-MP-19 (SP297) had low levels of NMPI. The M-50 had 1.20 wt% NMPI and KP-MP-19 contained 2.31 wt% NMPI. Typically, the lower the insoluble values the better the quality of the CF that can be produced from the pitch.

Besides physical impurities, like coke primary QI, many pitch-based materials contain some inorganic compounds. These can me minerals, clays, and metals. For PP, the inorganic compounds usually come from catalyst fines present in the decant oil. In the case of CTP they are carried over from the coal during the coking process. The metals are typically in the form of inorganic particles, however there can be some organometallic and/or coordination complexes, which are commonly in the form of porphyrins or carboxylic salts. Similar to coke-like primary QI, inorganic particles can cause localized areas of defects at the particle boundaries within CF, however the defects become more dramatic upon carbonization and graphitization due to the release of gas due to smelting and reduction of the metal complexes which can generate large defects into the CF. Primary QI, organic and inorganic, was removed from CTP6-W by filtration after dissolving in NMP. When this filtration occurs, the metals content drops from 3404 ppm down to 99 ppm of metals. Upon mesophase conversion, there is an increase in the metals concentration because about half of the organic phase is removed during the reaction. However, the increase is larger than double the metals content of the filtered CTP6-NMP. This may be due

to some of the limits of quantification for some of the metals considering that the largest increase in metals is due to silicon, phosphorus, potassium, and calcium, all of which had some of the highest concentrations for the limits of quantification. Table 4 shows the metals analysis for select isotropic and mesophase PP and CTP.

Table 4: Metals analysis for PP, PPM, CTP-W and CTP-NMP and CTPM.

Element Analyzed			Koppers PP		ACP PP		CTP 6		
			KP-PP-19	KP-MP-19	M-50-PP*	ACP-M1	CTP6-W	CTP6-NMP	CTP6MP SP315.6
ATOMIC NUMBER	ELEMENT NAME	ELEMENT SYMBOL	Conc µg/g	Conc µg/g	Conc µg/g	Conc µg/g	Conc µg/g	Conc µg/g	Conc µg/g
11	Sodium	Na	< 10	< 10	< 10	< 10	< 10	< 10	18
12	Magnesium	Mg	4.1	6.7	47.8	12.8	15.3	4.2	21.4
13	Aluminum	Al	46	89	79	12	197	< 1	23
14	Silicon	Si	100	820	190	190	2630	< 10	130
15	Phosphorus	P	< 50	212	88	78	< 50	< 50	77
16	Sulfur	S	2700	1970	4700	4800	5150	5100	3460
19	Potassium	K	< 10	< 10	12	12	56	< 10	31
20	Calcium	Ca	10	13	< 10	14	59	< 10	49
22	Titanium	Ti	2	3	2	< 1	9	< 1	2
23	Vanadium	V	< 1	3	5	5	3	3	4
24	Chromium	Cr	1	6	< 1	10	2	< 1	2
25	Manganese	Mn	0.4	1.1	0.2	3.8	2.2	0.1	0.4
26	Iron	Fe	97.8	153	9.4	110	192	64.6	45.6
27	Cobalt	Co	< 0.1	< 0.1	< 0.1	< 0.1	0.7	0.4	0.7
28	Nickel	Ni	0.4	1.5	0.4	5.2	1.2	< 0.1	3.6
29	Copper	Cu	0.2	5.7	0.1	12.9	0.9	0.4	3.7
30	Zinc	Zn	1.2	2.1	< 0.1	5.3	107	1.8	2.7
31	Gallium	Ga	0.2	0.1	< 0.1	< 0.1	4.4	0.8	1.5
32	Germanium	Ge	< 0.1	< 0.1	< 0.1	< 0.1	2.4	1.4	1.1
33	Arsenic	As	< 1	< 1	< 1	< 1	2	< 1	2
34	Selenium	Se	< 1	< 1	< 1	2	4	1	1
38	Strontium	Sr	< 1	< 1	< 1	< 1	2	< 1	< 1
42	Molybdenum	Mo	< 1	< 1	< 1	2	< 1	< 1	< 1
48	Cadmium	Cd	< 1	< 1	< 1	< 1	2	< 1	< 1
50	Tin	Sn	< 1	< 1	< 1	< 1	4	19	3
51	Antimony	Sb	< 1	< 1	< 1	< 1	< 1	< 1	2
56	Barium	Ba	< 1	< 1	< 1	< 1	2	< 1	< 1
57	Lanthanum	La	2	5	6	< 1	1	< 1	< 1
58	Cerium	Ce	< 1	< 1	3	< 1	< 1	< 1	< 1
81	Thallium	Tl	< 1	< 1	< 1	< 1	4	< 1	< 1
82	Lead	Pb	1	2	< 1	< 1	96	2	3
83	Bismuth	Bi	< 1	< 1	< 1	< 1	5	< 1	< 1
		Total Metals	**266.3**	**1111.2**	**354.9**	**475**	**3404.1**	**98.7**	**427.7**

Pitch materials are typically characterized by their SP since this relates to the amount of volatiles loss and mesophase content during mesophase conversion. Isotropic pitch and mesophase pitch samples were characterized using a Mettler Toledo DP70 Dropping Point apparatus according to ASTM D3104. Table 5 shows the SP for the various samples.

Table 5: SP for various isotropic and mesophase samples using the Mettler Toledo method.

	Sample	Label	Cup 1	Cup 2	Mean	Diff.
Isotropic CTP	CTP 3A	CTP 3-SP138	138.2	138.2	138.2	0.0
	CTP 3B2 (distilled)	CTP 3-SP166	166.2	166.7	166.5	0.5
	CTP 4A	CTP 4-SP115	114.9	115.1	115.0	0.2
	CTP 5A	CTP 5-SP102	102.1	102.3	102.2	0.2

	CTP 6A	CTP 6-SP105	105.8	106.5	106.2	0.7
	CTP 6B	CTP 6-SP106	106.4	106.6	106.5	0.2
	CTP 6C	CTP 6-SP111	111.6	111.4	111.5	0.2
	CTP 6D (distilled)	CTP 6-SP125	125.7	125.7	125.7	0.0
	CTP 6E (distilled, deeper cut)	CTP 6-SP147	147.4	147.5	147.5	0.1
	CTP 7A	CTP 7-SP114	113.6	114.1	113.9	0.5
	CTP 7B (distilled)	CTP 7-SP129	128.8	128.6	128.7	0.2
	CTP 7C (distilled, deeper cut)	CTP 7-SP142	142.7	142.3	142.5	0.4
	CTP 7D (distilled, deeper cut)	CTP 7-SP145	145.1	145.4	145.3	0.3
Mesophase CTP	CTP 6A Mesophase reaction date: 9/24/2018	CTP 6-MP-9/24	-	-	280.3	-
	CTP 6D Mesophase reaction date: 10/8/2018	CTP 6-MP-10/8	-	-	348.7	-
	CTP 6D Mesophase reaction date: 10/11/2018	CTP 6-MP-10/11	-	-	292.9	-
	CTP 6D Mesophase reaction date: 11/1/2018	CTP 6-MP-11/1	-	-	219.6	-
	CTP 6D Mesophase reaction date: 11/2/2018	CTP 6-MP-11/2	-	-	236.9	-
	CTP 6C Mesophase reaction date: 11/6/2018	CTP 6-MP-11/6	-	-	318.9	-
	CTP 6C Mesophase reaction date: 11/8/2018	CTP 6-MP-11/8	-	-	320.8	-
	CTP 6D Mesophase reaction date: 11/10/2018	CTP 6-MP-11/10	-	-	294.5	-
	CTP 6D Mesophase reaction date: 11/12/2018	CTP 6-MP-11/12	-	-	320.2	-
	CTP 7B Mesophase reaction date: 11/15/2018	CTP 7-MP-11/15	-	-	340.2	-
	CTP 6E Mesophase reaction date: 11/19/2018	CTP 6-MP-11/19	-	-	304.8	-
	CTP 6E Mesophase reaction date: 11/20/2018	CTP 6-MP-11/20	-	-	333.5	-
	CTP 6E Mesophase reaction date: 11/28/2018	CTP 6-MP-11/28	-	-	331.9	-
	CTP 7 Mesophase reaction date: 3/27/2019	CTP 7-MP-3/27	-	-	331.4	-
	CTP 7 Mesophase reaction date: 4/5/2019	CTP 7-MP-4/5	-	-	339.4	-
	CTP 7 Mesophase reaction date: 4/17/2019	CTP 7-MP-4/17	-	-	330.2	-
	CTP 7 Mesophase reaction date: 5/8/2019	CTP 7-MP-5/8	-	-	340.2	-
	CTP 7 Mesophase reaction date: 6/11/2019	CTP 7-MP-6/11	-	-	328.0	-
	CTP 6 Mesophase reaction date: 6/28/2019	CTP 6-MP-6/28	-	-	320.9	-

	CTP 7 Mesophase reaction date: 7/9/2019	CTP 7-MP-7/9	-	-	318.5	-
	CTP 7 Mesophase reaction date: 7/18/2019	CTP 7-MP-7/18	-	-	317.5	-
	CTP 6 Mesophase reaction date: 8/12/2019	CTP 6-MP-8/12	-	-	305.6	-
	CTP 7 Mesophase reaction date: 8/20/2019	CTP 7-MP-8/20	-	-	340.0	-
	CTP 7 Mesophase reaction date: 8/28/2019	CTP 7-MP-8/28	-	-	335.8	-
	CTP 7 Mesophase reaction date: 9/4/2019	CTP 7-MP-9/4	-	-	313.8	-
	CTP 6 Mesophase reaction date: 9/20/2019	CTP 6-MP-9/20	-	-	320.4	-
	CTP 6 Mesophase reaction date: 11/25/2019	CTP 6-MP-11/25	-	-	308.9	-
	CTP 6 Mesophase reaction date: 12/5/2019	CTP 6-MP-12/5	-	-	313.8	-
	CTP 6 Mesophase reaction date: 12/11/2019	CTP 6-MP-12/11	-	-	316.1	-
	CTP 6 Mesophase reaction date: 12/19/2019	CTP 6-MP-12/19	-	-	314.0	-
	CTP 6 Mesophase reaction date: 1/8/2020	CTP 6-MP-1/8	-	-	300.1	-
	CTP 6 Mesophase reaction date: 1/14/2020	CTP 6-MP-1/14	-	-	302.2	-
	CTP 6 Mesophase reaction date: 1/21/2020	CTP 6-MP-1/21	-	-	305.2	-
	CTP 6 Mesophase reaction date: 1/29/2020	CTP 6-MP-1/29	-	-	310.4	-
	CTP 6 Mesophase reaction date: 2/5/2020	CTP 6-MP-2/5	-	-	315.6	-
	CTP 6 Mesophase reaction date: 2/12/2020	CTP 6-MP-2/12	-	-	314.7	-
	CTP 6 Mesophase reaction date: 3/3/2020	CTP 6-MP-3/3	-	-	317.6	-
	CTP 6 Mesophase reaction date: 3/24/2020	CTP 6-MP-3/24	-	-	317.1	-
	CTP 6 Mesophase reaction date: 4/16/2020	CTP 6-MP-4/16	-	-	314.5	-
Isotropic PP	Motor Carbon Elements Petroleum Pitch	MCE-PP	127.0	127.6	127.3	0.6
	M-50	M-50	121.5	121.7	121.6	0.2
	M-50 A (Filtered)	M-50 A	124.6	125.0	124.8	0.4
	ACP Pitch	ACP 10	94.2	94.2	94.2	0.0
	Koppers Petroleum Pitch 2019-1261	KP-PP-19	116.2	116.3	116.3	0.1
	Koppers Petroleum Pitch 2019-1261 (Filtered)	KP-PP-19A	122.3	122.5	122.4	0.2
	Koppers Petroleum Pitch 2020-0784	KP-PP-20	121.6	121.6	121.6	0.0
	Koppers Petroleum Pitch 2020-0784 (Filtered)	KP-PP-20A	122.6	122.6	122.6	0.0

Mesophase PP	ACP Mesophase (2019)	ACP-MP	329.9	329.5	329.7	0.4
	ACP Mesophase (2020)	ACP 20	313.6	312.7	313.2	0.9
	Koppers Mesophase	KOP MP 1	297.8	297.5	297.6	0.3
	Koppers Mesophase 2019-1741	KP-MP-19	297.0	297.7	297.4	0.7
	Koppers Mesophase 2020-0289	KP-MP-20-0289	294.4	288.2	291.3	6.2
	Koppers Mesophase 2020-0655	KP-MP-20	299.6	299.8	299.7	0.2
Isotropic Gilsonite	347 Grade	347 Grade	178.3	179.0	178.7	0.7
	ER 125	ER 125	141.5	142.3	141.9	0.8
	IR 200 Trial #1	IR 200	286.1	289.4	287.8	3.3

The SP test is run in duplicate and in several cases if the difference between the two cups is high (more than a few degrees) it can be an indication of a heterogeneous sample that will not produce continuous fibers during melt spinning. This is the case for KP-MP-20-0289, and in fact the sample phase separated so that the more liquid phase actually dropped from the cups during the test before the bulk of the sample melted. Analysis of the surface of the SP sample can also be used as an indicator of fiber spinning success. Samples that flowed and produced smooth continuous flow, initially like a tear drop followed by a continuous thread of uniform shape and shiny texture connected to the cup, generally spun fibers well. Figure 12 shows samples from the SP test for PPM that spun well (KP-MP-19) and KP-MP-20-0289 which did not.

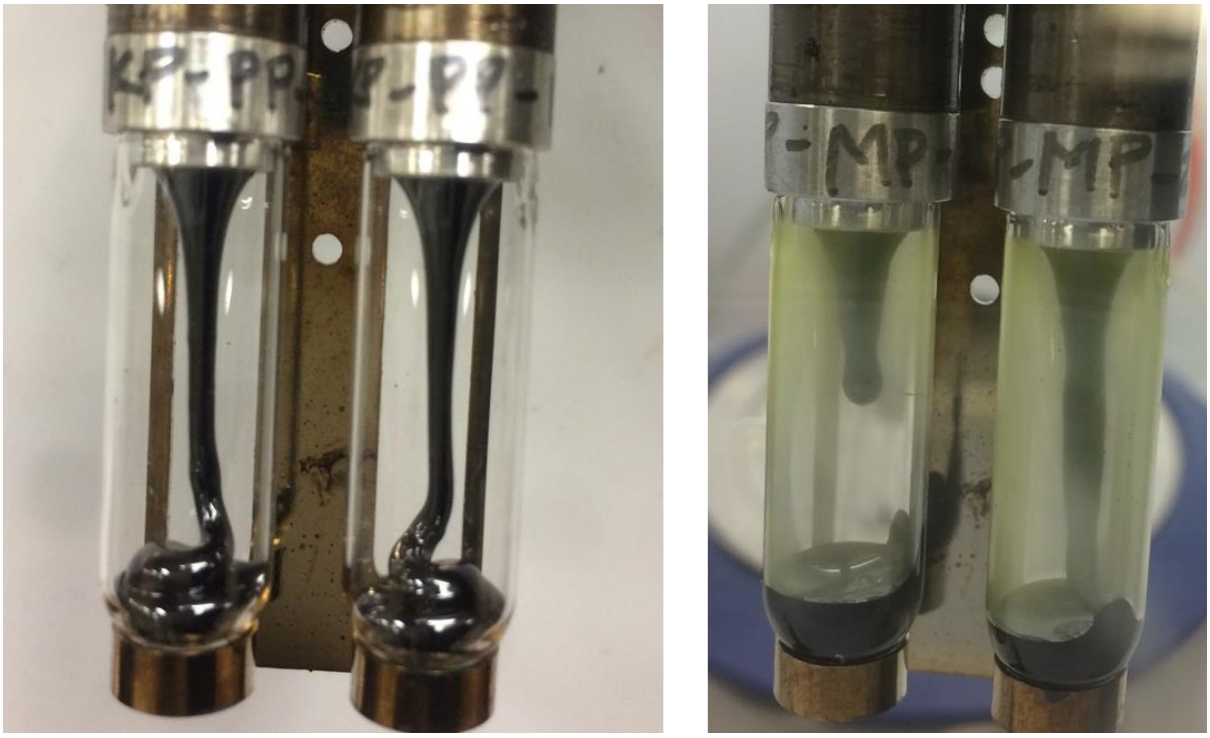

Figure 12: Photograph of SP test samples for KP-MP-19 (left) that spun continuous fibers well and KP-MP-20-0289 (right) which did not spin continuous fibers well.

Thermogravimetric (TGA) analysis under an inert atmosphere such as nitrogen is useful for characterizing hydrocarbon materials by quantifying the amount of volatile material that can evaporate from the sample up to about 395°C. Above this temperature, pyrolysis becomes significant, and loss of volatiles becomes dominated by the smaller fragments liberated by the cracking reactions and volatiles loss of heavier fragments; as well as some heavier molecules that are not cracked. As the temperature increases, volatiles from non-cracked material becomes less and the weight loss becomes increasingly dominated by pyrolysis products. Most pyrolysis events are completed < 600 °C and the resulting material left is the non-volatile carbon residue which is generally cross-linked coke. Significant weight loss above 600 °C usually corresponds to hydrogen loss and an increase in aromatization and aromatic cross-linking. At temperatures above 600 °C if the inert gas is switched to air, then combustion of the carbon residue occurs and any weight left after this is the remaining inorganic ash. The amount of volatiles below 395 °C are important, because if there is a significant amount of volatiles in this region gas will be liberated during the melt spinning process leading to discontinuous fibers and air bubbles in the fibers. It was observed that pitch materials with more than a few percent of volatiles did not spin well or produce high quality CF.

Figure 13 shows the derivative of the TGA weight loss curve (DTGA) comparing some of the various isotropic feedstocks. DTGA clearly distinguishes the heavy rapid pyrolysis (>395 °C) of gilsonite compared to some of the other feedstocks. It can also be seen that the LTCTP (CTP3)

has more pyrolysis carbon than the HTCTP samples. During mesophase production most of the volatile material below 400 °C is distilled from the sample.

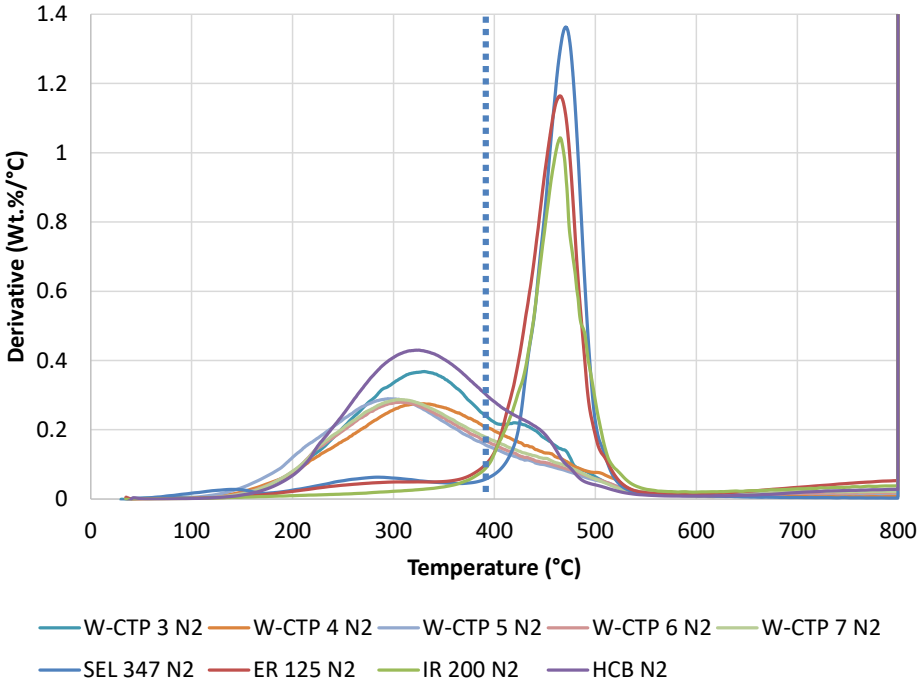

Figure 13: DTGA profile using a nitrogen atmosphere for HTCTP and LTCTP, gilsonite and HCB. The dotted line indicates where volatiles due to pyrolysis begin to dominate (>395 °C).

TGA was also performed under and oxidizing atmosphere to understand more about the reactivity of the pitch materials. Figure 14 shows a comparison of some of the feedstocks DTGA profile using air. From the DTGA there are three main regions: volatile loss (<395 °C), pyrolysis (395-500 °C), and combustion (> 500 °C). DTGA under air makes it more clear the separation between these various regions. DTGA in air also shows that the reactivity with oxygen is greater for the gilsonite, LTCTP and HCB compared to HTCTP. Compared to the other materials, HTCTP air combustion initiates, peaks and extends out at much higher temperatures. This is consistent with the fact that feedstocks containing more methyl and alkyl substituents are more reactive towards oxidation (Lavin, 1992).

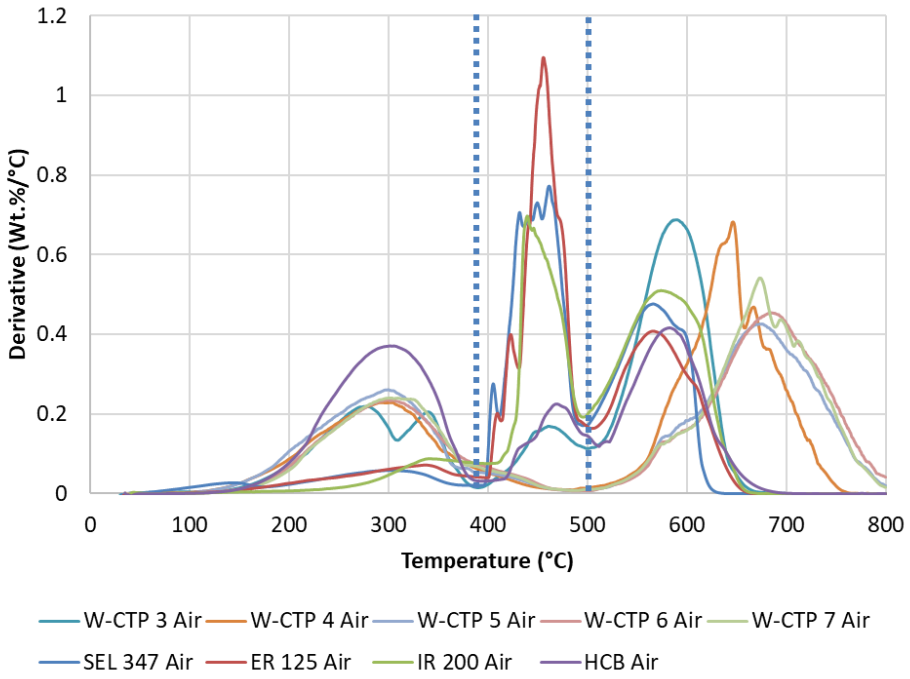

Figure 14: DTGA profile using an air atmosphere for HTCTP and LTCTP, gilsonite and HCB. The dotted line indicates where volatiles due to pyrolysis begin to dominate.

With respect to mesophase formation, DTGA using nitrogen or air shows that there is a decrease in volatiles and pyrolysis carbon. This is consistent with the increase in the carbon residue (coking index) which will be discussed later. When TGA is performed under air or nitrogen on mesophase samples the volatiles and pyrolysis carbon decreases and there is a relative increase in the combustion carbon relative to isotropic pitch. For both the CTP6M and ACP-M1—that produced CF that met DOE targets—they both show very minimal volatiles relative to the corresponding isotropic pitch. Figure 15 shows DTGA profiles for CTP6 and CTPM at various levels of mesophase conversion under nitrogen and air, and DTGA of PP (M-50) and PPM. Table 6 shows the TGA data for isotropic feedstock materials performed under nitrogen and air for various temperature regions, and Table 7 shows data for filtered feedstock samples, CTPM, PP and PPM for the same regions. Table 8 shows combined TGA data under nitrogen separating volatiles from pyrolysis and Table 9 shows data under air for the same regions.

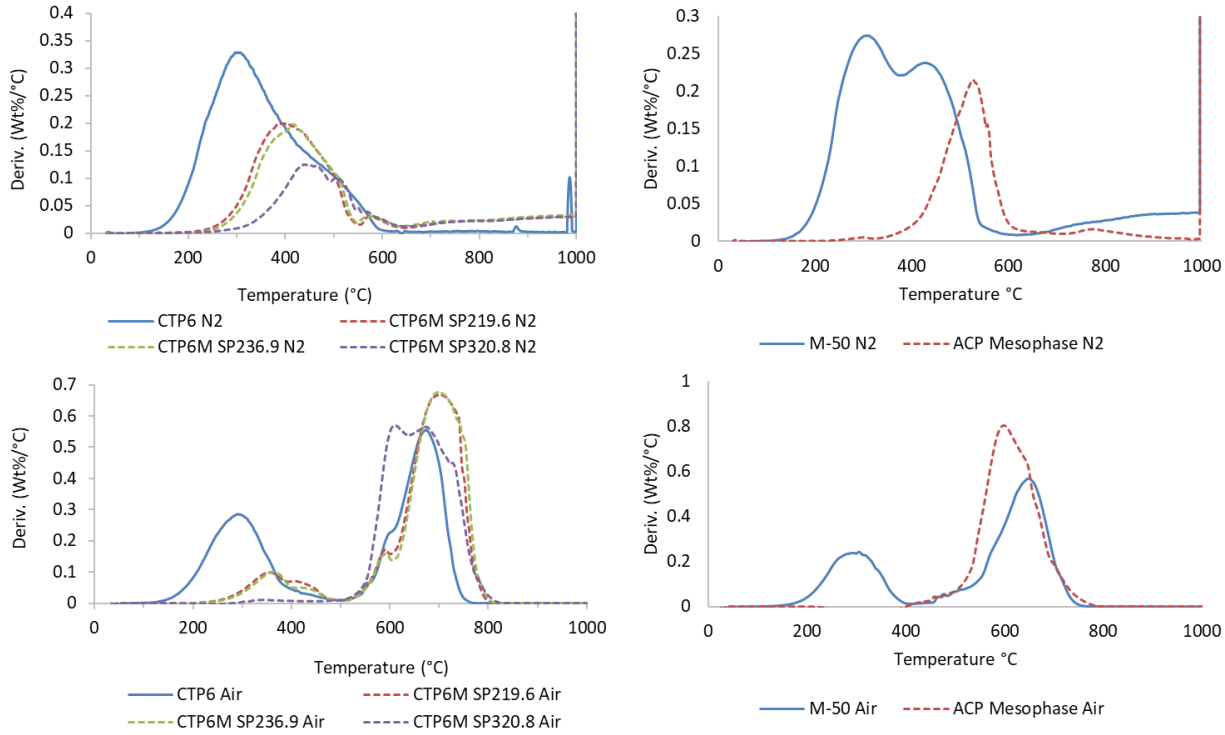

Figure 15: DTGA data for CTP6 and CTP6M (left) at different levels of mesophase conversion and M-50 PP and ACP-M1 (right) under nitrogen (top) and under air (bottom).

Table 6: TGA data showing the weight percent loss of whole isotropic feedstocks for various temperature ranges for experiments performed under a nitrogen atmosphere and under an air atmosphere.

Atoms.	Sample Name	Volatiles Range 30 to 395°C (%)	Pyrolysis 1 395 to 500°C (%)	Pyrolysis 2 500 to 1000°C (%)	Combustion for 15 minutes (%)	Pyrolysis 2 + Combustion	Residue (%)	Closure (Weight %)
N_2	W-CTP 3	55.28	14.68	5.75	23.78	29.53	0.57	100.06
	W-CTP 4	43.65	8.40	29.44	16.74	46.18	1.87	100.10
	W-CTP 5	46.98	6.46	27.31	17.19	44.50	1.98	99.92
	W-CTP 6	44.43	9.43	10.15	34.73	44.88	1.19	99.93
	W-CTP 7	44.79	6.92	30.75	17.54	48.29	0.32	100.31
	SEL 347	13.18	51.91	33.43	0.00	33.43	1.51	100.03
	ER 125	11.52	53.18	34.46	0.00	34.46	0.84	100.00
	IR 200	6.73	47.14	45.71	0.00	45.71	0.38	99.95
	HCB	65.70	22.43	3.44	8.73	12.17	-0.22	100.08
	Sample Name	Wt. Loss 30 to 395°C (%)	Combustion 395 to 500°C (%)	-		Combustion 500 to 1000°C (%)	Residue (%)	Closure (Weight %)
Air	W-CTP 3	26.09	11.90			61.25	0.72	99.96
	W-CTP 4	32.80	3.07			62.53	1.53	99.94
	W-CTP 5	37.20	1.73			59.63	1.35	99.91
	W-CTP 6	33.10	3.42			62.95	0.56	100.03
	W-CTP 7	33.11	2.10			64.25	0.45	99.91
	SEL 347	11.86	43.43			43.60	1.14	100.03
	ER 125	10.59	48.14			40.40	0.83	99.96
	IR 200	10.95	32.44			55.71	0.86	99.96
	HCB	48.94	13.11			38.15	-0.16	100.04

Table 7: TGA data showing the weight percent loss of filtered isotropic feedstocks, PP, PPM, and CTPM for various temperature ranges for experiments performed under a nitrogen atmosphere and under an air atmosphere.

Atoms.	Sample Name	Volatiles Range 30 to 395°C (%)	Pyrolysis 1 395 to 500°C (%)	Pyrolysis 2 500 to 1000°C (%)	Combustion for 15 minutes (%)	Pyrolysis 2 + Combustion	Residue (%)	Closure (Weight %)
N_2	CTP3-NMP	51.23	18.54	5.60	24.54	30.14	0.10	100.01
	CTP4-NMP	44.30	12.65	14.49	28.48	42.97	0.12	100.04
	CTP5-NMP	46.90	9.33	21.49	22.23	43.72	0.07	100.02
	CTP6A-NMP	45.76	9.63	26.17	18.27	44.44	0.19	100.02
	CTP6B-NMP	47.40	8.95	25.74	17.90	43.64	0.02	100.02
	CTP6C-NMP	50.91	15.26	7.31	26.28	33.59	0.18	99.94
	CTP6D-NMP	44.66	11.66	13.80	29.19	42.99	0.72	100.03
	CTP6E-NMP	38.73	13.12	14.85	32.85	47.70	0.49	100.04
	CTP7-NMP	47.17	8.73	26.07	17.84	43.91	0.19	100.00
	CTP7DC-NMP	39.80	10.78	29.54	19.74	49.28	0.14	100.00
	CTP6 SP 219.6	14.99	17.31	12.42	55.18	67.60	0.13	100.03
	CTP6 SP 236.9	12.18	17.25	14.08	56.35	70.43	0.13	99.99
	CTP6 SP 320.0	3.53	11.50	14.44	70.32	84.76	0.21	100.00
	CTP6 SP 294.5	13.06	15.70	12.91	57.88	70.79	0.45	100.00
	CTP6 SP 320.2	4.09	11.88	10.82	72.60	83.42	0.61	100.00
	CTP7 SP 340.2	1.35	7.03	14.37	77.38	91.75	-0.26	100.13
	CTP6 SP 304.8	7.29	15.96	12.84	64.05	76.89	-0.11	100.03
	CTP6 SP 333.5	1.61	6.88	14.59	76.96	91.55	-0.04	100.00
	CTP6 SP 331.9	1.97	7.35	16.16	74.36	90.52	0.19	100.02
	M-50	41.90	22.52	14.61	20.75	35.36	0.20	99.98
	ACP-M1	0.92	8.48	17.93	72.39	90.32	0.20	99.92
	Sample Name	Wt. Loss 30 to 395°C (%)	Combustion 395 to 500°C (%)	-		Combustion 500 to 1000°C (%)	Residue (%)	Closure (Weight %)
Air	CTP3-NMP	24.98	13.36			61.36	0.30	100.00
	CTP4-NMP	35.38	1.91			62.82	-0.21	99.90
	CTP5-NMP	39.37	2.03			58.61	-0.03	99.98
	CTP6A-NMP	38.26	2.82			58.94	-0.04	99.98
	CTP6B-NMP	38.22	2.46			59.34	0.05	100.06
	CTP6C-NMP	38.34	2.57			58.95	0.15	100.00
	CTP6D-NMP	31.23	2.55			60.45	5.83	100.06
	CTP6E-NMP	26.66	3.55			69.56	0.21	99.99
	CTP7-NMP	36.01	2.98			60.96	0.05	100.00
	CTP7DC-NMP	31.28	2.68			65.91	0.16	100.03
	CTP6 SP 219.6	8.60	4.41			86.79	0.22	100.01
	CTP6 SP 236.9	7.99	3.49			88.34	0.12	99.94
	CTP6 SP 320.0	0.63	0.76			98.22	0.33	99.93
	CTP6 SP 294.5	7.11	3.14			88.99	0.73	99.97
	CTP6 SP 320.2	0.09	0.54			98.28	1.04	99.95
	CTP7 SP 340.2	0.18	0.39			99.58	0.14	100.29
	CTP6 SP 304.8	0.99	1.64			97.34	0.00	99.97
	CTP6 SP 333.5	0.46	0.30			100.10	0.08	100.93
	CTP6 SP 331.9	0.42	0.34			99.93	0.29	100.98
	M-50	30.23	3.01			66.71	0.09	100.04
	ACP-M1	2.55	3.19			99.09	0.30	100.03

Table 8: TGA data showing the weight percent loss under nitrogen for various temperature ranges.

N2 Atomos.	Name	Nitrogen Volatiles Range Room Temp to 395°C (%)	Nitrogen Pyrolysis Range 395°C to 1000°C (%)	Air Combustion 15 minutes (%)	Air Residue (%)	Closure (Weight %)
Isotropic CTP	CTP3-NMP	51.23	24.14	24.54	0.10	100.01
	CTP4-NMP	44.30	27.14	28.48	0.12	100.04
	CTP5-NMP	46.90	30.82	22.23	0.07	100.02
	CTP6A-NMP	45.76	35.80	18.27	0.19	100.02
	CTP6B-NMP	47.40	34.69	17.90	0.02	100.02
	CTP6C-NMP	50.91	22.57	26.28	0.18	99.94
	CTP6D-NMP	44.66	25.46	29.19	0.72	100.03
	CTP6E-NMP	38.73	27.97	32.85	0.49	100.04
	CTP7-NMP	47.17	34.80	17.84	0.19	100.00
	CTP7DC-NMP	39.80	40.32	19.74	0.14	100.00
CTPM	CTP6M SP 219.6	14.99	29.73	55.18	0.13	100.03
	CTP6M SP 236.9	12.18	31.33	56.35	0.13	99.99
	CTP6M SP 320.0	3.53	25.94	70.32	0.21	100.00
	CTP6M SP 294.5	13.06	28.61	57.88	0.45	100.00
	CTP6M SP 320.2	4.09	22.70	72.60	0.61	100.00
	CTP7M SP 340.2	1.35	21.40	77.38	-0.26	100.13
	CTP6M SP 304.8	7.29	28.80	64.05	-0.11	100.03
	CTP6M SP 333.5	1.61	21.47	76.96	-0.04	100.00
	CTP6M SP 331.9	1.97	23.51	74.36	0.19	100.02
	CTP6M SP 305.2	4.61	27.26	68.05	0.19	100.11
	CTP6M SP 310.4	4.46	25.32	69.73	0.47	99.97
	CTP6M SP 316.1	3.60	28.25	67.19	0.89	99.93
	CTP6M SP 314.0	3.32	27.96	68.09	0.67	100.04
	CTP6M SP 315.6	3.33	27.25	68.42	1.00	100.00
	CTP6M SP 314.7	4.27	25.42	68.65	1.59	99.93
	CTP6M SP 317.6	3.90	24.43	70.13	1.41	99.87
	CTP6M SP 317.1	3.76	25.32	72.37	-1.36	100.09
	CTP6M SP 314.5	4.48	26.35	69.45	-0.34	99.94
PP	M-50	45.74	29.97	23.44	0.8722	100.02
	ACP 10	51.27	20.47	26.62	1.662	100.02
	KP-PP-19	47.64	23.87	26.92	1.831	100.26
	KP-PP-20	47.50	24.96	26.99	0.6078	100.06
PPM	ACP-MP	1.70	24.86	73.64	-0.20	100.00
	KOP MP 1	7.67	27.81	63.47	1.06	100.01
	KP-MP-19	6.76	37.22	56.18	-0.20	99.96
	KP-MP-20-0289	18.01	20.24	61.06	0.68	99.99
	KP-MP-20	19.07	25.29	55.04	0.65	100.05

Table 9: TGA data showing the weight percent loss under air for various temperature ranges.

Air Atomos.	Name	Air Volatiles Range Room Temp to 395°C (%)	Air Combustion 395°C to 1000°C (%)	Air Residue (%)	Closure (Weight %)
Isotropic CTP	CTP3-NMP	24.98	74.72	0.30	100.00
	CTP4-NMP	35.38	64.73	-0.21	99.90
	CTP5-NMP	39.37	60.64	-0.03	99.98
	CTP6A-NMP	38.26	61.76	-0.04	99.98
	CTP6B-NMP	38.22	61.80	0.05	100.06
	CTP6C-NMP	38.34	61.52	0.15	100.00
	CTP6D-NMP	31.23	63.00	5.83	100.06
	CTP6E-NMP	26.66	73.11	0.21	99.99
	CTP7-NMP	36.01	63.94	0.05	100.00
	CTP7DC-NMP	31.28	68.59	0.16	100.03
CTPM	CTP6M SP 219.6	8.60	91.20	0.22	100.01
	CTP6M SP 236.9	7.99	91.83	0.12	99.94
	CTP6M SP 320.0	0.63	98.98	0.33	99.93
	CTP6M SP 294.5	7.11	92.13	0.73	99.97
	CTP6M SP 320.2	0.09	98.82	1.04	99.95
	CTP7M SP 340.2	0.18	99.97	0.14	100.29
	CTP6M SP 304.8	0.99	98.98	0.00	99.97
	CTP6M SP 333.5	0.46	100.40	0.08	100.93
	CTP6M SP 331.9	0.42	100.27	0.29	100.98
	CTP6M SP 305.2	0.75	98.70	0.54	99.99
	CTP6M SP 310.4	0.43	100.59	-1.04	99.98
	CTP6M SP 316.1	0.21	99.63	0.16	100.01
	CTP6M SP 314.0	0.16	99.81	0.05	100.02
	CTP6M SP 315.6	0.36	99.30	0.37	100.02
	CTP6M SP 314.7	0.22	99.03	0.75	100.00
	CTP6M SP 317.6	0.36	99.18	0.45	99.99
	CTP6M SP 317.1	0.10	100.35	-0.48	99.96
	CTP6M SP 314.5	0.35	100.40	-0.76	99.99
PP	M-50	29.95	69.36	1.86	101.17
	ACP 10	37.04	62.03	1.75	100.81
	KP-PP-19	31.03	68.32	1.64	100.99
	KP-PP-20	30.44	69.02	1.23	100.69
PPM	ACP-MP	2.095	101.05	1.93	105.07
	ACP 20	1.122	100.96	0.73	102.81
	KOP MP 1	0.131	99.13	1.72	100.98
	KP-MP-19	0.517	99.11	0.87	100.50
	KP-MP-20-0289	8.924	90.47	1.54	100.94
	KP-MP-20	11.67	87.88	0.41	99.96

For mesophase samples subjected to TGA under air, oxygen uptake could be observed, especially if the samples were relatively void of volatiles below ~360 °C. Once volatiles in the pitch materials begin to increase below ~400 °C, and especially ~360 °C, the weight loss from

the volatiles begin to mask the oxygen uptake. Figure 16 shows the oxygen uptake by TGA under air for PP mesophase ACP-M1, and Figure 17 shows a comparison of the oxygen uptake for CTP mesophase samples produced with varying mesophase and volatiles content. The plots in Figure 17 show that oxygen uptake doesn't appear until around 220-230 °C for both PP and CTP based mesophase materials.

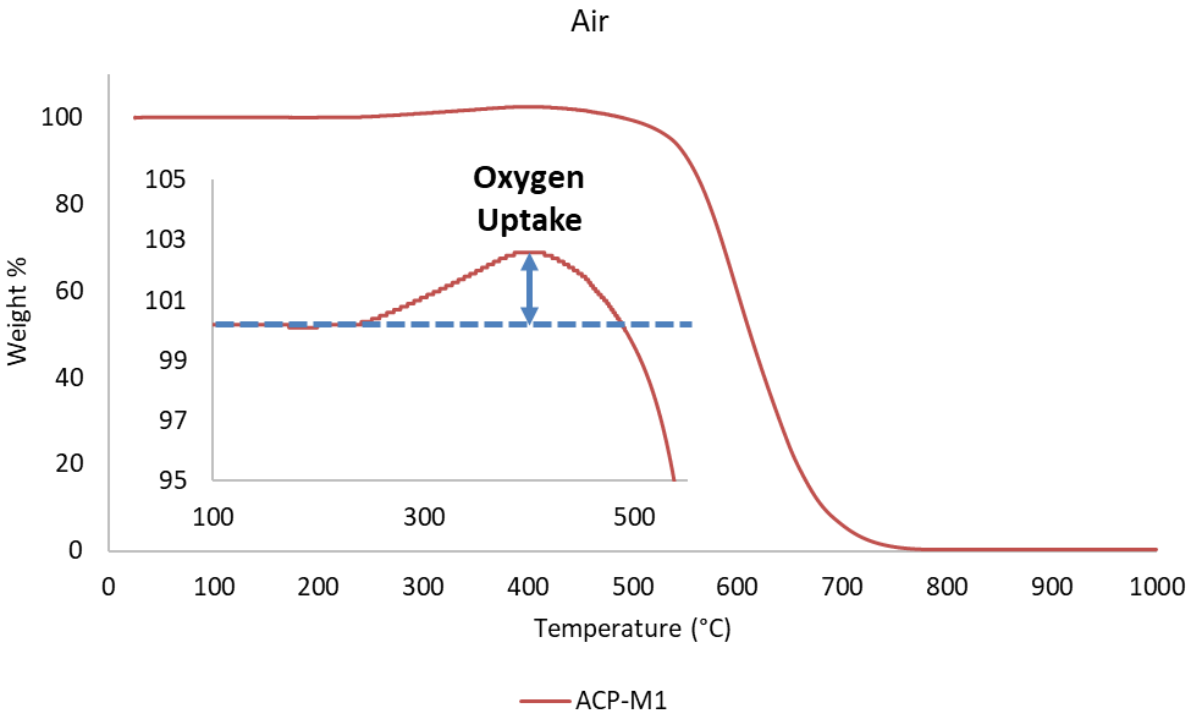

Figure 16: Weight loss profile for PP mesophase sample ACP-M1. The inserted plot shows an expanded region of interest where oxygen uptake can be observed.

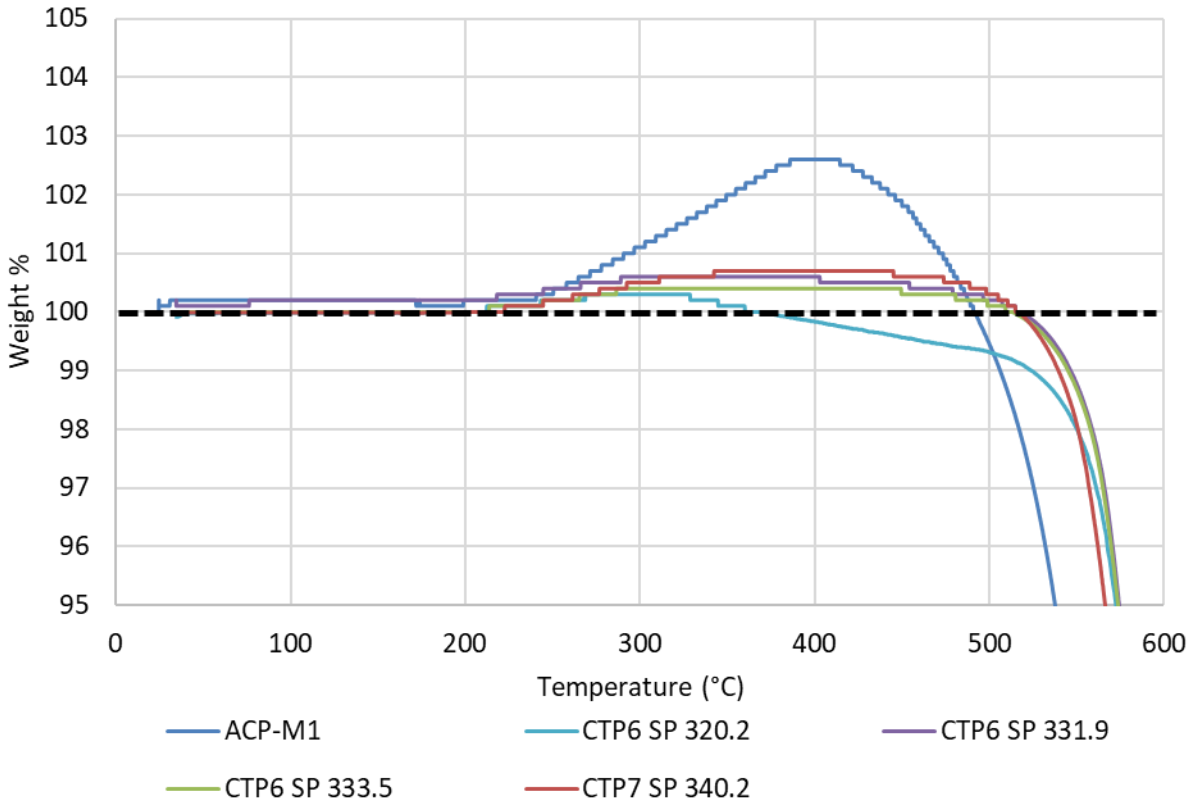

Figure 17: Weight loss profile for ACP-M1 and the CTPM samples.

From the data in Figure 17, it appears that the PPM takes up a significantly larger amount of oxygen than the CTPM samples. However, to make an appropriate comparison between the oxygen uptake, it is important to compare between two samples that have the same amount of weight loss under nitrogen in the region <400 °C. Figure 18 shows that the mesophase sample CTP7M SP340.2 does have about the same amount of weight loss compared to the ACP-M1 sample. Since these two samples have about the same amount of weight loss <400 °C then it can be reasonably assumed that PPM does take up significantly more oxygen than the CTPM.

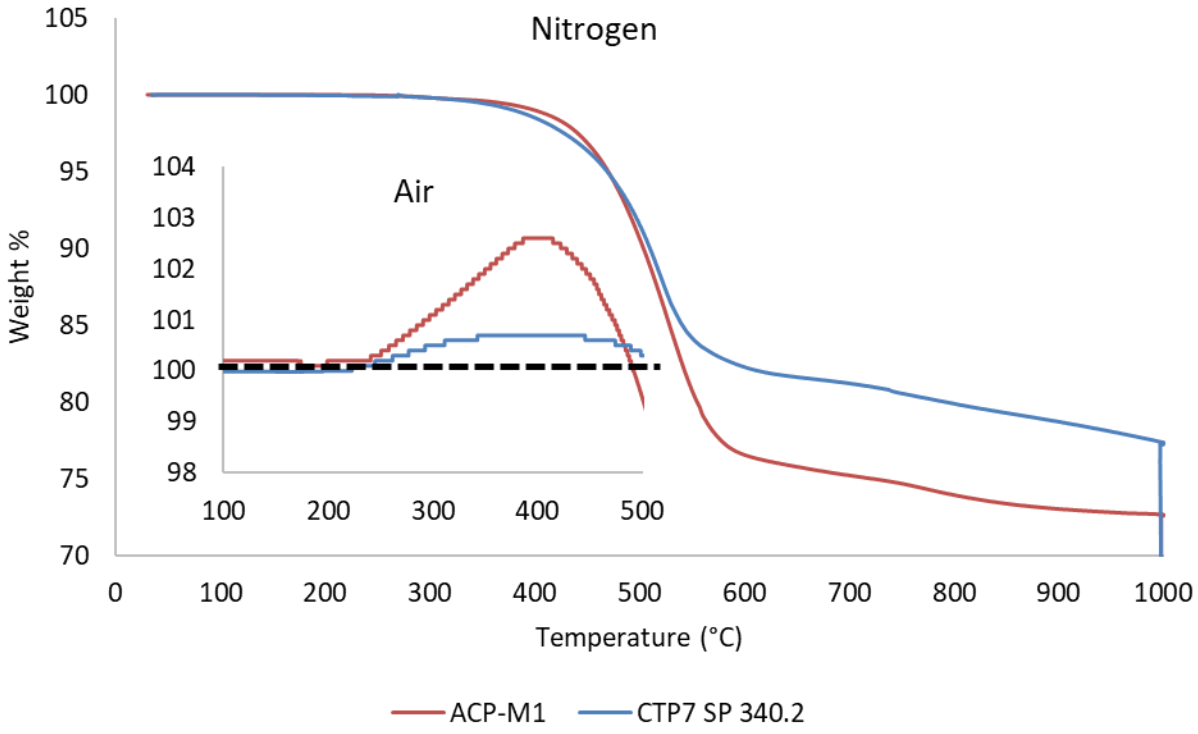

Figure 18: TGA weight loss curve for PPM and CTPM under nitrogen with the inset plot showing the TGA under a select region under air demonstrating the oxygen uptake (above the black dotted line).

TGA was also used to approximate the 500 °C coking index (CI), which is a measurement often used to assess the amount of carbon residue in CTP materials that does not pyrolyze. This amount is the non-pyrolyzable carbon residue is called many different names, but for this work we referred to it as the CI. Typical carbon residue experiments, such as are performed for the micro carbon residue test (MCRT), take the sample up to 500 °C under an inert atmosphere which is then held isothermal for some time. For the TGA, CI determination was performed with samples held at 500 °C for 15 minutes (D4530-15, 2020). The CI by TGA for the various feedstock and mesophase samples are given in Table 10. During mesophase conversion, as the lighter molecules are distilled off, and larger molecules are formed during the mesophase reaction, the fixed carbon content increases. This is shown in the correlation between the softening point and the CI in Figure 19.

Table 10: CI values determined by TGA.

	Sample Name	Coking Index
Whole CTP	W-CTP 3	28.0
	W-CTP 4	36.0
	W-CTP 5	37.7
	W-CTP 6	37.8
	W-CTP 7	37.9
Isotropic CTP	CTP3-NMP	29.2
	CTP4-NMP	34.9
	CTP5-NMP	36.2
	CTP6A-NMP	34.4
	CTP6B-NMP	34.7
	CTP6C-NMP	40.7
	CTP6D-NMP	42.5
	CTP6E-NMP	49.0
	CTP7-NMP	37.7
	CTP7DC-NMP	50.3
CTPM	CTP6M SP 219.6	69.3
	CTP6M SP 236.9	70.8
	CTP6M SP 320.0	84.2
	CTP6M SP 294.5	74.5
	CTP6M SP 320.2	84.5
	CTP7M SP 340.2	88.2
	CTP6M SP 304.8	81.3
	CTP6M SP 333.5	90.5
	CTP6M SP 331.9	89.8
	CTP6M SP 305.2	75.1
	CTP6M SP 310.4	75.4
	CTP6M SP 316.1	80.7
	CTP6M SP 314.0	77.9
	CTP6M SP 315.6	80.1
	CTP6M SP 314.7	78.3
	CTP6M SP 317.6	79.0
	CTP6M SP 317.1	79.9
	CTP6M SP 314.5	79.5
PP	M-50	35.4
	ACP 10	27.3
	KP-PP-19	31.5
	KP-PP-20	31.2
PPM	ACP-MP	93.6
	ACP 20	-
	KOP MP 1	-
	KP-MP-19	73.1
	KP-MP-20-0289	-
	KP-MP-20	65.6
Gilsonite + Others	SEL 347	21.1
	ER 125	21.5
	IR 200	34.7
	HCB	15.2

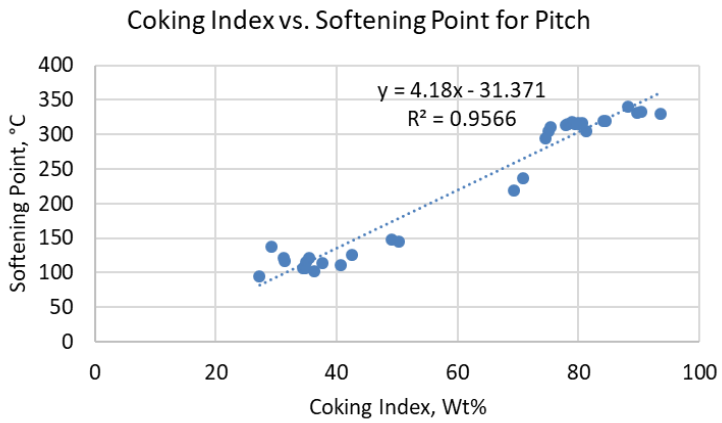

Figure 19: Correlation between the TGA CI and softening point for isotropic and mesophase CTP and PP materials.

The standard method to test the CI is using the MCRT method. This method was also run on the samples to validate the TGA data. Table 11 shows the MCRT data for select samples and Figure 20 shows the correlation between the SP and the MCRT data. There is a higher correlation with the SP for the MCRT data than with TGA, with the exception of the LTCTP sample.

Table 11: MCRT data for isotropic and mesophase CTP and PP samples.

	Sample ID	MCRT
Whole CTP	W-CTP 3	43.8
	W-CTP 4	56.1
	W-CTP 5	52.7
	W-CTP 6	56.5
	W-CTP 7	-
Isotropic CTP	CTP3-NMP	44.4
	CTP4-NMP	52.4
	CTP5-NMP	49.6
	CTP6A-NMP	51.8
	CTP6B-NMP	-
	CTP6C-NMP	-
	CTP6D-NMP	-
	CTP6E-NMP	-
	CTP7-NMP	-
	CTP7DC-NMP	-
CTPM	CTP6M SP 219.6	81.2
	CTP6M SP 236.9	83.5
	CTP6M SP 320.0	91.2
	CTP6M SP 294.5	83.2
	CTP6M SP 320.2	92.8
	CTP7M SP 340.2	94.5
	CTP6M SP 304.8	90.0
	CTP6M SP 333.5	94.2
	CTP6M SP 331.9	94.1
	CTP6M SP 305.2	91.4
	CTP6M SP 310.4	91.7
	CTP6M SP 316.1	92.7
	CTP6M SP 314.0	93.0
	CTP6M SP 315.6	92.3
	CTP6M SP 314.7	92.1
	CTP6M SP 317.6	92.6
	CTP6M SP 317.1	93.3
	CTP6M SP 314.5	92.8
PP	M-50	50.8
	ACP 10	46.6
	KP-PP-19	53.1
	KP-PP-20	53.3
PPM	ACP-MP	94.0
	ACP 20	91.7
	KOP MP 1	-
	KP-MP-19	-
	KP-MP-20-0289	-
	KP-MP-20	88.3
Gilsonite + Others	SEL 347	-
	ER 125	-
	IR 200	-
	HCB	-

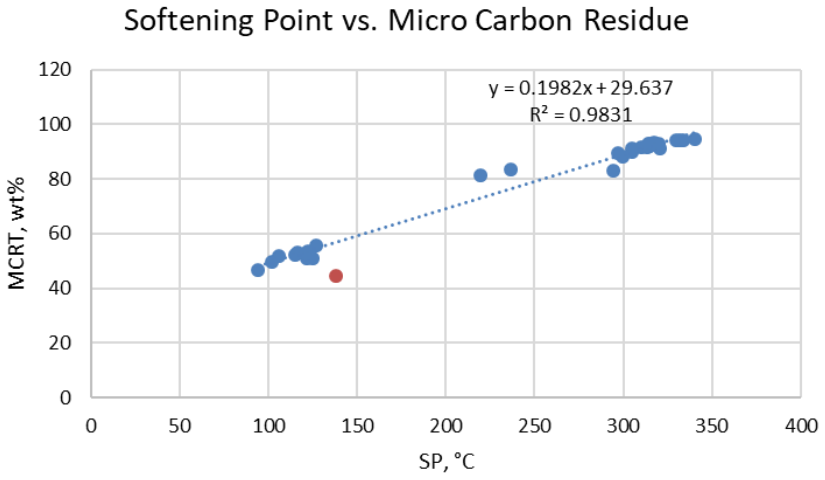

Figure 20: Correlation between the SP and the MCRT for isotropic and mesophase CTP and PP samples. The outlier is LTCTP.

Differential scanning calorimetry (DSC) is another method that shows the thermally related flow properties, like the SP, of pitch-based materials. Table 12 shows DSC data for various glass transition properties from modulated DSC for isotropic feedstock materials. The glass transitions were difficult to reliably obtain at temperatures significantly above 200 °C with the current instrument. Figure 21shows the correlation between the glass transition end point and the SP.

Table 12: DSC glass transition properties of various isotropic pitch feedstocks.

Sample Name	Heating 2°C/Min						
	Tg (H)		Tg (I)		Tg onset	Tg end	Width
	°C	J/(g·°C)	°C	J/(g·°C)	°C	°C	°C
W-CTP 3	48.7	0.35	48.0	0.35	22.7	75.4	52.7
W-CTP 4	48.8	0.30	45.3	0.31	33.1	64.4	31.3
W-CTP 5	38.0	0.30	35.5	0.30	23.1	52.9	29.9
W-CTP 6	47.5	0.30	42.5	0.31	32.1	62.5	30.4
W-CTP 7	49.8	0.29	46.7	0.29	34.8	65.5	30.7
CTP3-NMP	56.3	0.42	55.8	0.42	24.4	88.1	63.7
CTP4-NMP	46.9	0.29	47.8	0.29	33.7	59.7	26.0
CTP5-NMP	36.3	0.33	37.4	0.33	20.2	52.5	32.2
CTP6A-NMP	41.9	0.30	42.5	0.29	29.0	54.9	26.0
CTP7-NMP	47.7	0.36	47.3	0.36	32.1	63.4	31.3
CTP7DC-NMP	61.4	0.28	64.2	0.28	44.5	78.2	33.8
M-50	54.8	0.25	59.1	0.25	42.8	66.9	24.2
SEL 347	53.0	0.48	61.4	0.47	-5.3	111.3	116.6
ER 125	48.6	0.35	53.0	0.34	5.7	91.6	86.0
IR 200	83.7	0.28	87.2	0.27	17.3	150.7	133.3

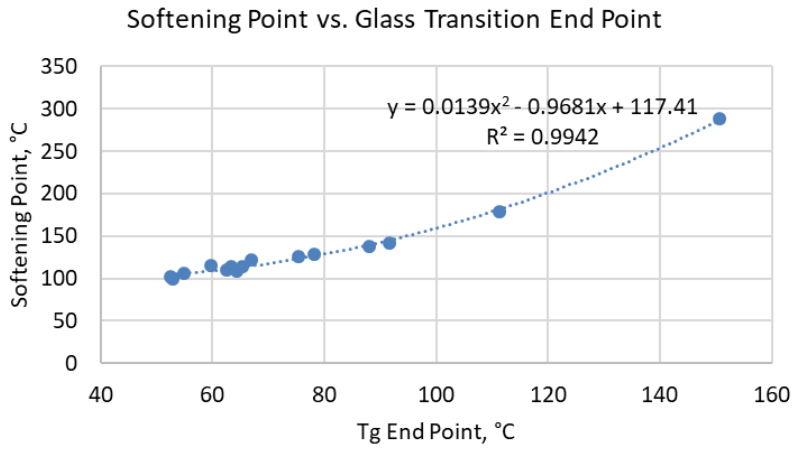

Figure 21: Comparison of the Tg end point with the SP for various isotropic feedstocks.

HTCTP typically has a higher aromaticity than PP. This is because PP is derived from FCC bottoms which contain 2- to 5-ring species but contains predominantly 4-ring species substituted with a significant amount of methyl groups and other alkyl groups up to C4 (Mochida, Korai, & Hieida, 1991). During the processing of FCC oil to produce pitch, aromatic growth reactions take place to produce dimers, trimers, and tetramers of the primarily 4-ring FCC feedstock. During this mild pyrolysis process there is also a significant amount of dealkylation that occurs, however most of the PP molecules still contain one or more methyl groups (Thies M. C., 2014). Table 13 shows the CHNOS composition for the various isotropic pitch samples. From the CHNOS data, it is clear that HTCTP is more aromatic than PP, and these are more aromatic the other materials with gilsonite being the least aromatic. Chemically, more than a few percent of heteroatoms can also interfere with mesophase formation. Therefore, it is desirable that the total NOS be below about 3 wt%. HTCTP contains significantly less oxygen than incomplete pyrolysis low-temperature CTP3. CTP also contains more nitrogen PP but gilsonite contains the most nitrogen. Gilsonite also has more oxygen than CTP and PP.

Table 13: CHNOS data and aromaticity (H/C) for isotropic pitch feedstocks and mesophase precursors.

	Sample ID	Carbon	Hydrogen	Nitrogen	Oxygen	Sulfur	Total	H/C
		% w/w	% w/w	% w/w	% w/w	% w/w		
Whole CTP	W-CTP 3	85.56	6.42	1.01	6.49	0.21	99.69	0.90
	W-CTP 4	91.29	4.21	0.99	1.47	0.98	98.94	0.55
	W-CTP 5	92.07	4.29	0.90	1.10	0.55	98.91	0.56
	W-CTP 6	92.97	4.08	0.91	0.89	0.60	99.45	0.53
	W-CTP 7	92.83	4.24	0.96	1.02	0.48	99.53	0.55
	CTP3 NMP	86.59	6.18	1.09	6.53	0.19	100.58	0.86

Filtered CTP	CTP4 NMP	92.92	4.28	1.09	1.28	0.95	100.52	0.55
	CTP5 NMP	93.94	4.23	0.97	1.17	0.57	100.88	0.54
	CTP6A NMP	93.91	4.14	0.95	0.99	0.57	100.56	0.53
	CTP6B NMP	93.94	4.24	0.97	1.09	0.57	100.81	0.54
	CTP6C NMP	93.31	4.42	0.97	0.99	0.55	100.24	0.57
	CTP6D NMP	94.67	3.93	0.90	0.85	0.54	100.89	0.50
	CTP6E NMP	94.17	4.32	1.15	0.83	0.55	101.02	0.55
	CTP7A NMP	93.71	4.27	1.00	1.21	0.48	100.67	0.55
	CTP7B NMP	93.66	4.25	0.95	1.14	0.48	100.48	0.54
CTPM	CTP6 MP SP 219.6	94.69	3.92	0.91	0.61	0.47	100.60	0.50
	CTP6 MP SP 236.9	94.65	3.95	0.84	0.58	0.45	100.47	0.50
	CTP6 MP SP 320.0	94.76	3.72	0.83	0.54	0.40	100.25	0.47
	CTP6 MP SP 294.5	94.73	3.86	0.85	0.53	0.42	100.39	0.49
	CTP6 MP SP 320.2	95.05	3.71	0.87	0.49	0.39	100.51	0.47
	CTP7 SP 340.2	94.87	3.72	0.91	0.63	0.33	100.46	0.47
	CTP6 MP SP 304.8	94.68	3.79	0.84	0.52	0.41	100.24	0.48
	CTP6 MP SP 333.5	95.18	3.67	0.85	0.49	0.38	100.57	0.46
	CTP6 MP SP 305.2	94.71	3.65	0.78	0.46	0.39	99.99	0.46
	CTP6 MP SP 310.4	94.52	3.64	0.78	0.49	0.39	99.82	0.46
	CTP6 MP SP 315.6	94.53	3.62	0.78	0.37	0.39	99.69	0.46
	CTP6 MP SP 314.7	94.54	3.62	0.81	0.44	0.39	99.80	0.46
	CTP6 MP SP 317.6	94.67	3.62	0.81	0.40	0.38	99.88	0.46

	CTP6 MP SP314.0	94.64	3.72	0.74	0.60	0.37	100.07	0.47
	CTP6 MP SP314.5	95.50	3.69	0.74	0.50	0.40	100.83	0.46
	CT 6 MP SP316.1	95.51	3.71	0.76	0.60	0.38	100.96	0.47
	CTP6 MP SP317.1	95.10	3.72	0.75	0.53	0.37	100.47	0.47
PP	M-50	94.43	5.50	0.19	0.61	0.55	101.28	0.70
	ACP 10	93.85	5.69	0.07	1.43	0.28	101.32	0.73
	KP-PP-19	94.61	5.44	0.15	0.25	0.30	100.75	0.69
	KP-PP-20	95.41	5.64	0.08	0.20	0.12	101.45	0.71
PPM	ACP-M1	95.08	4.27	0.27	0.29	0.55	100.46	0.54
Gilsonite + Other	347 Grade	85.37	10.21	2.55	1.13	0.38	99.64	1.44
	ER125	85.38	10.94	2.52	1.26	0.31	100.41	1.54
	IR200	84.04	9.96	3.16	2.26	0.34	99.76	1.42
	HCB	86.96	9.77	0.73	0.61	2.30	100.37	1.35

With respect to mesophase formation, for CTP relative to CTPM and PP relative to PPM, there is a further increase in aromaticity primarily due to hydrogen loss leading to aromatic growth, and some dealkylation (Zander, 2000) and other transformations. It should also be noted that for CTP there is also a decrease in NOS heteroatoms.

Feedstock CTP, PP, and gilsonite were characterized using the WRI patented (US 20130067991) Saturates, Aromatics, Resins-Asphaltene Determinator (SAR-AD^{TM}) separation—which is a combined chromatographic and solubility separation. The SAR-AD is an automated separation using high pressure liquid chromatography instrumentation with four different columns with four different solvents to separate material into 8 different fractions. These fractions represent classes of compounds based on an increase in aromaticity, heteroatom content and solubility/association tendencies. Figure 22 shows an example chromatogram with explanation of the various fractions. Quantification of the fractions provided by the SAR-AD provide a fingerprint of petroleum materials which has been shown to correlate to various physical properties (Delfosse, et al., 2016; Delfosse, et al., 2016; Glaser, et al., 2016). Table 14 gives the SAR-AD data for the various feedstock materials and Figure 23 shows an example fingerprint for some of the materials used in this study. SAR-AD data shows that HTCTP (Kershaw & Black, 1993; Fan, Fei, Chen, & Li, 2017) and PP materials have similar compositions, in that the chlorobenzene soluble portions have the most Aromatics 3 fraction which contain mostly 4 and 4+ ring fused aromatics (Thies M. C., 2014). PP does have more of the smaller ring aromatics (2-4 rings) than CTP. SAR-AD data also shows that the feed for PP contains mostly contains 3- to 4-ring

aromatics, consistent with the previous discussion of the material. Note that the cut off for 4-ring aromatics is largely based on the structure of the ring system. CTP does contain significantly more polar materials than PP as shown by the significant amount of chlorobenzene insolubles. This higher polarity material is like why CTP produces higher SP material than PP at the same relative amount of mesophase as judged by cross-polarized light optical microscopy.

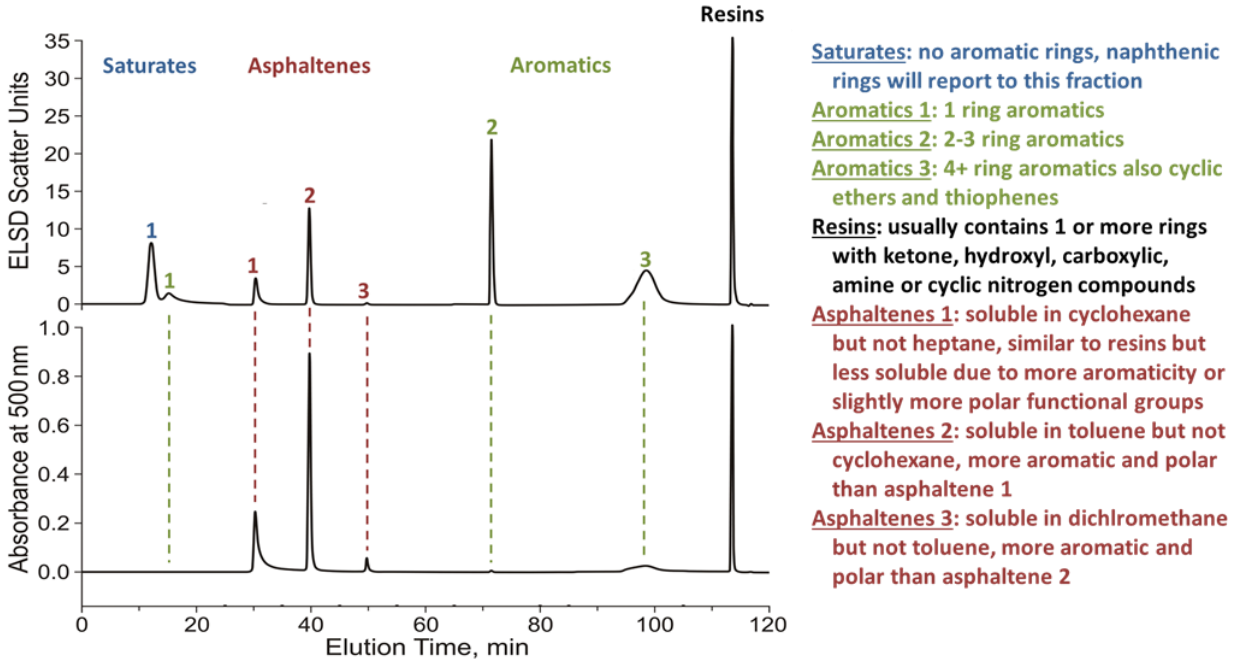

Figure 22: Example SAR-ADTM chromatogram using and evaporative light scattering detector (approximate weight percent) and a variable optical absorbance wavelength detector set at 500 nm (concentration of brown colored material). Details to the right of the chromatogram explains some of the compositional details for what reports to the various fractions.

Table 14: Evaporative light scattering detector (ELSD) data from SAR-AD analysis for CTP, PP, and other feedstock materials. ELSD data is approximately equal to weight percent present in the fractions.

			Maltenes					Asphaltenes			
	Sample ID/ELSD Data	Chlorobenzene Insolubles	Sat	Arom 1	Arom 2	Arom 3	Resins	CyC_6	Toluene	CH_2Cl_2	Total
CTP	CTP3-NMP	85.67	2.59	1.32	12.88	46.54	16.22	0.93	16.82	2.70	20.45
	CTP4-NMP	29.67	0.00	0.00	3.34	76.90	3.32	1.34	12.28	2.83	16.45
	CTP5-NMP	33.67	0.00	0.00	4.56	76.99	3.26	1.03	11.29	2.86	15.18
	CTP6-NMP	33.50	0.00	0.00	4.15	77.14	2.84	0.94	12.14	2.80	15.87
	CTP7-NMP	28.00	0.00	0.00	4.38	73.46	3.67	1.02	13.98	3.49	18.48
	CTP7DC-NMP	29.17	0.00	0.00	2.30	75.48	2.84	1.10	14.31	3.97	19.38
PP	M-50	-	0.10	0.01	8.61	67.70	3.22	1.23	16.41	2.72	20.36
	ACP-10	-	0.19	0.03	20.42	61.25	0.92	0.05	14.86	2.27	17.19
	KP-PP-19	-	0.15	0.00	16.51	66.71	0.24	0.03	14.06	2.30	16.39
	KP-PP-20	-	0.22	0.02	14.85	68.21	0.15	0.04	14.34	2.17	16.55
PP Feed	Slurry/Decant Oil KP-PP-19	-	17.12	0.31	49.93	31.95	0.34	0.00	0.35	0.00	0.35
Gilsonite + Others	ER 125	0.00	2.94	0.97	2.17	11.09	58.81	7.50	15.71	0.83	24.04
	SEL 347	0.00	2.99	0.40	1.86	8.71	32.76	9.40	42.33	1.55	53.28
	IR 200	6.83	0.85	0.41	0.89	5.38	23.48	4.87	61.84	2.27	68.99
	HCB	-	16.89	8.65	20.51	39.04	7.70	0.13	5.98	1.10	7.21
	RAS	-	15.84	8.85	12.00	19.22	14.05	1.43	22.55	6.06	30.04

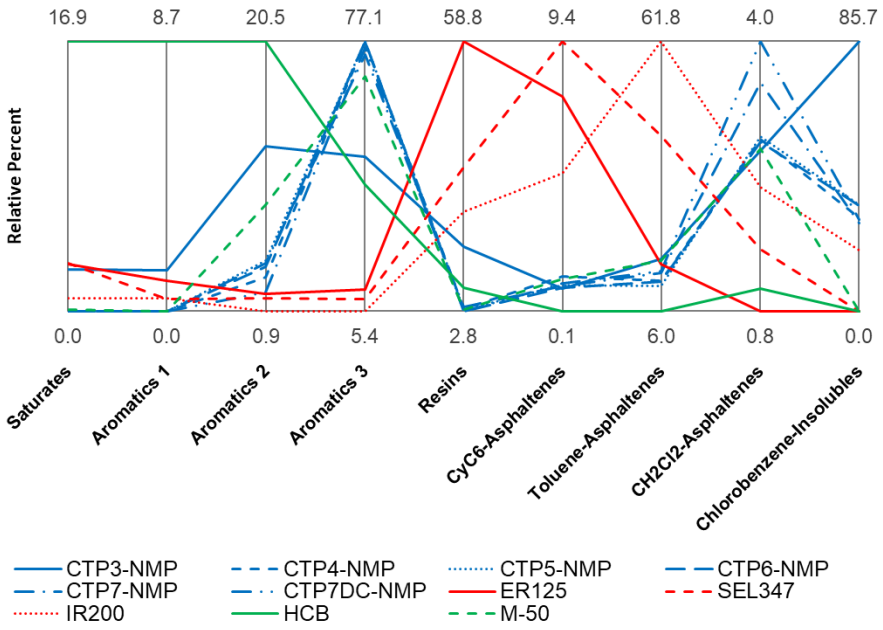

Figure 23: Parallel plots of SAR-AD data showing the fingerprints of some of the materials evaluated under this work. CTP samples are in blue, gilsonite materials are in red, and PP materials are in green. Most of them show clear and distinct composition patterns that will be exploited in the prediction models. Note: the data for the SAR-AD fractions are normalized to 100% for what was initially dissolved in chlorobenzene, they have not been scaled relative to the amount of material which dissolved in chlorobenzene.

To help with some of the modeling efforts, to understand the carcinogenicity, and to provide more details about the composition, the PAH content of select materials were determined by GC-MS. Select PAH values for select materials are shown in Table 15. It is clear that HTCTP contains significantly more PAHs than PP due to the severe pyrolysis conditions for which it is produced. Effluent from production of CTPM and PPM both contain high levels of PAHs while CTP effluent contains significantly more. CTPM and PPM samples have a majority of the smaller PAHs converted to larger PAHs or distilled out of the reaction into the effluent. This leads to low levels of these lighter PAHs in the mesophase materials.

Table 15: PAH quantification by GCMS for select PAHs for select samples. A PAH level of zero indicates that the values were below the limits of quantification. ACP20 is a PPM mesophase sample produced by ACP.

PAH	CTP3	CTP4	CTP5	CTP6	CTP7	CTP6M SP314	CTP6M SP320	CTP6 Effluent	KP-Decant Oil	M-50	ACP20	KP-PP-19	KP-MP-19	KP-PP Effluent
	ppm													
Naphthalene	0	0	0	0	0	0.69	1.6	0	15	0	1.3	0	0	32
Acenaphthylene	0	5	7.9	3.5	2.2	0	0	0	0	0		0	0	0
Acenaphthene	1.8	200	470	180	100	9.3	10	1700	18	0	1.1	0	0	31
Fluorene	8.4	300	880	120	82	0.22	0.54	60	36	0	1.2	0	0.50	8.3
Phenanthrene	120	7000	16000	5700	3200	1.1	2.0	1900	410	51	17	0	9.0	85
Anthracene	82	2200	4000	2400	1400	0.81	0.94	900	100	36	8.5	0	11	44
Carbazole	28	1700	2400	1300	780	0.10	0.24	1100	0	0	0.69	0	0	6.7
Fluoanthrene	330	19000	28000	26000	19000	2.0	2.3	22000	40	51	13	23	3.4	61
Pyrene	500	16000	24000	23000	17000	5.9	8.3	19000	550	860	150	280	17	380
Chrysene	830	15000	20000	26000	18000	3.1	7.4	27000	1300	960	87	640	19	560
Benz(a)anthracene	740	16000	22000	25000	17000	1.2	5.5	27000	2400	1600	74	1500	24	700
Benzo(b)fluoranthene	1200	21000	29000	38000	26000	6.8	18	43000	230	610	33	490	36	1800
Benzo(k)fluoranthene	1000	13000	17000	21000	13000	5.4	15	28000	79	480	16	180	17	
Benzo(a)pyrene	1400	20000	22000	35000	23000	26	49	43000	800	2400	240	2700	350	9800
Indeno(1,2,3-C,D)pyrene	2100	15000	15000	23000	15000	73	250	25000	0	160	29	230	170	3200
Dibenz(a,h)anthracene	1700	4400	4200	6800	4600	26	26	6500	120	320	27	420	130	3500
Benzo(ghi)perylene	2100	15000	16000	20000	15000	130	450	20000	380	1300	220	1600	1200	17000
Total ppm	12140.2	165805	220957.9	253503.5	173164.2	291.62	846.82	266160	6478	8828	918.79	8063	1986.9	37208

To understand the evolution of pyrolysis products during mesophase formation, the effluent from CTP7M was studied under different conditions. Effluent begins to emerge from the reactor above 300 °C but below 390 °C when pyrolysis begins to dominate. During this stage it is expected that the volatile species liberated are primarily lighter pitch components and the effluent is more oil like. After mesophase conversion temperature 410-420 °C is reached a relatively constant evolution of effluent is observed during the course of the reaction. This effluent was collected after the reaction temperature was reached and, in some cases, two different phases of the effluent were observed as a more powdery material and a more glassy material. GC-MS showed that the initial reactor effluent consists of lighter PAH material from the distillation of the pitch and that later effluent is more concentrated in larger conjugated ring molecules (Table 16). As a confirmation, SAR-AD also showed that the pyrolysis effluents are more concentrated in 4+ aromatic rings (Table 17). The composition shows that the effluent is highly aromatic and should be able to be recycled back into isotropic pitch processes.

Table 16: GCMS results for the amount of fused ring molecules of CTP7 distillates prior to pyrolysis and CTP7 effluent after production of mesophase. The effluent had two different morphologies: powder and glass. Approximate percentages were taken by integrating areas of the chromatograms.

Before Pyrolysis	%	After Pyrolysis Powder	%	After Pyrolysis Glass	%
2 membered	0.12	2 membered	1.58	2 membered	0.06
3 membered	5.55	3 membered	1.58	3 membered	0.12
4 membered	29.9	4 membered	2.17	4 membered	0.99
5 membered	50.9	5 membered	11.9	5 membered	9.77
6 membered	12.8	6 membered	70.8	6 membered	71.5
7 membered	0.768	7 membered	11.9	7 membered	17.6

Table 17: SAR-AD for CTP7M effluent generated after pyrolysis conditions were reached.

		Maltenes					Asphaltenes			
Sample ID	Det	Sat	Aro 1	Aro 2	Aro 3	Resins	CyC_6	Toluene	CH_2Cl_2	Total
Reactor Effluent	ELS	0.00	0.00	0.51	94.61	2.27	0.00	2.40	0.21	2.60
Powder	500 nm			0.09	87.25	3.74	0.00	6.72	2.20	
Reactor Effluent	ELS	0.00	0.00	0.22	94.17	2.59	0.39	2.43	0.20	3.02
Glassy	500 nm			0.00	88.80	3.46	0.83	5.37	1.54	

The reactor effluent is a soft material that is completely soluble in dichloromethane, and about half of the total material is soluble in heptane. When the effluent material is dissolved in a solvent, or is spread as a thin film, the material is orange/red to red in appearance. GCMS of the

volatile and eluted portion of the material showed that it contained mostly molecules with 6-fused rings (~70%) with the bulk of the other material containing 5- and 7-fused ring systems. Several interesting compounds were observed such as rubicene and coronene, both 7-fused ring molecules. The amount of this material is highly concentrated in the effluent compared to the starting CTP. During the collection of the effluent, it was observed that some the effluent deposited in the collection flask as flakes of orange material while some of the material was extruded from the effluent tube as a more reddish glassy material. These two morphologies of the effluent material were analyzed independently to determine if there was a significant difference in the chemical composition of these materials. It was found that the glassy material was more enriched in larger fused ringed structures than the powder (Table 16).

Fourier transform infrared spectroscopy (FTIR) spectra were previously recorded for all the samples using the KBr method. The KBr was dried in a muffle oven prior to use to control the amount of water in the sample. Samples were ball milled with KBr under an inert atmosphere prior to producing the KBr pellet. After acquiring the spectra, the baselines were corrected and spectra were normalized to the methyl umbrella, usually around 1377 cm^{-1}, so that relative concentrations of the other functional groups could be compared on a methyl basis. The various functional group wavenumbers that were used to characterize the material by FTIR are show in Table 18.

Table 18: Various wavelength assignments for CTP and PP materials. The 724 cm-1 for CH2n rocking, where n > 4, is omitted since this is only relevant for gilsonite, asphaltenes and other materials with longer alkyl groups.

Functionality	CTP-based Wavelength (cm^{-1})	PP-based Wavelength (cm^{-1})
Phenolic O-H/Carboxylic O-H Stertch	3525.06	3525.06
Pyrrolic N-H/OH Stretch	3420.67	3420.67
Phenolic O-H Stretch Intermolecular	3357.29	3357.29
Aromatic C-H Stretch	3044.11	3044.11
Assymetric CH3 stretch	2956.50	2956.50
Assymetric CH2 stretch (some CH3)	2914.00	2921.08
tertiary C-H Stretch	2894.98	2894.98
Symmetric CH3 Stretch	2868.89	2868.89
Symmetric CH2 Stretch	2855.84	2855.84
Ar C=C ring stretching mode	1601.28	1601.28
Ar -CH2, CH2 or CH3 bend 1	1452.15	1452.15
Ar -CH2, CH2 or CH3 bend 2	1437.24	1437.24
Methyl symmetric bend	1375.72	1375.72
C-O, C-C, O-H bend 1	1334.71	1334.71
C-O, C-C, O-H bend 2	1317.94	1317.94
C-O, C-C, O-H bend 3	1260.15	1260.15
C-O, C-C, O-H bend 4	1237.78	1237.78
C-O, C-C, O-H bend 5	1202.36	1202.36
C-O, C-C, O-H bend 6	1176.26	1176.26
C-O, C-C, O-H bend 7	1161.35	1161.35
C-O, C-C, O-H bend 8	1150.16	1150.16
C-O, C-C, O-H bend 9	1129.66	1129.66
C-O, C-C, O-H bend 10	1111.02	1111.02
C-O, C-C, O-H bend 11	1062.55	1062.55
Sulfoxide	1032.72	1032.72
C-O, C-C, O-H bend	946.98	946.98
Isolated Ar C-H bend	871.00	878.00
Ar C-H bend 2H (CH2 and CH3 rocking modes) 1	834.00	838.86
Ar C-H bend 2H (CH2 and CH3 rocking modes) 2	822.08	822.08
Ar C-H bend 2H (CH2 and CH3 rocking modes) 3	812.00	812.76
Ar C-H terminalH4	750.00	745.65

By FTIR there is a clear distinction in isotropic materials in that HTCTP is distinct from LTCTP, and LTCTP appears more similar to PP. FTIR spectra for a representative sample from each of these is shown in Figure 24 along with assignments. From the Figure it is clear that LTCTP and PP have significantly more aliphatic groups (~2978-3840 cm^{-1}) than HTCTP, which is expected due to the sever pyrolysis used to produce HTCTP. Other differences are that LTCTP has less aromatic hydrogen (~3040 cm^{-1} and the Ar-H out-of-plane bends) which is likely due to its great degree of substitution with aliphatic and also oxygen containing functional groups (6.5 wt.% oxygen). It also appears that HTCTP may have more cata-condensed aromatic structures than PP, however this may be masked by the alkyl substitutions in PP.

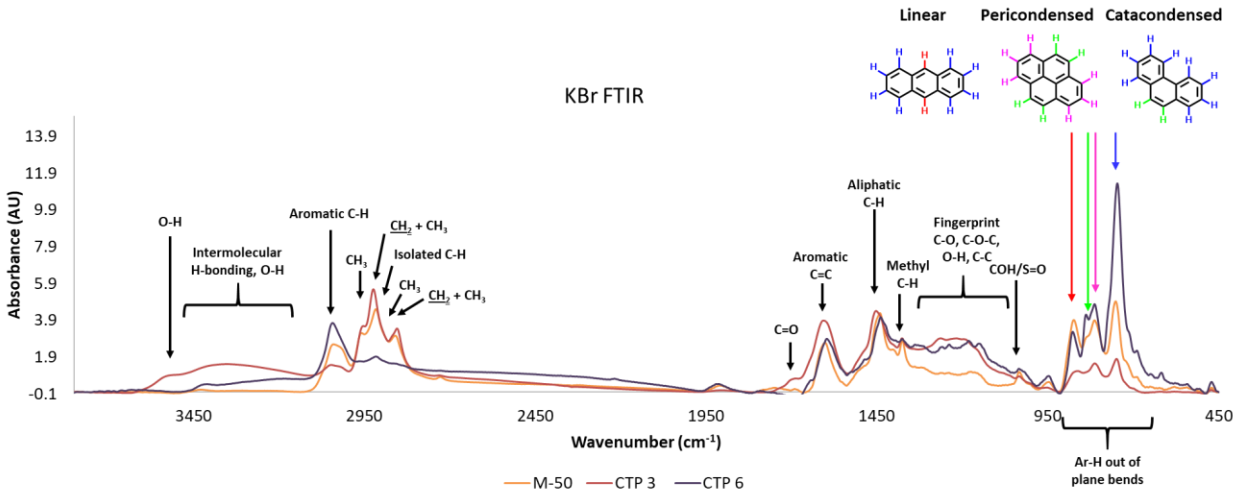

Figure 24: FTIR of HTCTP (CTP6), LTCTP (CTP-3) and PP (M50) with assignments.

By comparing CTP to CTPM, and PP to PPM, some general trends were observed, while normalizing to the methyl band at 1377 cm^{-1}. Upon mesophase conversion there is a loss of aliphatic and aromatic C-H stretches (12978-2840 cm^{-1} and 3044 cm^{-1}, respectively) and there is a decrease in the less substituted out-of-plane blends for 3 neighboring Hs and 4 neighboring Hs (812 and 750 cm^{-1}, respectively). These changes are consistent with the loss of hydrogen and aromatic growth leading to larger ring systems where terminal rings with 3 and 4 neighboring H are relatively reduced. Also, the aliphatic C-H bending mode around 1437 cm^{-1} becomes less for both PP and CTP materials upon conversion to mesophase. Figure 25 shows FTIR spectra for PP and PPM, Figure 26 shows a zoomed in region showing the out-of-plane bending mode, Figure 27 shows FTIR spectra of CTP and CTPM and Figure 28 shows FTIR spectra of CTP and CTPM at various stages of mesophase conversion.

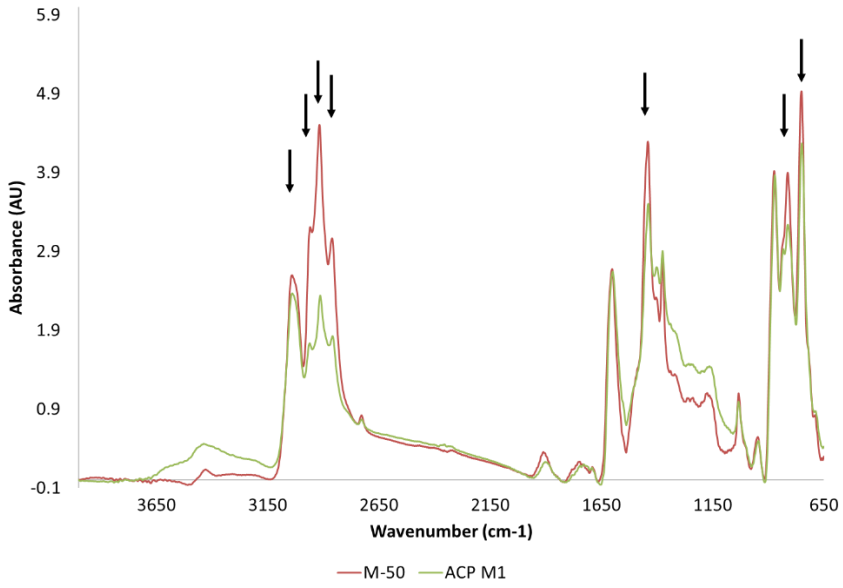

Figure 25: FTIR of PP and PPM. Arrows indicate changes in major functional groups relative to the methyl band at 1377 cm^{-1} when going from isotropic pitch to mesophase.

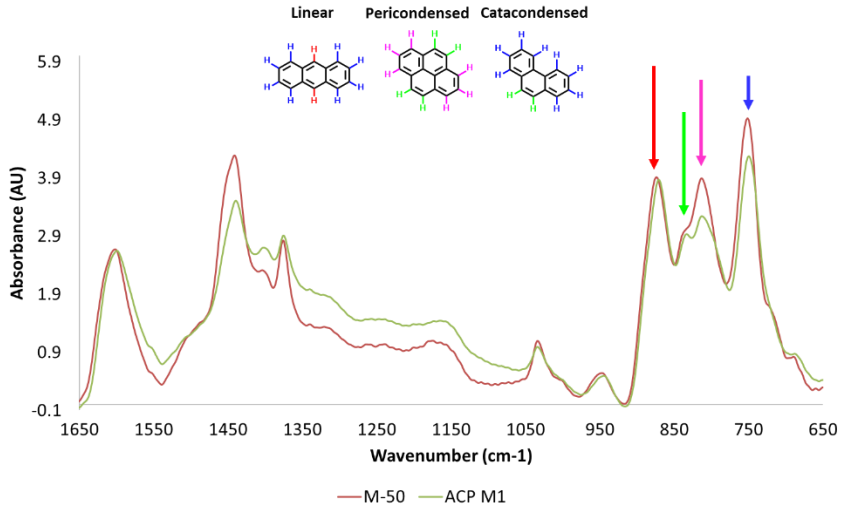

Figure 26: FTIR of PP and PPM focusing on the out-of-plane bend (aromatic substitution) region. Arrows indicate changes in major functional groups relative to the methyl band at 1377 cm^{-1} when going from isotropic pitch to mesophase.

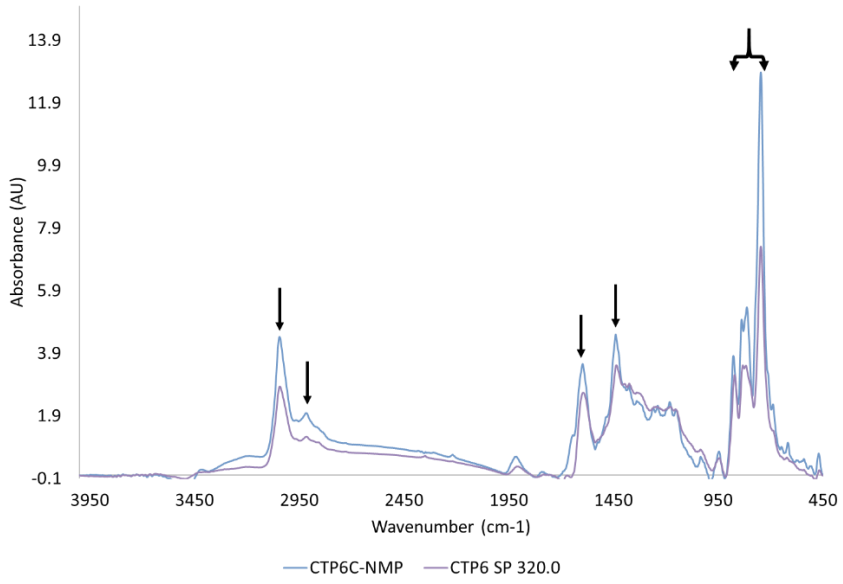

Figure 27: FTIR of CTP and CTPM. Arrows indicate changes in major functional groups relative to the methyl band at 1377 cm^{-1} when going from isotropic pitch to mesophase.

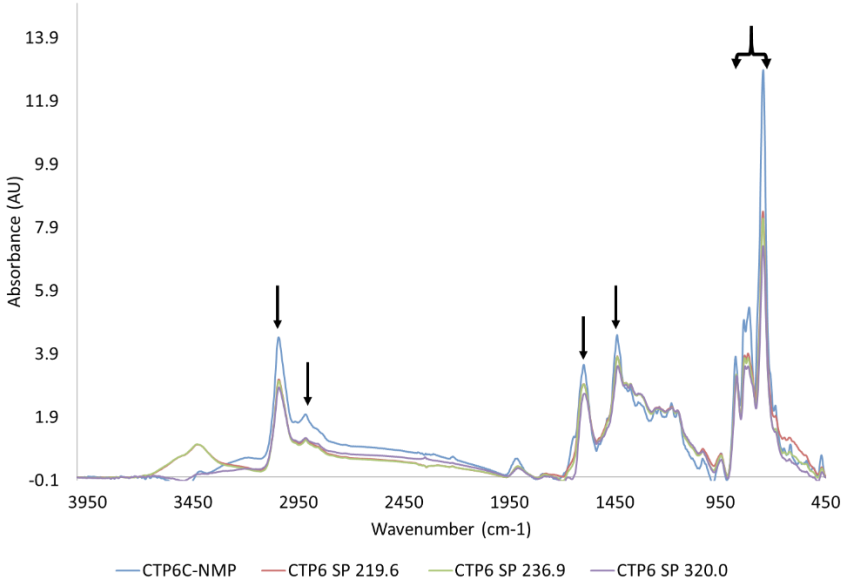

Figure 28: FTIR of CTP and CTPM at various stages of mesophase content as indicated by the SP.

The SP should is indicator of the degree of dehydrogenation which should also be an indicator of hydrogen content. In fact, comparing the SP to the absorbance at 1442 cm^{-1} (in the range of the C-H alkyl bend) a good correlation was observed between the different materials (Figure 29).

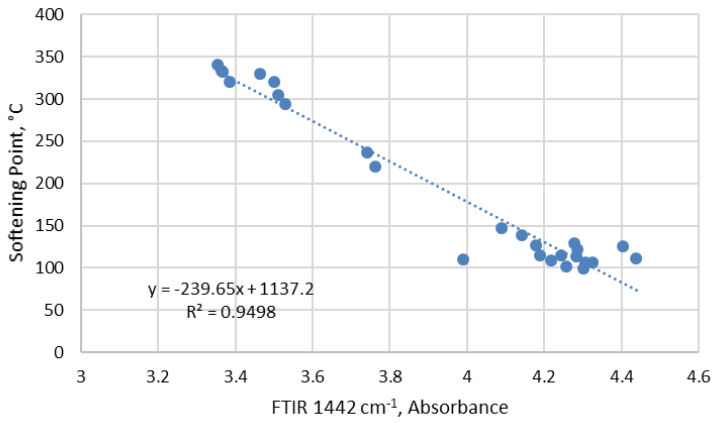

Figure 29: Correlation between the SP and the FTIR C-H alkyl bend at 1442 cm^{-1} for HTCTP, CTPM, LTCTP, PP and PPM.

Since LTCTP and PP contain significantly more alkyl groups than HTCTP, other correlations such as with the H/C ratio were not as good as when only focusing on HTCTP materials. Figure 30 shows the correlations between SP and 1442 cm^{-1} and the H/C ratio and 1442 cm^{-1}. Other correlations with the H/C ratio were apparent when compared to the amount of substitution occurring as indicated by the out-of-plane bends. Figure 31 shows some correlations between the peaks of peaks the out-of-plane bands which change the most upon mesophase conversion and also some closely related areas in the out-of-plane bands which gave slightly better correlations which were not at the peak of the bands.

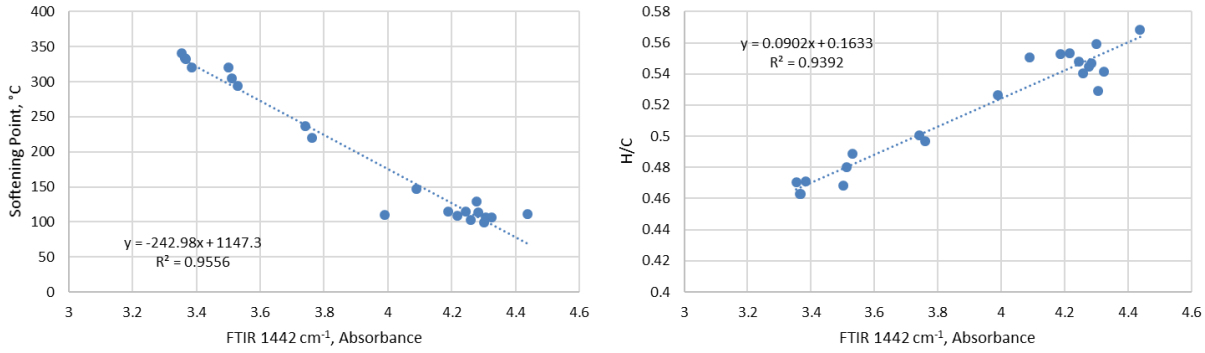

Figure 30: Correlation between the SP and the FTIR C-H alkyl bend at 1442 cm^{-1} for HTCTP and CTPM (left) and correlation between HTCTP and CTPM with the same IR band.

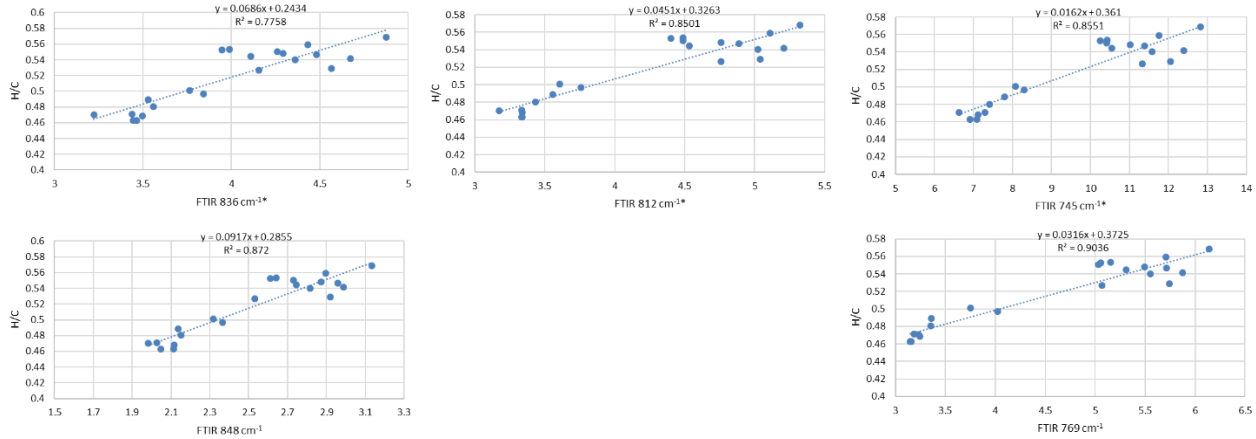

Figure 31: Correlations between various aromatic out-of-plane C-H bends and the H/C ratio of HTCTP and CTPM. Top shows correlations at the maximum of the peaks that change the most during mesophase conversion and the bottoms shows regions next to these peaks which gives a higher correlation.

FTIR data was also analyzed by comparing some other ratios of average functional groups to find correlations with physical properties. Some of the ratios used to study the functional groups are shown in Table 19. There are many other possible indices which may also be studied (Azemani & Rabbani, 2016).

Table 19: Various ratios of wavelengths used to provide some level over average structural information (Guillen, Iglesias, Dominguez, & Blanco, 1992; Li, Du, Li, Hou, & Ye, 2015; Dordevic, et al., 2012; Menendez, Bermejo, & Figueiras, 2000).

Description	**Index**
Chain Index 1	ICH3(2956)/ICH2(2921)
Chain Index 2A	CH2(1452)/CH3(1376)
Chain Index 2B	1437/1376
Aromatic Index 1	C=C(1601)/(C=C(1601)+CH2(1437)+CH3(1376)
Aromatic Index 2	ArC-H(3044)/(ArC-H(3044)+CH2(2921))
ortho-substitution index	746/(876+839+813+746)

When evaluating these metrics there are clear trends between different materials between gilsonite, PP, LTCTP and HTCTP, and there were clear differences between PP and PPM. However, between various levels of conversion of mesophase there were no clear global trends. Table 20 shows the calculated values for the various FTIR metrics from Table 19.

Table 20: Calculated values for the various ratios from Table 19.

	Sample ID	Chain Index 1	Chain Index 2A	Chain Index 2B	Aromatic Index 1	Aromatic Index 2	ortho-substitution index
		ICH3(2956)/ICH2(2921)	CH2(1452)/CH3(1376)	1437/1376	C=C(1601)/(C=C(1601)+CH2(1437)+CH3(1376)	ArC-H(3044)/(ArC-H(3044)+CH2(2921))	746/(876+839+813+746)
Whole CTP	W-CTP 3	0.634	1.382	1.280	0.337	0.194	0.361
	W-CTP 4	0.718	1.055	1.234	0.276	0.616	0.497
	W-CTP 5	0.769	1.107	1.246	0.273	0.667	0.495
	W-CTP 6	0.640	0.942	1.106	0.222	0.504	0.524
	W-CTP 7	0.702	1.002	1.184	0.256	0.613	0.503
Isotropic CTP	CTP3-NMP	0.662	1.486	1.350	0.347	0.208	0.342
	CTP4-NMP	0.692	1.188	1.365	0.279	0.602	0.495
	CTP5-NMP	0.676	1.042	1.219	0.248	0.556	0.500
	CTP6A-NMP	0.775	1.115	1.289	0.290	0.647	0.474
	CTP6B-NMP	-	-	-	-	-	-
	CTP6C-NMP	-	-	-	-	-	-
	CTP6D-NMP	-	-	-	-	-	-
	CTP6E-NMP	-	-	-	-	-	-
	CTP7-NMP	0.749	1.108	1.276	0.295	0.622	0.478
	CTP7DC-NMP	0.781	1.115	1.286	0.304	0.653	0.474
CTPM	CTP6M SP 219.6	0.910	1.050	1.289	0.302	0.723	0.441
	CTP6M SP 236.9	0.908	1.039	1.285	0.302	0.727	0.438
	CTP6M SP 320.0	0.924	0.945	1.200	0.285	0.698	0.435
	CTP6M SP 294.5	0.821	0.978	1.213	0.283	0.622	0.442
	CTP6M SP 320.2	0.929	0.946	1.190	0.287	0.698	0.426
	CTP7M SP 340.2	0.931	0.928	1.177	0.295	0.704	0.426
	CTP6M SP 304.8	0.935	0.968	1.224	0.292	0.714	0.430
	CTP6M SP 333.5	0.959	0.932	1.191	0.286	0.712	0.426
	CTP6M SP 331.9	0.958	0.931	1.185	0.289	0.715	0.418
	CTP6M SP 305.2	0.919	0.953	1.207	0.285	0.699	0.429
	CTP6M SP 310.4	0.912	0.991	1.243	0.292	0.724	0.422
	CTP6M SP 316.1	0.880	0.930	1.179	0.278	0.675	0.438
	CTP6M SP 314.0	0.925	0.975	1.223	0.289	0.715	0.424
	CTP6M SP 315.6	0.902	1.003	1.254	0.294	0.725	0.420
	CTP6M SP 314.7	0.919	0.981	1.237	0.289	0.716	0.423
	CTP6M SP 317.6	0.918	0.968	1.215	0.291	0.697	0.424
	CTP6M SP 317.1	0.886	1.092	1.314	0.310	0.758	0.410
	CTP6M SP 314.5	0.903	1.032	1.270	0.297	0.738	0.413
PP	M-50	0.710	1.346	1.425	0.280	0.359	0.311
	ACP 10	0.707	0.972	1.118	0.271	0.343	0.305
	KP-PP-19	0.677	1.104	1.271	0.251	0.351	0.310
	KP-PP-20	0.671	1.130	1.250	0.255	0.296	0.298
PPM	ACP-MP	0.726	1.017	1.192	0.293	0.500	0.299
	ACP 20	0.708	1.040	1.210	0.288	0.482	0.283
	KOP MP 1	-	-	-	-	-	-
	KP-MP-19	0.699	1.107	1.264	0.298	0.496	0.280
	KP-MP-20-0289	0.657	1.024	1.234	0.276	0.490	0.314
	KP-MP-20	0.685	1.011	1.195	0.288	0.485	0.287
Gilsonite + Others	SEL 347	0.766	1.262	0.060	0.215	0.028	-
	ER 125	0.749	1.348	0.058	0.194	0.043	-
	IR 200	0.718	1.228	0.077	0.240	0.023	-
	HCB	-	-	-	-	-	-

Oxidation of as spun pitch-based fibers is an important step in the path towards CF production. The oxidation step causes crosslinking of aromatic units within the fibers—locking them in place which preserves the structure of the fiber through increasing the melting and boiling point of the cross-linked molecules within the fiber. This change in molecular properties is what allows the fibers to be carbonized at high temperatures around 1000 °C. Without this step, it is not possible to carbonize the fibers as they will simply melt and a significant amount of carbonaceous

material would be volatilized. Stabilization of green fibers is an energy and time consumptive process which, has different optimization parameters for different materials and fibers. Stabilization proceeds different between CTPM and PPM (Zheng, Maeda, Tokumitsu, & Mondori, 1993). However, it is very different in terms of chemistry when dealing with PAN-based fibers. PAN stabilization causes a series of exothermic condensation reactions to occur to create aromatic units, the ladder structures, and crosslinking of aromatic units (Ozcan, Vautard, & Naskar, 2014). For PAN this is all done under tension to maintain polymer alignment, with tightly controlled temperatures to prevent thermal runaway, and the process is often controlled by incorporating various reactive comonomers in the PAN formulation. In general, the degree of stabilization is correlated with the tensile strength of CF (Ingaki, 2000) (Figure 32).

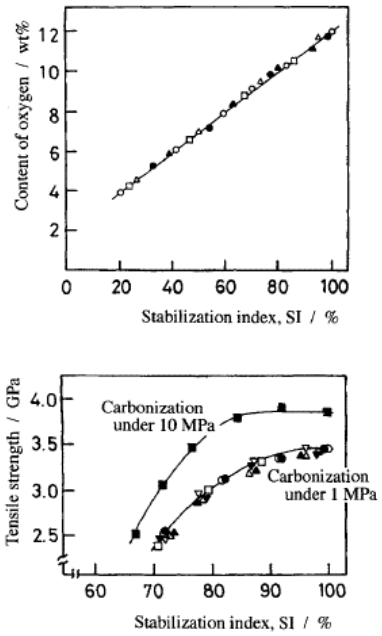

Figure 4-7 Dependence of oxygen content after stabilization (a) and tensile strength of carbon fibers (b) on the stabilization index SI of PAN fibers prepared by using different comonomers such as methyl acrylate, sodium acrylate and acrylamide [Ogawa and Saito, 1995].

Figure 32: Relationship between stabilization and Carbon Fiber properties for PAN fibers.

With this in mind, fibers spun from CTP6, ACP-M1and bio-PAN from BP1, were placed in a thermogravimetic analyzer and heated up to 250-300 °C under nitrogen or air and held isothermal for 180 min to probe their sensitivity towards oxidation and understand the oxygen uptake behavior of these different materials. For the first set of experiments, the samples were all heated to the stabilization temperature appropriate for bio-PAN fibers since this material requires the lowest stabilization temperature of the materials. Weight loss profiles for this experiment of the different materials performed under air and under nitrogen are shown below in Figure 33.

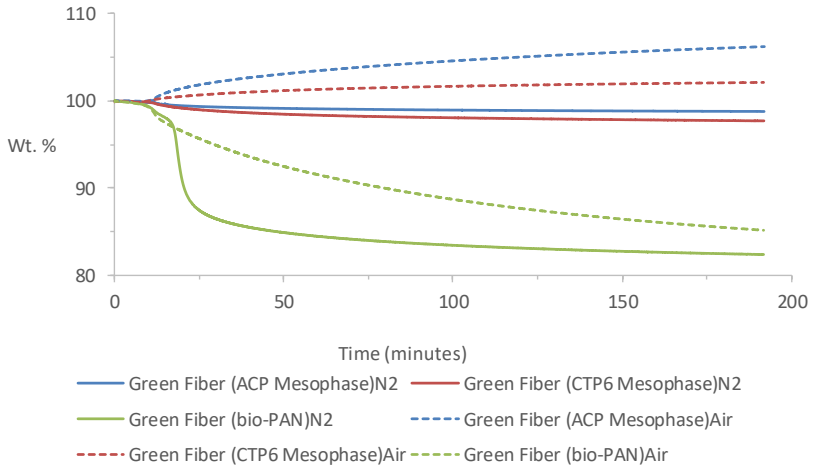

Figure 33: TGA weight loss curves (250-300 °C) under an air atmosphere and under a nitrogen atmosphere for the 3 different materials from BP1 that met DOE mechanical property requirements (elongation was slightly low for bio-PAN).

By subtracting the weight loss due to volatilization under nitrogen from the weight changes in the samples after heating in air the amount of oxygen uptake can be determined for these materials. Figure 34 shows the subtraction of the air and nitrogen weight loss curves resulting in the net oxygen uptake for these different materials. From the subtracted weight loss curves, differences between the oxidation properties of these different materials becomes apparent. The results shows that bio-PAN oxidizes very rapidly under these conditions taking up more than 8 wt% of oxygen before it begins to lose weight due to additional reactions. When comparing the two different pitch samples, it is clear that the ACP-M1 sample is more sensitive towards oxidation at this temperature as it takes up more oxygen more quickly than the CTP6M SP320 sample. This has implications on how best to optimize these different materials. Considering that both of these materials have similar softening points this means that the CTP6M SP320 sample will need to be stabilized at longer times to achieve the same level of oxygen uptake. It is not clear if CTP needs to reach the same level of oxygen uptake as the PP in general, this must be taken into consideration before making determinations about economic impacts of the different oxygen uptake behaviors of the two materials.

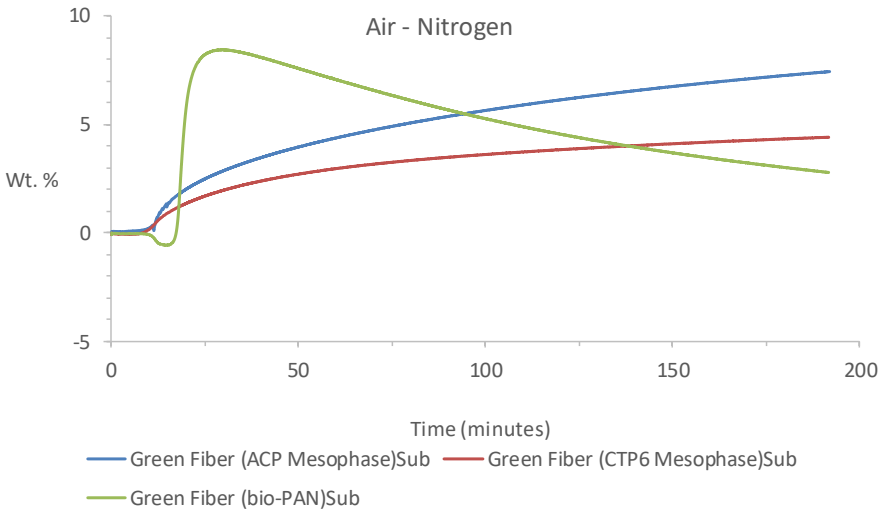

Figure 34: Resulting weight loss curves after subtracting the TGA weight lost curve of the materials collected under nitrogen and under air shown in Figure 3. This subtraction shows the oxygen uptake for the different materials.

Since the temperature used in this experiment were not optimized for actual stabilization temperatures appropriate for pitch fibers, the pitch samples did not reached a stead state of oxidation. As a result, the experiments were repeated at a temperature more relevant to pitch stabilization temperatures (300-350 °C). By visually inspecting the TGA samples, it can be clearly seen that the presence of air greatly stabilizes the green fibers. Figure 35 shows a photograph of the TGA samples for CTP6M SP320 heated under air and under nitrogen. The sample heated under air maintained the fiber structure while the sample heated under nitrogen melted into a puddle of pitch. Figure 36 shows the TGA weight loss curves for the two pitch samples heated under air and under nitrogen, and Figure 37 shows the subtraction of the nitrogen experiment and air experiment weight loss curves for the two pitch samples to provide the net oxygen uptake. From the weight loss curves in Figure 37 the CTP mesophase has a rapid oxidation event that completes in less than 15 minutes and the weight increase is slow for the remaining time. For the PP mesophase sample, it takes up about twice as much oxygen than the CTP mesophase and the transition to a quasi-steady state (flattening out of the weight increase) occurs over a longer time and is significantly broad. Additionally, after about 1.5 hrs the oxidized PP mesophase begins to undergo weight loss.

Figure 35: Photograph showing isothermal TGA (300-350 °C) of green fibers from CTP6M SP320 performed under air (left) which retains the structure of the crushed fibers and the experiment performed under nitrogen (right) resulting in complete melting of the fibers.

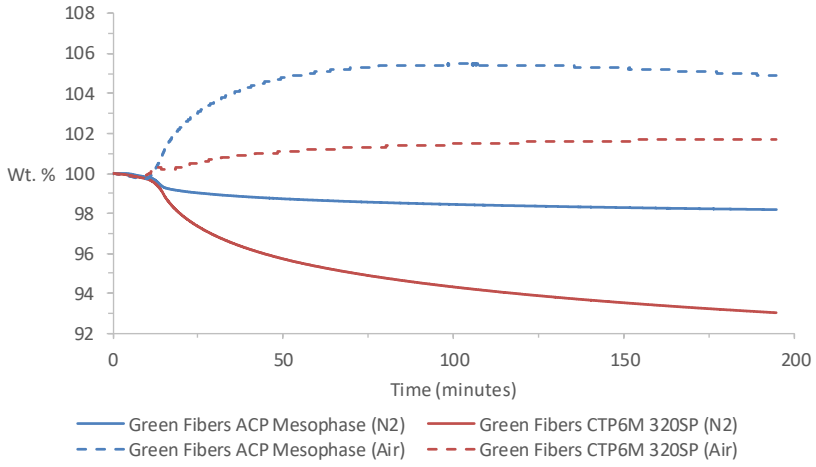

Figure 36: TGA weight loss curves (300-350 °C) under and air atmosphere and under a nitrogen atmosphere for the petroleum-based ACP Mesophase and coal based CTP6M 320SP.

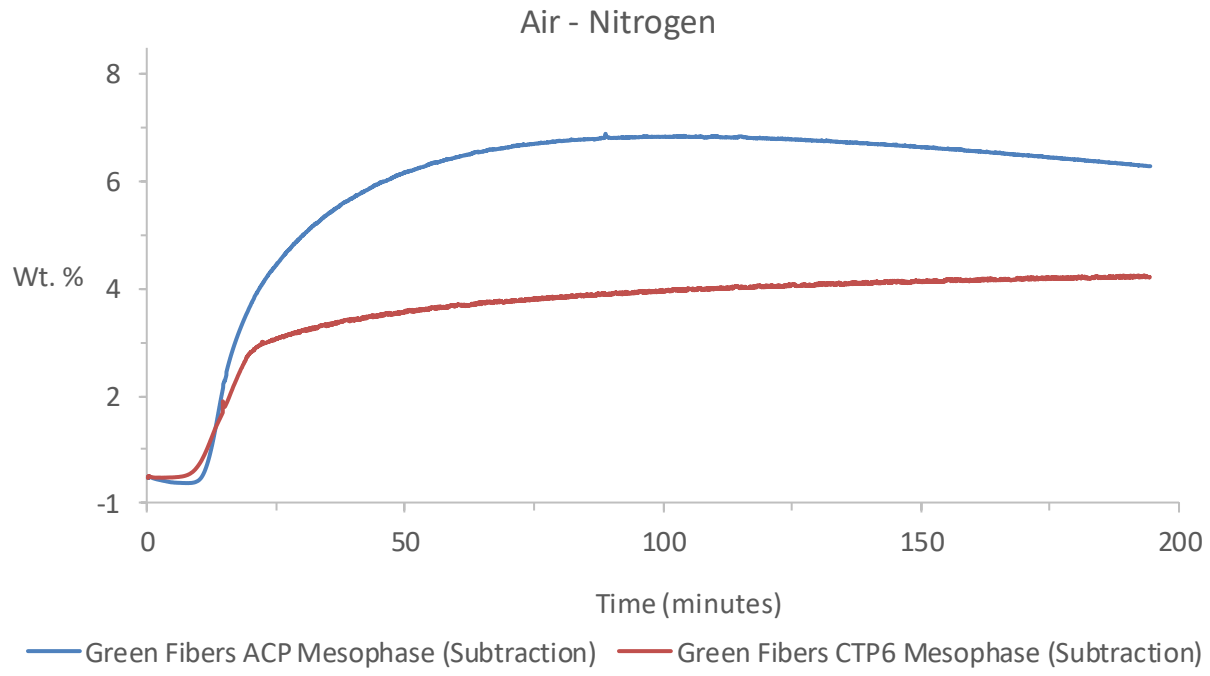

Figure 37: Resulting weight loss curves after subtracting the TGA weight lost curve of the two different pitch materials collected under nitrogen and under air shown in Figure 36. This subtraction shows the oxygen uptake evolution between these two different materials.

The difference in the oxidation behavior between these two materials is likely due to the lower aromaticity of the PP material as it contains more methyl groups, small alkyl groups and bridging CH_2 (fluorene and acenaphthene type) groups compared CTP (Menendez, Blanco, Santamaria, Dominquez, & Blanco, 2002). Oxidation is known to occur readily at α-aliphatic carbon attached to aromatic units (Menendez, Blanco, Santamaria, Dominquez, & Blanco, 2002). To determine some of these chemical differences, FTIR spectra were obtained on the ACP-M1 and CTP6M SP320 after heating under nitrogen and under air. Figure 38 shows the FTIR spectra for the ACP mesophase TGA samples treated in air and under nitrogen, and Figure 39 shows the FTIR spectra for the CTP6M SP320 TGA samples treated in air and under nitrogen.

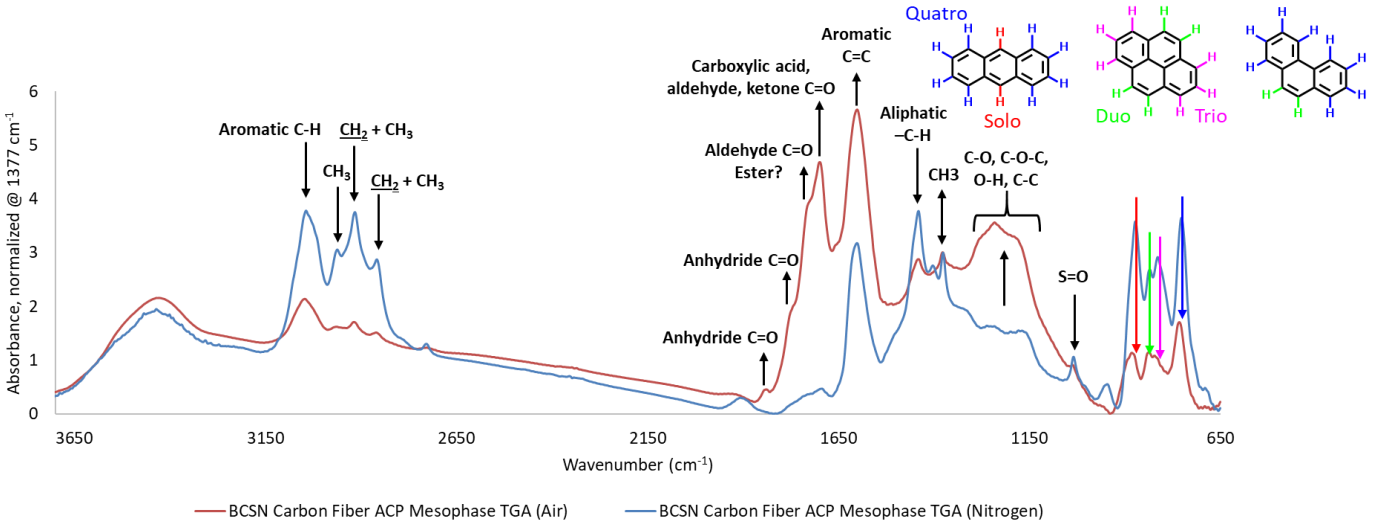

Figure 38: FTIR spectra of ACP mesophase after treated under air and under nitrogen in a TGA which was held isothermal at 250-300C for 180 minutes. Some tentative spectral assignments are provided.

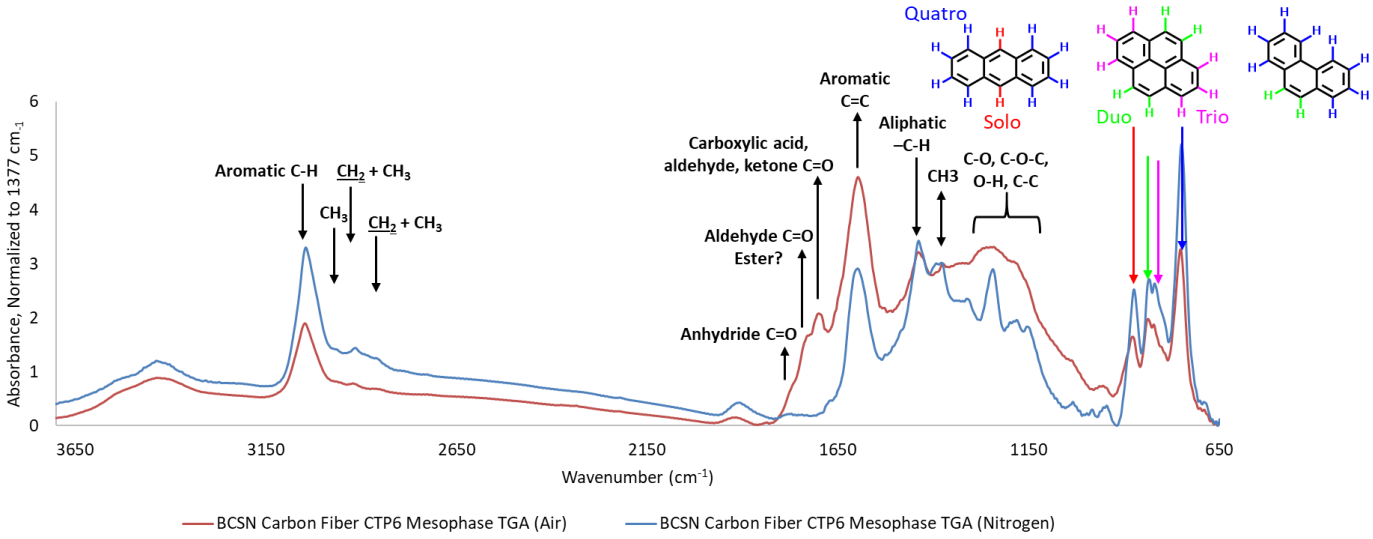

Figure 39: FTIR spectra of CTP6M SP320 after treated under air and under nitrogen in a TGA which held isothermal at 250-300C for 180 minutes. Some tentative spectral assignments are provided.

When comparing the spectra for the two materials (ACP mesophase vs. CTP6M 320SP) treated under nitrogen, for the ACP mesophase it is clear that it contains significantly more methyl and short chain alkyl CH_2 material (~2900 and ~1438 cm^{-1}) than the CTP material. It is also clear that both materials have significantly different aromatic substitution patterns. For the PP, it contains significantly more isolated (solo) aromatic C-H protons relative to the CTP, whereas CTP contains significantly more aromatic rings that contain four neighboring protons on the same aromatic ring (quatro). This is consistent with the fact that CTP is highly enriched in PAH molecules with only a few molecules containing substituents, whereas the ACP-M1 is derived

from PP from slurry oils. Slurry oils are highly enriched in 4-fused aromatic ring systems substituted with short aliphatic groups. These differences in the materials will cause different oxidation behaviors at various positions within molecules depending upon the structure of the aromatic unit and the number and type of substituents on the aromatic units. The connectivity of the aromatic units, substituents and geometry has a tremendous influence in the electron density within the conjugated π-systems.

Upon treating the green pitch derived fibers in an air atmosphere, several observations can be made from the FTIR spectra:

1. Decrease in aromatic-hydrogen (decrease in 900-715 cm^{-1} and 3040 cm^{-1})
2. Relative increase in carbon-carbon aromaticity (1600 cm^{-1}), a decrease in aliphatic substituents (bands centered around 2900 cm^{-1} and 1440 cm^{-1})
3. Slight decrease in sulfoxide for ACP-M1 (1034 cm^{-1})
4. Significant increase in oxygen containing carbonyl (C=O) groups (around 1775, 1730 and 1700 cm^{-1}: anhydride; aldehyde; carboxylic, aryl aldehyde or aryl ketone; respectively)
5. Significant difference in the amount of C=O amount and type between ACP-M1 and CTP6M 320SP, likely due to aliphatic content and aromatic substitution patterns in the ACP-M1
6. Significant increase in various C-O- absorption bands 1340-1030 cm^{-1}
7. Solo aromatic hydrogen (875 cm^{-1}) appear to be relatively more sensitive towards oxidation than other aromatic hydrogens, especially in the ACP-M1

Similar TGA experiments under air and nitrogen were performed using the bio-PAN green fibers. Figure 40 shows the FTIR spectra of the fibers after TGA treatment.

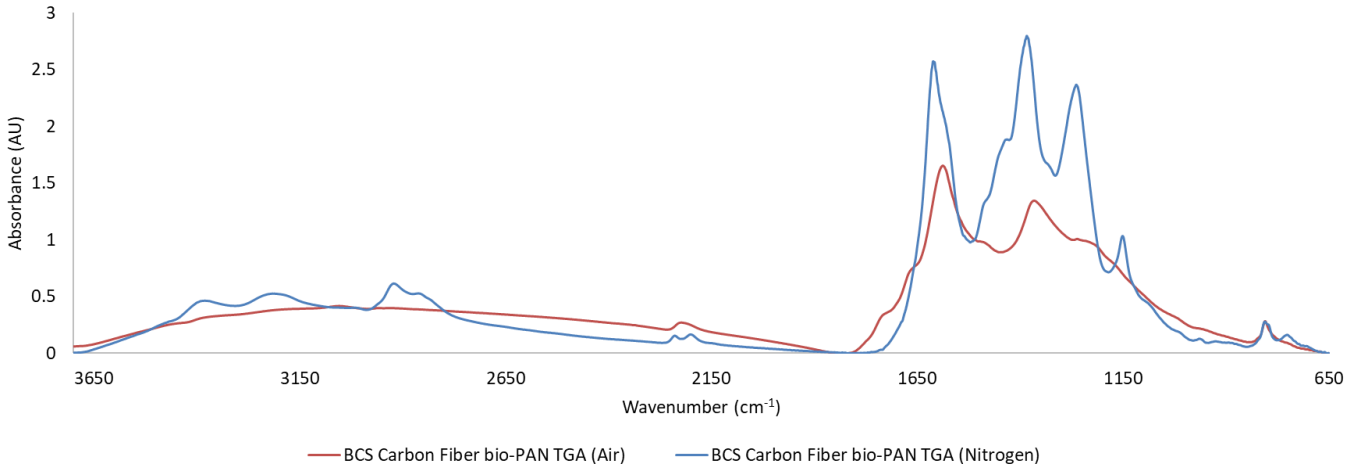

Figure 40: FTIR spectra of CTP6M SP320 after treated under air and under nitrogen in a TGA which held isothermal at 250-300C for 180 minutes.

Time of flight mass spectroscopic methods are well suited for determining the molecular weights (MW) of large molecules. The technique is often applied to studying polymers and biological based materials such as proteins, and is also likewise well suited for analysis of petroleum and coal-based materials. These materials are not amenable to analysis by gas chromatography coupled to mass spectroscopy GC-MS because of their low volatility, and analysis by size exclusion chromatography can lead to erroneous values due to self-aggregation of heavier ends. A popular type of time-of-flight mass spectroscopy is matrix assisted light desorption (MALDI), where the matrix is used to assist in the donation of a proton to the analytes. The same method can also be applied to aromatic molecules without using the matrix since aromatic molecules can be easily ionized by the laser. Operating in this manner is referred to laser desorption ionization mass spectroscopy (LDI). This method has been used to characterize various heavy aromatic hydrocarbon materials from coal and petroleum (Hortal, Martinez - Haya, Lobato, Pedrosa, & Lago, 2006; Hortal, Hurtado, Martinez - Haya, & Mullins, 2007; Sabbah, et al., 2010; George, et al., 2010). Although arguably MALDI with the appropriate matrix, or other LDI types of techniques, can give more information, especially at higher molecular weights (Pomerantz, Hammond, Marrow, Mullins, & Zare, 2009; Rogel & Moir, 2015), LDI can provide valuable insight.

Isotropic and anisotropic materials for CTP, PP and gilsonite samples were analyzed by LDI. Prior to analysis the laser power was optimized using coronene and 9,9'-bianthracene. Laser powers that are two low will lead to weak ionization and detection whereas too high of a laser power can lead to fragmentation and additional reactions to produce artificially larger material.

For the HTCTP samples, the average MW was around 290 Daltons and no significant compounds were detected below 216 Daltons and significant amounts of material was not detected above about 550 Daltons. The low end of the MW corresponds to 4-memberd fused rings and this is consistent with the distillation cut point of this material. Material around the average MW of 300 Daltons contain 6- to 7-membered rings. The major species in the HTCTP

samples are the same between the different sources except that they vary in relative concentrations (Figure 41). The spectra are very similar to HTCTP obtained by MALDI (Fan, Fei, Chen, & Li, 2017). The groupings of MW ranges are separated by 24 Daltons corresponding to 2 carbon atoms which is the minimum change needed for of adding one aromatic ring. The molecules within the grouping differ by the number of hydrogens, as isomers with different connectivity. More minor groupings are separated by another carbon. The molecular diversity within these step changes for the number of rings are also due to some methyl substituents and 5-membered rings.

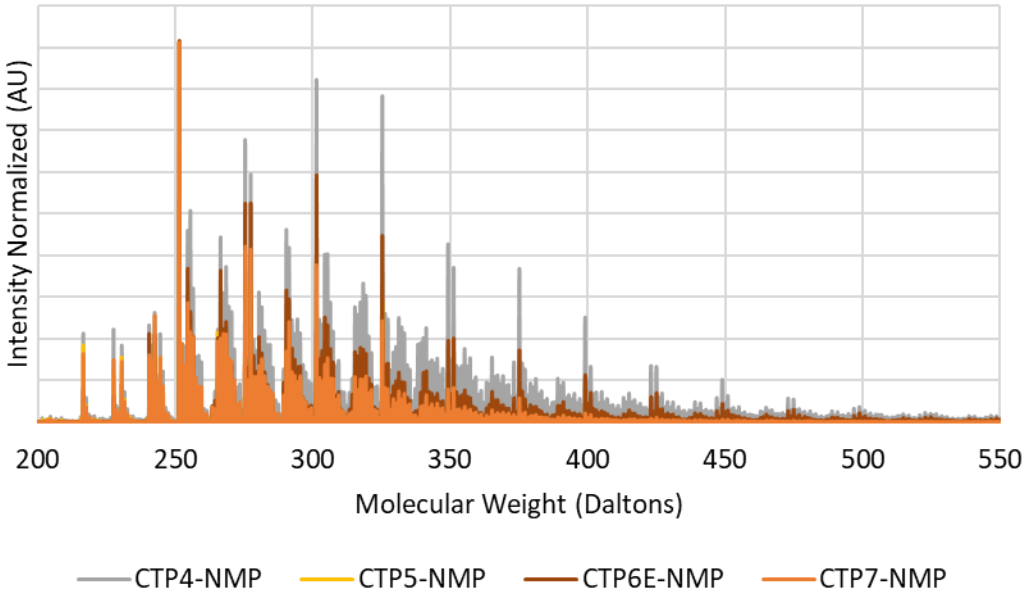

Figure 41: LDI spectra for HTCTP samples.

For the LTCTP, this material had about the same higher and lower MW ranges, however it did show relatively more material at higher MW than the high temperature HTCTP samples. Figure 42 shows the LDI spectra of CTP3-NMP and CTP6-NMP for comparison. LTCTP contained significantly more molecular diversity, which is due to the greater presence of alkyl groups, oxygen groups, and likely more prevalent C-C linkages between smaller aromatic units.

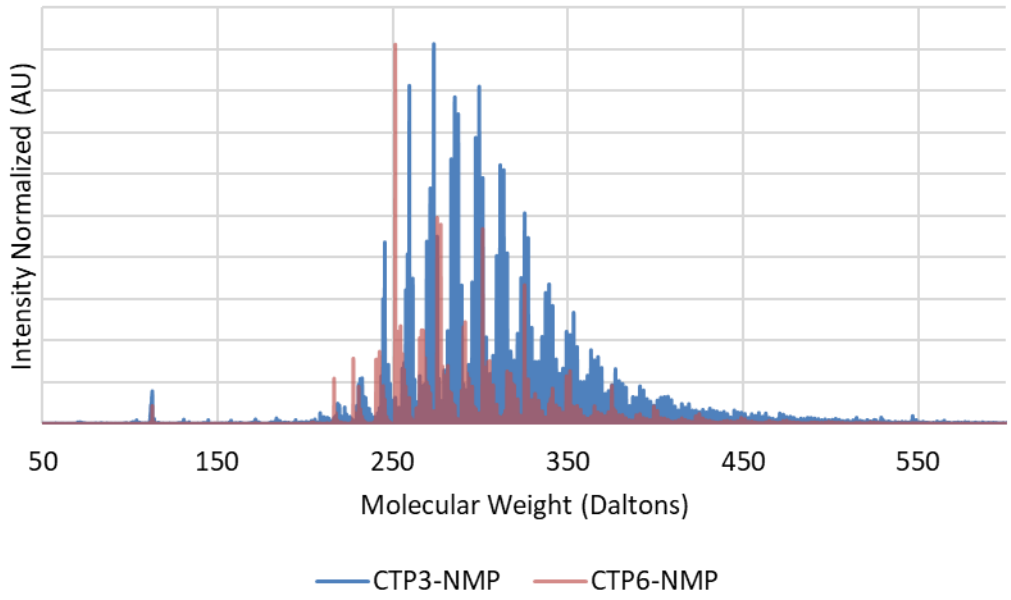

Figure 42: LDI spectra of CTP3-NMP and CTP6-NMP. Signal at 112 Daltons is an impurity present in all the samples.

When comparing the LDI spectrum between the isotropic PP and HTCTP there are drastic differences as shown in Figure 43. The PP spectra shows a multi-modal distribution with lower MW material, near the range of the bulk of the CTP material, and a significant amount of higher MW material. For PP the low MW material has an average of around 300 Daltons and the nigh MW material has an average of around 471 Daltons. This is consistent with the monomers and dimers observed by others (Thies M. C., 2014). However, the trimers and tetramers are not as apparent with LDI as with MALDI.

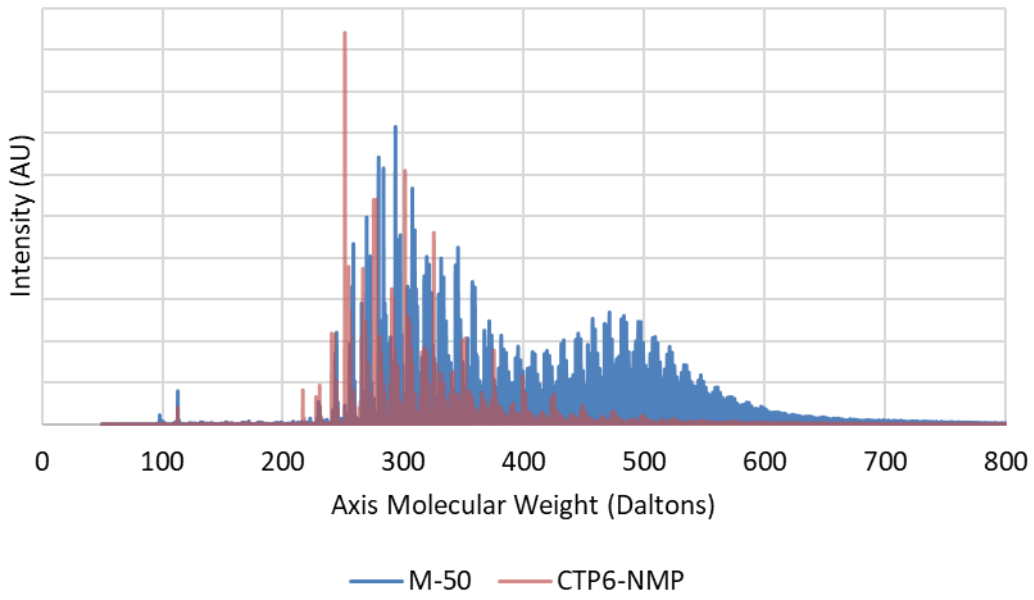

Figure 43: LDI spectra for isotropic PP M-50 and CTP6-NMP.

During mesophase conversion of PP the monomers become either distilled out or consumed, and the MW distribution of the resulting mesophase is very similar to the dimer portion of the original PP at around 470 Daltons, and trimers at around 740 Daltons become more obvious. Figure 44 shows the LDI spectrum for PP and PPM.

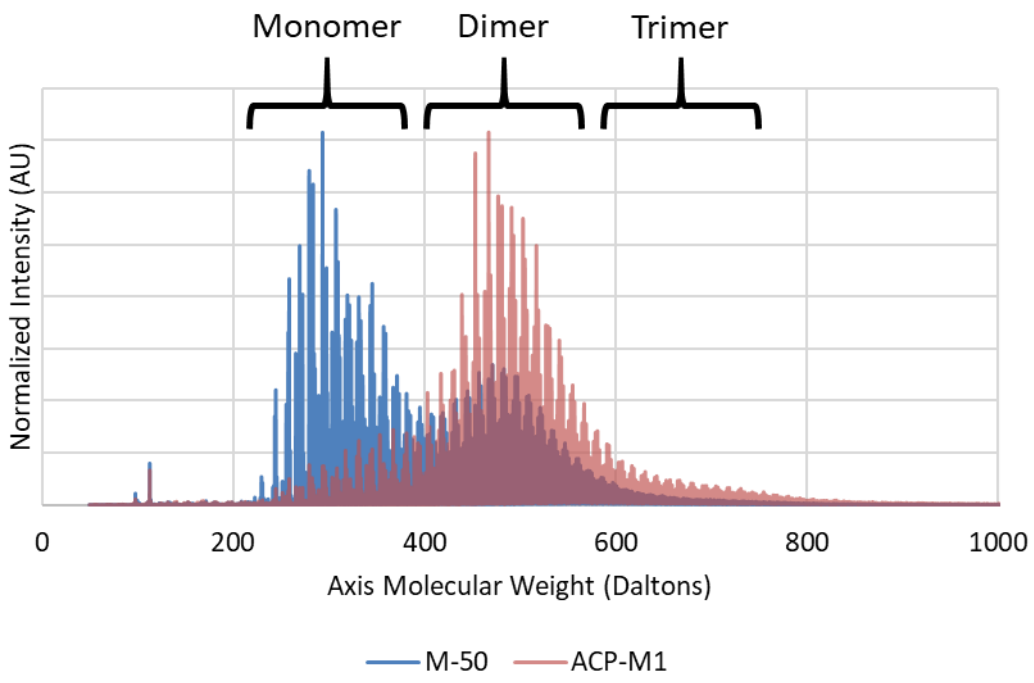

Figure 44: LDI spectra for M-50 and the corresponding mesophase ACP-M1.

Similar shifts to higher MW material upon mesophase conversion were observe for the CTP materials when converted to CTPM. In general, there was a progress to higher MW with higher levels of mesophase conversion (higher SP) for mesophase produced from CTP6-NMP. Figure 45 shows the progression in MW as the SP increases from 219.6 °C to 236.9 to 320 °C, and Figure 46 shows how the MW shifts to even higher values at higher conversion to give a mesophase of around 90+% with a SP of 333.5 °C.

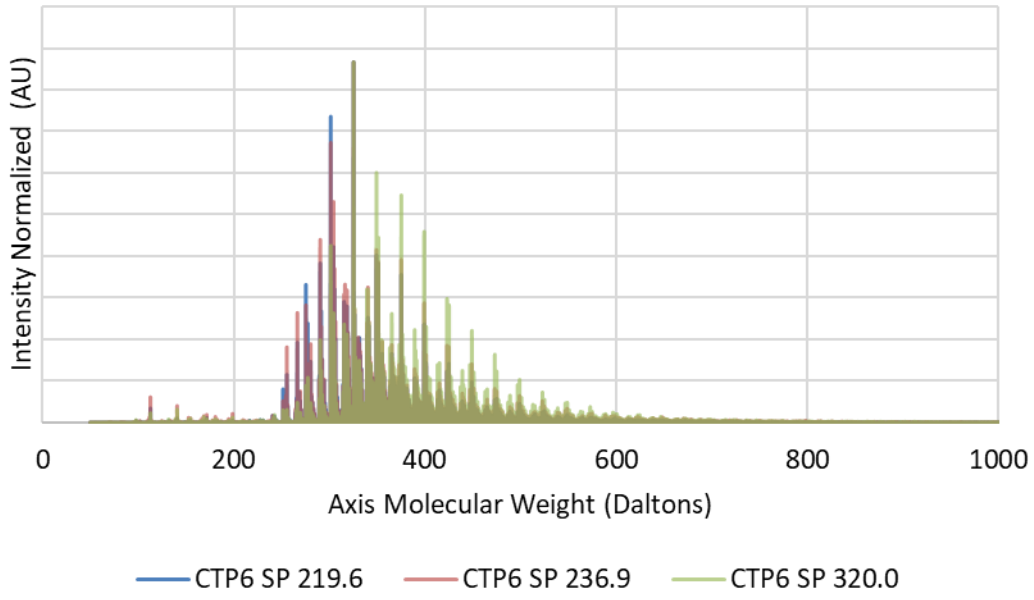

Figure 45: LDI spectra showing the progression to higher MW material during mesophase conversion to produce more mesophase and a higher SP for CTP6.

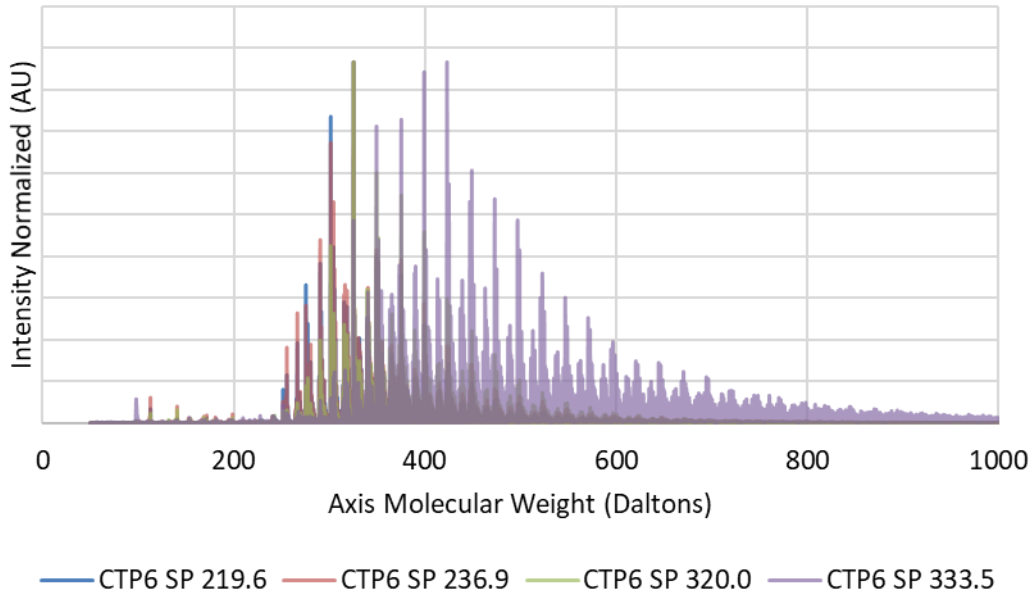

Figure 46: LDI spectra from Figure 24 also showing the highest conversion of mesophase achieved (90+%) for CTP6 with a SP of 333.5 °C.

A similar shift to higher MW was also observed for isotropic CTP7-NMP when converted to mesophase pitch with a SP of 340.2 °C. Figure 47 shows the LDI spectra for CTP7-NMP and the corresponding mesophase pitch with a SP of 340.2 °C.

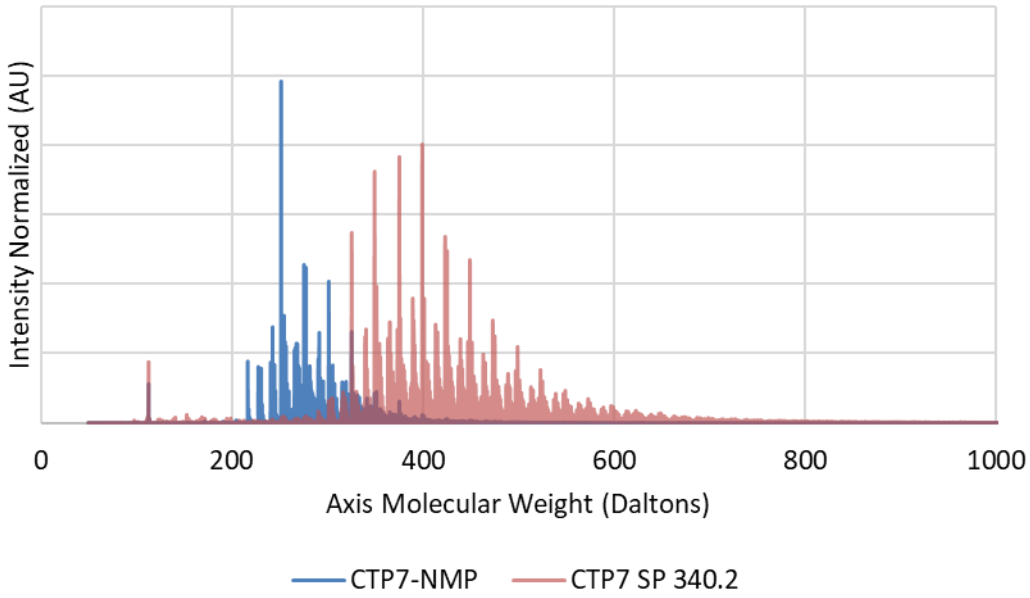

Figure 47: LDI spectra for isotropic CTP-7 and the corresponding mesophase CTP7 SP 340.2 °C.

LDI spectra for ACP-M1 was compared the CTP6 SP 320.0. Both of the mesophase samples produced CF with mechanical properties that were very similar and met the DOE targets and they had the same SP. From the LDI spectra in Figure 48 it appears that the PPM had significantly higher MW material than CTPM.

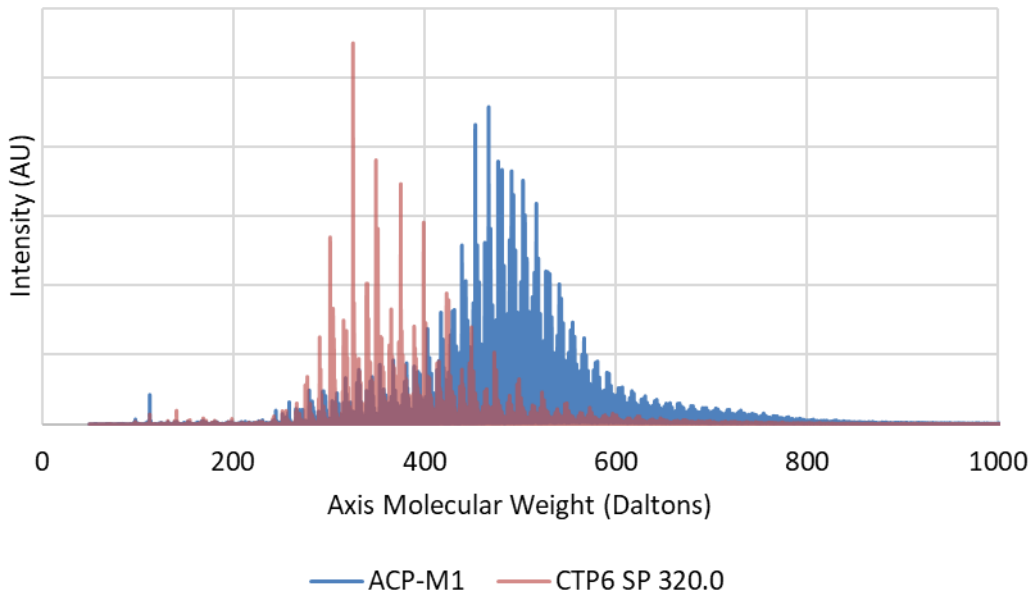

Figure 48: LDI spectra comparing PPM and CTPM.

During LDI analysis, it is likely that lower MW mesophase molecules and left-over isotropic pitch are preferentially ionized and detected in the mesophase samples. To verify this, ACP-M1 and CTP6 SP333 were added to NMP and sonicated to remove smaller MW material. After settling, the NMP solution was decanted and fresh NMP was added. The procedure was repeated several times until the NMP solutions were slightly brown. The NMP extracted solids were then dried and 1000 ppm were suspended in NMP. Despite several washes the mesophase was still sparingly soluble. A different extraction was performed using a Soxhlet extraction with NMP under nitrogen for several days until the extracts appeared nearly colorless. For the ACP-M1 extracts, LDI samples from the NMP suspension were prepared from the colored solution after allowing the insoluble material to settle, from the mixed suspension and from the solids layer after settling. These samples show a progression from lower MW material to higher MW material. Figure 49 shows the LDI spectra for the various NMP extracted ACP-M1 samples after resuspension in NMP.

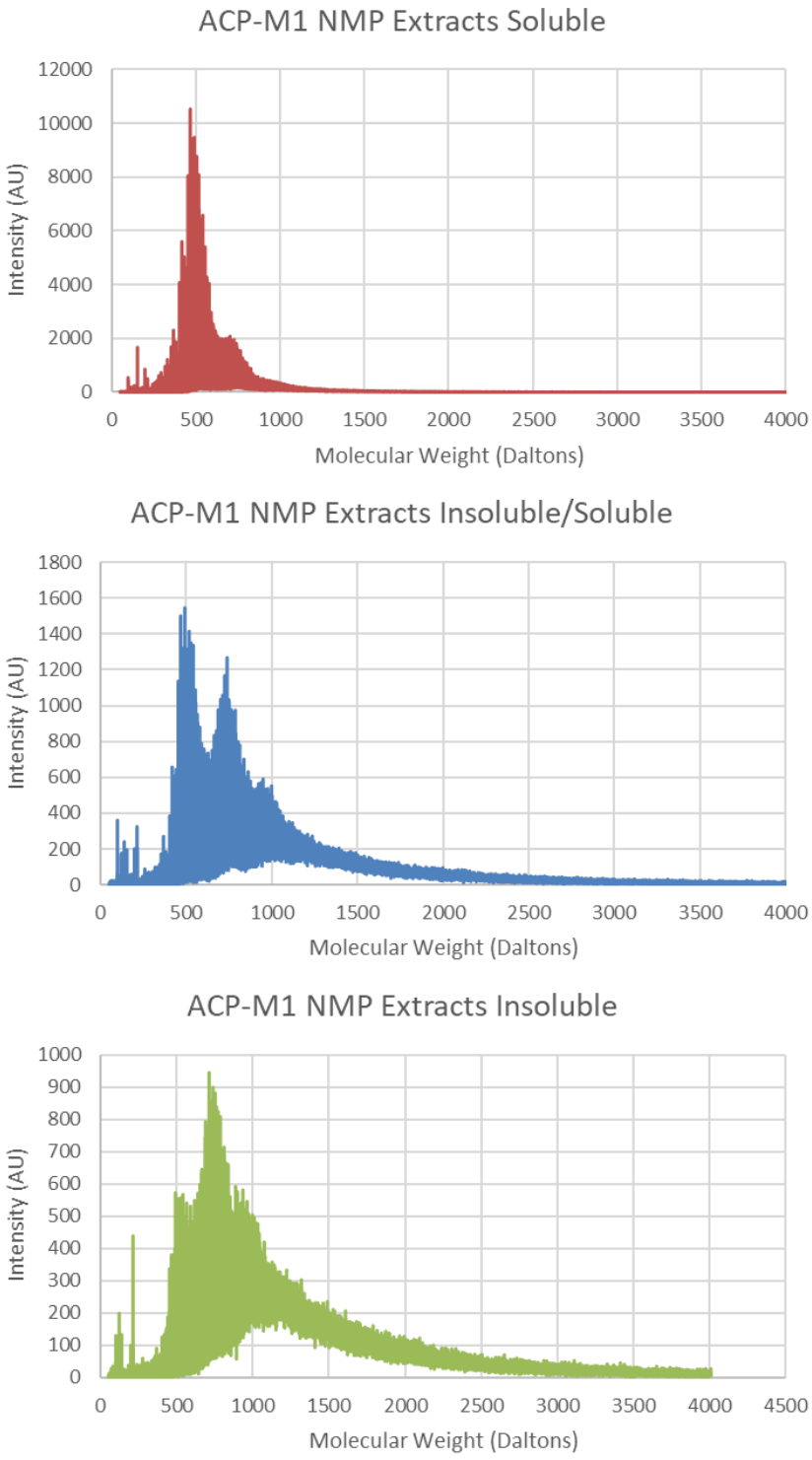

Figure 49: LDI spectra for ACP-M1 after extraction by NMP to remove lower molecular weight mesophase and isotropic pitch. The extracted material was suspended in NMP and allowed to settle. The material still soluble in NMP is shown in the top plot, that material that was not soluble in the NMP is shown in the bottom plot and the mixed-up suspension is shown in the middle plot.

From the plots in Figure 49 it is clear that the residual NMP-soluble material, after NMP extraction, was still enriched in dimeric material around 470 Daltons, but there was also a considerable amount of trimeric material centered around 740 Daltons. There is considerably more trimeric material present than compared to the whole mesophase sample. When analyzing samples prepared from the whole suspension (NMP-soluble with NMP-insoluble) there is a considerable increase in the trimeric material around 740 Daltons and also tetrameric material apparent at around 940 Daltons. Analysis of the NMP-insoluble solids showed that the dimeric material was further decreased, and the bulk of the material was trimeric and tetrameric. The significant amount of tailing in the spectra shows that there are probably some aggregates due to π-π stacking of the aromatic molecules.

A similar analysis of the CTP6M SP333 mesophase was also performed. For this sample, the NMP-insoluble material was concentrated with molecules having an average MW of around 720 Daltons (Figure 50) which is very similar to the trimeric material found in the ACP-M1 material. The LDI spectra of this least soluble portion from the CTP6M SP333 indicates that there is a more homogenous distribution of molecules in this fraction compared to ACP-M1 (not multi-modal). It should be noted that the MW of this material is significantly higher than what was present in the previous spectrum of the whole CTP6M SP333 which had an average MW of 420 Daltons. This result shows that smaller MW aromatic molecules are in fact preferentially ionized.

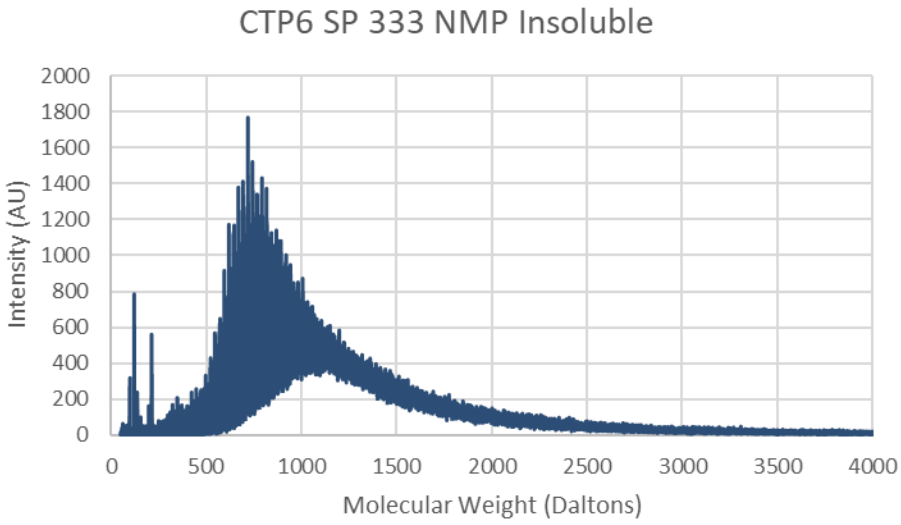

Figure 50: LDI spectrum of CTP6 SP 333 NMP-insoluble materials.

New LDI spectra were obtained using different parameters for the isotropic pitch, mesophase pitch, and soluble and insoluble mesophase fractions after extraction of the mesophases with NMP for PP and CTP materials. Spectra for the different materials various samples are shown in Figure 51. By comparing the spectra, it is clear that for CTP and PP there is a strong preferential ionization of smaller aromatic units. The preference for ionization of the smaller aromatic

molecules is more severe for the CTP as it appears that the only difference between the CTP and CTPM is the removal of smaller aromatics <300 Daltons, whereas for PP the bulk of the monomers are clearly absent in PPM. After extraction of the mesophase with NMP and then taking up the extracted samples in NMP very significant differences are observed in the LDI spectra. CTPM NMP-solubles after extraction now have an average MW around 448 Daltons and the insolubles have an average MW around 870 Daltons. For PP, the NMP-solubles after extraction contain dimers (average MW ~492 Daltons), trimers (average MW ~713 Daltons), tetramers (average MW ~974 Daltons) and higher MW species, and the insolubles contain very little dimers and trimers and is dominated by trimers (average MW ~995 Daltons), tetramers (average MW ~1201 Daltons) and higher oligomers.

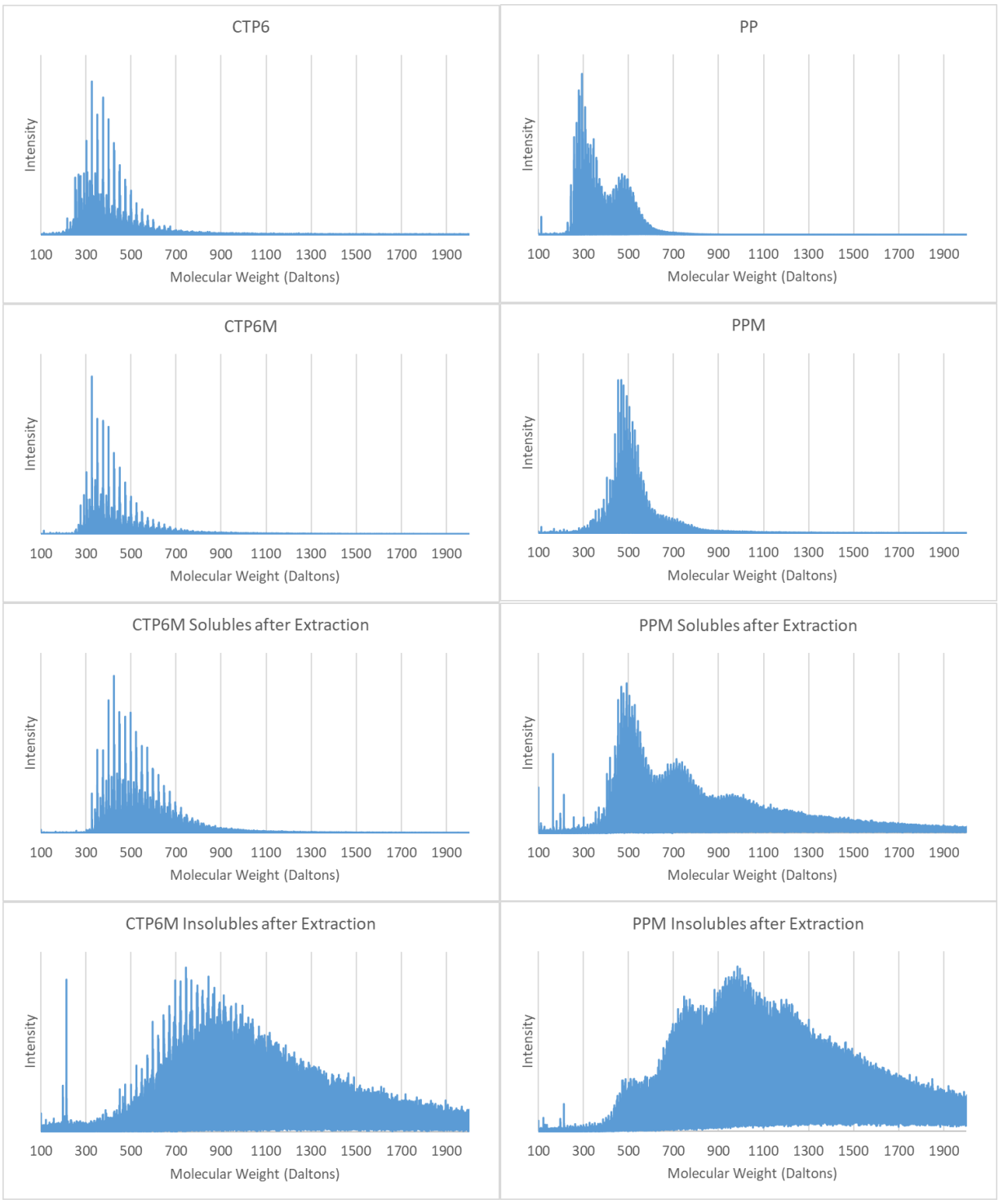

Figure 51: LDI spectra for isotropic pitch, mesophase pitch, and NMP soluble and insoluble mesophase fractions after extraction mesophase extraction with NMP for PP and CTP materials.

Fluorescence spectroscopy is a technique which detects molecules which have the ability to absorb photons near the IR region thought the UV region while generating photons at a different wavelength within the region. The region of photons that are usually of most interest are

wavelength falling within the visible region or those in the UV region up to about 250 nm. Fluorescence spectroscopy is highly sensitive and has a long history of being used to detect aromatic compounds in petroleum, coal, industrial quality control and for a variety of commercial and environmental applications. Pure aromatic compounds will display very distinct fluorescence emission spectra with some materials showing very broad featureless spectra while others will show much sharper spectra with multiple distinct features. Analysis of petroleum and coal liquids on the other hand, usually generate broad featureless spectra, because these spectra are the average over many different types of rings structures and different isomers for molecules with the same number of rings. Not only can fused aromatic rings have different isomers through connectivity (e.g. linear, cata-condensed and peri-condensed) affecting their fluorescence, but they can have fused ring systems where the conjugation is broken by the presence of 5-membered rings (alternant vs non-alternant) can cause quenching of the fluorescence making these molecules invisible by fluorescence (Zander, 2000). Furthermore, similar aromatic ring structures can be very different due to the presence of varying aliphatic or aromatic substituents which can be at different positions on the same fused ring system. Likewise, the same is also true when these materials contain heteroatoms in the form of various functional groups at various positions.

From a useful and perhaps over simplified analysis, previous work showed that the increasing molecular size of CTP molecules (larger fused ring systems), which were separated by sized exclusion chromatography, resulted in a linear increase in the emission maxima by fluorescence spectroscopy (Figure 52) (Zander & Haenel, 1990). Additionally, tars extracted from coals of varying maturity also become red shifted due to presumably larger conjugated condensed aromatic structures, and the trend was also confirmed with SEC (Li, Wu, Cai, & Kandiyoti, 1994) of the tars and from work by others (Herod & Kandiyoti, 1995; Islas, et al., 2003; Kraca, et al., 2009), for petroleum (Al - Muhareb, Morgan, Herod, & Kandiyoti, 2007) and asphaltenes of increasing size (Roenzin & Mullins, 2000; Mullins, 1998) and during the conversion of PP to PPM (Kershaw, 1995). Therefore, a similar type of analysis was used for the various CTP, PP and gilsonite materials.

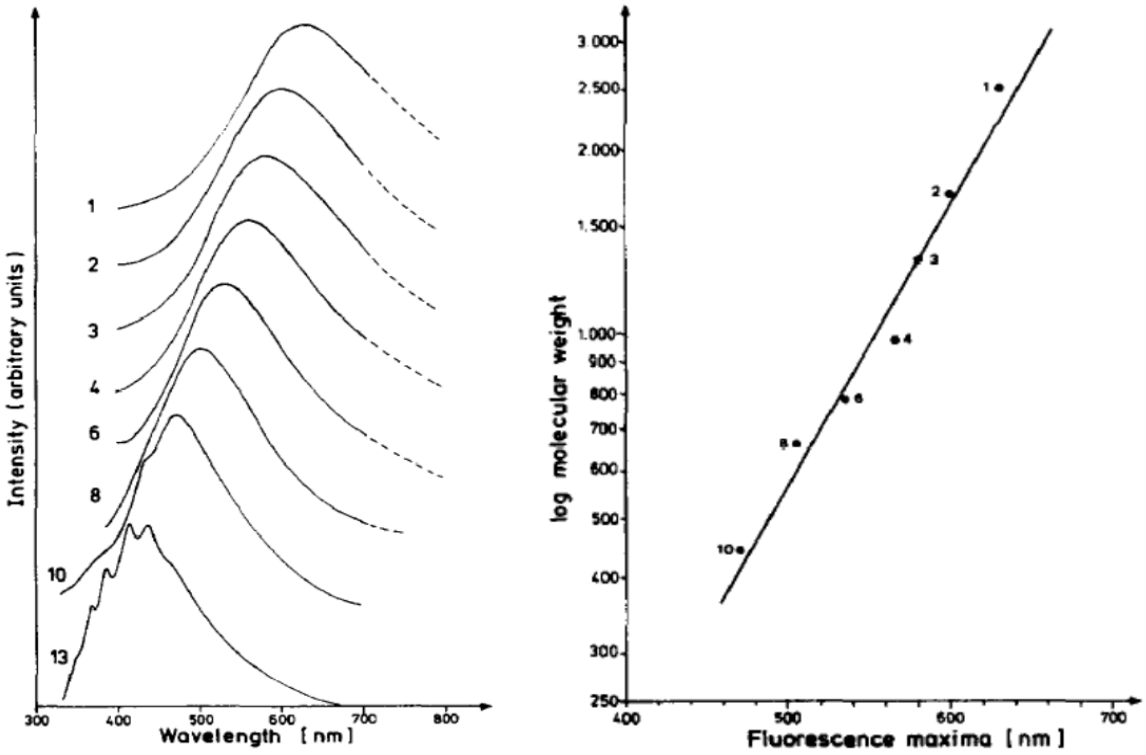

Figure 52: Relationship between size of CTP molecules and the emission maximum for fluorescence spectroscopy (Zander & Haenel, 1990).

Because of the complexity in the number of different molecules often present in petroleum and coal, there can be a range of wavelengths that correspond to different ring structures and the overlap between emission regions usually increases with the number of fused rings. This increasing overlap is because the number of possible isomers also increases with increasing number of fused rings. Figure 53 shows some general ranges corresponding to number of fused rings for petroleum and coal materials.

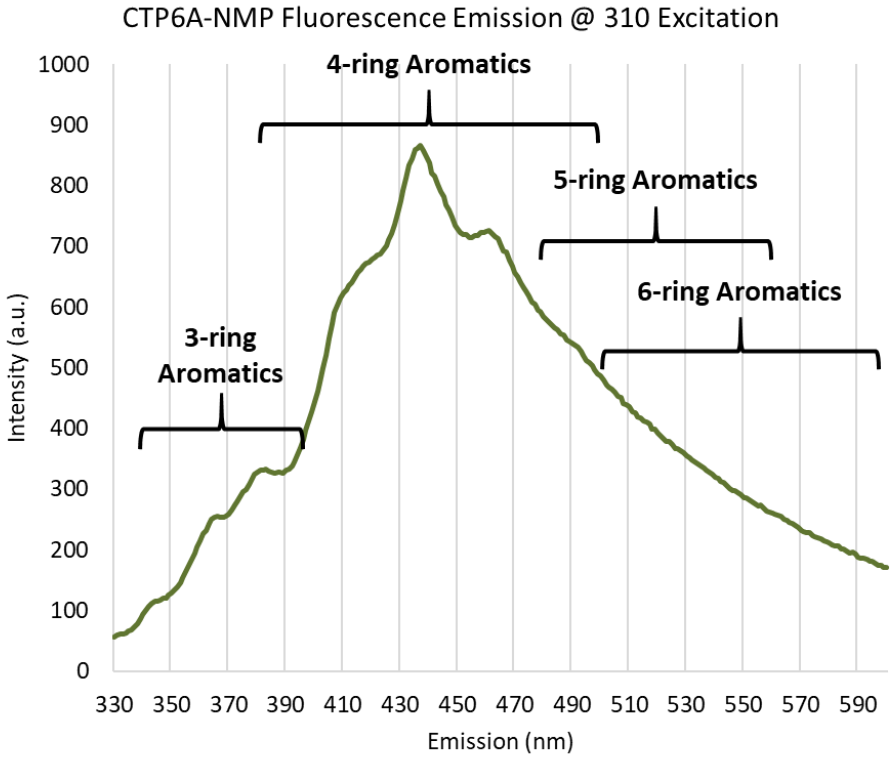

Figure 53: Fluoresce spectra for CTP6A-NMP while dissolved in NMP. The emission was recorded using an excitation wavelength of 310 nm. Ring assignments are based off of synchronous spectral data (Scotti & Montanari, 1998), other non-synchronous data of non-heteroatom containing aromatics suggests 370 nm corresponds to roughly 3 ring aromatics while an emission maximum around 430-500 nm corresponds to 7-11 rings (Mullins, 1998).

During mesophase conversion if isotropic CTP and PP materials, lighter more volatile smaller fused ring aromatic molecules become liberated in the effluent gas and aromatic rings begin to crosslink to form larger aromatic ring molecules. This trend is general as there are many other different types of ring opening reactions that can liberate smaller aromatic ring structures which also occurs in conjunction with cyclization and aromatization of aliphatic side chains and aromatic pendant groups. These various changes can be monitored by fluoresce spectroscopy (*Note: solution fluorescence spectroscopy has some limitation when it comes to characterizing mesophase because not all of the mesophase is soluble in the solvent*). As the average number of molecules with larger fused ring structures increase it is expected that there will be a likewise shift in the fluorescence spectrum of the materials towards higher wavelengths (red-shifted). This can easily be shown by mapping the excitation and emission spectra for the isotropic materials relative to their corresponding mesophase materials. This has been done in Figure 54 which shows that over a range of excitation wavelengths the maximum of the emission spectra becomes more red-shifted. Interestingly, the most intense set of emission spectra are also at different excitation wavelengths. For M-50 the most intense emission spectra occurs with a 310 nm excitation while for ACP-M1 the most intense emission spectra occurs using about at 350 nm excitation. This is consistent with the fact that larger aromatic molecules are usually more

efficiently excited using longer wavelengths. The excitation and emission matrix can also be view by looking at the data in a topographical layout. Figure 55 shows the data in Figure 54 as a topography plot.

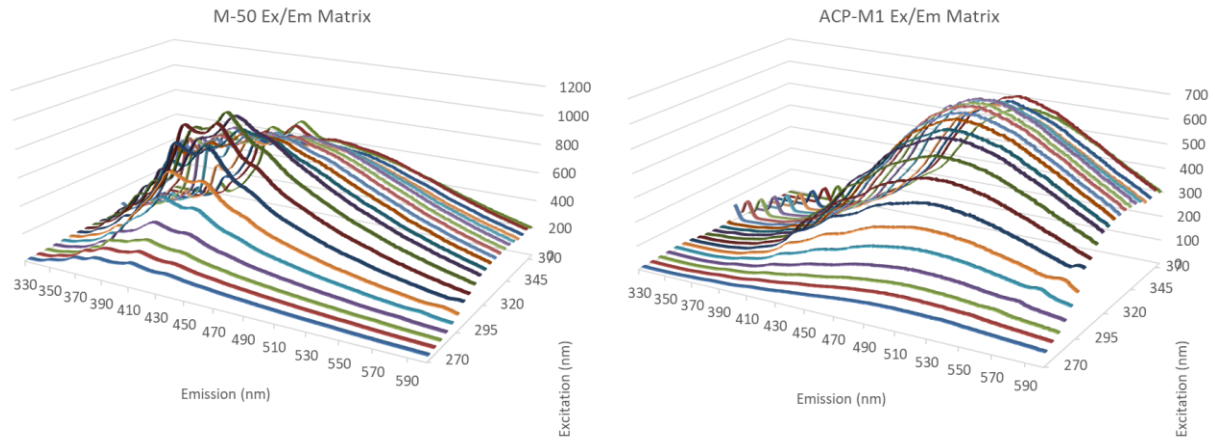

Figure 54: Fluorescence excitation and emission matrix for isotropic PP M-50 (left) and the corresponding anisotropic mesophase ACP-M1 (right).

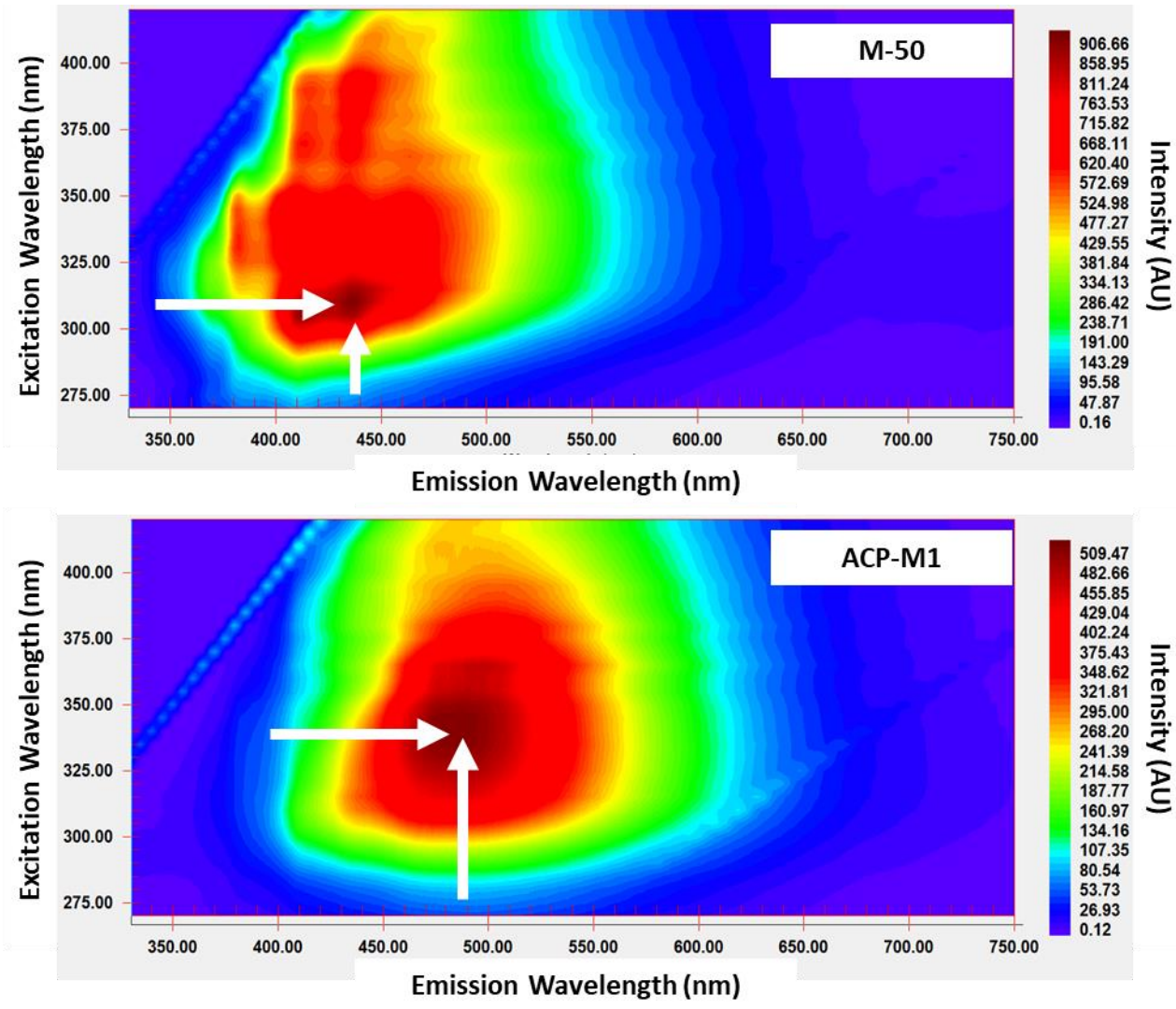

Figure 55: Fluorescence excitation and emission matrix shown as a topographical plot for isotropic PP M-50 (top) and the corresponding anisotropic mesophase ACP-M1 (bottom). The white arrows point to the wavelengths with the highest density of highest intensity in the emission spectra.

A similar shift in the excitation and emission is also observed for the isotropic CTP6-NMP and corresponding mesophase with a SP of 320.8 °C, as show in the topographical plot in Figure 56. Interestingly, in the case of both the PP and CTP materials, for the NMP-soluble portion, there appears to be a more homogenous distribution of molecules after thermal treatment to form the mesophase. This is most clearly inferred by the decrease in highly fluorescing molecules which occur at excitation wavelengths between 350 and 400 nm with emission wavelengths between 400 and 450 nm. This observation is consistent with the fact that the organization of liquid crystalline anisotropic material, produced from aromatic molecules, is enhanced if the molecules are more uniform as this will allow for more efficient stacking of the molecules.

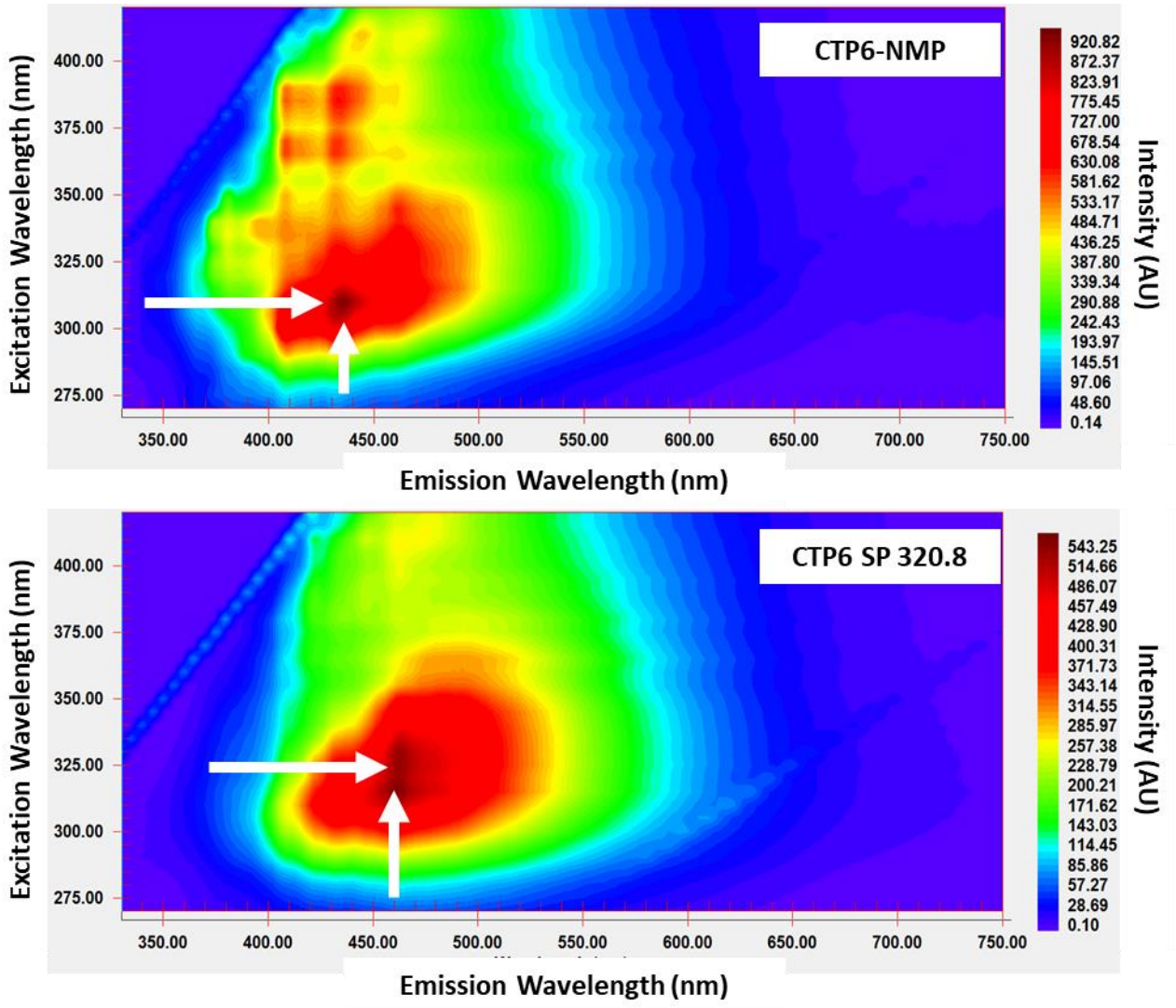

Figure 56: Fluorescence excitation and emission matrix shown as a topographical plot for isotropic CTP6-NMP (top) and the corresponding anisotropic mesophase with a SP of 320.8 °C (bottom). The white arrows point to the wavelengths with the highest density of highest intensity in the emission spectra.

From comparing the emission spectra of the HTCTP isotropic and mesophase samples, collected using a 310 nm excitation, some trends in material changes during mesophase formation could be determined. For simplicity, Figure 57 shows the emission spectra of CTP6-NMP and corresponding mesophase samples reacted to give increasing amounts of mesophase (increasing SP). From this plot it can be seen that the intensity of the band at around 435 decreases while the band at around 461 increases. This shift towards the red (increasing wavelengths) is an indication of a reduction of smaller aromatic rings for larger aromatic rings, as is expected during mesophase conversion. As shown in Figure 58, there appears to be a reasonable correlation between all of the high temperature isotropic CTP materials and mesophase samples at various levels of conversion. This is consistent with work performed on PP conversion to PPM (Kershaw, 1995).

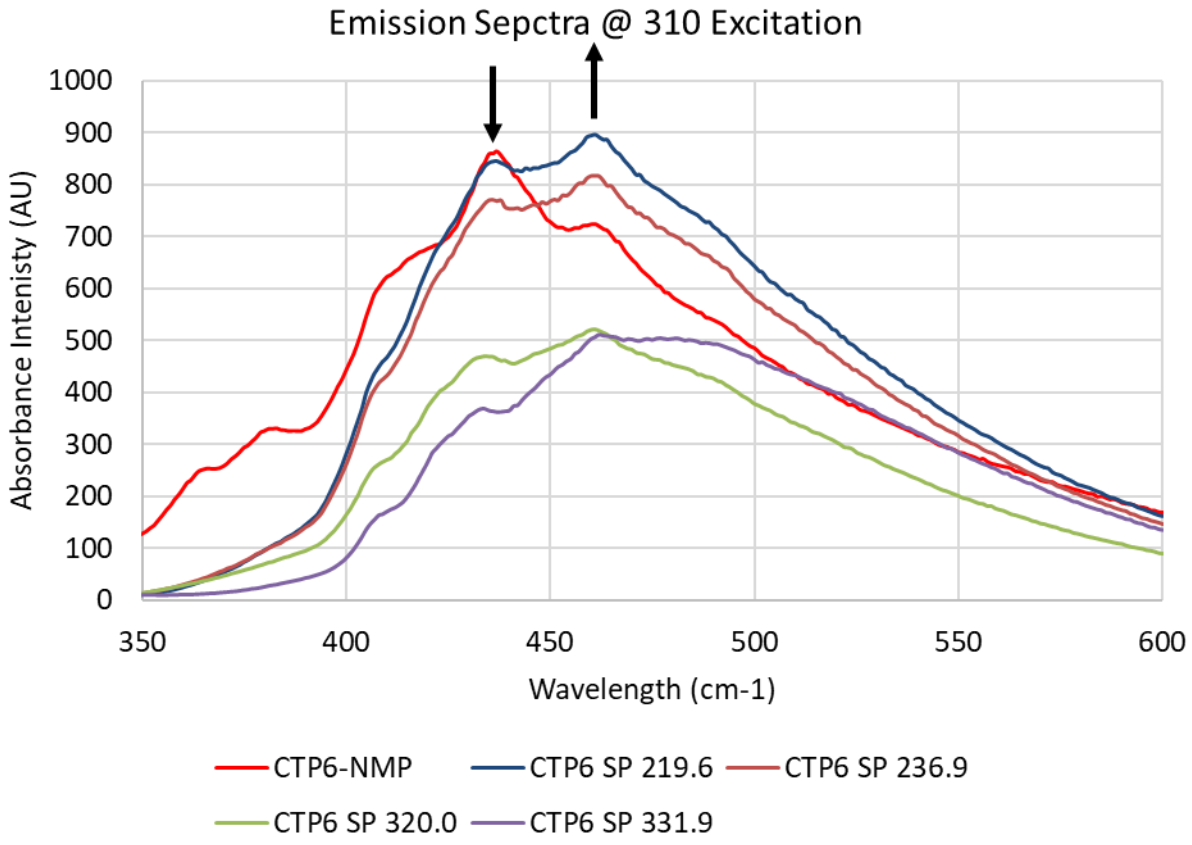

Figure 57: Fluorescence emission spectra collected using an excitation of 310 nm for CTP6-NMP and the same material converted to various levels of mesophase (increasing mesophase content with increasing SP). Band at 435 and 461 nm are marked.

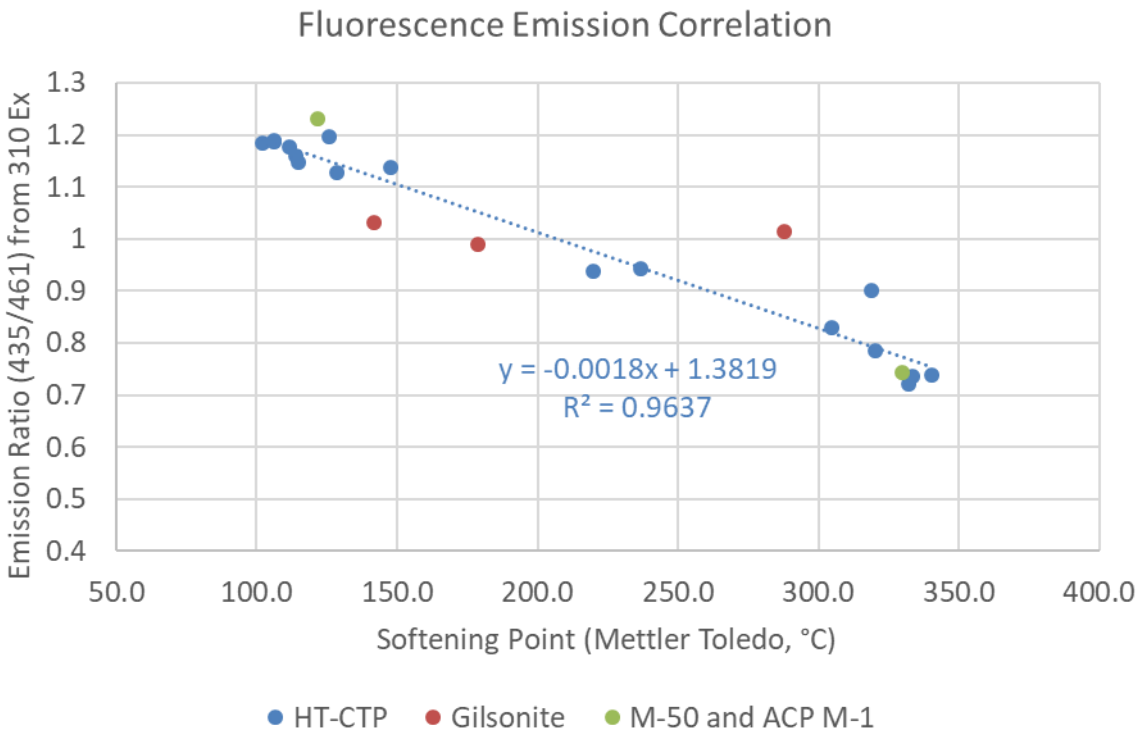

Figure 58: Comparison of the intensities for 435/461 ratio obtained from the emission spectra collected at 310 nm for the various isotropic and mesophase materials. Correlation in blue only shows the data for the high temperature (HT) CTP (excluding CTP3) isotropic and mesophase pitch.

Similar red-shifts in the fluorescence spectra can also be observed using synchronous fluorescence spectroscopy (SFS). SFS methods have been used to quantify the amount of fused ring aromatics in a variety of solvents and mixtures. This method scans both the excitation and emission wavelengths simultaneously where the difference in these wavelengths ($\Delta\lambda$) are held constant. By applying this technique, it is possible to identify and quantify various fluorescing PAHs in a mixture (Songasasen, Bangkedphol, & Pornsinlapatip, 2002; Li, et al., 2011; Lloyd, 1971). This often requires optimizing the $\Delta\lambda$ for each kind of PAH. For work on petroleum and coal materials the synchronous spectra can provide cut points between wavelengths corresponding to the number of rings in fused aromatic molecules. The concepts is similar to that shown above in Figure 53. These ranges vary depending upon various references; however, some useful ranges are:

- At $\Delta\lambda = 3$; one ring from 260-300 nm, two ring from 300-330, three ring from 340-400, four ring from 380-500, five ring from 480-560 nm and six ring from 500-600 nm (Scotti & Montanari, 1998)
- At $\Delta\lambda = 23$; one ring from 280-290 nm, two ring from 300-320 nm, 3-4 ring from 340-380 nm and 5+ ring >400 nm (Wakeham, 1977)

It is not expected that the CTP and PP samples would contain a significant amount of material below 300 nm since these materials have been distilled to remove most material containing 1-2 aromatic rings. In fact, this was true for all the isotropic CTP and M-50 samples. Depending upon the Δλ chosen different wavelengths can have a higher intensity as shown in Figure 59 (Δλ between 3 and 5 – 40 nm at 5 nm increments were investigated). Regardless of the Δλ chosen all the isotropic pitch materials showed significantly more intense bands at lower wavelengths than the corresponding mesophase samples. For example, for Δλ = 25 nm the band at around 400 nm is significantly more intense relative to the rest of the SFS spectra for the same material but with increasing mesophase conversion this band decreases in favor of the 450 nm band. This is similar to the Δλ = 30 nm has been found to be useful to provide a characteristic fingerprint of coal extracts (Clark, et al., 1987). This is consistent with a shift from 3-4 rings to 5+ ring systems. Shifts to higher MW mater following this same trend has also been observed by others (Menendez, et al., 2001) between CTP and CTPM and by severe air blowing of CTP and for PPM (Kershaw, 1995; Menendez, Blanco, Santamaria, Dominquez, & Blanco, 2002). A similar shift from smaller aromatics to larger aromatics was also observed for PP M-50 and ACP-M1, as shown in Figure 60.

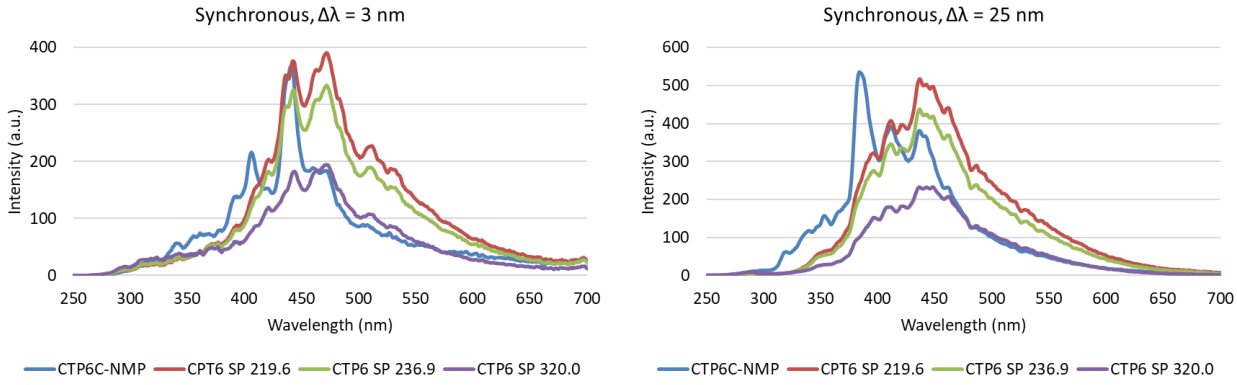

Figure 59: SFS spectra for CTP6-NMP and the material converted to mesophase pitch with increasing mesophase content (increasing SP) at a Δλ = 3 nm (left) and Δλ = 25 nm (right).

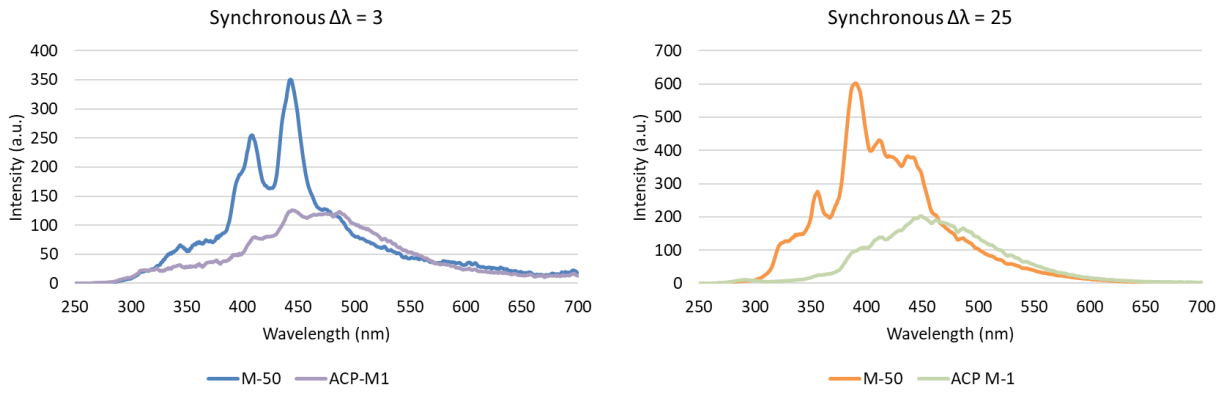

Figure 60: SFS spectra for PP M-50 and the material converted to mesophase ACP-M1 at a Δλ = 3 nm (left) and Δλ = 25 nm (right).

During the investigation of mesophase conversion, it was found that CTP7 (Koppers/China) and CTP 6 (Kopper/North America) pitches had significantly different reactivity to form mesophase. In the case of CTP7 it formed mesophase more quickly than CTP6. Based on CHNOS, SAR-AD, LDI, and FTIR data these pitches are very similar. By elemental analysis, it was shown that CTP7 is slightly less aromatic that CTP6 and contained slightly more oxygen. By SAR-AD analysis, CTP7 had more polar aromatic resins and asphaltenes but less chlorobenzene-insolubles. One of largest differences between the two is that CTP7 has significantly less primary QI (8%) than CTP6 (13%). This is reflected in the fact that coal coking oven in China operate differently than those in North America. It was also determined that CTP7 contains a larger fraction of higher molecular weight, or more associated, molecules than CTP6, which is consistent with CTP7 containing more asphaltenes. This was determined by performing size exclusion chromatography (SEC) in NMP as the eluting solvent and using only the NMP-soluble fractions from the two pitches for the analysis. Figure 61 shows the SEC chromatograms for the NMP soluble material from CTP6, CTP7 and M50 while eluting with NMP. During an SEC separation, quicker eluting material has a smaller molecular weight since it has a low residence time in the pore structure of the column packing material. From the chromatograms in Figure 61 it can be seen that CTP7 contains more, higher molecular weight material (lower retention time). Starting out with a greater amount of larger molecular weight molecules should reduce the amount of reaction time needed to convert CTP7 into mesophase, relative to CTP6.

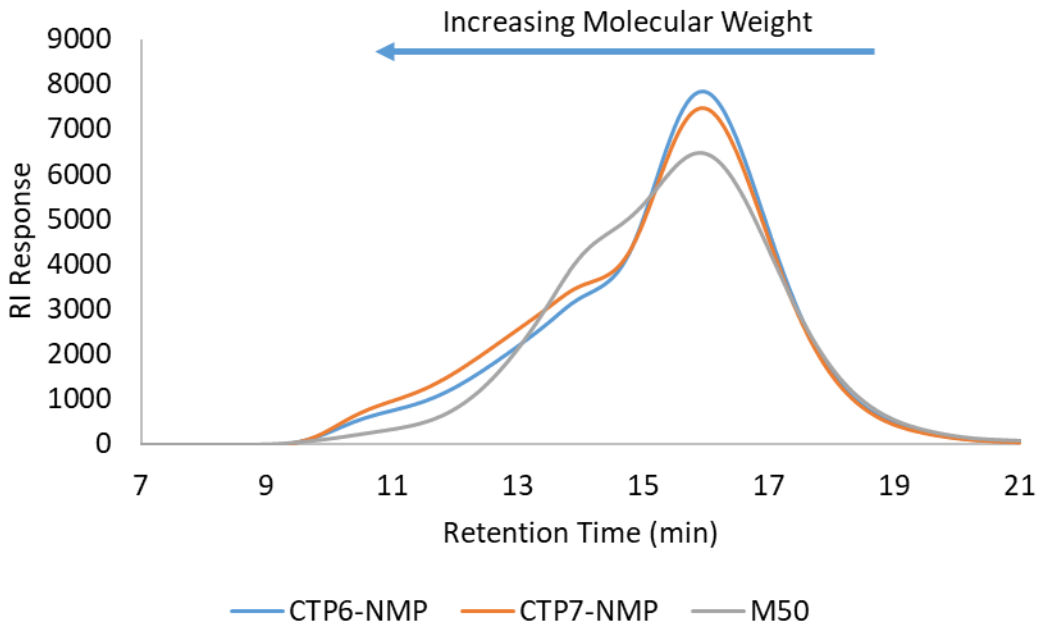

Figure 61: SEC chromatograms for CTP6-NMP, CTP7-NMP and M50 in NMP. Note "-NMP" designation means that the samples have already been filtered from NMP to remove the primary QI and distilled to remove NMP.

Bio-ACN and Bio-PAN

Bio-ACN was produced from sugars using a process developed by SRI and the process was scaled up during the course of this study. To help with the scale up, different impurities in several different biomass sugar feedstocks were identified as inorganic and organic and these compounds were tested for their effect on the efficiency of the bio-ACN process. Analyses were performed to map the various impurities found in biomass (woody, agricultural residue, and energy crops), relative to the various catalytic processes used to produce the sugars and eventually bio-ACN. If higher tolerances of impurities can be processed this would result in a cost savings by being able to use less pure and cheaper sugars. A minimum tolerance of various impurities (related to biomass and process conditions) will be established that ensure proper formation of ACN, PAN, and PAN-based CF at the lowest possible costs. It was the goal of this study to understand how these various impurities impacted bio-PAN quality and resulting CF properties. However, it was determined that producing a bio-ACN that contained ≥ 99.26% bio-ACN, ≤0.38% acetonitrile and ≤0.36% water was sufficient in quality to produce a stable bio-ACN that polymerized sufficiently to produce CF that meet DOE targets. The final target bio-ACN impurity level targets are shown in Table 21.

Table 21: Bio-ACN impurity targets.

Acrylonitrile (wt %)	99.4
Water (wt %)	0.3
Acetonitrile (wt %)	0.3

Impurities are found either in the biomass feedstocks (9 different biomass feedstock considered) and/or are introduced during biomass processing to extract the sugar (primary feedstock for acrylonitrile). Accounting for both, a concentration range (lowest to highest) was determined for each impurity. Following this determination, sugar feed solutions were spiked with each of these impurities (one at a time) at the maximum listed concentration to test the maximum impact that it can have on the bio-ACN production process.

Each test is conducted for a period of 2 to 3 days, on continuous a basis, liquid samples are collected and tested (ICP-MS for inorganic and HPLC/GC/GC-MS for organic) to determine breakthrough curves for impurities. Additionally, products are analyzed on HPLC to gauge the impact of impurities on catalyst activity.

Tested inorganic impurities showed no impact on bio-ACN production—particularly in terms of activity and durability of the catalyst. A unique trend was observed in the case of Na, Ca & Mg, in which higher concentrations of these metals were measured in the product stream than the feed. As a result of this observation water leaching test was performed on the fresh catalyst. ICP-MS results from this test reveal that Na, Ca and Mg leach out from the catalyst surface during the reaction, which is the cause for the significantly higher concentration of these metals in the product stream than in the feed. Nonetheless, the highest concentrations of these metals, observed in the product stream, are significantly below the acceptable levels in the finished product.

Organic impurities tested (formic acid, acetic acid, levulinic acid, hydroxymethylfurfural (HMF), furfural, glycolic acid, vanillin, syringaldehyde and benzoic acid) showed no impact of these impurities on the catalyst activity. Furthermore, the highest level of impurities was tested to be able to trace and analyze samples and realize maximum impact (in other words accelerated aging tests) on catalyst performance. However, it must be noted that the processed biomass derived sugars, which are used as feed material for this conversion process, typically contain lower levels of impurities than mentioned in Table 21, and as such they already meet ACN product specifications.

The "Bioenergy Feedstock Library" (https://bioenergylibrary.inl.gov/), prepared and compiled by the U.S. DOE and Idaho National Laboratory, has a comprehensive list of different biomass feedstocks and their impurity levels. This reference was used to select nine different biomass feedstocks. The percent of convertible sugars, lignin and inorganic impurities of these biomass feedstock were used to determine the three best candidates which are highlighted in Table 22.

Table 22: Inorganic impurities and their concentration in different biomass samples.

	% SiO_2	% Al_2O_3	% TiO_2	% Fe_2O_3	% CaO	% MgO	% Na_2O	% K_2O	% P_2O_5	% Cl
Corn Stover	3.09	0.17	0.01	0.083	0.42	0.24	0.03	0.95	0.13	0.04
Sugarcane Bagasse	5.49	0.5	0.03	0.166	0.19	0.09	0.09	0.31	0.07	0
Switchgrass	3.64	0.06	0	0.07	0.79	0.53	0.06	0.9	0.36	0.1
Wheat Straw	3.2	0.15	0.01	0.164	0.6	0.15	0.06	0.85	0.12	
Miscanthus	2.94	0.04	0	0.05	0.56	0.25	0.01	0.32	0.18	0.01
Sorghum	2.08	0.07	0	0.033	0.17	0.27	0.01	0.82	0.19	0.26
Hybrid Poplar	0.09	0.01	0	0.006	0.22	0.06	0.01	0.2	0.05	0
Grass Clippings	3.42	0.15	0.01	0.066	0.52	0.14	0.02	0.71	0.29	0
Lodge Pole Pine	0.38	0.04	0	0.059	0.09	0.03	0.06	0.07	0.01	0

For the production of Acrylonitrile, biomass feedstock needs to be processed via pretreatment and hydrolysis to extract the sugars. This processing step introduces additional organic impurities (Table 23). Commonly used hydrolysis methods include acid (HCl, H_2SO_4) hydrolysis, liquid hot water hydrolysis and enzymatic hydrolysis. Depending on the chemicals used and the concentration levels during pretreatment and hydrolysis, the levels of some organic impurities listed in Table 23 could vary from their respective levels in the biomass.

Table 23: Biomass Organic Impurity and Hydrolysis Summary

Wheat straw	Corn Stover Biomass	Sugar Cane Bagasse	Sorghum Straw	Hybrid Poplar
furfural	Acetate	Furans	Furfural	Aliphatic acids
acetic acid	HMF	Phenolics	acetic acid	Furans
formic acid	Furfural	Acetic Acid		Aromatic acids
	Phenolics			Furfural
				HMF

The biomass-based impurities, and the impurities resulting from biomass processing to sugar, have been accounted for when determining the concentration range of each impurity (Table 24and Table 25). Using the maximum levels listed in Table 24 and Table 25, sugar solutions were spiked with each impurity, one at a time, and tested for the resulting effect on catalytic activity. This will determine the maximum impact of each particular impurity on the process. Catalyst performance was tested for > 32 hours. Aside from analyzing catalytic performance, HPLC/GC/GC-MS, ICP-MS analysis was conducted on the product solution to determine what percentage of the feed impurities carried over into the product.

The results from Table 24 show that the catalytic activity is unaffected at the highest impurity levels which highlights the durability of the process in presence of these impurities. For Fe and K, nearly 100% of the impurity was observed in the product stream. For Si, P, Cl and Ti, there was also no significant impact on catalytic performance and nearly 0% of these impurities were observed in the product stream. For Mg, Ca and Na, the concentration of these impurities was higher in the product stream than what was injected in the feed stream. To understand this result, a catalyst leaching test was performed using pure water and fresh catalyst under the same operating conditions for 96 hours. ICP-MS results from this test indicate that the higher concentrations observed in the product stream is the result of these metals (Mg, Ca, Na) leaching from the surface of the catalyst. This explains the higher concentrations in the product stream. Nonetheless, the highest concentrations of these impurities observed in the product stream are significantly below the maximum allowable levels in finished product. The lowest levels of impurities generally found in commercial sugar feedstocks, as shown in Table 24, will not impact product specification since they occur at lower than specified.

Table 24: Range of inorganic impurities in biomass derived sugar, tested concentration for effect on production, percentage of feed impurities obtained in the product and resulting effect on performance. The numbers listed in column 2 and 3 correspond to the levels in pure sugar solution. The samples were analyzed using ICP-MS.

Impurity	Range of impurities in sugar (ppm)		Experimentally tested (ppm) with 10% sugar solution	% of feed impurity in the product	Remarks
	lowest	highest			
Fe	0.4	101	10.1	100%	Catalyst activity not affected
K	0.002	50	5.0	88%	Catalyst activity not affected
Si	0	2180	218.0	9%	Catalyst activity not affected
Mg	0.002	4	0.4	379%	Catalyst activity not affected Mg leaching from catalyst
Ca	0.006	8	0.8	960%	Catalyst activity not affected Ca leaching from catalyst
P	0.0004	100	10.0	0%	Catalyst activity not affected
Cl	0.0009	60	6.0	7%	Catalyst activity not affected
Ti	4.0	19	1.9	0%	Catalyst activity not affected
Na	0.0003	1.8	0.18	1452%	Catalyst activity not affected Na leaching from catalyst

The lowest amounts of organic impurity listed in Table 25 are the current levels of the impurities present in the commercially available cellulosic sugars obtained from vendors. The highest level of impurities shown are the worst-case scenario. In order to observe the effect of impurities on catalyst performance in an accelerated manner, and detection of impurities in the product, the highest levels of organic impurities were chosen for tests. The rationale is that if the highest level of impurity does not deactivate the catalyst, then the lowest levels will have much less impact. SR tested commercially obtained cellulosic sugars as feed that contained both organic and inorganic impurities. These tests were conducted to observe the overall impact when all the inorganic and organic impurities are present, as opposed to individual impurity tests. The level of each impurity present in this feed falls within the range selected for individual impurity tests.

The results confirmed no deactivation of the catalyst, and the intermediate product quality did satisfy purity standards for further downstream processing.

It is important to note that the first reaction step in conversion involves hydrocracking of sugars to glycerol and glycols. As such, under these conditions certain organic impurities undergo direct hydrogenation or C-C cleavage followed by hydrogenation. As seen in Table 25, acetic acid is not expected to hydrogenate under the operating conditions however, there is a greater possibility of hydrogenation of formic acid and levulinic acid under the operating conditions, considering the nature of the catalyst. As a result, 100% of the acetic acid is detected in the product whereas significantly lower levels of formic (1%) and levulinic (18%) acids are detected in the product stream. Similarly, (hydroxymethylfurfural) HMF, furfural and syringaldehyde are not hydrogenated and observed in the product stream at concentrations equal to the injected concentration. A few compounds (vanilin, syringaldehyde and benzoic acid) are not reported in the literature extensively, however there are a few papers that mention the presence of these compounds in very low concentrations, due to hydrogenation schemes employed. For the sake of completeness, we have tested the catalyst performance in the presence of these trace impurities as well. The levels of these compounds reported are below the detection limits of analytical methods used, as a result, 10 times higher concentrations of these three compounds were used for testing. At those concentrations as well, the catalyst activity was not affected.

Table 25: Range of organic impurities in biomass derived sugar, tested concentration for effect on production, percentage of feed impurities obtained in the product and resulting effect on performance. The numbers listed in column 2 and 3 correspond to the levels in pure sugar solution.

Impurity	Range of impurities in pure sugar (ppm)		Experimentally tested (ppm) with 10% sugar solution	% of feed impurity in the product	Remarks
	lowest	highest			
Formic Acid	4180	11080	1108	18%	Catalyst activity not affected
Acetic Acid	15880	51340	5134	100%	Catalyst activity not affected
Levulinic Acid	850	7200	720	1%	Catalyst activity not affected

HMF	4160	5740	600	100%	Catalyst activity not affected
Furfural	1500	3000	300	100%	Catalyst activity not affected
Glycolic Acid	4730	6200	500	21%	Catalyst activity not affected
Vanilin	NA	60	60*	56%	Catalyst activity not affected
Syringaldehyde	NA	30	30*	100%	Catalyst activity not affected
Benzoic Acid	NA	60	60*	70%	Catalyst activity not affected

* Using HPLC

The study of inorganic as well as organic impurities showed that the catalyst was found to be stable and capable of withstanding the highest levels of commonly found impurities.

ASPEN simulations and distillation runs on a lab scale distillation column were performed for the separation of organic impurities that may end up in the finished product. Table 26 shows the percentage of each impurity in the product stream with their boiling points. The goal of simulations and experiments is to find the amount of each impurity that carries forward for the second reaction step and the remaining that will be discarded with by-products/waste water.

Table 26: Reactant and products of hydrogenation reaction for organic impurities present in the biomass samples. The third column shows the percentage of impurities observed in the product and the last two columns show the boiling point of the product (or reactant where applicable).

Reactant/ Impurity	Product	% Impurity in product	BP of reactant (°C)	BP of product (°C)
Formic Acid	Methanol	12%		65
Acetic Acid	Acetic Acid	100%	118	
Levulinic Acid	γ-Valerolactone (GVL)	4%		207
HMF	DMF	100%	114	
Furfural	Furfuryl Alcohol	100%	161	
Glycolic Acid	Ethylene Glycol	21%		197
Vanilin	Cresol/Vanilyl Alcohol	56%	285	201
Syringaldehyde	Syringyl Alcohol	100%	192	
Benzoic Acid	Cyclohexane Carboxylic Acid	70%	249	232

From Table 26, it is noted that the compounds having boiling points below the boiling point of ethylene glycol (197 ºC) are easily separated by distillation and will not appear in the product glycerol stream. In addition, the last three compounds in Table 26 are rarely reported in the literature and their composition is extremely low. These three compounds, although having higher boiling points than ethylene glycol, are present in very small amounts and are not expected to cause any difficulties in the finished product purity. Nonetheless, ASPEN simulations and laboratory results did indicate successful removal of these impurities from glycerol.

As a representative case, Figure 62 shows ASPEN simulation results for a product stream containing glycerol, ethylene glycol (EG), propylene glycol (PG), water and acetic acid at 100 torr vacuum. Note that this model mimics the B/R instrument batch distillation column that SRI used to perform distillation runs. Figure 62 shows that the acetic acid concentration in the glycerol stream drops to near zero after 3.8 hours (or after 160 ºC). As a result, the purity of glycerol stream obtained is 99.42% at the end of ~4 hours. It should be noted that other components (EG, PG, water) are already separated at those temperatures (at 100 torr) and do not occur in glycerol stream.

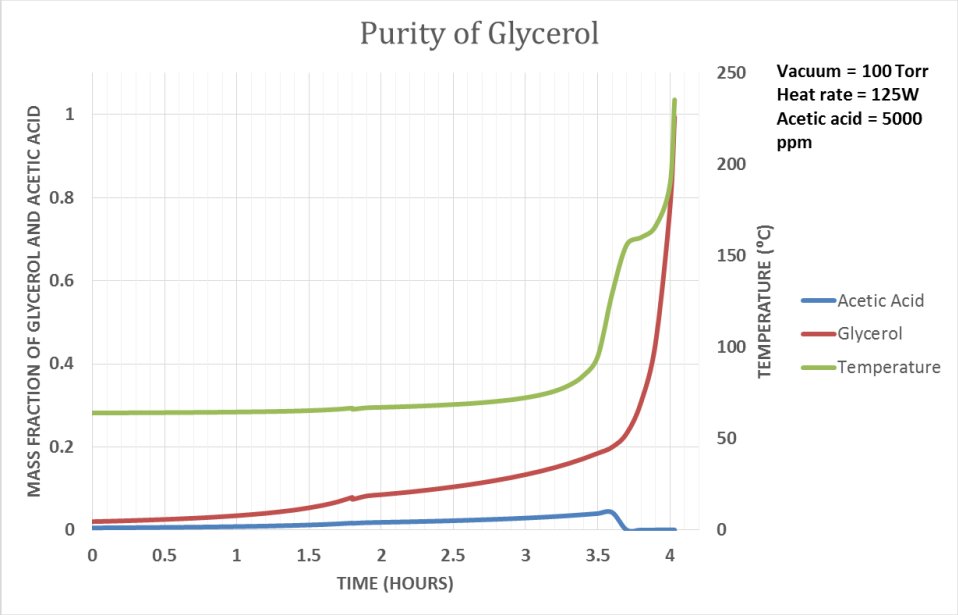

Figure 62: Representative results from ASPEN distillation simulation for separation organic impurity such as Acetic acid in its highest observed concentration in biomass derived sugars.

No significant inorganic or organic effect on catalyst performance or on bio-ACN quality was observed and production of bio-ACN proceeded to scale up. High purity acrylonitrile (99.7% on dry basis) was obtained and send to ORNL for bio-PAN production. The other observed process driven impurities were acetonitrile and water as mentioned in Table 21.

Carbon Fiber Fabrication and Physical Properties

During BP1 several isotropic pitch materials were studied from coal, petroleum, gilsonite, as well as some CTPM, PPM (from ACP), textile grade PAN and bio-PAN. It was found in BP1 that isotropic CTP could produce CF that nearly met DOE targets (strength: 227.1 Ksi, modulus: 21.2 MSi, elongation: 1.02 %, diameter: 6.7 µm), while CTPM, PPM, textile grade PAN and bio-PAN met DOE targets. After initial scouting work in BP1, only CTPM, PPM and bio-PAN were selected for scale up in BP2 for multifilament spinning for the pitch-based materials and larger tows for the bio-PAN. Scaled up materials from CTPM and bio-PAN produced CF that met DOE targets, but scaled up PPM from Koppers did not meet the elongation requirements. Moving towards BP3, CTPM was omitted and further scale up of PPM and bio-PAN was achieved and the underlying reasons for improving the elongation for PPM was identified.

The following discussion shows the progression of PAN-based materials, CTP, CTPM and PPM. It should be noted that CF processing conditions, and other CF related experimental data and results are either omitted or are encrypted. This is due to the fact that certain aspects of CF production are export controlled and a high degree of attention was placed on protecting sensitive information.

PAN-Based Fibers

Early spinning and evaluation for PAN based materials were tuned using textile grade PAN feedstocks. Textile grade PAN, which deviate from traditional CF grade PAN for several reasons, is commonly used material in many knitted products. It is comprised of polymer chains with sub-optimal molecular weight and co-monomer subunit composition. These factors combine to reduce the potential of producing CF from textile grade PAN products. Despite this, the production of general purpose CF from textile spinning lines represents a significant opportunity to improve the affordability of CF products. ORNL has made significant optimizations to the solution spinning of textile grade PAN powder in order to prepare CF with suitable automotive-grade properties. Figure 63 is a curve generated from textile grade PAN fibers by an automated single filament tester (Favimat, Textechno) averaging fifteen textile PAN filaments solution spun at ORNL. A high quality, well-structured precursor is an essential precondition for reaching CF with acceptable attributes. The polymeric precursor templates the structural evolution of the fiber in the subsequent heat treatments, ultimately dictating the properties of the final CF. The precursor characterized in Figure 63 exhibit acceptable peak strength and strain. Filament diameter is another critical consideration, as thick fibers prevent proper development of the chemical structure during the ensemble of diffusional processes that occur during stabilization and carbonization. Additionally, the cross section of the precursor fibers should be as circular as possible to prevent stress concentration in the final CF state when the dense material is predisposed to brittle failure modes. The inset in Figure 63 is a sectioned precursor bundle suspended in epoxy perpendicular to the spinning direction. The circumference of the fiber cross-sections were determined using optical microscopy imaging software. For this batch of fibers, the diameter was shown to be 14.36 μm ± 0.8, within the ideal range for stabilization and carbonization. The conformal fiber geometries and size suggests that the utilized spinning parameters are allowing for proper coagulation dynamics to effectively draw the fibers down.

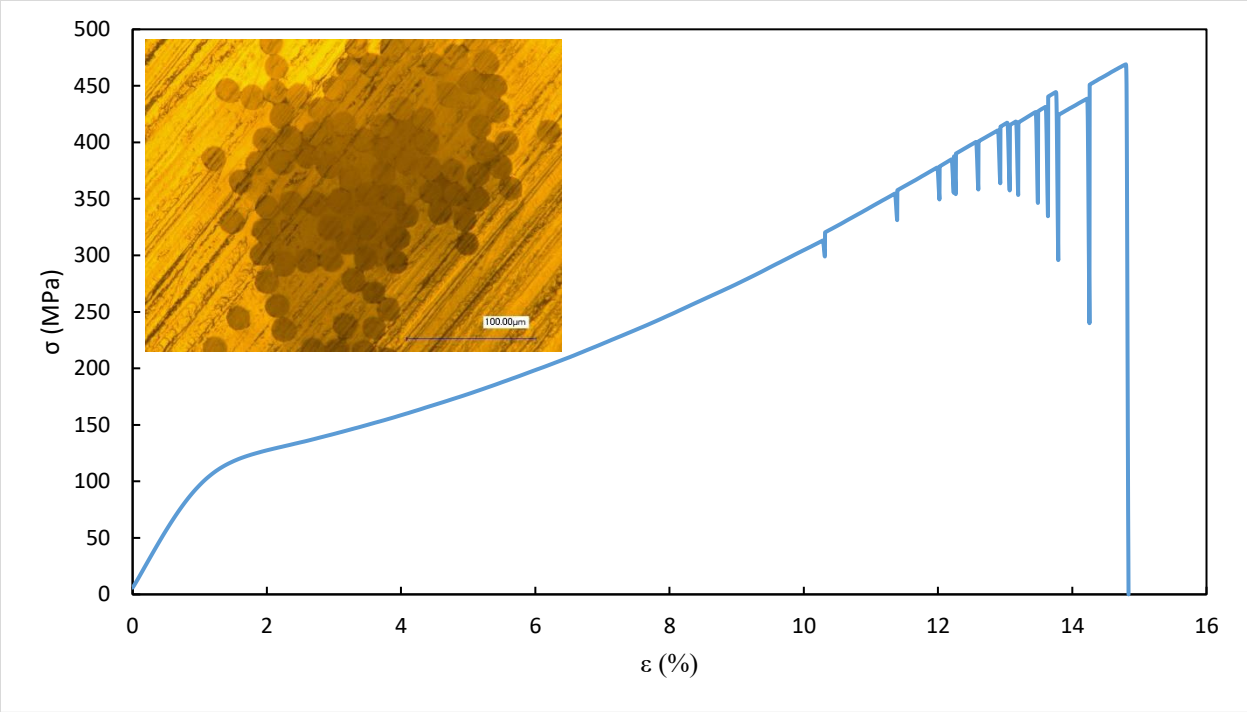

Figure 63: Stress vs. strain plot for textile grade polyacrylonitrile fibers solution spun at ORNL. Uniform diameters and filament circularity are shown in the inset.

Following solution spinning, fibers were combined into 540 filament tows and subjected to a multi-stage continuous oxidation process. This essential step produces long-range inter-segmental cross-links, stabilizing the polymeric fibers into a thermoset to preserve the fiber structure during final carbonization. Nitrile moieties, subjected to thermal oxidation, undergo simultaneous dehydrogenation and cyclization reactions leading to an increase in the density of the fibers. Density development as a result of the stabilization for the four-step process utilized by ORNL's CF processing line is shown in Figure 64. After confirming successful thermoset formation, the flame-resistant fibers were carbonized in a two-stage continuous process under an inert atmosphere. An optical micrograph and the final CF properties are displayed in Figure 65a and 65b, respectively. In Figure 65a, a uniform CF surface morphology is observed for fibers displaying an average diameter of 7.55 µm ± 0.6, consistent with the expected mass loss that occur during the combination of thermal treatments. Figure 65b shows the tensile plot for stress vs. strain for ten textile PAN derived CF specimens. Average strength and modulus for this material were found to be 2575 MPa (373.6 ksi) and 189 GPa (27.5 Msi), respectively. These exceed the performance targets while preserving an average peak ε of 1.12.

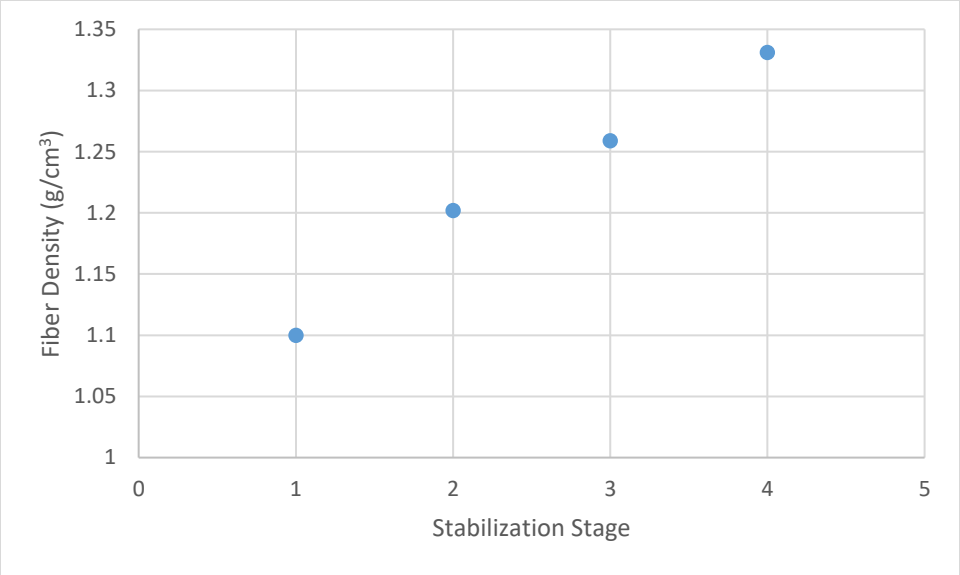

Figure 64: Density evolution as a function of stabilization stages showing proper formation of the thermoset.

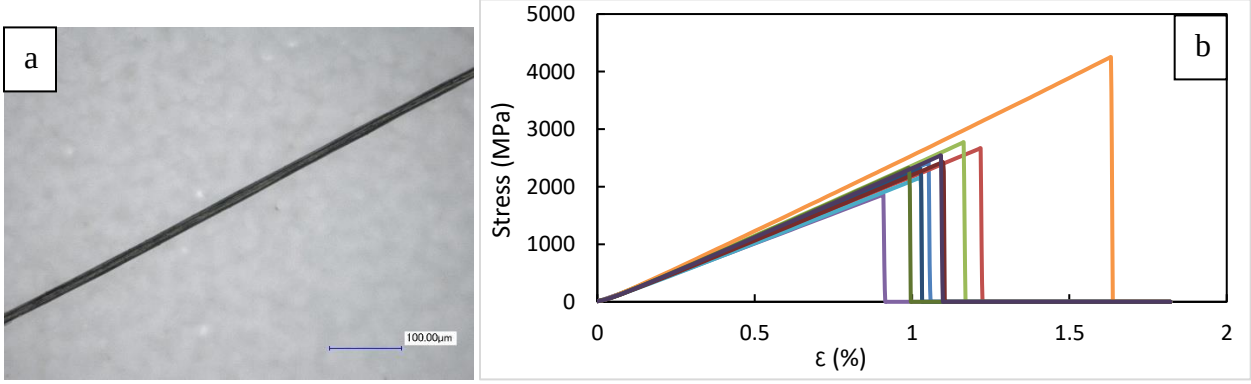

Figure 65: (a) Optical micrograph of final carbon fiber with average diameter of 7.55 µm. (b) Stress vs strain plot for 10 carbon fiber samples derived from textile grade PAN.

Bio-PAN synthesis and solution-spinning trials were refined to produce fibers that exceeded DOE targets. Smaller batches of bio-PAN were successfully spun into CF that met DOE requirements with fibers that were less than 20 microns in diameter and with bio-PAN with molecular weights between 136-199 kDa. General trends showed that the higher molecular weight polymer did produce CF with higher strength, modulus and elongation. After refining the conditions, a larger batch was spun to produce fourteen individual spools of 108 filaments each. These were combined to provide a tow of ~ 250 ft long and 1512 filaments of bio-PAN CF. SEM analysis of the CF cross-section shows a turbostratic carbon structure free of any microscopic voids (Figure 66).

Figure 66: Left shows as spun bio-PAN fibers, middle spool shows black stabilized and carbonized bio-PAN fibers and the right image shows a SEM micrograph showing a cross-section of bio-PAN Carbon Fiber with a trubostratic carbon structure.

After each spinning trial, multiple fibers were selected and analyzed for their mechanical properties to understand the variability related to the precursor and the spinning method. Figure 67 shows the statistical data for the stress and % elongation to failure for bio-PAN fibers that was spun to 13.5 microns.

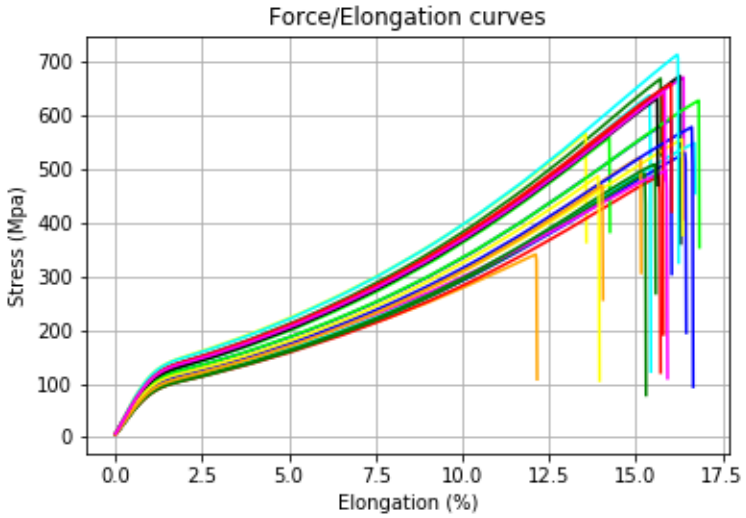

Figure 67: Example fiber data for bio-PAN fibers produced with at 15 wt% solids dope and spun to 13.5 microns (data is for illustration purposes and is pre stabilization and carbonization).

Following the synthesis and wet-spinning of a batch of bio-PAN precursor (bioPAN_4), the material was converted to a large format tow. Fourteen individual spools (108 filaments each) were combined in two sequential steps to form a final tow length and filament count of ~300 ft and 1512 filaments, respectively. Previous scale up trials lead to CF properties well above the strength and stiffness criterion but lacking in average peak strain %. The CF conversion parameters were adjusted to target a more ductile fiber and resulted in the property set summarized in Table 27. Bio-PAN CF produced at ORNL exceeds all the property goals and clearly shows it as a viable alternative to petrochemically derived feedstocks. A scanning

electron micrograph of the CF cross-section is displayed in Figure 68, which shows a turbostratic carbon structure free of any microscopic voids. A CF tow with a final length of approximately 250 feet was tested for tow-level properties at the University of Wyoming. These results have promising implications to both the cost, stability and sustainability of CF production going forward. Table 28 is a summary of bio-PAN fibers produced during BP1 and BP2.

Table 27: Summary of Carbon Fiber properties derived from bioPAN_4 precursor.

Diameter (µm)	Modulus (Msi)	Peak Strength (ksi)	Peak ε %
7.74 ±0.53	30.0 ± 1.0	328.9 ± 54.0	1.11 ± 0.15

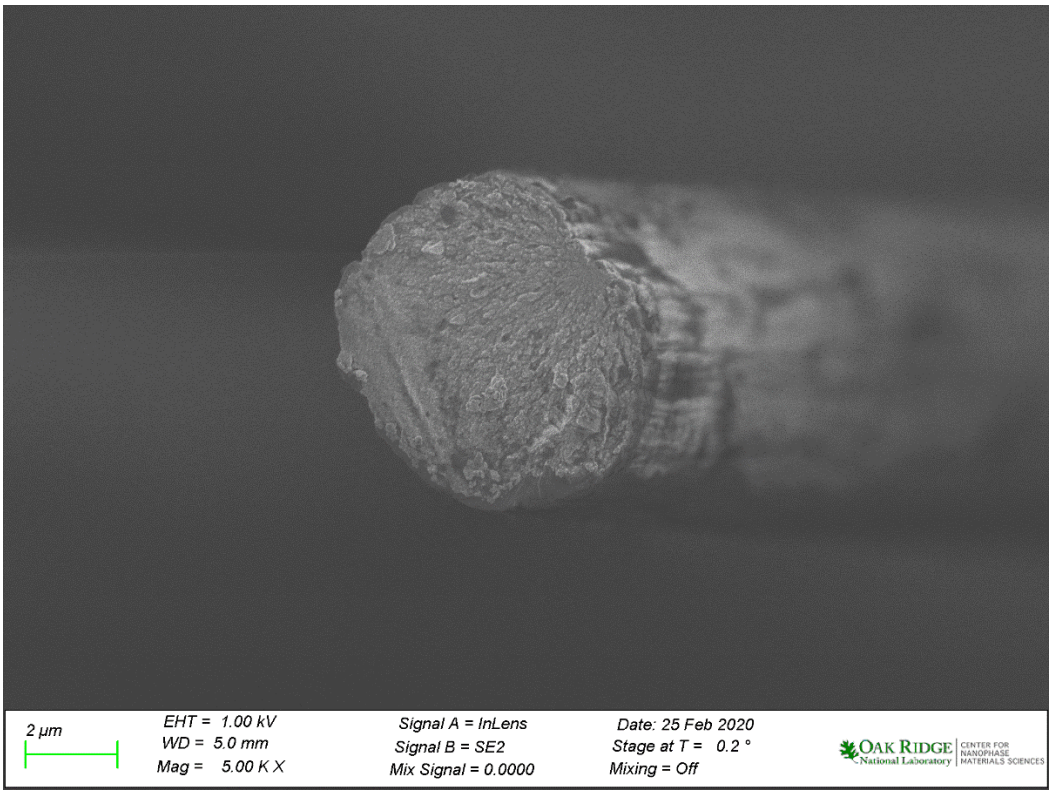

Figure 68: Scanning electron micrograph of a representative bioPAN_4 Carbon Fiber.

Table 28: Bio-PAN Carbon Fiber properties produced during BP1 and BP2 that meet DOE strength and modulus targets. Note that the elongation was < 1% for some samples which was corrected by polymer formulation and Carbon Fiber processing.

Sample	Peak σ		Modulus		Peak ε	Diameter
	Mpa	Ksi	Gpa	Msi	mm/mm	µm
BioP1	194 ±337	282.7	248±7.8	38.2	0.86	-
BioP2-2	3630±580	526.7	282±5.2	40.9	1.20±0.11	5.45±0.44
BioP3	2190±324	317.8	227±3.8	32.9	0.98±0.10	7.26±0.63
BioP4	-	328.9±54.0	-	30.0±1.0	1.11±0.15	7.74±0.53

Promising Pitch Based Isotropic CTP Fibers

In order to achieve appropriately high properties from pitch feedstocks, it is essential to understand the melt rheology of these materials to produce sub 15 μm in diameter precursor filaments. Early attempts produced filaments above 20 μm diameter and strengths in the low hundreds of megapascal range. By selecting the correct feedstock and fine-tuning the spinning parameters, sub 15 μm pitch fibers were successfully produced. Figure 69a shows the as-spun pitch fibers spun from feedstock CTP6-NMP, received from WRI. Superficial fiber morphology is uniform and free of any significant defects. Diameter measurements resulted in an average of 12.7 μm for this as-spun material. Single filaments were stabilized and subsequently carbonized up to a final temperature of 1000 °C. The final pitch CF morphology and diameter (average - 6.7 μm) are exhibited in Figure 69b. Again, the uniform nature of the CF surface suggests that the thermal treatments were applied correctly without producing observable porosity. CF derived from the isotropic CTP were tensile tested and a representative specimen is plotted in Figure 70. Interestingly, the average peak strength was 1416 MPa (205 Ksi) while the average modulus was found to be 121.8 GPa (17.7 Msi) these are slightly below DOE targets for the strength and modulus. The high strength of the isotropic CTP is intriguing and is worth further investigation since eliminating the mesophase production step towards producing CF would be a significant cost savings. However, there are some practical limitations to using isotropic pitch. The primary limitation is how to efficiently stabilize the fibers in a continuous manner over short durations which would need to be addressed to be commercially viable. Table 29 shows some of the properties of CTP6-NMP CF compared to CF produced from the other select isotropic pitch materials.

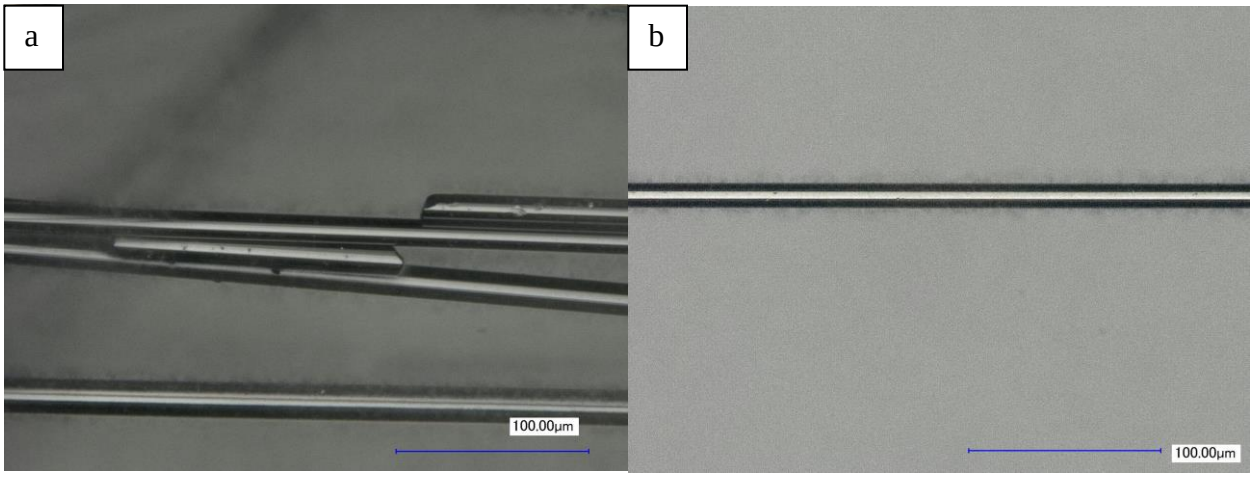

Figure 69: (a) Optical micrograph of as-spun CTP6-NMP (average diameter of 12.7 μm). (b) Pitch derived CTP6-NMP Carbon Fiber single filament (average diameter 6.7 μm).

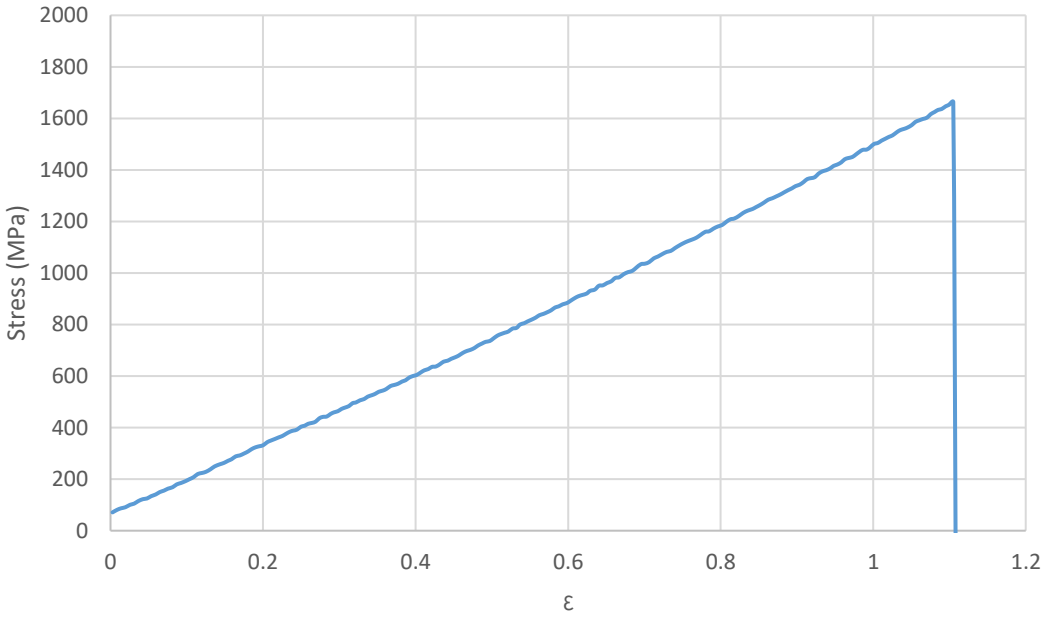

Figure 70: Representative tensile specimen on a stress vs strain plot derived from CTP6-NMP feedstock.

Table 29: Carbon Fiber Properties for select isotropic pitch spun materials.

Sample	Peak σ		Modulus		Peak ε	Diameter
	Mpa	Ksi	Gpa	Msi	mm/mm	µm
M50_bsA_bcA	891.4	129.3	49.1±	7.1	1.27	-
GILSEL347_bsA_bcA	258.8±62.4	37.6	18.6±6.7	2.7	1.25	23.83±4.35
CTP3_bsA_bcA	161.3±45.6	23.5	19.2±8.1	2.8	0.79	22.08±4.63
CTP3NMPs_bsA_bcA	484.4±169.8	70.3	29.7±8.5	4.3	1.51	15.44±5.54
CTP4NMPs_bsA_bcA	286.1±87	41.5	33±9.4	4.8	0.84	10.68
CTP6NMPs_bsA_bcA	1565.4±209.6	227.1	146.1±21.8	21.2	1.02	6.7
CTP6NMPsDC_bsA_bcA	412.3±186.1	59.8	38.4±4.4	5.6	0.96	12.49
CTP7NMPsDC_bsA_bcA	367.8±86.6	53.4	28.2±5.8	4.1	1.19	23.79

Mesophase Pitch Carbon Fiber

Several CTPM precursors were produced by WRI and evaluated at ORNL for melt spinning and qualification. ORNL successfully produced low diameter filaments, stabilized and carbonized them to CFs from two CTPM pitches. In some cases, some of the CF properties we slightly shy of DOE targets. However, slight changes to the spinning in CF diameter, stabilization procedure, and carbonization procedure change the properties of the CF. For instance, decreasing the CF diameter will increase the strength and make stabilization more efficient (Chung, 1994), and increases in carbonization temperature will typically lower the strength and strain but increase the modulus (Manocha, 2007). Other types of trends have been documented. Large scale up would be further useful for understanding all the parameters of mesophase quality and spinning and processing.

As previously mentioned, mesophase from CTP6-NMP (CTP6M) was produced under different conditions. The mesophase sample with a SP of 320°C was used to produce CF that met DOE targets with 361 Ksi strength, 26 Msi modulus and 1.17% strain to failure. Some aspects of the processing which has an impact on the structure relation were investigated. For some spinning trials of CTP6M SP320, both radial and random wave morphology of the crystalline domains were observed by SEM (Figure 71). In some cases if the stabilization temperatures were too high, relative to the SP of the material, then various defects were observed from inter-filament fusing (Figure 72). Additionally, if the stabilization time and temperature were not adequate then the core of the fibers were not fully stabilized which led to burned-out hollowed fibers after carbonization (Figure 73).

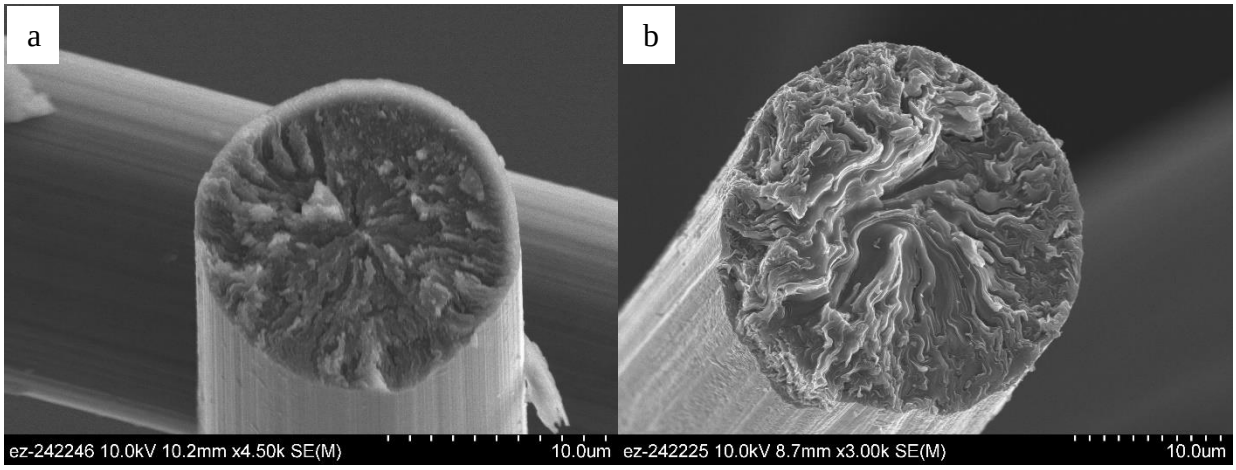

Figure 71: Scanning electron micrographs of well-stabilized CTP6M 320 displaying radial (a) and random wave (b) type patterns.

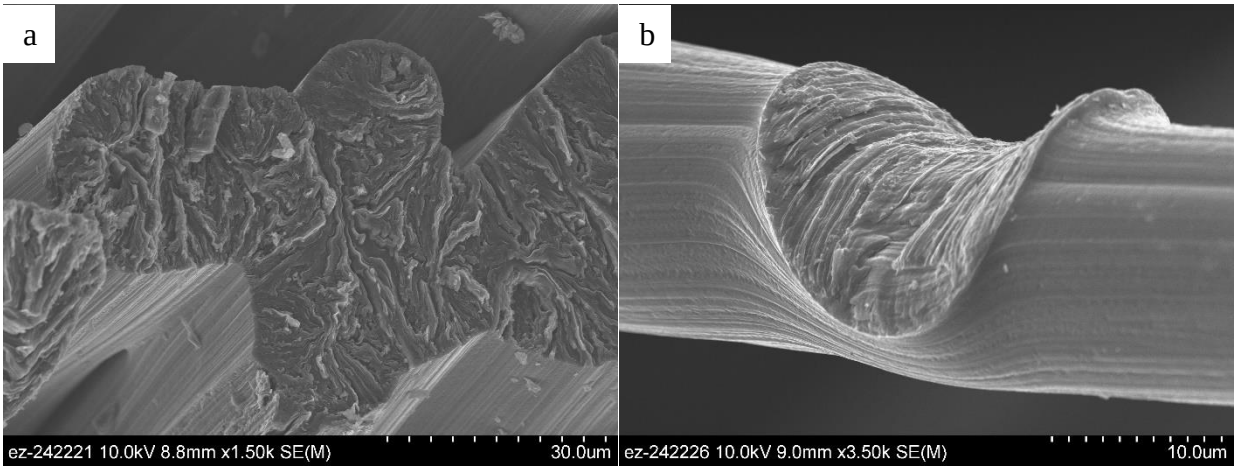

Figure 72: Scanning electron micrographs of fibers displaying inter-filament fusion for aligned (a) and off-axis (b) fiber bundles.

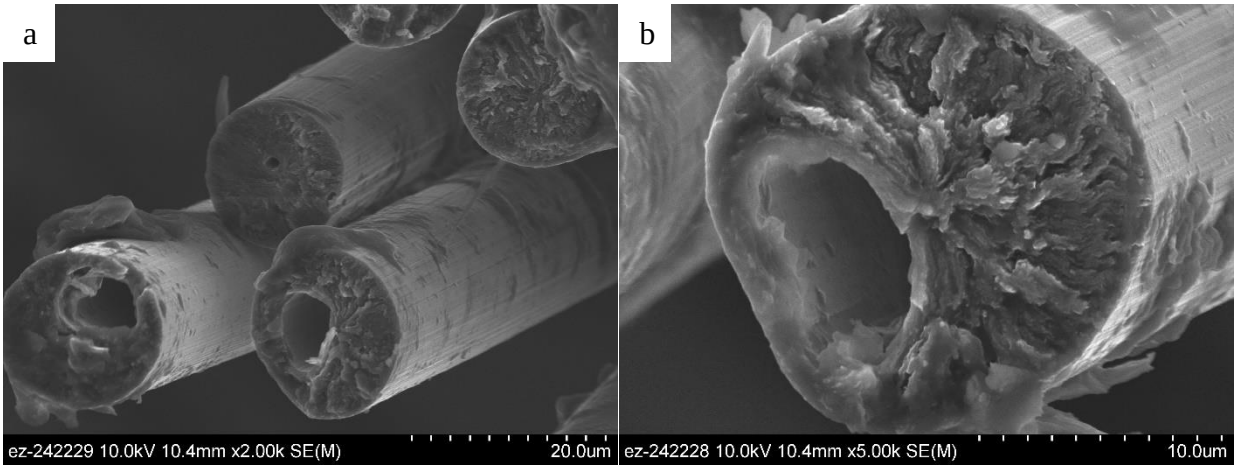

Figure 73: Scanning electron micrographs of fibers showing the effects of entrapped, poorly-stabilized regions leading to various size voids.

CTP6 (North American – Koppers) and CTP7 (Chinees – Koppers) were selected for scale up. Scaled up batches in a 1 L reactor of CTP6M were produced with a SP around 315-320 °C. Scaled up batches for CTP6M SP 320 for single filament test had a strength of 333.6 Ksi, a modulus of 34 Msi and a strain of 0.95%. Combined batches of CTP6 SP315 and SP317 produced 21 filament tows with a strength of 260 Ksi, 24 Msi and a strain of 1.0%. CTP7 produced mesophase more quickly than CTP6 and in many cases mesophase pitch with a SP higher than 320 °C was produced. This caused some issues in the single-shot melt spinning equipment due to the temperature tolerances for the seals. Despite the higher SP, CTP7M SP330 and CTP7M SP340 were evaluated. Both precursors were melt spun at 30-40 °C above softening point and are shown in Figure 74. Diameters less than 15 μm are essential for achieving performance CFs. The fibers produced from the CTP7M exhibited excellent spinnability, producing monofilament with consistent diameters between 9-12 μm. Inspection of the fiber surfaces showed defect free, smooth surface finishes.

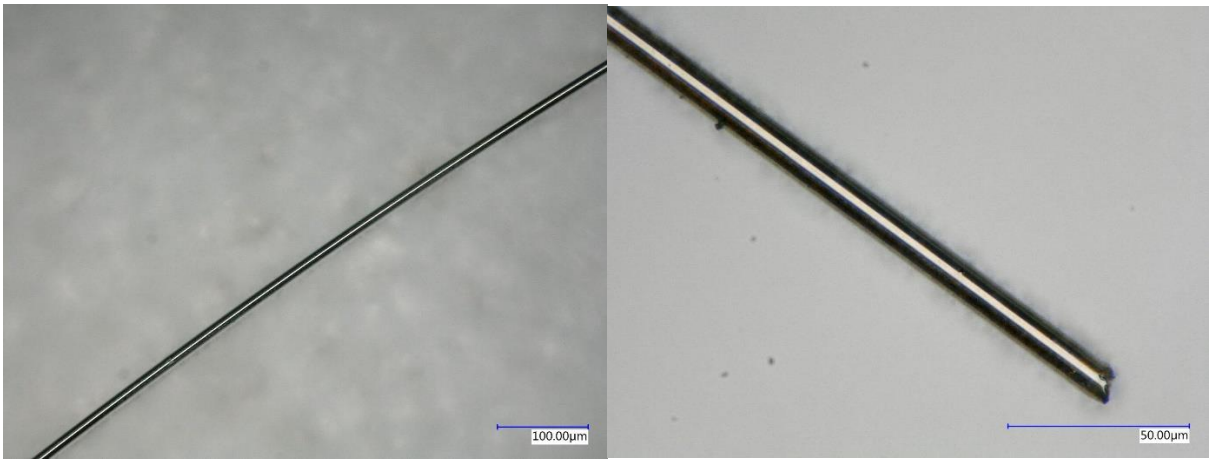

Figure 74: Optical micrographs of CTP7M SP330 (a) CTP7M SP340 (b) showing fibers with sub 15 µm diameters and defect free surfaces.

Following successful melt-spinning, the CTP7M precursor fibers were subjected to TGA analysis. Sufficient yield for carbonaceous materials is an essential pre-condition for quality CFs. Materials which do not form a pyrolyzed char (carbon residue = coking indes) are incapable of making CFs. Additionally, compositions which form higher yields will result in an a more profitable process. Figure 75 compares temperature ramps of as-spun mesophase fibers of CTP7M and CTP6M for comparison. A heating rate of 10 ˚C/min under flowing nitrogen gas was used. In Figure 75 it can be seen that the CTP6M with an approximate softening point of 298 °C has both the lowest final carbon yield (~ 62%) and earliest degradation onset at approximately 300 °C. Samples CTP6M SP320 and CTP7M SP330 have identical thermal properties as evidenced by the overlap in the two curves and exhibit a final yield of over 70%. The pitch with the highest yield is CTP7M SP340, which also has the highest softening point. The monotonic relationship between softening points and yield shown here is due to the increasing mesophase content in the pitch composition. From the data shown here, the new mesophase formulations appear to have the requisite properties to be ideal precursor materials. The entire library of developed mesophase pitches by WRI have over 60 % yield.

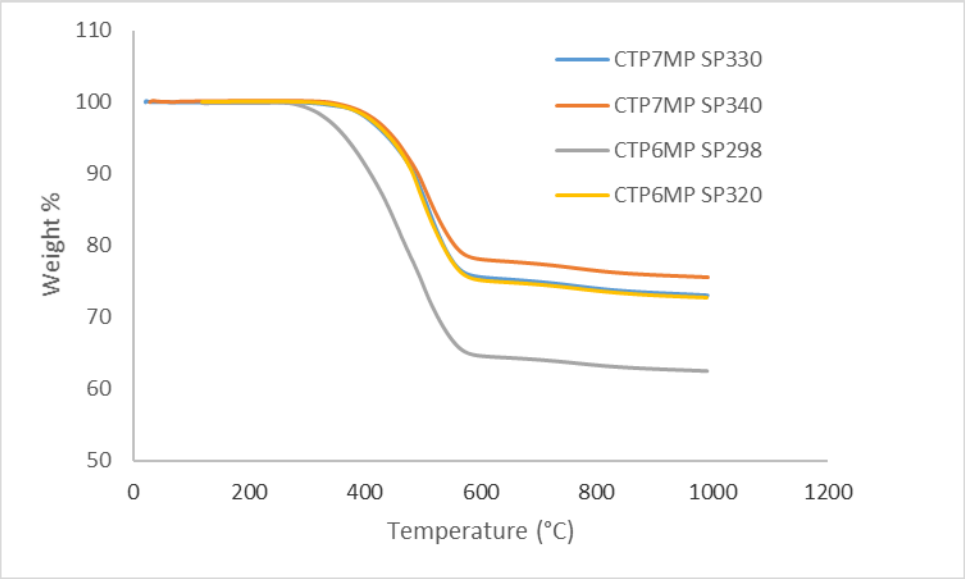

Figure 75: Fractional weight loss as a function of temperature in nitrogen for the WRI mesophase formulations.

For the higher SP CTP7 samples, as-spun filaments were stabilized in air using a variety of ramp rates, isotherms, and final temperatures and subsequently carbonized. A summary of average properties is shown in Table 30. We found that the CTP7M SP340 samples had consistently low peak ε, consistent with a high defect density fiber given the moderate carbonization temperatures used in this study (1200 °C). This occurred irrespective of the stabilization protocol and was elucidated upon detailed analysis of the as-spun filament cross sections shown in Figure 76. Large, sub-surface defects are apparent in the cross section of the CTP7M SP340 filaments. This finding suggests that gases evolving during spinning, create voids which are then entrapped in the fiber during solidification. These voids persist through the thermal treatments and lead to catastrophic failure of the filaments prematurely. The lower softening point sample, CTP7M SP330, displays ductility consistent with low defect densities. As a result, the strength was improved to nearly 2 GPa in the second stabilization trial. The second stabilization trial produced CF that met DOE strength targets (289.5 Ksi) but was short on modulus (16.3 Msi). However, this sample did have a significant amount of strain (1.6%) that could allow these fibers to be further stabilized to increase the modulus.

Table 30: Summary of carbon fiber properties produced from CTP7M materials.

Sample ID	Avg Diameter (µm)	Peak Strength (MPa)	Modulus (GPa)	Peak ε %
CTP7M SP340 (1)	11.4	1188	140	0.72
CTP7M SP340 (2)	10.5	1077	155	0.63
CTP7M SP330 (1)	10.8	1319	84	1.4
CTP7M SP330 (2)	10.5	1995	112	1.6

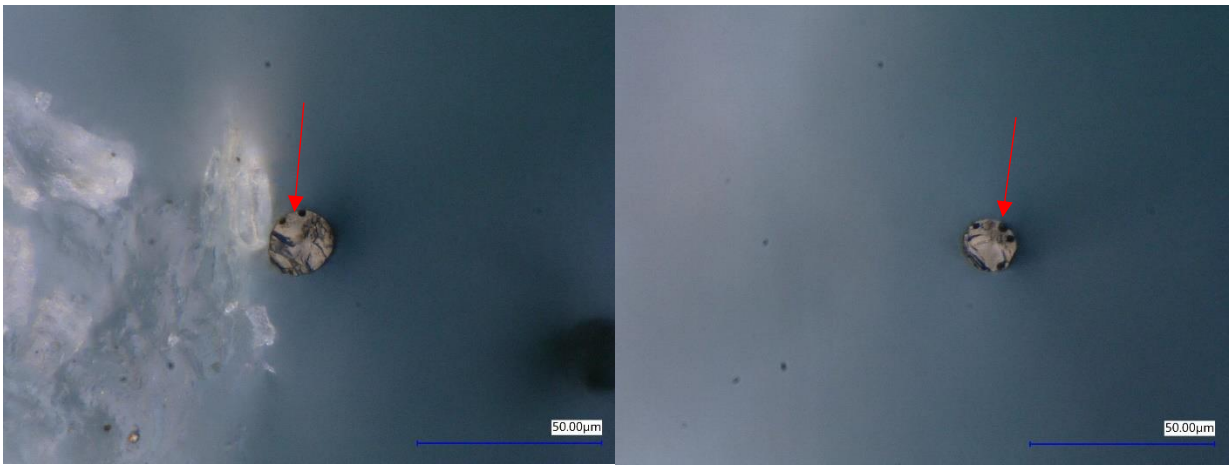

Figure 76: Cross sections of CTP7M SP340 filaments showing large voids in the cross-sectional volume.

CTP6M SP321 and CTP7M SP328 were able to be spun to fibers of approximately the same size diameter (Figure 77) and CTP6M SP321 produced highly ordered wavy radial microstructure upon carbonization (Figure 78). Thermal stability for CTP6M and CTP7M at the melt at temperatures needed to spin the material, and resistance to degradation, can be reflected in a consistent viscosity as a function of time. Figure 79 and Figure 80 show the viscosity as a function of time for CTP6M and CTP7M, respectively, subjected to a continuous oscillatory shear deformation over the course of 1 h, just below their respective SP as measured by WRI. Both samples exhibit predictable and gradual viscosity increases as a function of time, with CTP7M showing almost no change in viscosity after the initial 15 minutes. These promising results suggest that the mesophase compositions have excellent thermal stability at these temperatures and should not deteriorate during the extrusion dwell time in an isothermal condition. In addition to thermal stability, the material's viscous response to temperature also needs to be well understood. A gradual decrease from approximately 1200 Pa·s to 230 Pa·s is observed (Figure 81) for the CTP6M material from 320 to 400 °C, suggesting that the material does not undergo any substantial thermal crosslinking or degradation over the range of expected temperatures required for melt spinning. These pitch materials from scaled up mesophase

synthesis processes show favorable spinnability and thermal stability but need to be evaluated based on mechanical properties to confirm viability before and additional scale up is ultimately attempted.

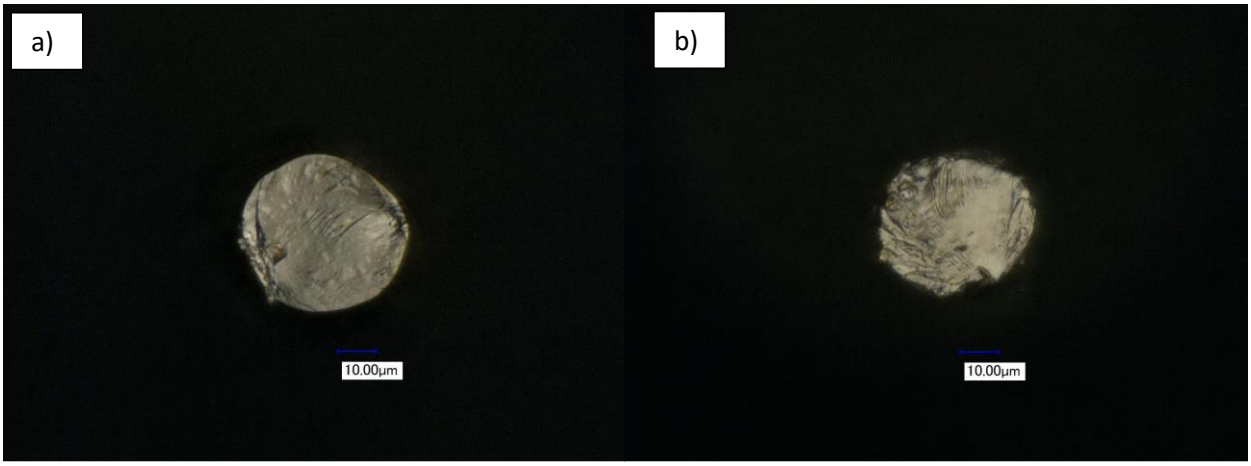

Figure 77: Optical micrograph of as-spun CTP6M SP321 (a) and CTP7M SP328 (b).

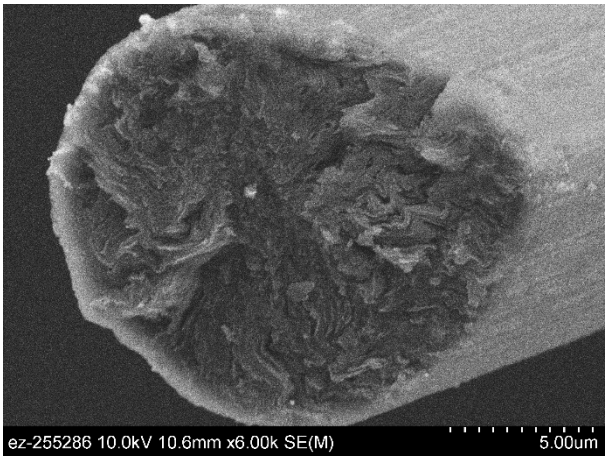

Figure 78: Scanning electron micrograph of CPT6M SP321 carbon fiber cross-section.

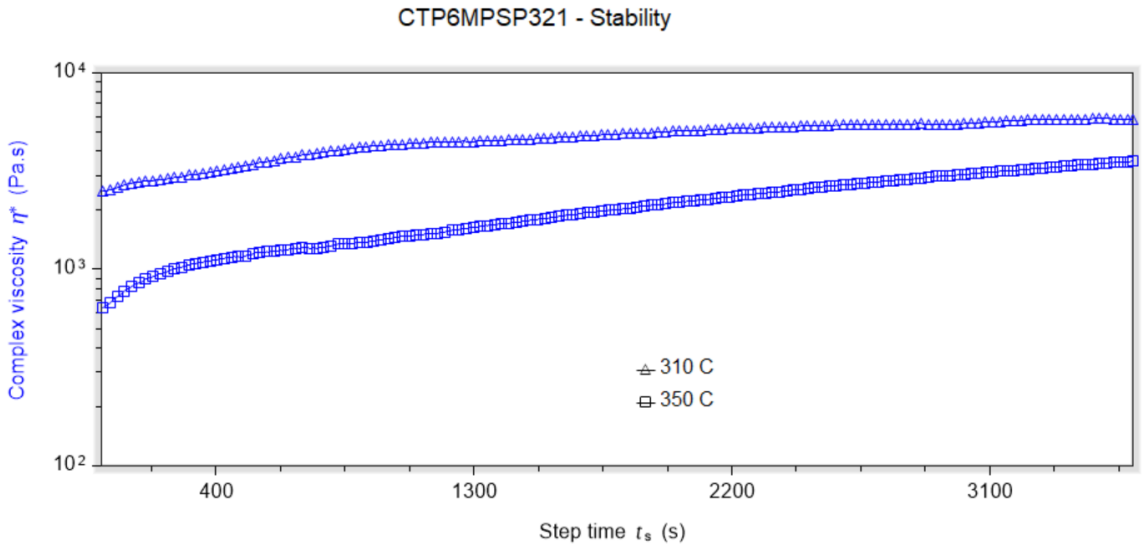

Figure 79: Oscillatory shear rheology test displaying stability of CTP6M SP321 pitch over the course of 1 h.

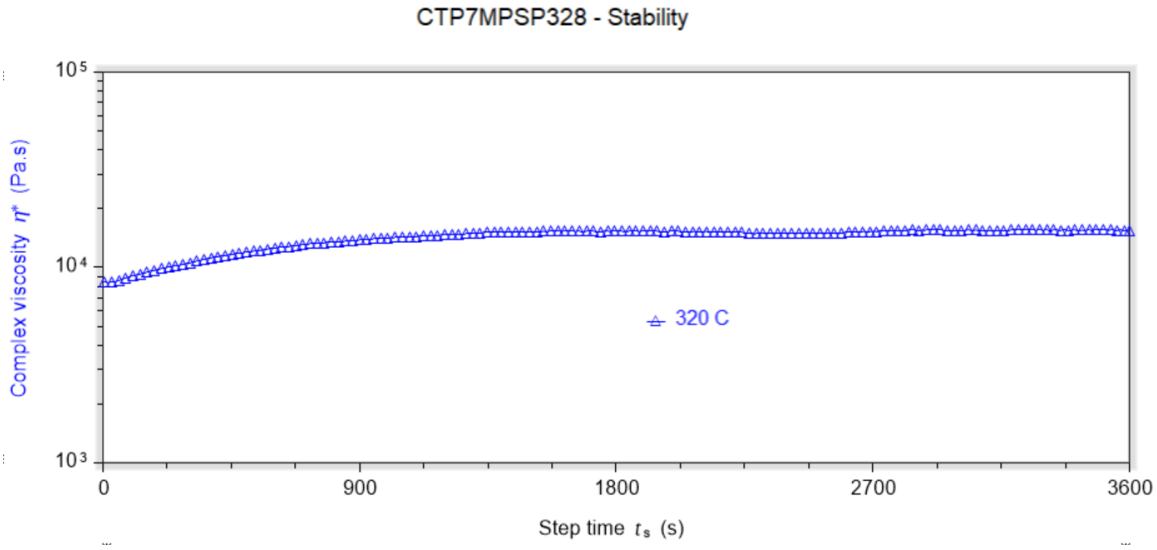

Figure 80: Oscillatory shear rheology test displaying stability of CTP7M SP328 pitch over the course of 1 h.

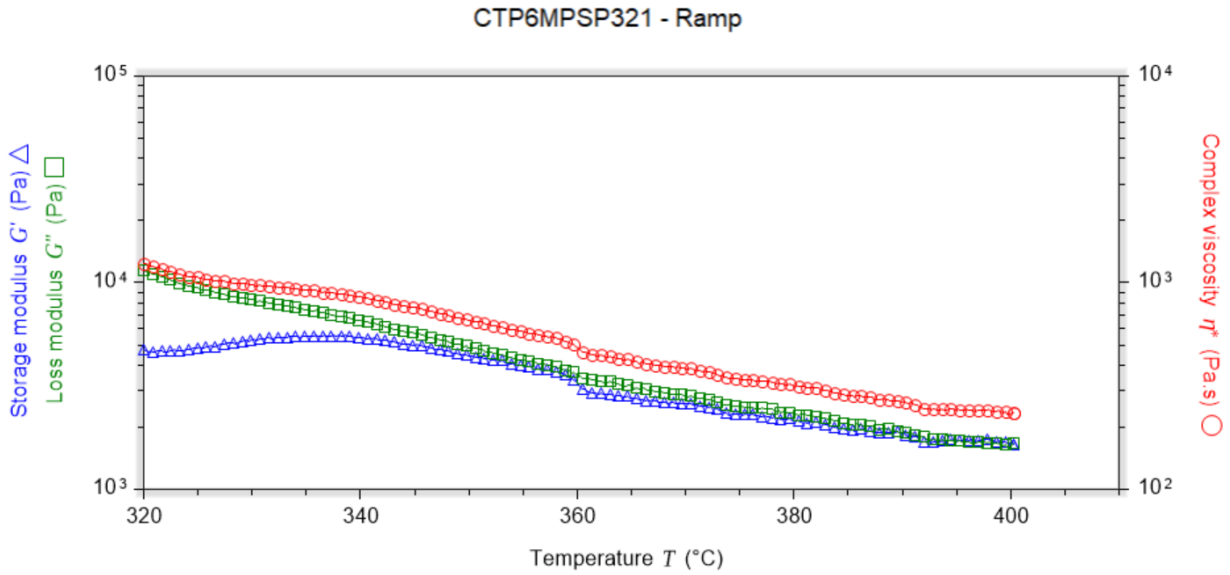

Figure 81: Oscillatory shear rheology test displaying stability of CTP6M SP321 pitch over the course of 1 h.

Additional CTP6M with slightly lower SP were also produced at a larger scale and evaluated. Samples designated as CTP6M with measured softening points of 320 °C and 314 °C were both successfully melt spun into fine fully dense fibers. After several combinatorial spinning, oxidation and carbonization trials on CTP6M SP320 significant improvements to the achievable properties were obtained. Average strength, diameters modulus, and % elongation were 333.6 Ksi, 17.4 µm, 34.0 Msi, and 0.95, respectively. This shows that the scaled up mesophase synthesis has preserved the requisite quality from the smaller scale reactions schemes. Additionally, the property set observed here indicates that by slightly tuning the processing window the peak elongation can be improved at the expense of some expected losses in fiber stiffness. Figure 82 shows the results of the initial spinning and carbonization trials on CT6MP SP314, both showing a dense and mostly defect free exterior. Oscillatory shear rheology was performed on CT6MP SP314 (Figure 83 and Figure 84) in both a ramp and isothermal mode. In concert, this rheology study shows that the material has a good response to increasing temperature with a decrease in viscosity of almost an order of magnitude in a temperature window of only 60˚C. The isotherms shown in Figure 84, show the expected trend of lower viscosity for the higher temperature and a crossover point around 1000 s, suggesting that at 400˚ C the material is reacting to undergo additional condensation and should be spun where the material is stable for a longer processing period.

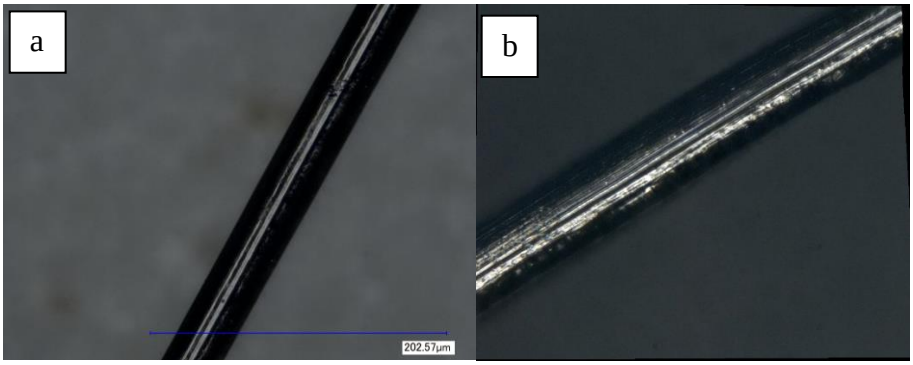

Figure 82: Optical micrographs showing the surface morphology and feature set of CTP6M SP314 fibers. As spun (a) and carbonized (b) are both shown.

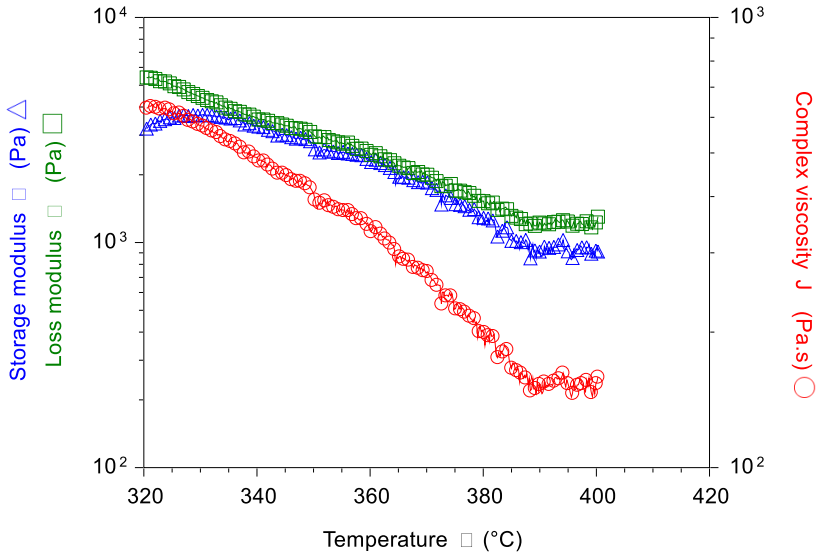

Figure 83: Oscillatory shear rheology performed on CTP6M SP314 at a ramp rate of 2 ℃/min

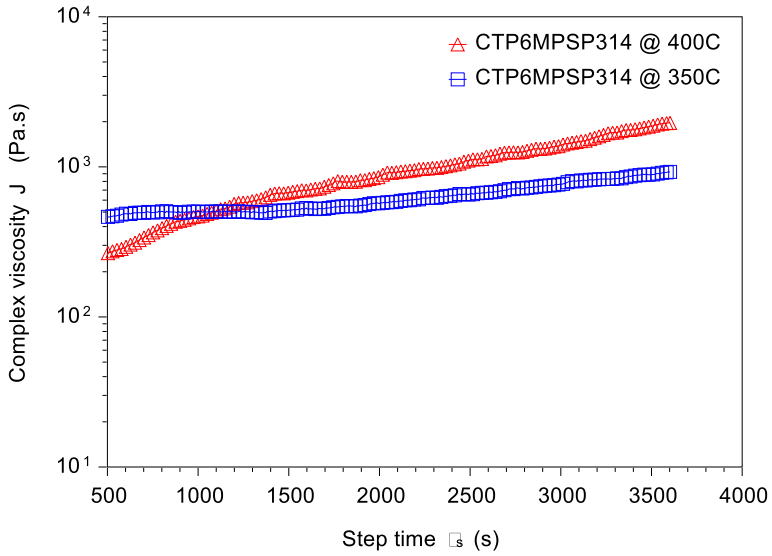

Figure 84: Oscillatory shear rheology isotherm studies for CTP6M SP314.

Large-scale multi-filament melt spinning trails with CTP6M

To produce a larger batch for multifilament spinning of CTP6M two of the pitches with softening points separated by only 0.7 °C (SP 314.0 and SP314.7) were analyzed for melt stability as well as their rheological response to flow. Figure 85 overlays both materials on an isothermal (85a) and ramp (85b) in oscillatory shear experiment. From the combined figures, the melts indicate that they can remain well within a spinnable viscosity window for an hour or more. As expected, the materials show nearly identical melt flow properties and were combined to make a single, larger batch for melt spinning purposes.

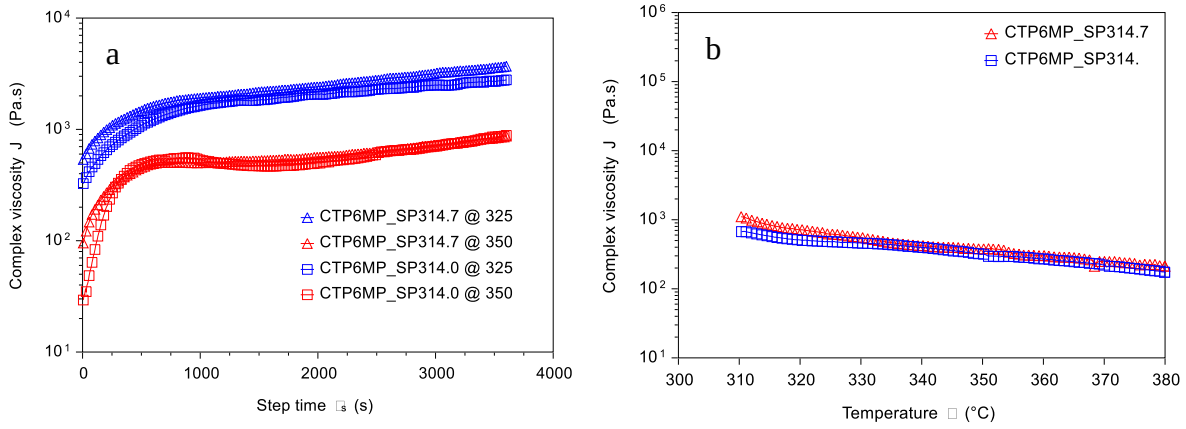

Figure 85: CTP6MP_SP314.0 and CTP6MP_SP314.7 overlay of oscillatory shear melt rheology for isothermal conditions (A) and ramp of 2 °C/min (B).

Combined CTP6M using samples with SP of 314.0 and 314.7 were successfully spun using the multi-filament extruder. Figure 86a shows the fiber take up running at speed, in process. The surface finish is shiny and consistent suggesting that the fibers are smooth and of consistent diameter. Notably, the pitch filaments were tolerant of the use of a roll traverse enabling consistent distribution of the filaments along the roll length. The fibers were liberated from the roll using a sharp razor (Figure 86b) for analysis and stabilization. Optical microscopy (Figure 86c and 86d) show dense fibers, free of microscopic surface or internal defects. Multiple rolls of fibers were collected under various extrusion and take up parameters, however the smallest filaments exhibit a diameter between 35 to 40 µm. Additional multifilament melt-spinning trials were accomplished with CTP6M SP315+. Fibers that were 18-21 microns were achieved with strength at 260 ksi, modulus at 24 Msi and elongation above 1%. Some fibers have a modulus over 25 Msi, therefore within error, the fibers do meet all of DOE specifications.

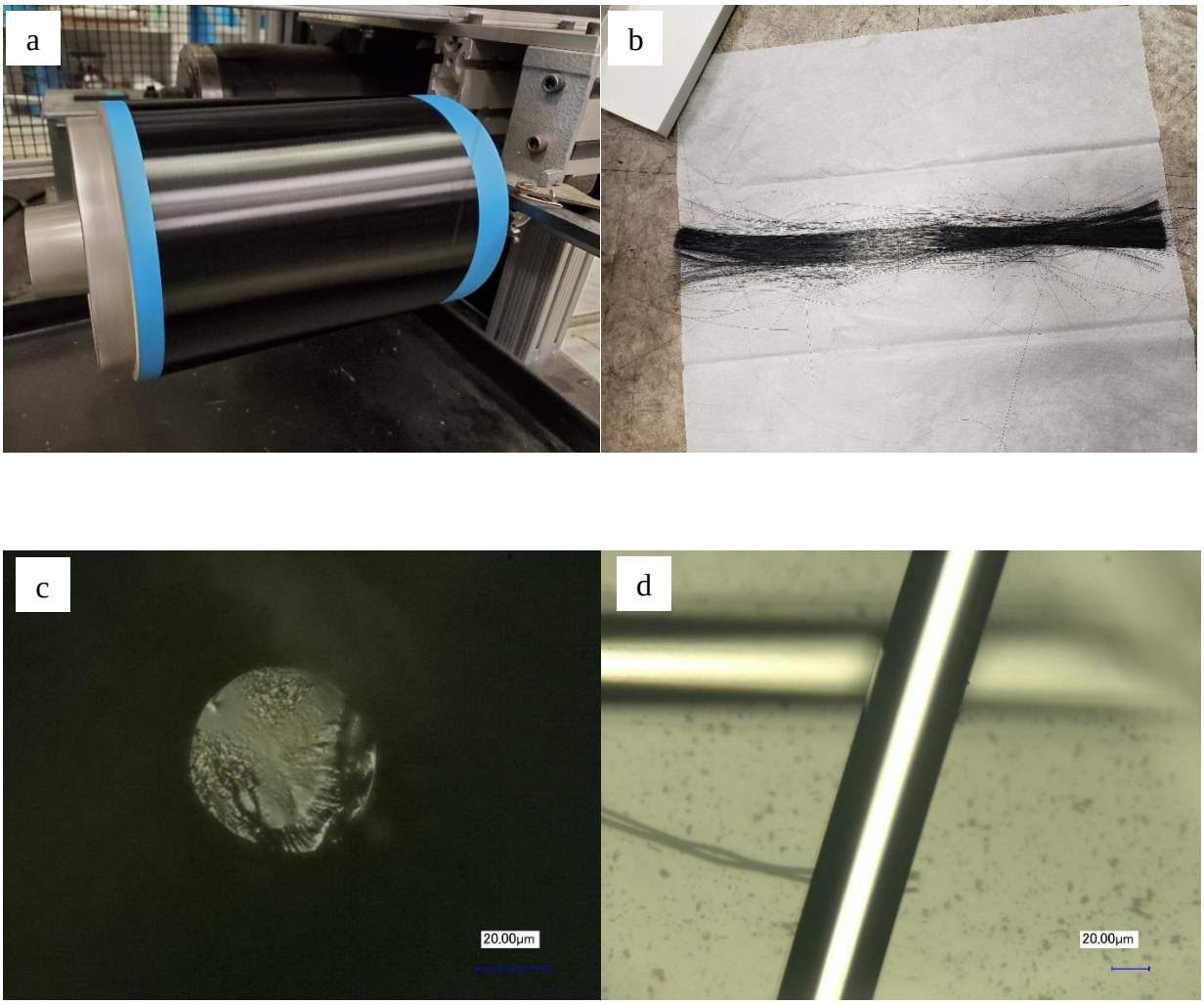

Figure 86: (A) CTP6M filaments being taken up the large-scale melt extruder. (B) Free filaments removed from the roll. Representative cross-section (C) and longitudinal (D) micrographs of single filaments produced on the multi-filament extruder.

PPM Carbon Fiber Production

A sample of PPM (ACP-M1) was produced by ACP from their proprietary technology from their ACP-10 isotropic pitch. The ACP-10 PP is produced from FCC oil and is similar to previously commercially available M-50 pitch. This sample was hot filtered to remove any residual inorganic contaminants. The sample was 95+% mesophase with a SP of 329.7 °C. Filtered ACP-M1 produced CF that met DOE specifications with a strength of 347.9 Ksi, a modulus of 25.2 Msi and a strain of 1.18%. Further heat treatment of the sample to graphitization temperatures decreased the strength (243.3 Ksi) and strain (0.57%) but increased the modulus (36.6 Msi).

Additional samples of ACP-M1 were not able to be obtained and Koppers joined this effort in January of 2020 to provide additional samples of PPM for testing during the end of BP2. Koppers provided a PPM SP298 (KOP MP 1) and single filament CF that were 21 µm gave a strength of 263 Ksi, a modulus of 56 Msi and a strain of 0.57%. Despite several attempts it was

not possible to get a strain above 1% with this material. The underlying reason for this low strain is detailed in later in the Phase 2 Topical Report. Additional Koppers samples KP-MP-19 and KP-MP-20 were received and found suitable to produce CF.

A petroleum derivative mesophase pitch (KOPMP, same as KPPM) was also analyzed during this quarter for determination of spinnability. Rheological properties in response to an oscillatory shear field are summarized in Figure 87. With a measured softening point of 298 °C, the material displays a stable complex viscosity below 2 x 10^3 at an isothermal temperature of 325 °C. The data indicates that the KOPMP is suitable for spinning.

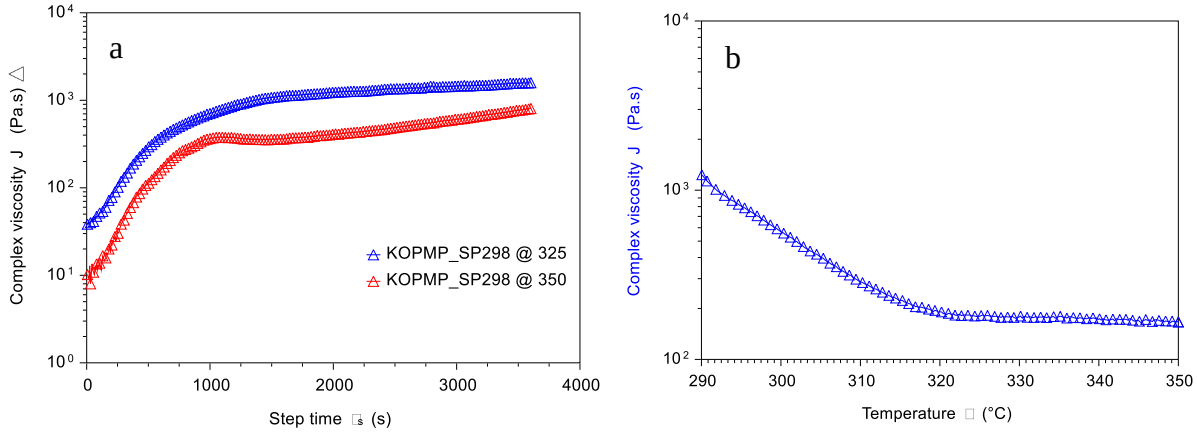

Figure 87: KOPMP_SP298 oscillatory shear melt rheology for isothermal conditions (A) and ramp of 2 °C/min (B).

TGA was also used to determine the onset of mass loss under nitrogen. CTP6M shows a region of stability until approximately 360 °C while the KOPMP begins to deteriorate around 280 °C (Figure 88). These values establish effective ceiling temperatures for the pitch materials within the extrusion path. In conjunction with the melt rheology, a safe spinnability window can be established between the boundaries of thermal degradation and viscous flow. To ensure consistent packing of the screw head in the extruder, the pitch feed material must be relatively uniform and resistant to caking along the flow path. The resulting combined batches were manually passed through a 2.7 mm sieve and the < 500 µm fines were removed to optimize these properties. Approximately 440 g of suitably sized material was prepared and purged prior to large melt-spinning. The same methods have been applied to CTP6M 315.6-316.1 batches were spun on the large scale, multi-filament extruder and reported later in the Phase 2 Topical Report.

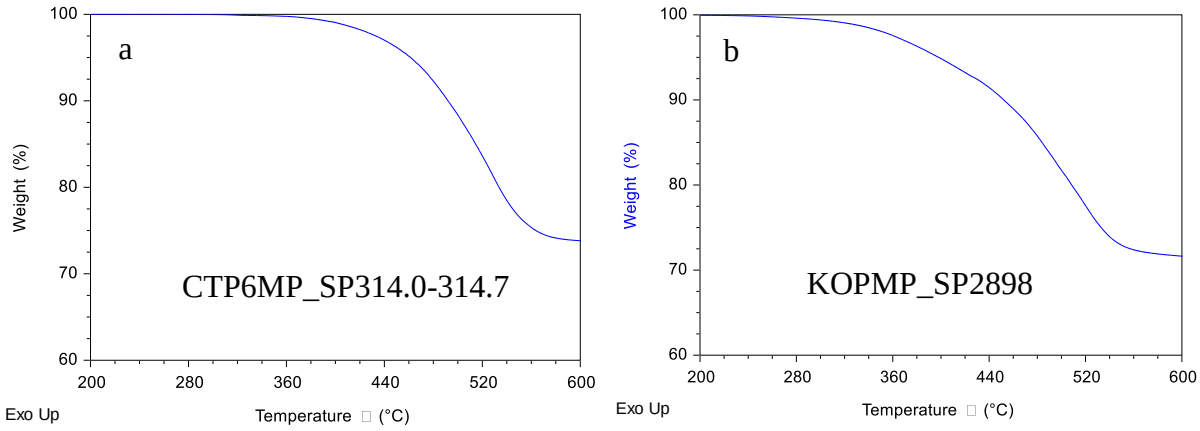

Figure 88: Thermograms of CTP6M (A) and KOPMP (B) indicating the onset of mass losses due to thermal degradation.

Table 31 shows a summary of properties for some of the CTPM and PPM samples prepared during BP1 and BP2.

Table 31: Carbon Fiber properties for select CTPM and PPM materials for PB1 and PB2.

Sample	Peak σ		Modulus		Peak ε	Diameter
	Mpa	Ksi	Gpa	Msi	mm/mm	µm
CTP6MP (CARB)	2491.3	361.5	182.5	26.5	1.17	-
CTP6M SP320 Average	-	333.6	-	34.0	0.95	17.4
CTP6MPSP314+_bs	1080.7±167.3	156.8	133.6±10.8	19.4	0.93±0.17	37.04±1.72
CTP6MPSP315+_bsN_bcH	1561.2±291.7	226.5	132.1±7.8	19.2	1.14±0.19	21.42±0.74
CTP6MPSP315+_bsO_bcH	1610.6±406.1	233.7	140.1±11.4	20.3	1.12±0.24	21.40±0.76
CTP6MPSP315+_bsP_bcH	1547.9±337.3	224.6	130.6±4.2	19.0	1.15±0.20	21.54±0.71
CTP6MPSP315+_bsQ_bcH	1360.3±282.8	197.4	109.3±17.4	15.9	1.21±0.21	20.73±1.08
CTP6MPSP315+_bsR_bcH	1504.0±352.3	218.2	127.1±14.9	18.4	1.15±0.21	21.01±1.2
CTP6MPSP315+_bsS_bcH	1296.0±174.1	188.0	115.0±10.3	16.7	1.12±0.11	20.89±1.09
CTP6MPSP315+_bsT_bcI	1731.6±143.4	251.3	162.2±8.0	23.5	1.05±0.05	21.39±0.67
CTP6M SP315+, 21 filament tows	-	260.0	-	24.0	1	-
CTP6MPSP321_bsC_bcF	1319.3±137.1	191.4	46.6±6.5	6.8	2.00±0.16	31.56±7.12
CTP6MPSP321_bsE_bcF	832.5±145.5	120.8	65.2±14.0	9.5	1.01±0.27	16.02±1.49
CTP6MPSP321_bsG_bcF	1215.1±93.0	176.3	70.8±16.7	10.3	1.33±0.21	16.70±2.35
CTP6MPSP321_bsH_bcF	51.7±12.0	7.5	4.6±1.0	0.7	1.14±0.25	17.39±1.71
CTP6MPSP321_bsO_bcF	731.1±452.2	106.1	71.0±31.1	10.3	0.73±0.26	17.58±1.58
CTP6MPSP320_bsF_bcF	1631.8±188.7	236.8	86.7±16.9	12.6	1.44±0.21	18.92±1.25
CTP6MPSP320_bsO_bcF	1080.4±370.5	156.8	92.0±20.3	13.3	0.93±0.18	18.95±1.75
CTP7MPSP340_bsF_bcB	1245.1±268.1	180.7	163.5±34.1	23.7	0.69±0.11	9.08±1.46
CTP7MPSP340_bsJ_bcB	1361.7±1071.2	197.6	124.7±65.7	18.1	0.82±0.33	10.03±3.15
CTP7MPSP330_bsC_bcC	1245.5±182.0	180.7	51.4±13.2	7.5	1.73±0.25	19.36±2.40
CTP7MPSP330_bsD_bcB	1258.1±284.8	182.6	47.5±11.0	6.9	1.91±0.32	21.68±4.15
CTP7MPSP330_bsI_bcB	1458.7±207.4	211.7	83.7±18.6	12.1	1.41±0.19	10.52±2.11
CTP7MPSP330_bsI_bcC	1221.2±202.8	177.2	51.4±13.2	7.5	1.72±0.25	19.10±2.56
CTP7MPSP330_bsG_bcB	935.9±225.5	135.8	74.8±7.4	10.9	1.11±0.16	18.98±2.97
CTP7MPSP330_bsG_bcC	905.4±258.2	131.4	84.9±13.9	12.3	0.91±0.20	16.29±2.16
CTP7MPSP330_bsH_bcB	806.7±175.8	117.1	91.2±13.4	13.2	0.77±0.09	9.24±1.15
CTP7MPSP328_bsF_bcF	181.3±186.9	26.3	22.7±21.5	3.3	0.68±0.54	42.87±13.62
CTP7MPSP328_bsC_bcF	572.7±179.3	83.1	25.7±9.4	3.7	1.43±0.33	43.78±2.73
CTP7MPSP340_bsE_bcB	1228.6±371.5	178.3	139.8±32.7	20.3	0.76±0.15	11.03±1.26
CTP7M SP340 (1)	1188	172.4	140	20.3	0.72	11.4
CTP7M SP340 (2)	1077	156.3	155	22.5	0.63	10.5
CTP7M SP330 (1)	1319	191.4	84	12.2	1.4	10.8
CTP7M SP330 (2)	1995	289.5	112	16.3	1.6	10.5
ACPMP1 (CARB)	2398.5	348.0	173.9	25.2	1.18	-
ACPMP1 (GRPH)	1677.3	243.4	252.6	36.7	0.57	-
KOP MP1	-	263.0	-	56.0	0.57	21

Figure 89 shows a plot representing of some of the isotropic materials, CTPM and PPM samples that were investigated in BP1 and BP2 with DOE targets defined. Table 32 shows the best performing materials from BP1 and Table 33 shows the best preforming materials form BP2.

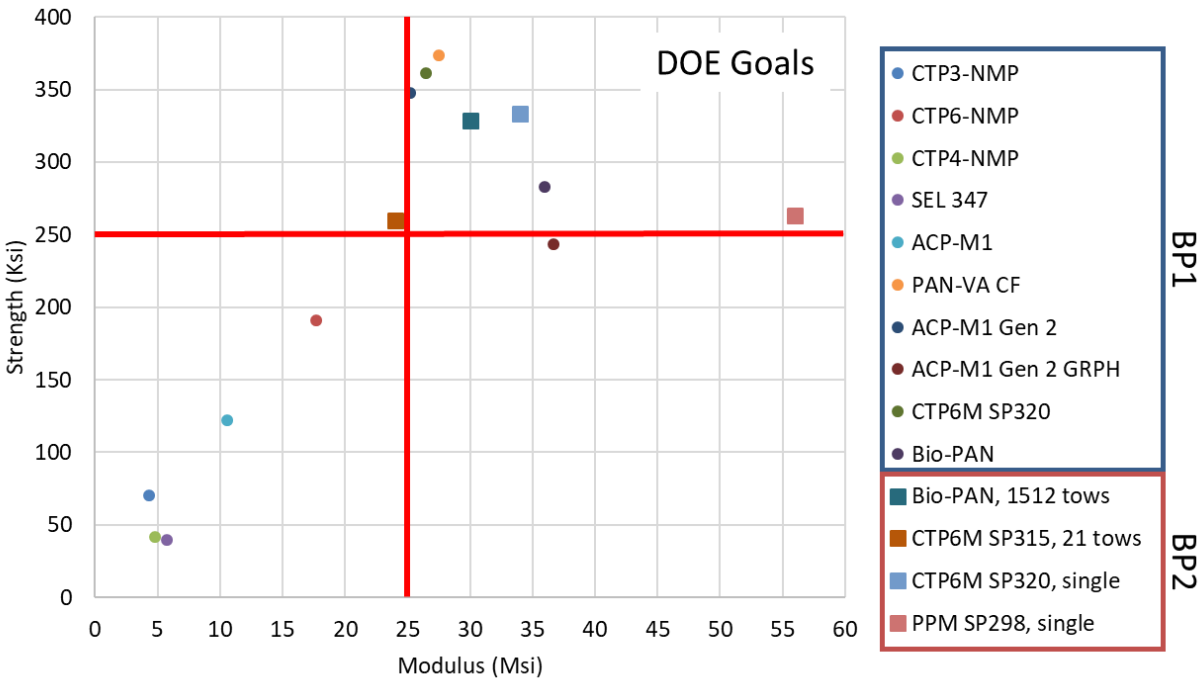

Figure 89: Summary of select Carbon Fiber properties.

Table 32: Mechanical property data for precursors developed in BP1 from some of the best CF produced from bio-PAN, CTPM and PPM.

Precursor	Strength (Ksi / MPa)	Modulus (Msi / GPa)	Strain (%)
Biomass-derived Precursors			
Bio-PAN	283 / 1948	36 / 248	0.86
Coal-derived Precursors			
CTP6M SP320	361.3 / 2491.3	26.5 / 182.5	1.17
Petroleum-derived Precursors			
ACP-M1	347.9 / 2398.5	25.2 / 173.9	1.18

Table 33: Carbon Fiber mechanical property data for scaled up precursors during BP 2.

Precursor	Strength (Ksi)	Modulus (Msi)	Strain (%)
Biomass-derived Precursors			
Bio-PAN (1512 filament tow, 7.7 µm)	328.9 ± 0.53	30.0 ± 1.0	1.11 ±0.15
Coal-derived Precursors			
CTP6M SP315+ (21 filament tow,	260	24	1.0
CTP6M SP320 (single filament, 17.4 µm)	333.6	34	0.95
Petroleum-derived Precursors			
KP-MP-19 (single filament, 21 µm)	263	56	0.57

Micro-Level Models and Simulations

Micro-level modeling began at the molecular level using both molecular dynamics (MD) and coarse-grained (CG) approaches. CG approaches use assumptions to simplify the number and type of atoms in a molecule so that not every atom must be accounted for during computations. This method allows for an increase in the number and/or size of molecules which can be modeled while significantly reducing computational power and time. To make meaningful GC models it is important that the assumptions represent molecular functionality for the true rate limiting chemical pathways. This means that important (most reactive) molecular features are accounted for as a group (a coarse grain) so that they can participate in reactions while more benign atoms are grouped together as another type of molecular feature (a different coarse grain). During the modeling efforts for the pitch-based systems it was found that a fully atomistic model was important to understand the proper assignment of atoms to form proper grains and a decision was made to pursue fully atomistic methods since there is a wide range of molecular diversity and assumptions for CG may not appropriate. On the other hand, the challenge in describing the polymerization of high molecular weight PAN within a purely atomistic approach is computationally expensive, can be largely mitigated through the overall simplification of the PAN model through GC-MD.

During BP1 and BP2 pitch-based modeling focused on understanding the best ways to model mesogen growth, stabilization and the relationship to CF properties. Ultimately it was found that hydrogen abstraction for proxy aromatic molecules may be the limiting feature for pitch-based

systems which may be adequate to describe the molecular arrangement of aromatic molecules to predict CF properties. This was also confirmed by the fact that the models could also predict the densities of resulting CF.

For PAN-based fibers, the pathway for PAN synthesis moving from polymers to the ladder structure towards cross-linking ladder structures was successfully modeled by the CG approach. The models were able to predict several CF properties, including density, and to give the correct direction trends between the various stages of PAN formation relative to physical properties, such as the modulus.

In all modeling cases, strength and elongation could not be modeled within the atomistic/CG models (as the size of the model is constrained to within a few nm) without imposing assumption on the role played by the microstructure, in the form of impurities, voids, grain boundaries, microstructural features. Indeed, strength is largely driven by defect density and so it is also a function of CF diameter, which is in the micro-scale. Upscaling the nano-scale models to account for an accurate description outside of it scaling boundaries, cannot not be immediately achieved. Rather than introducing scaling theoretical models to describe strength and elongation, with limited means of validation, the worked focused on materials properties capable of scaling directly from the atomic to the macro scale, such as density and elastic modulus and their evolution in relation to fundamental properties expressing the chemistry of the various feedstocks and the CF fabrication process.

Completing the modeling at each stage of CF processing—e.g. spinning, stabilization, carbonization, graphitization, etc.—was not possible due to the inability of ORNL to share this data with MIT due to export control. Later in the Phase 2 Topical Report some of these aspects were accounted for by ORNL developing an encryption for the various processing parameters.

Fully Atomistic Pitch-based Molecular Dynamics Modeling

An initial approach to molecular modeling was a combination of molecular dynamics (MD) methods (including the use of reactive force fields, ReaxFF, to account for the chemistry of in carbonaceous materials) to build structurally accurate, sample specific models, starting from a set of molecular “fingerprints”. These models, as detailed below have been optimized to represent, chemical and process reactions, as well as to predict, from the atomic models to global mechanical properties, as show in Figure 90.

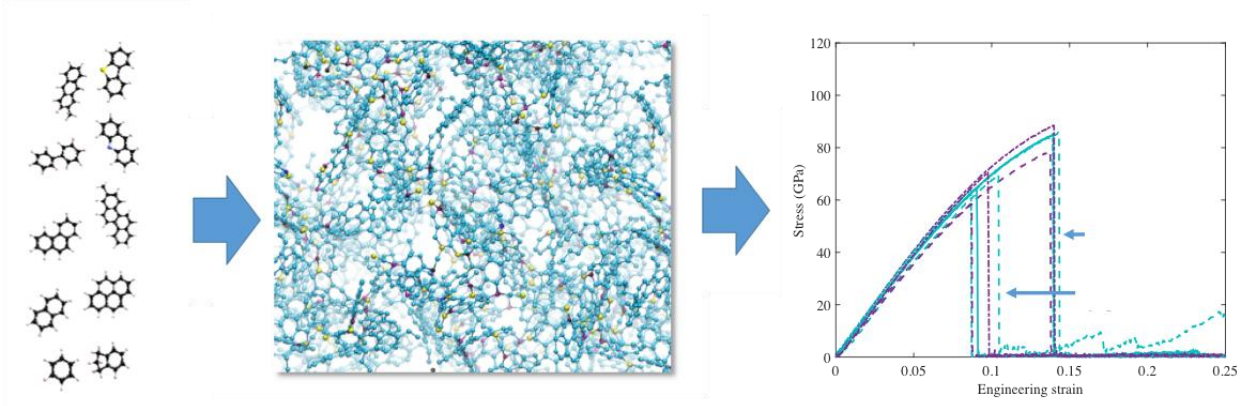

Figure 90: Schematic representation of the flow process in designing bottom-up atomistic, sample-specific, models (middle) from molecular fingerprints of carbonaceous materials (left) which are able to characterize global mechanical properties such as stress-strain.

A suite of process parameters and related frameworks were developed for modeling the evolution of atomistic models under high temperature processes relevant to CF production, while accounting for a wide range of environmental conditions during these processes, such as:

- Pyrolysis, combustion, oxidation/precarbonization, carbonization, graphitization
- Gas phase reactive chemical reactions (oxygen, hydrogen, free radicals, nitrogen)
- Bidirectional modeling of reaction kinetics that will allow for a direct, and unique, correlations of simulated molecular dynamics reaction times and reaction temperatures to actual experimental reaction equivalents. Table 34 shows correlations between MD-simulated parameters to equivalent experimental data.

Table 34: Example of reaction MD-simulated times temperatures equivalent to experimental process times at an experimental temperature of 450 °C. This is derived from Arrhenius reaction kinetics with minimal assumption based on a collection of experimentally derived activation energies.

Exp. Time (s)	MD time (s)	MD temperature (K)
~ 100	10^-9 (1 ns)	~1800
~ 1000	10^-9 (1 ns)	~2200
~ 100	10^-10 (100 ps)	~2200
~1000	10^-10 (100 ps)	~2600
~100	10^(-11) (10 ps)	~2600
~1000	10^(-11) (10 ps)	~3300

Predictive structure-to-function relations between atomistic models and global mechanical properties have been identified. By using well defined and studied test models based on graphene composites for validation, a suite of MD tools has been built to obtain stress-strain relations, modulus and elongation fractions from the atomistic models. Through the reaction kinetics algorithms described above, a direct correlation of the predictive mechanical behavior can be

established with the experimentally measured performance from the corresponding real sample. Establishing such direct, sample specific, correlation between atomistic models and their global behavior with real materials is a core mission of the modeling effort in this project (Figure 91, right). The functional understanding of sample specific mechanical performance and behavior (elastic, plastic regimes, etc.), is directly correlated to the structural evolution within the model, allowing the identification of the origin and onset of failure or plastic deformations within the structure (Figure 91, left).

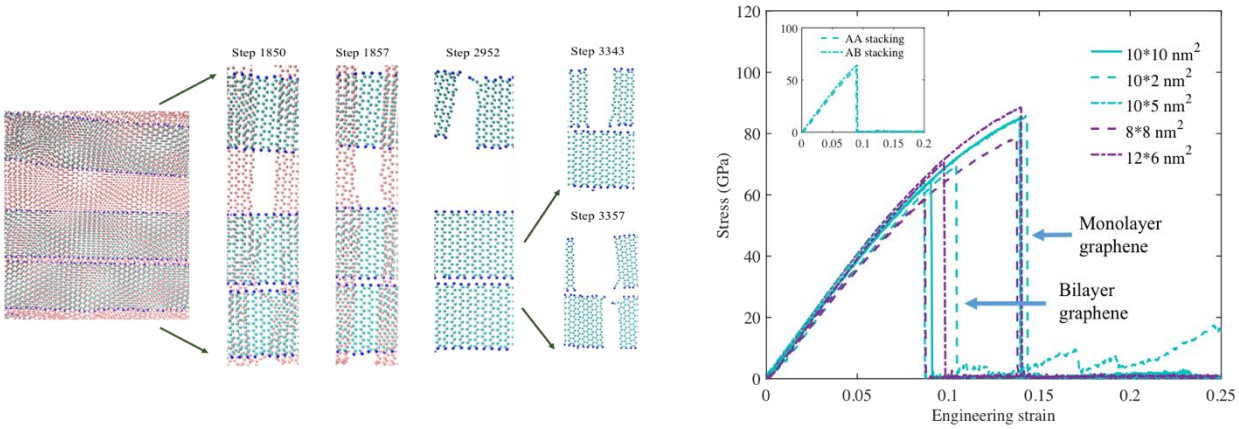

Figure 91: Simulated mechanical performance, through a stress-strain relation (right) is simulated from atomistic models of a test-system of graphene sheets and ribbons (left).

Initially, instead of using a broad range of molecular fingerprints to construct realistic models, such proxy models are constructed using only a very limited, yet carefully selected set of molecules (2-3 at most, Figure 92). Through selection criteria for the molecules, proxy models were used to maximize expected and explained unexpected phenomena (for example the role of anisotropy in the molecular structure for the formation of mesophase pitch).

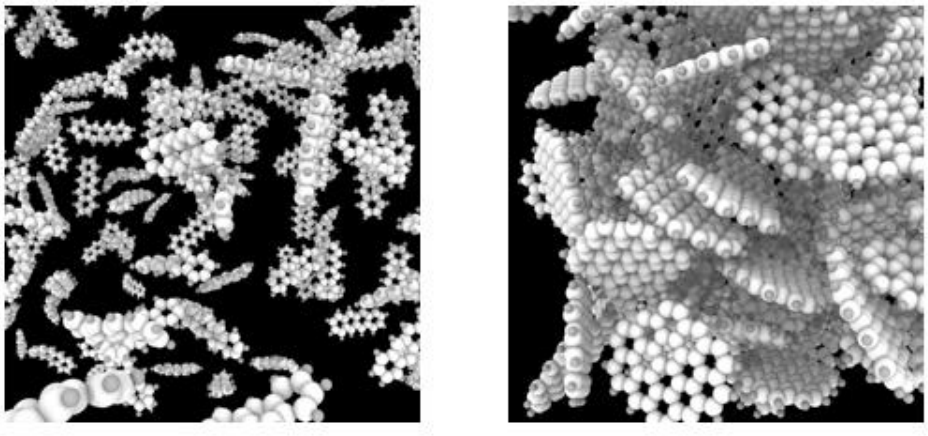

Figure 92: Simplified molecular proxy models using two types of selected molecules. In this example, tetracene (left), vs 14-ring aromatic cluster (right). Proxy models are created by mixing and converging carefully selected molecular sets with different proportions/concentrations. These models are then used to probe the role of structure (in this case molecular anisotropy) and chemical functionality when the system is subjected to a particular step of the CF synthesis. A first application is for the understanding of the formation of anisotropic mesophase pitch in relation to structure.

One of the main goals of the modelling effort in this program is to be able to use the developed molecular framework developed to guide, understand and predict the evolution of pitch throughout each phase of the CF production, in relation to the chemistry and microstructure. A detailed investigation was performed for the relation between molecular anisotropy and molecular alignment under conditions similar to mesophase formation and melt-spinning. This was done using a dual-molecular system (tetracene + 14 isotropic aromatic cluster) under conditions where mesophase is known to form (420-430 °C), with the application of uniaxial strain, the molecular evolution of the proxy model towards alignment can be studied. Results showed that anisotropic model aromatic systems (14-ring clusters, Figure 93) appear to show better molecular alignment, compared to isotropic model molecules (such as tetracene, Figure 94). However, when such clusters are added in small concentrations to tetracene, all molecules in the ensemble exhibit an enhanced alignment towards the stress direction (Figure 95). Temperatures in excess of 400 °C are needed to initiate cluster stacking.

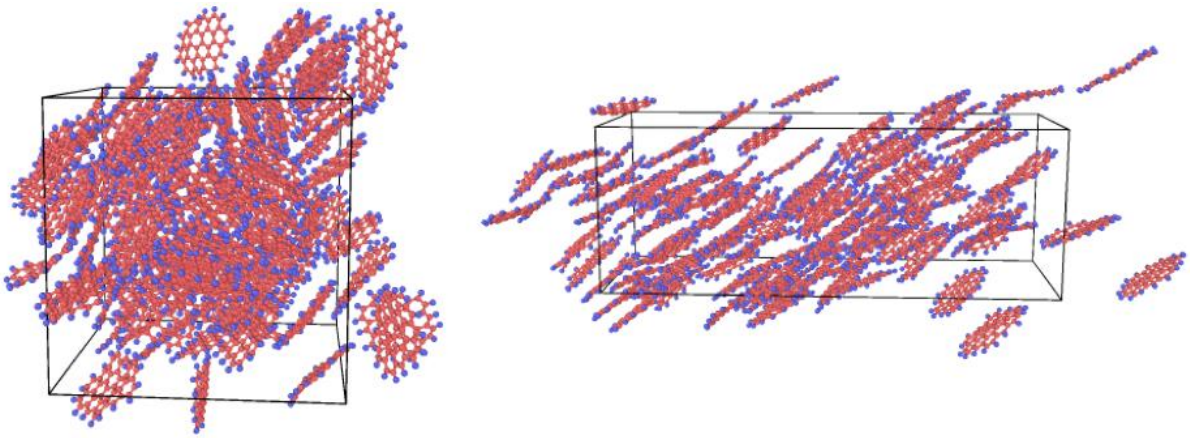

Figure 93: Ensemble of 14-ring aromatic clusters converged at room temperature (left). Simulation under uniaxial stress at 430 °C leads to preferred orientation and stacking along the stress direction (right).

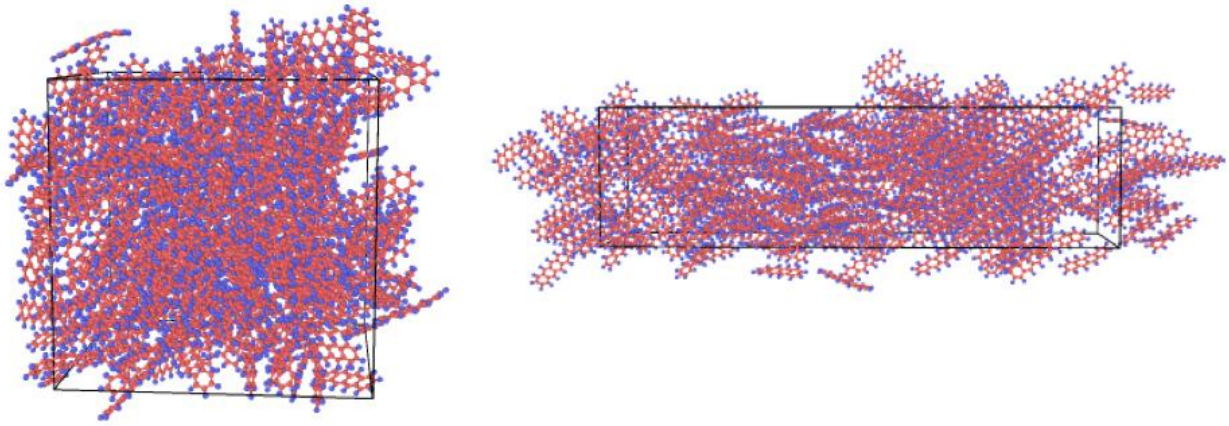

Figure 94: Tetracene ensemble converged at room temperature (left). Simulation under uniaxial stress at 430 °C does not lead to preferred orientation along the stress direction (right).

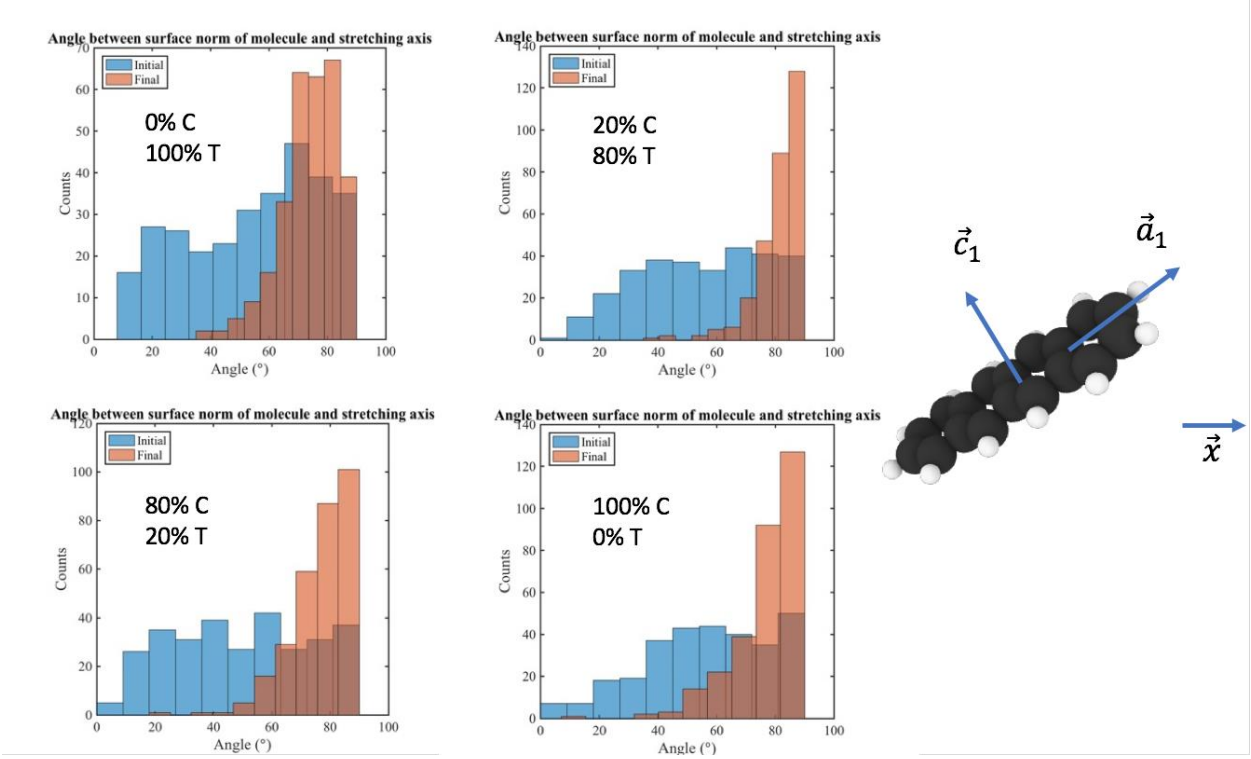

Figure 95: The distribution of alignment angles between the normal to the molecule c1 and the applied stress direction x is plotted for a series of mixtures between tetracene (T) and 14-ring aromatic clusters (C) at room 400C. A sharp distribution of molecular alignment along the stress direction (where c1 is perpendicular to x) is obtained for tetracene molecules is obtained when adding a small concentration of large clusters (20%C, 80%T)

Using the full molecule-to-CF genomic modeling method developed with the initial proxy molecules a set of CF models were created starting from different molecular sets that are reported in literature as proxies for CTP (all modeling from this point on only deals with HTCTP), CTPM and PPM, as shown in Figure 96 (Jian, Zhu, Adams, Grossman, & Ferralis, 2021).

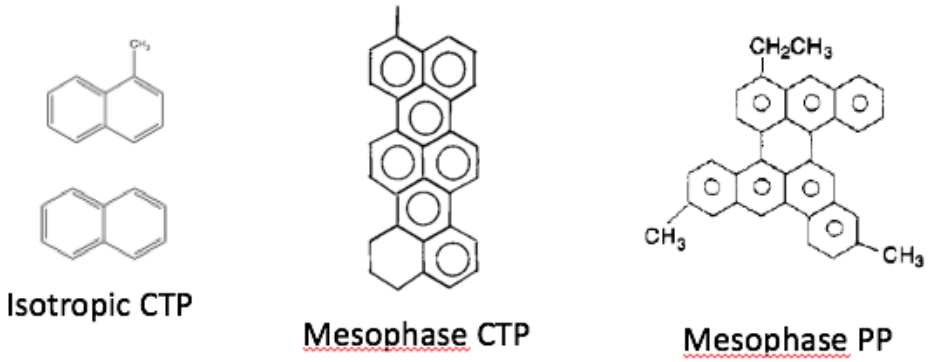

Figure 96: Individual molecular sets used as initial molecular fingerprints to create isotropic CTP (Korai, et al., 1998) (CTP, left), CTPM (Korai, et al., 1998) (center) and PPM (Kershaw, et al., 1993) (right).

A naphthalene-based pitch model was created to simulate both the formation of mesogens (formation of larger aromatic molecular intermediates to the mesophase), and stabilization products (oxygen is not yet accounted for so this is pseudo stabilization that will be referred to a pre-carbonization) of a purely isotropic pitch. The initial pre-carbonization of the overall framework was carried out as previously described and the larger intermolecular model has physical and chemical characteristics in agreement with experimentally reported naphthalene-based system (Figure 97).

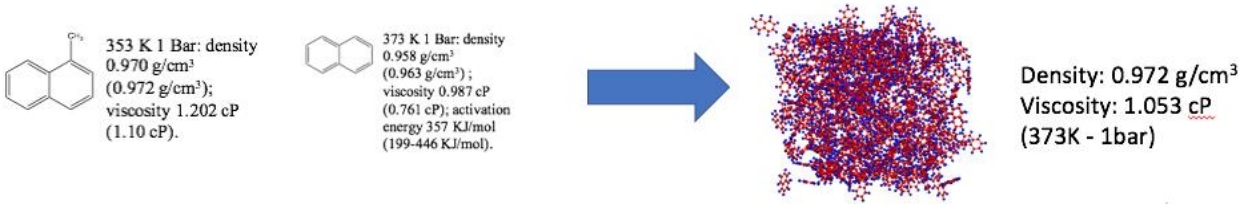

Figure 97: Comparison between simulated and experimentally reported properties of individual naphthalene-based molecules when pre-carbonized within a simulation box. The found parameters are well in agreement with experimental values with accuracy within 30%.

Pre-carbonization conditions employed during MD were based on experimental conditions reported in the literature. For isotropic pitch, these reactions are carried out at 2800-3200K (time: 720 ps), which corresponds to the experimental temperature of 670K (time: 1h), using the calculated activation energies for the conversion. After this step, the histogram of produced molecules consists of a large macromolecular cluster of interconnected aromatic fragments (number of overall carbon atoms: 380-2500, depending on the temperature), and a subset of small molecules (Figure 98). Higher processing temperatures significantly increases the size of the largest macromolecular ensemble, both in terms of the number of carbon atoms and size of aromatic clusters. This is expected, as aromatic cluster expansion depends on thermal activation. Higher processing temperatures result in a significantly reduced number of small aromatic clusters. In this initial set of simulations, only the largest aromatic cluster system was used for graphitization into CF, under the assumption that smaller molecules remain in gas phase and are therefore expelled. Thresholds for gas phase transitions for each small byproduct molecule were identified (Jian, Zhu, Adams, Grossman, & Ferralis, 2021) for a more accurate characterization of the molecular framework that is used for graphitization. We note that no preferential molecular alignment of aromatic units occurred within the molecular framework, after pre-carbonization or after graphitization, a model consistent with that of an isotropic pitch.

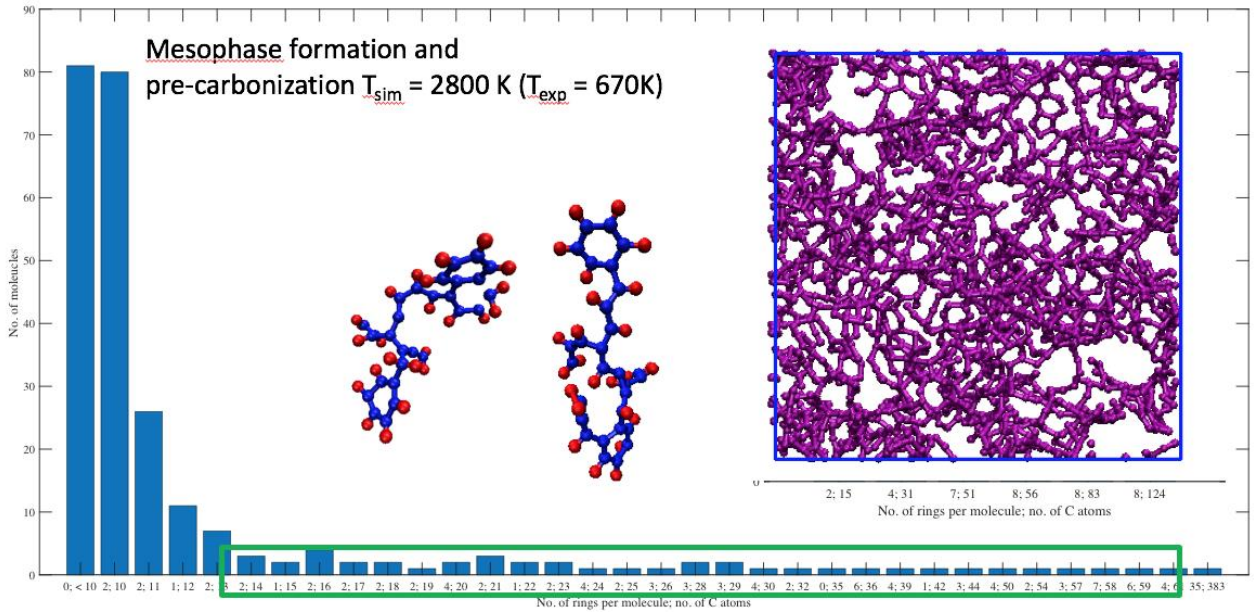

Figure 98: Histogram with the byproduct molecules resulting from the pre-carbonization step. Small molecules within the green box were not considered for graphitization. Only the largest (structure depicted in the imbedded panel at the upper right; distribution of number of rings and carbon atoms for the largest clusters) molecular framework was used for graphitization into CF.

A similar set of models are created using mesogen molecules representative of mesophase CTP for a naphthalene analogue system (Korai, et al., 1998) (as shown in Figure 96, center) and PP. Under similar processing conditions (temperature, time, pressure), a similar histogram can be generated to visualize the byproduct molecules when starting from the mesogens (Figure 99) (Jian, Zhu, Adams, Grossman, & Ferralis, 2021). Indeed, a large interconnected molecular framework is formed, and a set of much smaller aromatic molecules are produced. Just as in the case of the isotropic CTP, those small molecules were discarded before simulating graphitization. Since those molecules are already represent a larger aromatic cluster, compared to the single molecules in the isotropic pitch, the expectation is that at the same processing conditions the number of aromatic rings within the framework will not significantly increase in size compared to the initial mesogens. Indeed, this is observed and consistent with the hypothesis that aromatic cluster size expansion depends directly on the processing temperature. It also appears that by starting with the larger aromatic mesogen molecules that less lighter molecules are formed which would lead to less CF shrinkage and a higher carbon yield. An extensive formation of interconnections across the individual mesogens into the large framework is also similarly observed. We note that the observed overall trend is similar for both molecular frameworks generated using both CTP and PP mesogens, despite the different chemical functionality.

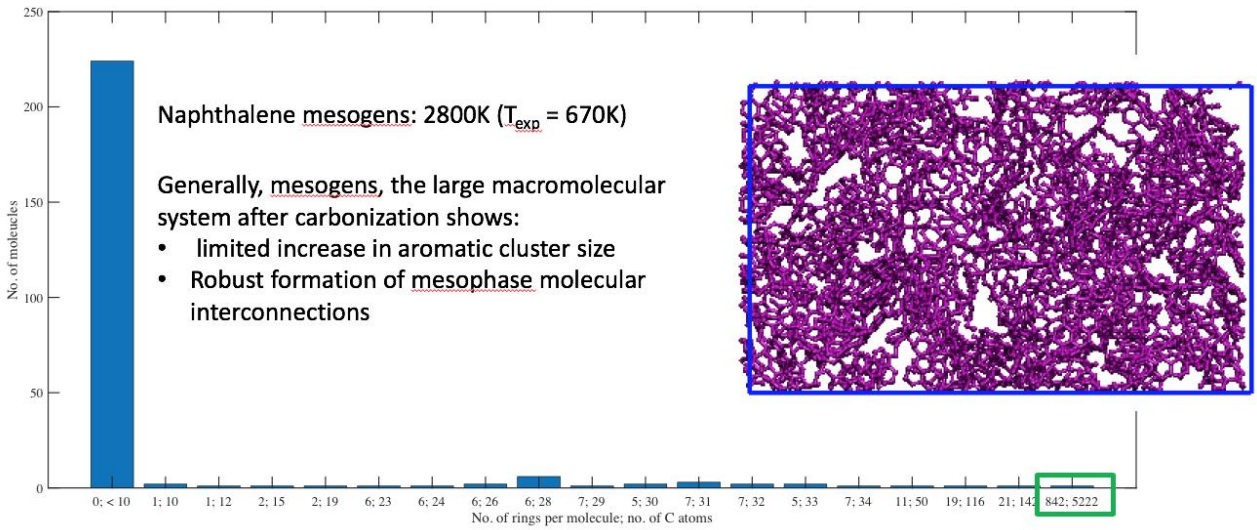

Figure 99: Histogram with the byproduct mlecules resulting from the precarbonization step starting from CTP mesogens molecules. Only the largest (structure depicted in the panel; distribution of number of of rings and carbon atoms for the largest clusters are shown under the panel) molecular framework is then used for graphitization into CF.

It was explored how different carbonization temperatures affect the molecular alignment of aromatic clusters within the produced framework (Jian, Zhu, Adams, Grossman, & Ferralis, 2021). While no alignment is observed at any temperature for isotropic pitch, it is clearly observed for mesogen frameworks (Figure 100). The initial random distribution of angles between the surface normal of each mesogens, evolves into a distribution around a fixed angle, with observed formation of stacking. This is preserved during processing at carbonization and graphitization.

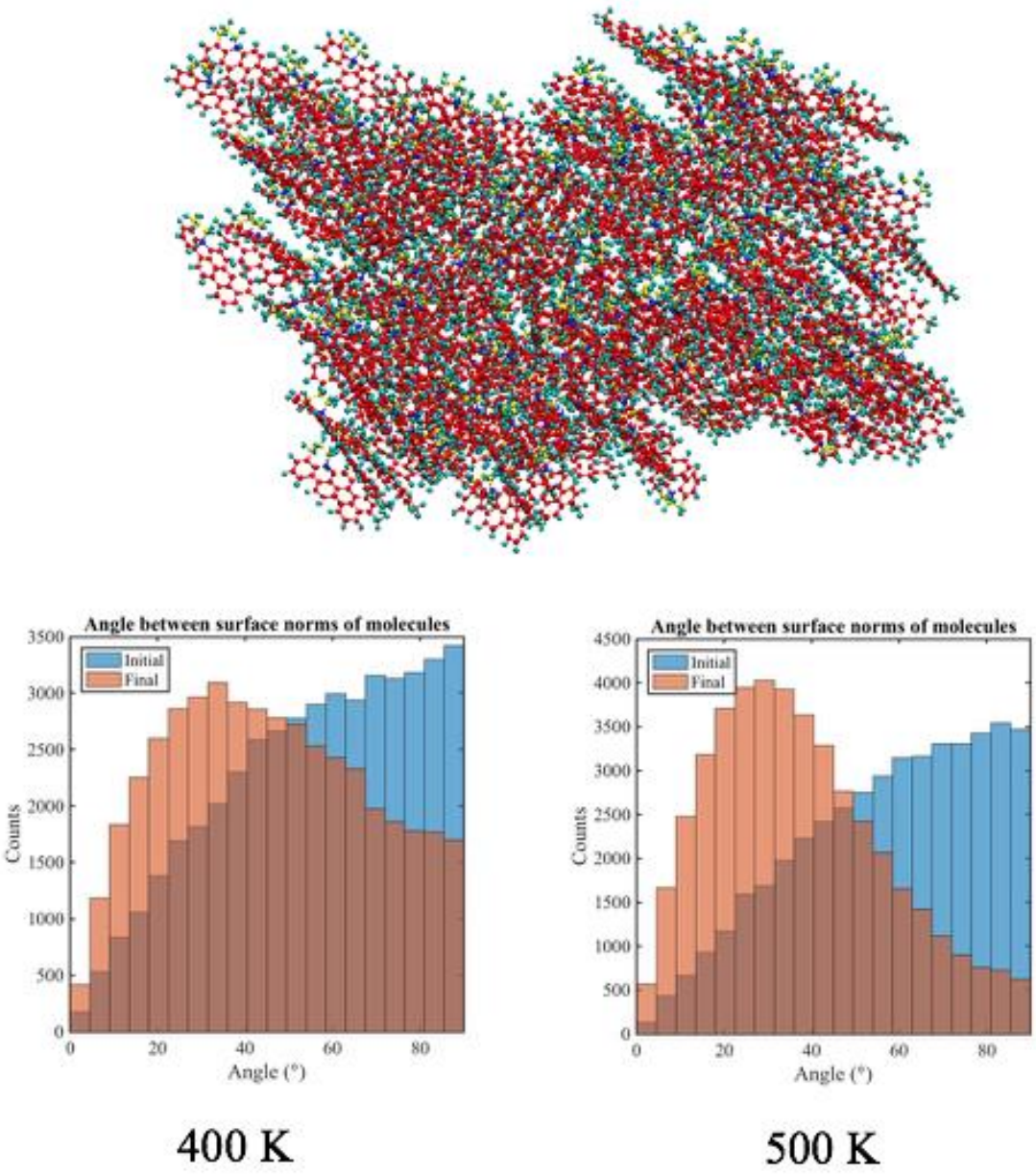

Figure 100: Distribution of alignment angles between the normal to the molecule c1 and the applied stress direction x is plotted for the CTPM using mesogens (carbonization model is depicted on top).

Initial graphitization conditions applied to the molecular framework were selected, once again, using processing parameters consistent with the experimentally used synthesis conditions. Using the testing protocols developed early in the program to probe the mechanical properties of graphene nanoribbons (such as stress-strain relationship, Young's modulus (YM)), we evaluated these properties for CF obtained from the three systems described earlier, namely CTP, CTPM and PPM. The effects of applied pressure under graphitization were explored for pressure ranging from no pressure to bulk values. When graphitization is carried out at low surface pressure (~50 mmHg (Huang X. , 2008) or < ~4 Torr (Noda, et al., 1965) YM for isotropic and

mesophase naphthalene-based CTP is 20 and 60 GPa respectively, which is in agreement (within 30%) with the values for CF experimentally synthesized under similar conditions (Figure 101, left). When pressure is applied during graphitization with values consistent with high bulk pressure (10 Kbar), YM increases for the two systems to 220 and 389 GPa respectively (Figure 101, right), which is also consistent with the performance of experimentally synthesized naphthalene-based CF under similar processing conditions. It is notable that YM for mesophase CF is consistently between 2 to 3 times larger than that of isotropic CF. In comparing the CF mechanical performance of CTP and PP mesophase, we observed no notable differences in YM values and stress-strain performance. Using different mesogens formation temperatures also does not appear to have a significant effect on the performance. It should be noted that molecular frameworks obtained in the carbonization step for CTP and PP carried out at identical processing conditions are chemically similar (i.e. with similar aromatic content, aromatic cluster size, etc.).

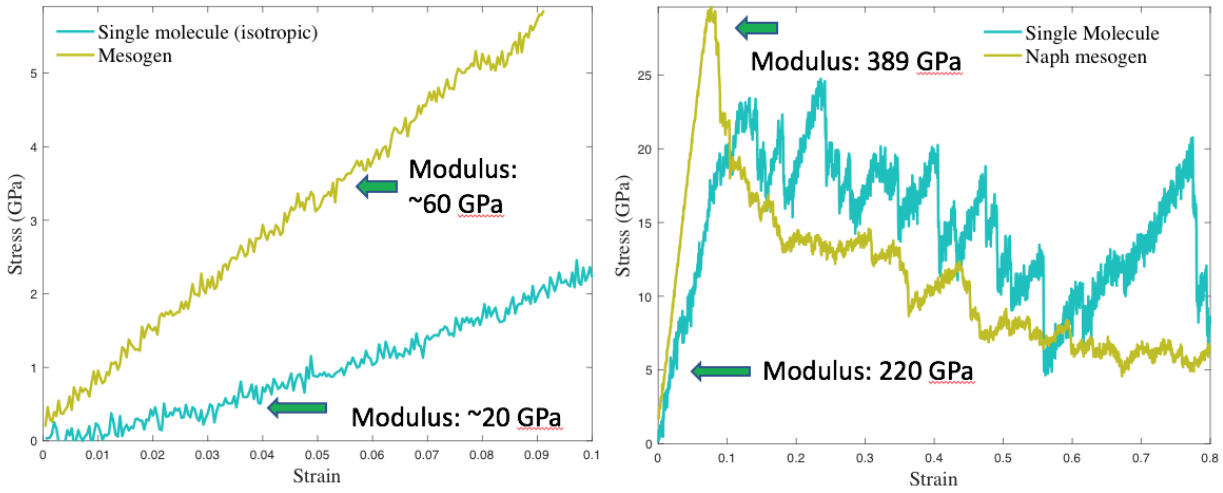

Figure 101: Stress-strain relationships and Young's moduli for isotropic and mesophase CTP, under different graphitization pressures: low surface pressure (left) and high bulk pressure (right).

The initial, experimentally validated results on CTP and PP isotropic and mesophase systems were obtained under standard, yet not optimized, processing conditions. Four research directions were explored to identify structure-functional relationships between the precursors and CF performance: 1) evaluation of intermediate reaction byproducts during mesophase formation and carbonization steps; 2) statistical identification of the distribution of aromatic clusters and interconnection after the pre-carbonization step; 3) effects on cluster alignment in relation to processing conditions; 4) breaking down the single mesophase formation/pre-carbonization step into a more realistic two-step process. In parallel, we are evaluating more complex initial molecular systems beyond the naphthalene system developed so far, which are capable of capturing more complex aromatic chemistry, heteroatoms, etc.

Building on the insight from the naphthalene-based precursors to construct simulated CF, more realistic molecular choices capable to accurately describe the chemical subtleties of coal- and petroleum-based precursors were developed during BP1. For this purpose, a computational

framework was developed to simulate CF synthesis from various coal-based and petroleum-based precursors. The molecular choice that was adopted to identify realistic precursors to CF synthesis—with reduced complexity and with simplified processing conditions (i.e. no oxidative processing steps)—allowed the generation of synthetic models that are correctly validated with experimental conditions and final CF mechanical properties.

In BP2, a precursor-to-CF atomistic framework has been adopted to resolve major limitations set in the framework in BP1, namely: 1) improve our prediction accuracy by implementing oxidation/stabilization stage into our computational framework, and 2) adopt realist molecular sets that are experimentally validated to be representative of the precursors currently used by the Consortium. The latter requires a thorough understanding on the growth pathways of PAHs during mesophase formation.

Molecular sets to be used for full atomistic models that satisfy two requirements: 1. They realistically capture the most common molecules in pitch; 2. The flexibility in their composition and fractionation should be used to investigate different CTP and PP. Based on internal experimental LDI data from WRI and literature (Fan, Fei, Chen, & Li, 2017), all CTP and PP appear to have a wide but well determined range of molecules within 3 and 13 aromatic rings). Different CTP or PP will have different distributions and if significantly different feeds or process are used the types of molecules can be different. In this study the PP is produced from slurry oil consisting of mostly 3- and 4-membered rings and the catalyst processes cause most slurry oils today to contain very similar sets of molecules. Also, the CTP produced from metallurgical coal and they were all identified to contain about the same type of molecules and the distributions of these molecules were only slightly different between the different CTPs. By choosing a well determined set of molecules that are experimentally determined to be the most common in CTP, we expect to build models with different compositions by adapting the fractionation of each constituent from the molecular set. In the case of PP, the presence of base aromatic systems with different methyl functionalization is accounted for.

The following molecules were chosen to represent in varying degree of concentrations to represent CTP: acenaphthene, phenanthrene, anthracene, chrysene pyrene (with methyl group), benzo[a]anthracene, benzo[a]pyrene, triphenylene, benzo[ghi]perylene. Many of these smaller 3- and 4-ring molecules are not actually present in CTP, however they are the fundamental building blocks which lead to larger dimeric structures formed by the crosslinking of these molecules. Using these molecules will provide an understanding of some reasonable substitution patterns crosslinking these PAH molecules to form larger PAHs that will help to understand crosslinking patterns when forming larger mesogens.

It is worth noting that the well documented mechanism of supramolecular formation. Cluster merging to mesophase formation, based on dimer-based molecular interaction, provides the relationship between some of the molecule chosen, as well as those that are supposed to be generated in the modeling. In the atomistic modeling, no constrains over the possible reaction pathways are set within the ReaxFF framework. Therefore, a validation of the reasonableness of

the model was performed using Density Functional Theory (DFT) so that modeling results are consistent with experimental assumption (Figure 102). Besides providing guidance on the fidelity of ReaxFF based models to capture the correct evolution towards mesophase and further downstream CF synthesis, such studies will help identify the role of contaminants during mesophase.

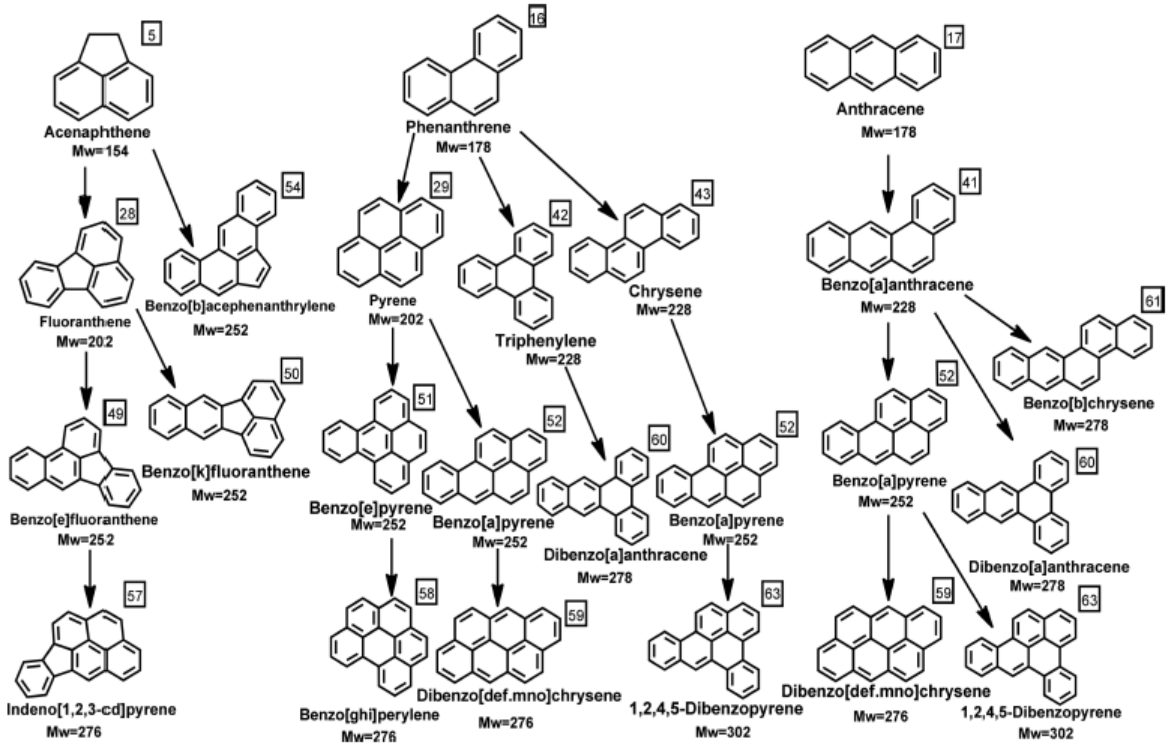

Figure 102: PAH growth (Fan, Fei, Chen, & Li, 2017) under investigation as the validation step by DFT. Taken energy input from higher level calculations, atomistic simulations can be performed at a much larger length scales by employing several hundred molecules.

The details of PAH reactions during CF processing are crucial for the quality of product, and ultimately designing/optimizing the fabrication processes. However, these details are largely unclear or empirically based on known reaction kinetics. Accurate *ab initio* methods were applied to scrutinize the reaction pathways proposed in the literature (for example listed in Figure 102), and then search possible alternatives in a high-throughput manner. This goal was accomplished in three steps, as shown in Figure 103, with progressing computational complexities. In the first stage, computational methods were calibrated for the calculation of reaction enthalpies with well-established reactions. This step focuses on the validity/accuracy of DFT and various functionalities. The next step switches to saddle-point search using nudged elastic band (NEB) method. After the calibration, this method was used to study the effects of H_2O and O_2 in CF processing (see later). Following the second step, the pathway searching was automated, and high-throughput pathway searching was achieved. The results from these studies are not only important for CF synthesis, but also for general PAH reactions, such as those involved in astrophysics, combustion, and environment pollutants.

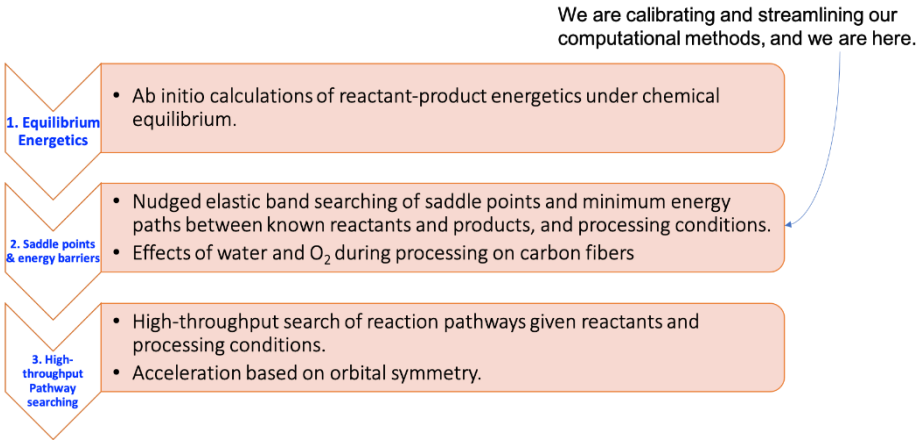

Figure 103: An overview of the proposed roadmap for our ab initio studies on PAH reactions in Carbon Fiber processing.

Calculations of chemical and reaction energetics, based on B3LYP hybrid functional and Pople basis sets, have shown satisfactory agreement with known published results. At this point, given a hypothesized pathway, the energy evolution can be calculated accurately. However, most of our questions involve only reactants or products, or even both might be hypothesized. Therefore, potential energy surfaces (PES) need to be calculated. Several strategies were tried, such as *ab initio* molecular dynamics, PES scanning, and umbrella sampling. Results showed that NEB is an acceptable method for this work in terms of its balance between computational expense and reliable accuracy.

As the first step, computational methods and numerical setups were tested. For this purpose, a calibration was performed with the combination of B3LYP hybrid functional, augmented by 6-311+G(d,p) basis, with two model reactions (Figure 104). The first reaction is a HACA process, in which hydrogen is abstracted and acetylene is added, leading to a 5-ring addition. The energies calculated, also plotted in Figure 104(left), agree well with literature values (Unterreiner, Sierka, & Ahlrichs, 2004). The second reaction is the oxidation process. The energetics for the hypothesized pathway also agrees with the literature (Barckholtz, Fadden, & Hadad, 1999). Using this method the energies have been calculated for all the reactions listed in Figure 102.

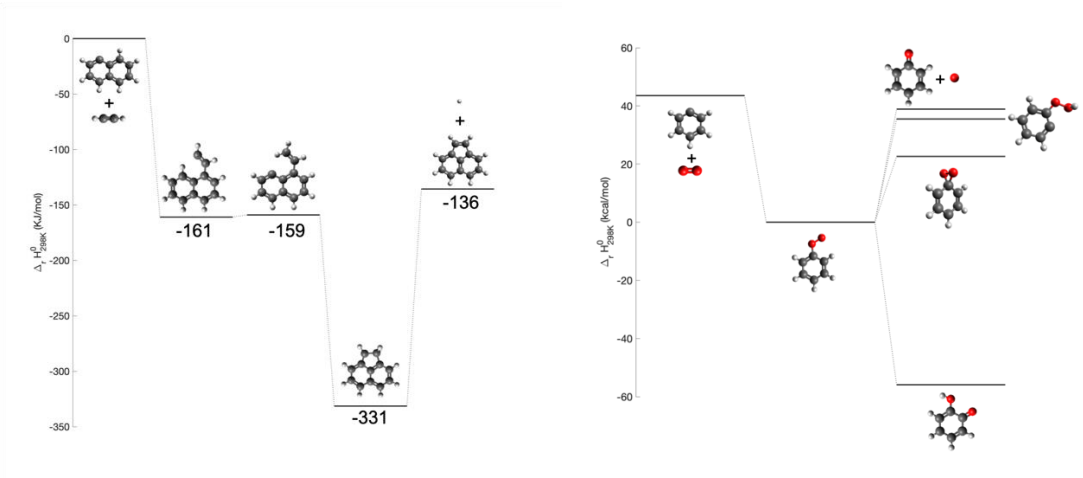

Figure 104: Calibration of B3LYP/6-311+G(d,p) for two model reactions. Left is ring addition via hydrogen abstraction acetylene addition mechanism. The results compare well with B3LYP/SV(P) results reported in values (Unterreiner, Sierka, & Ahlrichs, 2004). The right is oxidation reaction, and the results agree with B3LYP/6-31G(d) calculation in (Barckholtz, Fadden, & Hadad, 1999).

Following the thermochemical calculations in Step 1, the computational tool for PES searching was further calibrated. For this purpose, Nudged elastic band (NEB) was applied on a well-studied Diels-Alder reaction between ethylene and 1,3- butadiene,

$$C_4H_6+C_2H_2\rightarrow C_6H_8$$

The results are summarized in Figure 105, in which NEB found a minimum energy pathway and the energy barrier 23.2 KJ/mol (300K) is in good agreement with the values reported in literature (Huang, Geissler, & Chandler; Lischka, Ventura, & Dallos, 2004).

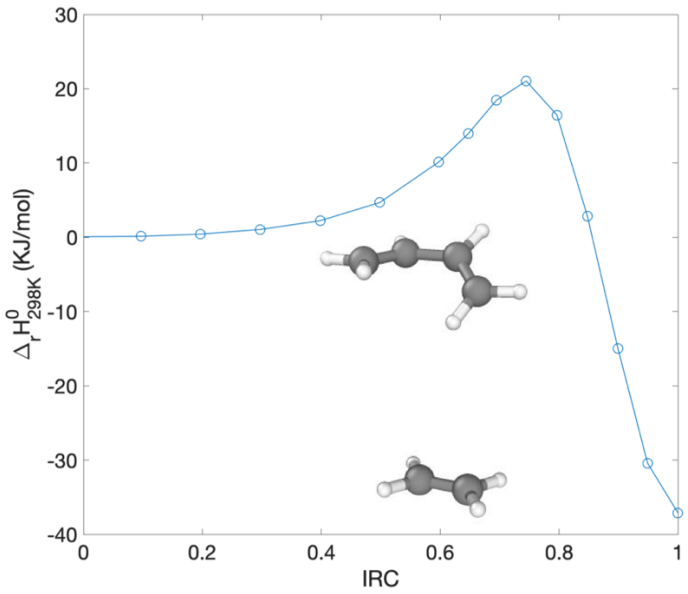

Figure 105: Minimum energy pathway searched by NEB using B3LYP/6-311+G(d,p) for a Diels-Alder reaction C4H6+C2H2® C6H8, our results agree well with the literature values.

With the calibrated first-principles methods, the calculations were extended in the next step systematically to a hypothesized reaction pathway, as shown in Figure 102. This pathway was proposed in (Fan, Fei, Chen, & Li, 2017) for CTP, based on experimental measurements using high-resolution matrix-assisted laser desorption/ionization time-of-flight mass spectrometry combined with other analytical techniques. However, these reactions are largely hypothetical, and a systematic scrutiny will provide insights valuable for better applications of CTP as well as fundamental understandings to the overall PAH reactions in natural carbonaceous materials.

The following system shown in Figure 106a was constructed to mimic CF synthesis from compounds identified in coal tar using gas chromatography–mass spectrometry (Figure 106b). Adopting computational streamline developed in BP1, the final modulus of the resultant fiber was listed in Figure 106c in comparison with previous monodispersed system (taking mesogen as one example, same processing conditions). It can be seen that CF synthesized from polydispersed systems with random oriented molecules show a smaller modulus, in close proximity to the value reported in literature for isotropic tar (Hawthorne, Baker, Bentall, & Linger, 1970).

a)

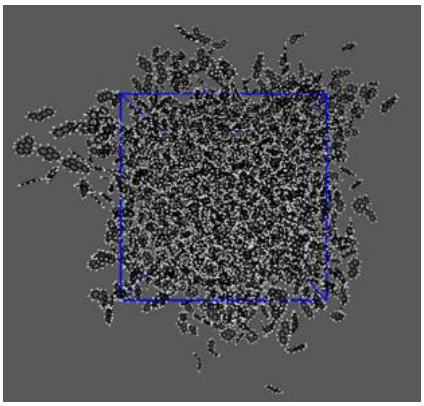

b)

Compound	Coal Tar ppm wt/wt
Acenaphthylene	16
Fluorene	2050
Phenanthrene	14800
Anthracene	6200
Pyrene	22000
Benzo[a]anthracene	17700
Chrysene	16500
Benzo[b]fluoranthene	13400
Benzo[k]fluoranthene	5100
Benzo[a]pyrene	10500
Indeno[1,2,3-cd]pyrene	5200
Dibenz[a,h]anthracene	1500
Benzo[g,h,i]perylene	4000
Total Above Detction Lim.	118966

c)

Materials	Modulus (GPa)
Mesogen	60
Coal tar	33

Figure 106: a) A representative configuration of the polydispersed system, b) compounds, as well as their concentrations, used in constructing the configuration, and c) comparison of Carbon Fiber modulus synthesized from different materials.

Extending from the energetic calculations, the first-principles investigation is carried out in three phases: i) NEB search of saddle points and minimum energy paths has been implemented, which allows the characterization of reaction kinetics, more than earlier thermochemical calculations; ii) an automatic pathway proposing framework has been developed. This framework considers the given mechanisms and symmetry of molecules, and can enumerate all possible pathways; iii) the mechanism of hydrogen abstraction acetylene addition (HACA) has been extended to polynucleus condensation, the latter is closely related to mesogen formation. Each phase is described in the following.

Building on the energetic calculations using DFT, the NEB algorithm widely used in solid-state physics is implemented to search for saddle points and minimum energy paths between known reactants and products. The conventional approach of proposing pathway relies mostly on chemical knowledge and experience, which is also true in the processing of carbonaceous materials. For instance, a pathway shown in Figure 107a, was hypothesized for the indenopyrene (Fan, Fei, Chen, & Li, 2017), among many others. The energy states and corresponding barriers are calculated (Figure 107b). While the former tells the thermodynamics and equilibrium states, the barriers newly calculated during this quarter would be valuable for kinetics. The kinetics give an indication of how fast the reactions can occur as a function of temperature. All the hypothesized pathways have been assessed similarly (not shown here).

However, the conventional approach has two shortcomings: i) inaccurate pathways might be proposed, and ii) additional possible pathways might be missed. Taking the example of molecule, the originally hypothesized pathway is shown to be energetically unfavorable, since the energy states of product is about 100 kcal/mol higher than reactant. To search for alternative pathways, a top-down algorithm was developed to automatically enumerate all possible pathways. The example for molecule is shown in Figure 107c. Considering the symmetry of

product, by gradually splitting C_2H_2 or C_4H_4 radicals while adding hydrogens (Figure 107c, inset), the process is the reverse reactions of HACA. This also gives a way of automatic pathway enumeration to propose all possible pathways for given rules. For molecule, 7 pathways are proposed. Note that this algorithm is geometrically based, and the results in Figure 107c are shown for HACA mechanism.

Extending to other mechanisms is straightforward, such as polynucleus condensation. Similar to the above HACA mechanism, an automatic algorithm could be developed based on molecular symmetry. However, for polynucleus condensation (e.g. Figure 107d), an alternative approach based on charge density was attempted. For instance, the algorithm is shown for pyrene dimerization and trimerization (Figure 107d). The HOMO state and total charge densities are shown in Figure 107e-f. While HOMO states are believed to be most reactive, they show little evidence for bond splitting. Instead, varying total charge density leads to the weak bonds (Figure 107f, right), which suggests the possible mechanisms of dimerization, as denoted by the arrows. Similar calculations are also performed for the pyrene trimer (not shown here), and the automation of pathway proposing framework based on charge density is under development. This pathway proposing framework can be considered as an enhanced version of the above geometry-based framework, but would complement each other in enumerating all possible pathways.

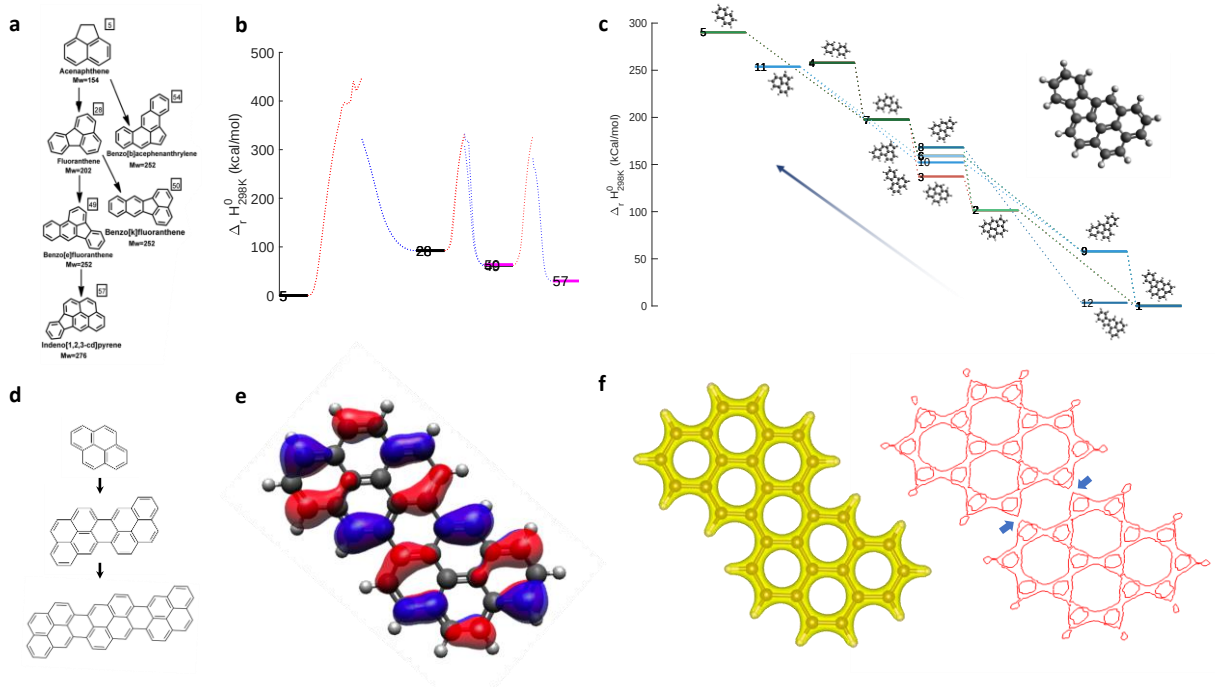

Figure 107: (a-c) first-principles energetic calculations based on hydrogen abstraction acetylene addition mechanism. A hypothesized pathway for molecule [57] shown in (a) is assessed with regards to both energetics and minimum energy path (b). (c) the automatic enumeration of all possible pathways for [57]; (d-f) polynucleus condensation mechanism for pyrene dimerization and trimerization (d), (e-f) HOMO and total charge density of pyrene dimer.

Atomistic Modeling of Coal Tar and Petroleum Pitch

While an integrated framework that connects coal and PP feedstocks and fiber mechanical properties has been developed and calibrated during BP1, such framework relied on reactive force fields simulations (ReaxFF) to determine the chemical evolution of feedstocks, from small molecules to mesogens to CF. Building on the extensive atomistic characterization of the individual components during BP2 (mesogens formation energies and reaction pathways), next the formation and alignment of mesophase for realistic CTP and PP molecular models were investigated, with the development of predictive rules linking chemical functionalization, molecular size, and molecular interactions to the final molecular alignment of mesophase and ultimately of the CF. In particular, both the physical and chemical processes during mesogen formation were studied. It is hypothesized that such process of great complexity is composed of self-assembly (physical) and polyaromatic ring growth (chemical). This work was designed in a way to decouple the physical and chemical processes: the former focuses on the dynamics of self-assembling using classical molecular dynamics, and the latter focuses on the possible synergetic effects of mesogenic phase on ring growth based on density functional theory calculations.

In this research, the dynamical process of mesogen self-assembly was investigated, focusing on the effects of side groups attached to the aromatic units on the quality and rate of mesogen formation. This assumes that all the mesogen units have been produced, and it focuses on how the molecular units self-assemble into an aligned mesogen phase, which is complementary to the second work explained below. As shown in Figure 108, both artificial and natural pitches, represented respectively by naphthalene and FCC pitches, are studied. To obtain statistically significant results, five independent replicas are sampled, each of which contains 1000 molecules and will run through 10ns dynamics simulation. Figure 108 shows the aligned systems for N1 and N2 molecular packings at 500K.

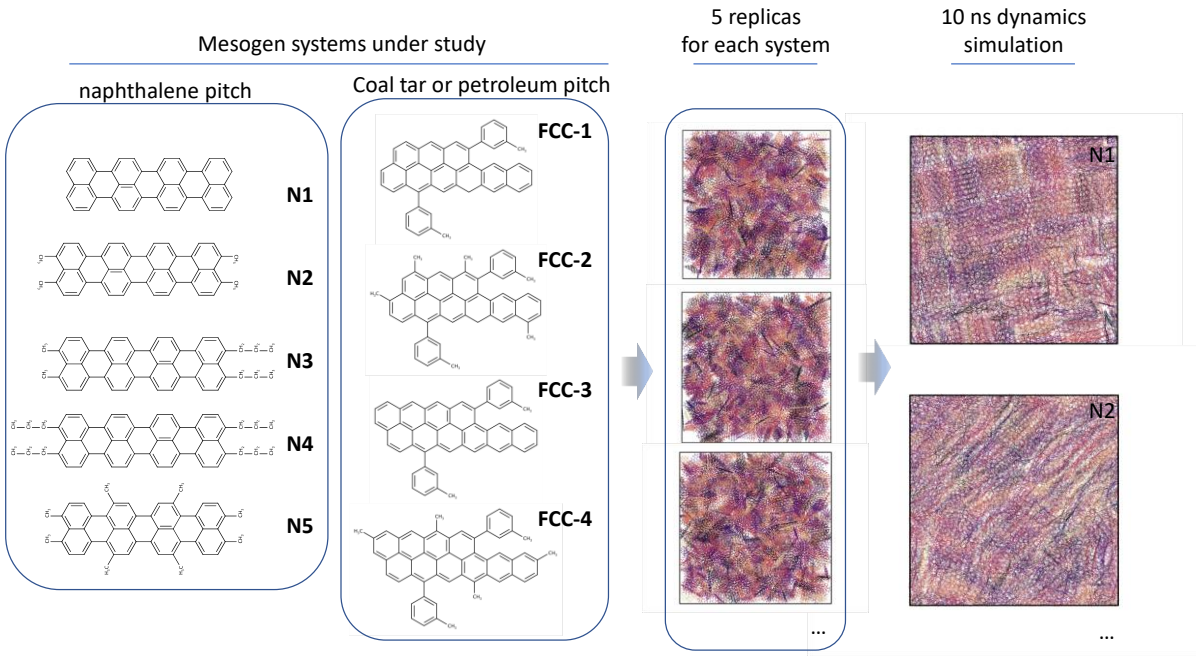

Figure 108: The naphthalene and CTPs are being studied. For each of the system, five independent random packings are sampled, followed by 10 ns dynamics simulation with classical molecular dynamics. Two examples are shown for N1 and N2 systems, where self-assembled alignment could be visually identified.

Based on these results, two quantitative metrics were defined to quantify the alignment and self-assembling. On one hand, the distribution of molecular orientations could be used to identify the alignment and possibly the number of grains in the system. One example is shown in Figure 109 (a-c), where the visual alignment evolution can be quantified by the concentration of orientations, denoted by the peaks. Ideally, the system should exhibit only one peak, which suggest the whole system aligns in a single direction. However, considering the time scale and phsically possible existence of grains, multiple peaks could coexist. On the other hand, to define the quality and speed, the oritentaional entropy is defined as

$$S(\theta) = -\sum P(\theta)\log P(\theta)$$

where $P(\theta)$ is the distribution of angles between the molecular orentation and a reference direction, such as $(0,0,1)$ in this case. The results for the example in Figure 109 (a-c) are shown in Figure 109(d). It is interesting to note that $S(\theta)$ at equilibrium states can be used to compare the alignment quality, and the slope approaching the equilibrium states, $\mathrm{d}S(\theta)/\mathrm{d}t$, can be calculated to quantify the speed of self-assembling (aligning) process.

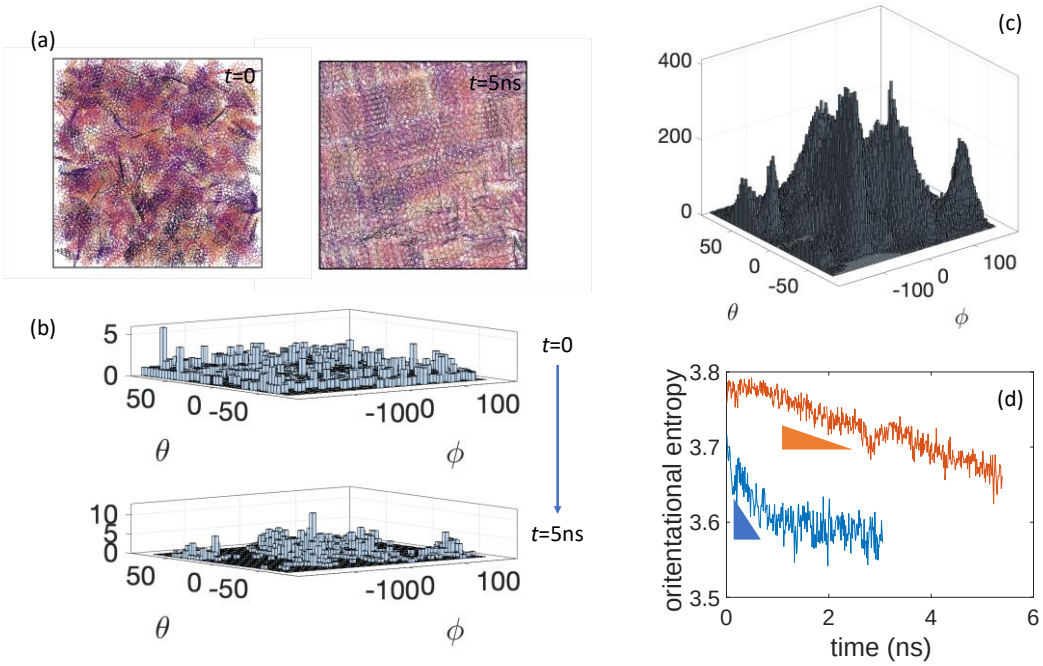

Figure 109: (a) Snapshots from dynamical simulations showing the evolution molecular orientation and alignment from N2 system. (b) angle distribution for the two snapshots at 0s and 10ns, where concentration of specific angles can be observed. (c) the distribution of molecular orientations for all snapshots during last 1 ns simulations. (d) orientational entropy as a function of time for N1 (red) and N2 (blue) systems, where quality and speed can be defined respectively by the equilibrium entropy and slope as they approach to equilibrium states.

To explain the observations of side-groups on varying self-assembling speed and quality, two competing effects are currently under investigation. On one hand, the mesogenic unit should possess sufficient mobility that allows the individual molecules to adjust their orientations. The molecular mobility of different molecules with different side groups is quantified by molecular diffusivity as

$$D = \frac{1}{6}\lim_{t\to\infty}\frac{d}{dt}\langle u^2 \rangle_t \quad ,$$

where the mean squared displacements $\langle u^2 \rangle_t$ is defined by

$$\langle u^2 \rangle_t = \frac{1}{N}\sum_{i=1}^{N}|R_i^t - \bar{R}|^2 \quad .$$

The mobility for the naphthalene-tetramer variant units is summarized in Table 35.

Table 35: The diffusivity of naphthalene-tetramer variants. (units 〖μm〗^3/s)

N1		N2	N3	N4	N5
0.4		1.7	2.2	2.1	2.6

The novel insight from this work consists in the identification of the role of side-groups in the molecular mobility of mesogens units, in essence their rheological behavior. In general, side functionalization by short methyl groups increases the mobility of naphthalene tetramers. However, on the other hand, entropic effects will compete with the mobility effects tending to favor disordered distributions. This latter effect of entropic driven force falls outside of the current work, but it will the subject of future investigations to estimate at different temperatures the change in viscosity of these molecular system based on their functionality, by identifying the transition temperature from a “solid-like” system to a highly viscous, yet fluid system. This can ultimately be compared with the experimental measurements of the pitch softening point.

A second direction concentrated on the effect of molecular absorption for ring addition. By investigating how large mesogen units impact the chemical reactions between smaller reactants, new predictive pathways for optimal alignment, and utilization of smaller molecular systems can be achieved. On the latter point, during mesophase formation extensive mass loss is generally observed, due at least in part, to outgassing of lighter aromatics units. By investigating how the low molecular weight aromatic unit interacts with larger mesogen units, and the strength of the interaction, this may point to strategies for maximization of small molecule retention and reduction of mass loss during mesophase formation by seeding with larger aromatics. The premise of this is the presence of larger mesophase units, either introduced externally or chemically generated during processing, where smaller reactants would be absorbed onto their surface. This absorption can hypothetically allow the alignment of molecular orbitals, which favors ring growth, as it was found during the first and second quarters (see the FCC pitch example in Figure 110 a). This work starts from the study of absorption followed by the energetic calculations for radical production and molecular orbital analysis. Figure 110 (b-c) shows the case of naphthalene pitch.

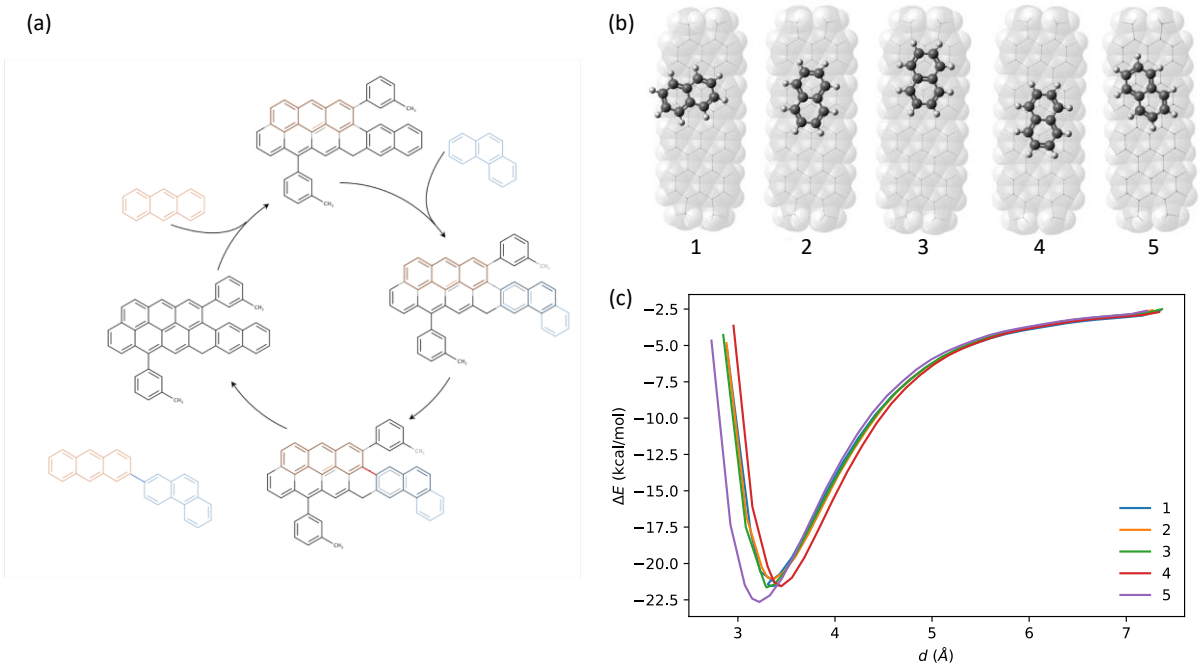

Figure 110: (a) The hypothesized self-catalytic mechanism due to absorption of small reactants onto the mesogen units, which allows alignment of molecular orbitals that in turn facilitate the reactions. (b) five absorption configurations studied according to symmetry, and (c) energy as a function of molecular distance, the absorption energies for different configurations are all around -21 kcal/mol.

Considering the symmetry of naphthalene trimers, five absorption cases are studied (shown in Figure 110(b)) based on DFT. FCC pitches have also been studied similarly and are not shown here. The energy as a function of distance between a naphthalene molecule and a naphthalene trimer is shown in Figure 110 (c). The equilibrium distance is around 3.4 Å, with absorption energy around -21 kcal/mol, which is around 1/5 of C-H bond dissociation energy (103 kcal/mol) and could introduce non-negligible effects on the reactions, such as radical production and chain reactions. Such results point to the strong interaction between small molecules and larger mesogens, with a potential increase in molecular retention. Some of these concepts will require further investigations further as they tend to contradict some well-known trends in mesophase formation. For instance, high quality mesophase (a narrower molecular weight distribution) is produced by sparging the mesophase reaction to continuously remove lower molecular weight material. Low quality mesophase (more bimodal distribution of lower molecular weight and much higher molecular weight materials) is produced if lower molecular weight molecules are not liberated during the reaction.

To connect the raw materials and product under a consistent model, the key missing part of the modeling framework is the simulation of the chemical reactions. So far it has been demonstrated the evaluation of individual pathways, and an automatic exploration algorithm for all possible pathways was developed. This framework and results are shown in Figure 111. It will be discussed in the following that this framework will allow consistently simulating the cross-scale processes in CF synthesis, including oxidation.

This newly developed framework combines ML and kinetic Monte Carlo, as shown in Figure 111(a), which consists of three main parts: molecule generative model, energetic prediction, and pathway ranking. The generation model of molecule configurations is currently based on rule-based algorithms, followed by ReaxFF and then DFT relaxations. This model can be extended to other generative models, such as GCGAN algorithms. In this work, four example families of reaction mechanisms are mixed, as shown in Figure 111(b), including i) hydrogen abstraction acetylene addition (HACA), ii-iii) peri- condensation via mono- and di-radicals, and iv) binding by oxygen. Shown in each category are four example reactions, (A., B., C., D.).

As reported earlier for individual pathways, the Gibbs energy of each generated molecule, with vibrational entropy considered, are calculated based on DFT or ML prediction based on molecular graph convolutional neural network (MGCNN) model (Xie & Grossman, 2018). The choice of DFT or MGCNN is based on prediction uncertainty of MGCNN model. If the uncertainty or error is higher than 5%, then DFT is revoked and the results are added into the database, and the model is retrained. However, as shown in Figure 111(c), with MGCNN model trained on 1700 molecules, only 1% of the verification set exceed the 5% error threshold. Therefore, the ML model is reliable for Gibbs-energy prediction.

With the molecular enthalpy (H) and Gibbs energies (G), we can estimate the reaction thermodynamics. For instance, for the reaction $A_1 + A_2 \rightarrow B_1 + B_2$, the reaction enthalpy is calculated as

$$\Delta H = \sum_{B_i} H_{B_i} - \sum_{A_i} H_{A_i}$$

In Figure 111(d), 1700 pathways are shown for each of the four example reactions in Figure 111(b). The energy landscape exhibits a maximum of 200 kcal/mol difference between reaction enthalpies for all the 1700 pathways.

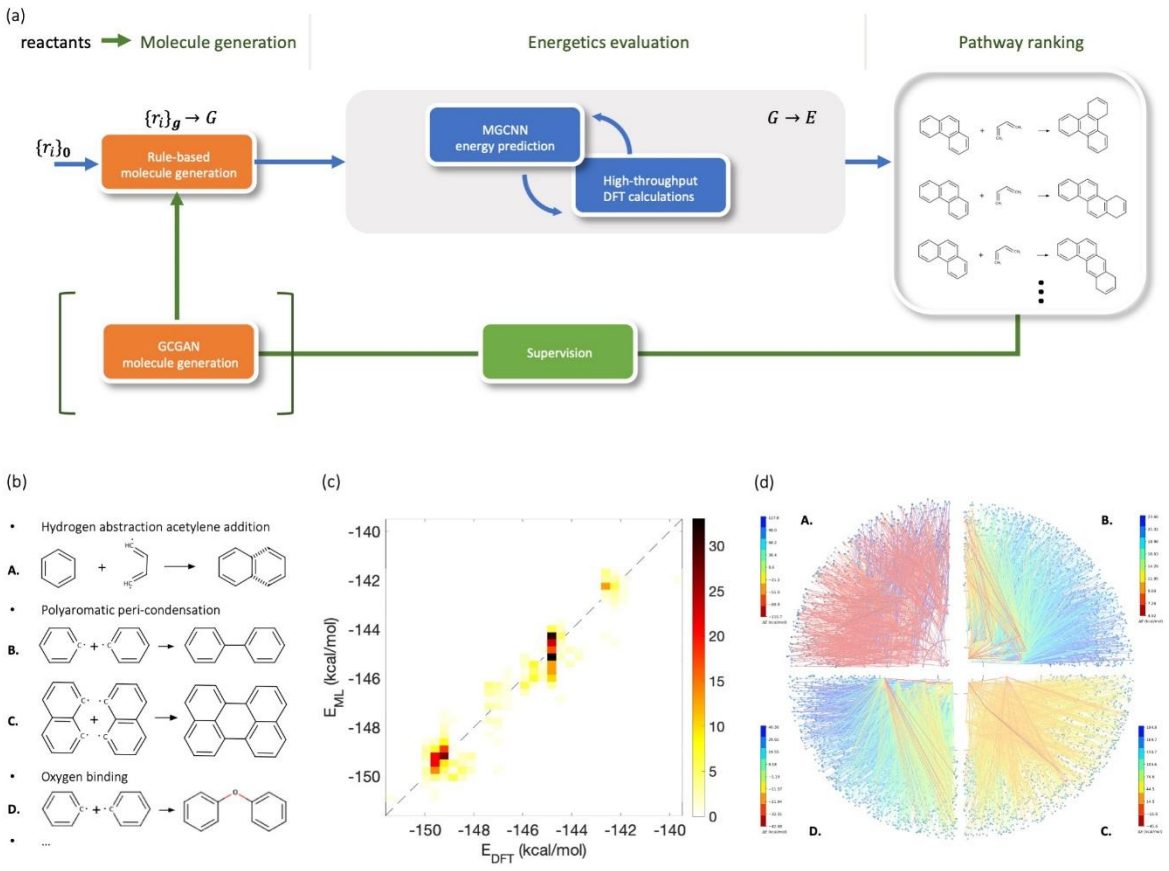

Figure 111: The computational framework and results for four types of reactions. (a) The numerical framework consists of molecule generative models, energy calculation and prediction, and pathway ranking. The choice of density functional theory or machine learning for energetics calculation is based on prediction error. (b) Four example rules for PAH reactions, including HACA (A.), radical aromatic condensation (B. & C.), and oxygen binding (D.). (c) Molecule-graph convolutional neural network (MGCNN) prediction of enthalpy versus DFT values. The prediction error of machine learning model is within 5% for 99% molecules. (d) The ranking of the four example reactions in terms of enthalpy reduction. The molecules considered are generated in 3 generations. The number of generations and kinds of reaction rules can be extended.

The resulting combination of atomistic simulation tools developed during BP2 for modeling the synthesis of pitch-based CFs that lead us to develop a new modeling framework that does not rely on chemical and physical assumptions. The extensive exploration of reaction dynamics from first principles, including a chemically justified identification of oxidation chemistry during the CF stabilization step, provides a robust framework for the creation of chemical rule-based synthesis of CF. This framework was used to accomplish the stated milestones for BP2, and in particular: 1. Create a realistic set of ensembles of small molecules and derived mesogens for pitch. 2. Identify reaction chemistries in presence of oxygen to simulate the oxidative step 3. Generation of CF from the ensembles with the expected improved accuracy in mechanical behavior. We note that this is a different approach than that used in BP1, where molecules were hand selected and reaction pathways not identified. Besides obtaining more realistic models, BP2

produced the fundamental understanding of several phenomena during the synthesis process that are helping to enable: 1. Understanding and optimization of the role of oxygen functionalities during stabilization in molecular alignment; 2. Correlation between initial molecular configuration and pitch processing (in relation to rheology); 3. Optimization of synthesis processes. Each will be described in the following sections.

1. Equilibrium of reaction graph.

The equilibrium states of the reactions are calculated by van't Hoff equation,

$$\log K = -\frac{\Delta H}{RT} + \frac{\Delta S}{R} \quad ,$$

in which the reaction entropy can be estimated *via* DFT. With the above framework and pathway ranking, we are able to estimate the equilibrium abundance of each chemical.

2. Kinetic Monte Carlo simulations

The ensemble of ranked pathways will be transferred to next quarter for kinetic Monte Carlo simulations, which is the last piece to connect raw materials and product. After that, the framework could produce dependence of mechanical properties of CFs as functions of chemistry of raw materials and thermodynamic conditions. An important step in the modeling was the transition from a monodisperse system to polydisperse system. The molecules were chosen from GCMS measurement, as summarized in Figure 112. The molecule sizes range from 3 to 6 rings, and the effects of branch groups were studied later. The choice of a selected subsets of experimentally derived molecular systems that can realistically represent the CTP, is justified within the previously developed framework based on the machine-learning and kinetic Monte Carlo, as shown in Figure 113. While an essentially infinite number of molecules (initial and mesogens) can be selected, we chose an experimentally derived set as a matter of simplicity, consistency, and reliability. It follows that the synthesis of CF here described can be applied to any particular molecular set of choice, including the derivation of larger molecular systems (mesogens) from the atomistic framework.

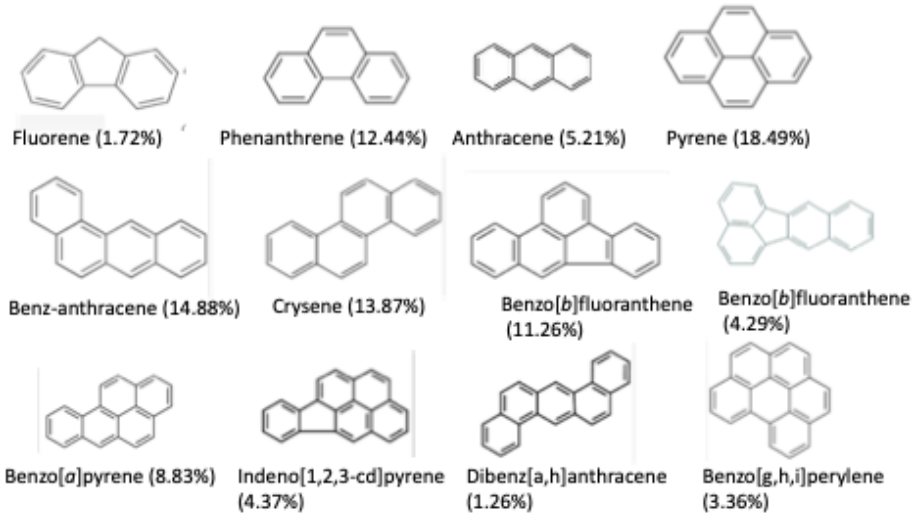

Figure 112: Molecule models from GCMS measurement. Ring sizes from 3 to 6 are observed and no other pendant groups are considered. It should be noted that 3 membered rings are not prevalent in CTP because they are distilled out from the coal tar with the anthracene oil fraction. However, they are included to understand the impact of smaller molecules on the modeling.

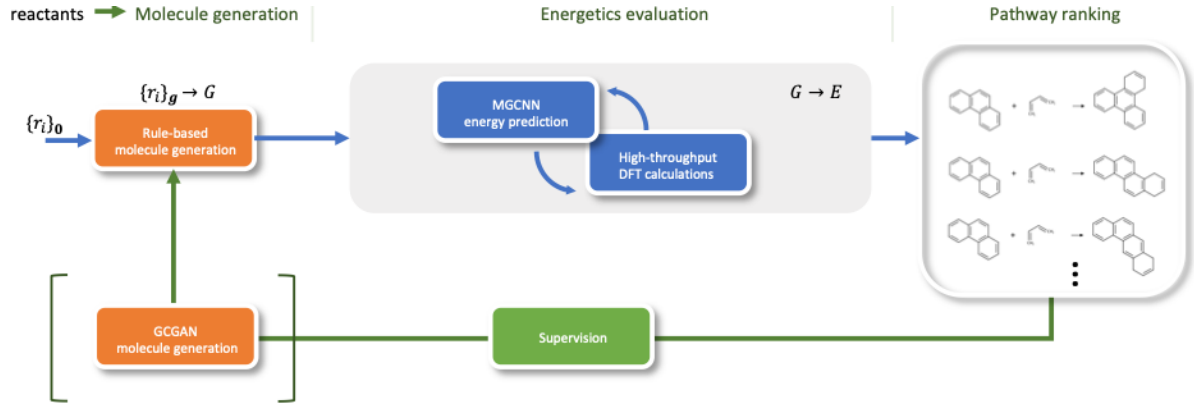

Figure 113: The computational framework and results for four types of reactions. (a) The numerical framework consists of molecule generative models, energy calculation and prediction, and pathway ranking.

Molecular dynamics based on ReaxFF were extensively performed to probe the reactions between the chosen molecules. As shown in Figure 114, the temperature of the system was ramped from 3K to 3000K in 0.3 ns, which will be held constant for 0.7 ns. During this period, the number of molecules (*N*m) keeps reducing, suggesting small molecules are combining and bigger rings are produced. Meanwhile, the number of different species (*N*s) increases, because small radicals are also produced (Figure 114, (b), B. and C.). The overall number of molecules is going down, but that the diversity in the species produces is increasing, which can be understood from the reaction of phenathrene (a three-ring system) grows into to several different larger species but also produces several different gaseous species. This could be seen from the change of molecule masses, *M* (Figure 114, top right). While small molecules/radicals are produced, the backbone rings are combined to form larger rings. At the end of the 1ns simulation, the system is composed of one whole molecule, along with small gaseous radicals—similar to the

disproportionation which occurs upon coke formation. This is also shown in Figure 114, bottom. The color denotes the molecule ID. As times goes from 0 to 0.6 ns, the variation of color (molecule ID) reduces, indicating that all original small rings chosen from GCMS have reacted with each other, resulting in a larger carbon network.

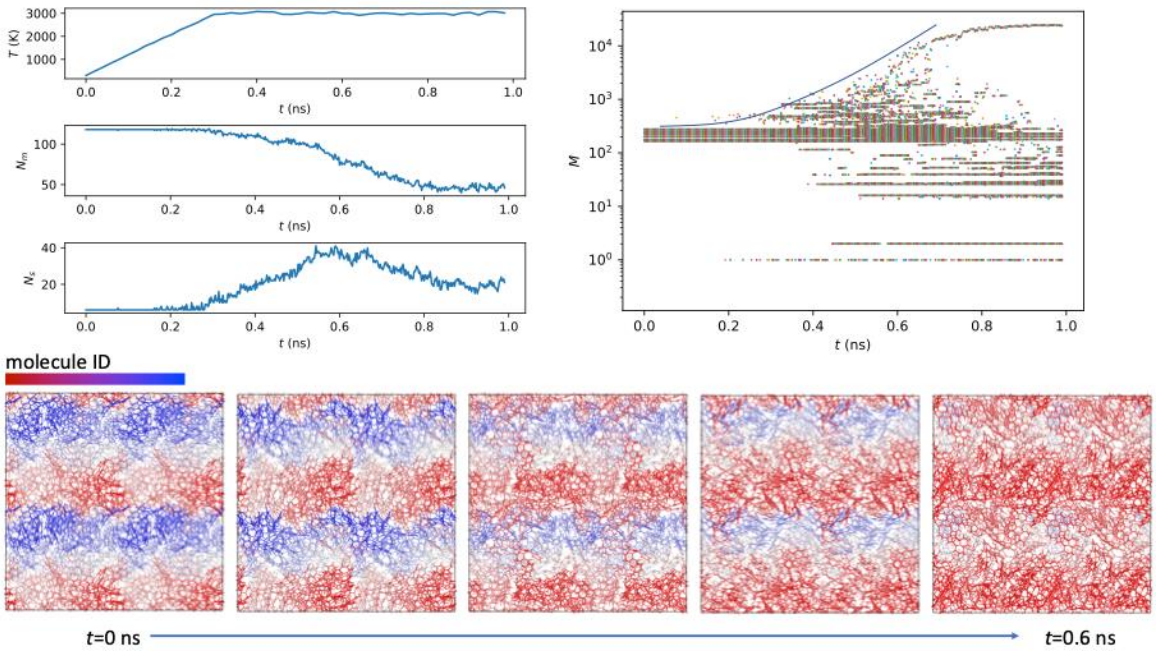

Figure 114: The numerical processing approach and corresponding reaction dynamics.

It was found that the configuration of the above carbon network could be controlled by the processing conditions. Rigid-body simulations are adopted to accelerate and control the dynamics of mesogen units. More specifically, the molecules are considered as rigid bodies, and their rotational degree of freedom were not constrained. In this way, isotropic and aligned fibers could be numerically produced (see Figure 115), which allows to study the effects of molecular alignment on mechanical properties, such as Young's modulus.

As shown in Figure 115, the fiber with aligned molecules has a higher Young's modulus than the isotropic fiber by ~50%. In this section, the processing conditions (pressure/density) was explored. In Figure 115, fibers with both isotropic and aligned configurations are studied. For each situation, two different densities are given, Dx_Dy. Dx is the density under which the reactions are performed, mimicking the reaction condition. Dy is the density of relaxed structure, which is the normal density of the fiber product. For both isotropic and aligned cases, the Young's modulus increase with density, ranging from very small, tens of GPa to 600 GPa. For the same density, aligned fibers consistently have higher modulus than isotropic fibers. The enhancement even increases with density, indicated by the slope of the dashed lines in Figure 116. It is also interesting to note that the procedure of pressure relaxation also has an observable impact on the quality control. This can be seen by comparing the cases of "aligned_D2.7_D2"

and “aligned_D2.7_D2_iso”. The latter relaxes the stress in the carbon network in a coupled manner, while all remaining cases are uncoupled. By this single change in pressure, the variation of Young’s modulus of the former is significantly larger than the latter. This observation suggests that, more than reaction conditions that control the overall product density, the relaxation conditions also play an important role in the mechanics of fiber product, particularly the quality control.

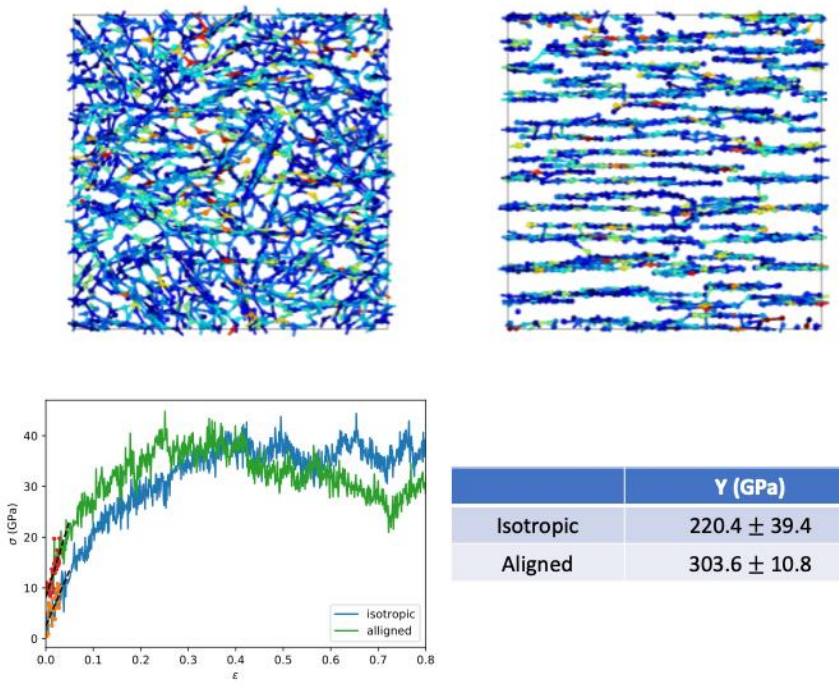

	Y (GPa)
Isotropic	220.4 ± 39.4
Aligned	303.6 ± 10.8

Figure 115: Upper: two examples of isotropic and aligned fibers generated using the approach described in the text. Bottom: strain-stress analysis for these two systems. The Young's modulus of aligned system is 50% higher than the isotropic case.

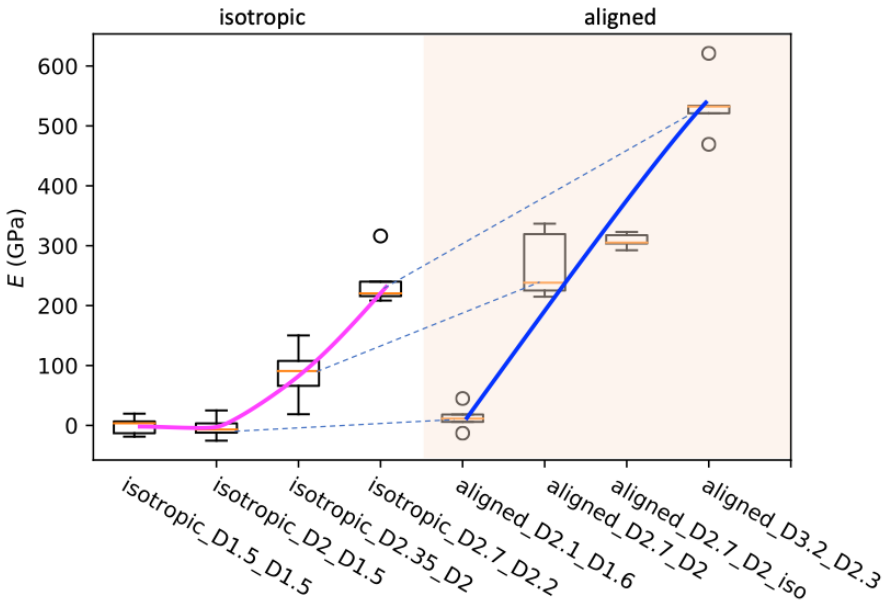

Figure 116: Young's modulus for Carbon Fibers processed under different conditions. The unshaded cases are isotropic fibers, while the shaded are aligned fibers. For each case, the Dx_Dy denotes the density under which the reactions underwent (Dx) and the final relaxed density (Dy).

As shown, the resulting micro-models are able to capture the realistic representation of coal/petroleum/PAN-based (see later for PAN) processing of CF as well as the mechanical properties for the final CF properties to be validated with experimental values which are in agreement within the ±15% error for the project. Note that the micro-models do not capture the variety of parameters into a "single" CF. The modeling framework developed by the MIT allows for the *causal* characterization of the effects of microstructure, functional chemistry, and processing conditions to the final CF properties. By providing either correlation charts between mechanical performance metrics and either structural or procedural parameters. To achieve this hundreds of individual models for CF were produced that can be directly used to directly guide the experimental processing of fibers with consistent yield.

Given the goals to both explain the performance variability in the CFs experimentally synthesized, and to guide the selection of optimal processing parameters, screening was performed of the modulus in relation to microstructure for both isotropic and mesophase fibers. An overview of the variability of moduli for the CF synthesized is shown in Figure 117(a). It has been hypothesized that the degree of molecular alignment has substantial benefit on the modulus of CF. This is statistically valid from the experimental data in Figure 117(a). However, it is noted that isotropic fibers could also achieve rather high modulus under specific, yet undetermined processing conditions. Mesophase pitch shows a more uniform distribution in modulus. Three key elements were further developed: 1. The ability to obtain high modulus fibers from isotropic pitch is practically significant, because it would remove the requirement of mesogen preparation as a necessary condition for high modulus CFs. 2. Furthermore, identifying the microscale processing descriptors (bonding configuration, oxidation, etc) that are immediately responsible

for the mechanical response is key for being able the use of these models for prediction and experimental planning. 3. Finally, a macro-scale descriptor (predictor) that can be directly experimentally measured for CF to predict, through these models, the resulting modulus, can allow a direct application of the models themselves to the experimental synthesis.

For these three goals, hundreds of models were constructed using ReaxFF. The results are summarized in Figure 117(b-d). In addition to separating the evolution for isotropic and mesophase fibers, we introduce CF density during processing as the macroscopic key metric that appears to regulate and determine the final fiber modulus. Selective de-hydrogenation (Figure 117(c)) can be devised to mimic either the effects of controlled oxidation (by selecting the atomic sites that will first de-hydrogenate and interconnect), or differences due to the presence of functional groups usually associated with PP. It is remarkably notable that the modulus of isotropic fibers shows values well in agreement with experiments with excellent accuracy. This is also the case for mesophase pitch fibers. Overall, mesophase fibers generally have higher modulus than isotropic cases. However, for both cases the modulus increases monotonically with fiber density. For instance, both the isotropic and mesophase cases with similar density of 2 g/cc show similar modulus around 200 GPa. A major difference between the two cases is in the presence, for isotropic pitch of an “activation density”, below which the CF will have marginal or poor modulus.

As density denotes the spatial closeness, the existence of radicals is equally important. To this end, the effect of branch groups was studied, which was simulated as hydrogen removal (see Figure 117(d)). It is observed that both hydrogen (group) removal and fiber density are essential. In other words, a larger number of branch groups at the edge of aromatic cores (characteristic of PP) and the closer they approach (higher density), a higher modulus could be expected for the produced fibers. To show the reaction dynamics, the case where branch groups are removed with different speed was simulated, as shown in Figure 117(d). A large variation (low correlation) between removal speed and fiber modulus was shown. This infers, as shown above, that the density and amount of branch groups are determining factors. This needs to be investigated more closely in future work, because there may be different density domains for different materials. For example, PP materials may have a lower density range and have a lower intrinsic ability to pack tightly due to branching groups than CTP materials. Another aspect that needs to be further developed is the observation that 5 membered rings are often found in PP, which is likely due to participation in the methyl groups in aromatic growth.

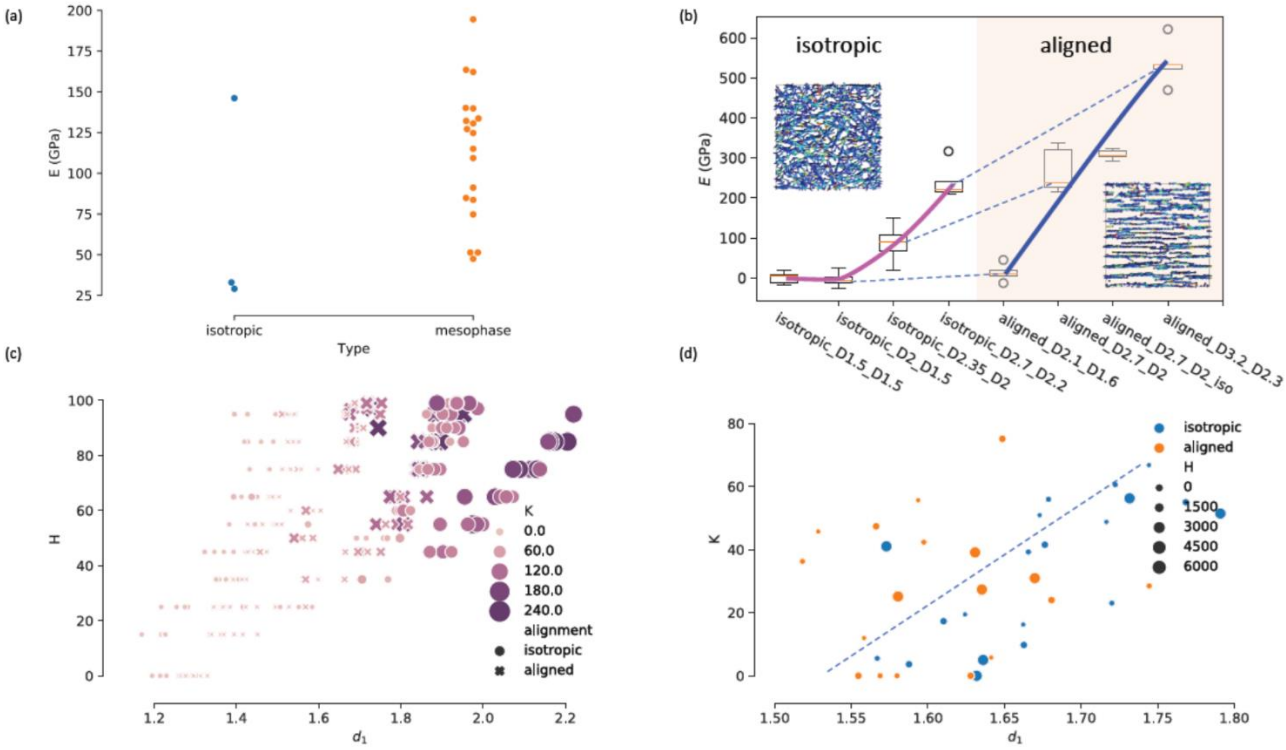

Figure 117: The effects of molecular alignment, density and hydrogen removal.

While the models produced are accurate in capturing the performance metrics observed experimentally more validation is needed for the direct relation between density and modulus. The novelty and potential for guiding the experimental synthesis provided by these models: essentially, given an initial estimate on the molecular structure of the initial pitch, basic process conditions (such as temperature) and processing and final density, the search for optimally performing fibers can be directly found by using the charts provided by this approach.

Furthermore, to reveal the atomic mechanisms that are activated with variations of density, detailed bonding analysis were conducted to estimate how the bonding configuration impacts the mechanics of CFs. This was explored more comprehensively in BP3, for example, by counting different types of bonds, including bonding order, in-plane versus out-of-plane bonds, and simply the newly built bonds during reactions. The ability to directly correlate density with formation of bonds, can provide not only an atomic scale mechanism to justify the essential role of density, but also it can guide for further optimization of the initial pitch (for example by mixing different pitches, or additives) to achieve higher interconnectivity (and higher modulus) at lower density.

Finally, by projecting the bonds towards the tensile direction, a universal descriptor was developed that governs the mechanics of CF, regardless of isotropic or aligned cases, from the atomic bonding information.

Modeling Oxidative Stabilization during Carbon Fiber Synthesis

An important feature of CF production is oxidative stabilization. Stabilization is used to crosslink the aligned molecules in the as spun fibers so that they can be subjected to carbonization and graphitization temperatures without deforming (melting) and/or altering the fiber geometry. Admittedly stabilization is diffusion limited, however, the aim of this modeling effort is not to model the rates of diffusion for optimal stabilization, but rather to uncover which molecular features are most affected by stabilization so that new strategies may be implemented to improve stabilization.

Recent work done by (Senda, et al., 2019) demonstrated the applicability of ReaxFF (atomistic reactive potentials heavily employed in this project) in probing oxidation pathways of isotropic pitch. Adopting similar ideas, investigations were first carried out on a model PAH compound (molecular structure shown in Figure 118a) by injecting a certain amount of oxygen molecules into well-aligned mesophase developed in BP1 (initial configuration shown in Figure 118b). Oxygen-Hydrogen (O-H) distance were tracked (Figure 119a) at the end of the simulation, as well as Oxygen-Carbon (O-C) distance (Figure 119b), and this was used to further classify the bonding environment of oxygen into a) only one bond being formed (O-C and O-H), and b) two bonds being formed (C-O-C and H-O-H) as shown in Figure 119c. For visualization, a typical schematic representation for C-O-C is shown in Figure 119d.

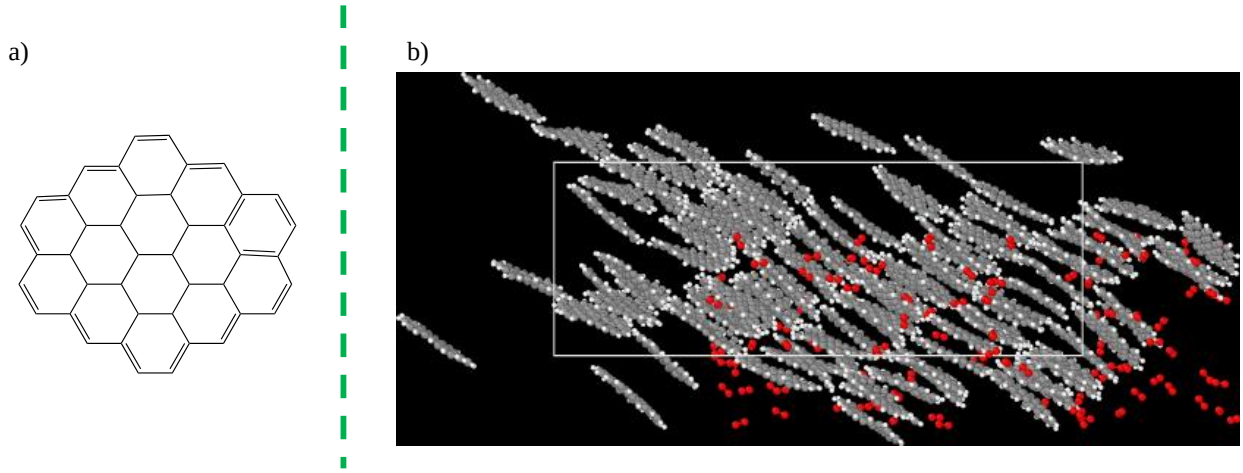

Figure 118: a) Molecular model chosen for testing (superior stability at high T=2800 K here), and b) initial configurations: grey balls represent carbon atoms; white ones represent hydrogen atoms; and red ones represent oxygen atoms. Model PAH compounds are in mesophase form (developed in BP1).

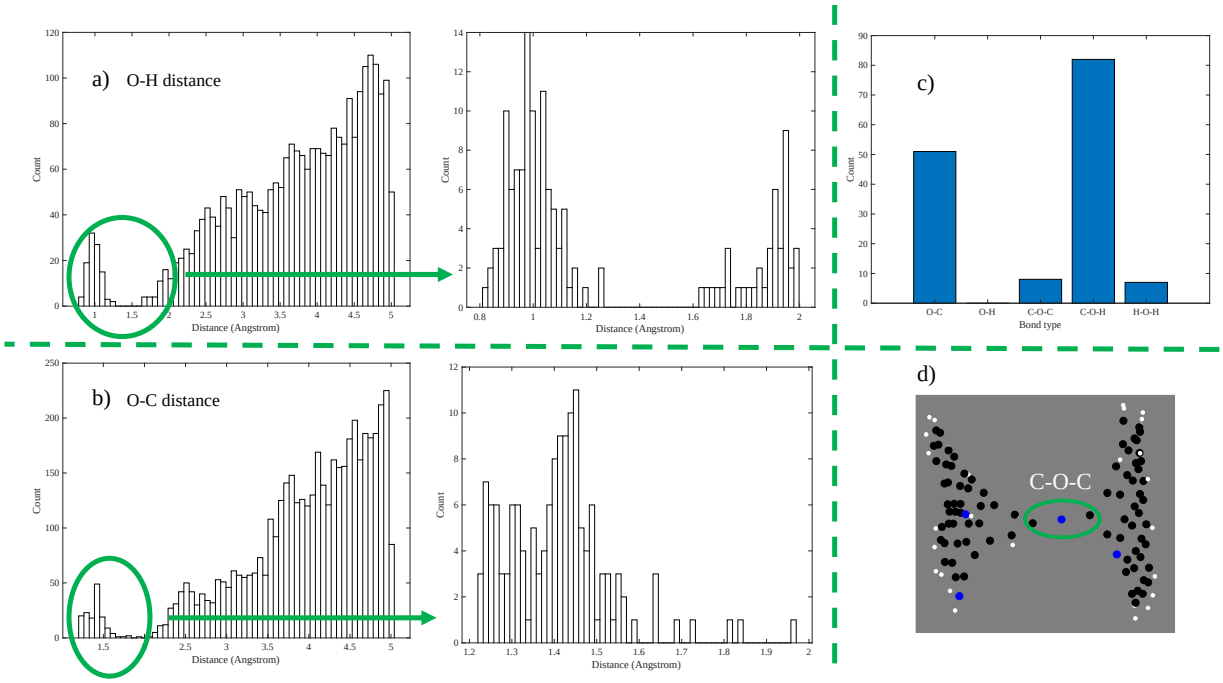

Figure 119: a) O-H distance at the end of the simulation, indicating bond formation (<1.2 Å indicates bonding) between oxygen and hydrogen atoms; b) O-C distance at the end of the simulation, indicating bond formation between oxygen and carbon atoms (< 1.6 Å indicates bonding); c) bonding environment of oxygen atoms: majority of the oxygen atoms are involved in either O-C or C-O-H bonding; d) schematics: black dots represents carbon atoms; white dots represent hydrogen atoms; and blue dots represent oxygen atoms. The grouping of black and white dots on the left represents on large PAH molecule and the grouping of black and white dots on the right represent another large PAH molecule. One type of C-O-C bonding environment is highlighted, where one oxygen atom serves as the linker between two PAH molecules. These results demonstrate the formation of oxygen linkers in the oxidation/stabilization stage.

Based on the above testing, further investigation was performed on the oxidation of a mesogen derived from naphthalene and methyl-naphthalene as well as representative PP molecule (molecular structures shown in the insets of Figure 120a) and b), respectively. Compared to the PAH model, the presence of methyl functional groups greatly increases the instability of the molecules, reflected by that oxidation can occur at much lower T: 1200 K for these two molecules but up to 2800 K for larger PAH shown in Figure 118. However, decomposition was also introduced by the enhanced instability, confirmed by the apparent formation of various small molecules, such as H_2O, CO_2, etc. To maximize the percentage of oxygen linkers, further investigations were carried out at much higher simulation temperatures.

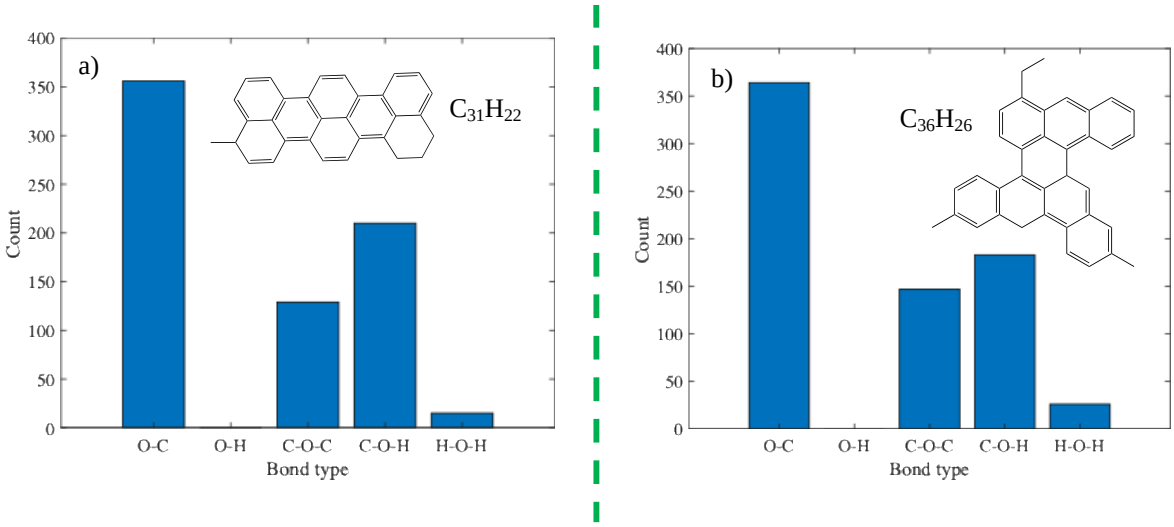

Figure 120: Oxygen bonding environments formed in a) mesogen, and b) PP: both are obtained at 1200 K, under which no oxidation was observed for the PAH compound tested in Figure 118.

From Figure 121 it is shown that after the initial heating up stages, the lowest temperature at which mesogen molecules are stable is 1400 K, while the counterpart for PP is 1800 K. Considering their chemical structures, this observation suggests that the inclusion of sp^3 carbons at the core areas could introduce more significant instability to the compounds.

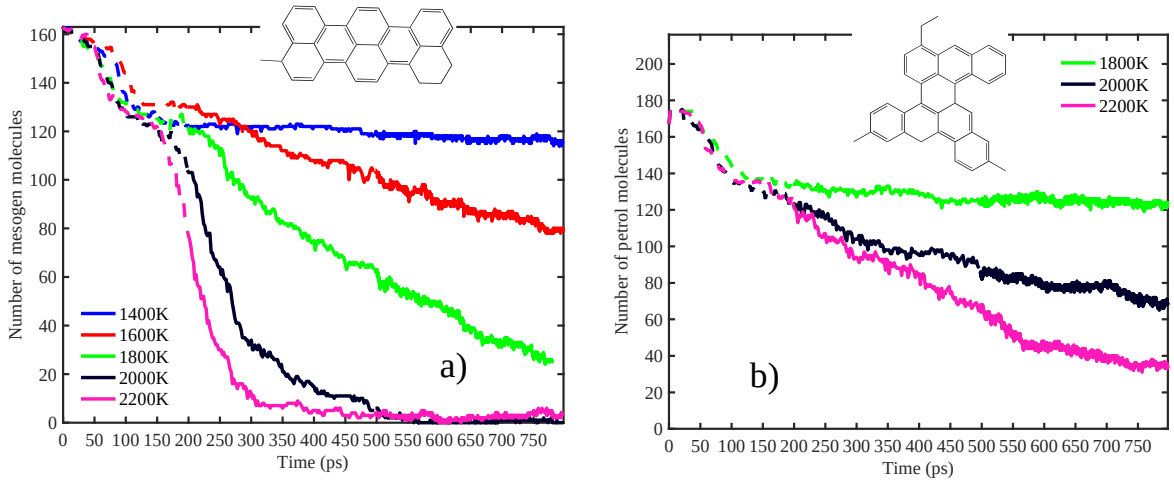

Figure 121: Reaction rate of coal tar and PP mesogens as a function of simulation time.

Considering bonding environments, in total, 4 neighbor types were first identified for oxygen atoms: a) O=C: the oxygen atom is only connected to one carbon atom; b) C-O-C: the oxygen atom is connected to two carbon atoms; c) C-O-H: the oxygen atom is connected to one carbon atom and one hydrogen atom; d) H-O-H: the oxygen atom is connected to two hydrogen atoms. Figure 122a-b show the neighbor types of oxygen atoms at temperature = 2200 K, each of which consists of a group of bars corresponding to different simulation time. Simulations showed that neighbor types of O=C, C-O-H, and H-O-H show an overall increasing trend with simulation time, while neighbor type C-O-C exhibits an increasing trend followed by a decreasing trend.

Representative structures for O=C, C-O-C, and C-O-H are shown in Figure 122c, and it should be pointed out that these structures are similar to those reported in literature (Senda, et al., 2019). To track the interdependence of each neighbor type, Figure 123 shows the formation of C=O, H-O-H, and C-O-H neighbor types. In Figure 123a), the oxygen atom initially was present in the form of C-O-C, and subsequently evolved into C=O neighbor types (carbon dioxide); in Figure 123b), the oxygen atoms directly pull off hydrogen atoms connected to carbon to form H-O-H neighbor types, i.e. water molecules; and in Figure 123c), the oxygen atom first was present in the form of free oxygen atom, followed by forming C-O-C neighbor type, and finally evolved into C-O-H neighbor types. Overall, it is noted that C-O-C neighbor types are more likely to evolve into C-O-H or C=O neighbor types (Figure 123a-b).

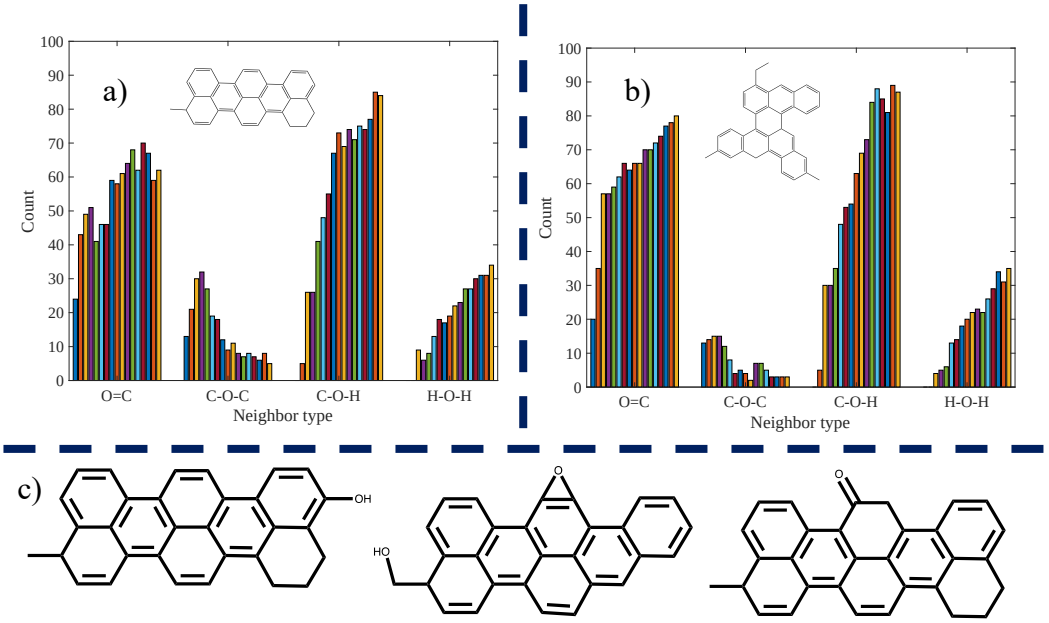

Figure 122: Neighbor types of oxygen atoms at temperature = 2200 K: a) mesogen and b) petroleum pitch; c) representative oxidized structures.

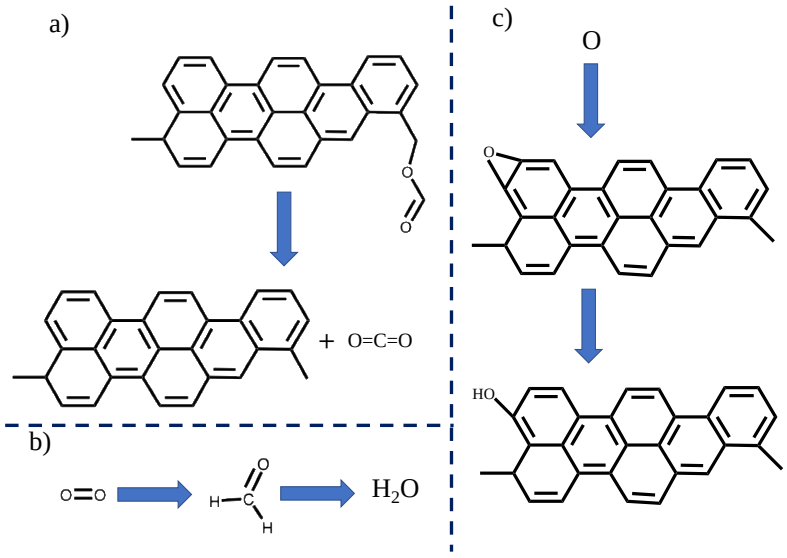

Figure 123: a) Transformation of C-O-C neighbor type to C=O neighbor type, b) formation of water molecules, and c) transformation of C-O-C neighbor type to C-O-H neighbor type.

With the following developments, now it is also feasible to track types of carbon atoms (*sp2* vs. *sp3*) involved in each of the 4 oxidized neighbor types. The ability to activate reactive sites, for each molecule in the system within the computational framework of ReaxFF, relies on the removal of hydrogen atoms decorating each aromatic molecule. While this approach may appear unphysical, based on the work developed within this project in BP2 it is justified within the computational constraints (i.e. simulated temperature/reactions time). Here, within ReaxFF, molecular activation through H-atom removal on a 2-molecular system leads to similar results in terms of final molecular conformation and bonding. Such strategy was instrumental in characterizing the stabilization process during CF in BP3.

An intriguing question is the integration within this framework of the oxidation step. Early in BP2, oxidation was investigated directly, with addition of oxygen atoms within the ReaxFF framework. This led to the formation of unrealistic molecular systems, due to an unconstrained reaction competition between de-hydrogenation and oxidation. A new approach was developed later in BP2, where a systematic study was performed on 2-molecule systems to identify reaction pathways mediated by oxygen, and edge site reactivity (Figure 125).

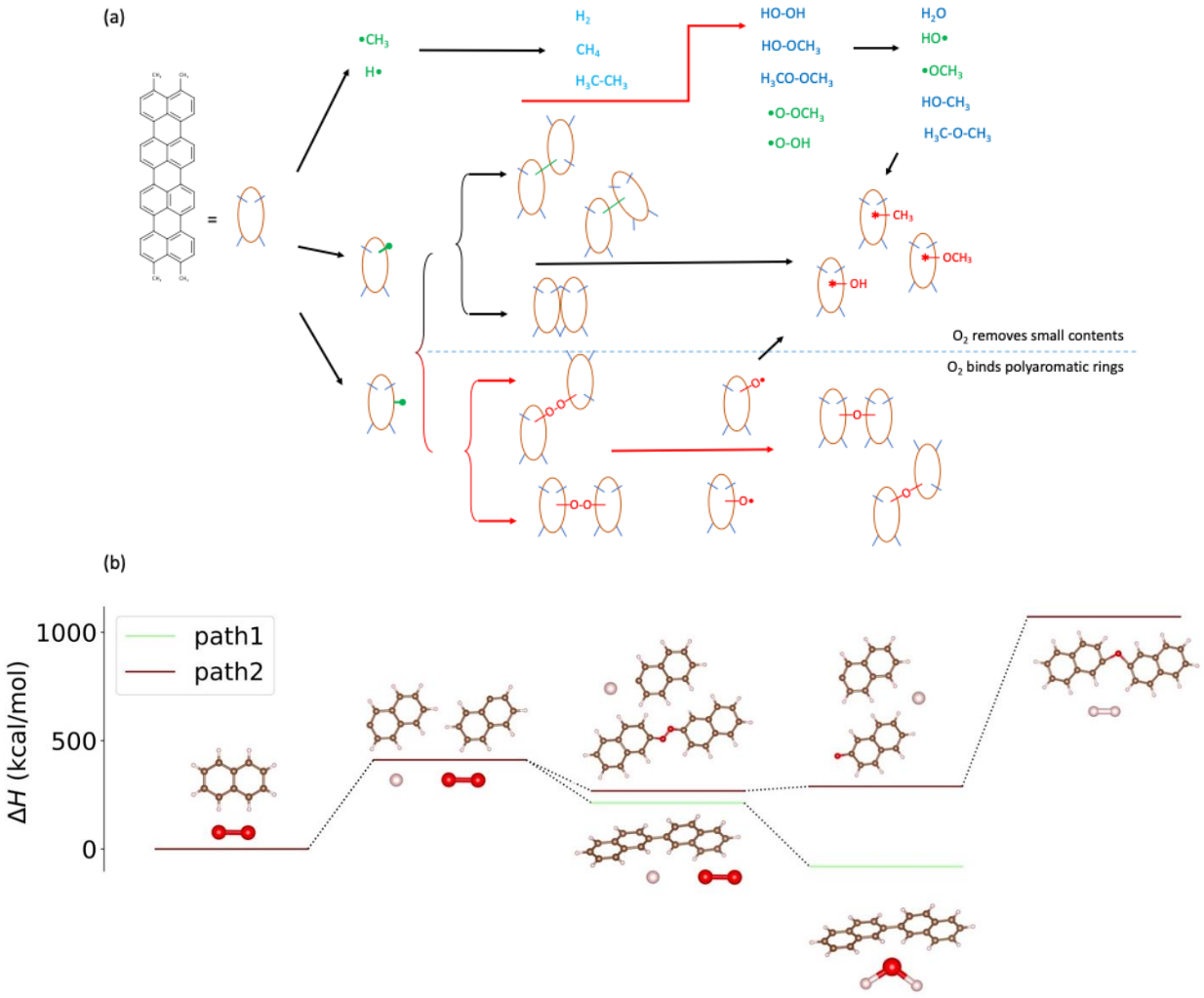

Figure 124: (a)The schematic of oxidation of a model molecule. The hypothesis is that oxygen takes away the small radicals and/or binds large polyaromatic radicals. (b) The example of naphthalene oxidation.

Within this framework, ongoing work is taking place to evaluate the role of oxidation through an indirect evaluation of selected active reactive sites for each molecule. In essence, rather than stripping all molecules of their H-atoms, a variable number will be retained based on the reactivity. Similarly, functional groups for PP will be added as hyper-reactive sites. The ability to tune which sites will be active will facilitate the correlation between effective dehydrogenation, oxygen site activation and functionality.

Coarse-Grained Pitch-based Modeling

During BP1, preliminary evaluation of a Coarse-Grain (CG) modeling approach to upscaling model size and reaction times was performed. Upscaling atomistic bottom-up models to account for mesoscale features (extended reaction times and model sizes in the hundreds of nm) is computationally challenging with current MD based tools and computational resources. The evaluation of the upscaling, in terms of reaction times and sizes, in relation to the mechanical

behavior can potentially be achieved using a CG modeling approach. With this approach, fragments and molecular fingerprints are used to build the original atomistic models. These fragments and molecular fingerprints are represented as homogeneous “grains” or “beads” with well-defined chemical and physical behavior. By retaining the molecular interconnectivity from the original atomistic model, much larger CG models can be constructed, as shown in Figure 125. GC was initially used, along with atomistic models, to probe how the predicted the global mechanical behavior is affected by the length scale, ultimately determining a scalable predictive approach to be deployed within the produced in this program.

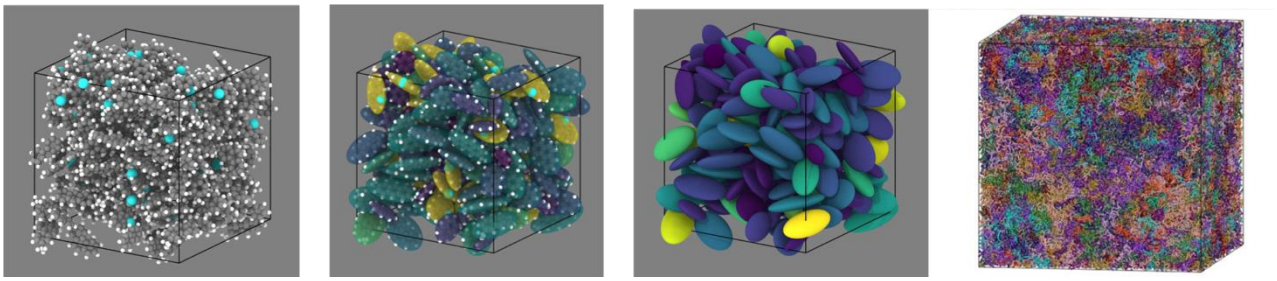

Figure 125: Coarse-Grain approach in model upscaling. The atomistic model of a tar proxy (far-left) can be reduced in its complexity by replacing each fingerprint with a “bead” with a well defined average chemical and physical behavior (center-left). The resulting CG model (center-right) allows for a significant simplification over the original, allowing for upscaling computational time, model size and reaction times into the mesoscale (far-right).

Realistic, coarse-grained models must use representative “average” grains to represents molecular entities. It allows for the description of microstructure, while leveraging on a much-reduced computational cost to reach larger scale simulations with many more molecules and interactions Figure 126. A significant effort was devoted in the development of algorithms to translate atomic molecular structures in coarse grains, while retaining average chemical and physical parameters. In the implementation, there is no limits in the number of different grains that can be created and combined in the models.

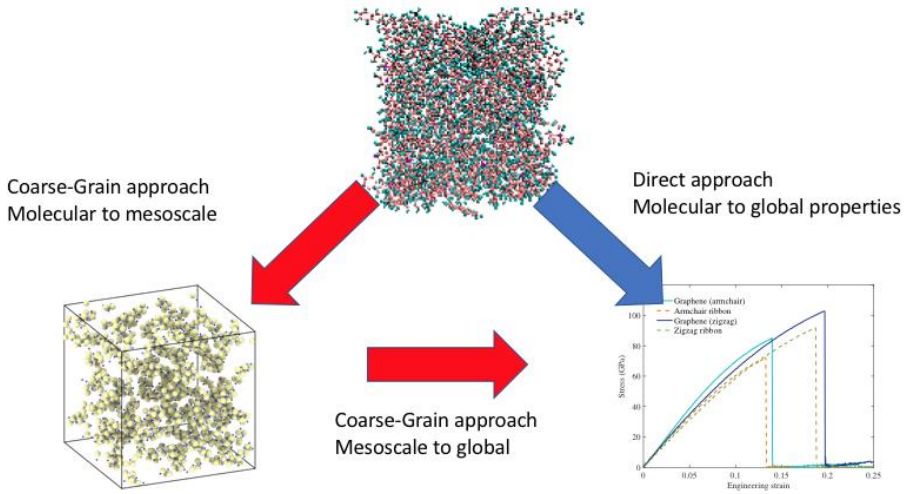

Figure 126: Coarse-Grain approach in model upscaling. The atomistic model of pitch (top) can be reduced in its complexity by replacing each fingerprint with a "bead" with a well-defined average chemical and physical behavior (bottom-left). The resulting CG model allows for a significant simplification over the original, allowing for upscaling computational time, model size and reaction times into the mesoscale. Either model can be used to evaluate, within the sample size, macroscopic behavior (mechanical properties, etc.), each with a particular emphasis based on the atomistic structure (atomistic models), or macromolecular arrangements (CG models).

Fully atomistic (FA) models were used to investigate the alignment of precursor pitch molecules and its dependences on several factors, including temperature, strain and additive molecules. However, due to the high computational cost of the FA models, the simulated system could only handle a limited number of molecules (~300), making it difficult to describe extended pitch systems realistically and to show long-range molecular alignments. CG modeling was used to reach larger time and length scale to enable more realistic representations of pitch as complex mixtures of molecules with the goal of achieving better comparability with experiments. This naturally raises two questions: 1) how the geometric information of the molecules in a CG model can be preserved; and 2) how intermolecular interactions can be accurately described.

This was tested by developing a CG model while taking the above two points into consideration. In the model, ellipsoidal beads were used to represent the pitch molecules, which reasonably described their volumes and shapes. Adopting the Ellipsoid method (Grotschel, Lovasz, & Schrijver, 1988), we obtained the values of σ_x, σ_y, and σ_z (three axes of the ellipsoid) for a set of common pitch molecules as listed in Table 36. To account for the non-covalent intermolecular interactions, the RE-squared force field (Senda, et al., 2019)(FF) (Everaers & Ejtehadi, 2003) was adopted that expresses the interaction energy as a function of both the separation distance and the relevant orientation of each pair of molecules. To calibrate the FF for a specific chemical species, an automated script was written, optimizing the FF parameters to reproduce the energy (averaged over a set of different configurations) predicted by the fully atomistic models. Applying this parameterization protocol, in Table 36, a complete set of parameters for the proposed molecules was obtained, enabling CG molecular dynamics (MD) simulations for this complex system. A CG configuration capable of representing a realistic pitch system (e.g. the

molecule species and their fractions are close to the experiment) was prepared. As shown in Figure 127, our preliminary CGMD simulation results show that the system is stable at 600K and has the tendency of self-aligning in several small domains.

Table 36: CG parameters for several molecules commonly found in coal-tar pitch

Molecules	A_{12} (Kcal/mol)	σ_c (Å)	σ_x (Å)	σ_y (Å)	σ_z (Å)	E_x	E_y	E_z	Error
Tetracene	7245.40112	4.1763	5.3062	2.0774	0.3784	4.6874	1.6367	0.49489	0.0087
Benzo(e)fluoranthene	4338.45706	4.3677	5.1923	3.2261	0.35089	2.5861	1.5914	0.29271	0.0091
Pyrene	6108.73218	4.3384	3.9336	2.8528	0.35564	3.1418	2.0181	0.39755	0.0044
Chrysene	5875.01887	4.2579	5.0952	2.512	0.36191	3.9241	1.6269	0.40085	0.0065
Phenanthrene	5622.42289	4.1114	4.0016	2.3749	0.39268	7.3815	1.9391	0.53895	0.0084
Benz[a]anthracene	6427.98595	4.249	4.9517	2.4688	0.36225	4.3362	1.7969	0.43439	0.0102
Anthracene	8618.49645	4.147	3.9732	2.0875	0.36341	4.5459	2.0178	0.59215	0.0063
Benzo[a]pyrene	5641.90689	4.3398	4.947	2.9764	0.35005	3.1945	1.743	0.34711	0.0053
Indeno[1,2,3-cd]pyrene	6123.63303	4.3399	4.7664	3.1608	0.35561	2.7798	2.1152	0.36149	0.0056
Benzo[k]fluoranthene	6962.57412	4.3586	5.0063	2.6474	0.35007	3.1671	2.0246	0.39349	0.0084
Benzo[g,h,i]perylene	7403.66927	4.3751	3.9888	3.4245	0.3567	2.6334	2.1444	0.39834	0.0049

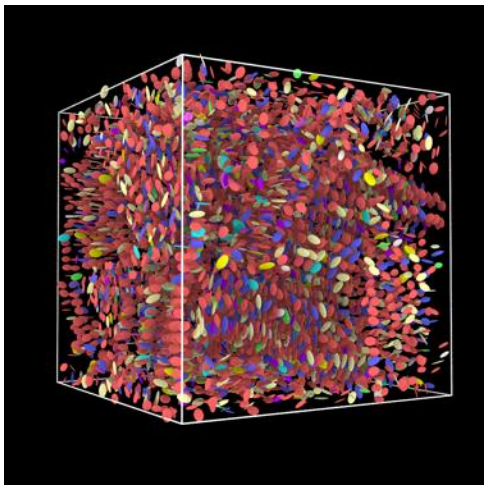

Figure 127: Simulation snapshot from a CGMD simulation that contains 8,000 pitch molecules.

Due to time limitations needed to evaluate various assumptions in the correct choice of representing grains, and the discovery that the FA models could accurately represent CF modulus and density, no further work was pursued for the CGMD system for pitch-based system and the remainder of pitch-based computations were performed using MD and ReaxFF. CGMD, however, was extensively studies for PAN based systems, which is described later.

PAN-Based Modeling with CGMD

Due to the largely repetitive nature of PAN and the very large MW (>100,000 Daltons) a CG approach is appropriate and necessary to best capture molecular features of the polymers and their transformation into CF. An over simplified approach to GCMD was initially applied where each ACN unit was represented as a grain (Figure 128). These models were able to predict the bio-PAN and literature CF properties for modulus at greater than 70%, often greater than 80%.

Figure 128: A simplified GC model for PAN and the ladder structure of PAN where each molecule of ACN in represented as a grain.

The major limitation of the approach followed in BP1 was in the ability to realistically capture—with no assumptions—the evolution of bio-ACN to bio-PAN, crosslinking and ultimately CF production. A rigid set of rules was followed in the CG framework, which while correctly working in perfect conditions (i.e. in absence of contaminants), was not sufficiently flexible to allow for the presence of contaminants. The models were improved by moving from CG beads that encompass the full monomer, to beads that capture the C and N atoms including the H, the new framework which is more sensitive to the presence of contaminants in any step of the process, but with limited impact on computational efficiency.

As shown in Figure 129a, the ACN monomer was represented by four beads, that included most of the geometric information of the monomer, with taking the considerations of both the accuracy and efficiency. Compared with the previous model, where each molecule was abstracted by only one bead, the new model kept necessary information about the internal structure of ACN, which was crucial for modeling the later CF fabrication stages, such as the ladder structure formation and sheet expansion. In the current model, the polymerization was accomplished by creating chemical bonds between specific beads to link the ACN monomers. The degree of polymerization, quantified as the number of new bonds in the CG simulation, could be expressed as a function of time (Figure 129b, right), qualitatively reproducing the experimental results in the literature (Sherigara & Yashoda, 1999) and Figure 129b, left). The detailed polymer chain formation process, especially the local polymer conformation, was also reasonably captured in the CGMD simulation. In addition, the model was designed such that the simulations could be performed under different loading conditions, e.g., Figure 129c provided a series of simulation snapshots showing the polymerization under uniaxial tension, a simplification of the steering applied in realistic synthesis. The temperature and pressure of this simulation were set to 330K, and 1 atmosphere respectively, both close to the experimental setup. This CG framework allows systematic study of the PAN polymerization process, and lays foundation for realizing the simulations of later oxidation and graphitization stages.

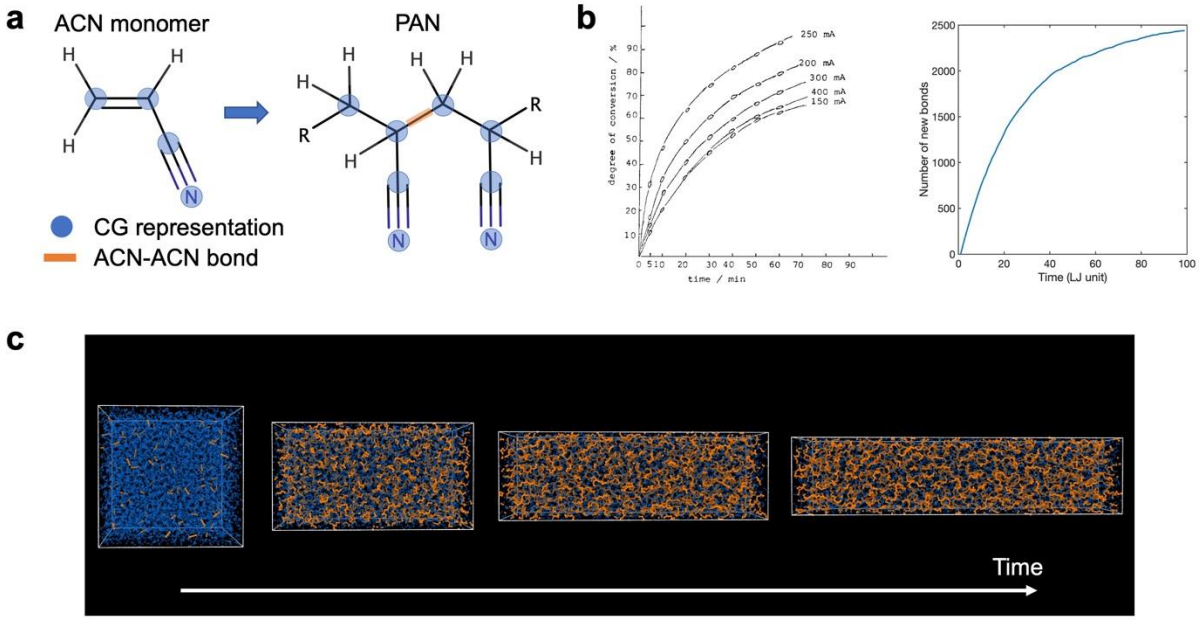

Figure 129: (a) Schematic of the coarse-grained PAN model. (b) Comparison of the polymerization process measured by experiments1 and CG simulations. (c) CG simulation snapshots showing the polymerization of ACN monomers under uniaxial tension.

CGMD Models for Simulating PAN-based Carbon Fiber Synthesis

The development of a PAN-CF models using our current CGMD framework relied on the accurate description of the chemical transformation from linear PAN to ladder structure, a process that is critical to stabilize the system prior to carbonization and graphitization stages (Fitzer, Frohs, & Heine, 1986). The developed united-atom model included information of initial radical generation, ring closure, adjacent radical formation and ring propagation, to capture the details of the PAN cyclization, as demonstrated in Figure 130. During this process, the associated local geometry changes, such as the bond angle and dihedral angle constraints, were also taken into the consideration. A more realistic example was given in Figure 131, where the model showed the process of an isolated long PAN chain gradually turning into the ladder structure, with external forces applied on both ends of the chain (to mimic the stretching condition). The development of this model solves the main technical challenge in simulating the PAN stabilization, and lays foundation for realizing simulations of the full fabrication process of PAN-based CF.

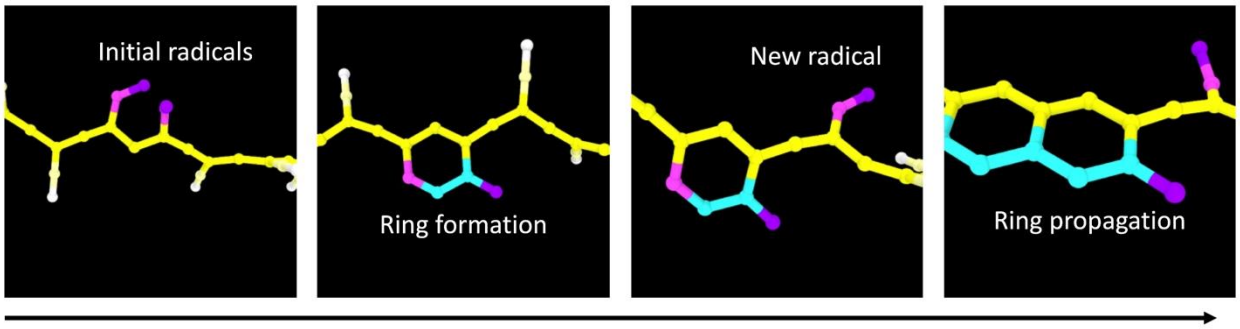

Figure 130: Details of the radical cyclization process along the polymer chain.

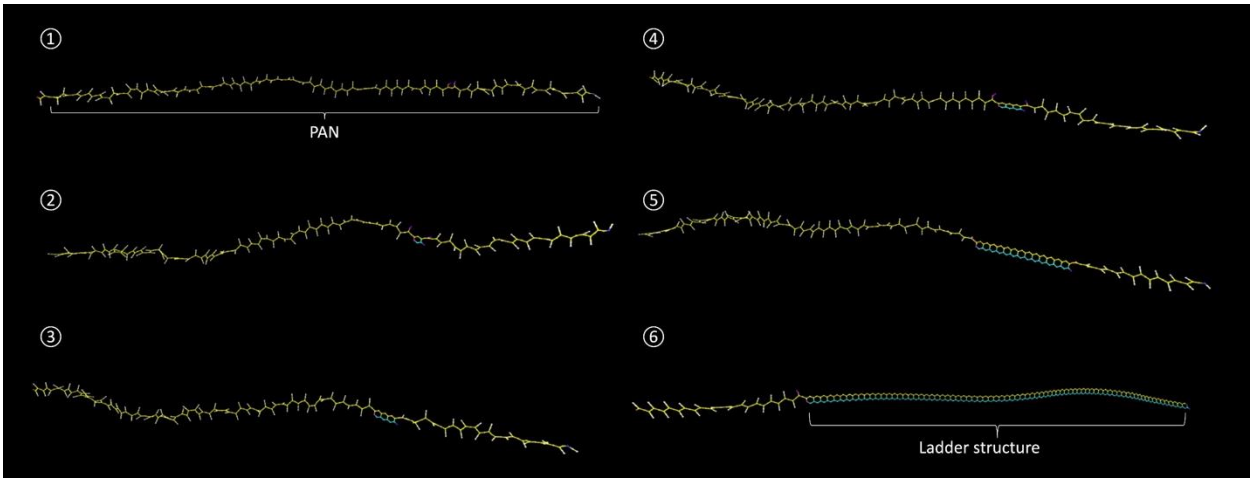

Figure 131: Snapshots from one CG simulation showing the formation of ladder structure from PAN.

The CGMD model was further refined, introducing a template-based algorithm for handling chemical reactions in the simulations. This improvement enabled comprehensive descriptions of both topological and geometrical changes associated with the reactions (e.g. bond formation/break) in an automatic manner. With this development, the model can account for various reactions during the PAN-based CF synthesis process, including radical generation, radical annihilation, ring closure, chain propagation and termination, etc. As shown in Figure 132(a), (b) and (c), the capability of the improved model to capture the molecular-level details was demonstrated, as well as the conformational evolution of the polymer in the PAN polymerization and the later ladder structure formation stage. In addition, the number of reactions were analyzed for the synthesis for each reaction type (Figure 132(d)), from which the synthesis pathways could be identified and understood.

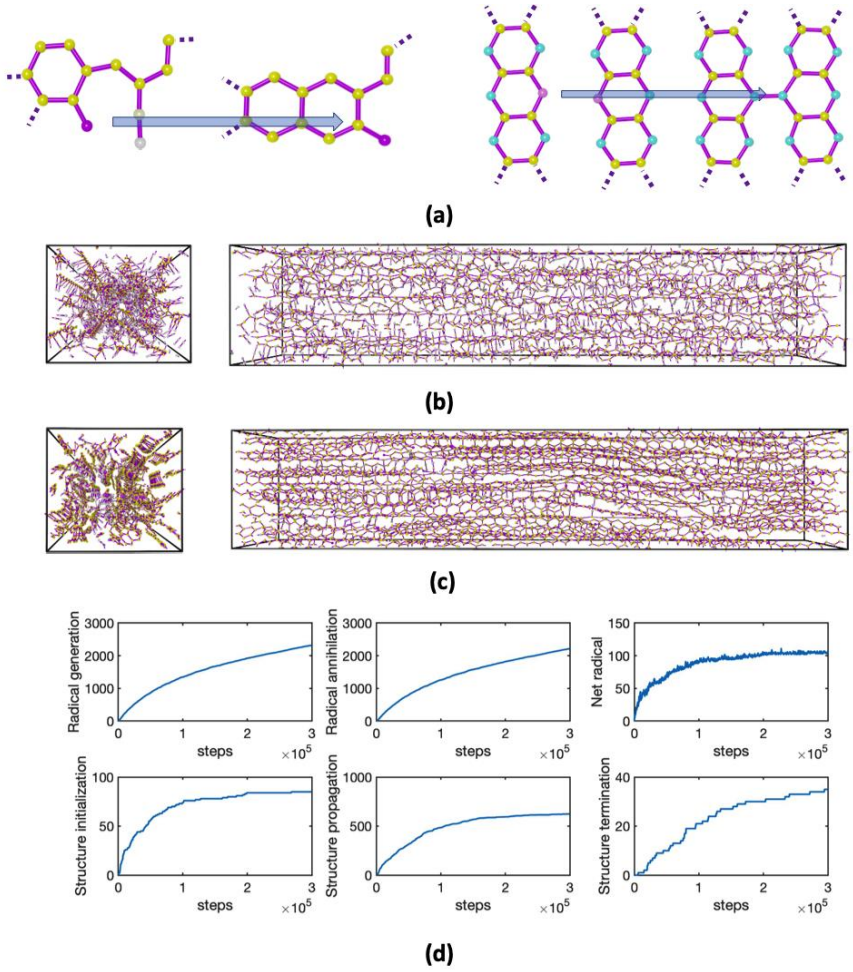

Figure 132: (a) **Molecular-level details of the template-based bond formation algorithm; (b) CGMD simulation snapshot showing the polymerization process; (c) CGMD simulation snapshot showing the ladder formation process; (d) The counts of radical generation, radical annihilation, net radical, isolated ring closure, ladder structure prorogation and termination are plotted as a function of simulation steps.**

With further refinements the CGMD computational framework received the ability to describe major chemical reactions during the entire PAN-based CF synthesis. This is achieved by adopting and implementing the direct bond formation method and the template-based algorithm. As shown in Figure 133(a), the model captures the microstructure evolution from the initial random distribution of the acrylonitrile monomer, to the well aligned ladder structure, to the highly cross-linked fiber network. In Figure 133(b), we demonstrate the capability of the framework to quantify the alignment of the ladder structure. Specifically, we provide the distribution of the shape anisotropy κ, which is defined as $\kappa^2 \triangleq \frac{3}{2}\frac{\lambda_x^4+\lambda_y^4+\lambda_z^4}{(\lambda_x^2+\lambda_y^2+\lambda_z^2)^2} - \frac{1}{2}$, where λ_x, λ_y and λ_z are the trace elements of the diagonalized gyration tensor for each chain structure. In Figure 133(c), the number of close rings with different sizes in the simulated CF materials was counted, which allows us to estimate the aromatic fraction of a given fiber configuration. Tensile test (up to 2% strain) were performed on the simulated fiber. From the slope of the stress-strain curve shown in Figure 133(d), the Young's Modulus is calculated. In Table 37, this value is compared with experimental CF, showing a very good agreement (error is ~5%). These results validate the applicability and reliability of the developed CG framework, as a powerful tool to systematically investigate the PAN-based CF synthesis related problems.

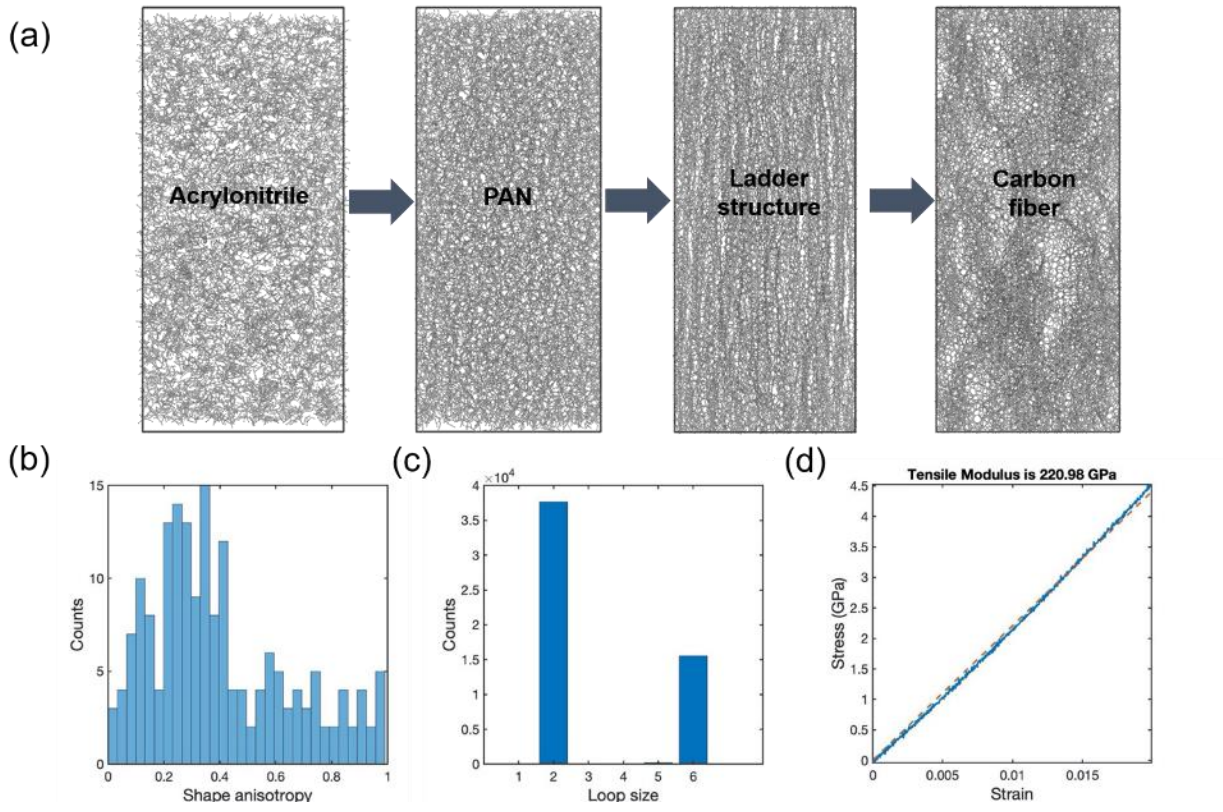

Figure 133: (a) Microstructure evolution during the PAN-based Carbon Fiber synthesis captured by the CGMD simulations. (b) The distribution of the shape anisotropy of the ladder structures. (c) The counts of rings with different sizes in the Carbon Fiber system. (d) The stress-strain relationship of the simulated Carbon Fiber.

Table 37: Young's modulus predicted by the CGMD model compared with the experimental value.

	Young's modulus
CGMD	221 GPa
Experiments	231 GPa (Solvay Thornel T-300)

The newly developed CGMD modeling framework was used to conduct a comprehensive correlative analysis on the PAN-based CF synthesis. Over 100 simulations were performed with systematically varied parameters in each processing step, including temperature, pressure, time and external stressing force. As a direct result from the simulations, the modulus of the final CF were extracted, along with several materials properties in intermediate process steps as effective system descriptors. This allowed us to identify the correlations among these system descriptors and the fiber modulus (as shown in Figure 134). Through such correlation, structural parameters that are highly correlated with mechanical performance were evaluated for significance from a physical point of view. For example, from Figure 134, we identified a very strong correlation between the number of ladder structures and the graphitic fraction, which is physically expected and justified. These results also show that a higher graphitic fraction leads to a higher CF density and modulus. These findings affirm the importance of the fiber stabilization stage, and through a quantification of such relationship, it can be immediately used to guide and predict the mechanical performance of a specific fiber.

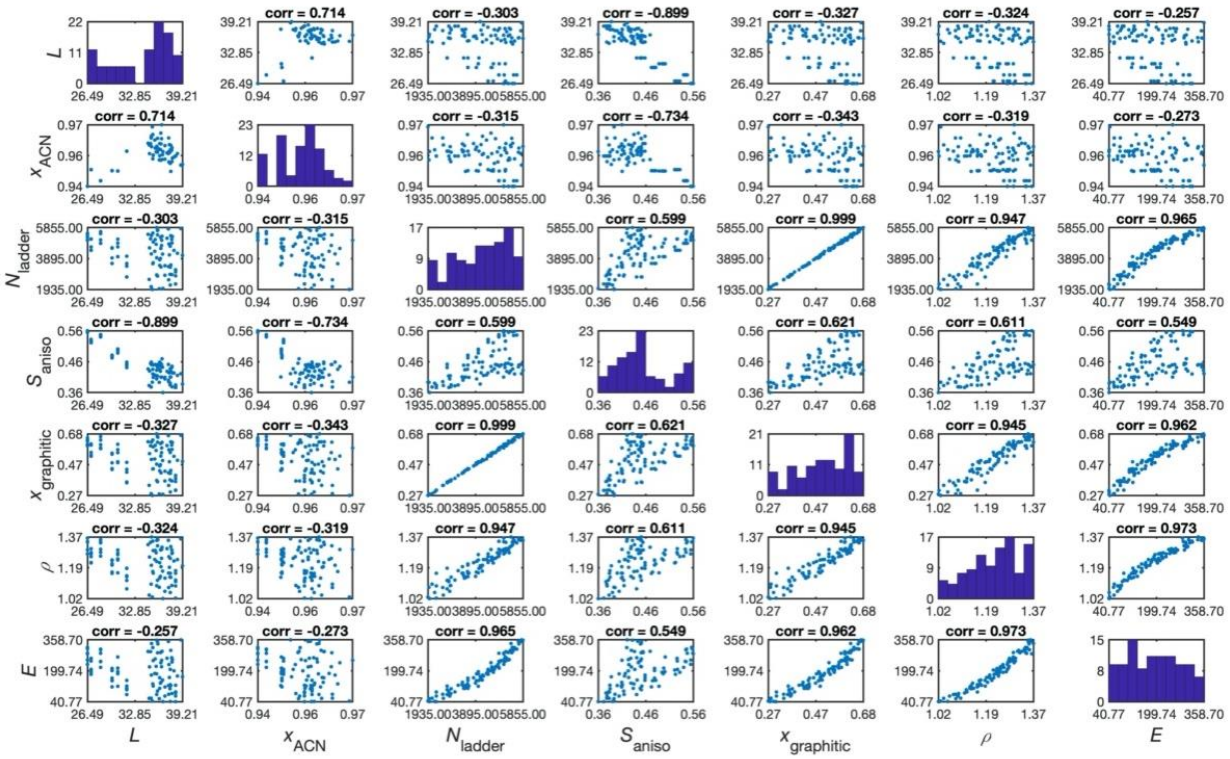

Figure 134: Correlations among the system descriptors and the fiber mechanical properties.

Other properties besides modulus were investigated as a metric for mechanical performance. By a quick optimization of the MD algorithm, bond-breaking was tested, which led to the identification, from the hundreds of models available, not only of the performance under the linear (elastic) regime in the stress-strain curve, but also an estimate on the peak stress/strain, max elastic elongation and mechanics during deformation. As previously noted, however, the scale-dependent nature of these properties prevents from a direct comparison with actual experimental measurements for elongation and strength, due to their dependency on the mesoscale structure.

Machine Learning (ML) Predictive Analysis

An important aspect of this work is to develop predictive tools which can help identify and guide the selection of appropriate feedstocks as well as determine which sets of materials and processing will result in successful CF production. In the original goals within this project, a vertically integrated approach in the data to be used was envisioned, from feedstock molecules, the impurities, the processing to product intermediates for CF spinning (mesophase or PAN), spinning and all the various CF processing steps, while moving to CF tow-level properties. During BP1 and BP2 it was not possible to include the various CF spinning and processing steps due to export control issues which prevented sharing of data between MIT and ORNL. This was overcome in BP3 (see Phase 2 Topical Report section). A major focus in BP1 and BP2 was the

impact of impurities on bio-PAN, from available data, and the various pitch, mesophase pitch and pitch-based CF properties.

The highly flexible suite of data processing and ML tools have been applied to generate predictive models and the resulting correlative analysis of manufacturing and characterization of the properties of precursors for CF from process parameters and chemical variability. Two main tasks were accomplished towards the proposed goal: 1) A ML framework using neural networks based on a Deep Multi-Layer Perceptron (MLP) (Rosenblatt, 1961; Rumelhart, Hinton, & Williams, 1985) capable of multi-label, classification (Ferralis N., 2018); 2) Algorithms to generate reliable training data from available feedstock processing parameters and chemical reactions throughout the manufacturing process. These methods were put to test and customized for the predictive determination of impurities in the production of ACN from biomass, and streamlined for the purpose through a collaboration with the consortium member SRI. Using variability in chemical composition and chemical balances throughout the multistep ACN synthesis, training sets were developed to predict the concentration of impurities in ACN (such as water and acetonitrile) from an initial extensive set of impurities in addition to biomass source (Figure 135). The efficient implementation of the neural network, through Keras and TensorFlow (Keras, 2018; TensorFlow, 2021), allows the rapid generation of trained predictive models (~training is carried out in ~ 30 minutes) with accuracies >98%. Such models can be readily applied for ultra-rapid (<50ms) inference and prediction.

The successful implementation of predictive algorithms for ACN, was optimized further through more accurate estimates of chemical balances, impurities concentrations, etc. A similar approach was also under development for CTP and PP. Rather than focusing on the prediction of the role of impurities in ACN synthesis from a processing perspective, the focus was to use characterization data to predict the structural and chemical behavior of CTP and PP from unknown CTP and PP. A major collaboration between WRI and the MIT team helped identify a selection of valuable CTP and PP characterization parameter and the availability of actual supporting data needed for the implementation of the predictive models.

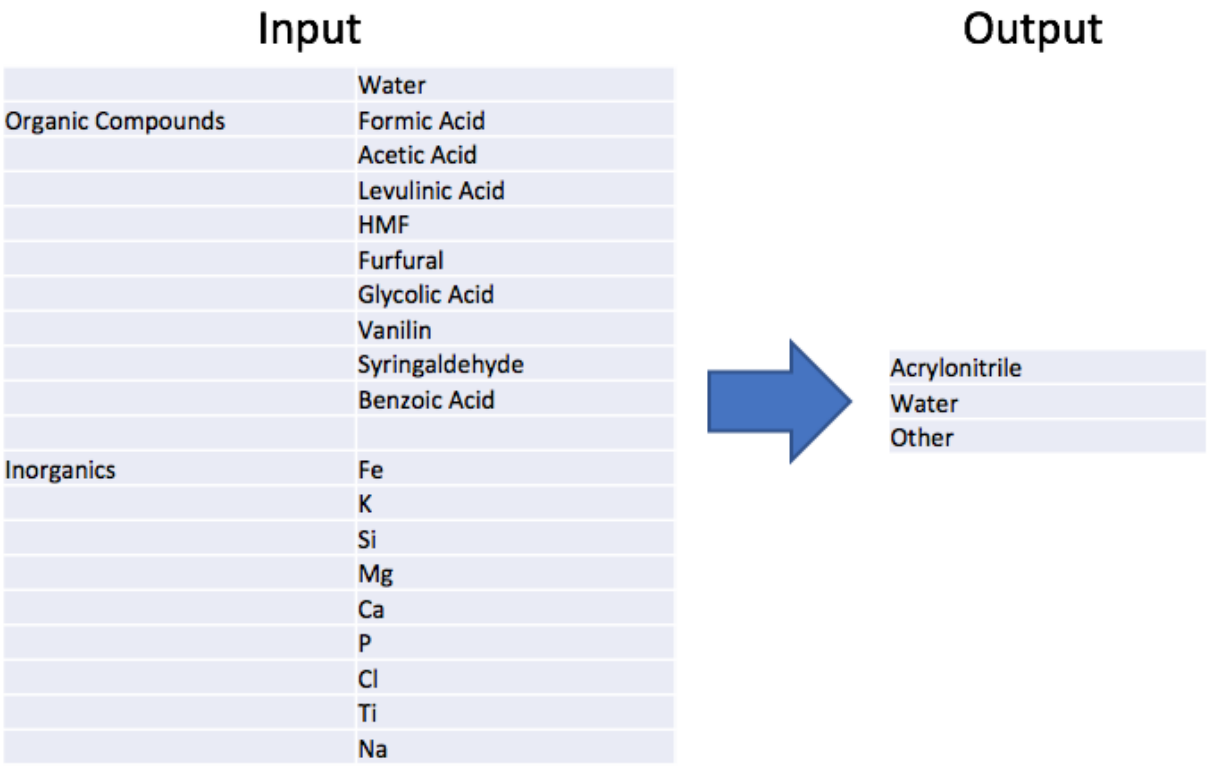

Figure 135: Workflow schematic of the predictive ML algorithm for impurities in biomass acrylonitrile processing (output) from the initial impurities in biomass (input).

The universal holistic approach to ML of synthetic processes and characterization data relied uniquely on processing indiscriminately the overall comprehensive collection of data, with no discrimination within the training data of parameters that are directly relevant to the synthesis process or performance. This approach was applied in the prediction of either reaction products, or chemical-physical characteristics of a particular precursor for PP and CTP fibers. While the prediction accuracies met the required target (with hundreds of ML predictive models available in the project data-management), the heuristic nature of the holistic ML approach provided only limited insight, physical and chemical, on the possible reaction pathways, correlations across processing and characterization parameters. In essence, while the assumption has been, so far, that all parameters matter equally, the Artificial Neural Networks (ANN) within each model may perform differently in predicting different parameters, this based on the fact that the variability of training data may be different for each parameter. Furthermore, a reduction in the parameter phase space is known to reduce the complexity of the ANN and more importantly, the actual ability to universally represent a CF system with minimal redundancy and overfitting.

During BP1, a major universal ML framework was developed for its application for the prediction of either reaction products, or chemomechanical characteristics of a particular precursor. This framework was extensively applied specifically for the petroleum-based data, not only to create hundreds of predictive models based on characterization data, but to allow a

ranking of the most effective correlation models. In essence, while the assumption has been, so far, that all parameters matter equally, the neural networks within each model may perform differently in predicting different parameters, this since the variability of training data may be different for each parameter. Data showed (Figure 136), for example, that pair linear correlations between characterization and prediction parameters differs within each pair, and through smart selection, this can be used to restrict the dimensionality of the training set by removing uncorrelated parameters, or to systematically combine correlated vs anti-correlated parameters. The narrowing of important correlated terms will reduce overfitting while providing chemical and physical insights behind the correlation. This approach is referred to as a "targeted approach" while simply inputting all data indiscriminately is a typical "holistic" approach.

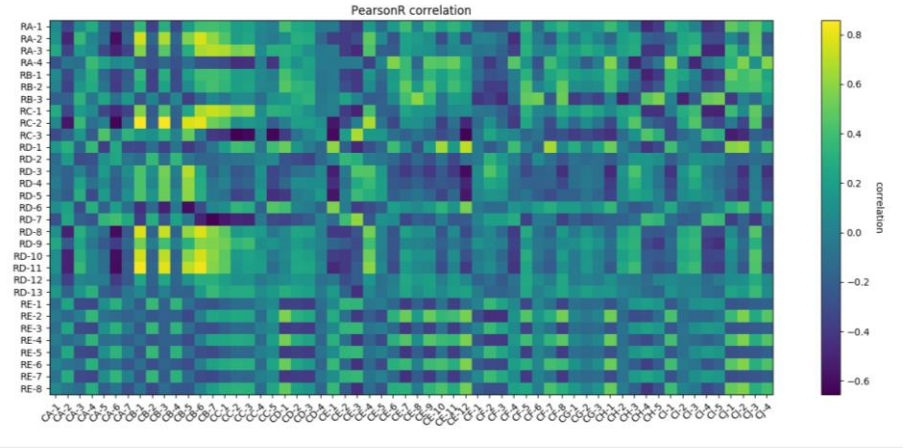

Figure 136: Pearson R correlation between characterization-based parameters (x-axis) and prediction parameters (y-axis). This visual characterization allows for a rapid identification of linear correlations between pairs of parameters, or anticorrelation or no correlation. A multi-dimensional approach to this (through combination of similarly correlated parameters in hyperspace) will be carried out using ML.

A robust, rapid and visually efficient method was developed for a rapid identification of correlations and cross-correlations between any relevant characterization, process and performance parameter. By utilizing fast processing algorithms, based either on the Spearman (for monotonic correlation) or Pearson approaches (for linear correlation), pair linear correlations and anticorrelations between parameters are visualized through custom heat maps (Figure 137). Through smart selection, this can be used to restrict the dimensionality of the training set by removing the uncorrelated parameters, or to systematically combine correlated vs. anti-correlated parameters. This approach was also used to identify possible cross-correlations within characterization data (for example, chemical vs thermal, spectroscopic vs elemental, etc.).

The overall understanding that can be obtained from these maps is multi-fold:

1. Identification of specific reaction pathways, where for example an increase in H:C can be directly associated in the evolution of parameters such as polydispersity and aromatic content.

2. Identification of cause-effects in processing precursors

3. Massive reduction in dimensionality of the training dataset, by excluding parameters uncorrelated with processing or performance. This also leads to a natural mitigation of overfitting in ML, as it will be described below.

4. Verification of the *bona fide* of the actual validation set used to validate ML algorithms, and indication of potential requirements for additional training data.

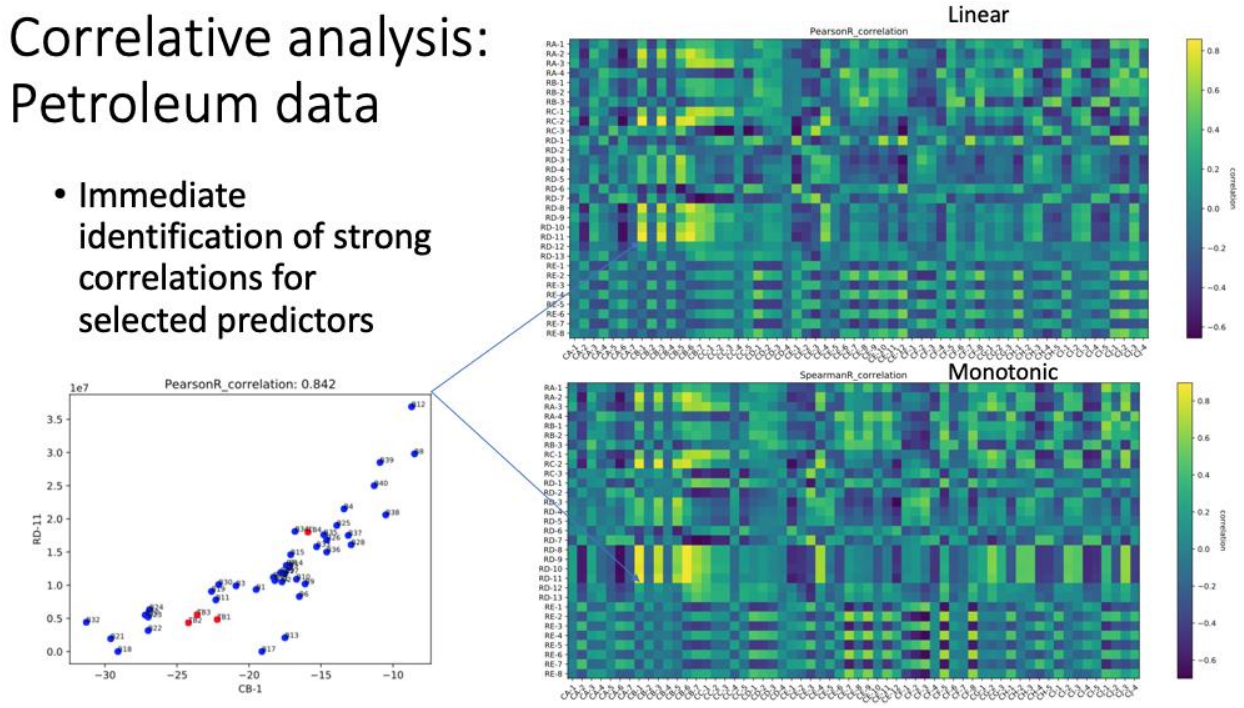

Figure 137: Pearson and Spearman correlation maps to identify correlations and anti-correlations between characterization (C* data) and performance data (R* data). For each pair, 2D plots are generated including all the training and validation data. Blue dots in the inserted plot at the lower left show data used for the training, while the red dots represent validation test data points.

The last two points above have been further explored in relation to the development of ML algorithms which are called "targeted," as opposed to "holistic." Essentially, by setting a correlation (or anti-correlation or both) threshold for non-trivial pairs of parameters, such set of parameters are used to build ML predictive methods. The absence of uncorrelated data drastically reduces the risk of overfitting, and points to a more efficient operational process, since only a few parameters are required for prediction. As it is shown in Figure 137, selected parameters correlated (or anti-correlated or both) are used to produce ML predictive models. Differently from BP1 and early in BP2, in addition to classification, regression has been used for prediction. While classification is friendlier in principle, in that it allows for the classification to be validated directly through a value of accuracy, the limited quantity of training data, and the broad number of predictive parameters renders each class artificially broad. Regression was tested instead, where a specific performance parameter for PP and CTP data was obtained from regression, rather as belonging to a specific class. While regression does not lend to the direct assessment of accuracy, the mean average error (MAE) of the predicted regression values compared to the validation value can be used instead. As shown in Figure 138, MAE values

below 0.1 correspond to accuracies higher than 95%. It is worth noting that, despite the use of the targeted method, not all subsets of correlated data produce high accuracy, low MAE predictive values. This is in fact extremely important, and only possible because of the correlation analysis: in the holistic approach, high MAE, low accuracy models can be achieved without knowing the origin of such poor prediction capabilities. Here, rather, by plotting each pair of parameters (as shown in Figure 137, bottom left; and Figure 138, bottom right) a direct visualization of the fidelity of the training set in representing the validation data is possible. As it is shown, for example, in Figure 137, CB-1 and RD-11 are highly correlated within the training data; however, the validation data, highlighted in red, does not follow the same trend. Essentially, this indicates that the training data is biased against the validation set, leading to poor predictive performance. This limitation and the method here presented, provides however a clear path forward to improve on the training dataset to remove such bias.

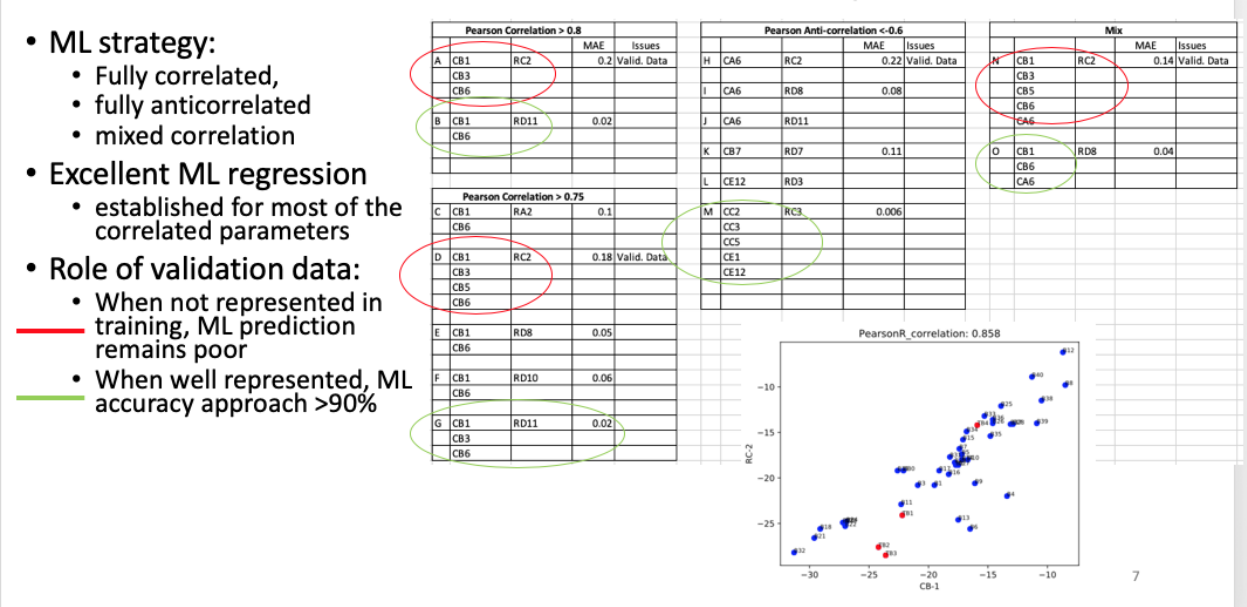

Figure 138: Using the correlation analysis and by setting correlation and anti-correlation thresholds, targeted regression ML models are generated. The fidelity of such regression models (evaluated through the mean average error, MAE, against the validation dataset) is used to determine the presence of potential bias in the training data, or to be used on the field when such models are accurate within the set expectation values.

The combined correlative analysis and ML regression analysis was then broadly and directly adopted throughout this project with the goals of: 1. Assessing the relevant performance, process and characterization parameters needed to create efficient and non-redundant predictive ML models; 2. Verify the quality and fidelity of the training dataset against the available validation dataset; 3. Offering an operational strategy for the creation of efficient ML models within and beyond this program (Figure 139).

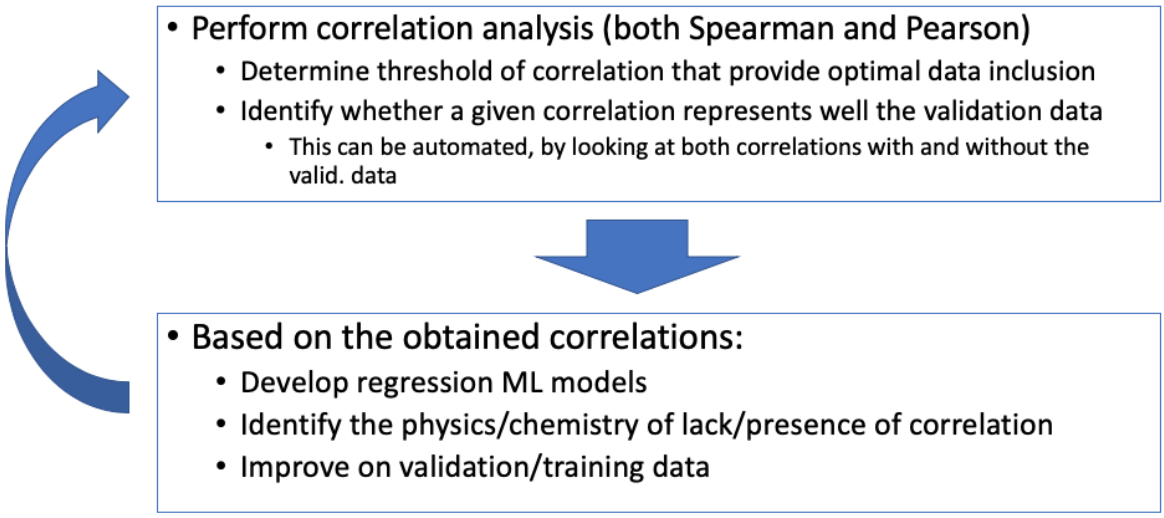

Figure 139: Proposed "targeted" method for an efficient generation of ML predictive models and physical insight through correlation analysis.

As a direct application of the method here developed, the robust, rapid and visually efficient method was exploited for identifying correlations between the characterization and processing data for the Petroleum dataset provided by WRI (Figure 140), and used to establish chemical and physical reaction pathways. For example, from the heat maps highlighting the correlations between the characterization data (C-data, Figure 141), and the performance data (R-data, Figure 142), pathways can be defined and visualized depending on the strength of the correlation, its type (direct or inverse) and shape. A parametric correlation pathway map was created by WRI based on such correlative analysis, and a representative example is shown in Figure 142. While apparently complex, it provides clear pathways of otherwise non-trivial pathways between different parameters. For example, two parameters that may not be directly correlated, may be correlated through an intermediary parameter. Furthermore, clear, and often times orthogonal pathways exist for different parameters allowing for the definition of predictive models that may rely on completely independent sets of characterization and performance parameters. Through this method ("stepwise approach") intermediate artificial neural networks can be developed to interlink uncorrelated parameters, but also to predict intermediate, non-available parameters. It is therefore a powerful tool that provides new insight while compensating for the lack of data, and that can be used to define operational processing method that are optimized to use in the correct sequence, only a selected number.

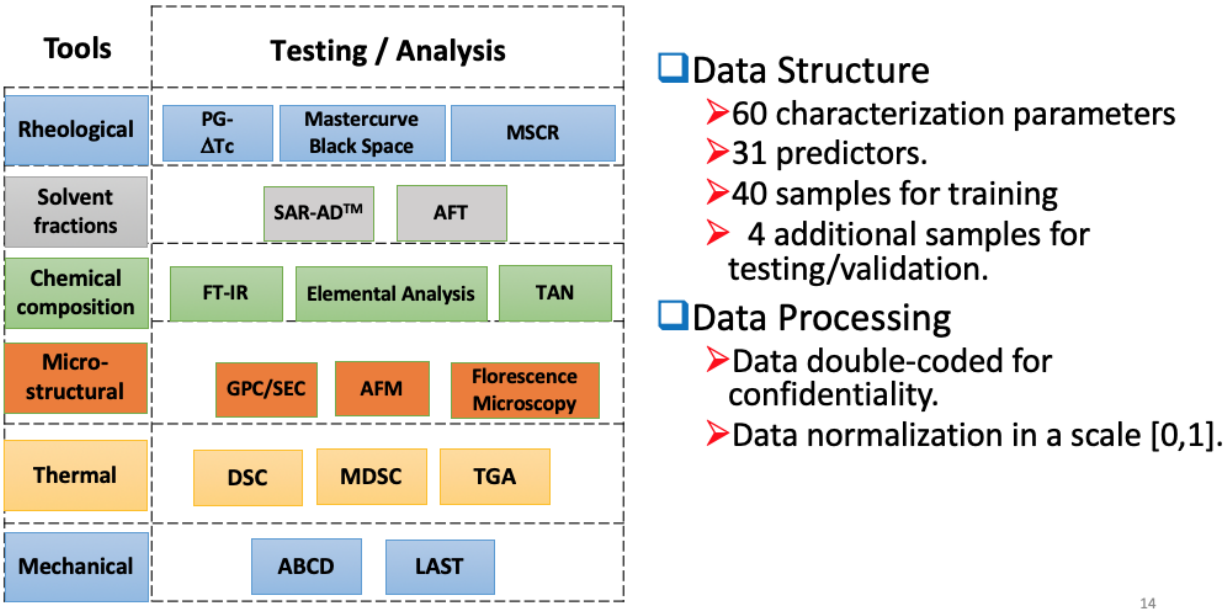

Figure 140: Summary of the characterization and processing data available for the Petroleum dataset, both for training and validation.

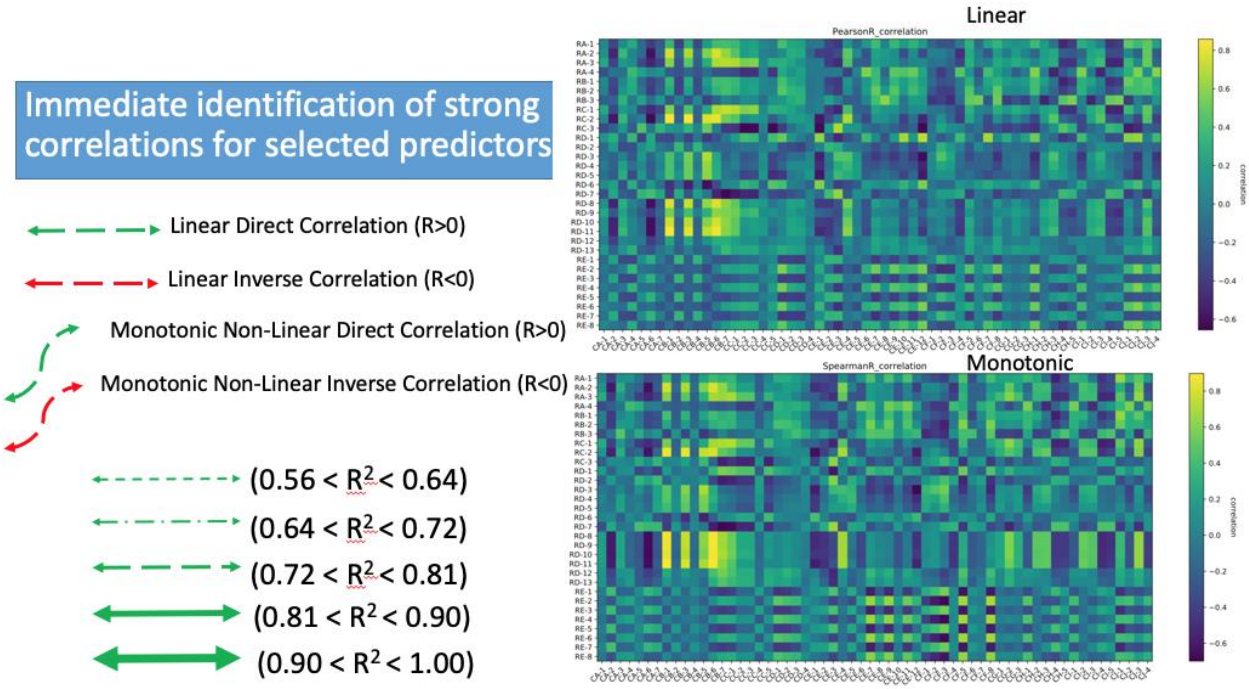

Figure 141: Definition of correlation pathways based on the strength, type and shape of the correlation, obtained from correlation characterization (C) and performance (R) data, as visualized in the heat maps.

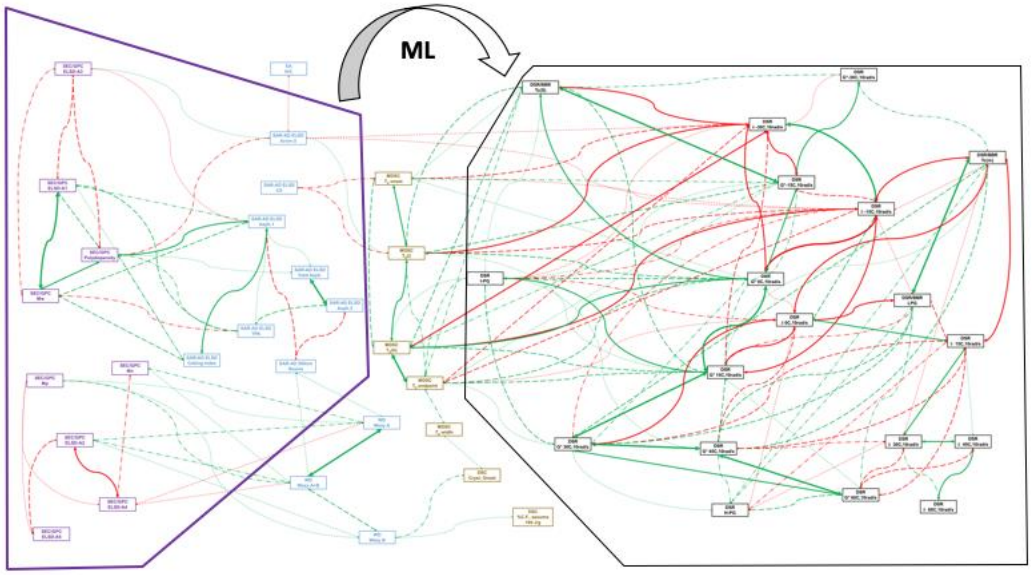

Figure 142: Parametric correlation pathway map based on correlative analysis of characterization and performance data, is used to define, physically and chemically justified, parameters to be used to construct ML models. Such map is used also to identify non-trivial relationships between physical parameters that might not be directly correlated.

As shown in Figure 142, and ad hoc selection of parameters can be easily obtained to train ML models that are both highly accurate and physically justified (Figure 143).

Targeted (27 parameters) vs. holistic (60 parameters);
55% reduction in the input layer size.

Sum of Square Errors	Holistic	Targeted
Cont. H-PG	200	39
Cont. I-PG	33	12
Cont. L-PG	38	76
Tc(m)	47	79
Tc(S)	80	58
Total	398	264

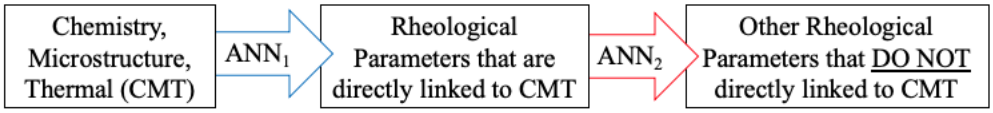

Stepwise Approach

Figure 143: Comparison in MAE between Holistic and Targeted methods, using the stepwise approach.

Most data available for PP and CTP feedstocks were in the form of either single value parameters or indirectly derived parameters from raw data based on predefined algorithms. Yet, significantly more data is available in the form of raw spectra. So far, the project has not made use of such data to develop predictive ML algorithms, mainly because of the lack of selectivity in the data that is truly useful within the algorithms. Essentially, the risk of overfitting and extreme redundancy makes the balance between information and cost not worthy of inclusions in training datasets. Based on the work on correlative analysis, the same strategy has been applied to raw spectra. Correlation plots have been produced, where spectra from the training dataset (including Fluorescence, FTIR, LDI) are correlated with physical characteristics of the CTP (for example, softening point, SP). For example, the correlation with softening point of the LDI spectra is shown in Figure 144, and the correlation between FTIR data and the CI and SP are shown in Figure 145. The correlation plots allow for the identification of specific features (peaks, bands, spectral regions, etc.) that highly correlate with the performance parameters. These features can be then easily extracted and used directly within the training dataset. In addition, physical insight is gained: in the example shown in Figure 144, it is noticeable that with increasing SP, there is a higher amount of molecular systems with molecular weight > 350D, which is expected.

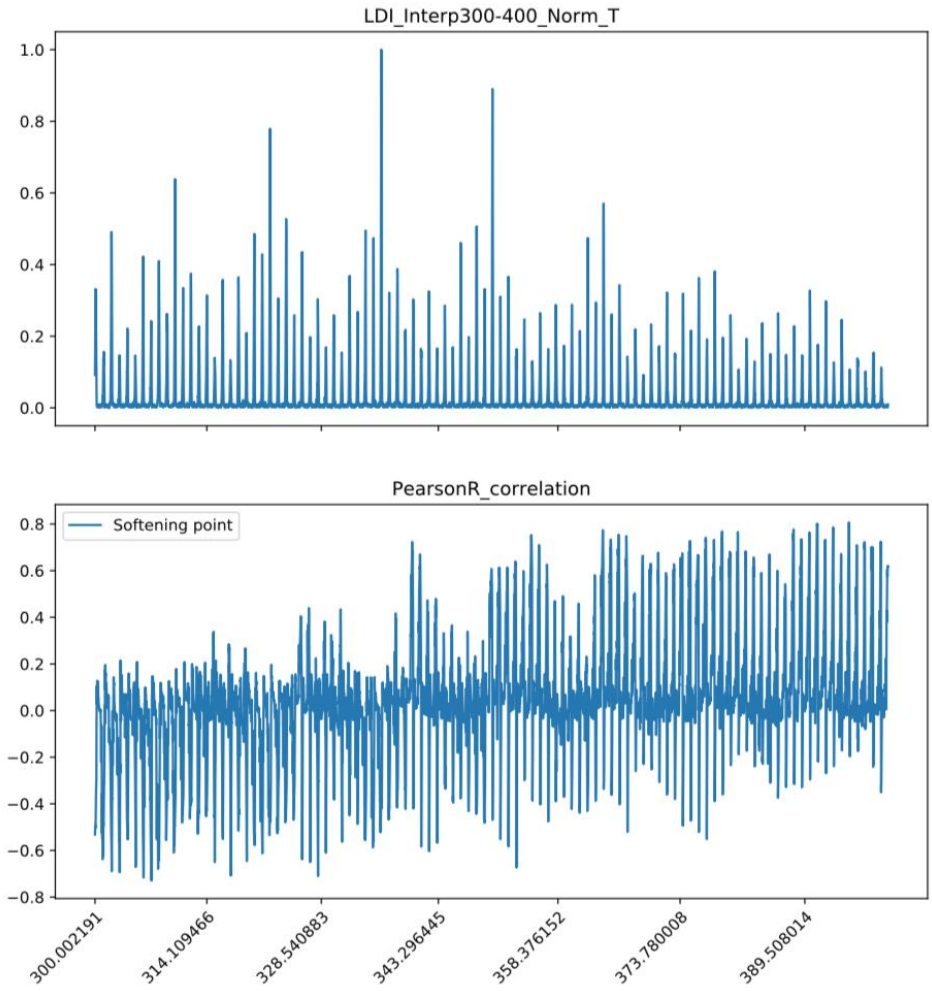

Figure 144: Correlation plot of LDI data for coal-tar pitch is plotted (below), along with a representative LDI spectra over the same range (above). The numbers at the bottom is the molecular weight.

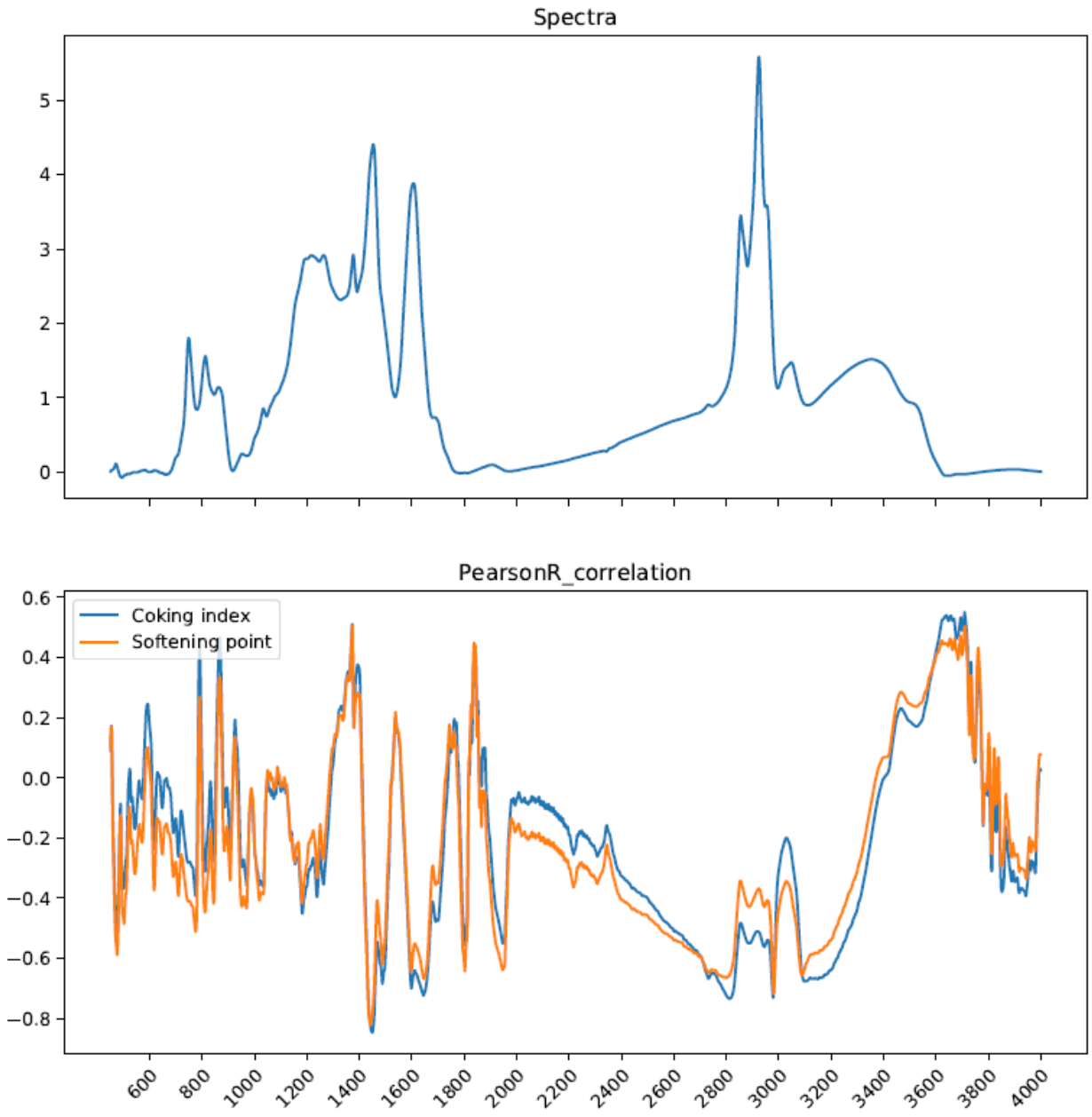

Figure 145: Correlation plot of FTIR data for CTP with CI and SP is plotted (below), along with a representative FTIR spectra over the same range (above). The numbers at the bottom are the wavenumbers.

Through a comprehensive analysis within the full set of raw spectra available for pitch-based data, new characterization parameters were identified and used directly to develop ML predictive models. It is noteworthy that while different spectra may correlate to the same parameter, they do so for completely different physical reasons. Therefore, they act on the ML as statistically independent parameters, adding more information, without increasing redundancy. The new characterization parameters that correlate well with SP (with Spearman correlation > 0.9, or < -0.9) are:

- FTIR: spectral feature at 1442 cm^{-1}, which is justified by corresponding to the bending modes of methyl groups. This feature is inversely correlated to SP, because the number of methyl groups is reduced for pitch with increasing SP.
- Fluorescence: features within the range [380-390] cm^{-1} with excitation at 330 cm^{-1}. This feature is inversely correlated with SP, as it corresponds to aromatic clusters with size 3-4, whose concentration decreases for pitch with higher SP. LDI: Average molecular weight: This is directly correlated with SP, as the higher concentration of larger aromatics leads to a material with higher SP.

Cost Estimation

Ramaco developed a front-end loading (FEL-1) cost estimate for the pitch-based feedstocks. Most of the data needed to build the cost analysis for bio-ACN was provided by SRI. For bio-PAN, PP and CTP all three materials were deemed to produce CF which satisfied the DOE requirement of <$5/lb. A summary of the economic analysis are provided below.

The following are key parameters that effect the economics of any new technology.

A. Annual Production Capacity

It was considered that existing pitch-based fibers will grow from its current global demand of less than 2,000 metric tons per year with the availability of lower priced fibers than the current $25-$50+ per pound. Further the existing 161,200 metric tons of PAN-based fiber capacity may permit partial substitution of pitch-based fibers. Based on a market report purchased by Ramaco there is in recent years a CF industry CAGR of 10+%. Assuming that it would not be a large commercial challenge for pitch-based CFs to displace PAN fibers provided that those fibers were of the same or better quality and at a lower price. Current business plans, such as those for Ramaco, expect to support the production of 10,000 metric tons per year of CFs and this figure has been used across the board for comparing raw materials and production routes as it is reasonable commercial scale for a new facility.

B. Capital Investment

Capital investment is largely based on the annual production capacity. In addition, the location of a site and whether it is greenfield or brownfield with some infrastructure is an important aspect of the overall process economics. Furthermore, the investment source likely requires a balance of debt and equity as neither private investors nor banks would want to bear the combined technical and commercial risk alone.

For the raw materials reviewed there is a distinct difference in investment. PAN substitutes like bio-ACN or lignin can reuse existing PAN solution spinning equipment with perhaps minor changes. Petroleum, coal tar or coal based pitches, either isotropic or mesophase, require new melt spinning production equipment.

For purposes of this analysis, the facility specified and costed out is in a facility with existing infrastructure and using incremental investment in the equipment needed to produce the precursor as well as the CF.

C. Coproduct Revenue

There is an inherent danger in using co or by-product credits as they have often been used to justify otherwise uneconomical processes. However, they are also a basic element of most petrochemical economic analyses. Chemicals, distillates and solid carbon by-products require some further market development, however there are existing target product quantities and market prices. Bio-ACN produces propylene glycol and ammonium sulfate coproducts. Organic distillates have many uses as solvents and aromatic oils. Carbon char is used as a soil enhancer, reductant in metal refining and thermal insulation.

D. Operating Expense

As in most scenarios for new process economics, raw material cost and operating costs can greatly impact the process economics. Expected yields of precursor from raw material as well as the projected CF yield from the precursor has been factored into the analysis.

Other operating expenses include the cost of hydrogen, utilities, maintenance and repair, labor and supervision, site management, insurance and technology license royalties. Corporate overheads are not included in this economic review as existing companies are expected to enter the business as a growth opportunity.

E. Production Costs of Carbon Fiber

Table 38 outlines the product yields to CF, the raw materials, co-product credits, and operating expense, including capital charges to produce CFs from each respective precursor. Advances continue to be made to lower the production costs of spinning CF. For example, 4M (http://4mio.com/) are advancing the use of laser technology in the oxidation step of fiber spinning to lower capital and operation costs. In the table's footnotes are the references and assumptions that will be refined as this project progresses.

Table 38 compares cost of production; it does not assume that these will be the expected commercial market prices. Such prices may be higher in order to provide higher business returns in order to attract investors.

Table 38: Summary of costs associated with assumptions for the TEA for various CF precursor material. PAN is derived from traditional petroleum sources using petroleum PAN feedstock costs, bio-ACN-PAN is using bio-ACN derived from sugars by SRI, Slurry Oil-direct is using traditional methods to produce PPM with no recycle, Slurry Oil-upgraded is using the ACP process which has a very high recycle rate, CTP (traditional) is what was used in this program and is the distilled bottoms from coal tar from coking ovens used to make metallurgical grade coke for the steel industry (after filtration of primary QI), and Coal (Dry) to DCL is taking upgraded Powder River Basin coal and using direct coal liquefaction methods.

	Carbon Fiber Feed Source					
	PAN[4]	Bio-ACN-PAN[2]	Slurry Oil - direct	Slurry Oil - upgraded[3]	Coal Tar Pitch (traditional)[5]	Coal (dry) to DCL[6]
Yield to isotropic pitch	N/A	N/A	25%	65%	N/A	34%
Yield isotropic to mesophase pitch	N/A	N/A	50%	65%	47%	55%
Yield of mesophase to CF	N/A	N/A	50%	50%	50%	50%
CF Yield from Source, %	45%	45%	6.3%	21.1%	23.3%	9.4%
Ton Feed / Ton CF	2.22	2.22	10	4.73	4.30	3.91
Feed Source, $/metric ton	$2,700	$3,287	$300	$300	$800	$28
Feed By-product Credit, $/MT feed	N/A	($2,423)	N/A	N/A	($241)	($166)
Net Feed Cost, $/metric ton CF	$6,000	$1,920	$4,800	$1,420	$2,405	($1,481)
Feed OPEX Cost, $metric ton CF	N/A	N/A	$9,856	$2,296	$1,720	$4,160
Spinning OPEX[1], $/metric ton CF	$8,802	$8,802	$3,593	$3,593	$3,593	$3,593
TOTAL CF COST, $/MT CF	$14,802	$10,722	$18,249	$7,309	$7,719	$6,273
TOTAL CF COST, $/lb CF	**$6.71**	**$4.86**	**$9.12**	**$3.65**	**$3.86**	**$3.14**

(1) US OPEX cost for spinning precursor into into carbon fiber. PAN-based carbon fiber manfactured costs for automotive sector average $18/ kg are @ $3.99/lb (Das, et al, Global Carbon Fiber Composites Supply Chain Competitiveness Analysis, CEMAC, ORNL, May 2016, p 51, p 64 Figure 4-12) including 12.4% capital charge. Pitch-based @ $1.63/lb (Warren, presentation Carbon Fiber Precursors and Conversion, ORNL) based on 12,000 lbs/year melt spinning with 12.4% capital charge.

(2) Cooperative Agreement DE-EE0008203, Q4 2018 report, page 60. Carbon fiber spinning Opex same as PAN.

(3) Boyer, et al, "New Process for Making Mesophase Pitch", Advanced Carbon Products, Carbon Fiber Conference, November 11, 2016. Minimal by-product recovery assumed.

(4) PAN feedstock cost based on $60/bbl crude oil. Cost @ 50% of range per "Global Carbon Fiber Composites Supply Chain Competitiveness Analysis, Sujit Das, Josh Warren, and Devin West Energy and Transportation Science Division, Oak Ridge National Laboratory, Susan M. Schexnayder, The University of Tennessee, Knoxville" PAN carbon fiber price based on S. Das presentation to Pittsburgh Coal Conference, September 2019.

(5) Coal tar pitch (@ 7% QI) to mesophase pitch conversion cost estimated at $400/ MT. Mesophase pitch has a by-product distillate credit at $500/MT.

(6) DCL conversion cost plus pitch to mesophase pitch conversion estimated at $4,160/ MT CF. By-product credit includes sales of excess coal liquids and solid carbon.

A techno-economic assessment was conducted for a 5000 MT/year biomass derived non-food sugar to acrylonitrile production plant. A complete process was simulated using ASPEN Plus using the experimental results obtained by SRI. Capital costs were estimated and averaged (with standard deviation) from three different sources. Figure 146a shows the pie chart of cost distribution for the biomass to ACN process. Raw materials, particularly sugar, were found to be the major cost driver (68%). Hence, a sensitivity analysis with respect to type and/or price of raw materials was conducted and shown in Figure 146b-d. Although cost of ACN shows high sensitivity to sugar price, the economics remains favorable (<$1/lb) for a wide range of sugar prices ($300-$450/MT). On the other hand, the overall cost of acrylonitrile production would be less sensitive to the price volatility of other raw materials, such as, NH_3 and H_2 (Figure 146c and d).

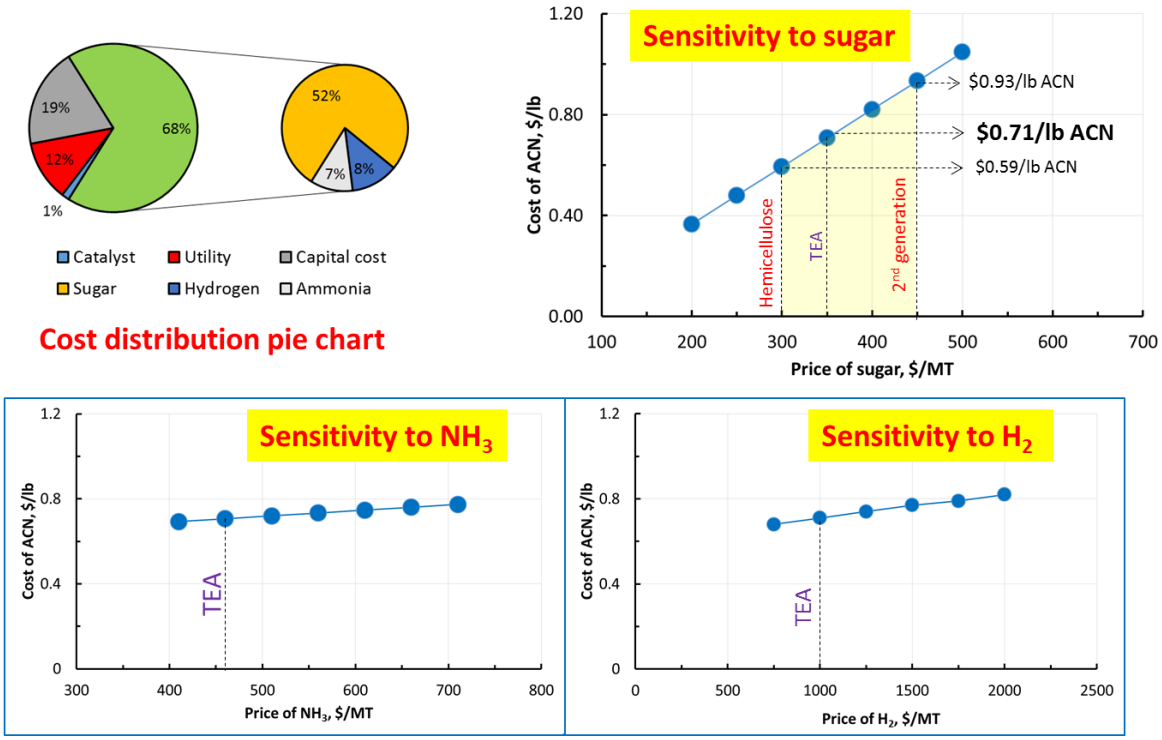

Figure 146: (a) Cost distribution pie chart for biomass to acrylonitrile production and bio-ACN production cost sensitivity with respect to (b) sugar, (c) NH3 and (d) H2 price.

Macro-Level Engineering Models and Analysis

An important aspect of this work was to determine strength and modulus properties of CF at the tow-level. This serves as a validation of the performance of the CF from the single filament test towards the expected performance at the composite level. As part of the initial scope of work, this program was to include investigation of creep properties. However, is was later confirmed that creep properties are dominated by the epoxy matrix properties and are not an inherent property of the CF material, and therefore not useful in characterizing and understanding the CF.

The various method to prepare the samples, the testing that was applied and the finite element analysis modeling that were applied to CF are described below

To test at the tow level CFs were used to make CF epoxy matrix composite specimens for characterization. Using a wet layup process, specimens will be manufactured to ASTM D-3039 standard. A known volume of CF were measured, and impregnated with a known volume of Hexion resin. This way, the volume fraction of fiber in the composite specimens will be known, allowing the theoretical strengths of the specimens to be calculated. These theoretical values were used as a rough benchmark for experimental accuracy. Once the fibers are impregnated, they are placed in a press clave, pictured in Figure 147, where the resin is cured.

(a) *(b)*

Figure 147: Pressure clave interior (a), and with top plate (b).

The press clave is used to apply an external pressure to the composite specimens while the system is heated. Specifically, a vacuum will be draw through port on the bottom plate while the system is heated to 120°C. Once the temperature reaches equilibrium, the vacuum will be slowly bled, and the system will be pressurized to 60 psi through the port on the top plate. The vacuum is used to for degassing while the resin undergoes curing, while the pressure is used to remove voids from the epoxy matrix to minimize faults in the specimens. Heat is applied to hasten the curing of the epoxy matrix, while also decreasing the viscosity of the epoxy to allow voids to be more easily forced out of the matrix. A vacuum bagging apparatus, shown in Figure 148, will be used to inhibit air from being forced into the matrix while the outer pressure is being applied.

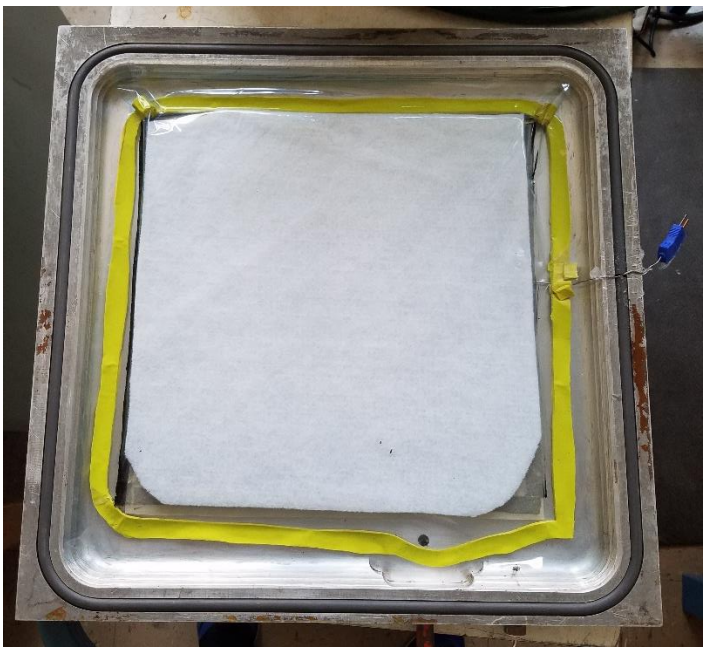

Figure 148: Vacuum bagging apparatus.

Once curing is complete, fiberglass epoxy matrix tabs will be adhered to the ends of the specimens. These tabs are used to accommodate forces placed on the specimen by the grips on the load frame. This load frame is an Instron 1125, which is a uniaxial, quasi-static, screw driven load frame, capable of exerting 100kN (~25kip) in both tension and compression. These specimens, pictured in Figure 149, due to their unidirectional nature, are significantly stronger in the axial direction (parallel to the fibers), than in the transverse direction (perpendicular to the fibers). Due to this high axial strength, relatively large forces are required by the grips to inhibit slippage of the specimen during loading. These forces are strong enough to cause premature failure at the grip-composite interface.

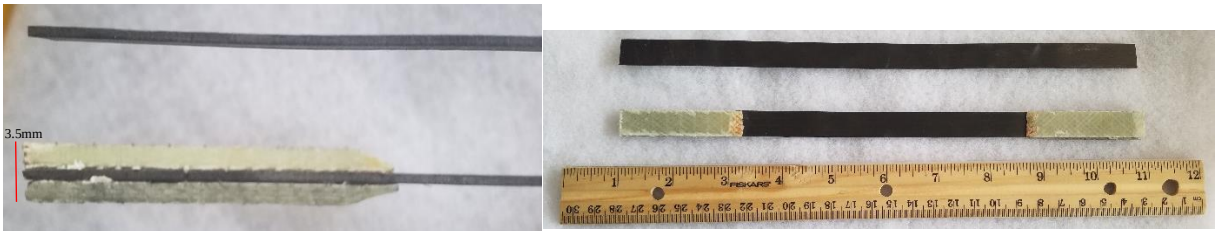

(a) *(b)*

Figure 149: Side view (a) and front view (b) of a tensile specimen with and without tabbing.

Once the tabs are properly attached to the specimens, the specimens will be run through a series of mechanical tests (tensile, iosipescu, etc.) to fully characterize the fibers.

12” by 12” sheets of prepreg CF tows were cut and stacked on a flat aluminum plates, which were coated in an industrial release agent. The plate and prepreg were then placed in a press-clave, pictured in Figure 150, and surrounded by cork tape. The cork tape keeps resin from spilling away from the composite plies during the curing process. Peel ply and bleeder cloth were

then placed over the top of the composite plies. This system was then surrounded in tacky tape and covered in release film to create a vacuum bagging set up. The press-clave was then placed in a heated press and heated while pulling vacuum to produce the standard to-level CF plate for ATM testing.

Figure 150: A photograph of the press-clave used for this work.

After manufacturing the tow-level CF plate, tabs were cut out of sheets of fiberglass to attach the plates for testing. The tabbing plates were placed in a tabbing jig, shown in Figure 151, covered in AF-126-3 structural film adhesive, and the laminate plate was placed on to the adhesive film. Adhesive film and tabbing plates were then placed on top of the laminate plate, and the entire system was heated and cooled and then samples were cut for mechanical testing.

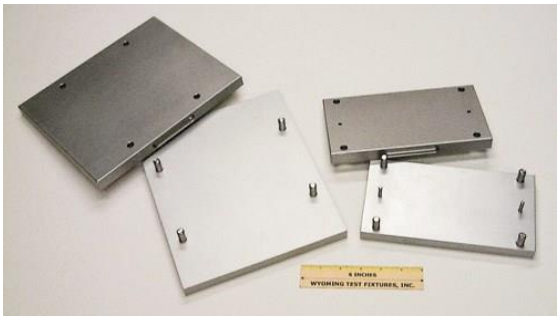

Figure 151: A photograph of the composite tabbing jigs used to prepare the tow-level Carbon Fiber plates for testing.

Currently, both sample sizes have been manufactured, but only the ASTM standard specimens have been mechanically tested. A photograph of the standard specimen with tabs is shown in Figure 152.

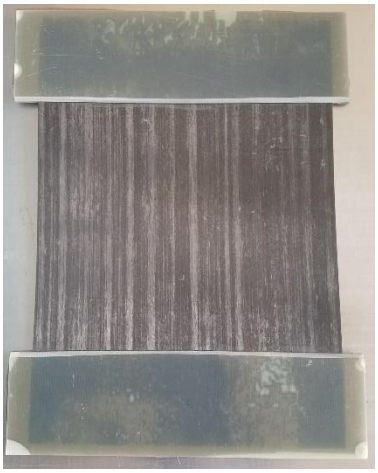

Figure 152: A photograph of a standard composite plate with tabs.

A wet layup manufacturing process was developed. Sheets have been prepared using Hexion resins to apply multiple plies until the laminate was 1 mm in thickness. Due to the variability with CF tows, the number of plies will vary between samples. The prepared system was then placed on to a larger metal platform and vacuum bagged and an identical tabbing procedure as the prepreg composite plate was followed for the wet layup composite plate.

Some issues have been encountered in tabbing wet layup composite plates, and were addressed. Specifically, as the adhesive film is heated, its viscosity is greatly decreased, and the force placed on the tabbing plates causes the adhesive film to spread out. This spreading places a transverse tensile stress on the composite plate and leading to some splitting. Useable samples can be scavenged from these split plates, but this is a less than satisfactory situation. Figure 153 shows photographs of a wet layup composite plate and a prepreg composite plate.

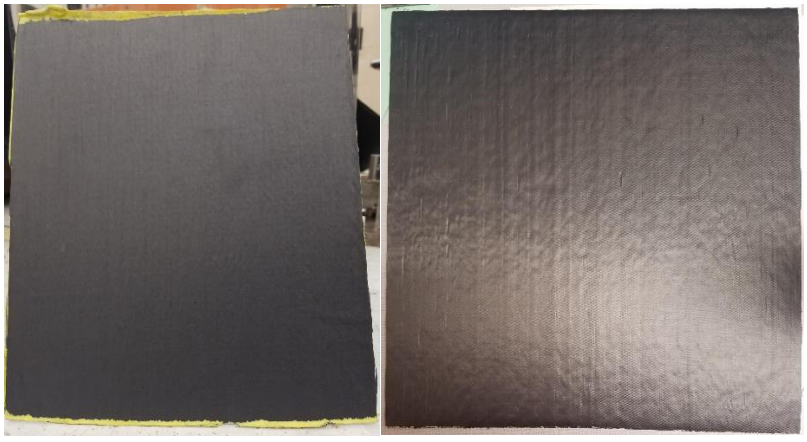

Figure 153: Wet layup composite plate (left) and a prepreg composite plate (right).

The ASTM standard for tensile testing of unidirectional CF polymer matrix composites (ASTM D3039), for example, calls for rectangular specimens, that are 10 in. long. The tow-level composites fabricated from CF developed in this project were sometimes significantly smaller

than this standard. Using these smaller than standard specimens requires verification that similar results can be obtained compared to ASTM standard specimens.

The process for this verification was straightforward: manufacture both ASTM standard specimens and smaller specimens, test them to failure and compare their properties to ensure equivalence. To achieve the most consistent properties for this comparison, commercial preimpregnated (prepreg) CF tows were used for this initial verification.

Previous work showed the importance of correctly modeling the fiber morphology to achieve more realistic strength properties. To this end, a model has been developed (Figure 154) to generate random fiber microstructures based on long-range (radial distribution function) and short-range statistics (nearest neighbor distribution), including distribution of major and minor radii of ellipse cross-sections.

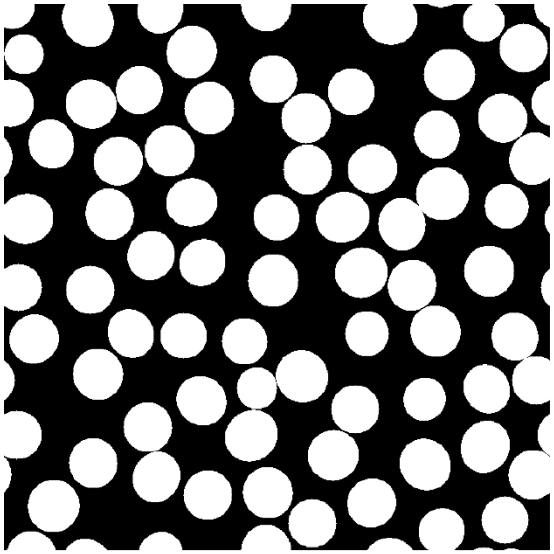

Figure 154: Random fiber model generated from long-range and short-range statistics.

These random models have been incorporated into a finite element framework for extraction of stiffness and strength properties (Figure 155 shows the mesh generated from this approach).

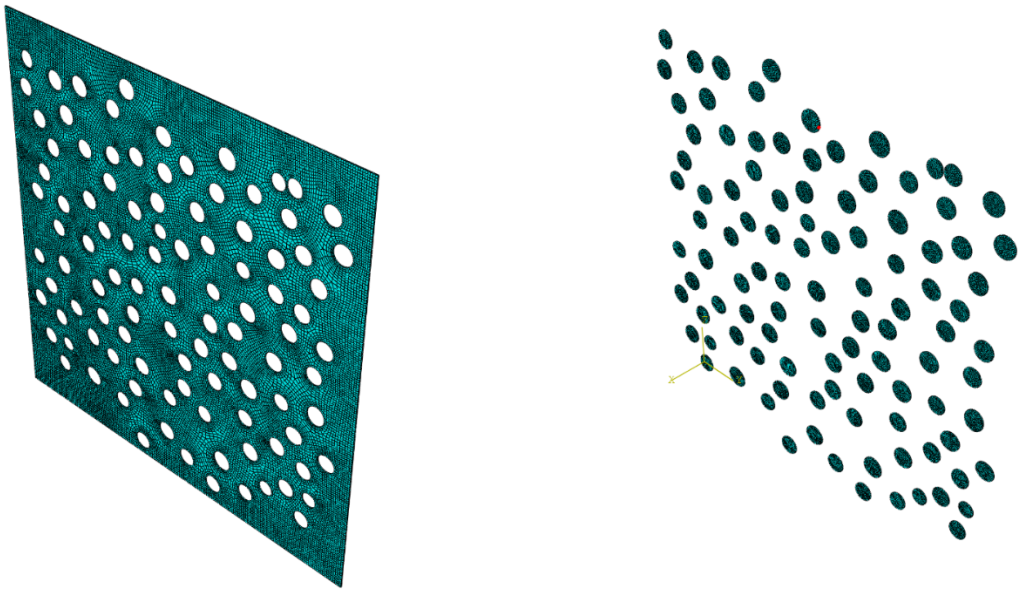

Figure 155: Meshed random fiber model.

It was discovered that there was an issue related to the periodicity at the corners that required resolution a corrected periodicity was incorporated into the microstructure generation model. Periodic boundary conditions on microstructure models were developed—this ensures that stress/strain/displacement fields are continuous across boundaries and do not introduce any spurious stresses. Figure 156 shows the idealized micromechanics model loaded in transverse tension with periodic boundary conditions.

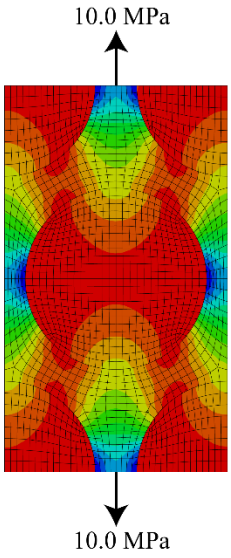

Figure 156: Idealized micromechanics model loaded in transverse tension with periodic boundary conditions.

Another key aspect of the work is to develop microstructure finite element models to predict the composite properties. To these ends, the primary objectives of the work of the University of Wyoming in support of this project were:

1. Provide a complete set of elastic properties for fiber characterization.
2. Assess the performance of particular fiber types in tow-level composites, from both static and durability perspectives.

The first objective of obtaining a complete elastic characterization of the CF requires a combination of simulation and experiment. Tow-level composites were fabricated and tested in longitudinal tension, transverse tension, and longitudinal shear, with appropriate composite tow-level elastic moduli computed. In conjunction with this experimental effort, a hexagonal representative volume element (RVE) was modeled using finite element analysis. By coupling knowledge of the elastic moduli of the matrix with the composite moduli properties obtained experimentally, the elastic properties of the fiber was computed using a gradient-based optimization algorithm. These outputs are shown in Table 39.

Table 39: Expected Outcomes from Elastic Property Characterization

Composite Properties (Experimental Testing)	Matrix Properties (Experimental Testing)	Fiber Properties (Simulation)
E_{11}^{C}	E^{C}	E_{11}^{f}
$E_{22}^{C} = E_{33}^{C}$	G^{C}	$E_{22}^{f} = E_{33}^{f}$
$G_{12}^{C} = G_{13}^{C}$		$G_{12}^{f} = G_{13}^{f}$
$\nu_{12}^{C} = \nu_{13}^{C}$		$\nu_{12}^{f} = \nu_{13}^{f}$
G_{23}^{C}		G_{23}^{f}

The second objective requires evaluation of mechanical performance of composite tow structures fabricated from the CF developed by ORNL. The performance metrics sought are static strengths and fatigue performance. Because multiaxial testing is extremely difficult and historically unreliable, simulations were used to predict the full range of strength under arbitrary loadings after benchmarking with experimental solutions for uniaxial loadings. To accurately predict strength in composites is significantly more challenging than predicting elastic modulus; this is because modulus is an average response of the system, while strength pertains to local failure initiation and propagation. To this end, an ensemble of stochastic finite element models using realistic microstructures with statistically similar microstructures is required. These microstructures are used in conjunction with failure modeling techniques such as the extended finite element method (XFEM), cohesive surfaces, and specialized user-defined materials to predict a distribution of strength and fatigue responses to arbitrary loadings.

FEA is often used to solve composite microstructure modeling problems. To infer CF properties a model for a hexagonal fiber packing RVE was developed. An example result from this model is shown in Figure 57.

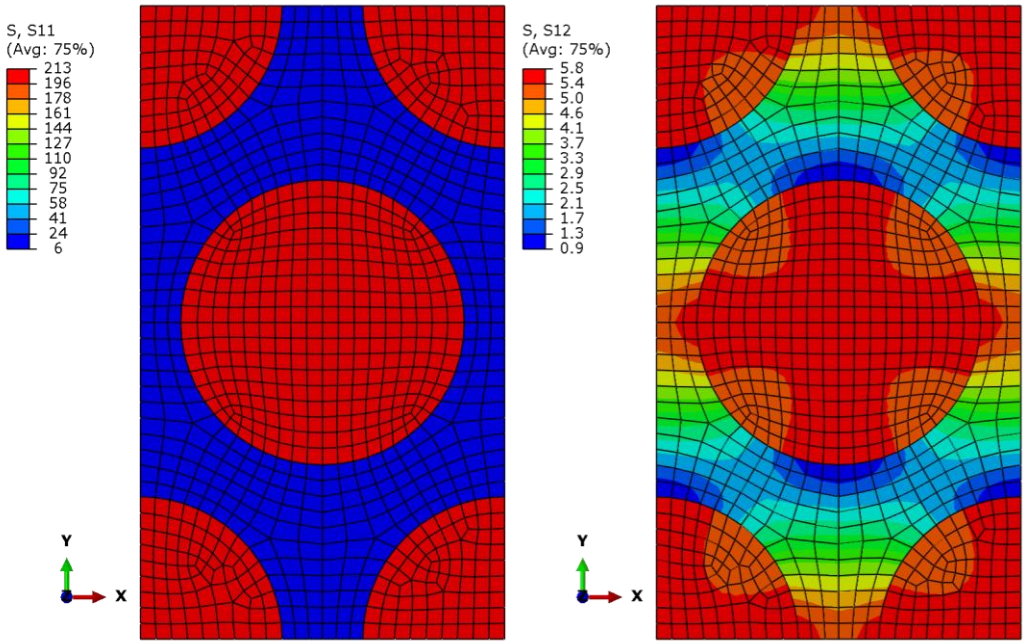

Figure 157: Hexagonal Fiber Packing Model (left) longitudinal normal stresses under longitudinal loading, and (right) longitudinal shear stresses under longitudinal shear loading.

As part of the preparation for the complete composite tow performance evaluation, stochastic failure methodology was developed. Figure 158 shows this model along with close-up images of cracking between fibers.

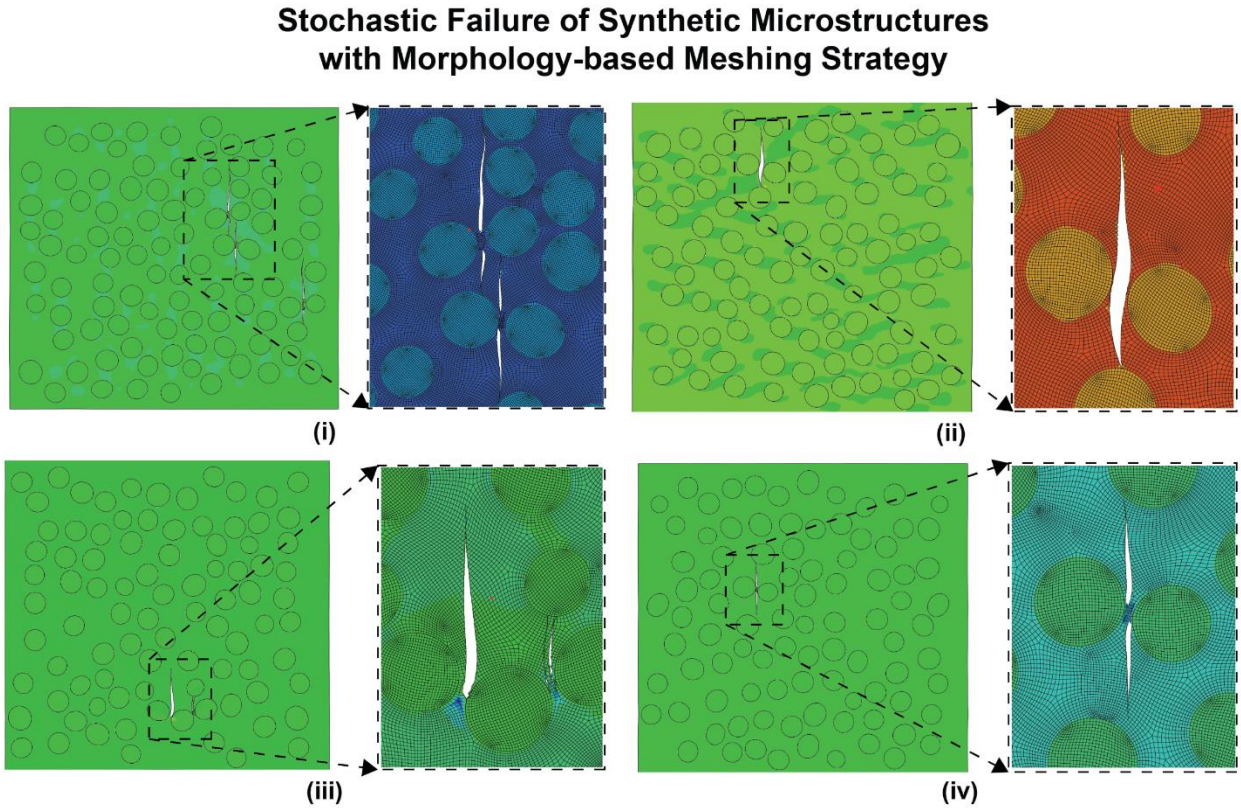

Figure 158: Four separate stochastic realization of a microstructure ensemble along with images of failure initiating between fibers under transverse loading.

Elastic Property Characterization

Digital image correlation (DIC) was investigated as a strain measurement technique for tow-level composites testing and characterization (Figure 159). Specifically, DIC was benchmarked via strain measurements on 0° tensile specimens. Good agreement was observed. A stress-strain diagram for one such DIC test is seen in Figure 160. Table 40 shows the characterization of the material properties using this strain measurement approach. In particular, the fiber longitudinal modulus is computed to be 414 GPa using the rule of mixtures, which is highly accurate for on-axis unidirectional tests. These results demonstrate the accuracy of DIC for measuring the strain of composites during mechanical testing, and will be used in all future tests.

Figure 159: DIC set up (a) and a tow-level specimen before and after testing at 0° failure (b) left and right, respectively.

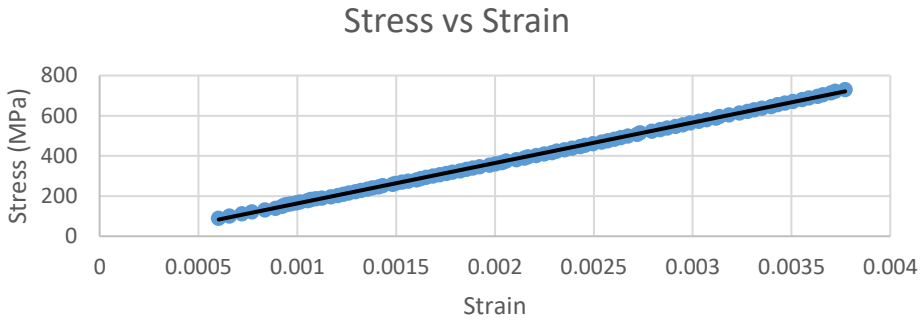

Figure 160: Stress vs strain curve generated from DIC data

Table 40: Results of back out method using DIC data

E_m(MPa)	E_f (MPa)	E (MPa)	ε_{fail}	σ_{fail}(MPa)	$V_{f,theo}$	$V_{f,act}$
3	414000	201301	0.38%	730.48	48.62%	48.92% ±1.28%

One Efficient way to characterize CF from nontraditional sources is to back out fiber properties from CF reinforced polymer matrix composites. In order to fully characterize the composite, and subsequently the fibers, four mechanical tests are required: a 0° tensile test, a 90° tensile test, a ±45° tensile test, and a rotated, thicker 90° tensile test. From these tests, values for E_{11}, E_{22}, v_{12}, v_{23}, G_{12}, and G_{23} can be found.

As verification for this proposed characterization method, 0° tensile test specimens have been manufactured using a wet layup technique and mechanically tested. In order to demonstrate the

quality of the wet layup process, the modulus of elasticity of each specimen can be compared. The accuracy of this "back out" method can also be verified using a simple rule of mixtures equation:

$$E_{composite} = E_{fiber}V_{fiber} + E_{matrix}V_{matrix}$$

Where E_i represents the elastic moduli of the respective materials and V_i represents the volume fraction of each material. This equation can be rewritten to calculate the theoretical fiber volume fraction of the composite,

$$V_{fiber} = \frac{E_{composite} - E_{matrx}}{E_{fiber} - E_{matrix}}$$

These specimens were made using Thornel P-55 pitch based fibers, and Epikote RIMR 135 from Hexion, which have known elastic moduli of 414 GPa and 3 GPa, respectively. The actual V_{fiber} can be directly measured by analyzing cross sectional images of the specimens with a MatLab script written by Dr. Seyed Sanei. The theoretical and actual V_{fiber} values are then compared. Figure 161 shows the consistency of the measured composite elastic modulus.

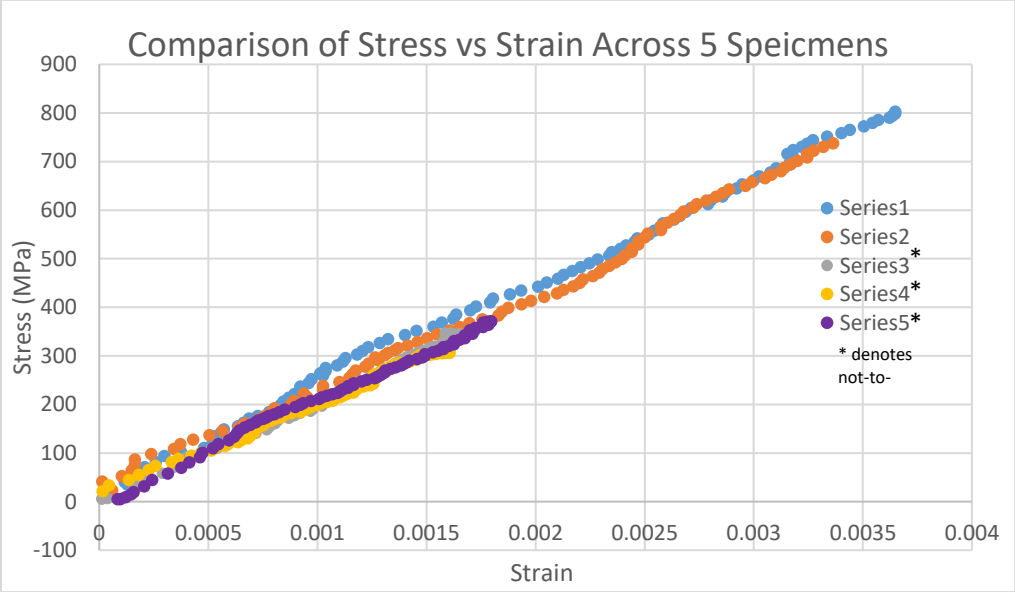

Figure 161: Stress vs strain plot for 5 wet layup specimens

These five specimens were then sectioned, polished, imaged, and analyzed. An epifluorescent lens is used to magnify the contrast between the fibers and matrix, seen in Figure 162.

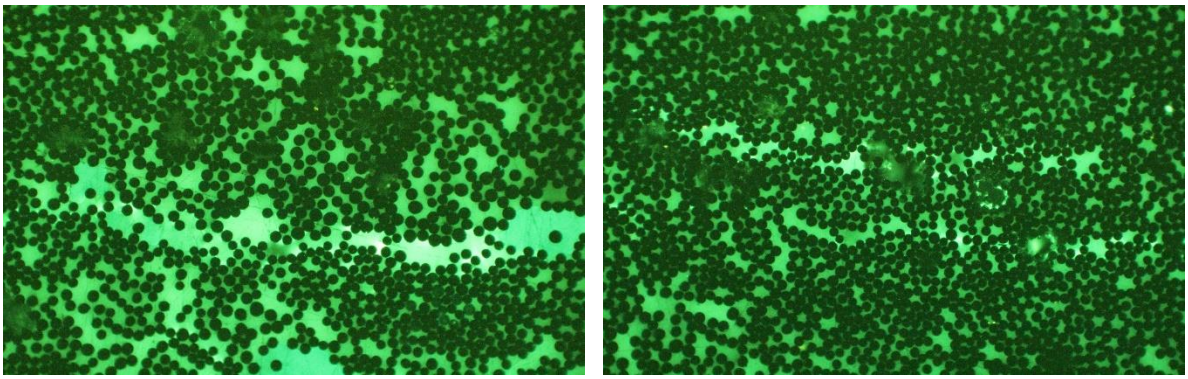

Figure 162: Cross sectional images from the Test 5 specimen, taken at 2 different locations

As seen in Figure 162, a considerable amount of bias can be introduced from the location on the specimen from which the picture is taken. In order to minimize this bias, 15 images are analyzed per specimen, across the length of two different sections of each specimen. Table 41 shows the theoretical versus measured V_{fiber}, with uncertainty.

Table 41: Theoretical vs Measured Vf with uncertainties and standard deviations (95% confidence interval)

Test	E (Gpa)	Theoretical V_f	Measured V_f	σ
3	246	59.1%	56.1% ±1.31%	2.29
4	216	51.8%	55.1% ±1.42%	2.26
5	245	58.9%	56.7% ±1.14%	1.93

This process will be repeated for the remaining mechanical tests to confirm their validity. This first round of tests has revealed areas of needed improvement. The stress versus strain curves of the 0° tests appear wavier than a typical curve generated from this test. This is due to the laser extensometer used to measure strain. The laser extensometer is meant for use with large strain specimens. As seen in Figure 163, the ultimate strain of these specimens is 0.35%. A more appropriate small strain measurement technique is digital image correlation (DIC), and will be implemented going forward. This will sharpen the results of each test.

The process for characterizing 0° composite specimens was refined via the introduction of DIC strain measurement techniques. Immediate improvement was observed, seen in Figure 32.

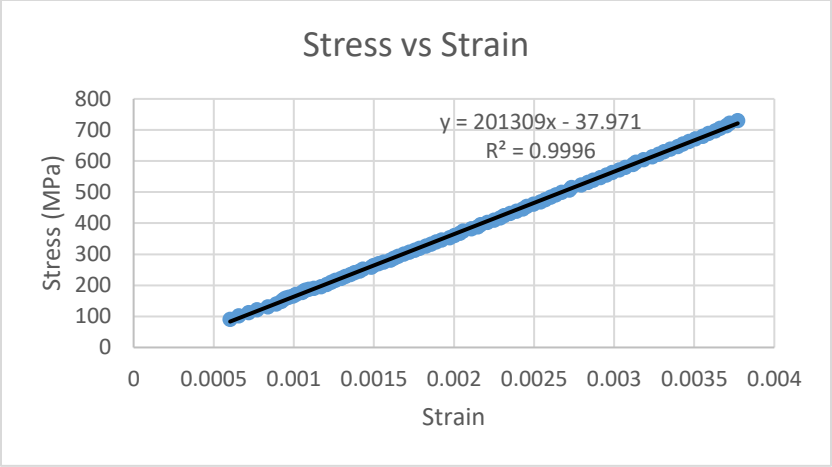

Figure 163: Stress vs strain plot for a typical DIC specimen.

It can be seen that classic brittle behavior is exhibited in the specimen, demonstrated by the R^2 value. The DIC strain measurements predicted a V_{fiber} of 48.6%, and the experimental counting method yielded a V_{fiber} of 48.9%. Going forward, DIC was implemented in all mechanical tests. From the 0° tests, Poisson's ratio in the 1-2 direction was also found to be 0.28 ±0.03. Compared to literature values of 0.31, the calculated value appears valid.

From this validation, 90° specimen manufacturing was investigated and attempted. Due to the nature of the hand layup technique, it was not thought possible to make specimen geometries that matched ASTM standard primarily because of time constraints associated with the manufacturing process. Because the elastic constants of a material are generally independent of geometry, shorter and thinner specimens were manufactured using the same process as the 0° specimens. The first iteration of specimens were much too thin to be properly handled and placed in the grips, often breaking prematurely. The second iteration of specimens was made to be significantly thicker, approximately 1mm as opposed to 0.5mm. It was assumed that the tabbing regime used for the 0° specimens would be appropriate for the 90° specimens. This assumption proved to not be valid, as the first plate to be tabbed came out of the tabbing jig wavy, despite being flat at the beginning of the tabbing process. After more iterations of tabbing, and changing the process parameters several times, it was realized that the structural adhesive being used was simply overkill for these specimens. The structural adhesive was replaced with Loctite Super Glue, which was strong enough to withstand the loading during tensile testing. Table 42 shows the successful results of the 90° tests.

Table 42: Transverse modulus results from six 90° specimens

Test	**1**	**2**	**3**	**4**	**5**	**6**
E_2 (GPa)	7.65	5.5	4.37	4.9	5.87	6.68

These tests yielded an average transverse modulus of 5.83 ±0.87 GPa, which compared to a literature value of 5.58 GPa, shows success.

Next, ±45° specimens were manufactured. Only 4 plies were used due to the time restrictions of manufacturing these specimens. Since no tabbing is required for these specimens, fewer iterations were required to obtain valid results. During testing of the first set of specimens, curling of the specimen edges was observed and attributed to the nature of tensile loading of balanced and symmetric ±45° specimens. Some of these tests were cut short due to a misunderstanding of the existence of a plastic deformation region on the stress strain diagram. Later tests were allowed to continue until fracture was observed. After this was corrected, further tests were run and an in-plane shear modulus of 2.85 ±0.18 GPa was found. Literature values of 3-4 GPa were found for fibers specifically, showing success in our composites. Table 43 contains all experimental results compared to values found in literature.

Table 43: Compiled experimental and literature values (* denotes fiber values)

	E_1 (GPa)	ν_{12}	E_2 (GPa)	G_{12} (GPa)	ν_{23}
Experimental	229 ±12	0.28 ±0.03	5.83 ±0.87	2.85 ±0.18	0.52 ±0.08
Literature	220	0.31	5.58	3-4*	N/A

G_{12} requires further validation because reliable composite values could not be found in literature. From MatWeb, Thornell P-55 pitch based CF reinforced composites have a shear strength of 55 GPa, which strongly agrees with the experimental data. It should also be noted that some rotated ±45° specimens were cut to demonstrate the quality and consistency of the plate. The rotated specimens were found to have a higher shear strength than the non-rotated specimens. These specimens were also shorter than the non-rotated specimens, meaning the likelihood of preexisting defects is decreased, which is manifested as larger strengths. The two orientations did not demonstrate any significant difference in shear modulus, showing the consistency and quality of the test. Table 44 shows the measured shear modulus for all ±45° specimens.

Table 44: Shear modulus results for 2 different orientations of ±45° specimens, all from the same initial composite plate

Specimen	**1**	**2**	**3**	**4**	**5**	**6**	**1R**	**2R**	**3R**	**4R**
G_{12} (GPa)	3.27	2.34	3.13	2.88	2.70	2.70	2.80	2.61	2.71	3.32

The next, and final, step in the verification process is to characterize the epoxy matrix. As mentioned earlier, Epikote RIMR 135 is being used for the composite matrix. Epikote publishes the material properties of their epoxy systems, however, the resin systems used are past the recommended use date, requiring characterization. Compared to the other components of this process, characterizing the matrix is relatively simple. ASTM D638 will be used to characterize the isotropic resin. Once the matrix has been characterized, the FEA model will be able to be tested for the composite system used and can be verified and troubleshot.

Shear property methodology for testing tow-level epoxy composites were also investigated. ASTM D5379 was used to manufacture v-notched beams, or Iosipescu beams, of varied orientations to experimentally derive shear properties from test specimens. Digital image correlation (DIC) and a beam test figure were used to derive specimen stress and strain, which are plotted in Figure 164 and Figure 165.

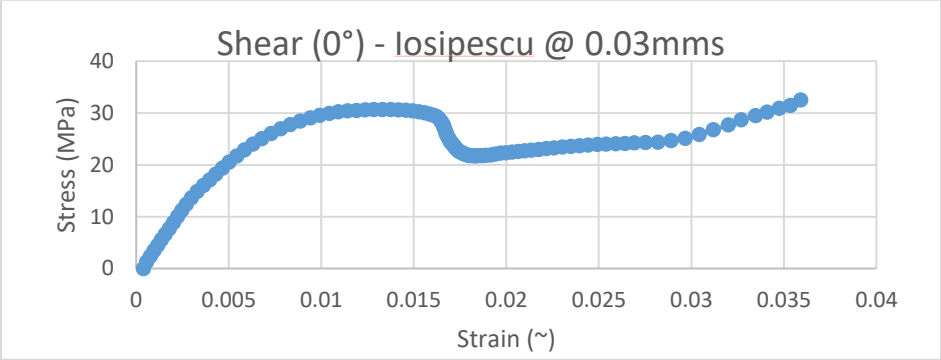

Figure 164: Stress vs strain data for a single 0° Iosipescu specimen loaded to failure.

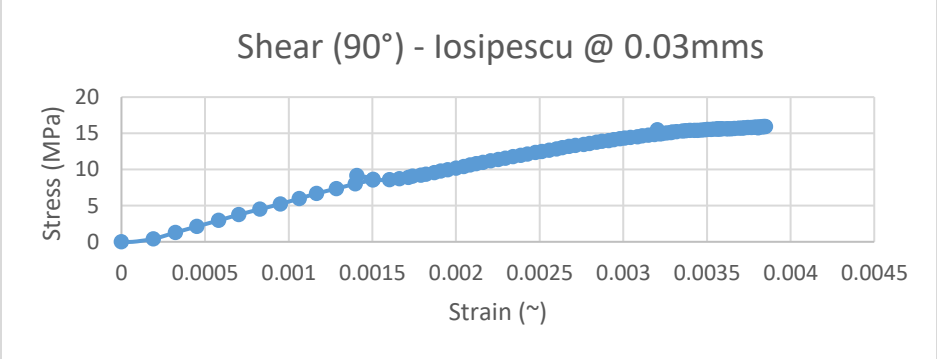

Figure 165: Stress vs strain data for a single 90° Iosipescu specimen loaded to failure.

These results were averaged over five tests, as per ASTM D5379 and are tabulated in Table 45. These values, along with those derived over the quarters from BP2, will be used to inform an FEA model to simulate the properties of a composite plate and confirm the validity of the suite of mechanical tests performed.

Table 45: Shear properties of Iosipescu specimens averaged over 5 tests.

Shear Strength	
Orientation	MPa
90°	9.94
0°	32.25

Strength Prediction Methodology

The focus of the modeling work in this quarter was stochastic transverse strength predictions for tow-level composites, but specifically the significance of the correct statistical descriptors vs. generic random models. In addition to obtaining the variation in transverse elastic moduli, strengths of an ensemble of microstructures under transverse biaxial loadings at different load ratios were also investigated in this work. Two different cases of biaxial failure stress envelopes were developed to demonstrate the variability in transverse strengths due to the presence of morphological variability in composite microstructures: (i) biaxial transverse tension (σ_{22} vs. σ_{33}) and (ii) transverse tension and transverse shear (σ_{22} vs. τ_{23}). It is worth mentioning here that these failure stress envelopes are very challenging to achieve experimentally. As stated previously, failure of the composite microstructures under transverse loading conditions were modeled using extended finite element modeling (XFEM) as implemented in the commercial finite element analysis (FEA) package ABAQUS to capture matrix fracture along with cohesive surfaces to capture fiber-matrix delamination. It should be noted that the current XFEM implementation in ABAQUS is suitable only for a limited number of non-interacting cracks (since an element cannot accommodate more than one crack), meaning cracks cannot coalesce. Moreover, within the crack domain (i.e., the enrichment region) a new crack can initiate only after all existing cracks have been completely separated. These limitations posed by the implementation of XFEM make it impossible to model matrix cracks that combine with each other; consequently, matrix fracture connecting interfacial failures and spanning across the entire composite microstructure meaning the ultimate failure could not be captured. A conservative approach of detecting the failure of the microstructure was adopted in this work where the first occurrence of a load drop ($f^{t+1} < f^{t}$) was determined to be the failure point of the microstructure.

In contrast to the traditional approach of reporting deterministic failure envelopes where only the average strength is reported, stochastic failure envelopes (SFEs) were utilized here as an effective means to incorporate reliability-based design. In SFEs, multiple failure loci/envelopes are reported such that each locus/envelope is associated with a particular level of reliability. In this study, SFEs were generated for the first quadrant of the 2D stress-space, since XFEM cannot be used to predict cracks under compressive loading. In addition to the stochastic failure

surfaces, the micromechanical failure mechanisms – failure initiation and propagation in the synthetic microstructures were also explored.

Stochastic failure envelopes under σ_{22} vs. σ_{33} loading

For this case, composite microstructures were loaded under biaxial tensile displacements in the transverse to fiber directions. Different ratios of biaxial displacements were applied on the microstructures, which can be expressed using the following definition of the angle between the applied displacements

$$\theta = \tan^{-1}\left(\frac{\delta_{33}}{\delta_{22}}\right) \tag{1}$$

This definition of the biaxial displacement ratio, or as we are calling it here, the biaxial load ratio is portrayed in Figure 167. Seven biaxial load ratios were used to generate the stochastic failure envelopes, with a minimum of 10 data points at each ratio level to quantify the variability in strength. These load ratios are as follows: $\theta = 0^\circ$ ($0/1$ ratio, uniaxial tension in the 2-direction), $\theta = 15^\circ$ ($0.2679/1$ ratio), $\theta = 30^\circ$ ($1/\sqrt{3}$ ratio) , $\theta = 45^\circ$ ($1/1$ ratio), $\theta = 60^\circ$ ($\sqrt{3}/1$ ratio), $\theta = 75^\circ$ ($3.7321/1$ ratio), $\theta = 90^\circ$ ($1/0$ ratio, uniaxial tension in the 3-direction). The UVE microstructures were loaded at both directions simultaneously by the appropriate ratio, since it has been showed in literature that loading path does not affect the failure envelope of a composite microstructure (Sun, et al., 2019).

The stochastic failure contours of the statistically equivalent microstructures were represented with three different levels of reliability and are presented in Figure 168. Since the failure

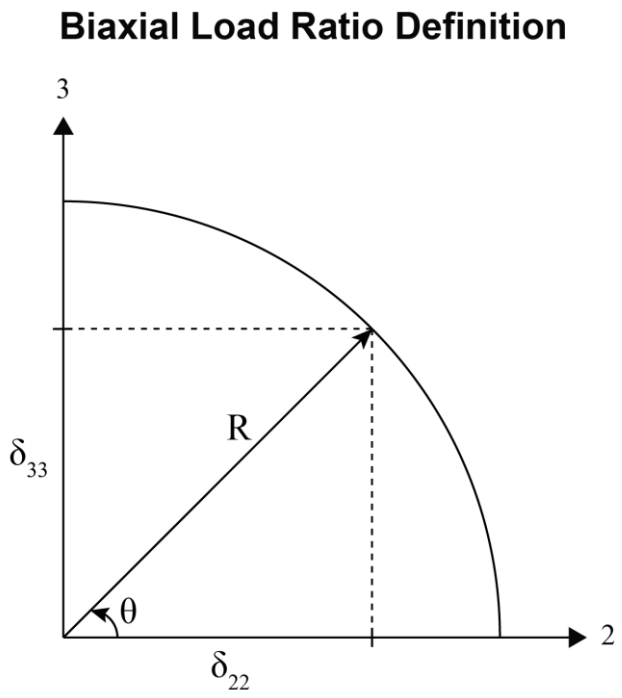

Figure 166: Definition of biaxial load ratio applied on the microstructures.

envelope is expected to be symmetric for the σ_{22} vs. σ_{33} loading scenario about the $\theta = 45^{\circ}$ axis, only four load ratio cases were required to be performed, namely $\theta = 0^{\circ}$, $\theta = 15^{\circ}$, $\theta = 30^{\circ}$, and $\theta = 45^{\circ}$. As it can be observed from the figure, the failure envelope shrinks as the reliability level increases. The 90% reliability locus is associated with the 10^{th} percentile of strength and is the most conservative one, while the 10% reliability contour is associated with the 90^{th} percentile of strength and the least conservative one. The stochastic average locus reports the mean value of the strength observed in the ensemble of microstructures, similar to the locus reported in a deterministic failure surface. From these reported failure surfaces, a small interaction between the two transverse tensile failure modes can be observed which causes the failure strengths to increase slightly. In the absence of experimental data, the predicted failure envelope was compared with computational data from the literature. A qualitatively similar failure envelope was reported by Zhang and Yan using a computational micromechanics-based modeling approach (Zhang & Yan, 2015).

It is also evident from the figure that there exists a significant amount of scattering in the strength data, with the COV ranging from 3.54% to 5.61%. This scatter for each load ratio level is reported in Table 46. The variation in strength is in complete contrast to the variation observed in the elastic properties of the composite. Moreover, the variation in strength is different for different load ratios, indicating the practice of using a single load safety factor for all load cases

is rather a conservative one. The variability in the strength observed in the SFEs of Figure 168 and quantified in Table 46 is a direct consequence of the variability existing in the morphology of the composite microstructures. The failure initiation spots and propagation paths are different for different microstructures, which is depicted graphically in Figure 169 (a)-(d) for microstructures loaded in uniaxial transverse tension. Four instances of failure are provided in this figure, each of them containing cracks propagating normal to the loading direction and at different locations to each other. It can be noticed from the figure that for all microstructures failure initiates where fibers are at close proximity to each other, creating regions of stress concentration. For this biaxial loading scenario, interfacial debonding is the initial mode of failure. These fiber-matrix debonds nucleate at the stress concentration regions and eventually a matrix crack appears and connects these interfacial debond regions, causing failure of the microstructure. However, due to the conservative failure definition adopted here, the complete evolution of the matrix cracks was not captured. The opening of the cracks presented in Figure 169 corresponds to the strain level at which load drop was detected, i.e., failure point of the microstructure. In Figure 170, failure plots of the same microstructure under different load ratios are presented. From this figure it can be observed that failure initiates at the same location of fiber cluster for all load ratios, however, the evolution path is different for different values of θ.

Table 46: Scatter of strength for biaxial transverse tensile loading at 4 load ratio levels.

θ	Number of samples	Mean value of the L2-norm of strength samples, $R_{samples} = \sqrt{S_{22}^{\ 2} + S_{33}^{\ 2}}$	COV (%)	Hexpack strength L2-norm at 0.45 FVF $R_{hexpack} = \sqrt{S_{22}^{\ 2} + S_{33}^{\ 2}}$	δ between $R_{hexpack}$ and $R_{samples}$ (%)
0°	10	55.35	3.54	72.46	23.61
15°	10	67.90	3.28	82.66	17.86
30°	10	79.35	3.88	91.76	13.52
45°	10	90.29	5.61	113.70	20.59

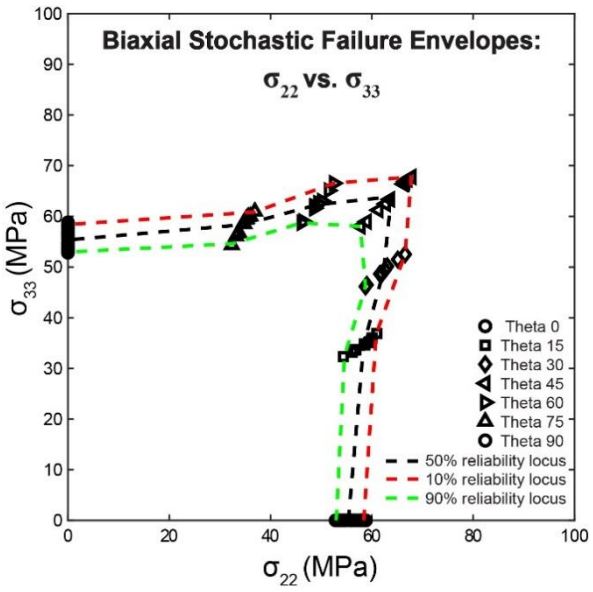

Figure 167: σ_{22} vs. σ_{33} **stochastic failure envelopes showing the variability in strengths due to morphological variation of the UVE microstructures.**

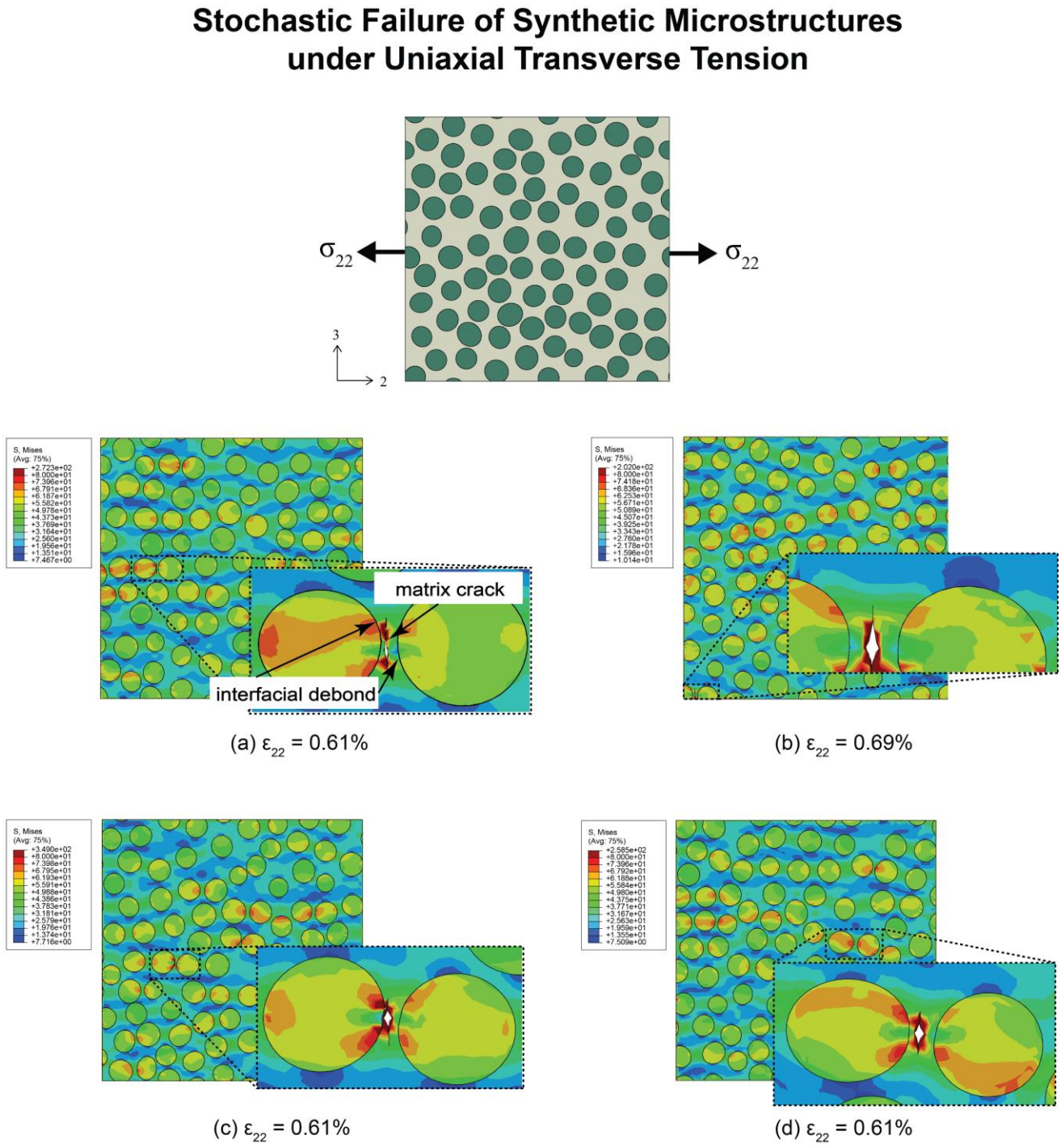

Figure 168: Finite element models with morphology-based meshing depicting interfacial debonds and matrix cracks initiating at fiber clusters and propagating perpendicular to the applied transverse tensile load are presented in sub-figures (a)-(d).

Stochastic Failure of a Synthetic Microstructure under Different Ratios of Biaxial Transverse Tension

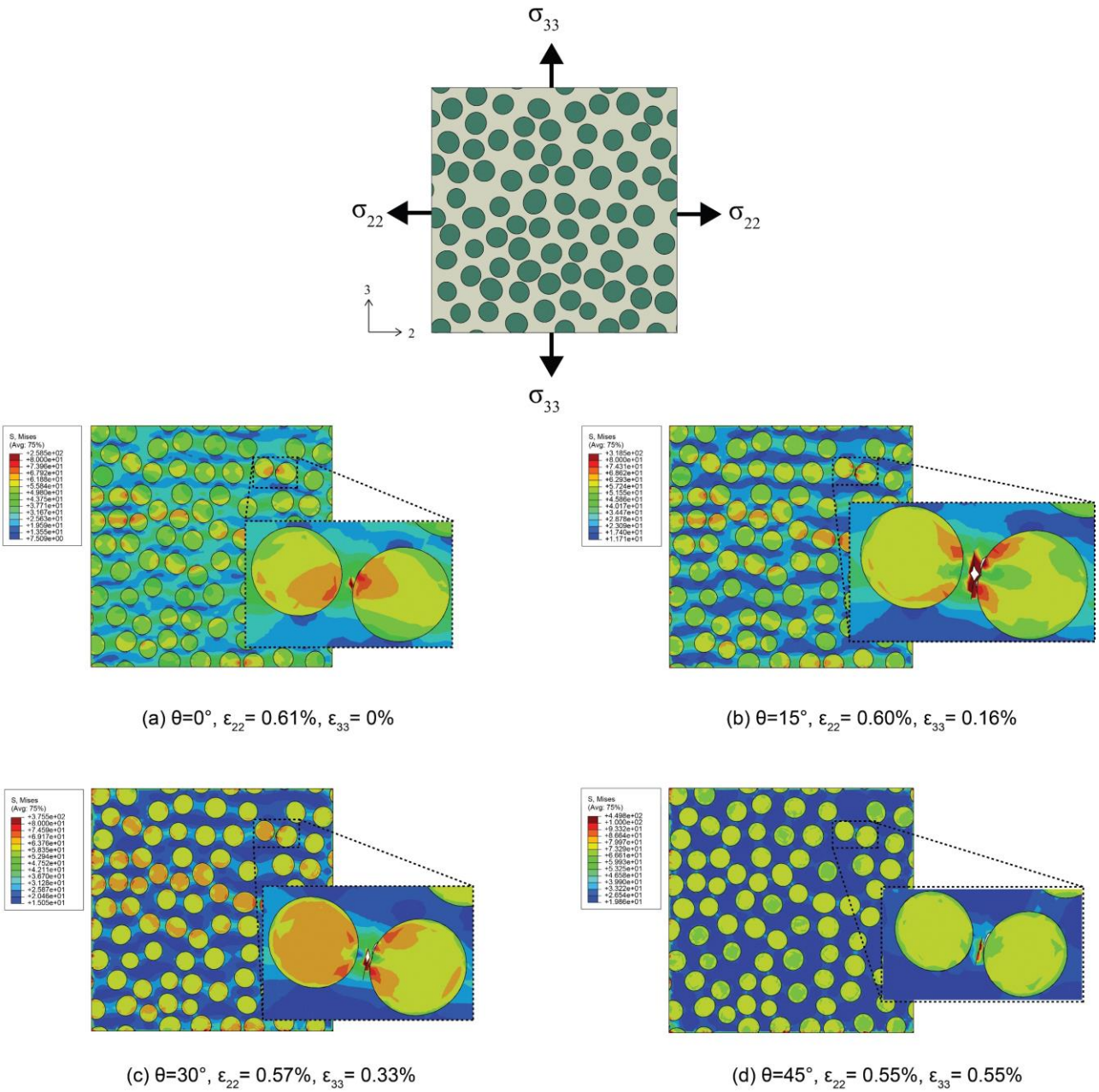

(a) θ=0°, ε_{22}= 0.61%, ε_{33}= 0%

(b) θ=15°, ε_{22}= 0.60%, ε_{33}= 0.16%

(c) θ=30°, ε_{22}= 0.57%, ε_{33}= 0.33%

(d) θ=45°, ε_{22}= 0.55%, ε_{33}= 0.55%

Figure 169: Failure initiation and evolution for the same synthetic microstructure, under different ratios of biaxial transverse tensile loading. For the tested microstructure, finite element model with morphology-based meshing depicting interfacial debonds and matrix cracks are presented in sub-figures (a)-(d).

The strengths of Hexpack models under transverse biaxial tension are also reported in Table 46. By comparing the strengths of the Hexpack model to the average strength values measured from the synthetic microstructures, it can be concluded that the idealized packing model provides a much higher estimation of strength than the average strength of the random microstructures at all load ratio levels. Failure of the hexagonal packing microstructure model under transverse uniaxial tension ($\theta = 0^{\circ}$) is presented in Figure 172. This figure provides a visual demonstration of why the idealized microstructure provides higher strength than the average synthetic microstructure – the regular distribution of fibers prevents the formation of the stress concentration regions as observed in the synthetic microstructures. As a result, the Hexpack model fails to provide good estimation of the average strength of the synthetic microstructures. Moreover, no insight on the variability of strength could be gathered from the analysis of such idealized packing of composites. The above discussion indicates that even though idealized packing models are reliable for predicting average elastic moduli, they cannot be used for predicting the average values of strengths.

The distribution function for the transverse tensile strength S_{22}^{T} gathered from the stochastic microstructure analysis is presented in Figure 171. Failure of 25 statistically equivalent microstructures was used to gather this distribution. Five widely used distributions were tested

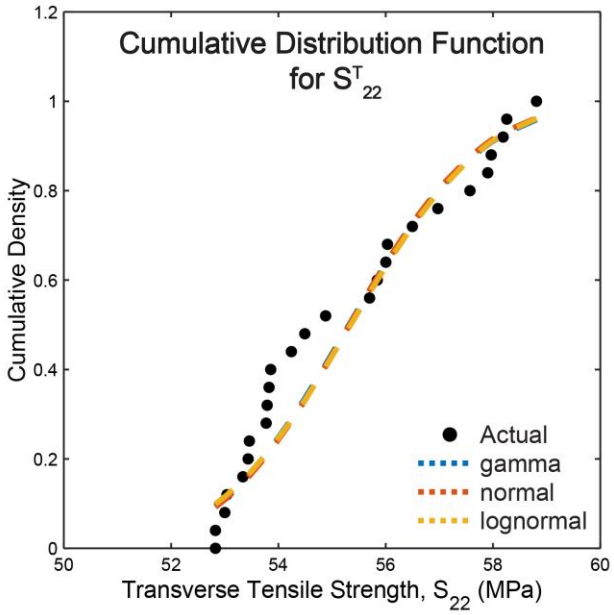

Figure 170: Cumulative distribution of transverse tensile strength, for 25 realizations of synthetic microstructures.

for providing a best fit to the uniaxial strength data. It can be observed from the figure that the normal distribution fits the strength data well, with parameters $\mu = 55.49$, $\sigma = 2.07$.

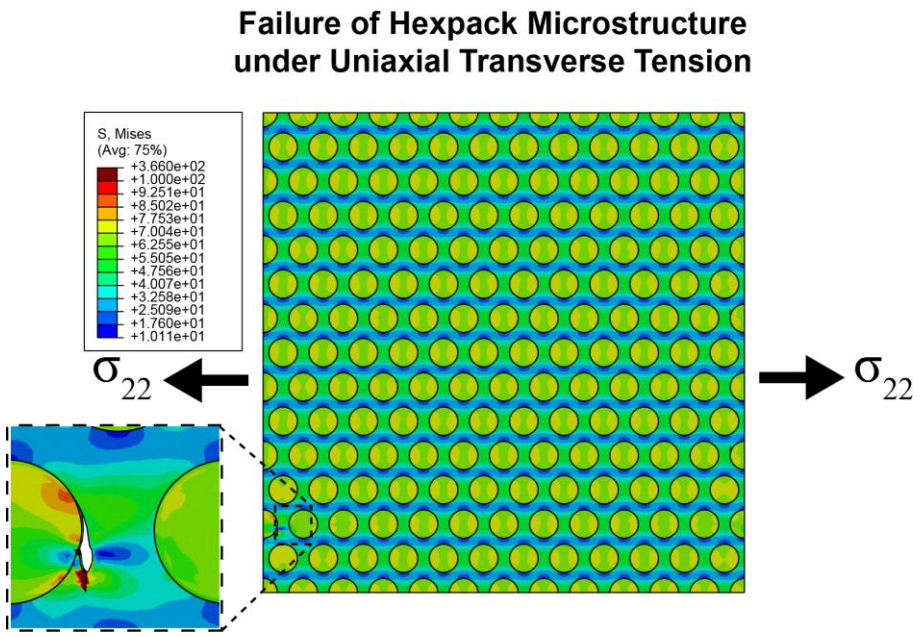

Figure 171: Failure of the hexagonal packing microstructure under uniaxial transverse tension. The regular packing of this microstructures prevents the formation of stress concentration zones as seen in the synthetic microstructures, thereby increasing the predicted strength of the hexpack microstructure.

The scatter of the transverse tensile and transverse shear strengths quantified from the stochastic analysis of synthetic microstructures were compared with experimental data from (Jensen, 2014) in Table 47. It can be observed that the COV values predicted from modeling are conservative compared to the experimental observations, albeit close. This originates from the >3% variability present in the fiber volume fraction of the experimental coupons, as well as the conservative failure definition used in this work.

Table 47: Comparison between experimental and modeling-based scatter of strengths.

	Experimental (FVF = 0.59)			Simulation (FVF = 0.45)		
	Average	**Std Dev**	**COV(%)**	**Average**	**Std Dev**	**COV (%)**
S_{22}^{T}	45.1	2.56	5.7	55.35	2.07	3.54
S_{12}	57.2	3.87	6.8	79.24	4.74	5.98

To measure the significance of matching the statistics of synthetic microstructure with actual microstructure, an analysis was performed with randomly seeded microstructures with no reorganization. The predicted statistics of the transverse tensile strength from the random microstructures were compared with their statistically equivalent counterparts in Table 49. It can be observed from the table that the mean value of strength predicted from the random microstructures are higher (about 7%), as well as the predicted scatter. This indicates that

matching the statistics of the synthetic microstructures is important to determine the accurate mean and scatter of real microstructures due to morphological variation, however, a random microstructure generating algorithm can come up with a good estimation of it.

Table 48: Scatter of strength for biaxial transverse tensile loading (S^T_{22}) for statistically equivalent and randomly seeded microstructures at 0.45 fiber volume fraction.

	Number of samples	Mean value of strength, S^T_{22}	COV (%)
Statistically equivalent microstructures	25	55.49	3.73
Randomly seeded microstructures	10	59.74	5.01

Creep Testing

Creep testing has also begun on composite specimens. This has been accomplished by utilizing (ASTMD7337, 2019), and fixtures used for 0° tensile tests. A servo-hydraulic load frame, operated in force control was used to stress samples as a constant force over 24 hours while strain data was captured using DIC. Creep was initially performed at a low force ratio on our composites to ensure repeatability within our test setup. Once confident, testing at higher force ratios were performed. The self-tightening grips used to perform creep tests needed to be adjusted to prevent application of torsional forces, which caused premature fracture of samples. Once adjusted however, creep tests, were successfully run at varied force ratios. Results from one such test is shown in Figure 172.

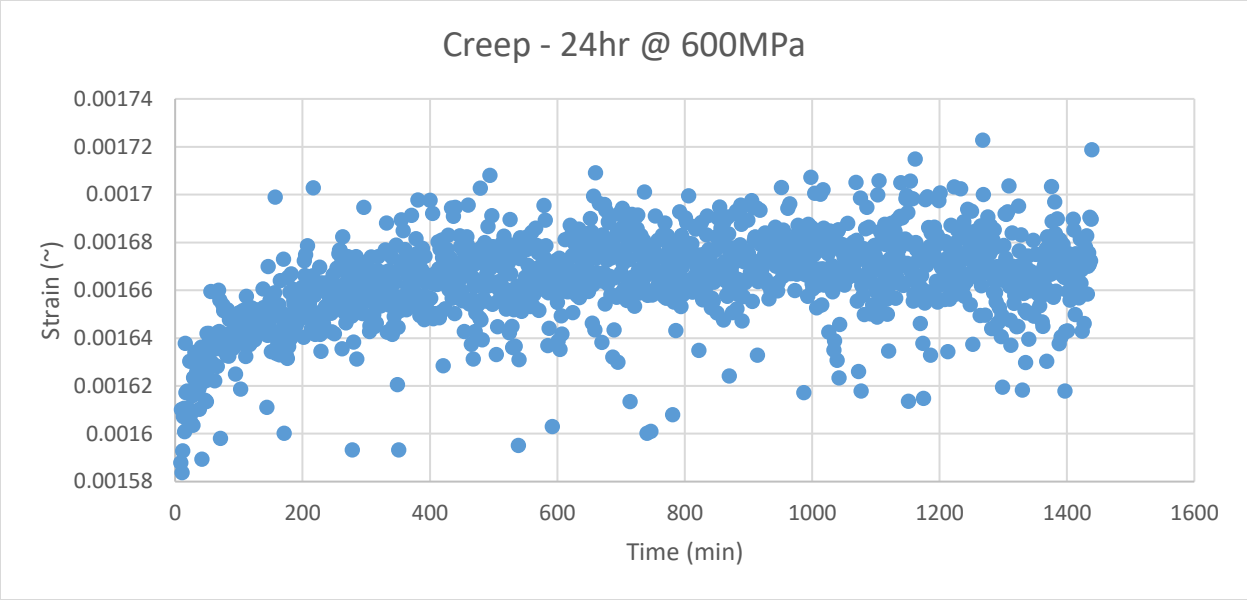

Figure 172: Creep test performed at 60% force ratio over 24 hours.

This process will be repeated for higher force ratios to generate a creep rupture trend line, as per ASTM D7337.

Unsized tows of bioPAN CF have been received from ORNL and are currently undergoing the full suite of mechanical tests laid forth in the test methodology developed over the last year. The properties derived from that testing will be used to inform an FEA model as well as compare directly to single fiber properties provided us with the bioPAN fibers.

Literature shows that CF is, at ambient conditions, resistant to creep rupture failure. Which suggests that 0° specimens would be unlikely to show creep. However, in specimens of different fiber orientations, creep can be observed in the epoxy matrix because, unlike CF, it will exhibit some level of viscoelasticity which could impact composite performance. Therefore, as an initial test, a 45° unidirectional hand-layup composite tested under a constant load, evaluated at 85% force ratio, was performed. The force ratio was determined by calculating the experimental failure stress of a composite with this geometry, shown in Figure 173, and then employing a servo-hydraulic load frame to submit the specimen to the maximum stress beneath that calculated threshold at which the instrument could maintain a stable force.

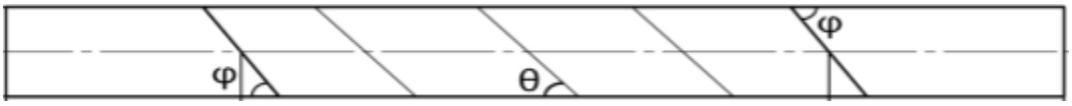

Figure 173: Representation of creep tensile specimen with Θ = 45° and Φ = 54°

As predicted, and as can be seen in Figure 174, even at ambient temperatures, well below the glass transition of the epoxy, the composite exhibited deformation over time. This test, performed over 24 hours, did not result in fracture, but extrapolating this data could indicate possible fracture over extended loading conditions. This was expected, as the orientation of the

fibers resulted in more of the load being borne by the epoxy matrix, which is prone to deformation under high load, and is representative of the stable increase in strain shown below.

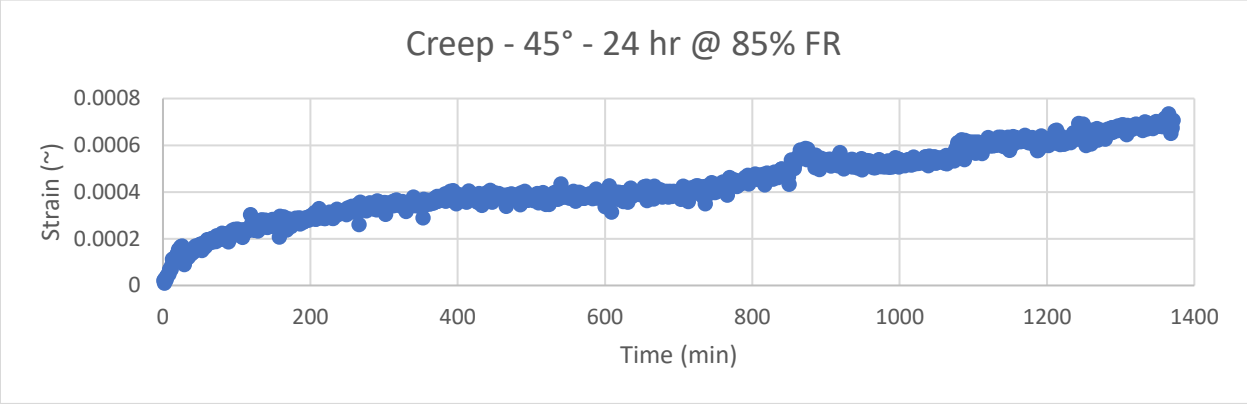

Figure 174: Creep test performed on a 45° specimen at 85% force ratio, or 10 MPa.

Creep tests were also performed on 0° unidirectional tensile specimens. The same setup as used in 45° tests was employed, except at force ratios of roughly 35%, 75% and 97% to observe behavior at various loads. These results can be seen in Figure 175, Figure 176 and Figure 177, respectively. The creep curves for each of these tests were similar, and no failures were observed even at 97% of the ultimate tensile strength. These results are reflective of typical creep testing, showing an exponential decay of strain as a function of time, such that samples are unlikely to fail at these loads over the lifetime of the composite. Further tests of these composites would need to be done at higher temperatures to evaluate long-term performance in various applications.

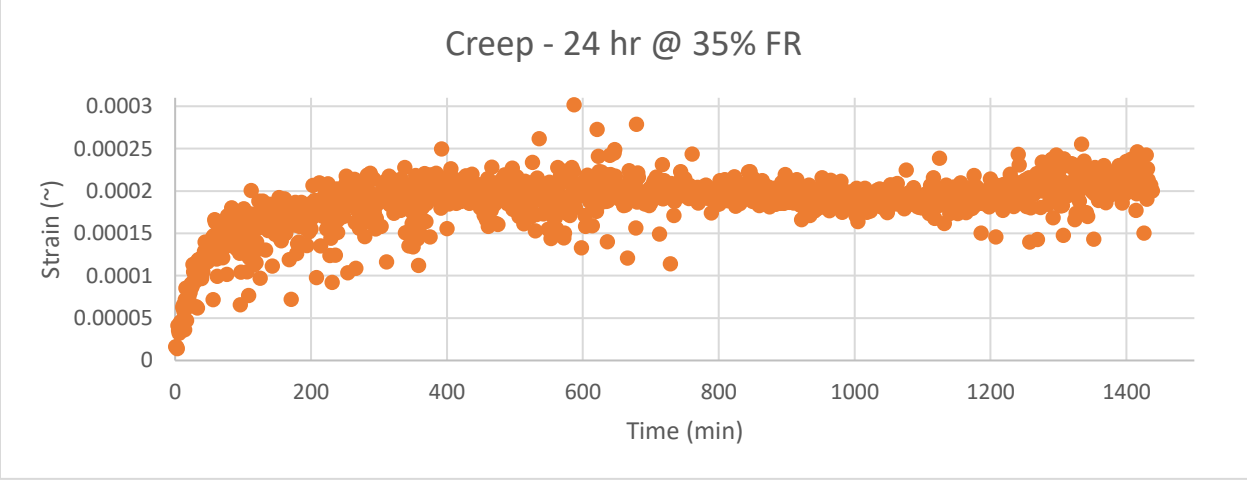

Figure 175: Stress-strain data from creep test performed on a 0° specimen at 35% force ratio, or 300 MPa.

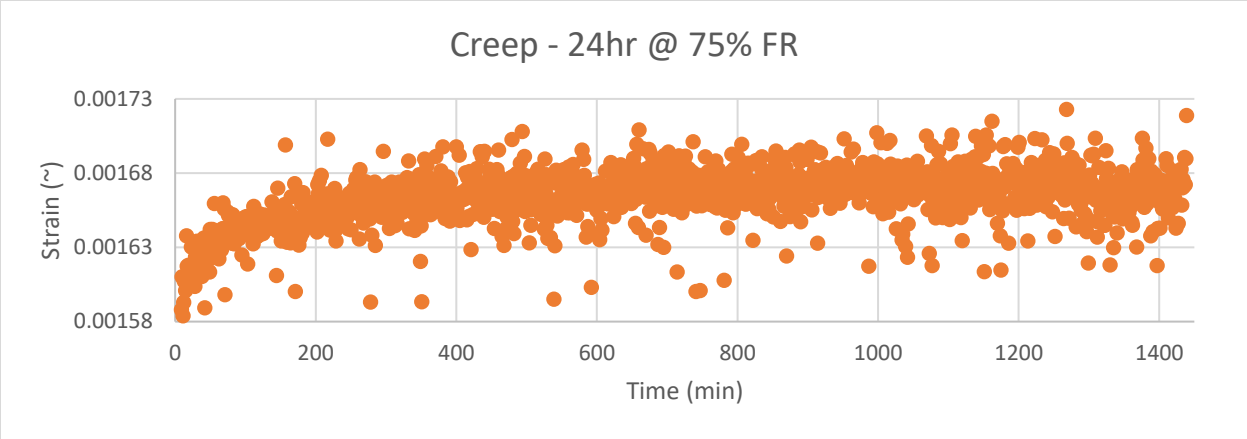

Figure 176: Stress-strain data from creep test performed on a 0° specimen at 75% force ratio, or 600 MPa.

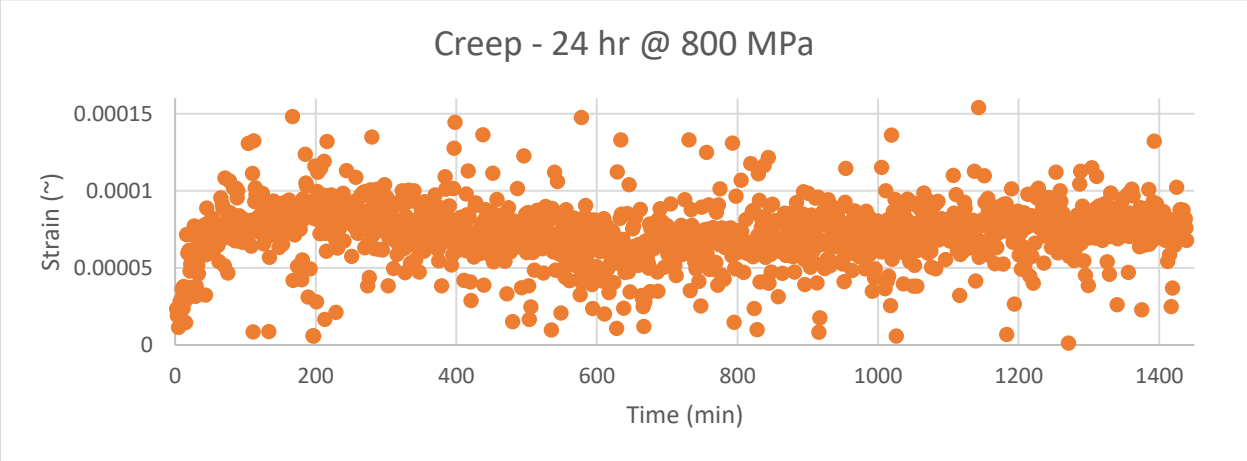

Figure 177: Stress-strain data from creep test performed on a 0° specimen at 97% force ratio, or 800 MPa.

Model Validation and Optimization for Carbon Fiber Elastic Properties

The bioPAN fibers manufactured at ORNL were subjected to the full suite of mechanical tests laid forth in the developed test methodology developed. The properties of these CF were provided, and the E_{11} modulus was compared to single fiber tests performed by ORNL to confirm our test methodology; this was also done for the pitch-based fibers that were used for trial testing. The results, which can be seen below in Table 49, showed that the composite layup testing methodology discussed above, were in accordance with single fiber testing performed at ORNL, confirming the composite testing method.

Creep tests are still yet to be performed on PAN fibers provided by ORNL. As of current, more bioPAN fibers need to be manufactured and shipped to UW before such testing can take place, at which point performance of those fibers can be compared to the surrogate fibers tested recently.

Table 49: Various properties of carbon fibers tested at UW with the composites method and at Oak Ridge National Labs using a single fiber test method.

Sample	E (Msi)	d (µm)	σ (ksi)	E (Msi)	ε
	UW	**Oak Ridge**			
Thornell P-55	60 ± 0.8	10.03±0.47	306.8 ± 64.3	57.5 ± 8.7	0.61 ± 0.10
Tonen (No-Sizing)	91.5 ± 5.2	9.62±0.42	325.0 ± 136.8	92.7 ± 5.9	0.41 ± 0.15
Tonen (AR)		9.61±0.30	430.8 ± 69.3	90.1 ± 5.5	0.55 ± 0.08

In order to obtain optimized properties of the experimentally tested composite materials and their respective fiber and matrix constituents, a hexpack model is utilized. A hexpack model is an idealized hexagonal packing of fiber reinforcement in a matrix material as shown in the Figure 178a. Using this approach, we can create a repetitive volume element as shown in Figure 178b, to which periodic boundary conditions are applied. This analysis is performed using a MicroMechanics plug-in in Abaqus – a commercial finite element package. In order to begin with the optimization, a material manager application from Autodesk is utilized. This application performs a preliminary optimization of the elastic constants calculated from the experiments. However, this optimization is only performed with respect to composite properties, as a result, optimized fiber and matrix properties are often largely different from the experimental values. In order to overcome this hurdle, we manually optimize composite as well as fiber and matrix properties.

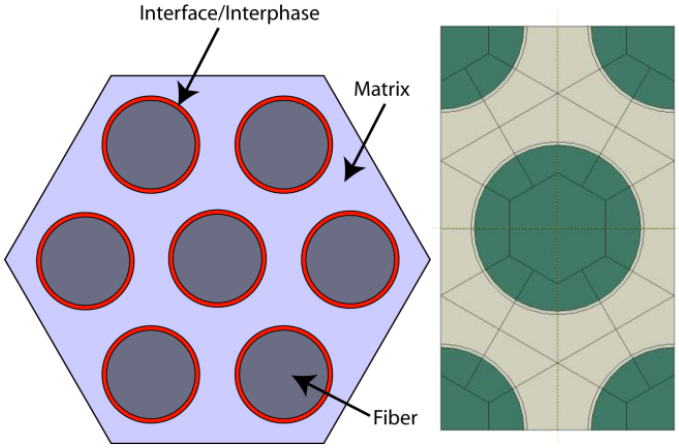

Figure 178: (a) Schematic of hexagonal packing; (b) Representative volume element for hexagonal packing.

(a) (b)

In order to manually optimize the material properties, it is crucial to understand the effect of fiber and matrix elastic constants on homogenized composite elastic constants. In general, we observed a few trends that would help us guide through the optimization process.

- Sensitivity of composite G_{12} to fiber G_{12} is very small è increasing fiber G_{12} to very high value results in very small increase in composite G_{12}
- Contrary to the previous trend, increasing matrix modulus substantially increases composite G_{12}
- Increasing the transverse fiber moduli E_{22} and E_{33} increases composite E_{22} and E_{33}
- Effect of the rest of elastic constants is negligible on the composite properties

Table 50-Table 58 represent a self-consistent set of material properties based on a hexagonal fiber packing for the three different tow-level composites that were fabricated. Table 50-Table 50 represent tow-level composite, fiber, and matrix properties, respectively, predicted by the finite element model for the Tonen fiber tow-level composite. Table 53-Table 55 represent tow-level composite, fiber, and matrix properties, respectively, predicted by the finite element model for the Thornell P-55 fiber tow-level composite. Table 56-Table 58 represent tow-level composite, fiber, and matrix properties, respectively, predicted by the finite element model for the 1K Bio-PAN CF tow-level composite.

Table 50: Tonen carbon optimized composite properties.

E11 (MPa)	E22 (MPa)	G12 (MPa)	v12	v23
3.101e5	4218	4575	0.281	0.511

Table 51: Tonen carbon fiber optimized properties.

E11 (MPa)	E22 (MPa)	G12 (MPa)	v12	v23
6.062e5	3232	2.095e4	0.2	0.499

Table 52: Matrix optimized properties for Tonen carbon composite.

E (MPa)	v
4954	0.35

Table 53: Thornell P-55 carbon optimized composite properties.

E11 (MPa)	E22 (MPa)	G12 (MPa)	v12	v23

2.175e5	5894	2808	0.301	0.514

Table 54: Thornell P-55 carbon fiber optimized composite properties.

E11 (MPa)	E22 (MPa)	G12 (MPa)	v12	v23
4.177e5	1.105e4	2.061e4	0.217	0.295

Table 55: Matrix optimized properties for Thornell P-55 carbon fiber composite.

E (MPa)	v
2820	0.397

Table 56: 1K Tow BioPAN carbon optimized composite properties.

E11 (MPa)	E22 (MPa)	G12 (MPa)	v12	v23
8.03E4	3062.6	3032.4	0.314	0.402

Table 57: 1K Tow BioPAN carbon fiber optimized properties.

E11 (MPa)	E22 (MPa)	G12 (MPa)	v12	v23
1.71E5	2.57E3	8E4	0.259	0.259

Table 58: Matrix optimized properties for 1K Tow BioPAN carbon fiber composite.

E (MPa)	v
3128	0.38

Ideally, a unidirectional composite material is visualized a hexagonally packed fibers as shown in Figure 178. However, real microstructures when observed under a microscope, exhibit an irregular hexagonal packing with other microstructure defects such as resin seams, voids etc. (Figure 179). Hence, in order to accurately predict material properties of composite materials, a microstructure that exhibits such variability needs to be utilized. In this study, we have utilized methods developed by (Sanei, Barsotti, Leonhardt, & Fertig, 2017) to generate random

microstructures with normal distribution. These microstructres are periodic as shown in Figure 180. Here the generated microstructures are pixel based.

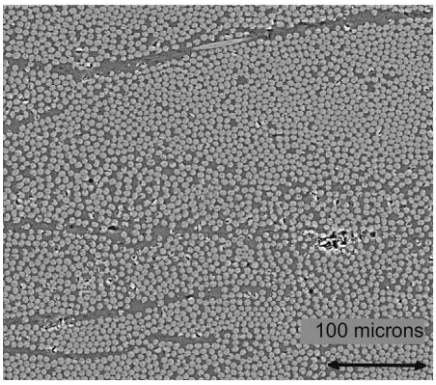

Figure 179: Microstructure as observed under microscope. Sanei et. al. 2017.

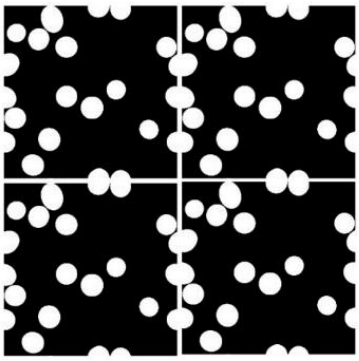

Figure 180: Showcasing periodicity in the generated random microstructure.[1]

These microstructures are then applied strain based periodic boundary conditions using micromechanics plugin in Abaqus. Six different load cases are applied to calculate homogenized composite properties. In this study, the optimized fiber and matrix properties are used as input to the 50 random microstructures for each composite. Average and standard deviation for each composite material is calculated which is plotted in Figure 181-Figure 184 and shown in Table 60-Table 62. Figure 181-Figure 184 also show corresponding elastic constants calculated from HexPack model. For a normal distribution, HexPack calculation should be a mean, which is not always the case in the current calculations. Hence, future study will need to simulate larger number of random microstructures to obtain a complete distribution of material properties.

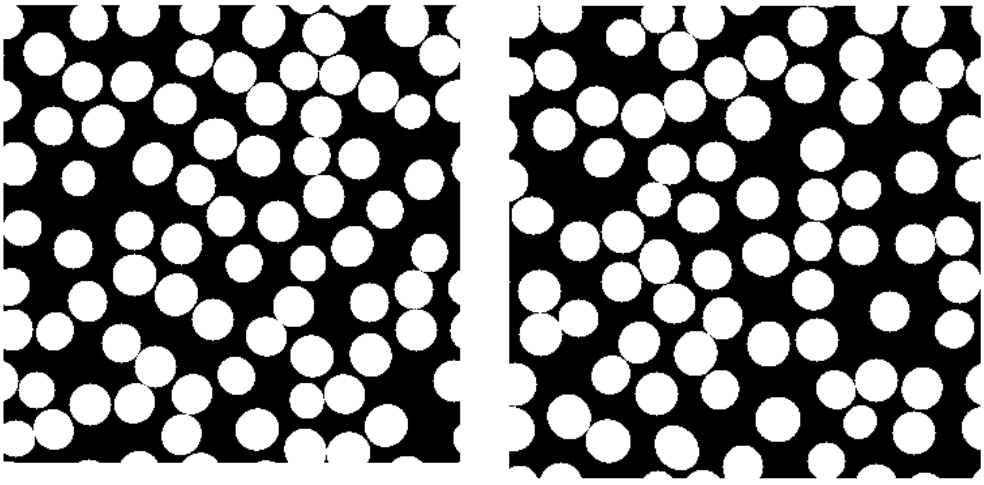

Figure 181: Examples of periodic Random Microstructure with normal distribution and fiber volume fraction of 0.46 corresponding to 1K Tow BioPAN carbon fiber composite.

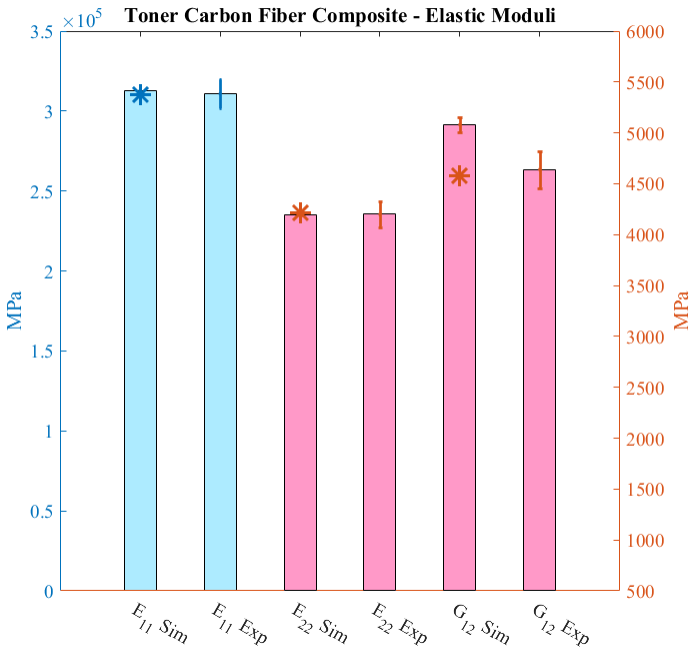

(a)

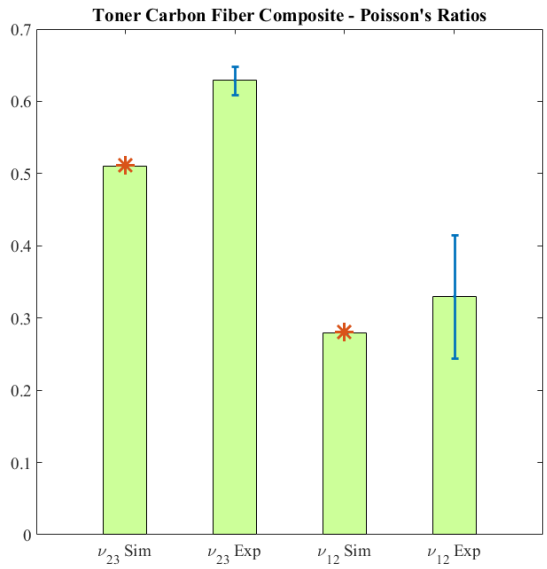

Figure 182: Tonen carbon fiber composite: Average and standard deviation of (a) Elastic modulus and (b) Poisson's ratios. Data marked by * are from Hexpack model.

(b)

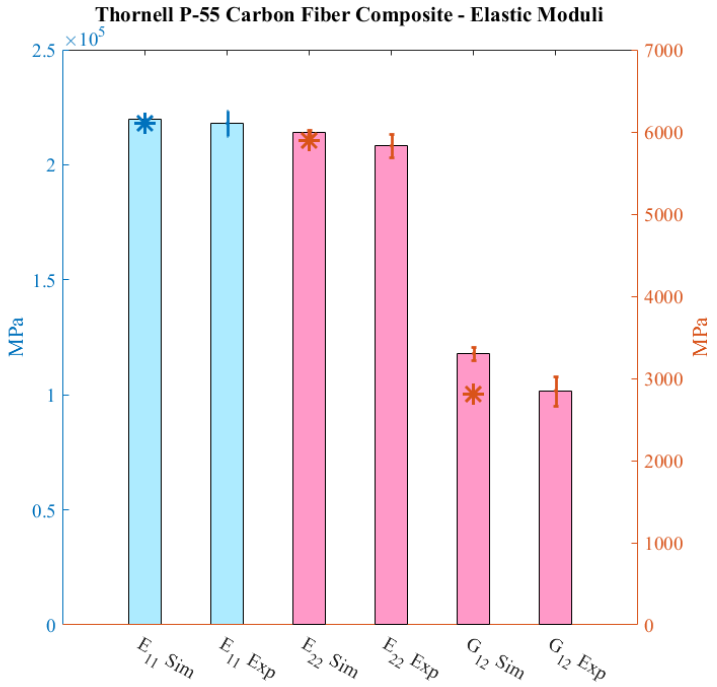

(a)

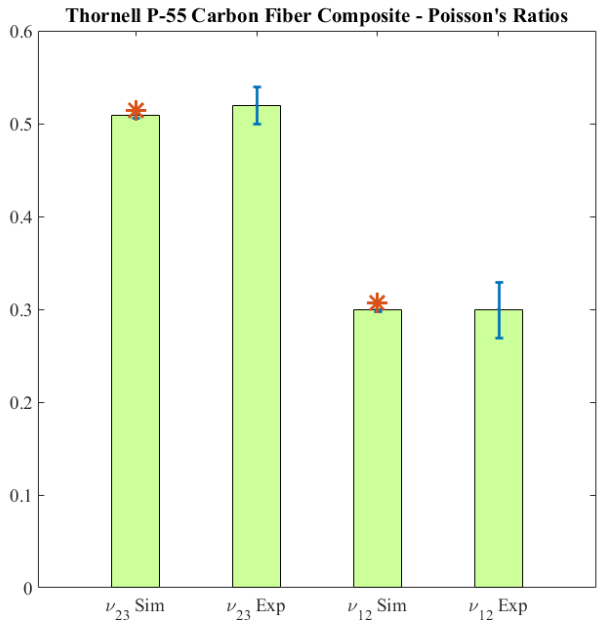

Figure 183: Thornell P-55 carbon fiber composite: Average and standard deviation of (a) Elasticmodulus and (b) Poisson's ratios. Data marked by * are from Hexpack model.

(b)

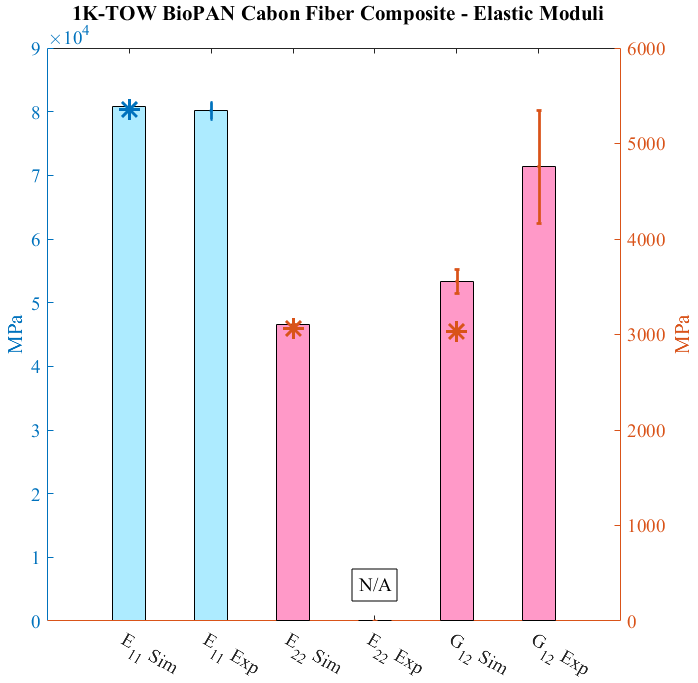

(a)

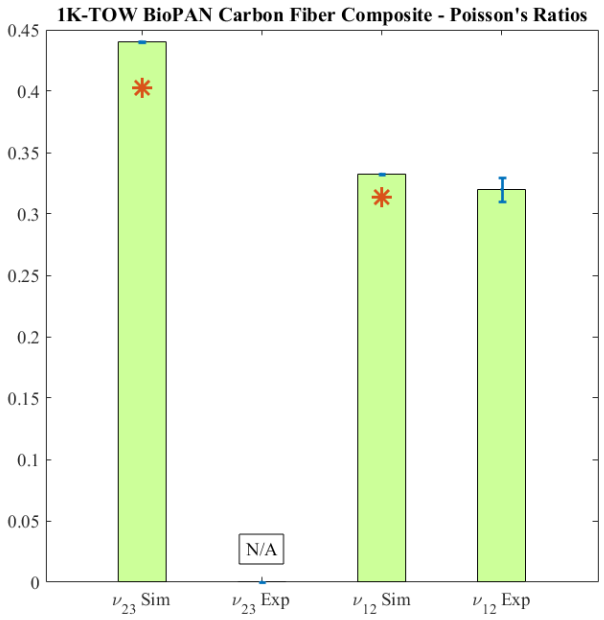

Figure 184: 1k Tow BioPAN carbon fiber composite: Average and standard deviation of (a) Elastic modulus and (b) Poisson's ratios. Data marked by * are from Hexpack model calculations.

(b)

Table 59: Tonen Carbon Composite: Elastic constants calculated from random microstructure generation.

E11 (MPa)	E22 (MPa)	G12 (MPa)	v12	v23
3.13E5±970.6	4198.5±5.6	5080±76.1	0.279±0.0004	0.51±0.0005

Table 60: Thornell Carbon Composite: Elastic constants calculated from random microstructure generation.

E11 (MPa)	E22 (MPa)	G12 (MPa)	v12	v23
2.19E5±685.36	5993.2±28.3	3303.1±81.5	0.299±0.001	0.509±0.002

Table 60: 1K Tow bioPAN Carbon Composite: Elastic constants calculated from random microstructure generation.

E11 (MPa)	E22 (MPa)	G12 (MPa)	v12	v23
8.08E4±289.5	3109.3±1.64	3556.7±125.8	0.3324±0.0002	0.44±0.0005

As shown in Table 60, that the matrix properties optimized for Tonen carbon is much higher than the experimental bulk properties. This is due to high value of composite G_{12} value. As noted in the optimization process, sensitivity of composite G_{12} is higher with respect to change in matrix moduli. Hence, in order to achieve, higher composite G_{12}, matrix moduli needed to be substantially high as well. Such big difference in the experimental matrix modulus and optimized modulus could be attributed to the fact that bulk matrix properties can be different than the matrix present in a composite, where the fiber-matrix interface could play a significant role.

In order to test this hypothesis, a hexpack model with an interface is generated in Abaqus. Interface properties are kept isotropic where modulus is much higher than bulk matrix modulus. As shown in Table 63, increasing interface modulus, results in increase in composite G12, while keeping the bulk matrix properties constant. This suggests that in some cases, modeling interface could be a necessary step. However, this analysis is not complete.

Table 61: Fiber, matrix and composite properties without (1st table) and with (2nd, 3rd tables) interface (units: MPa)

	E11	E22	E33	v12	v13	v23	G12	G13	G23
FIBER	6.06E+05	3232	3232	0.2	0.2	0.499	2.10E+04	2.10E+04	1078
MATRIX	3128			0.35					
COMP	3.11E+05	3387.424	3387.425	0.27518	0.27518	0.516834	**3109.526**	3109.526	1116.582
FIBER	6.06E+05	3232	3232	0.2	0.2	0.499	2.10E+04	2.10E+04	1078
MATRIX	3128			0.35					
INTERFACE	**8000**			0.35					
COMP	3.11E+05	3725.949	3725.95	0.27938	0.27938	0.514009	**3620.786**	3620.787	1230.463
FIBER	6.06E+05	3232	3232	0.2	0.2	0.499	2.10E+04	2.10E+04	1078
MATRIX	3128			0.35					
INTERFACE	**10000**			0.35					
COMP	3.11E+05	3813.706	3813.708	0.281098	0.281098	0.513861	**3701.639**	3701.64	1259.568

By using the optimization outlined above 1512 filament tows of bio-PAN of approximately 250 ft. of continuous fiber were evaluated. Due to the limited volume of fiber, composite samples were carefully manufactured to determine both the composite and single-fiber properties. With only a small volume, primary focus was given to manufacturing composites in 0° and ±45° orientations to obtain experimental values for E_{11} and G_{12}, respectively. Samples were prepared according to ASTM 3518M and ASTM 7205D.

Samples were loaded in tension to failure, using digital image correlation to monitor strain. Single-fiber properties were estimated using optical microscopy aided by a computer algorithm to estimate fiber fraction. Using stress-strain data, as well as fiber volume fraction, the estimated properties of a single fiber were directly compared to those initially derived by ORNL. Those results are tabulated in Table 62.

These results were in close accordance, with lower composite strength values due to suspected entanglement in the combined tow during manufacturing of tows at ORNL. This phenomenon is well documented in literature and can be confirmed with SEM.

To confirm the single-fiber properties derived at ORNL, single fiber tests were performed on a single bioPAN_4 fiber at the University of Wyoming. These average and standard deviation values are consistent with results provided by Oak Ridge.

Table 62: Single-fiber property of bio-PAN CF comparison between Oak Ridge and UW, using single fiber estimates and the composite method, respectively.

Fiber Property Comparison		
Test Method	Tensile Strength (ksi)	Strain (~)
Single Fiber Test (Oak Ridge)	328.9±54	.0111±0.0017
Composite Method (UW)	158.4±9.1	0.007±0.001
Single Fiber Test (UW)	250±27	0.01±0.001

A concern that arose in preliminary research suggested that poor fiber-matrix adhesion could impact experimental results since the bioPAN_4 was un-sized. To eliminate this concern, 90° tensile and compressive specimens were manufactured, see Figure 185, and tested to compare the value of E_{22} in both tests. Results for multiple bioPAN_4 and pitch-based fibers indicated no deviation in E_{22} suggesting that even the un-sized bioPAN_4 fibers were adequately adhering to the matrix in the composite manufacturing process.

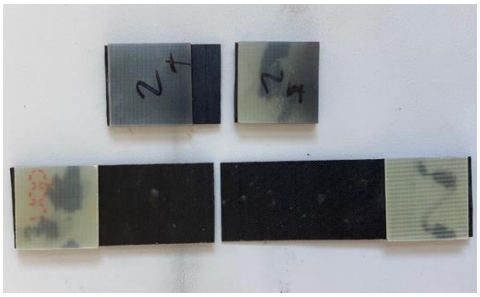

Figure 185: Compressive 90° specimen, (top) and, a tensile 90° specimen, (bottom). Dimensions are in accordance with ASTM D6641.

Initial creep tests were performed on a servo-hydraulic load frame. This method, however, introduces unnecessary noise that must be considered in post processing analyses. Furthermore, extended testing, greater than 24 hours, cannot be feasibly accomplished using a load frame.

Due to the difficulty of employing servo-hydraulic load frames for extended creep tests, an existing creep frame system at UW (Figure 186), combined with a DIC camera will be employed to observe creep at longer intervals. These tests will initially be performed on samples of 45° and 90° orientations. A diagram for this set up is shown in Figure 187.

Figure 186: Image of creep frame system

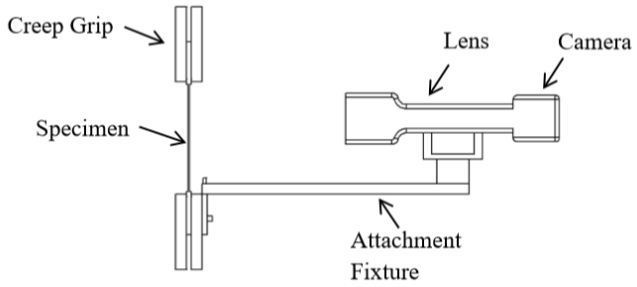

Figure 187: Schematic of creep specimen imaging setup adapted for creep frame.

Due to difficultly in melt-spinning pitch fibers, these pitch fibers were cut to approximately 10'' lengths and shipped in a bundle to the UW for testing. Figure 188 shows a photograph of CTP6M CF produced at ORNL.

Figure 188: ORNL pitch fiber sent to UW, (CTP6M SP315+).

Given the limited volume of fiber, approximately 1/3 previous shipments, composite testing was limited to 0° tensile tests. From these tests, peak tensile strain, strength and the E_{11} modulus were experimentally determined and compared to ORNL single fiber testing. Furthermore, given that un-sized pitch fibers are extremely fragile and subject to damage upon handling, single fiber tests were performed at UW to confirm that the samples were not damaged in transit. The results tabulated in Table 63 compare results of ORNL fiber tests, along with those performed at UW.

Table 63: Single-fiber property of CTP6M CF comparison between Oak Ridge and UW, using single fiber estimates and the composite method.

ORNL Pitch Fiber Property Comparison (CTPSP315+)				
Source	Diameter (µm)	Peak Strain (%)	Peak Strength (ksi)	Modulus (MSI)
ORNL	27.31±1.13	0.78±0.09	158.81±19.78	21.79±0.26
UW (single fiber)	27.2±0.2	0.58±0.01	188.1±12.3	21±3.5
UW (composite)	27.2±0.2	0.61±0.02	132±16.5	20.8±0.12

Results were in good accordance with ORNL values. Single fiber strengths were in agreement between UW and ORNL values, with lower composite strengths. The discrepancy between composite strengths and single-fiber strengths was to be expected, due to the lack of sizing on the fiber, and the required handling of fiber in composite manufacturing. The E_{11} modulus was in agreement across all tests, with very little variability in peak strains.

Due to the difficult nature of spinning green pitch, and the probability that future shipments may have lower overall fiber volume, we have developed a more resource-efficient approach to manufacturing composite coupons that will allow future shipments of pitch fiber from ORNL to be submitted to a broader suite of testing.

Carbon Fiber Strength to Weight Ratio Compared to Steel

In efforts to meet milestone requirements set forth for BP2, strength-to-weight (S-W) ratios for composites manufactured from bio-PAN fiber provided by ORNL were established. The S-W ratio of these composites were compared to LDV manufactuer steels.

The S-W ratio of composites using fiber provioded by ORNL were manufactured and submitted to tensile tests to establish an accurate tensile strength. Using this value, and the caluclated density of the composite, an S-W ratio was established. Using resources published in a report by Argonne National Laboratory investigating the material composition of US LDVs, the most common steels used in construction of US LDVs, by weight, the S-W ratio of these steels were be compared to our composites. The use of several high and low strength steels were included for further verification that the composites met the verification requirement.

As can be clearly seen in Table 64, the S-W ratio of the ORNL bio-PAN composite is between 6 and 10 times greater, or 600% to 1000% higher than the steels included above, which clearly exceeds the verification requirement. This result is to be expected, as many composites have much higher S-W ratios than steel. Furthermore, this result is consistent with S-W ratios of other carbon-epoxy composites that have been presented in contemporary literature.

Table 64: S-W, ratios of most commonly employed materials by LDV manufactures.

S-W of various LDV steels			
Material	Yield Strength (Mpa)	Density(g/cm3)	S-W (kNm/kg)
304 Stainless Steel	215	8	26.9
4340 Steel	710	7.83	90.7
1020 Steel	420	7.87	53.4
1040 Steel	415	7.845	52.9
1062 Steel	415	7.85	52.9
ORNL bio-PAN (composite)	540	1.14	474.8
Thornel P-55 (PP)	808	1.54	524.7
Tonen Corp (PP)	854	1.61	530.4
AS4 (PAN)	1028	1.44	713.9

Conclusions

Various feedstocks for CF production were investigated from coal, petroleum and biomass derived ACN. Other materials, such as gilsonite, showed promise as they could form isotropic general purpose CF, but these general purpose CF that were not able to meet DOE requirements. Significant improvements to gilsonite could be made by treating the material prior to spinning. Mesophase conversion of gilsonite was also attempted, but it was not easily controlled and would require a separate investigation. When working with isotropic pitch materials, it was discovered that isotropic HTCTP could produce CF that nearly met DOE targets. If high performance CF could be produced directly from isotropic pitch this could reduce the cost and energy input by circumventing the need to go through the mesophase production process. It is believed that isotropic HTCTP material could meet DOE targets with more control over the spinning and processing of the material. This was not further investigated primarily due to the long times initially needed for low temperature stabilization due to the low SP isotropic pitch. Low temperature continuous stabilization is not commercially implemented with current routine pitch based melt spinning production lines, without additional development. However, this result does call into question the importance of the mechanism of crystalline growth of pitch-based molecules to produce highly ordered molecules to produce high performance CF, and if it is necessary to move towards a more ordered mesophase. Obviously mesophase, due to its higher SP, is easier to process through melt spinning and stabilization and undergoes much less mass loss and fiber shrinkage during CF production.

PP and HTCTP were easily converted into mesophase PPM and CTPM, respectively, by standard methods, which was subsequently spun into CF that meet DOE targets. LTCTP did not form classical mesophase, which is likely due to a combination of increases aliphatic groups and the high oxygen heteroatom content. Bio-ACN was polymerized by traditional routes into bio-PAN which was spun into CF also easily meeting DOE targets. CTPM, PPM and bio-ACN materials were capable of being scaled up and the scaled up precursors were converted into tows that retained the material properties meeting DOE targets. When characterizing the tow-level

epoxy composites the strength was not retained due to defects in the materials upon shipping and while handling the material to produce the CF composites. Some of these issues may be helped the addition of sizing to the CF, however this was outside the scope of this project. By using a hexpack model with FEA it was easy to model and predict CF elastic properties within ±15%. This was developed using commercial pitch and PAN based CF and was validated using CTP and bio-PAN CF produced in this study. In this study, the modeling of the tow-level CF properties were generically referred to as macro-modeling.

A major focus of this study was to determine the best way to predict CF properties form the molecule feedstocks. In this study, this was generically defined as micro-modeling, although in reality it really starts at the nano-level and ends at the micro-level. The developed models were capable of predicting single fiber CF properties within ±15%. For the micro-modeling several methods were investigated and it was determined that GCMD was most fitting for the large repeating ACN units that comprise bio-PAN. After refining the assumptions to produce the grains, CGMD models were able to predict important stages of CF production, such as ladder formation during stabilization, and correctly predict physical aspects of commercial and bio-PAN CF, such as the modulus and density within ±15%. Slight overestimations of some elastic properties were fixed during BP3 as presented in the Phase 2 Topical Report.

For pitch-based molecules several modeling methods were investigated. These included GCMD, as well as a fully atomistic MD and DFT methods to predict the most reasonable (lowest energy) molecular structures produced in PPM and CTPM. However, it was found that a simpler approach, by using reasonable proxy molecules from the isotropic pitch, through a combination of the literature and the chemical characterization data (CHNOS, LDO, and FTIR), could be taken and used in MD and ReaxFF simulations to replicate experimental CF results well within ±15%. These models are chemistry based, relying on representative molecules present in the isotropic pitch, and they could easily predicted the density, modulus and other elastic properties without going back and adding factors to force the models to fit experimental data. Density was found to be a key parameter that could validate the micro-modeling efforts since it also accounts for molecular transformations which occur between the isotropic pitch, mesophase pitch/as spun fibers, stabilized fibers and carbonized CF.

ML was implemented to be able to perform predictions from the feedstock chemistry and composition to pitch properties, from pitch characterization to CF properties, and even from feedstock chemistry and composition directly to CF properties. By combining all the data indiscriminately, ML could easily predict pitch and CF properties with very low error. However, it is clear that using all the data, in a holistic approach, is limited due to overfitting. As such, the models were not capable of showing which chemical of physical properties were actually correlated with the performance, and which data was inconsequential. This was a further limited by the fact that massive amounts of variable data—that are typically needed to produce highly refined models—were simply not available with such a limited study. To provide more meaningful correlations, and predictions, a heat map approach was developed to first down-

select which types of data, or specific parameters from the data, were correlated with the material properties or performance. This method was defined as a targeted approach which greatly reduces overfitting. By using the targeted approach various correlations and predictions were made which now inform which molecules, chemistries, compositions and other properties are most favorable to producing desired properties and performance within ±15%. This type of approach should be able to guide feedstock and intermediate selection for other feedstocks, but needs validation for this specific purpose.

A major motivator for this work was to provide a roadmap for cheap materials which can be used to replace heavier steel load bearing and other metal and body components. It is well known that composites, especially CF composites, have a much higher strength-to-weight ratio than traditional steel. By surveying various steel metallurgies and comparing to tow-level CF composite data the CF produced in this study had a strength-to-weight ratio about 600% greater than steel used in the automotive industry and up to 1000% greater than other steel compositions.

Detailed techno economic analysis for scaling up CF production showed that bio-PAN CF could be produced at a cost significantly below $5/lb, which is not achievable for traditional petroleum based PAN. The primary reason for the bio-PAN cost advantage are significant co-product credits coming from propylene glycol and ammonium sulfate that are produced during the conversion of sugars to bio-ACN. The cost advantage for bio-ACN could in fact be more significant when considering potential impact of carbon credits and potential reduction of environmental pollution when using a bio-based renewable carbon feedstock. The cost analysis did also show that both PP and HTCTP could be also easily achieve a cost below $5/lb. Due to time and budget constraints bio-ACN and PP were further down selected for study in BP3 and are presented later in this report in the Phase 2 Topical Report section.

PHASE 2 (BUDGET PERIOD 3) TOPICAL REPORT

Executive Summary

This Phase 2 Topical Report summarizes BP3 results showing how the tools and methods developed in the Phase 1 Topical Report 1 are integrated and further developed to relate the atomistic properties of CF feedstocks to single filament CF properties and ultimately to the tow-level composite fiber properties. This was accomplished through detailed understanding of the feedstock molecules, how these are changed to produce CF precursors (mesophase or PAN), and the further development of the chemical structure during CF processing. These aspects were then integrated using NN to develop the relationships to the various physical properties of the CFs. This was ultimately validated with limited data available on the scaled up samples of CF produced under this program. CF properties such as elastic modulus, compressive modulus, shear modulus and Poisson's ratio could be predicted well within ±15%.

For bio-PAN modeling efforts, the initial coarse-grain CGMD methods were found to give and overestimation of some elastic properties. This was corrected by modifying the CGMD models to add back in the hydrogen atoms and allowing all the atoms to relax, thus converting it back to a fully atomistic model. This method was also adapted so that various bio-PAN processing parameters such as stretching force, stabilization temperature and stabilization time could be used to predict CF properties, as well as define limits of CF failure during CF production. It is obvious that this type of novel modeling could be further developed to help guide PAN-based CF production to target various CF qualities without needing to take a trial and error approach. For tow-level CF properties the various elastic components and density were also easily predicted within ±15%.

An important hurdle that was overcome for complete model integration was how to encrypt the CF processing data (spinning conditions and post processing of as spun fibers, e.g. stabilization and carbonization) without violating export control. This was important so that the processing, which is critical to CF properties, was not treated as a black box. A method was developed to encrypt the various CF processing parameters so they could be used for ML to develop web-based, user-friendly, platforms for predicting CF properties.

Model integration between the different scales (micro- to macro-level) was achieved using NN by considering the molecule properties and their connectivity during mesophase production and CF production (primarily through carbonization, although graphitization was considered), relating the localized molecular "sheet" properties to the CF microstructure, and finally to tow-level epoxy composite CF properties. Figure 189 shows the path developed to use NN to integrate models all the way from the atomistic-level to the CF tow-level CF properties. Model integration showed that, based on the chemistry of the feedstocks and precursors, it is possible to predict elastic CF properties and tow-level composite properties well within ±15%.

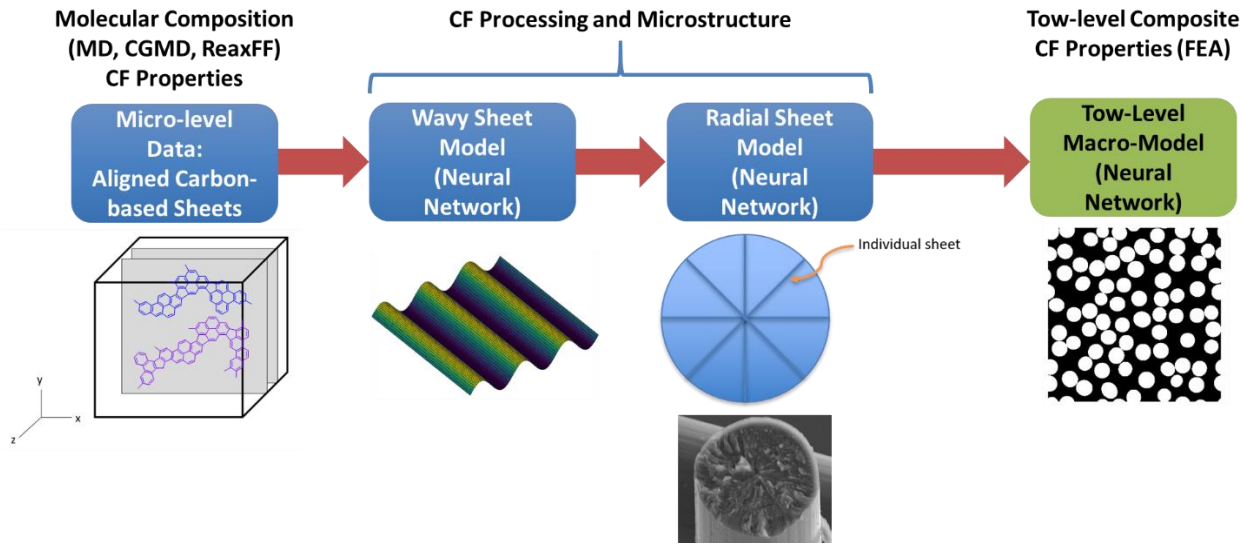

Figure 189: Schema for model integration representing how the micro-level modeling was integrated with tow-level composite data.

Several Kg batches of PPM were produced by Koppers. It was discovered that volatiles in some of the PPM batches were causing some inconsistencies in the spinning and CF properties. It was also demonstrated that primary carbonaceous insolubles, which was produced during the PP production, had a negative impact on CF properties. This was demonstrated by carefully filtering PP to remove the insolubles and producing PPM of the same SP for the filtered and unfiltered samples. CF from these filtered and unfiltered (referring to the isotropic pitch, not filtration of the mesophase) PPM were produced using the same melt-spinning processes. PPM produced from filtered PP produced significantly smaller diameter CF with higher strength and elongation, but lower modulus. Additional characterization data for the PP and PPM samples were also collected during this work to be used in further developments of ML.

DOE targets for strength (250 ksi), modulus (25 Msi), elongation (>1%) and cost at ≤$5/lb were all met with scaled up bio-PAN and PPM CF during BP3. Several large strides were made during this program to address different facets of pitch-based and PAN-based feedstocks, CF production and integration of models for a holistic approach to arrive at tow-level predictive capabilities. However, it is admitted that given the large scope of the project various aspects are more developed and validated than others, and additional work is needed to fully understand all aspects of CF production.

Micro-Level Models and Simulations

Pitch-based

A modeling framework built by the MIT team for pitch-based (either CTP or PP) was successfully completed. It allows for quantifying and predicting the effects of microscopic morphology and reaction dynamics on the fiber modulus, including molecular alignment, density

and radical production. Given the goals to both explain the performance variability in the CFs experimentally synthesized in this program and to guide the selection of optimal processing parameters, screening of the modulus in relation to microstructure for both isotropic and mesophase fibers was performed. An overview of the variability of moduli for the CF synthesized is shown in Figure 190(a). It has been hypothesized that the degree of molecular alignment has substantial benefit on the modulus of CF. This is statistically valid from the experimental data in Figure 190(a). However, we note that isotropic fibers could also achieve rather high modulus under specific, yet undetermined processing conditions. Mesophase pitch shows a more uniform distribution in modulus. Three key elements were studied: 1. The ability to obtain high modulus fibers from isotropic pitch is practically significant, because it would remove the requirement of mesogen preparation as a necessary condition for high modulus CFs. 2. Furthermore, identifying the microscale processing descriptors (bonding configuration, oxidation, etc) that are immediately responsible for the mechanical response, is key for being able the use of these models for prediction and experimental planning. 3. Finally, a macroscale descriptor (predictor) that can be directly experimentally measured for CF to predict, through these models, the resulting modulus, can allow a direct application of the models themselves to the experimental synthesis.

For these three goals, hundreds of models were constructed using ReaxFF. The results are summarized in Figure 190(b-d). In addition to separating the evolution for isotropic and mesophase fibers, density was introduced during processing as the macroscopic key metric that appears to regulate and determine the final fiber modulus. Selective de-hydrogenation (Figure 190(c)) can be devised to mimic either the effects of controlled oxidation (by selecting the atomic sites that will first de-hydrogenate and interconnect), or differences due to the presence of functional groups usually associated with PP—namely methyl groups. It is remarkably notable, that the modulus of isotropic fibers shows values in good agreement with experiments with excellent accuracy. This is also the case for mesophase pitch fibers. Overall, mesophase fibers generally have higher modulus than isotropic cases. However, for both cases the modulus increases monotonically with fiber density. For instance, both the isotropic and mesophase cases with similar density of 2 g/cm^3 show similar modulus around 200 GPa. A major difference between the two cases is in the presence, for isotropic pitch of an “activation density”, below which the CF will have marginal or poor modulus.

As density denotes the spatial closeness, the existence of radicals is equally important. To this end, we studied the effect of branch groups, which is currently simulated as hydrogen removal (see Figure 190(d)). It is observed that both hydrogen (group) removal and fiber density are essential. In other words, larger number of branch groups at the edge of aromatic cores (characteristic of petroleum pitch) and the closer they approach (higher density), the higher modulus could be expected for the produced fibers. Figure 191 shows a representation of CTP and CTPM molecules taken from (Fan, Fei, Chen, & Li, 2017) and (Fetzer, 2007), respectively, and Figure 192 shows PP and PPM molecules taken from (Thies M. C., 2014) (Burgess, Pittman, Marcus, & Thies, 2010) (Esguerra, Hoffman, & Thies, 2014) (Chen, et al., 2020). To show the

reaction dynamics, simulations were performed where branch groups are removed with different speed, as shown in Figure 190(d). The large variation (low correlation) between removal speed and fiber modulus shows counter-intuitively that the usually assumed important processing parameters, such as temperature, might not be key optimization variables.

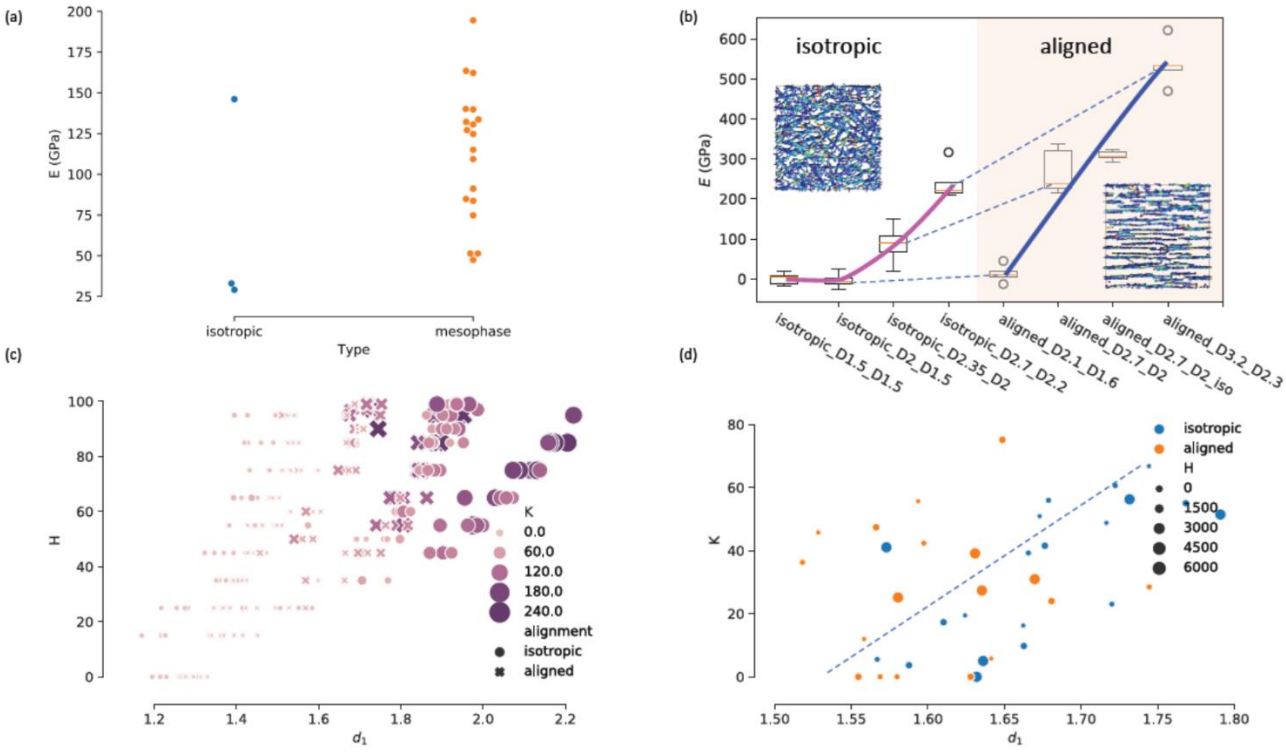

Figure 190: The effects of molecular alignment, density and hydrogen removal.

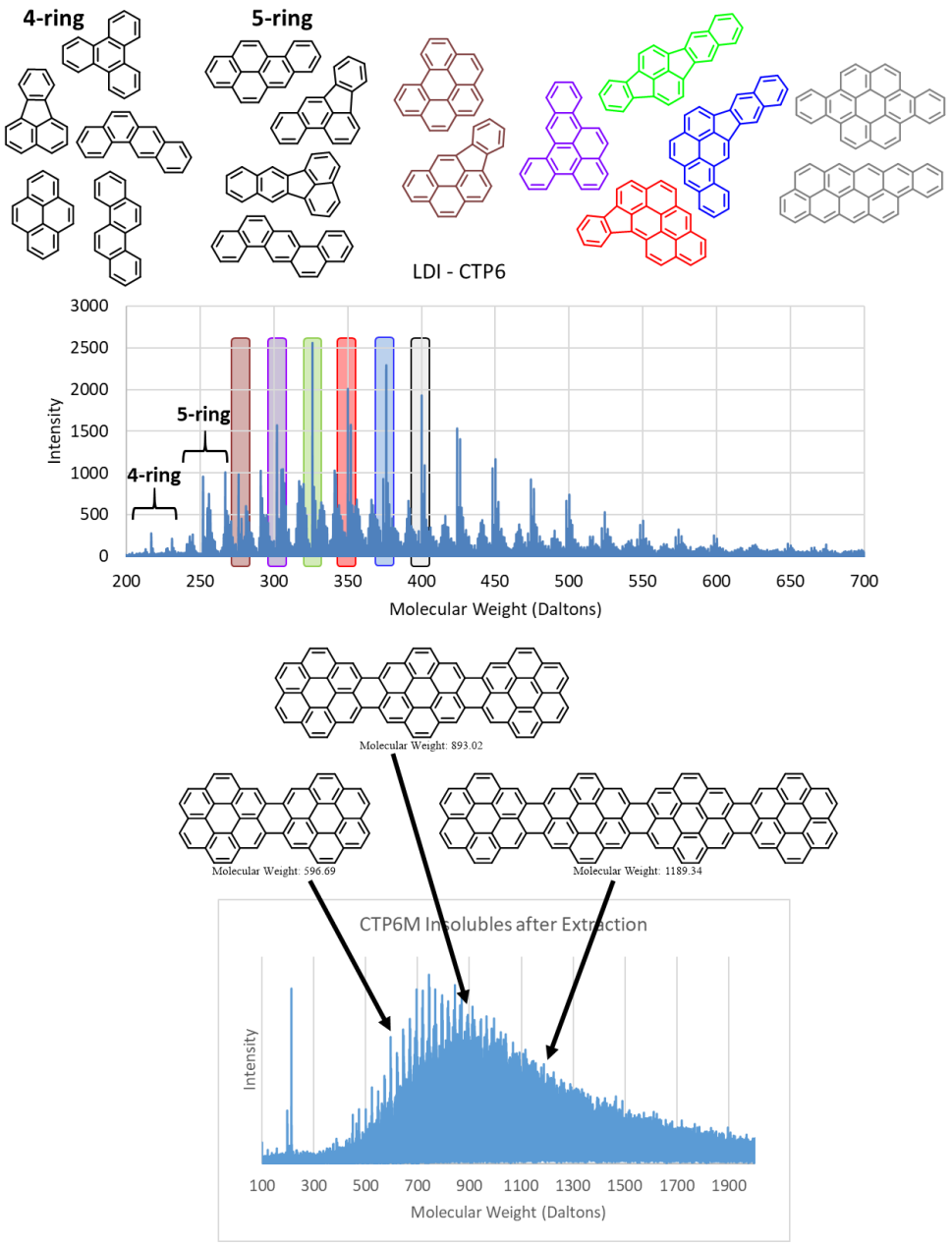

Figure 191: Top shows select CTP molecules relative to LDI spectra and the bottom shows hypothetical CTPM molecules relative to LDI based on coronene (Fetzer, 2007).

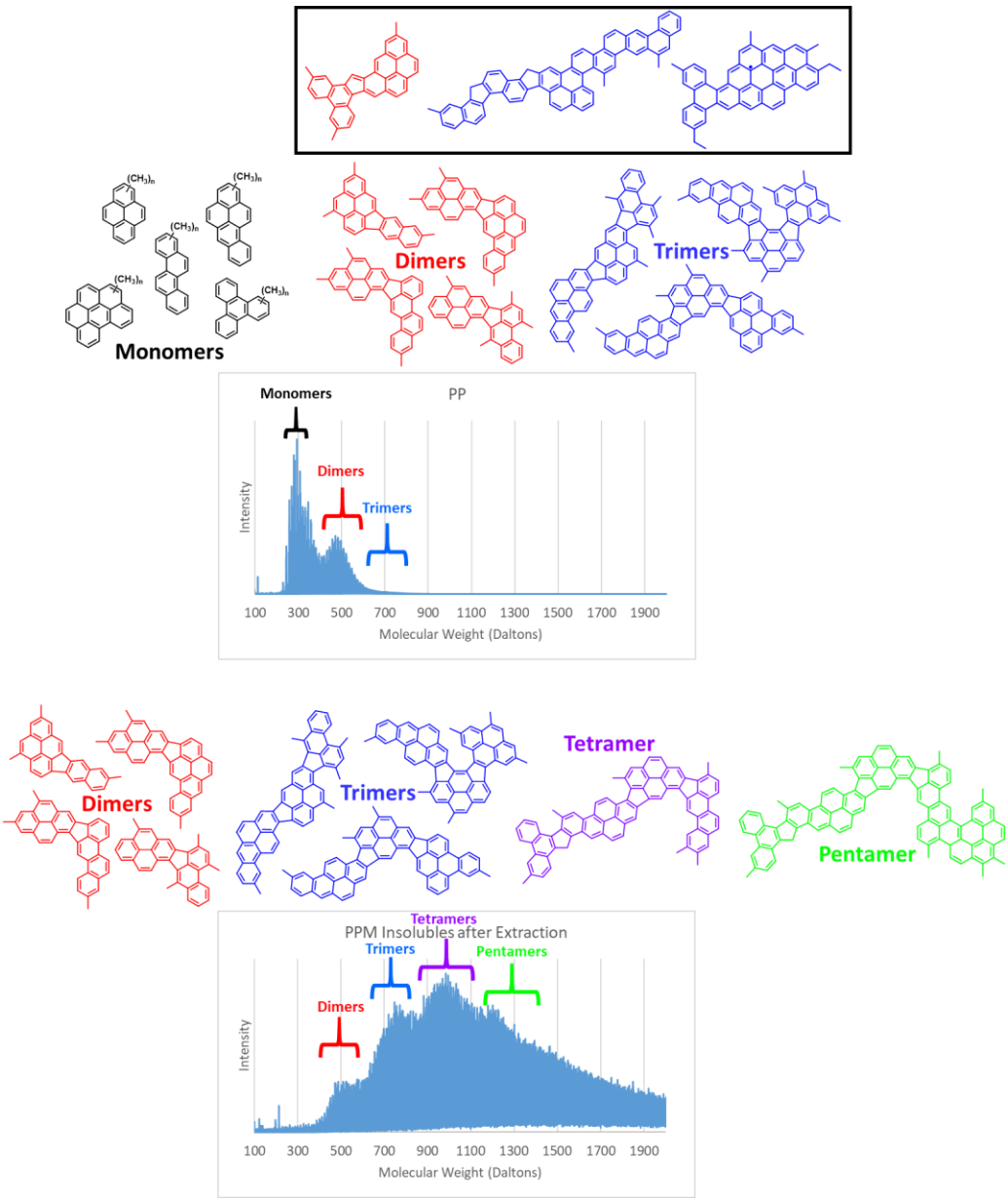

Figure 192: Top shows select PP molecules relative to LDI spectra and the bottom shows hypothetical PM molecules relative to LDI based on (Burgess, Pittman, Marcus, & Thies, 2010) (Chen, et al., 2020) (Esguerra, Hoffman, & Thies, 2014) (Thies M. C., 2014). The inset box in the top are actual molecular structure identified in PP using imaging techniques described in (Chen, et al., 2020).

The framework built by the MIT team for pitch-based (either coal-tar or petroleum) CF was further improved for the dual purpose to allow for: 1. A direct comparison between modeling prediction of modulus and density and the same parameters obtained from experimental data within the consortium; 2. Identify the role of molecular size/shape versus actual alignment on the ultimate mechanical properties of the CF. In this framework, for mesophase, the requirement of molecular alignment towards the direction of the fiber is decoupled from requiring the molecules to have significantly large size. In other words, while to achieve alignment during the experimental synthesis, large mesogen molecules are needed, in the modeling framework,

alignment can be achieved regardless of the formation of mesogens. It follows that when using small, yet aligned molecules, the reactive nature of the simulation (i.e. accounting for the realistic representation of the reactivity of the molecules themselves), results in a carbon network of large molecules akin those in mesogens. This was later validated at the end of the program against experimental data.

As an example, the molecular set chosen for the representation of isotropic and aligned pitch were taken from GCMS measurements from the pitch used for CF synthesis within this consortium, as shown Figure 193(a). By controlling molecular alignment, the modulus of both aligned and isotropic fibers were calculated. The results are shown in Figure 193(b), where each dot represent the relationship between the Young's Modulus and the nanoscale density of the material. The red dots correspond to aligned (mesophase) fibers, and blue dots to isotropic (unaligned) fibers. The larger dots and crosses are directly obtained from experiments carried out by the ORNL team with isotropic and mesophase pitch from WRI. It is worthy to note that the experimental data is simply overlaid on the modeling data, without fitting parameters, or offset readjustments. Overall, the agreements between the simulations and experiments are good, especially for the aligned case which is excellent. Furthermore, for modulus lower than 250 GPa, both isotropic and aligned fibers can achieve same-level modulus with slightly different density.

It should be noted that while the aligned case shows excellent agreement, in the case of isotropic CF, the density in the models seems to be overestimated. Some reasons for this discrepancy may be: 1. Role of molecular size and 2. Macro-scale vacancies/defects/boundaries. As noted, the initial molecules tend to be on the low-end of the molecular weight distribution for pitch. Small molecules that are aligned along the direction of the fiber, still produced aligned macromolecules (mesogens) in these models, with no detrimental effects on the overall density or modulus, due to the tendency of the aligned small molecules to form covalent bonding and therefore extended aromatic macromolecules. The same is not necessarily true for isotropic pitch, where the same small molecules, now isotropically distributed, may pack more tightly in our model than a molecular set with larger molecules, leading to an overestimation of the density, as observed. *Note: it should be noted that molecular changes due to the step of oxidative stabilization are not accounted for in these simulations.*

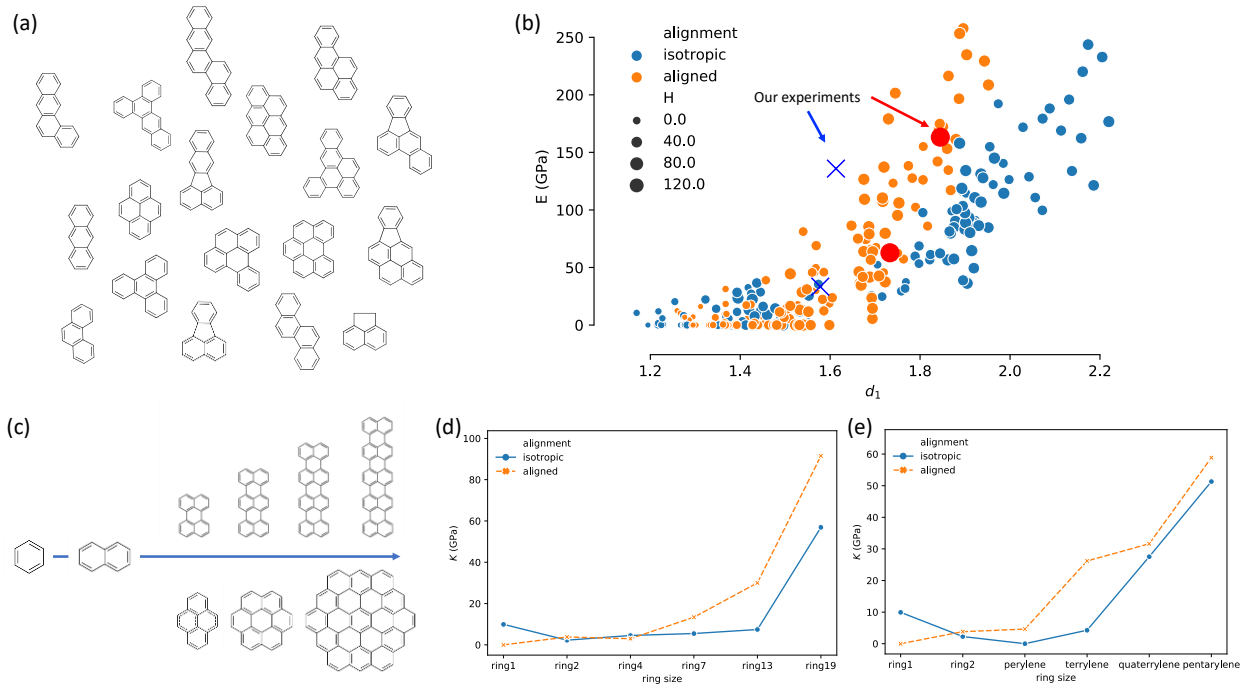

Figure 193: The effects of molecular alignment, density and hydrogen removal.

To highlight and resolve the controversy between isotropic and aligned pitch, simulations were performed where the same processing conditions are applied to the system, but different molecular sets are used. The molecules chosen are ideal molecules because they represent extreme cases in terms of size and shape (i.e. perfectly round or linear), starting from the smallest to very large, mesogen-like molecules (see Figure 193(c)). The moduli of the final resulting fibers are shown in Figure 193(d-e), respectively for linear and round molecules. It is worth noting that these results were carried out only at low-density. Some relevant observations can be drawn: 1. The difference in the modulus as the molecular size increases is minimal with regards to shape. 2. For both shapes, the modulus is marginally impacted for small molecules, such as less than 13 rings and smaller than terrylene. An increase in modulus is observed as the size increases, possibly because of an increase in packing density, and it is in line with what is captured with the simulations using realistic pitch molecules at low density. Based on these results at low density, it appears that the role of size and shape of the initial molecules does not alter the observed modulus vs density trend in pitch.

Earlier, the bond evolution was fit to Equation 1 and the value ‘a’ was taken as the representative value (Figure 194) because it represents the percentage of new bonds formed as time tends to infinity.

$$N = a[1 - exp(bt)] \qquad (1)$$

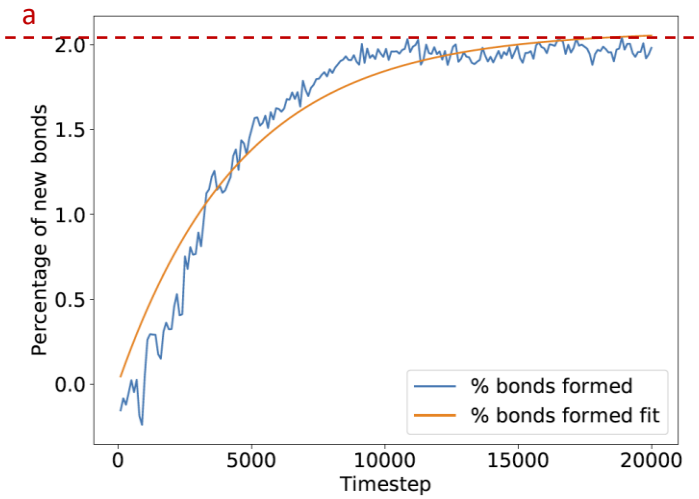

Figure 194: Percentage of new bonds formed evolving with timestep. The red dotted line indicates the value as time tends to infinity as is taken as the representative value.

The density and elastic modulus were subsequently plotted against the representative percentage of new bonds and Figure 195 were obtained. The plateau region in Figure 195a and the rapid increase in elastic modulus depicted in Figure 195b are confounding and urged us to consider an alternative method to analyze bonding in the simulated fibers.

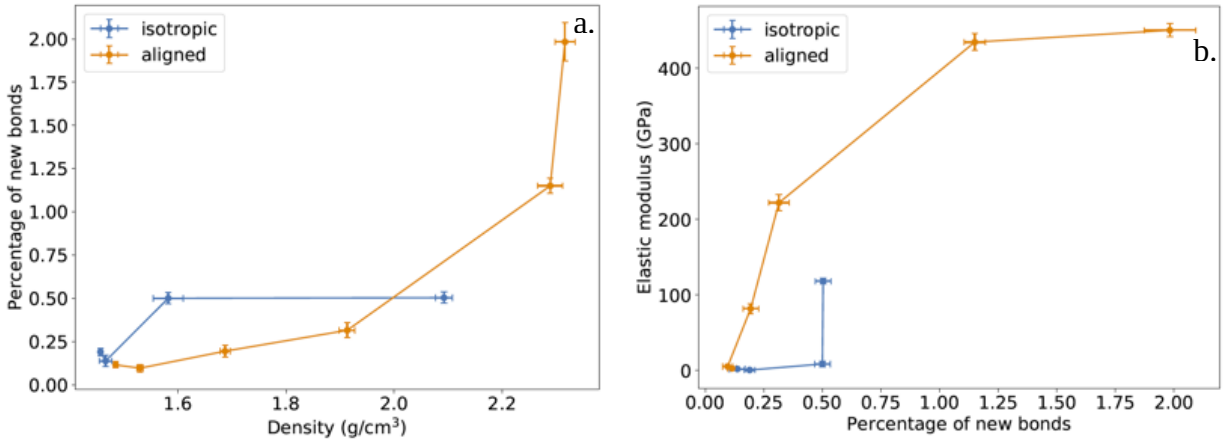

Figure 195: a. Percentage of new bonds as a function of density and, b. elastic modulus as a function of percentage of new bonds. The plateau region in 7a and the rapid spike in elastic modulus in 7b represent the unsuitability of this method of bonding analysis.

The elastic modulus is a function of number of bonds and the bond strength, among other parameters. Assuming the bond strength is constant on average, we thus expect to see an increased modulus with increase in bonds. One important feature is that modulus depends on bonds per unit volume instead of the bonds in the entire volume. Also, the modulus depends on the final number of bonds and not merely on the new bonds formed. These two changes were incorporated and the Figure 195 were modified into Figure 196.

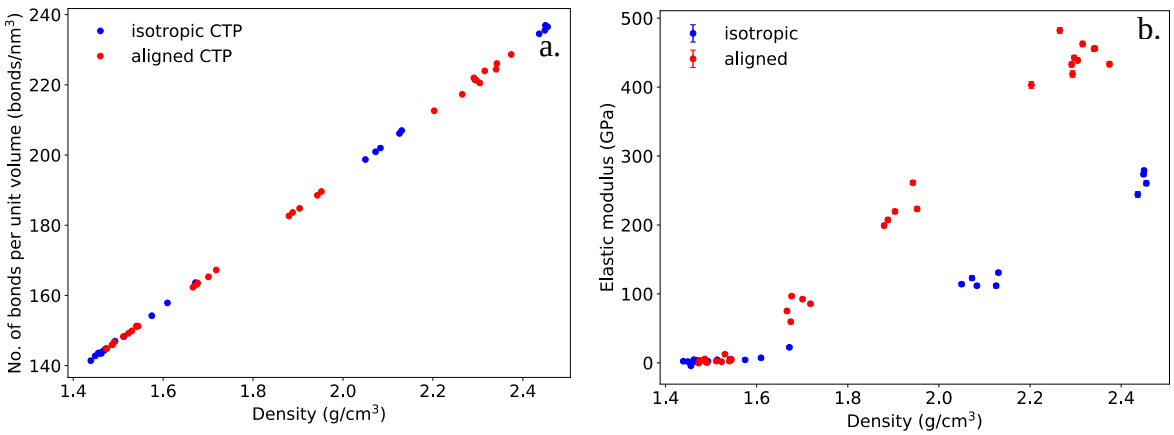

Figure 196: a. Bond density, and b. Elastic modulus as a function of density.

In particular, the Figure 196a shows a strong correlation between bond density and density for both isotropic and aligned systems. This implies that the difference in elastic modulus observed for isotropic and aligned systems stems completely from the difference in alignment and not because of the bonds present.

In order to study the effect of changing size of the aromatic molecules on elastic modulus and density, monodisperse systems were analyzed consisting of aromatic molecules ranging from 1 to 19 in ring size. Similar trends were observed in elastic modulus for a given density for both monodisperse and polydisperse systems, depicted in Figure 197, indicating that size might not be an important parameter in determining modulus.

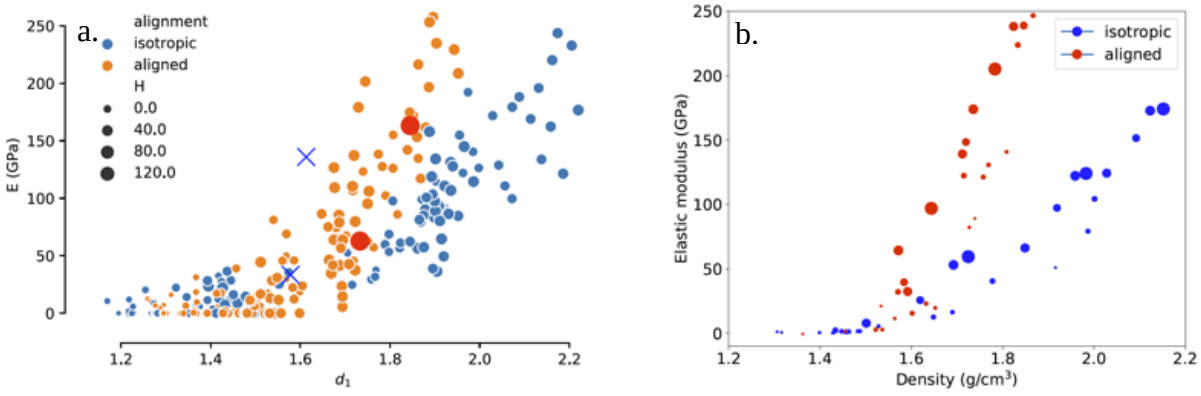

Figure 197: Elastic modulus vs density for a. polydisperse, and b. monodisperse CTP systems (the size of the circles is proportional to the ring size in 9b).

A more representative CTP sample consists of larger molecules in the weight range 300 – 400 g/mol comprising 75% of the entire sample by weight (based off of LDI-MS data). A modified system was made by adding the larger molecules depicted in the blue box of Figure 198 and deleting the smaller molecules present in the red box of Figure 198 (they are in very low amounts in CTP).

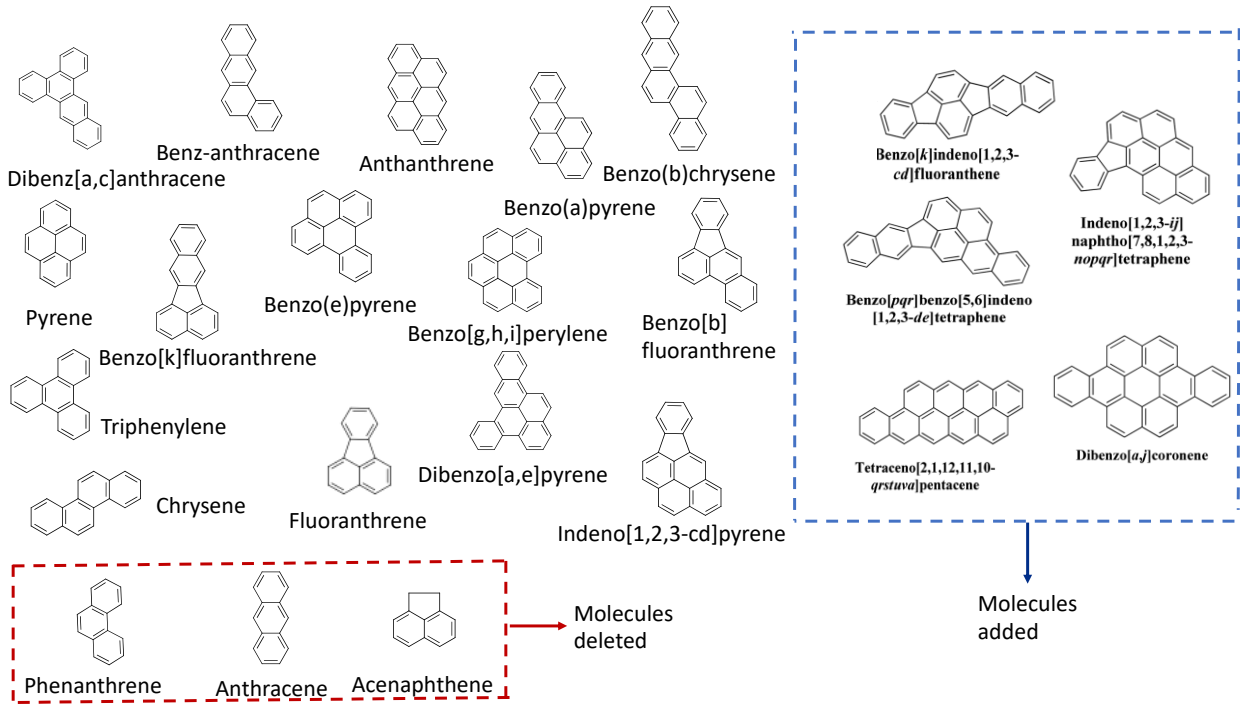

Figure 198: The molecular components of CTP systems. A modified system was made by adding the larger molecules in the blue box and deleting the smaller molecules in the red box.

The bond density vs density, plotted in Figure 199a, shows the same trend for all the 4 set of systems, highlighting that the eventual bond density is constant for a given density and is independent of the alignment of the fibers, as well as the sizes of the molecules. The elastic modulus follows a similar trend in the two aligned systems and the two isotropic systems, emphasizing the relative independence of the modulus on the molecule sizes present.

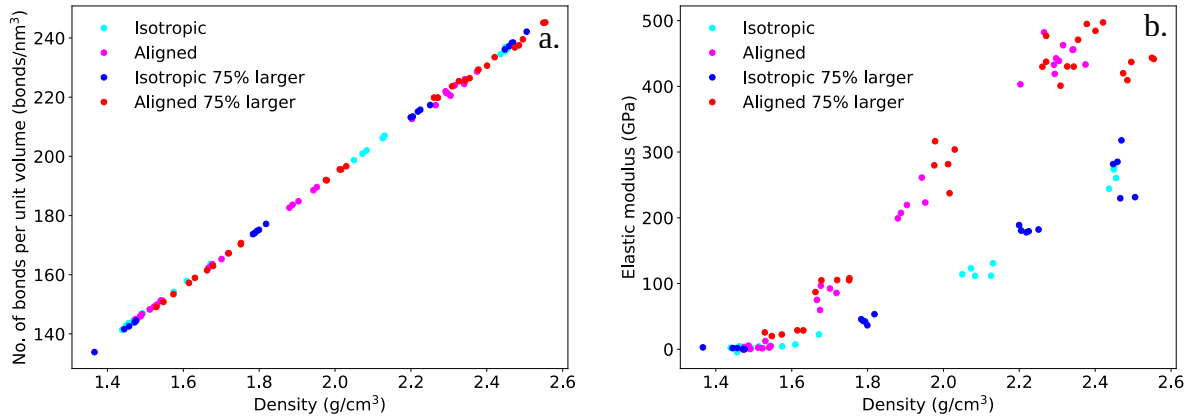

Figure 199: a. Bond density, and b. Elastic modulus as a function of density for the two CTP systems.

A comprehensive study on the resultant modulus and its dependence on alignment of the fibers was done for a variety of moduli: tensile longitudinal, tensile transverse, compressive

longitudinal, compressive transverse, longitudinal shear, and transverse shear. The Poisson's ratio was also calculated. All the properties are plotted in Figure 200, Figure 201 and Figure 202.

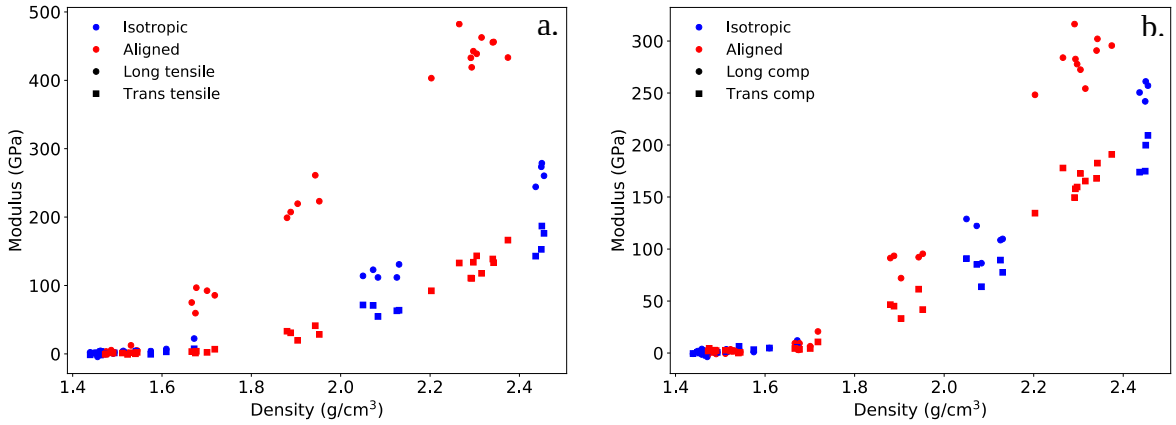

Figure 200: a. Tensile, and b. Compressive modulus vs density for CTP systems.

We observe, from Figure 200a, the longitudinal and transverse tensile moduli for the isotropic system lie between that of the longitudinal tensile and transverse tensile moduli for the aligned system, highlighting the direct correlation between orientation and modulus. While compressive moduli are smaller in magnitude when compared to their tensile counterparts in the aligned systems, the compressive moduli and the tensile moduli are similar for the isotropic systems (Figure 202a).

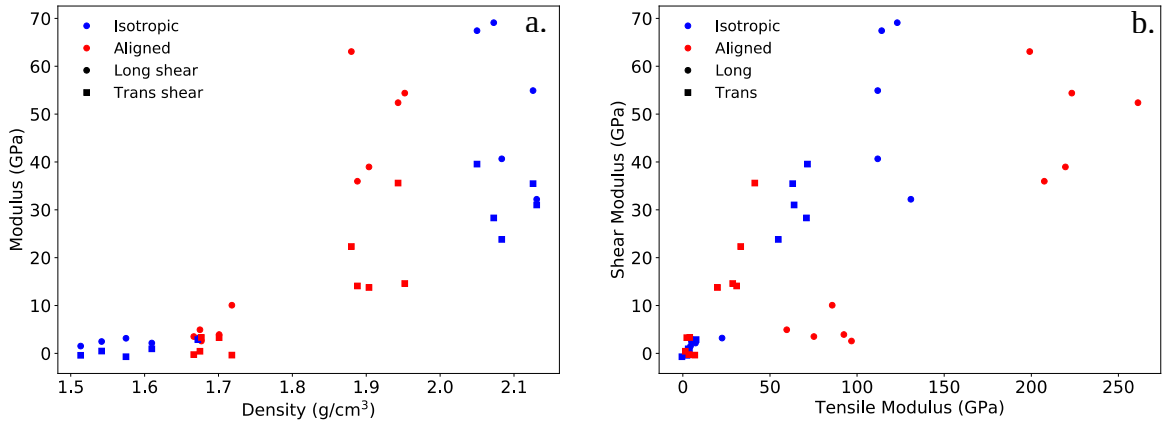

Figure 201: Shear modulus as a function of a. density, and b. their tensile modulus counterparts for CTP systems.

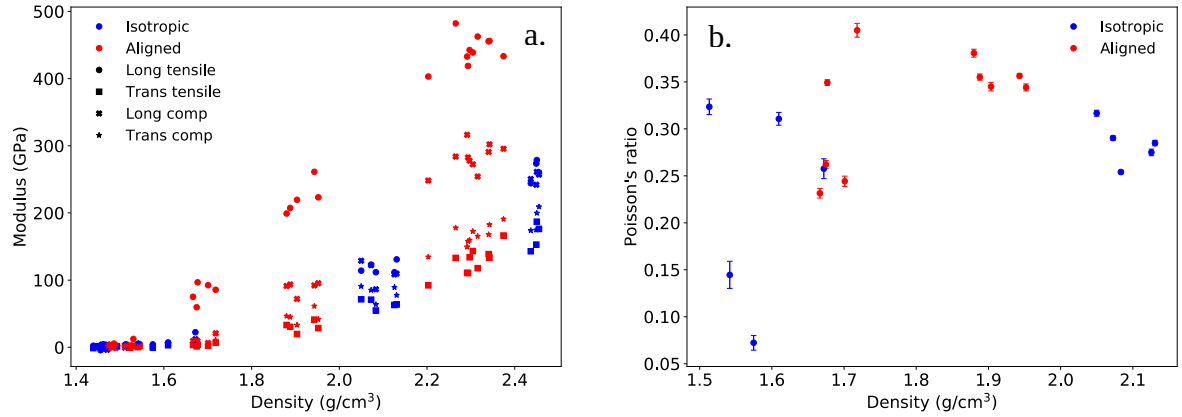

Figure 202: a. All moduli, and b. Poisson's ratio as a function of density for CTP systems.

Atomistic modeling of PP CFs was completed building on the framework that was used to model CTP CF. The basic framework is similar, in that a small subset of molecular compounds is chosen to represent the chemistry and composition of pitch and to subsequently build mesophase and isotropic systems. However, a major difference to be accounted for PP, is the presence of methyl groups decorating the aromatic cores. Since one of the major features of the ReaxFF modeling developed in this project consists in the selective removal of hydrogen to activate the reaction of molecules towards the formation of fibers, for PP several schemes were adopted to remove either aromatic or aliphatic hydrogen, or both, and their effects in the CF performance in relation to experimental data. As described below, a detailed bonding analysis was carried out to determine the nature of bonding configurations for PP and PPM, in relation to the system density. It was observed that the presence of methyl groups greatly enhances the ability of the system to form an extensive network of bonds compared to CTP. Furthermore, when not using graphitization during the synthesis process, the models indicate that high tensile *and* compressive moduli can be achieved at ultra-high density (> 2.2 g/cm^3) through the establishment of an extensive network of sp^3 bonds. Within the high-density regime (between 1.8 and 2.1 g/cm^3) the models are in good agreement with experimental data for both commercially available CF as well as CF produced within this project. To prove the modeling resilience to also describe graphitization (which achieves ultra-high moduli at density below graphite, 2.2 g/cm^3) additional steps in the modeling were introduced to perform high temperature annealing. The results indicate that the agreement in performance with commercial fibers is excellent.

The PP molecules used as precursors in this study are depicted in Figure 203. While CTP systems contain only aromatic hydrogen, PP systems also contain aliphatic hydrogen from mostly methyl groups. Applying the same procedure on the PP molecules show the applicability of the model to a more general set of pitch molecules. Additionally, via PP simulations, we can study the impact of aliphatic H and aromatic H removal on bonding and elastic modulus.

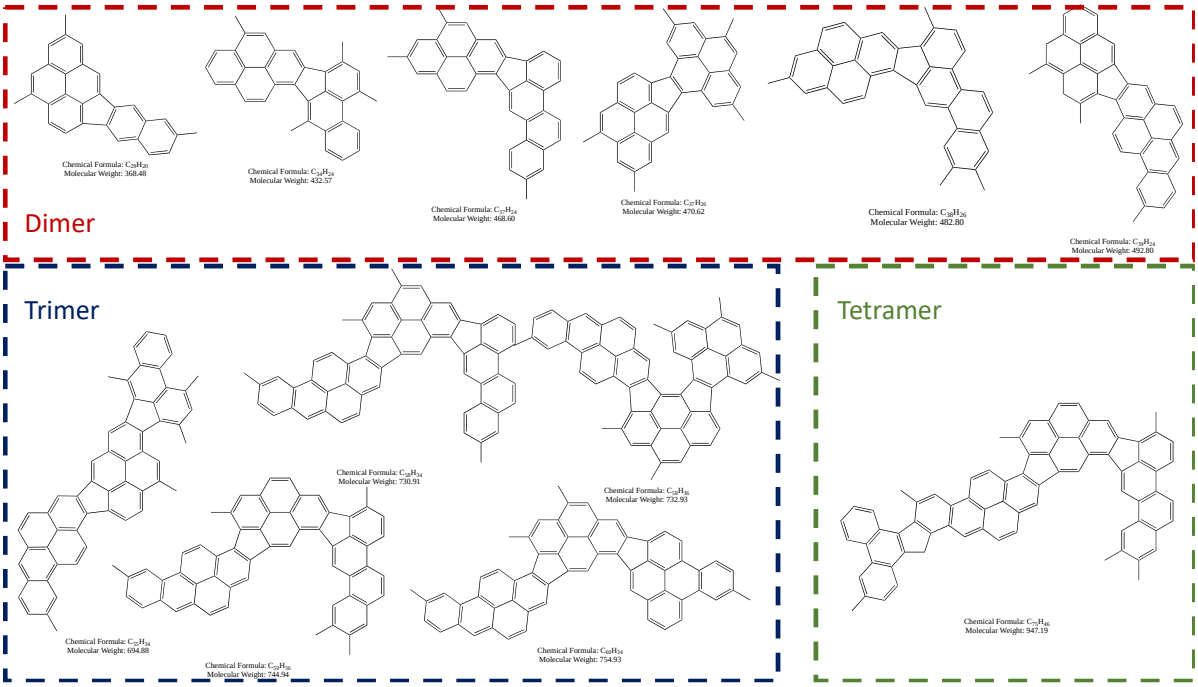

Figure 203: Petroleum pitch molecules used as precursor for obtaining CFs consist of dimers, trimers, and tetramers.

The presence of two different types of carbon-hydrogen atoms (H): aliphatic (primarily methyl, 5 membered ring methylene and 6 membered ring bridgehead methylene carbons were not considered) and aromatic H, allows investigation of their impact on the reactions and the eventual modulus obtained. With this as motivation, PP simulations were divided into 4 broad pathways. These pathways are chosen based on which type of H is removed (first). Removal of hydrogen atoms in the beginning of the simulation aids in activating the reaction sites and accelerating the reaction in the simulation setup. The first pathway corresponds to removing 95% of both aromatic and aliphatic H, while in the second and third pathway, we remove 95% of methyl H only and 95% of aromatic H only respectively. The fourth pathway corresponds to removing 95% of methyl H only first, allowing reactions to take place, and subsequently removing 95% of aromatic H only. These four pathways can provide valuable insight into the mechanism of the reactions and which H contributes the most to modulus. Figure 204 outlines the 4 different paths investigated.

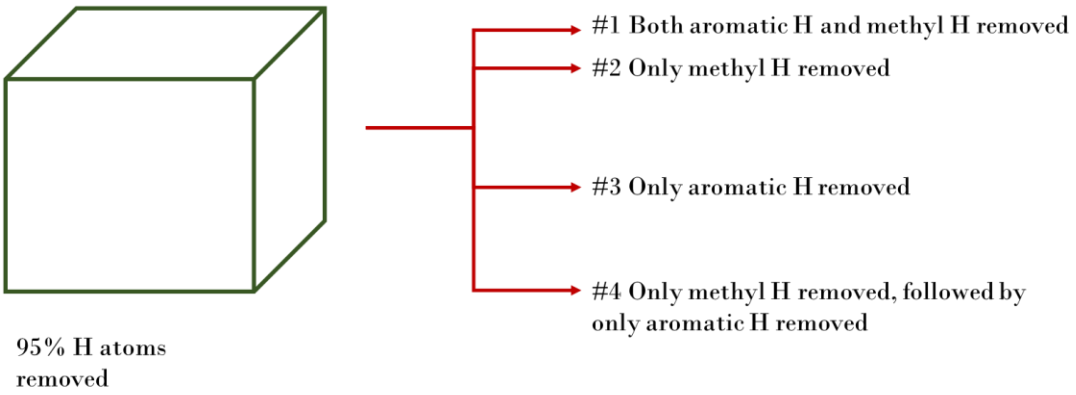

Figure 204: H removal pathways investigated for PP.

The elastic modulus vs density for the fibers obtained from all the four pathways along with experimental data is depicted in Figure 205. We observe remarkable agreement with experimental data. The experimental fibers which demonstrate much higher ranges of modulus are likely to have undergone a graphitization process.

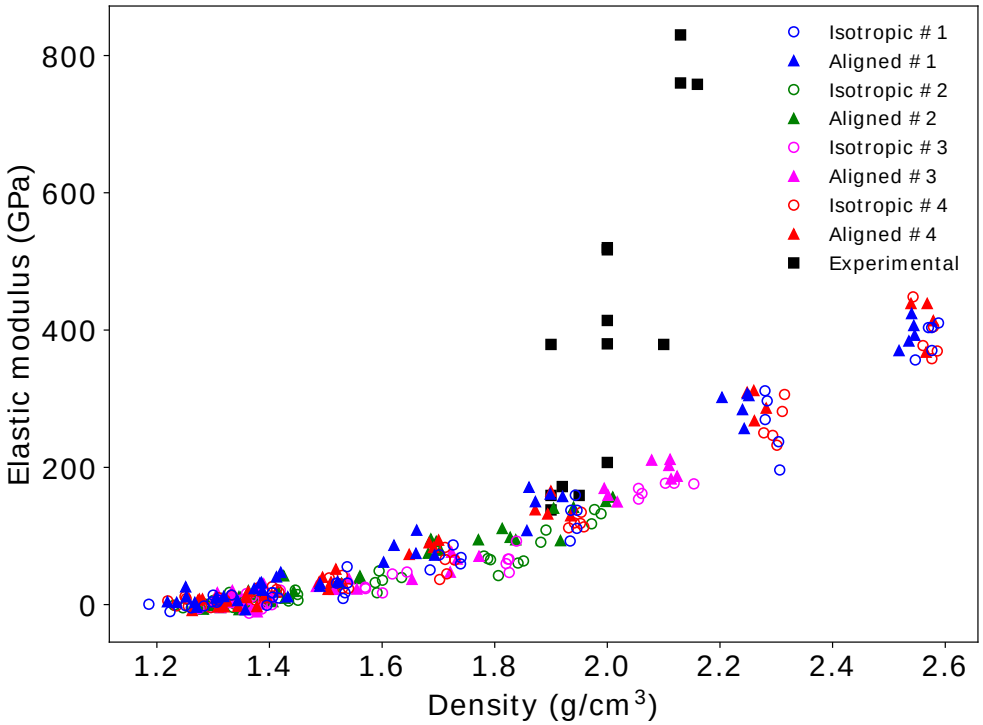

Figure 205: Elastic modulus vs density of CFs from petroleum pitch derived using all the four pathways.

From Figure 17, it is shown that pathways 1 and 4 result in similar elastic moduli. Moreover, while pathways 1 and 4 lead to high moduli, pathways 2 and 3 yield fibers lower in moduli compared to the former. This indicates the importance of the H in the reaction, emphasizing that both types of H are needed to form high moduli fibers.

Figure 206 highlights the relationship between density and bond density in the fibers generated from all the four pathways. Bond density is defined as the number of bonds per unit volume and varies linearly with density. Pathways 2 and 3 depict a higher bond density for a given density because of the lower number of H atoms removed and thus a larger fraction of C-H bonds present.

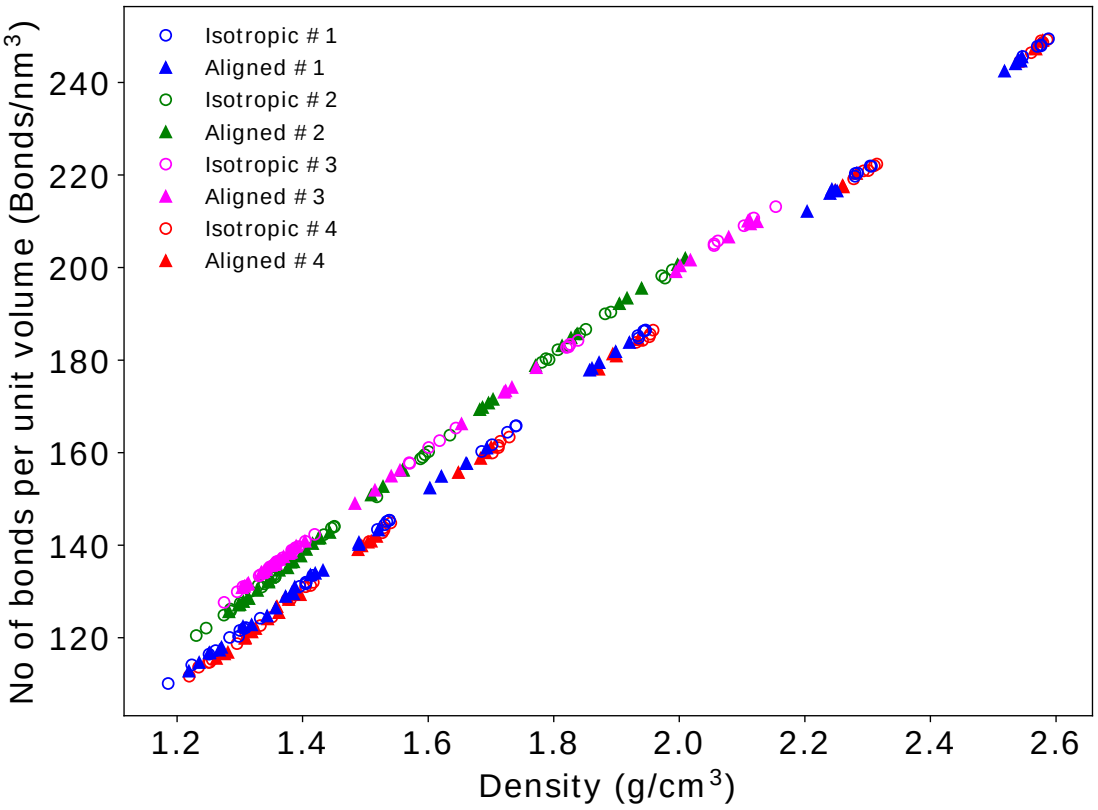

Figure 206: Bond density vs density of CFs from petroleum pitch derived using all the four pathways.

From Figure 206, it was observed that increasing density increases modulus of both isotropic and aligned fibers. While experimentally, high modulus fibers are synthesized by graphitization, this led to the belief that increasing the density can function as an alternative method of obtaining high modulus fibers. To investigate the nature of bonding at these high densities, we calculate the fraction of sp2 and sp3 bonds in the carbon fibers using equations 1 and 2.

$$change\ in\ sp2\ fraction = \frac{final\ sp2\ fraction - initial\ sp2\ fraction}{initial\ sp2\ fraction} \quad (1)$$

$$change\ in\ sp3\ fraction = \frac{final\ sp3\ fraction - initial\ sp3\ fraction}{initial\ sp3\ fraction} \quad (2)$$

Where the final (initial) sp2(3) fraction is the final (initial) number of sp2(3) carbon atoms divided by the total number of carbon atoms.

Figure 207 and Figure 208 depicts the change in sp2 and sp3 fraction as a function of density, respectively. It is shown that as density increases, the fraction of sp2 decreases while that of sp3 increases. From Figure 209 and Figure 210, there is also a positive correlation between sp3 content and elastic modulus. From these simulations, it was concluded that a significant sp3 carbon fraction is obtained which increases with increasing density.

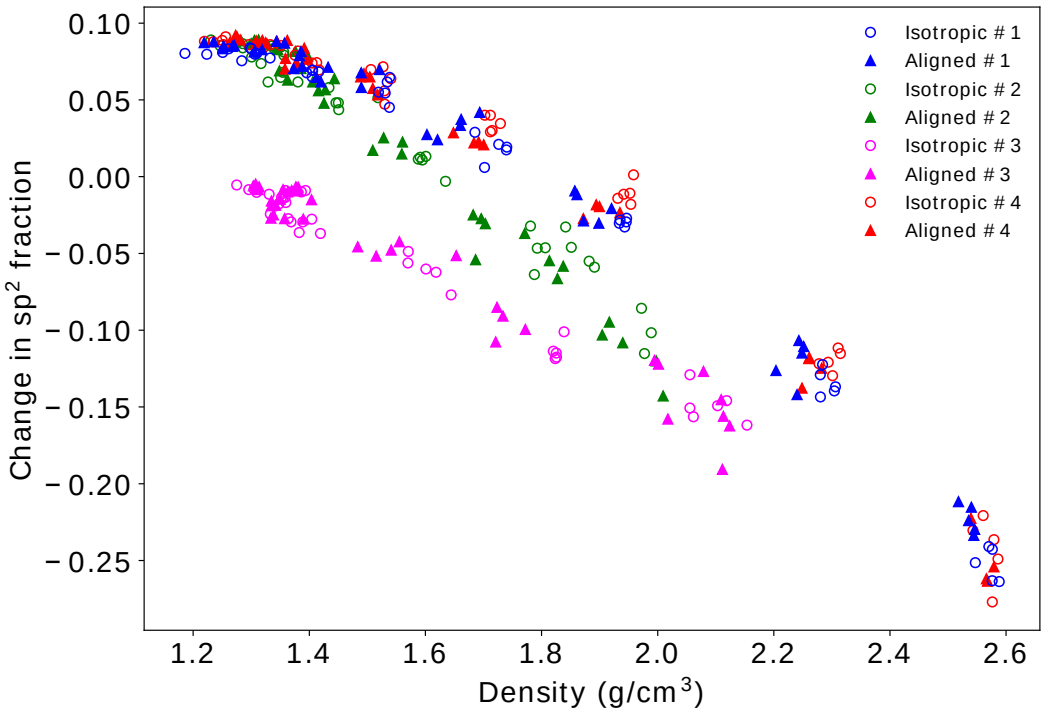

Figure 207: Change in sp2 fraction vs density for all the four pathways.

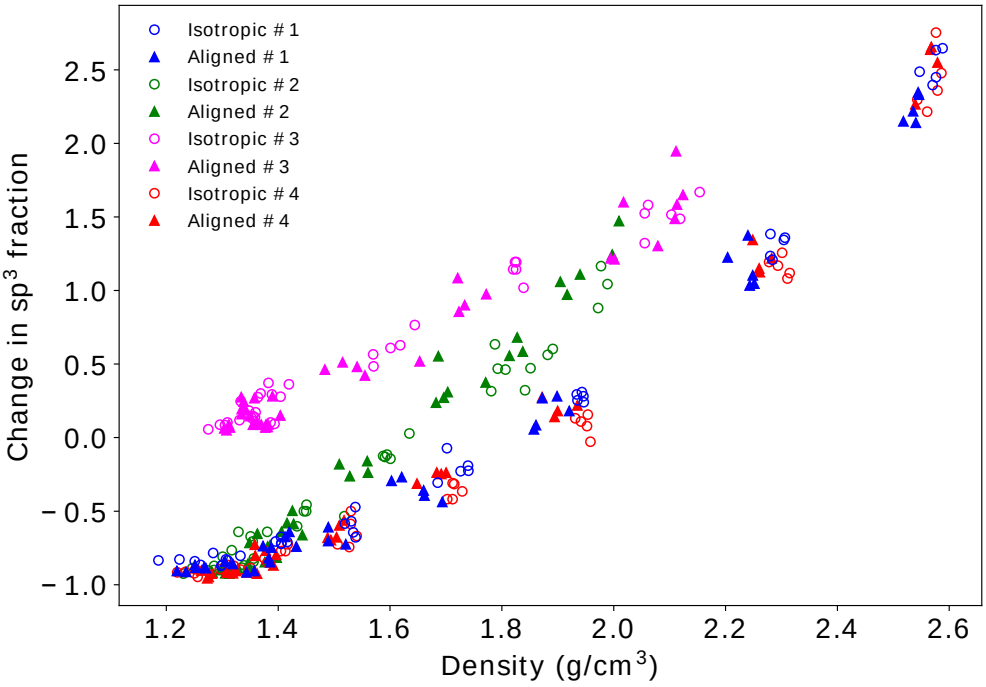

Figure 208: Change in sp3 fraction vs density for all the four pathways.

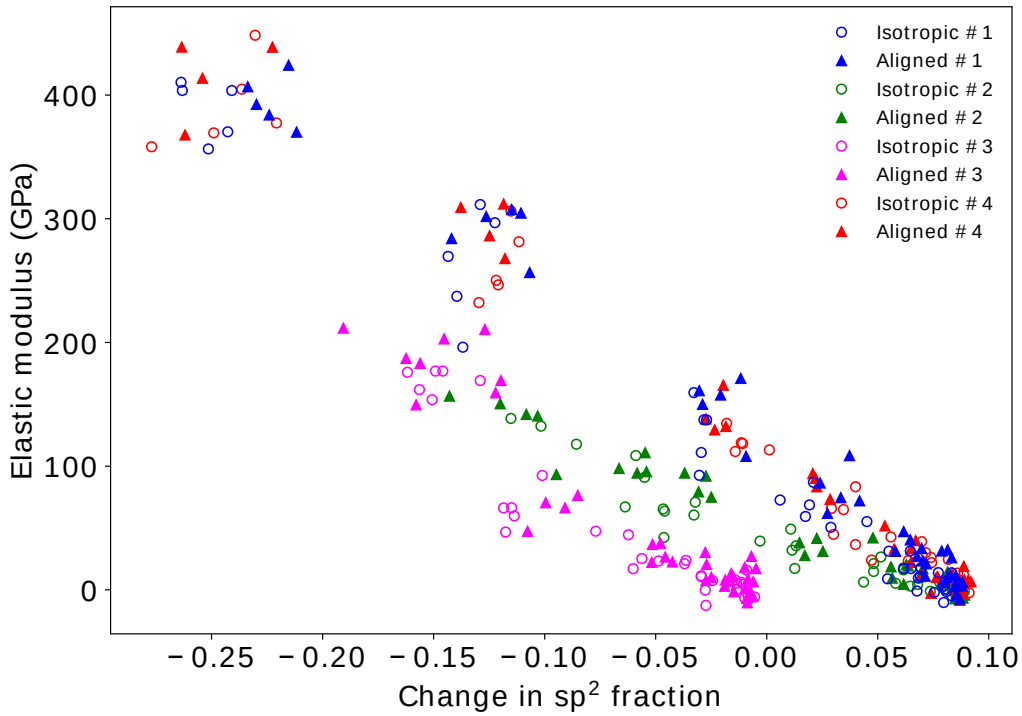

Figure 209: Elastic modulus vs change in sp2 fraction for all the four pathways.

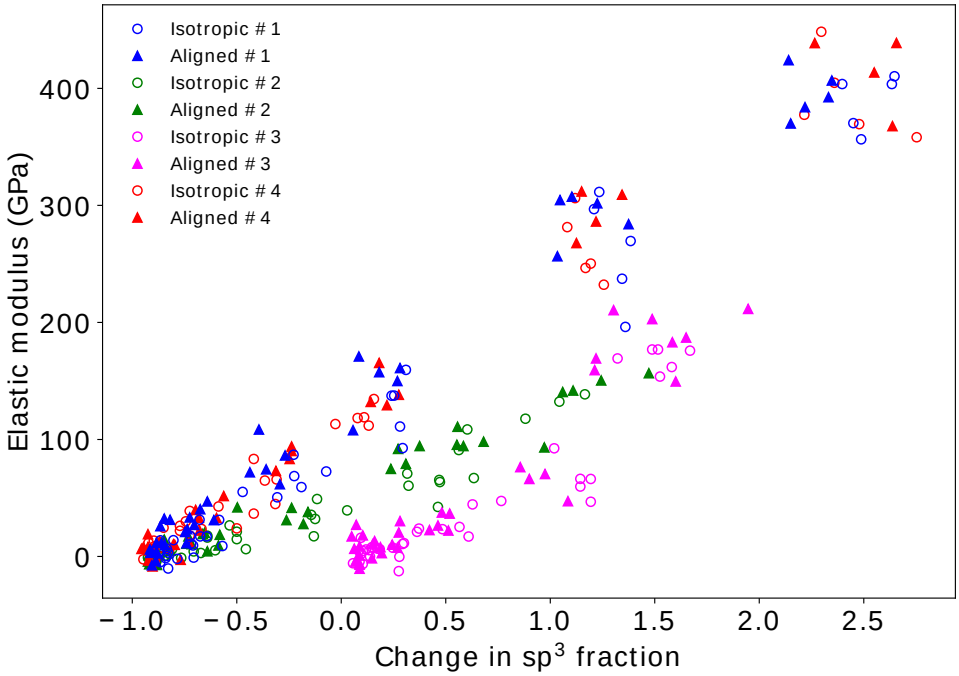

Figure 210: Elastic modulus vs change in sp3 fraction for all the four pathways.

An advantage displayed by CFs that have sp3 bonds incorporated in them is the enhanced compressive properties. Figure 211 depicts both tensile and compressive longitudinal modulus of CFs generated using pathway 1. We observe that the compressive modulus increases with density and displays modulus similar to its tensile counterpart at high densities.

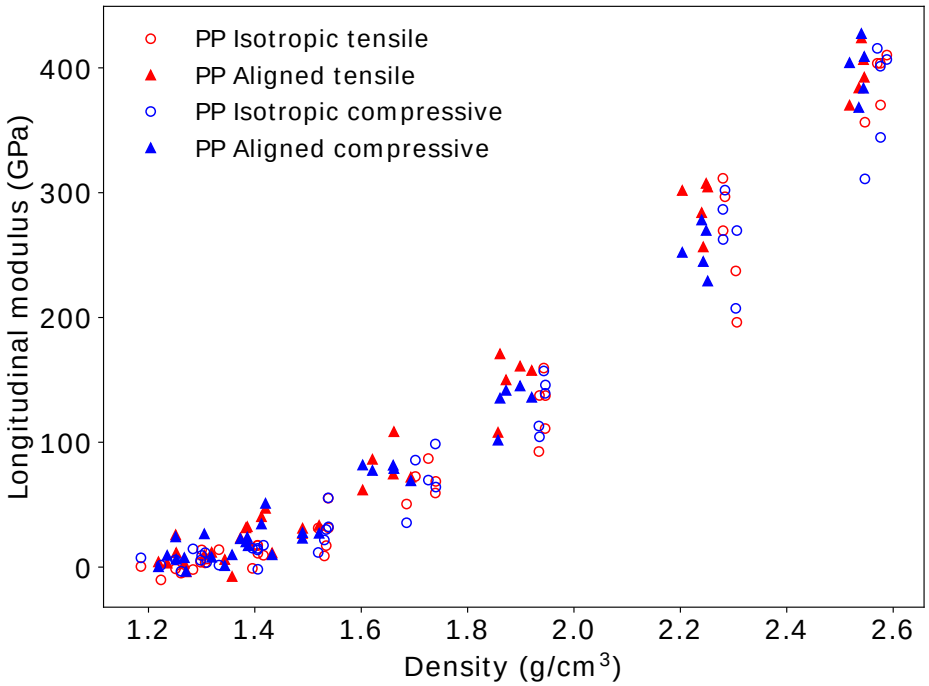

Figure 211: Tensile and compressive longitudinal modulus of CFs generated from petroleum pitch molecules using pathway 1.

While graphitization was not required to achieve the DOE target metrics, it was implemented in the framework to test its flexibility to model a different CF synthesis process which include such a step at ultra-high temperature, and validate it against commercial graphitized CFs. CF obtained using pathway 1 at around a density of 2 g/cm^3 were subjected to a graphitization step at around 3000 K. Figure 212 depicts the elastic modulus obtained. Graphitization was successfully simulated and generated CFs with a higher modulus compared to the CFs without the graphitization step, while achieving good agreement with experiment.

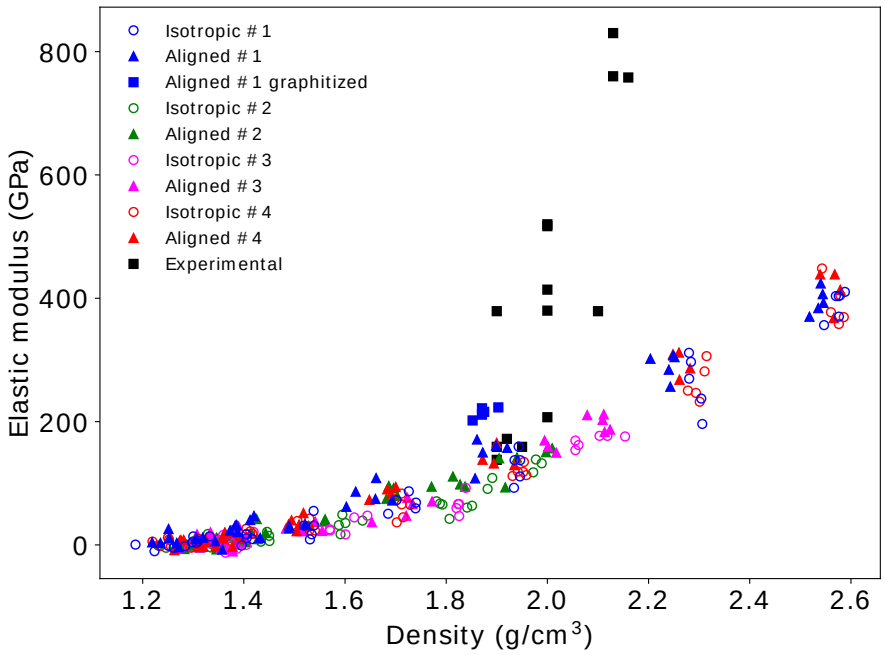

Figure 212: Elastic modulus vs density for all the pathways. Elastic moduli obtained via additional graphitization for some CFs generated using pathway 1 are also plotted.

A subset of PP-based CFs generated from pathway 1 with a density around 2 g/cm^3 were subjected to an additional graphitization treatment. The procedure is depicted in Figure 213. The CFs obtained were annealed at T_{high} K for t_{eqb} ps. After cooling down to room temperature, the modulus was calculated with a simulated tensile test. To optimize the parameters T_{high} and t_{eqb}, a range of values was tried for both, with T_{high} varied between 3000-7000 K and t_{eqb} between 5-200 ps. The modulus obtained are plotted in Figure 214. T_{high} of 3100 K was found to provide the highest modulus. While the modulus increased with t_{eqb} initially, it was found to saturate after t_{eqb} of 100 ps. The modulus obtained are in good agreement with experiments. The change in sp^2 and sp^3 fractions were plotted against density and results are displayed in Figure 215. Comparatively higher sp^2 fraction in graphitized CFs were observed.

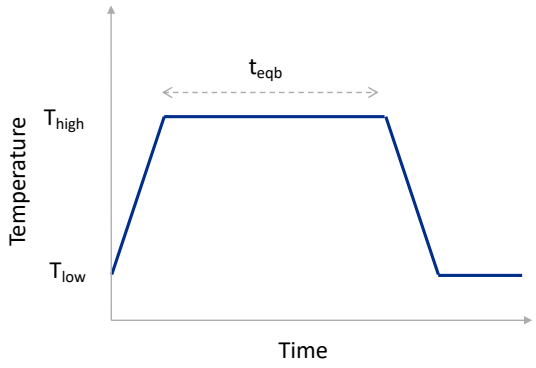

Figure 213: Procedure used for graphitization.

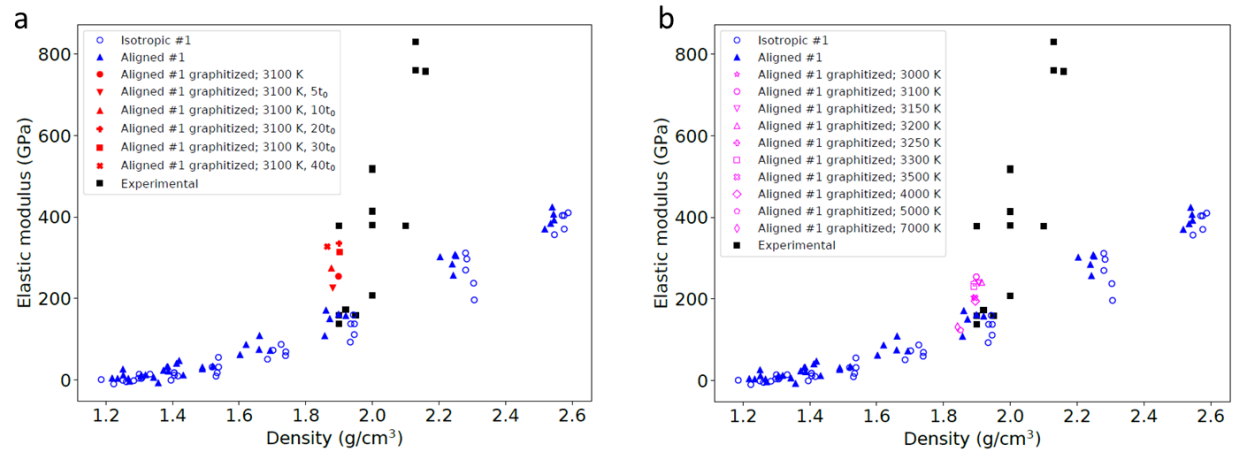

Figure 214: Elastic modulus as a function of density for PP-based CFs generated using pathway 1; graphitized fibers generated by a. varying T_high and b. varying teqb with T_high fixed at 3100 K.

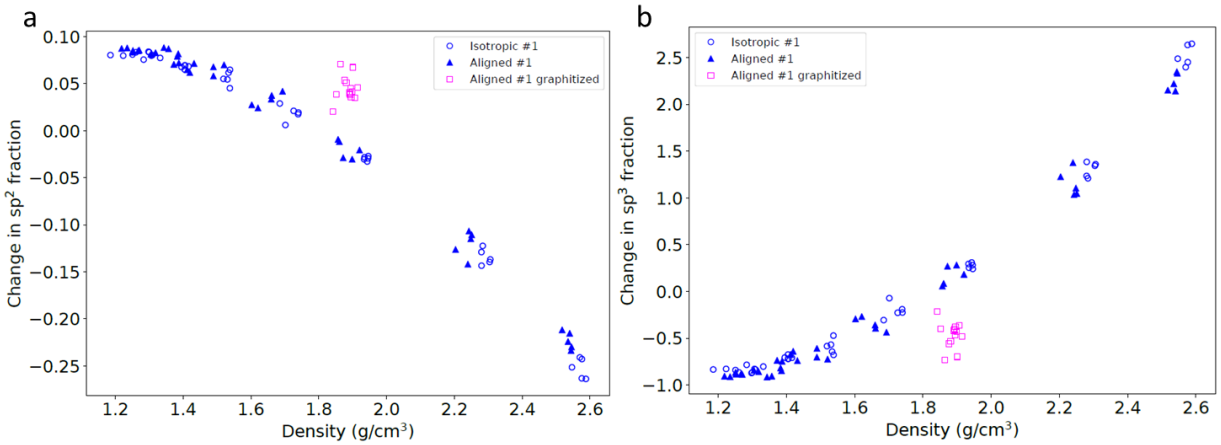

Figure 215: Change in a. sp2 and b. sp3 fraction as a function of density; graphitized CFs contain higher sp2 fraction compared to non-graphitized CFs.

It is worth noting that the simulated graphitized CFs (red data in Figure 216), differ significantly in their performance compared to CFs that were only carbonized. While we were not able to achieve the ultra-high values for modulus of some commercial graphitized fibers (black data in Figure 216), the trend of the simulated CFs clearly is in excellent agreement with the experimental data. Once again, this is obtained directly and without fitting the modeled data. Furthermore, the clear diversification in performance vs density between graphitized and ungraphitized CFs points to clear differences in the role of CFs and potentially proposing alternative routes for CF synthesis. Graphitization is, of course, the current method used to achieve very high modulus, and the effectiveness of the models here developed in capturing it is well represented by the asymptotic trend of the density to that of bulk graphite (2.266 g/cm^3). Yet, an alternative method, for which CF can achieve equally as high modulus, can be obtained by increasing the density beyond that of bulk graphite, essentially through a sp^3 rich network, rather than a sp^2 network.

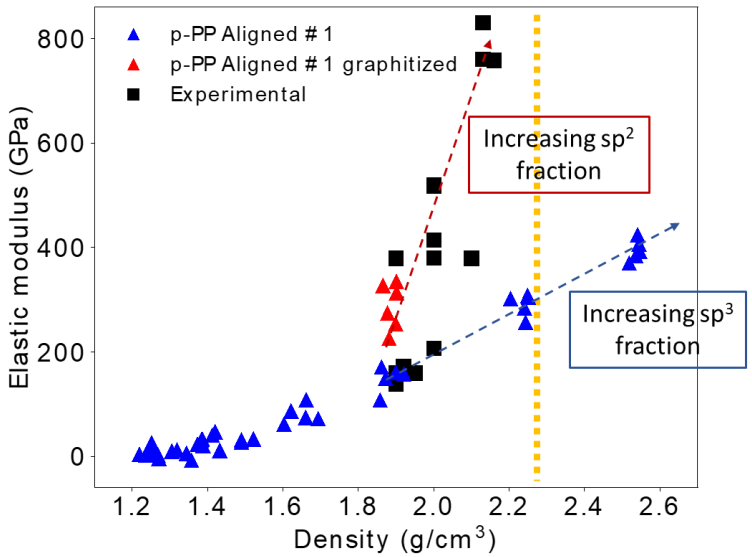

Figure 216: Blue triangles show the relationship between density and elastic modulus produced by the models. The theoretical maximum in density for sp2 graphite is around 2.27 g/cm3 (yellow dashed line). For the model to move towards higher densities additional sp3 bonding must occur. The black squares are experimental data from graphitized CF. Red triangles shows updated modeling to account for graphitized CF.

Achieving high density will require, from an experimental standpoint, a revised fabrication process. However, the benefits may go beyond the ability to use lower processing temperatures, but also removing the requirement of the use of mesophase pitch to achieve high modulus. As shown in Figure 217, both isotropic and mesophase pitch can be used at high density to obtain high performing CFs. Compared to graphitized systems, where only the tensile modulus achieves ultra-high values, high density CFs, may have very similar tensile and compressive modulus, enabling the applications of CFs in load bearing applications.

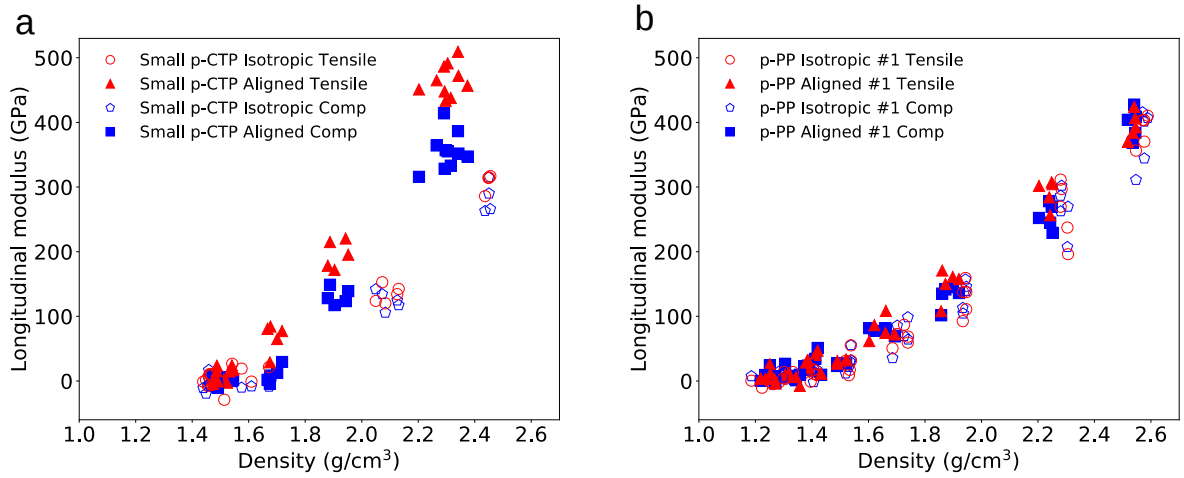

Figure 217: Tensile and compressive modulus as a function of density for CTP and PP.

Bio-PAN-Based

Using the newly developed CGMD modeling framework developed in BP2, the comprehensive correlative analysis on the PAN-based CF synthesis was further improved and optimized. Over 100 simulations were performed with systematically varied parameters in each processing step, including temperature, pressure, time and external stressing force. From these simulations, the modulus of the produced fiber was calculated. Information was extracted for several material properties in intermediate process steps as effective system descriptors. This allowed for identification of correlations among these system descriptors and the fiber modulus (as shown in Figure 218). Through such correlation, structural parameters that are highly correlated with mechanical performance were evaluated for significance from a physical point of view. For example, from Figure 218, a very strong correlation was identified between the number of ladder structures and the graphitic fraction, which is physically expected and justified. These results also show that a higher graphitic fraction leads to a higher CF density and modulus. These findings affirm the importance of the fiber stabilization stage, and through a quantification of such a relationship, it can be immediately used to guide and predict the mechanical performance of a specific fiber.

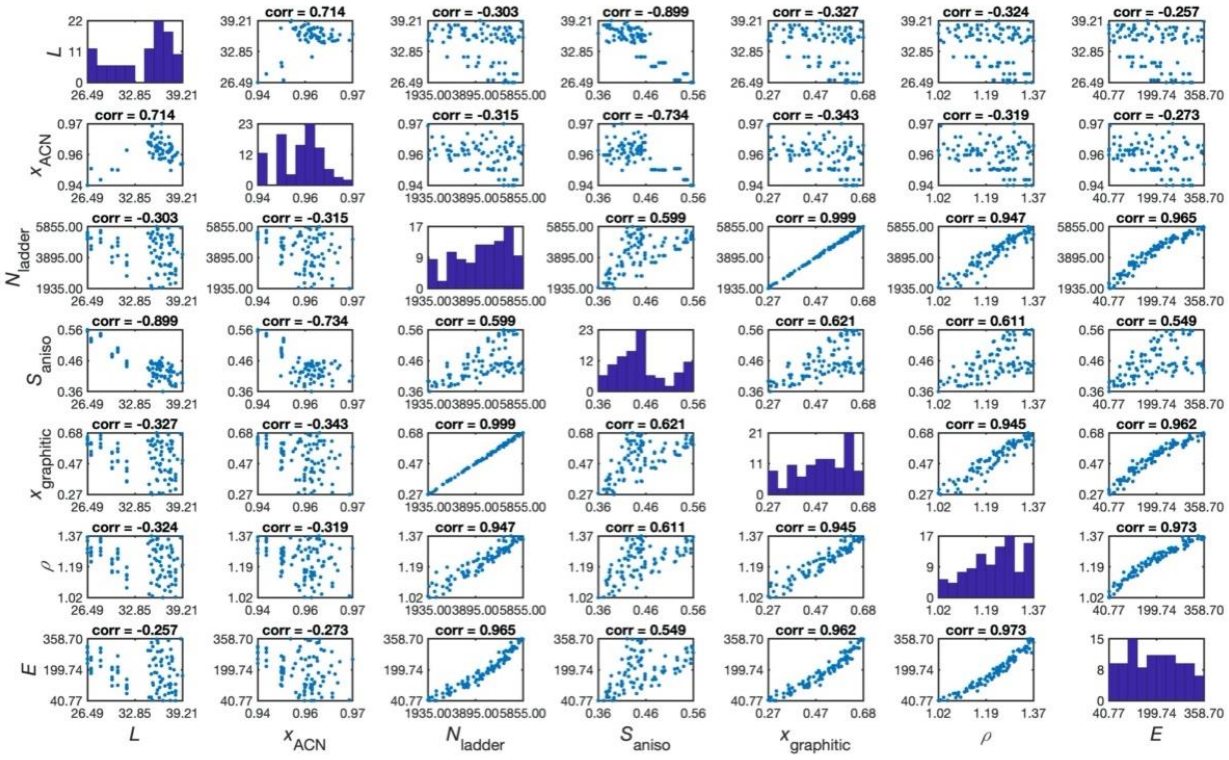

Figure 218: Correlations among the system descriptors and the fiber mechanical properties.

To compensate for the limited ability to represent bond forming and breaking within CGMD, the airebo force field (FF) was adopted as a classical FF capable of describing the bond forming and breaking based on the interatomic distances among the atoms. As shown in Figure 220, the CGMD FF with the airebo FF were compared, where a reasonable agreement could be seen from

both the structure and stress-strain relationship. In addition, based on this comparison, the parameters of the CGMD FF can be fine-tuned to further improve the consistency between the two force fields as well as the accuracy of modeling framework. With this new module, over 100 simulations were performed where the fiber was stretched up to their failure point, and the maximum elongation was recorded. In Figure 220, the maximum elongation and the strength were plotted versus the modulus, showing a negative correlation and a positive correlation respectively. These results are expected based on experimental results and provide a good validation of the robustness of the method. However, the absolute values of the elongation and strength are overestimated compared to experimental values, due to scaling factors (nanoscale vs macroscale elongation and strength), or to the absence of any defect, void etc. This was later addressed by converting the GCMD model to a fully atomistic model by including all the H and allowing them to relax, as described below.

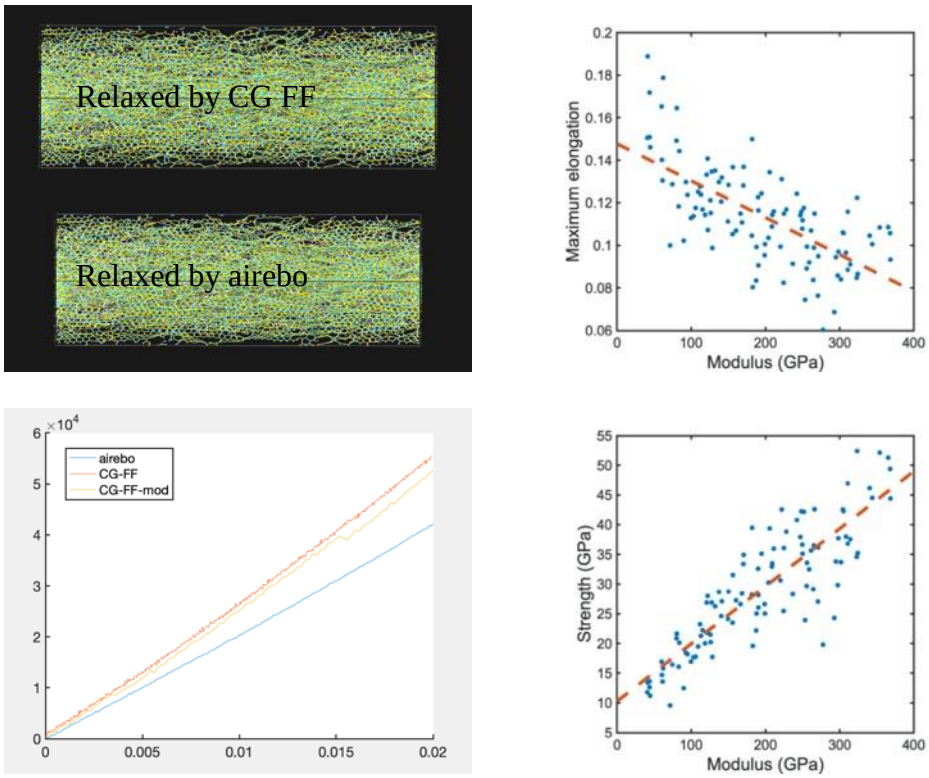

Figure 219: Comparison between the CGMD force field and airebo force field. Correlation between fiber elongation and fiber modulus.

Using the existing data, the relationship between the fiber modulus and the processing conditions was investigated in the CGMD simulations, such as the stretching force, temperature, pressure and time in each step (polymerization, stabilization and carbonization) (Figure 221). The model showed that the fiber's mechanical properties are more sensitive to the changes of stabilization conditions, compared with the variations of the conditions in other two stages. Based on these preliminary findings, it was decided to focus on the stabilization related parameter, to clarify the correlations among these parameters and their joint effects on the fiber properties.

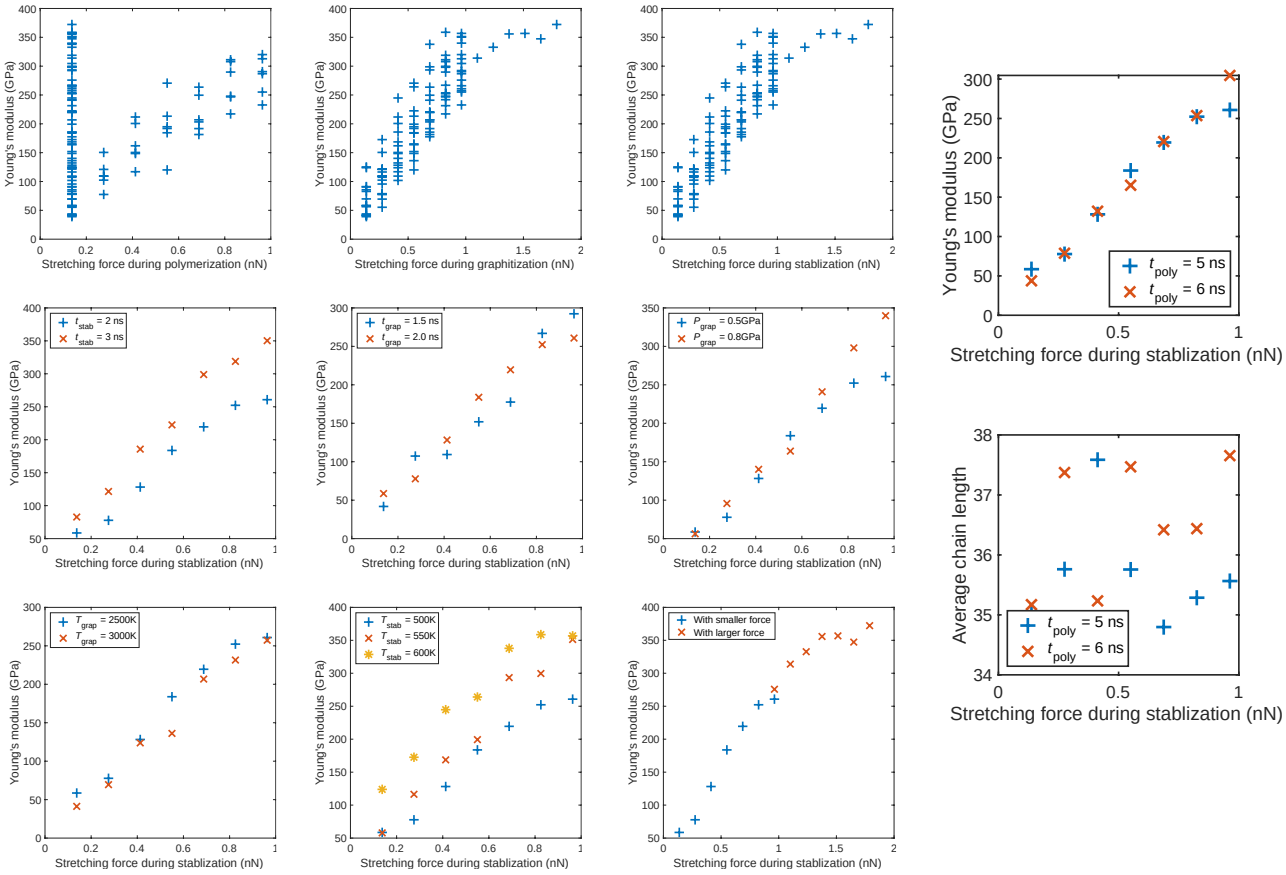

Figure 220: Relationship between Young's modulus and processing conditions in simulations.

As a further development if the CGMD modeling the CF manufacturing process was investigated at every primary step, including every relevant parameter controlling the synthesis of CF (Figure 221). By exploring the multi-dimensional parametric process phase space in relation to the structural and chemical characteristics of the resulting CF, in addition to the elastic performance of the CF, not one but hundreds of models have been generated, a first to our knowledge, for modeling PAN-based fibers. This allowed such modeling infrastructure not only to capture a realistic representation of one PAN fiber, but to allow predictive capabilities in the effects of processing PAN-based fibers into CF. Through correlative analysis (Figure 222), such correlations can be exploited directly for experimental implementation.

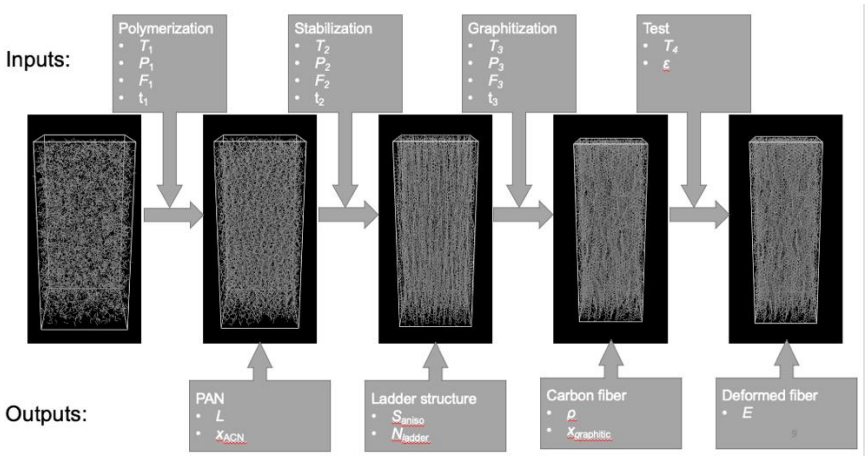

Figure 221: Evolution of the CG PAN-based CF in relation to synthesis parameters (input) and chemical, structural parameters of intermediate compounds and the final CF.

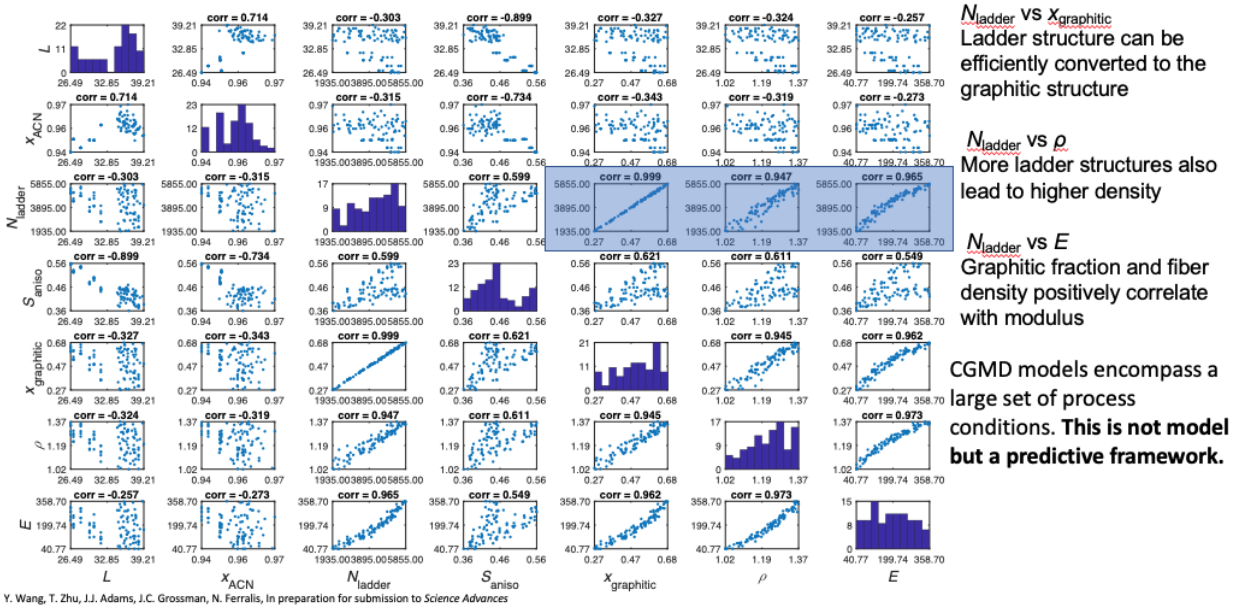

Figure 222: Correlative analysis between processing parameters and structural, chemical, and elastic characteristics of PAN-based fibers.

While the agreement with experiment of the elastic properties and densities are quantitatively good (with trends in excellent agreement), the approximations introduced with the CGMD, resulted in a slight overestimation on modulus, and a slight underestimation of density. This is somehow expected as such approximations limit the ability to capture the fine details of the bonding configuration (as H atoms are included into the modeling grains). This does not mean the CGMD approach is faulty, but rather that it allows a good approximation of the real system that can be achieved at a larger spatial and time scale. Therefore, CGMD approach should be, and needs to be, the primary approach for constructing realistic models for PAN-based fibers.

For a better representation of their performance and final structural properties, such models need to be reconverted back to fully atomistic models (Figure 223). It is worth noting that adopting a CGMD approach first and a conversion to atomistic later (as opposed to carrying out a full atomistic representations of hundreds of models) is still computationally more efficient and physically feasible that carrying out modeling using a full atomistic approach.

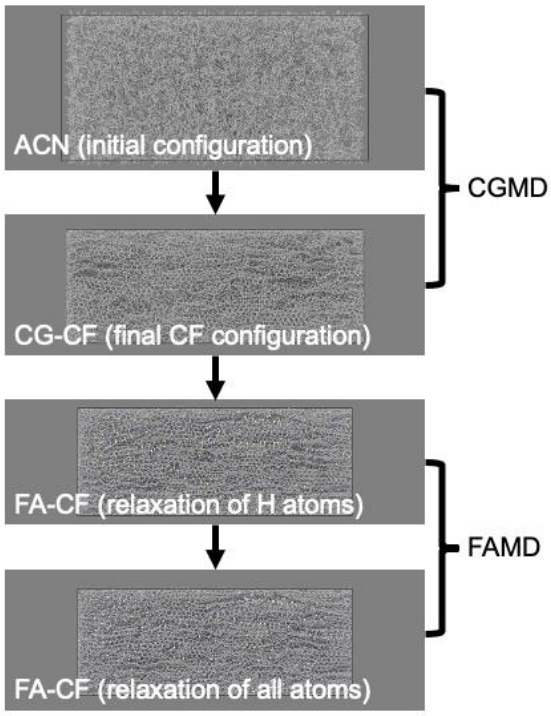

Figure 223: Conversion of CGMD to gain the molecular arrangement in the CF followed by fully atomistic MD to adjust the modulus and density to more completely and accurately predict experimental modulus and density.

The conversion from rules based CGMD to atomistic models is achieved on the final CGMD models by following the steps:

- Atom type assignment
- Appropriate hydrogen termination
- Relaxation of H atoms with fixing the other atoms
- Relaxation of the full configuration

Since bond relaxation is the only mechanism at play, the computational load needed for the conversion is minimal and straightforward. Once the atomistic models are available, elastic characterization is carried out similarly to the pitch based atomistic modeling, through stress-strain tests. Using this approach data shows that the obtained densities and elastic moduli are in excellent agreement with the available experimental data.

One additional feature that atomistic modeling can provide, if the bonding potentials are correctly implemented, is the ability to describe failure mechanisms, this is shown in Figure 224. As the atomistic description is particularly accurate, also in determining bond breakage, the determination of elongation and strengths may be achievable within this framework. Figure 225 shows an example of the microstructural evolution and volumetric strain at different strain levels, and Figure 226 shows how the stretching force, stabilization temperatures and stabilization time can be used to predict the CF modulus as well as the point at which failure will occur.

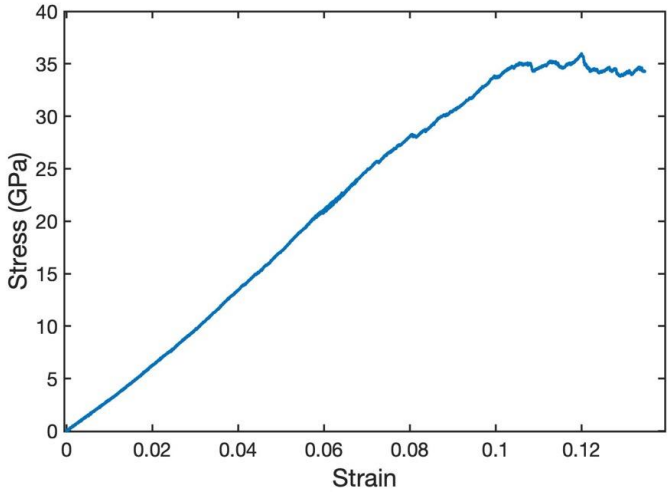

Figure 224: Stress-strain relationship predicted by FAMD using the ReaxFF force field (the same one for the pitch-based CF simulations)

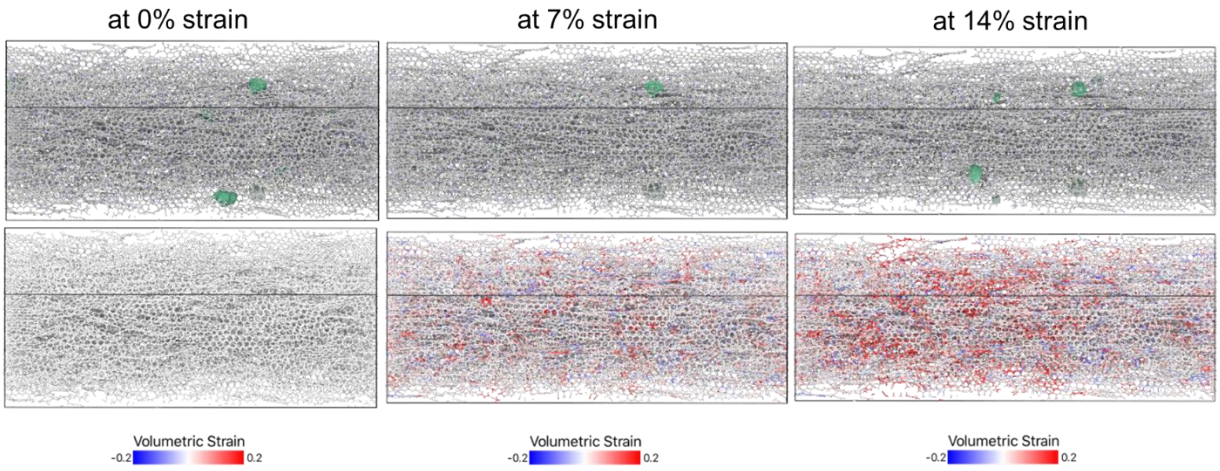

Figure 225: Microstructural evolution during PAN-based CF deformation at 0, 7 and 14% strain. Images at the top show the microstructural evolution during the simulation where the green polyhedrons represent the nano-voild in the CF (~1nm). The bottom images show atomic strain during the deformation process.

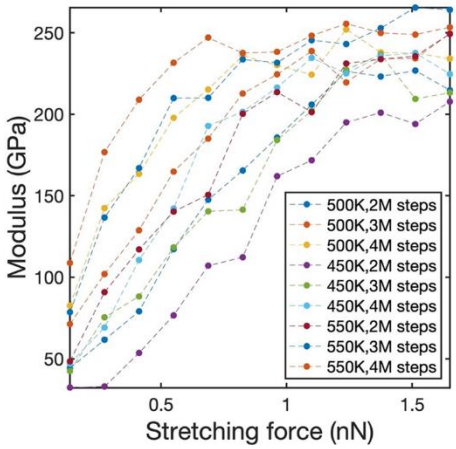

Figure 226: Results from the systematic investigation of PAN-based CF by varying stretching force, stabilization temperature and stabilization time.

As previously mentioned, when graphitization is not used (as CF produced in this project only require carbonization to achieve the DOE target metrics), the modeling framework points to the achievement of high tensile *and* compressive moduli at ultra-high density (> 2.2 g/cm^3) through the establishment of an extensive network of sp3 bonds. This was explored further by creating a comprehensive set of graphitized CF models, which are validated against graphitized commercial fibers with excellent agreement. The resulting framework highlights its flexibility in adapting to different methods for synthesis of CF fibers, that can be directly used by the end user to predict performance based on structure, precursor chemistry and fabrication parameters.

Similarly, the mechanical properties of PAN-CF obtained within the atomistic modeling framework through GC-MD, have been successfully validated with excellent accuracy being achieved. The resulting framework for PAN can provide flexibility in obtaining user-specific models based on specific structural, precursor and processing conditions. Furthermore, as previously shown, the large and comprehensive ensemble of models can be used, based on the end-user needs to identify correlations across processing or structural properties of the CF.

Given time constraints and the unavailability of density data for bio-PAN-based fibers, commercial CF fibers were used as validation points, obtained through materials databases such as MatWeb (http://www.mathweb.com). The validation against such fibers is shown in Figure 227, with excellent agreement. Excellent agreement is obtained with no adjustable fitting parameter, but it is obtained directly because of the modeling prediction.

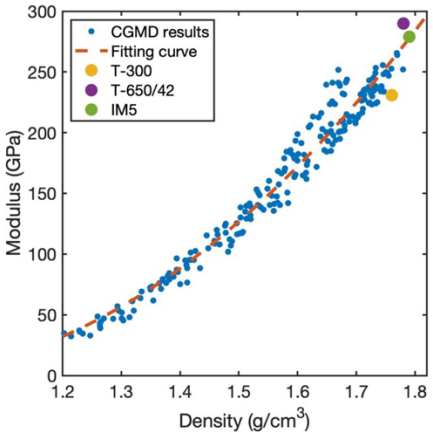

Types of PAN CF	Exp. *E* (Gpa)	Sim. *E* (GPa)	Error (%)
T-300	231	259	12.1
T-650/42	290	271	-6.6
IM5	279	277	-0.7

Figure 227: Validation of performance of PAN-based CF from commercial PAN fibers. The error is well within ±15%.

Macro-Level Engineering Models and Analyses

Up until this point, when testing CF-reinforced composites, experimental values for strain have been calculated using a digital image correlation (DIC) program. This method requires the use of a high-speed camera and a white-on-black background paint scheme applied to the specimen being loaded to track strains throughout the entire specimen's gauge length. This process results in very accurate strain measurements at small strains, but at higher strains (>1%) the black paint applied to the specimen to provide contrast for the white speckle patter can crack and distort results.

This distortion of results presents itself as irregular strain measurements just before specimen failure, as can been seen in Figure 228. Due to the distorted results, determining the exact strain-to-failure for composite specimens becomes more difficult. This is particularly problematic when trying to match composite properties with single-fiber properties provided by ORNL, and when only a few tests can be performed.

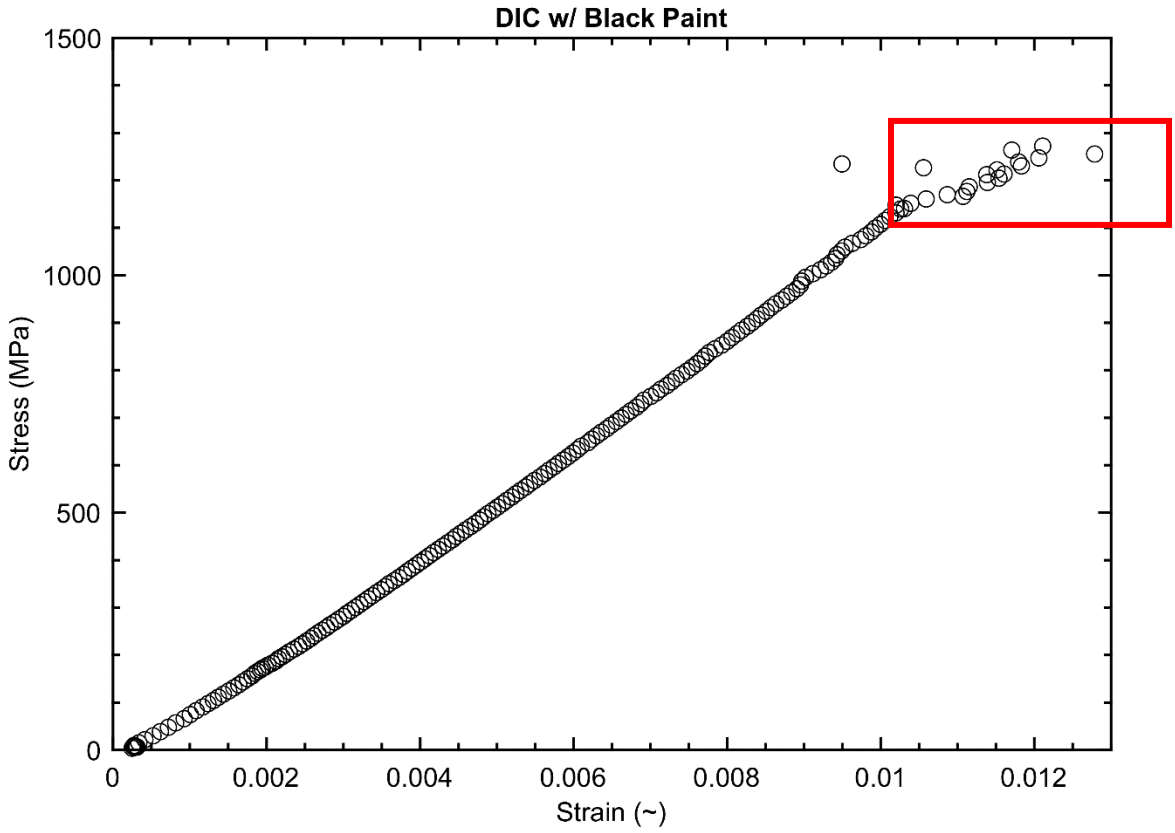

Figure 228: Example of paint cracking that results in irregular strain measurements beyond 1% strain, highlighted by the red box.

To remedy this, a new approach to DIC was developed for CF composites. Rather than applying a base-layer of black paint, a high gloss white paint speckle pattern was applied directly onto the composite coupons without a base paint layer. Because the composites are not as dark as an otherwise painted specimen, some technical camera specifications were modified: including exposure, gamma and brightness. This process was iterated until a suitable contrast for DIC to run without accumulating errors was achieved. Tensile tests were then run, and DIC processed to determine if improvements to the stress-strain plots and data were evident.

As can be seen in Figure 229, the adapted approach improved the accuracy of results, especially beyond 1% strain. As a result, the strain-at-failure can be more easily determined without the need for excessive testing. This is particularly important when testing composites using CF provided by ORNL. Many CF samples sent from ORNL have been low-volume, necessitating that only a few tensile specimens being fabricated. With a small sample size, high accuracy and test reliability are paramount; this adjusted DIC method allows for both.

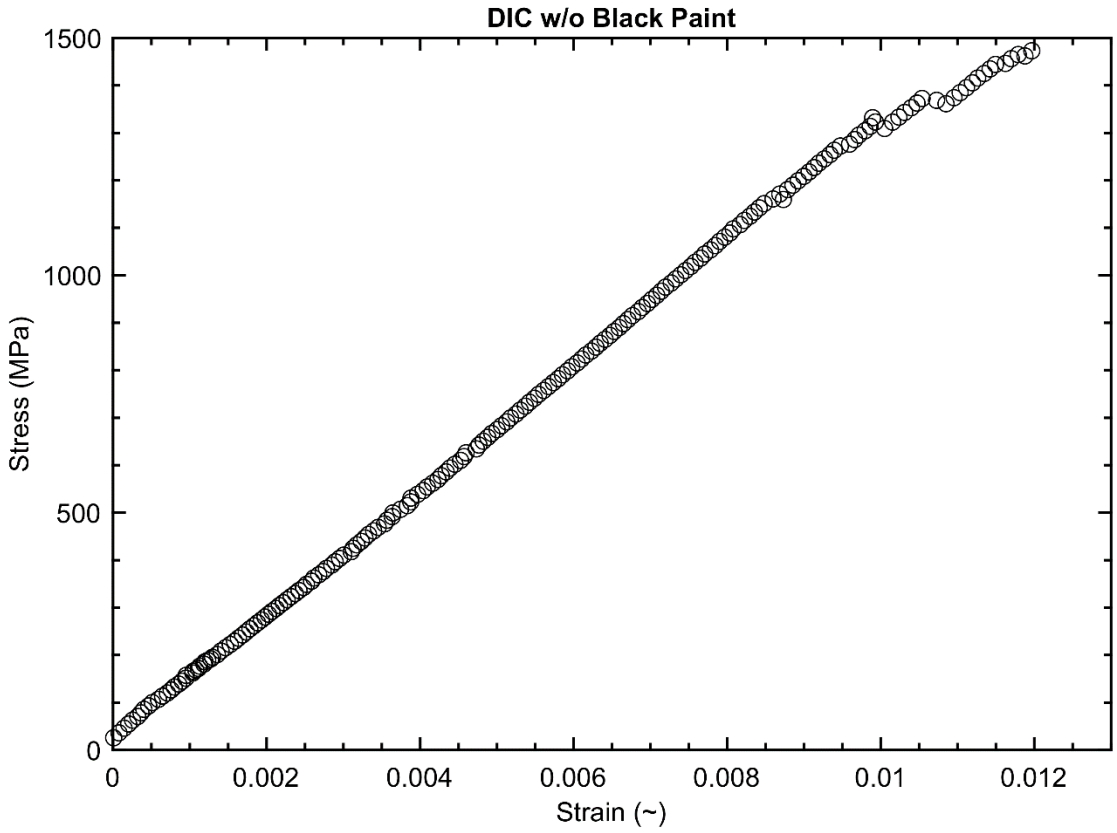

Figure 229: Example of adjusted DIC method without a black paint background that results in more predictable, and easily measured failure strain.

An example of the improvements in measurement consistency between tests can be seen in Table 65. The adjusted DIC method had more consistent and precise results, allowing for better measurements of composite performance.

Table 65: Comparison of failure strains for AS4 composites strained to failure in tension.

AS4 Composite Comparison b/w DIC Methods		
	Failure Strain	Std.
Standard DIC	0.013	±0.003
No Black Background	0.012	±0.0004

The developed macro-scale models, based on FEA, were tested on the scaled up PPM and bio-PAN CF. Given the limited volume of PPM CF tows, only 0° tow-level composite coupons were manufactured. The composite level properties derived from testing on these coupons are given in Table 66.

Table 66: Experimental constants derived from composites data. Data in this table is reflective of composite properties, not single fiber properties.

Experimental **COMPOSITE** Values		
Fiber Used	E_{11} (GPa)	0° Tensile Strength (MPa)
2939 KOP300 HT-Carbonized	49.18 ± 2.65	NA
2938 KOP300 HT-Carbonized	52.04 ± 3.11	NA
2933 KOP300 Graphitized	111.85 ± 16.42	NA

Table 67 contains fiber properties that were estimated using composite properties obtained at UW and the Rule of Mixture. Fiber properties estimated by ORNL are also included for comparison. Estimated fiber properties were in close alignment with ORNL's results for graphitized samples, but were slightly lower for carbonized samples.

Table 67: Single fiber properties estimated using the composite method.

Experimental **FIBER** Property Estimates				
Fiber Used	E_{11} (MSI) (**UW**)	E_{11} (MSI) (**ORNL**)	Strength (MPa) (**ORNL**)	Strength (MPa) (**UW**)
2939 KOP300 HT-Carbonized	17.24 ± 1.2	20.41	151.41	126.5 ± 13.7
2938 KOP300 HT-Carbonized	18.28 ± 0.98	21.26	157.18	101.2 ± 30.4
2933 KOP300 Graphitized	39.98 ± 1.7	41.78	227.32	208 ± 12.9

Two batches of 1.5k tows of bio-PAN CF (BP3SU2-2 and BP Batch 2) were fabricated only as 0° and 90° composite coupons due to the limited volume of fiber. The tow-level composite properties derived from testing on these coupons are given in Table 68**,** and Table 69 shows matrix level properties used in the EpiKote/bio-PAN composites.

Table 68: Experimental constants derived from composites data. Data in this table is reflective of composite properties, not single fiber properties.

Experimental **COMPOSITE** Values				
Fiber Used	E_{11} (GPa)	E_{22}(Gpa)	ν_{12}	0° Tensile Strength (MPa)
BP3SU2-2	80.99±5.31	4.86±0.85	0.33±0.01	619.78±36.2
BP (Batch 2)	74.8±4.50	4.84±0.77	0.32±0.01	473.2±50.68

Table 69: Calculated properties of neat resin matrix.

Matrix Properties (EpiKote 135)			
Modulus	Poisson	Tensile Strength	Shear Strength
GPa	~	MPa	MPa
2.72±0.11	0.35±0.017	67.64±1.11	19.64±2.52

Single filament CF properties provided by ORNL are shown in Table 70 and compared to single fiber properties that were estimated using the tow-level composite level properties obtained at UW with the Rule of Mixture. The measured tensile strength was lower than that provided by ORNL, but this was expected due to the fibers being un-sized and repeatedly handled in the composite manufacturing process. Single fiber properties could not be confirmed at UW by the time the project ended to date due to equipment maintenance. Without validation of the single filament CF properties the results from the tow-level composite tests for modulus values were ±15% considering the spread of error for the data. Strength and strain values were more variable due to handling of the unsized fibers.

Table 70: Bio-PAN fiber properties calculated from tow-level composites and single filament properties from ORNL for one of the samples for comparison.

Fiber Property Comparison			
Test Method	Tensile Strength (ksi)	Strain (~)	Tensile Modulus (Mpsi)
Single Fiber Test (BP3SU2-2) ORNL	288.97±29.3	.0106±0.009	27.15 ± 0.6
Composite Method (BP3SU2-2) UW	179.4±9.1	0.008±0.001	24.54±1.19
Composite Method (Batch 2) UW	134.18±14.6	0.0074±0.003	22.63±0.65

Machine Learning (ML) Predictive Analysis

A major effort was to refine and complete the development of ML models from encrypted data (to overcome the limitations imposed by export control on the CF processing data) to predict performance metrics of CF. The training dataset (obtained from ORNL as part of this consortium) was expanded, and while still not ideal in terms of covering the processing parameter phase space, it provided enough data for the ML to be successfully produced when combined with data augmentation methods. Refined augmentation methods based on hyperplane fitting of the parametric phase space was used to produce more data based on that provided by ORNL, without relying on pure randomization over the existing data. Previously, new data was created based on randomized data that was created based on expected deviations (experimental error or measurement uncertainty). This was improved by imposing expected inter-relations across parameters based on such deviations, limiting the production of unphysical data-points. Using this strategy from a dataset of 120 fibers, more than 3600 new data points were added. The prediction models for modulus, strain, and strength (in addition of a simple classifier determining, also using literature data, whether a CF could be produced from the provided processing parameters) achieved a Mean Absolute Error (MAE) of less than 5%, which is well below the required target metric for this project (±15%). Furthermore, to achieve universality across different feedstock, the training set was optimized to include pitch-based fibers as well as PAN-based CF. A selected yet chemically comprehensive small set of fibers was chosen as the validation set to determine the final accuracies and MAE, which for all the final models is ≤5%.

Furthermore, to reduce the learning curve and improve in the immediate utilization of such models (with no requirement in terms of software needed, and no training involved), the best candidate ML models for predicting CF performance from processing conditions, as well as precursor performance based on chemistry, new web-based ML interfaces were built. Through these simple “point-and-click” interfaces, any user can directly get predictions on the performance of either CF or precursors. It is worth noting, once again, that for processing conditions, the encryption key from ORNL need to be obtained for these models to be used, upon certification of compliance to Export Control. Any further detail, or request can be directed to the ORNL team within the consortium. Temporary URLs for the web interfaces are reported below. The same interface is available through the LightMAT consortium website.

ML models were translated into Javascript, and using TensorFlowJS, exported and converted to be used as web-based ML predictive tools. This approach was followed to create web-interfaces for prediction of pitch characteristics from chemical parameters, CF performance from processing conditions, and upscaling ML models to predict performance upscaling from micro-to-macro.

The ML models were created during BP2 based on the only available data from WRI. Using a targeted approach, a subset of characterization parameters was used to predict softening point and coking index. A screenshot of the prediction web-interface is shown below in Figure 40 using the temporary web page http://gridedgedm.mit.edu/tfjs/wri/.

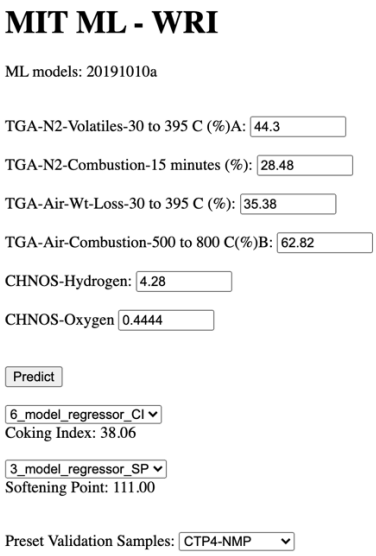

Figure 230: Screenshot from the web-based ML predictive tool that shows how analytical data are used to predict the coking index (carbon residue) and softening point for the pitch.

Similarly, the CF performance ML methods from processing data from ORNL were converted to web-interfaces. The C1 through C8 processing parameters are encrypted using a key available only to ORNL (and therefore unavailable to the MIT team). Of course, for a meaningful use of such models and web-interfaces, a prospective user will need to request and obtain access to such keys directly from ORNL. A screenshot of the prediction web-interface is shown below as obtained through the web page http://gridedgedm.mit.edu/tfjs/ornl/ is shown in Figure 231.

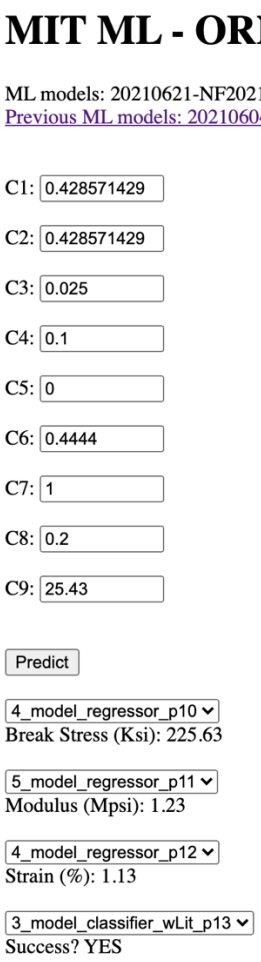

Figure 231: Screenshot from the web-based ML model to predict CF properties from encrypted CF processing data.

Finally, using ML models developed at the UW for upscaling micro-to-macro-modeling, similar interfaces were created to predict micro- (sheet-level) to CF and tow-level composite properties, as well as CF to composite models and downscaling composite to CF models. More explaination on where the sheet, fiber and composite properties come from are found in the micro- to macro-model model integration section. Each of such models and corresponding URL are shown in Figure 42 which were obtained through the temporary web page http://gridedgedm.mit.edu/tfjs/wyo/.

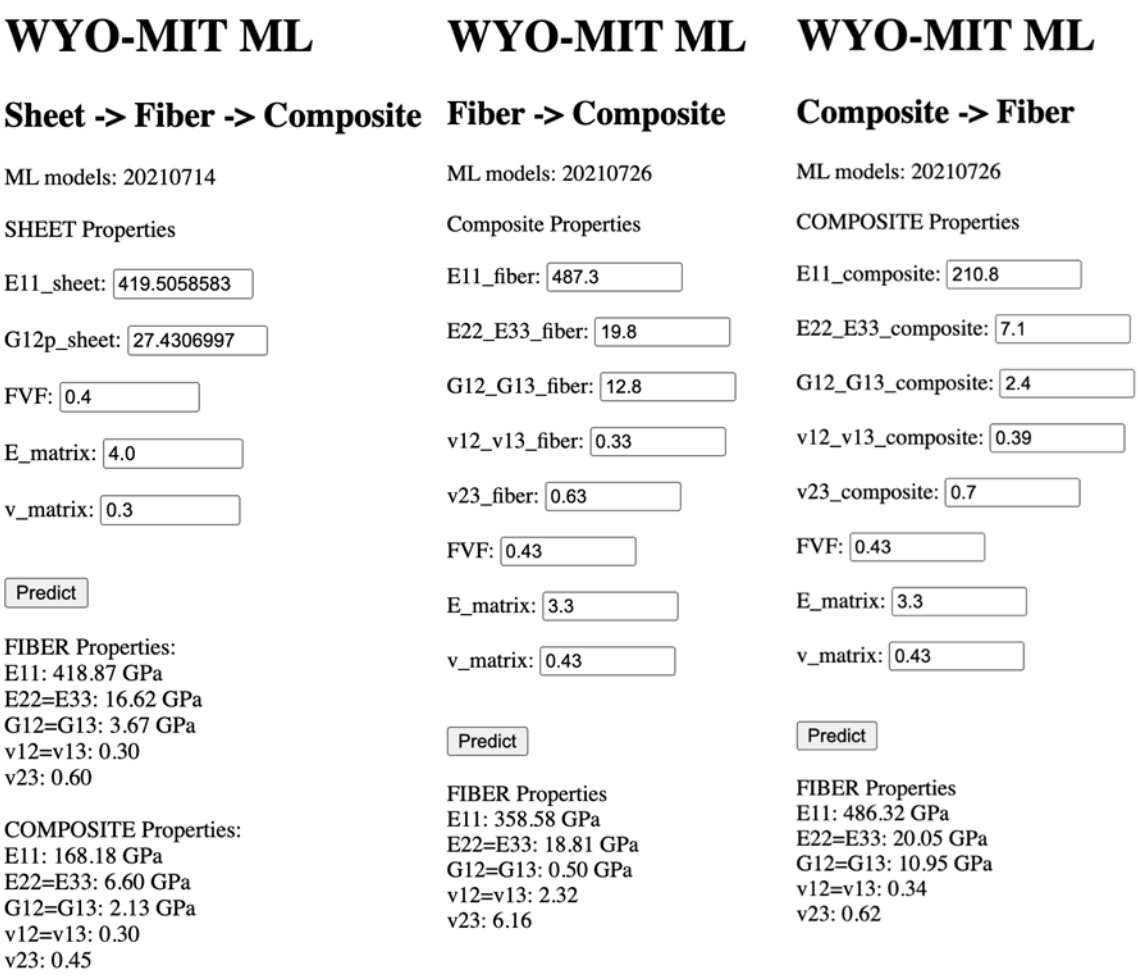

Figure 232: Output from the web-based ML models for the UW (WYO) and MIT integration of the micro- to macro-modeling to go from feedstock sheet chemistry through CF (fiber) to tow-level (composite) properties.

Micro and Macro-Level Model Integration and Validation

Prediction of Tow-level Composite Properties

An important goal for BP3 was to integrate the micro- and macro-models. To achieve this, work was performed to develop a NN capable of outputting the five elastic homogenized constants for a composite given the properties of the fiber and the matrix. In order to develop this tool, 20,000 composite microstructures were analyzed via the Abaqus micromechanics plugin. Each composite microstructure consisted of different material properties for the fiber and the matrix. Regarding the fiber, material properties ranged from, 30 – 75% fiber volume fraction, 80 – 500 GPa longitudinal modulus (E_{f11}), 2 – 20 GPa transverse modulus ($E_{f22} = E_{f33}$), 1 – 15 GPa in-plane shear modulus ($G_{f12} = G_{f13}$), 0.2 – 0.4 major Poisson's ratio ($\nu_{f12} = \nu_{f13}$), and 0.3 – 0.7 minor Poisson's ratio (ν_{f23}). Regarding the matrix, material properties ranged from, 1 – 4 GPa Young's modulus (E_m), and 0.3 – 0.45 Poisson's ratio (ν_m). The material properties for the fiber

and the matrix were used as the inputs to the NN and are summarized in Table 71. In addition, periodic boundary conditions were enforced and a 7 μm fiber radius was assumed. Ultimately, the output of the FEA model and the NN were the five elastic homogenized constants for the composite which are summarized in Table 71.

Table 71: Range of inputs for the fiber and matrix properties along with the outputs corresponding to the five elastic homogenized constants of the composite specimen used in the neural network.

INPUTS		OUTPUTS
Fiber		Composite
Fiber Volume Fraction	30 – 75%	Longitudinal Modulus E_{11}
Longitudinal Modulus E_{f11}	80 – 500 GPa	Transverse Modulus $E_{22} = E_{33}$
Transverse Modulus $E_{f22} = E_{f33}$	2 – 20 GPa	In-Plane Shear Modulus $G_{12} = G_{13}$
In-Plane Shear Modulus $G_{f12} = G_{f13}$	1 – 15 GPa	Major Poisson's Ratio $\nu_{12} = \nu_{13}$
Major Poisson's Ratio $\nu_{f12} = \nu_{f13}$	0.2 – 0.4	Minor Poisson's Ratio ν_{23}
Minor Poisson's Ratio ν_{f23}	0.3 – 0.7	
Matrix		
Young's Modulus E_m	1 – 4 GPa	
Poisson's Ratio ν_m	0.3 – 0.45	

The set of 20,000 data points were normalized in order to train the NN to predict the five effective elastic properties of the composite specimen. Two different NN architectures were tested. The first network architecture was designed with an input layer containing eight neurons and an output layer containing five neurons. The goal of this design was to utilize a single network to predict the composite properties. However, this architecture could not *accurately* predict all five properties. Thus, the second network architecture was designed with an input layer containing eight neurons and an output layer containing one neuron, as illustrated in Figure 233. Therefore, five separate networks were constructed to predict the composite properties individually. As a result, each network could be independently tailored to produce the best results.

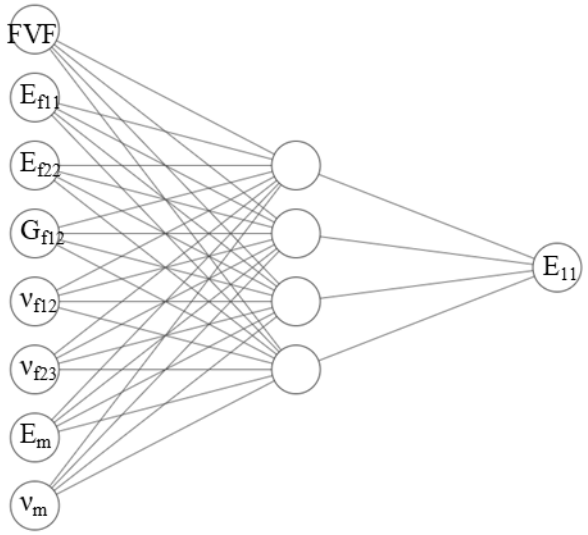

Figure 233: Neural network architecture used to predict the longitudinal modulus of the composite specimen.

All five networks were trained using the rectified linear (ReLU) activation function, the root mean square propagation (RMSprop) optimizer, and the mean square error (MSE) loss function. Other activation functions, optimizers, and loss functions were tested but yielded inferior prediction capabilities. Each network was trained for 100 epochs with a batch size of 32. These parameters produced excellent convergence of the loss function versus the number of epochs.

In order to test each network, the value of the predicted elastic constant was plotted against the true (observed) value of the elastic constant. Therefore, the ideal NN would yield a linear regression line in the form of $y = x$. Figure 234, Figure 235, Figure 236, Figure 237 and Figure 238 plot the predicted vs the observed value for each of the 5 elastic constants. In addition, Figures 44-48 also plot the corresponding linear regression line and the resulting MSE. From these figures, it is evident that the neural network's predictions are in good agreement with the true values. The four elastic constants E_{11}, E_{22}, G_{12}, and ν_{12} have excellent results with mean square errors less than or equal to 1.6E-4. The elastic constant ν_{23} in Figure 238 has the most deviation from the observed values, however, it still maintains a MSE of only 3.6E-4.

In conclusion, this project yielded successful results via five NN that can be used to accurately predict the five elastic homogenized constants for a composite specimen. Each network requires eight inputs corresponding to the fiber and matrix material properties. From these inputs the networks can be used to accurately predict the homogenized constants with a MSE of 3.6E-4 or less.

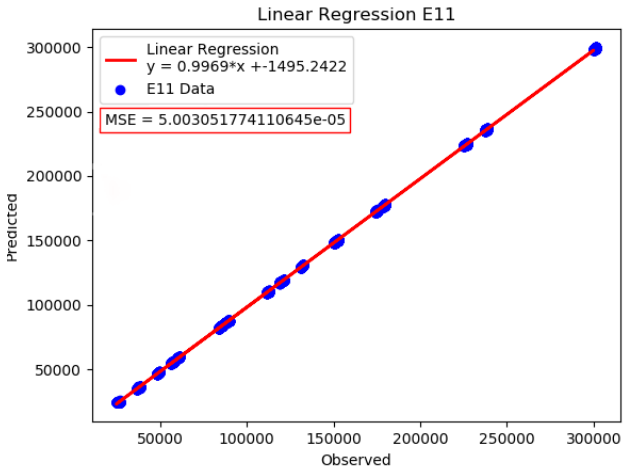

Figure 234: Predicted versus observed values for E11.

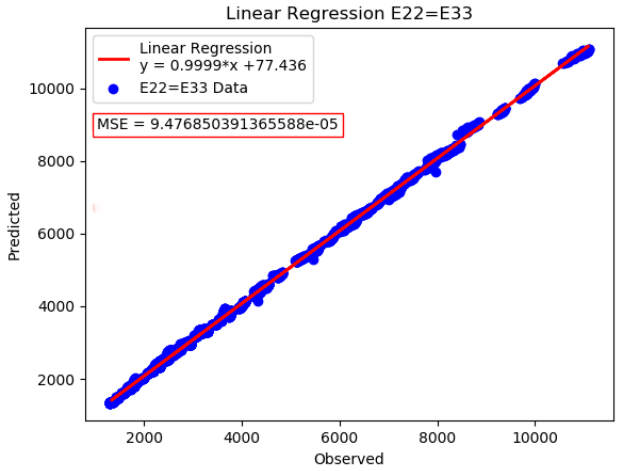

Figure 235: Predicted versus observed values for E22.

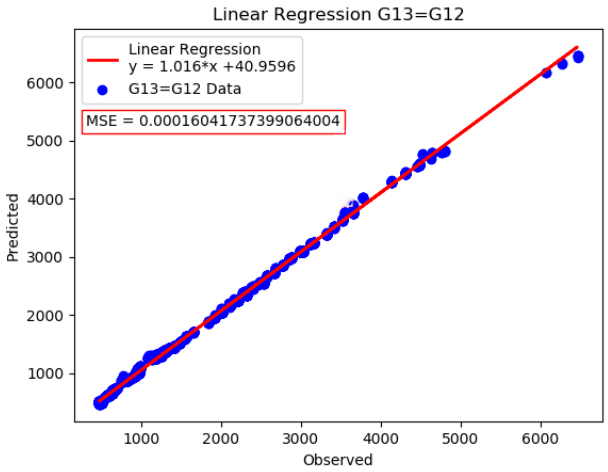

Figure 236: Predicted versus observed values for G12.

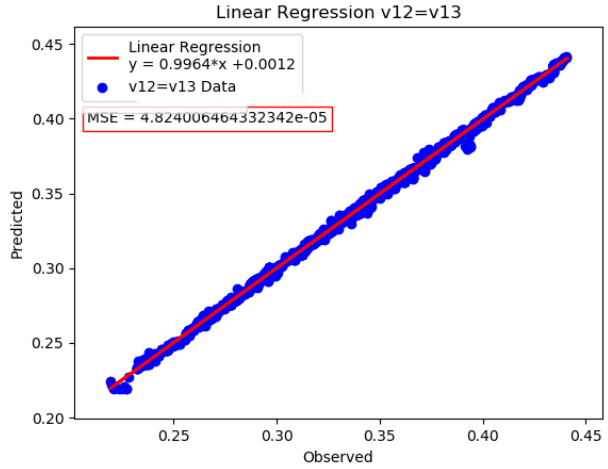

Figure 237: Predicted versus observed values for v12.

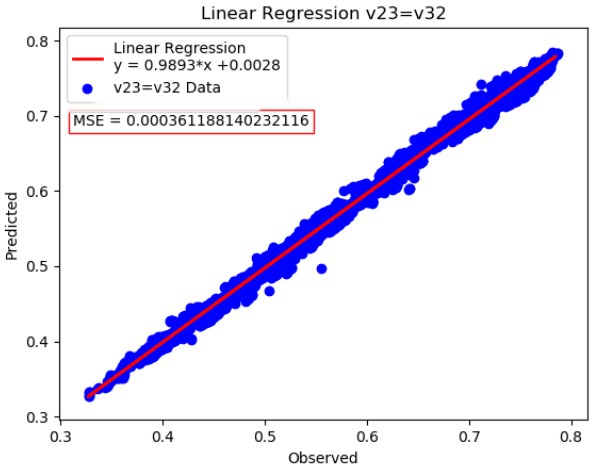

Figure 238: Predicted versus observed values for v23.

Prediction of Fiber Properties

Further work was performed to train a set of neural networks to predict fiber properties given the composite and matrix properties. The project was developed to better accommodate experimental setups. In general, it is easier to experimentally obtain the homogeneous composite properties than it is to obtain the fiber properties. As a result, this tool would permit the fiber properties to be quickly and easily backed out from the more readily obtained experimental data.

In order to develop this tool, 20,000 different composite microstructures were analyzed via the Abaqus micromechanics plugin. Periodic boundary conditions were enforced and a 7 μm fiber radius was assumed. The raw data was normalized to promote better convergence during the learning process. Based on the results from the previously developed composite micromechanics NN, the network architecture was designed with an input layer containing eight neurons and an output layer containing one neuron, as illustrated in Figure 22. Therefore, five separate networks were constructed to predict the five different fiber properties. By developing separate networks, each fiber property could be independently tailored to produce the best results. The material properties that were used as inputs and outputs to the set of neural networks is described below in Table 72.

Table 72: Inputs and outputs used in the neural network for fiber properties.

INPUTS	OUTPUTS
Composite	Fiber
Fiber Volume Fraction	Longitudinal Modulus E_{f11}
Longitudinal Modulus E_{11}	Transverse Modulus $E_{f22} = E_{f33}$
Transverse Modulus $E_{22} = E_{33}$	In-Plane Shear Modulus $G_{f12} = G_{f13}$
In-Plane Shear Modulus $G_{12} = G_{13}$	Major Poisson's Ratio $\nu_{f12} = \nu_{f13}$
Major Poisson's Ratio $\nu_{12} = \nu_{13}$	Minor Poisson's Ratio ν_{f23}
Minor Poisson's Ratio ν_{23}	
Matrix	
Young's Modulus E_m	
Poisson's Ratio ν_m	

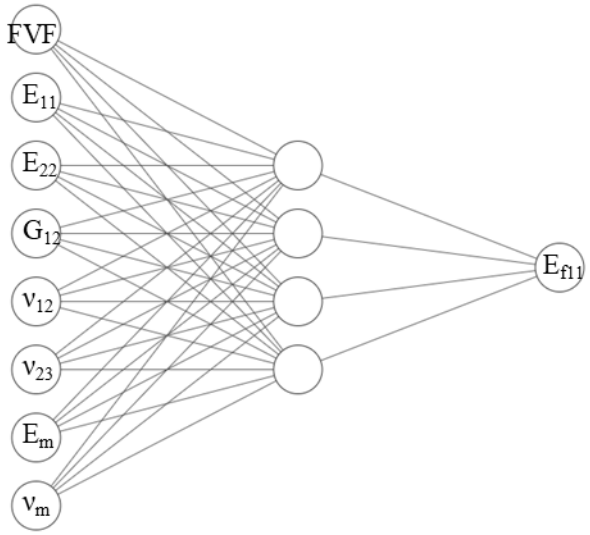

Figure 239: Neural network architecture used to predict the longitudinal modulus of the fiber.

All five networks were trained using the ReLU activation function, the RMSprop optimizer, and the MSE loss function. Other activation functions, optimizers, and loss functions were tested but yielded inferior prediction capabilities. Each network was trained for 100 epochs with a batch size of 32. These parameters produced excellent convergence of the loss function versus the number of epochs.

In order to test each trained network, the value of the predicted fiber property was plotted against the true (observed) value. Therefore, the ideal neural network would yield a linear regression line in the form of $y = x$. Figure 240, Figure 241, Figure 242, Figure 243 and Figure 244 plot the predicted vs the observed value for each of the five fiber properties along with the corresponding linear regression line to illustrate the overall network performance. From these figures, it is evident that there is a higher prediction error when trying to predict fiber properties given composite and matrix properties.

Table 73 quantifies the error in terms of a mean absolute percentage error (MAPE) and the MSE. The highest MAPE was only 3.05% for the prediction of ν_{f23}. However, this error is almost three times larger than the highest MAPE in the previously developed micromechanics neural network.

In conclusion, this project yielded a set of five trained neural networks that can be used to predict fiber properties given composite and matrix properties. Overall, the prediction error is relatively low with a maximum MAPE of 3.05%. However, given the nature of the original training data, it is believed that the error can be significantly reduced by generating a larger set of training data. Therefore, if this project is a path of interest, it is highly recommended that more data is generated.

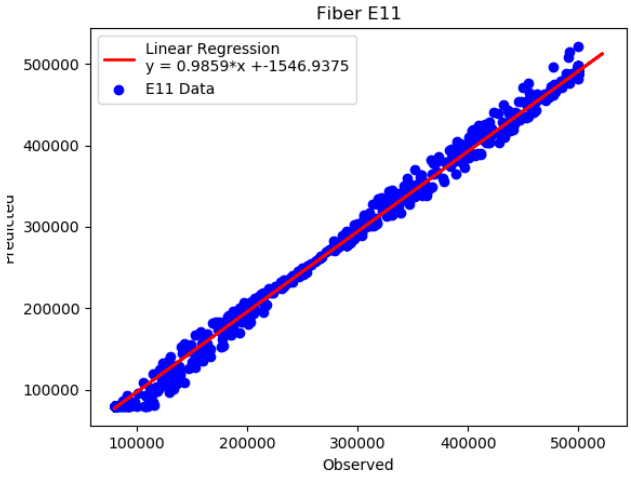

Figure 240: Predicted versus observed values for E11.

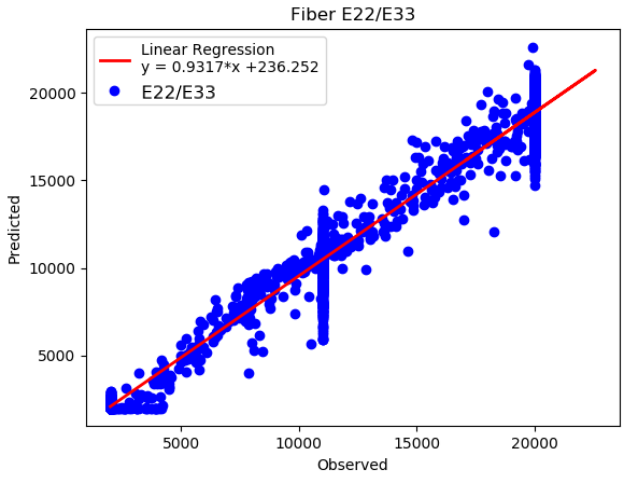

Figure 241: Predicted versus observed values for E22.

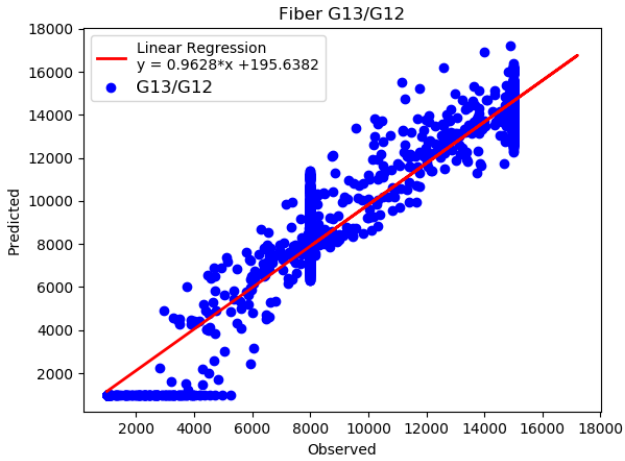

Figure 242: Predicted versus observed values for G12.

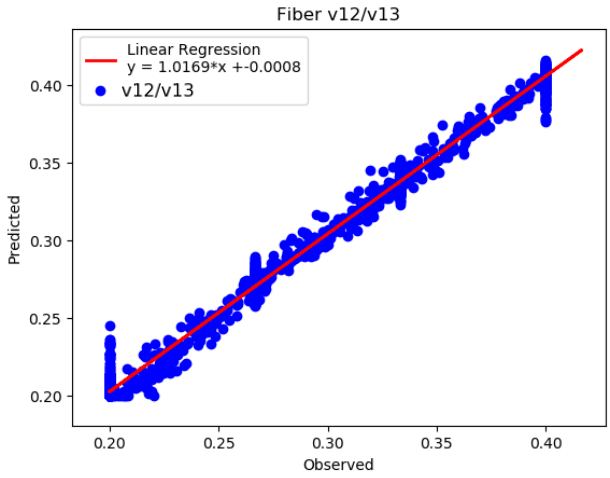

Figure 243: Predicted versus observed values for v12.

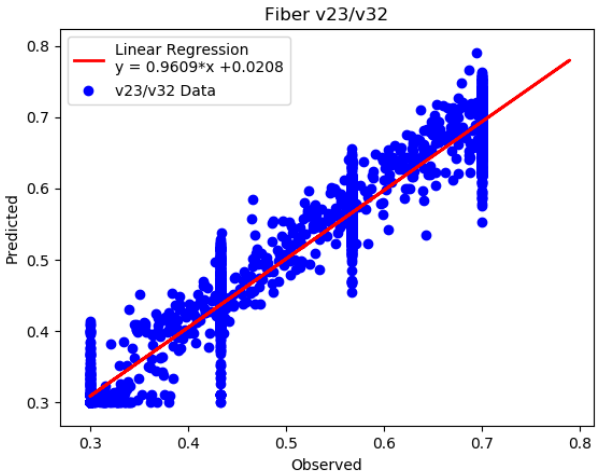

Figure 244: Predicted versus observed values for v23.

Table 73: Errors from fiber prediction.

Fiber Property	Mean Absolute Percentage Error (MAPE)	Mean Squared Error (MSE)
E_{f11}	0.95%	3.45E-4
E_{f22}	2.18%	3.93E-3
G_{f12}	2.38%	4.11E-3
ν_{f12}	1.68%	1.16E-3
ν_{f23}	3.05%	5.02E-3

High-speed Composite Property Predictions via Neural Networks

A key goal in this work was to link micro- to macro-scale composite properties through the development of high-speed prediction tools. In particular, a large focus was placed on predicting the properties of pitch-based fibers. These fibers contain a distinct radial distribution of wavy microstructural features. Therefore, when creating the finite element analysis (FEA) models, the goal was to integrate these observations in order to accurately capture the micro-scale details. While these models focused on pitch-based fibers, they were also extended to PAN-based (same for bio-PAN) fibers due to similarities in properties within the molecular dynamics atomistic simulations. Ultimately, this research removed the time consuming FEA models by training sets of NN to quickly and accurately predict properties from the micro- to the macro-scale. When compared to experimental data, the errors within the high-speed prediction tools were less than ±15%.

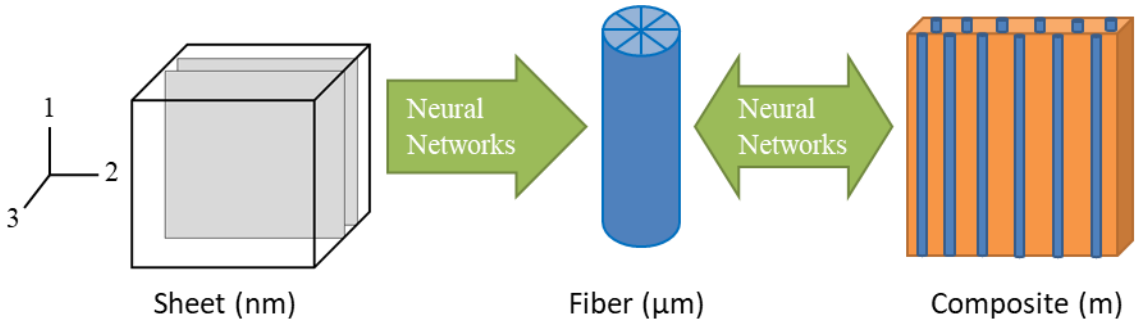

Figure 245: High-level visual of the micro/macro model, including the different scales, and the placement of the neural networks that promote fast property predictions.

In order to generate these tools, multiple sets of NN were trained to work between each length scale, as illustrated in Figure 245. At the nano-scale are sheets with properties that change based on fiber manufacturing techniques. These properties were obtained via MD atomistic simulations. From these simulations, two in-plane sheet properties, E_{11}^{*} and G_{12}^{*}, were collected and used to calculate the remaining sheet properties. The sheets were assumed to be orthotropic with some prescribed waviness and imperfect bonding between the sheets. Therefore, the sheet properties were assumed to fall within the prescribed bounds outlined in Equation 1.

$$\begin{aligned} E_{33} < E_{22} < E_{11}^{*} \\ G_{23} < G_{13} < G_{12} \end{aligned} \tag{1}$$

The equations that determine the remaining sheet properties are defined in Equation 2. The Young's moduli, E_{22} and E_{33}, were set as a fraction of the known property E_{11}^{*}. The modulus in the 2-direction was reduced to account for sheet waviness, while the modulus in the 3-direction was reduced to account for imperfect bonding between the sheets. The shear modulus, G_{12}^{*}, was also reduced by a fraction of E_{22}/E_{11}^{*} to account for sheet waviness. The shear modulus, G_{13}, was set as a fraction of G_{12} that was based on the ratio of an average out-of-plane shear modulus to the in-plane shear modulus. The shear modulus G_{23} was set as a fraction of G_{13} to maintain the bounds prescribed in Equation 1. Therefore, embedded within the nano-scale sheets are details pertaining to the waviness of the fiber microstructure.

$$\begin{aligned} E_{11}^{*} &= given & G_{12}^{*} &= given \\ E_{22} &= 0.15 * E_{11}^{*} & G_{12} &= G_{12}^{*}\left(\frac{E_{22}}{E_{11}^{*}}\right) \\ E_{33} &= 0.1 * E_{11}^{*} & G_{13} &= \left(\frac{(E_{33}/2)}{G_{12}^{*}}\right) * G_{12} \\ & & G_{23} &= 0.3 * G_{13} \end{aligned} \tag{2}$$

When combined together, the nano-scale sheets make up the micro-scale CFs. In order to account for the radial distribution of waves, the pseudo-orthotopic sheets were revolved radially about the center of the fiber. Within the FEA model, this microstructure detail was captured via a radial material orientation of the fibers within the hex-pack representative volume element, as illustrated in Figure 246.

At the macro-scale, the CF was combined with the matrix to form the overall composite. The CF and the matrix were given a range of properties defined in Table 74, based on typical values recorded in experimental data. The individual fiber and overall composite properties were determined by applying an in-house volume averaging software package.

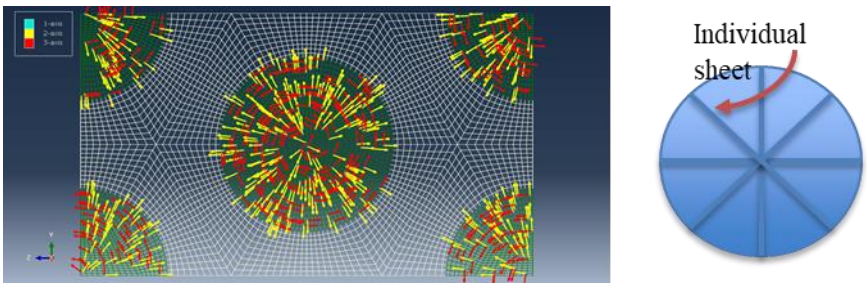

Figure 246: Material orientation within the FEA model to generate the radial features.

Table 74: Range of fiber and matrix values used within the FEA models.

RANGE OF PROPERTIES	
Fiber	
Fiber Volume Fraction	30 – 75%
Longitudinal Modulus E_{f11}	80 – 500 [GPa]
Transverse Modulus $E_{f22} = E_{f33}$	2 – 20 [GPa]
In-Plane Shear Modulus $G_{f12} = G_{f13}$	1 – 15 [GPa]
Major Poisson's Ratio $\nu_{f12} = \nu_{f13}$	0.2 – 0.4
Minor Poisson's Ratio ν_{f23}	0.3 – 0.7
Matrix	
Young's Modulus E_m	1 – 4 [GPa]
Poisson's Ratio ν_m	0.3 – 0.45

Suites of NN were developed to create the high-speed prediction tools that linked the micro- to macro-scale composite properties. In order to develop these tools, ~35,000 composite structures were analyzed and compiled via the Abaqus micromechanics plugin and an in-house volume-averaging software package. The collected data was normalized and split so that 80% was used as a training data set and 20% was used as a test data set. Various neural network architectures were investigated to determine the optimal configuration for prediction accuracy. Ultimately, the ideal architecture for this particular application was an input layer, hidden layers, and an output layer containing a *single* neuron as illustrated in Figure 247. This type of configuration resulted

in a single network used to predict a single property. Therefore, multiple NN were used to predict all of the properties required to define a component of the composite. Each network was trained using the ReLU activation function, the RMSprop optimizer, and the MSE loss function. Other activation functions, optimizers, and loss functions were tested but yielded inferior prediction capabilities. In the end, the overall combination of network architecture and model parameters produced excellent convergence of the loss function versus the number of epochs.

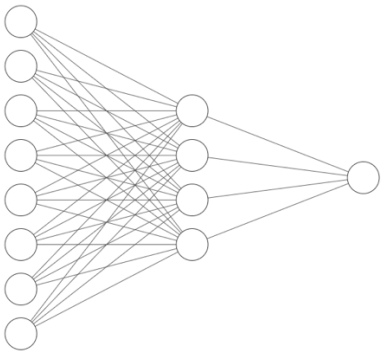

Figure 247: Example neural network used to predict a single property.

One of the primary goals of this work was to efficiently upscale properties from the micro-level sheets to the macro-level composite via the implementation of NN. The micro- to macro-scale tool requires the user to input information about the sheet properties, the fiber volume fraction, and the matrix properties, as defined in Table 75. These inputs then run through a series of NN to predict the complete array of fiber and composite properties.

Table 75: Inputs and outputs for the micro-level to macro-level property prediction tool.

Inputs		Outputs 1	Outputs 2
Sheet E_{11}	80 – 500 [GPa]	Fiber E_{11}	Composite E_{11}
Sheet G_{12}	1 – 300 [GPa]	Fiber $E_{22} = E_{33}$	Composite $E_{22} = E_{33}$
FVF	0.3 – 0.75	Fiber $G_{12} = G_{13}$	Composite $G_{12} = G_{13}$
Matrix E	1 – 4 [GPa]	Fiber $\nu_{12} = \nu_{13}$	Composite $\nu_{12} = \nu_{13}$
Matrix ν	0.3 – 0.45	Fiber ν_{23}	Composite ν_{23}

The first set of NN links the sheet properties to the fiber properties. Figure 248 illustrates the performance of the trained networks when predicting each individual fiber property given the sheet properties as indicated by the user. A visual examination reveals excellent training results as the observed versus predicted values converge along the red line given by the equation $y = x$. Table 4 reveals numerical details of the training performance in terms of the MAPE described in

Equation 3. In the first column is a normalized MAPE that allows the magnitude of the errors to be directly compared. In the second column is a true MAPE which indicates the amount of error given the true magnitude of each individual property. The normalized MAPE indicates that the fiber property ν_{12}=ν_{13} had the largest amount of error at 0.41%, while the true MAPE indicates that the fiber property G_{12}=G_{13} had the largest amount of error at 1.07%. However, all of the errors were relatively insignificant indicating well trained networks that can be used to accurately predict fiber properties.

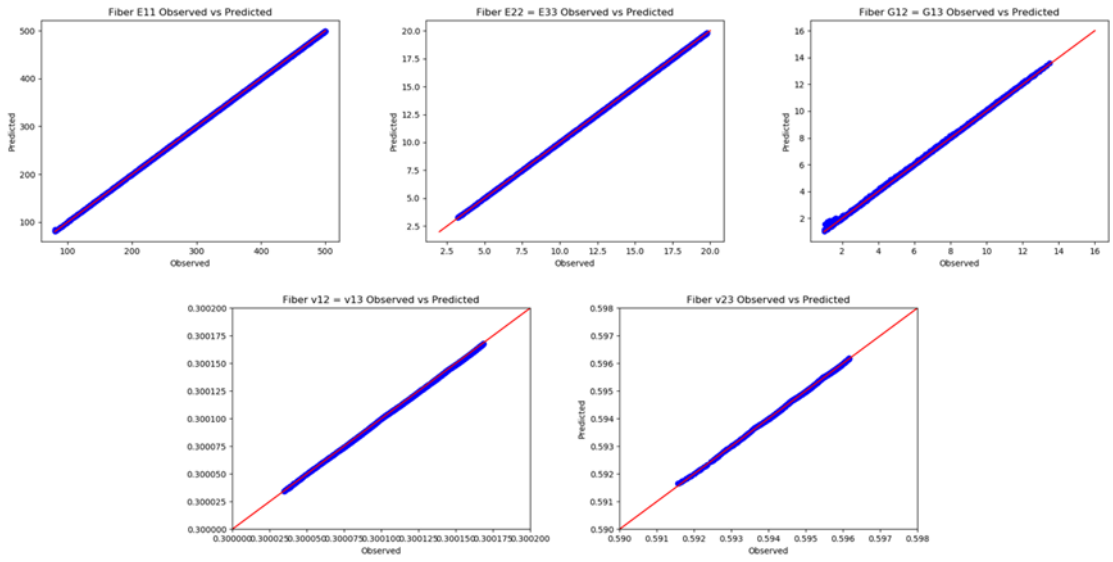

Figure 248: Observed versus predicted fiber property values for the micro-scale to macro-scale model. These networks took sheet properties as inputs and output predicted fiber properties.

The second set of NN links the fiber properties to the composite properties. Figure 249 illustrates the performance of the trained networks when predicting each individual composite property given the fiber properties from the previous set of NN. A visual examination reveals good training results as the observed versus predicted values converge along the red line given by the equation $y = x$. Table 76 reveals numerical details of the training performance in terms of the MAPE described in Equation 3. In the first column is a normalized MAPE that allows the magnitude of the errors to be directly compared. In the second column is a true MAPE which indicates the amount of error given the true magnitude of each individual property. The normalized MAPE indicates that the composite property ν_{23} had the largest amount of error at 0.93%, while the true MAPE indicates that the composite property G_{12}=G_{13} had the largest amount of error at 2.07%. However, all of the errors were relatively small indicating well trained networks that can be used to accurately predict composite properties.

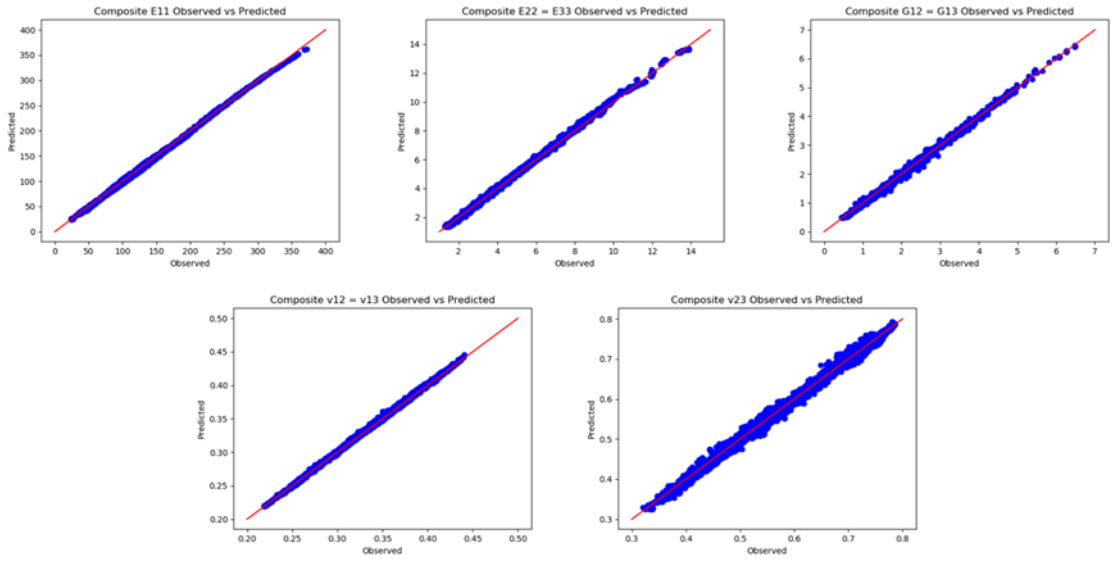

Figure 249: Observed versus predicted composite property values for the micro-scale to macro-scale model and the macro-scale upscaling model. These networks took fiber properties as inputs and output predicted composite properties.

$$MAPE = \frac{100}{n}\sum_{i=1}^{n}\left|\frac{Observed_i - Predicted_i}{Observed_i}\right| \quad (3)$$

Table 76: Mean absolute percentage error (MAPE) for the predicted fiber and composite properties in the micro-scale to macro-scale model and the predicted fiber properties in the macro-scale upscaling model.

Property	Normalized MAPE	True MAPE
Fiber E_{11}	0.0429%	0.0965%
Fiber $E_{22}=E_{33}$	0.0397%	0.1012%
Fiber $G_{12}=G_{13}$	0.2932%	1.0660%
Fiber $\nu_{12}=\nu_{13}$	0.4134%	0.0003%
Fiber ν_{23}	0.1724%	0.0022%
Composite E_{11}	0.2043%	0.8458%
Composite $E_{22}=E_{33}$	0.4412%	1.7725%
Composite $G_{12}=G_{13}$	0.4158%	2.0674%
Composite $\nu_{12}=\nu_{13}$	0.5465%	0.5508%
Composite ν_{23}	0.9283%	1.1918%

In order to test the performance of the micro- to macro-scale model, the tool's predictions were compared to experimental composite values. The experimental composite was comprised of an EpiKote 135 matrix and bio-PAN BP3SU2-2 fibers. The properties of the experimental matrix, fiber, and composite are detailed in Table 77. The experimental data was input into the model along with sheet properties of E_{11} = 169.2 GPa and G_{12} = 10.37 GPa. The model was then executed and high-speed predictions were made regarding the fiber and composite properties. Table 78 outlines the predicted values along with their percent error when compared to the experimental values. A majority of the errors were relatively insignificant and all of the errors met the milestone goals of <15%. Therefore, the micro- to macro-scale tool can provide high-speed and accurate predictions for both the fiber and composite properties.

Table 77: Experimental data for PAN-based fibers.

Experimental Matrix Properties (EpiKote 135)		Experimental Fiber Properties (bioPAN BP3SU2-2)		Experimental Composite Properties		
E [GPa]	ν	E_{11} [GPa]	FVF	E_{11} [GPa]	E_{22} [GPa]	ν_{12}
2.72±0.11	0.35±0.017	169.2	0.47	80.99±5.31	4.86±0.85	0.33±0.01

Table 78: Micro-scale to macro-scale model prediction of fiber and composite properties. The percent error is with respect to the experimental values.

Predicted Fiber Properties			Predicted Composite Properties		
E_{11} [GPa]	169.3	0.59% Error	E_{11} [GPa]	81.94	1.17% Error
			$E_{22} = E_{33}$ [GPa]	4.45	8.02% Error
			$\nu_{12} = \nu_{13}$	0.33	0.61% Error

Another primary goal of the work was to produce a macro-level model capable of efficiently upscaling and downscaling properties between the fiber and the composite. The macro-level upscaling tool requires the user to input fiber and matrix properties while outputting predicted composite properties. The macro-level downscaling tool requires the user to input matrix and composite properties while outputting predicted fiber properties. The high-speed predictions were carried out via a series of neural networks.

The NN utilized in the micro-scale to macro-scale model, between the fiber and the composite, were isolated and implemented within the macro-level upscaling tool. Therefore, the performance of the set of NN are illustrated in Figure 249 with numerical details highlighted in Table 76. However, the NN utilized in the macro-scale downscaling tool had to be trained to accurately predict fiber properties. Figure 250 illustrates the performance of the trained networks when predicting each individual fiber property given the composite and matrix properties as indicated by the user. A visual examination reveals an increased amount of scatter during the downscaling process. However, this is to be expected as property relationships are more ambiguous than during the upscaling process. Despite the increased scatter, the observed versus predicted values still maintain a good amount of convergence along the red line given by the equation: $y = x$. Table 79 reveals numerical details of the training performance in terms of the

mean absolute percentage error MAPE described in Equation 3. In the first column is a normalized MAPE that allows the magnitude of the errors to be directly compared. In the second column is a true MAPE which indicates the amount of error given the true magnitude of each individual property. The normalized and true MAPE indicates that the fiber property ν_{23} had the largest amount of error at 5% and 4.12% respectively. However, all of the errors were $\leq$5% indicating well trained networks that can be used to accurately predict fiber properties during the downscaling process.

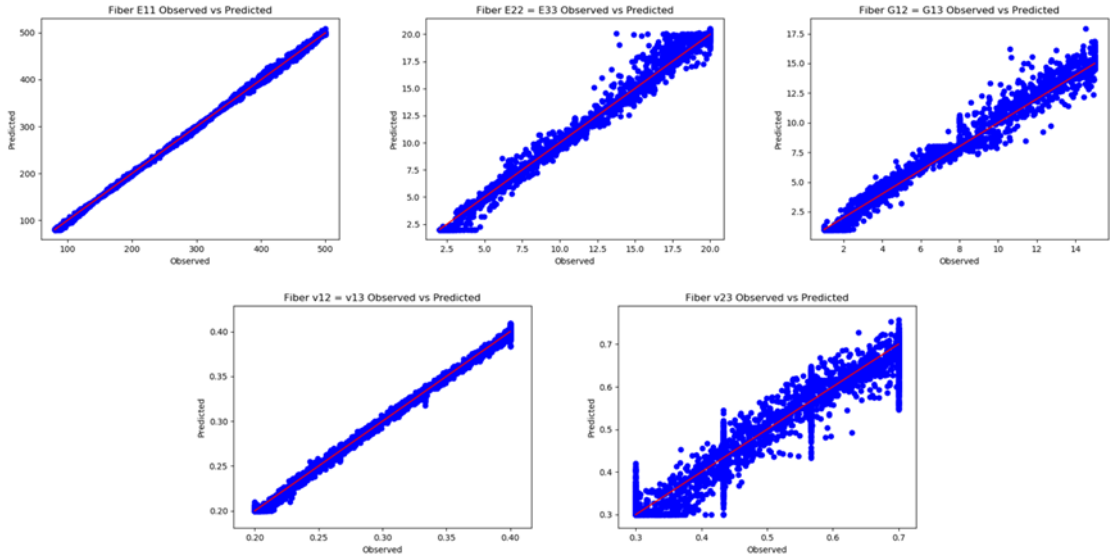

Figure 250: Observed versus predicted fiber property values for the macro-scale downscaling model. These networks took sheet properties as inputs and output predicted fiber properties.

Table 79: MAPE for the predicted fiber properties in the macro-scale downscaling model.

Property	Normalized MAPE	True MAPE
Fiber E_{11}	0.2463%	0.6024%
Fiber E_{22}=E_{33}	0.8984%	2.4934%
Fiber G_{12}=G_{13}	1.2676%	3.9085%
Fiber ν_{12}=ν_{13}	0.6290%	0.6290%
Fiber ν_{23}	4.9959%	4.1232%

In order to test the performance of the macro-scale model, the tool's predictions were compared to two different sets of experimental composite values. The first experimental composite was

comprised of an EpiKote 135 matrix and ORLN CTPSP315+ fibers. The properties of the experimental matrix, fiber, and composite are detailed in Table 80. The experimental composite data was input into the downscaling macro-model to predict the fiber properties, while the experimental fiber data was input into the upscaling macro-model to predict the composite properties. The two models were then executed and high-speed predictions were made regarding the fiber and composite properties. Table 81 outlines the predicted values along with their percent error when compared to the experimental values. All of the errors were relatively insignificant and easily met the milestone goals of <±15% error.

Table 80: Experimental data for pitch-based fibers.

Experimental Matrix Properties (EpiKote 135)		Experimental Fiber Properties (ORLN CTPSP315+)		Experimental Composite Properties
E [GPa]	ν	E_{11} [GPa]	FVF	E_{11} [GPa]
2.72±0.11	0.35±0.017	298.58	0.48	143.41

Table 81: Macro-scale model prediction of downscaled fiber properties and upscaled composite properties. The percent error is with respect to the experimental values.

Predicted Fiber Properties (Downscaling)			Predicted Composite Properties (Upscaling)		
E_{11} [GPa]	300.73	0.72% Error	E_{11} [GPa]	144.26	0.59% Error

The second experimental composite was comprised of an EpiKote 135 matrix and bio-PAN BP3SU2-2 fibers. The properties of the experimental matrix, fiber, and composite are detailed in Table 77. The experimental composite data was input into the downscaling macro-model to predict the fiber properties, while the experimental fiber data was input into the upscaling macro-model to predict the composite properties. The two models were then executed and high-speed predictions were made regarding the fiber and composite properties. Table 82 outlines the predicted values along with their percent error when compared to the experimental values. While the errors were slightly higher than the pitch-based fiber, they all met the milestone goals of <15% error. Therefore, the macro-scale tool can provide high-speed and accurate predictions for both downscaling the fiber and upscaling the composite properties.

Table 82: Macro-scale model prediction of downscaled fiber properties and upscaled composite properties. The percent error is with respect to the experimental values.

Predicted Fiber Properties (Downscaling)			Predicted Composite Properties (Upscaling)		
E_{11} [GPa]	165.29	4.61% Error	E_{11} [GPa]	81.94	1.17% Error
			$E_{22} = E_{33}$ [GPa]	4.45	8.02% Error
			$\nu_{12} = \nu_{13}$	0.33	0.61% Error

The results of the prediction tools for the macro model and the micro-to-macro model are fully tabulated and summarized in Table 83 and Table 84 for the PAN-based fibers and the pitch-based fibers respectively. The micro-to-macro model utilizes the nanoscale sheet properties, obtained from the MD atomistic simulations, to predict fiber properties that are then used to drive the prediction of the overall composite properties. The macro model backs out predicted fiber properties given the more readily obtained experimental composite properties. Ultimately, both models yielded predicted properties that were in good agreement with experimental values and were well within the required 15% error.

Table 83: Experimental data for bio-PAN-based fibers.

Component	Model	Property	Predicted	Experimental	% Error
Fiber	Micro-Macro	E_{11} [GPa]	169.3	169.2	0.06
Fiber	Macro	E_{11} [GPa]	165.29	169.2	4.61
Composite	Micro-Macro	E_{11} [GPa]	81.94	80.99	1.17
Composite	Micro-Macro	E_{22} [GPa]	4.45	4.86	8.44
Composite	Micro-Macro	ν_{12}	0.33	0.33	0.00

Table 84: Experimental data for pitch-based fibers.

Component	Model	Property	Predicted	Experimental	% Error
Fiber	Macro	E_{11} [GPa]	300.73	298.58	0.72
Composite	Micro-Macro	E_{11} [GPa]	144.26	143.41	0.59

In summary, the micro/macro integration utilizes a complex web of connections between neurons of multiple NN to provide near instantaneous and accurate predictions. However, the user simply interacts with elegant, straightforward, high-speed tools that require no FEA modeling experience as previously required for these types of problems. These tools can be used to help guide manufacturing decisions, because embedded within the nano-scale sheets (micro-level) are details unique to the manufacturing processes of the fibers. In the end the micro/macro tools met the milestone goals of <±15% error thereby enabling fast and accurate composite property predictions. Admittedly more work is needed to address and validate variation in CF shape (e.g. Pac-Man) and morphology (e.g. random wave) and also molecular diversity from other feedstock materials.

Scaled-up Carbon Fiber Precursor Processing and Analyses

Pitch-based Scaled-up CF Processing and Analyses

Building on the large format spinning efforts from the previous BPs, several additional CTP6M batches were successfully spun. Large diameter fibers (35 µm+) were readily achieved in initial trails, however due to the diffusive limitations during oxidative stabilization the targeted diameter for additional trials were 20 µm and below. To assist with the achievement of these goals additional spinnerets were designed with various L/D ratios (extrusion of pitch) and smaller apertures. To accommodate the lower material flux in the reduce diameter spinnerets, new designs allowing for lower flow rates on the metering pump while retaining ideal back pressure levels were submitted to the manufacturer and ordered. A batch of mesophase designated as CTP6MP315+ was spun to filaments of various diameters. Ultimately, diameters in the mid to low 20 µm range were achieved at the highest take-up speeds for the CTP6MP315+ material. Increasing take-up speeds led to consistent filament breakup. Figure 251a shows the fibers on a roll exhibiting a uniform glossy texture. Figure 251b and Figure 251c show micrographs of the fiber without the presence of any microscale defects in the as-spun and CF, respectively. In order to determine an appropriate conversion protocol, the as spun fibers were placed in a TGA and characterized in regards to their mass uptake and pyrolytic yield. Figure 252a is a simple ramp rate in air indicating a maximum air uptake between 300-400 °C. Figure 252b shows the overall pyrolytic yield under nitrogen. In Figure 252c, the as-spun fibers are subjected to a uniform ramp rate of 0.5 °C/min but with various final isothermal temperatures. The 325 °C final temperature ramp shows the highest overall mass uptake in the given window, while at 400 °C combustion leads to degradation of the fiber over the same time period. A representative CTP6MP315+ CF property set is summarized in Table 85. These CF meet DOE goals within the error stated in the measurements. Additional optimizations on the large format spinning line should allow for stable formation of smaller fibers more comparable to industrially manufactured pitch based CF, however due to budget and time constraints no further work was performed on CTPM materials.

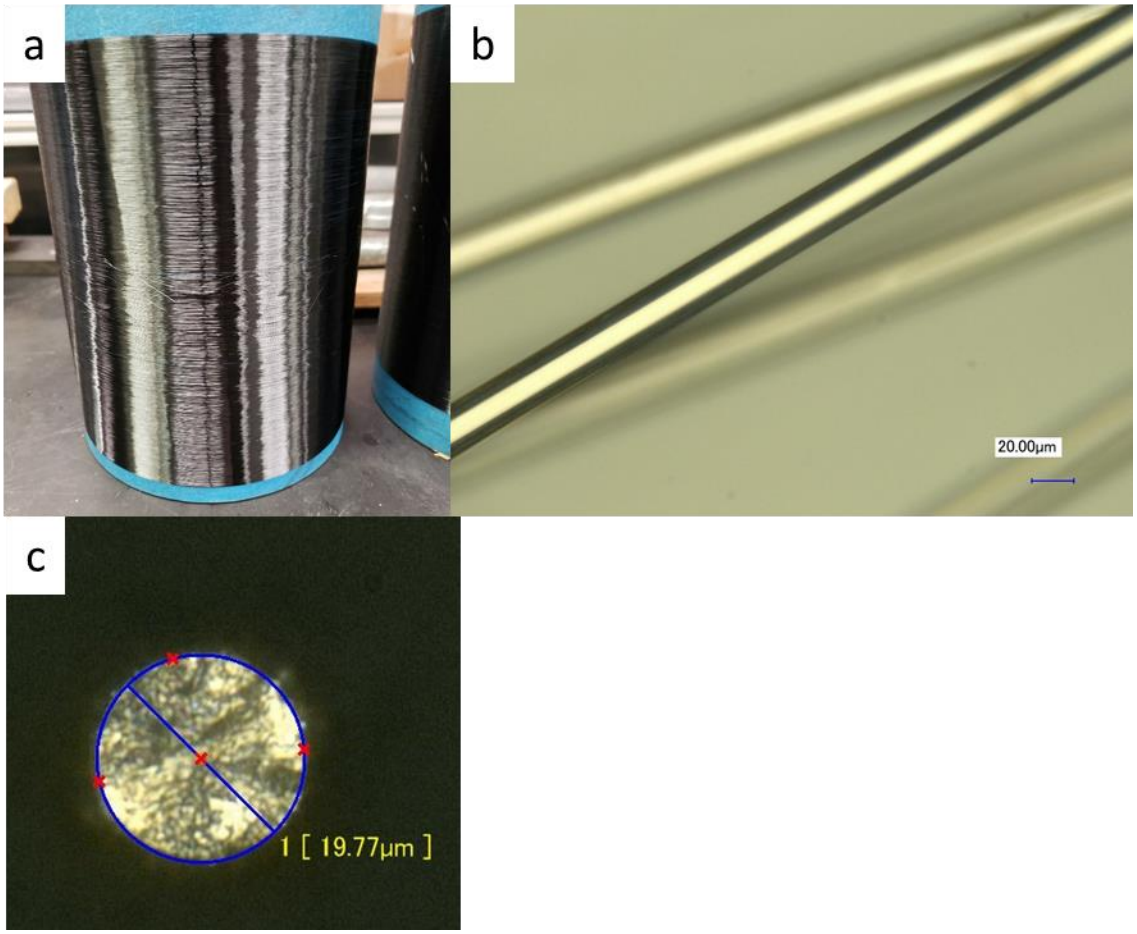

Figure 251: (a) CTP6MP315+ fibers on a roll. (b) Micrograph of as spun CTP fibers with diameters in the mid 20 µm range. (c) CF from CTP6MP315+ indicating a dense cross-section and some structural development consistent with mesophase conversion.

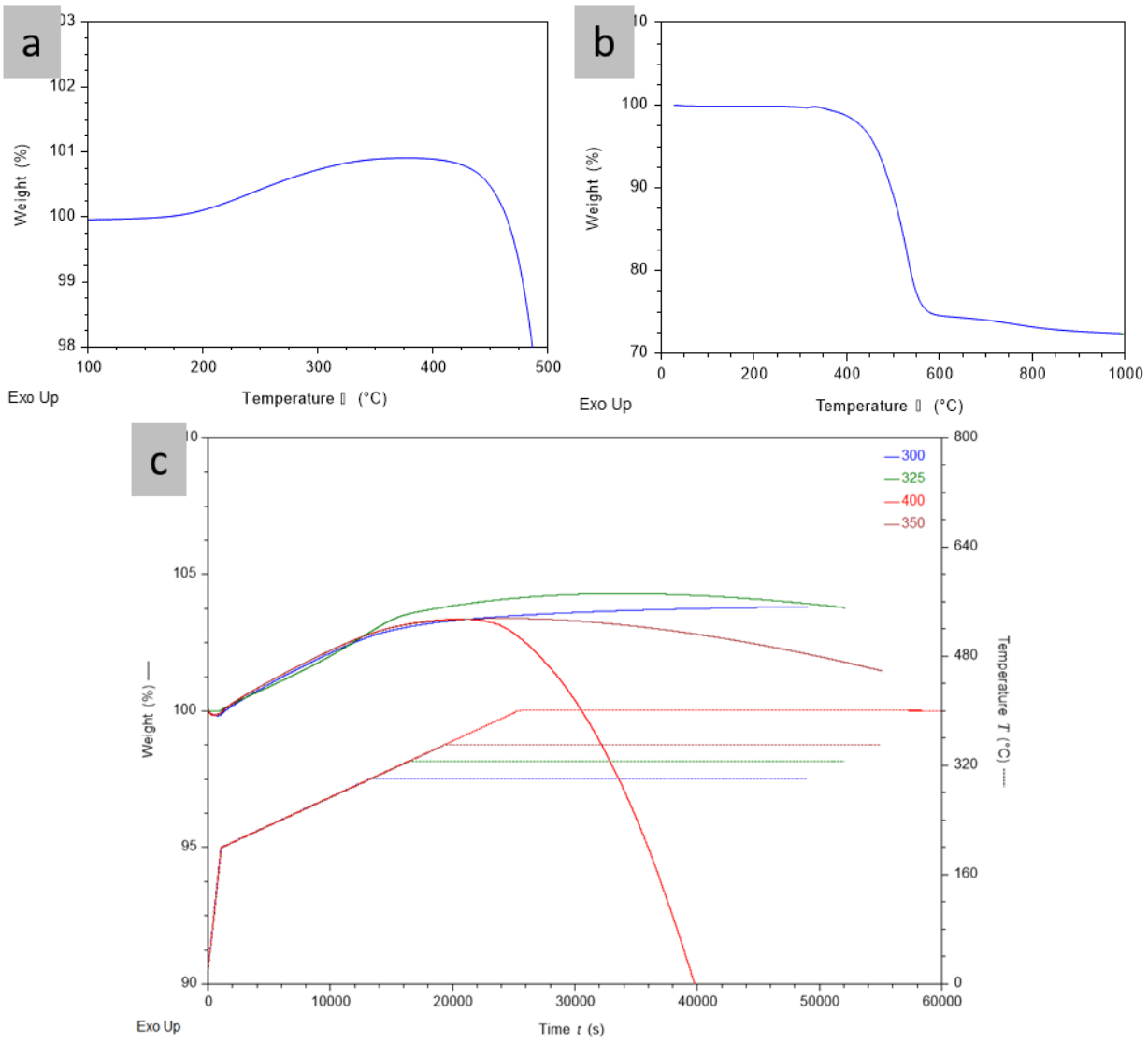

Figure 252: CTP6MP315+ thermograms in (a) air at 2°C/min and in (b) N2 at 10°C/min. (c) Sensitivity of the mass uptake to final isothermal condition (denoted in legend). All samples subjected to a 0.5 °C/min ramp rate to their respective isotherm and soaked for an additional 10 h.

Table 85: Semi-optimized conversion condition to date for CTP6MPSP315+ and resulting properties.

Diam (µm)	Peak Stress (ksi)	% E	Mod (Msi)
21.4±0.8	248.1±66.5	1.18±0.21	20.4±1.6

In addition to the melt conversion activities on CTPM systems, a petroleum derived mesophase produced by Kopper's with a SP of 296.7 was further developed (KP-MP-19). Utilizing the guideless developed form previous rheological characterization, the material was successfully

melt spun on the multi-filament extruder. Figure 13a and 13b show the surface of as-spun and CF form the KP-PM-19. From Figure 13c the cross sections of the CF can be seen, displaying radial reflections consistent with the associated mesophase texture development. With this conversion approach we do not see evidence of considerable defects on the surface or fiber bulk. Comparing Figure 14 to Figure 12, we observe clear differences between the PPM and CTPM oxidation behavior. Most notably, for an equivalent ramp rate, the oxygen uptake is approximately double relative to the coal-based counterpart (Figure 14a). Decreased temperature stability in air and faster oxygen uptake kinetics are observed (Figure 14b). Utilizing this information, conversion trials have been initiated to determine the best processing window for the material at each diameter. The initial mechanical data is summarized in Table 6.

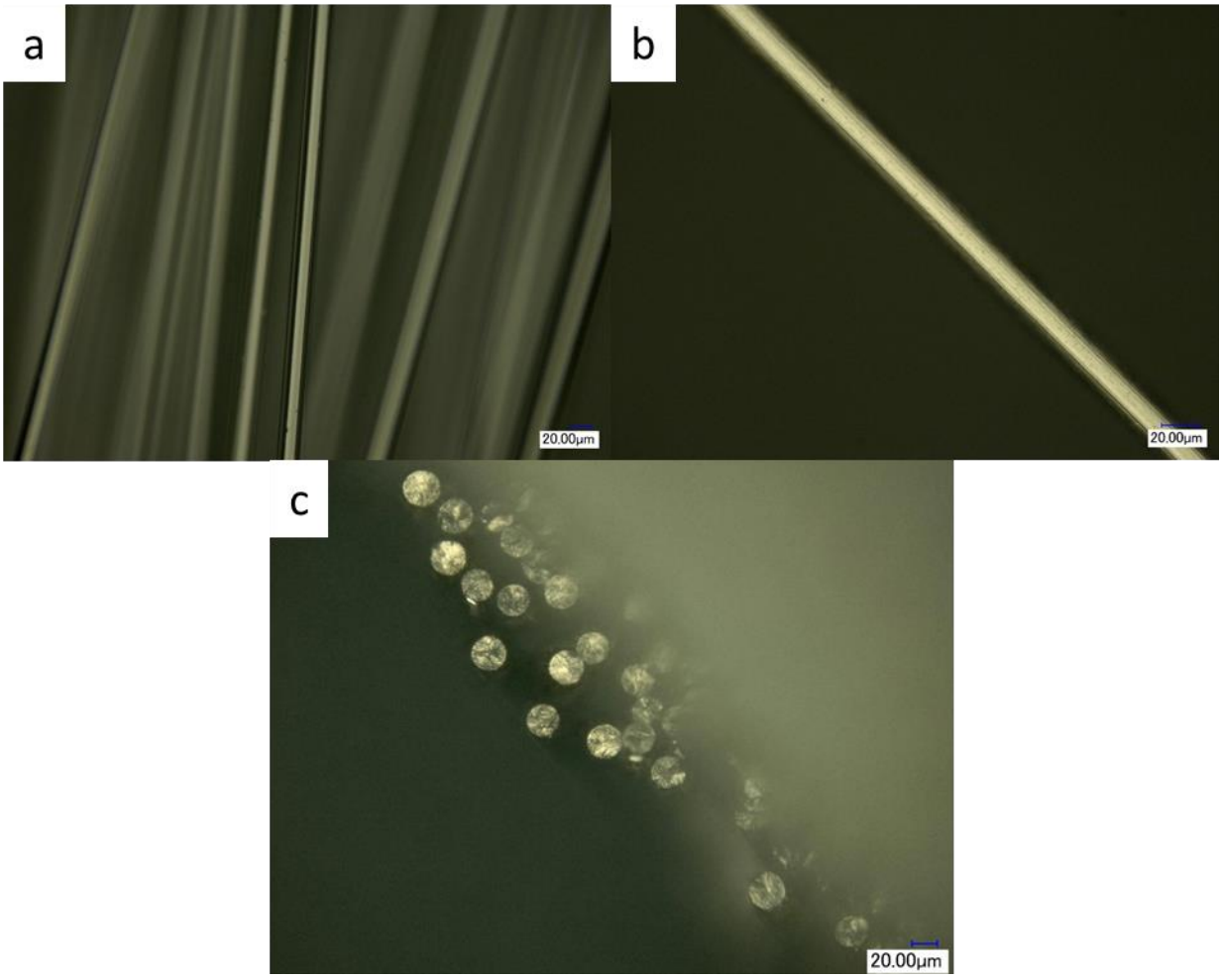

Figure 253: (a) Micrograph of KP-MP-19 fibers as-spun. Micrograph of KP-MP-19 CF along the (b) axial and (c) transverse direction.

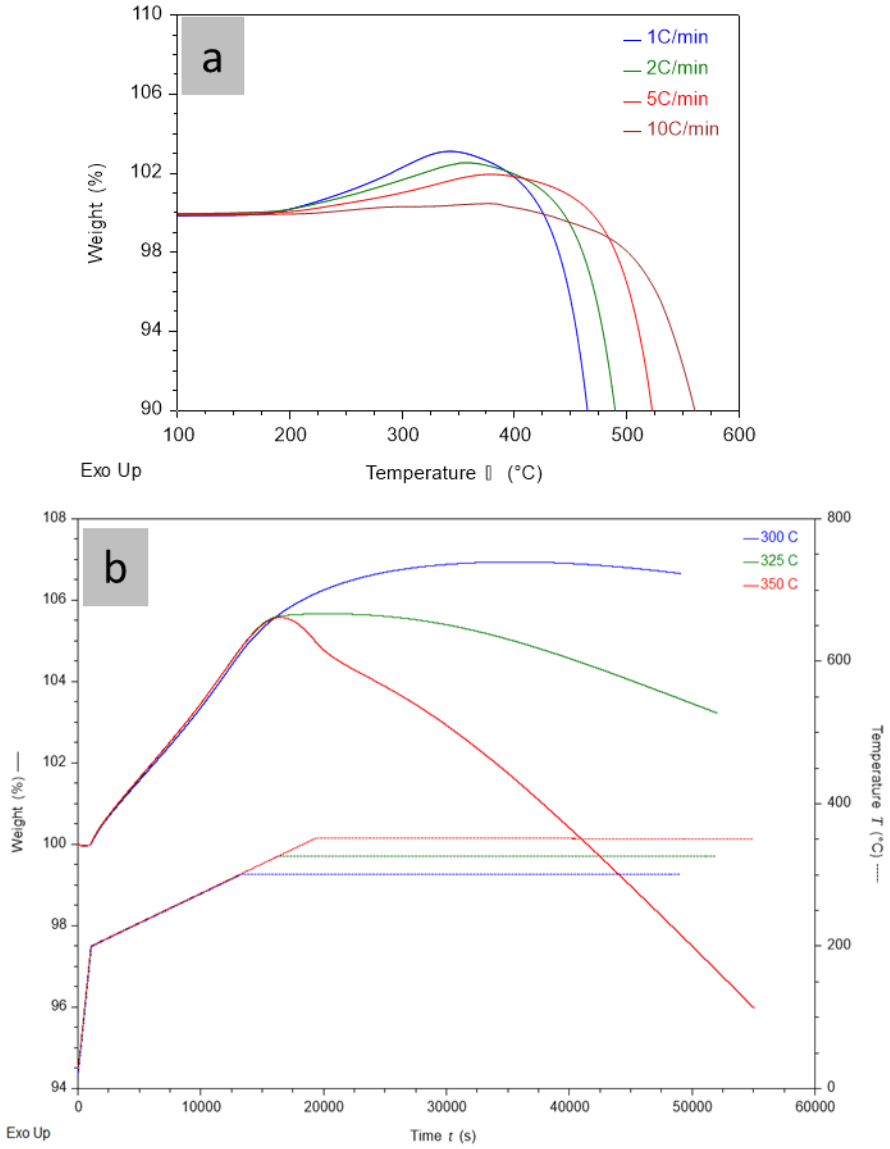

Figure 254: (a) Thermograms in air at ramp rates from 1-10 °C/min for the KP-MP-19 material. (b) Sensitivity of the mass uptake to final isothermal condition (denoted in legend). All samples subjected to a 0.5 °C/min ramp rate to their respective isotherm and soaked for an additional 10 h.

Table 86: Initial mechanical properties from large scale spun KP-MP-19 carbon fibers.

Diam (µm)	Peak Stress (ksi)	% E	Mod (Msi)
23.2±1.5	140.2±7.67	0.67±0.18	23.4±1.2

The initial spinning trial for KP-MP-19 with a modified pump assembly produced filaments down to approximately 20 µm in diameter using a wide variety of spinning conditions. Additional trials are needed to reduce the fiber diameters further and achieve the targeted

strength, stiffness, and elongation property goals. KP-MP-19 was successfully spun and carbonized. Micrographs of the carbonized filaments are noticeably absent of micropores or distortions of the fiber perimeters, suggesting that the conversion conditions are appropriately preserving the fiber morphologies during thermal processing. Figure 255 shows spools of the fibers from various multifilament spinning trials and a micrograph showing the fiber diameters are less than 25 µm.

Figure 255: Left photo shows multifilament spinning of KP-PP-19. Middle photo shows several spools of as spun fibers produced under different conditions to reduce the CF diameter. Right photo shows as spun fibers with a diameter less than 25 µm.

New PPM material, KP-MP-20-0655 (KP-PM-SP300), for large-scale melt spinning was evaluated initially by shear rheology for processing on the large-scale multi filament melt spinning. Thermal stability was evaluated in several isothermal temperatures above the softening point via oscillatory shear rheology. Figure 256a for the KP-PM-SP300 shows slightly less stability than a commercial PPM as evidenced by larger magnitudes of viscosity increases over the test duration. Interestingly, the commercial PPM showed a stronger apparent viscosity dependence on temperature compared to the Kopper's PPM (Figure 256b). KP-MP-SP300 and a commercial mesophase pitch show the required rheological behavior for multi-filament melt spinning.

In addition to the rheological properties, PPM materials oxidation response and yield were characterized via TGA. Ramp rates of 0.5 °C/min and 1 °C/min were used to replicate a ramp rate followed by an extended 10 h isothermal hold at temperatures ranging from 275 °C to 350 °C in air. The tests were completed by performing pyrolysis at a rate of 10 °C/min to a final temperature of 1200 °C. For mesophase plotted in Figure 257 and Figure 258, isotherms at a temperature of 275 °C provided the highest final yields. The mesophase materials once spun into fibers will utilize the trends observed in these studies to produce an optimized processing route.

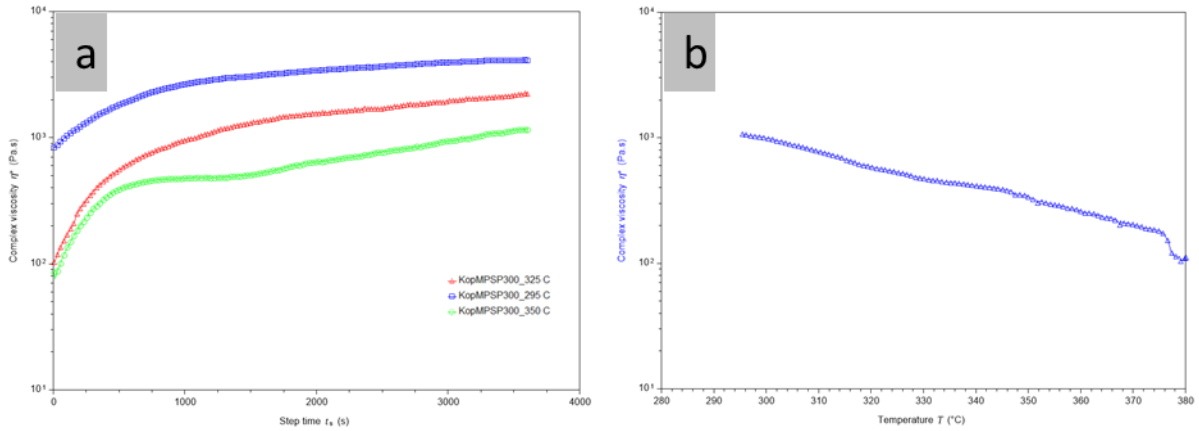

Figure 256: (a) **Oscillatory shear rheology used to evaluate reactive stability in an isothermal condition for KP-PM-SP300.** (b) **Viscosity vs. temperature at a rate of 2 °C/min.**

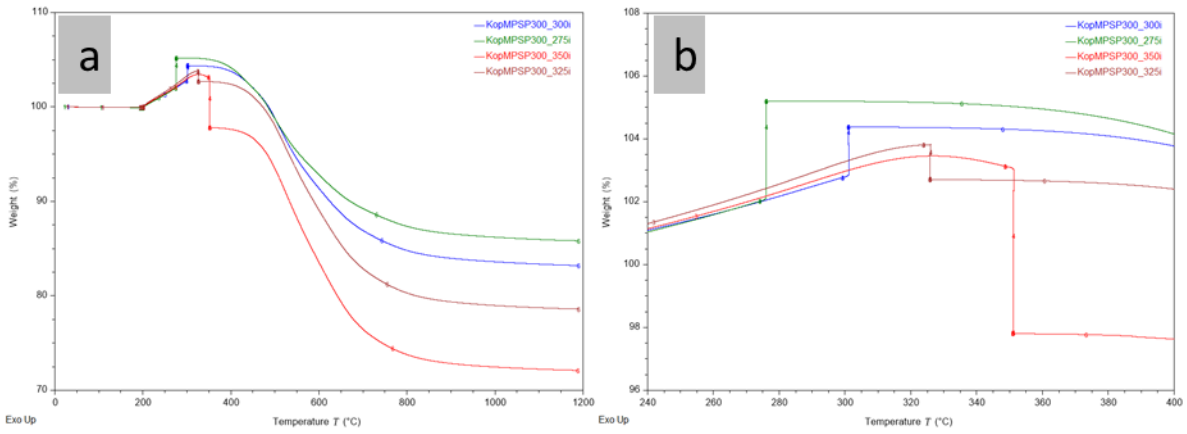

Figure 257: (a) and (b) **simulated conversion kinetics for KP-PM-SP300 at a ramp rate of 0.5 °C/min. Isothermal regions are expanded for clarity (b).**

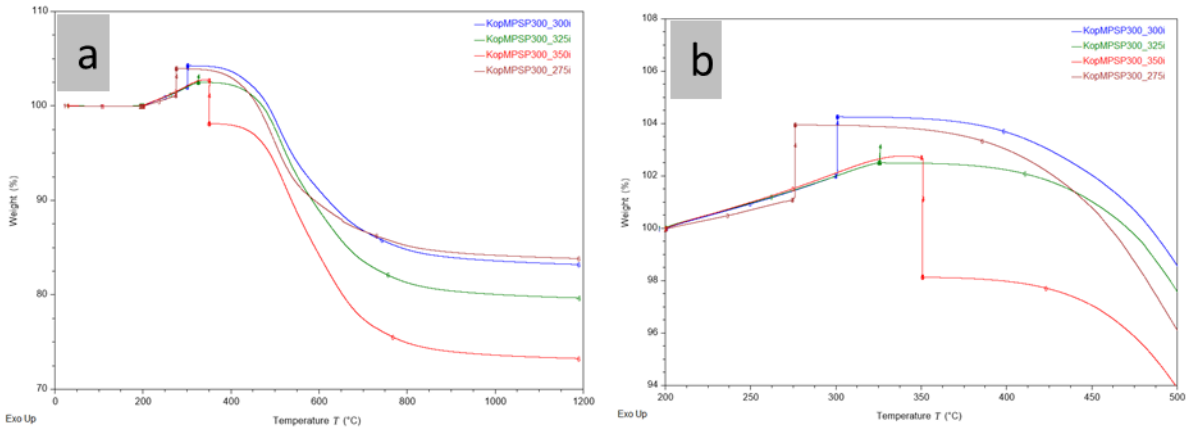

Figure 258: (a) and (b) **simulated conversion kinetics for the KP-PM-SP300 at a ramp rate of 1 °C/min. Isothermal regions are expanded for clarity (b).**

KP-PM-SP300 was spun utilizing the multi-filament spinning unit and the diameter was minimized during spinning. Fibers exhibiting diameters of 20-45 µm were produced and shown

in Figure 259. Diffuse light scattering points can be observed in the surface finishes of the carbon fibers suggesting some irregularities in the surface structure and are shown in Figure 259b. Small bundles of the lower diameter fiber groupings were stabilized in air and carbonized under nitrogen to a final temperature of 1500 °C. The highest strength sample with an average diameter of 22 µm demonstrated 202 ksi strength, 1.08 % elongation and 19 Msi modulus.

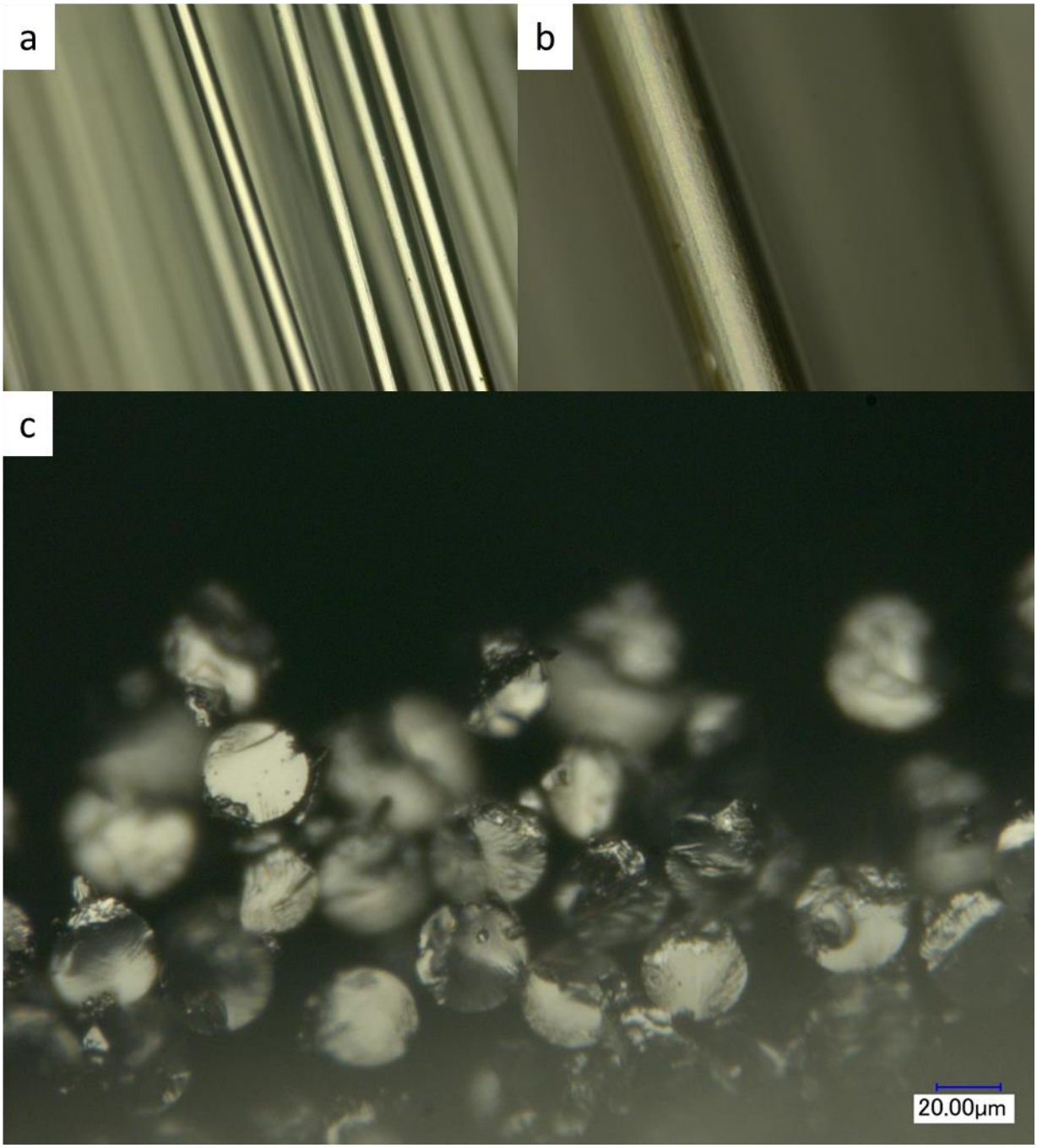

Figure 259: Optical micrographs showing the surface structure of KP-PPM-SP300 as-spun fibers at 500x (a) and 1000x (b) magnification. As-spun fiber cross-sections shown in (c).

Additional spinning trialed produced fibers that varied in size from diameters in the 25 µm range and above. A roll containing the smallest fibers (23.35 µm) was oxidized using an optimized condition set and subsequently carbonized to achieve a final peak strength of 259 ksi, 25 Msi and 1.21 % strain, which meet DOE targets. Using this processing route, a large format bundle was collected and some of the sample was sent to the UW for tow-level testing (Figure 260). Another portion of this material was converted and ultimately graphitized at temperatures >2000 °C. As expected, the graphitization lead to an increase in the modulus to 42 Msi but reduce the strength and % elongation to 227.3 ksi and 0.6 %, respectively. Ultimately, this shows that the CF properties can be tuned based on the desired application which may favor stiffness or strength assuming the fibers can be spun to small diameters and oxidized appropriately.

Figure 260: Approximately 12 g bundle of petroleum mesophase pitch carbon fiber sent to UW for composite testing.

Structure Development in PPM and CTPM Fibers

X-Ray scattering experiments in the wide and middle angle regimes was used to study the structural development in the PPM and CTPM systems used for this project. As-spun fiber was progressively converted first using oxidation in air, followed by carbonization in inert atmosphere to a moderate temperature of 1100 °C. It was observed that the major reflection associated with the mesophase polydomains $1.75 < q < 2$ for the green fiber displayed an orientation bias along the fiber axis. For both the PPM and CTPM the intensity of the peak broadens slightly with oxidation, suggesting a loss of orientation. Interestingly, the presence of a large scale structure ($q \sim 0.5$) is observed for the fibers up to 700 °C (Figure 261 and Figure 262)

and disappears after 1100 °C. Full indexing and quantification of the order parameters should be completed to yield a general model for understanding the morphology in pitch-based fibers.

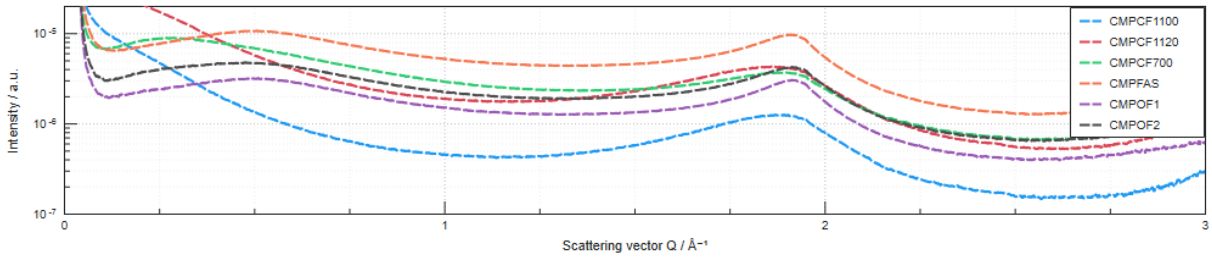

Figure 261: I(q) in the WAXS regime for CTPM used in this study showing the structure of green fiber through 1100 °C.

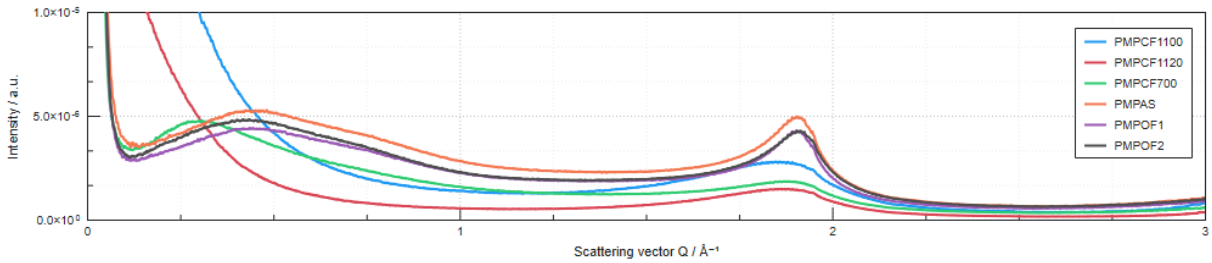

Figure 262: I(q) in the WAXS regime for PPM used in this study showing the structure of green fiber through 1100 °C.

CF Quality Relative to Primary QI in PP

It was discovered that the Koppers PP contained 2-3 wt% of primary carbonaceous (coke-like) primary quinoline-insolubles (QI). To understand the effects of organic QI in isotropic PP on the spinnability and properties of the derived CF, WRI prepared and delivered several samples of PPM of approximately the same SP from filtered and unfiltered PP. Multiple trials were undertaken for each mesophase sample utilizing spinning temperatures ranging from 320-350 °C. Minimized as-spun diameters for each supplied material are summarized in Table 87 and denoted by SP. All materials produced sub 20 µm green fibers, free of major surface defects. Notably, the filtered sample was able to achieve sub 10 µm diameters, equivalent to legacy high modulus pitch CFs. PPM fibers were then converted to CF using an oxidative stabilization followed by carbonization to temperatures between 1000-1400 °C. High resolution scanning electron micrographs of the filtered samples are shown in Figure 263. The single filament tensile results for the samples show a clear contrast in peak stress and elongation between the filtered and unfiltered compositions. Unfiltered pitch starting materials show a consistent inability to achieve > 0.7 % elongation, while the filtered alternatives easily achieve > 1.4 % in equivalent processing envelopes. Similarly, the average peak strength of PPM derived from unfiltered isotropic pitch do not exceed 150 ksi compared to approximately 260 ksi from the filtered. This suggests that filtration of the isotropic feed material is likely essential to achieve all key property

goals simultaneously for the project. Table 88 shows CF properties for filtered PPM and Table 89 and Table 90 show CF properties for two separate similar SP PPM samples. Direct observation at fracture surfaces with optimal microscopy has not yielded conclusive evidence of inclusion type defects but additional work is needed to definitively identify the origin of these performance differences.

Table 87: PPM samples and their minimum as-spun fiber diameters.

PPM SP	As-Spun Diam (µm)
307.2 Unfil	12-16 µm
307.9 Unfil	18-22 µm
308.1 Filtered	7-10 µm

Table 88: Mechanical properties of PPM SP308.1 filtered sample CF.

Sample	Break Stress (ksi)	Diameter (µm)	Modulus (Mpsi)	Strain (%)
2279	209.25	7.16	15.59	1.25
2309	214.84	6.57	16.84	1.20
2300	186.43	6.90	15.48	1.16
2298	264.94	7.46	16.82	1.45
2305	265.97	6.90	15.84	1.51

Table 89: Mechanical properties of PPM SP307.2 unfiltered sample CF.

Sample	Break Stress (ksi)	Diameter (µm)	Modulus (Mpsi)	Strain (%)
2304	144.4	12.7	23.6	0.61
2302	125.4	14.0	20.8	0.61
2299	132.5	13.2	20.9	0.64
2306	129.1	10.6	19.8	0.67

Table 90: Mechanical properties of PPM SP307.9 unfiltered sample CF.

Sample	Break Stress (ksi)	Diameter (µm)	Modulus (Mpsi)	Strain (%)
2270	111.44 (33.86)	17.23 (0.48)	23.98 (0.42)	0.51 (0.14)
2301	118.89 (23.13)	17.04 (0.98)	24.23 (0.43)	0.53 (0.08)
2265	73.92 (29.98)	16.17 (0.57)	15.64 (0.00)	0.36 (0.16)

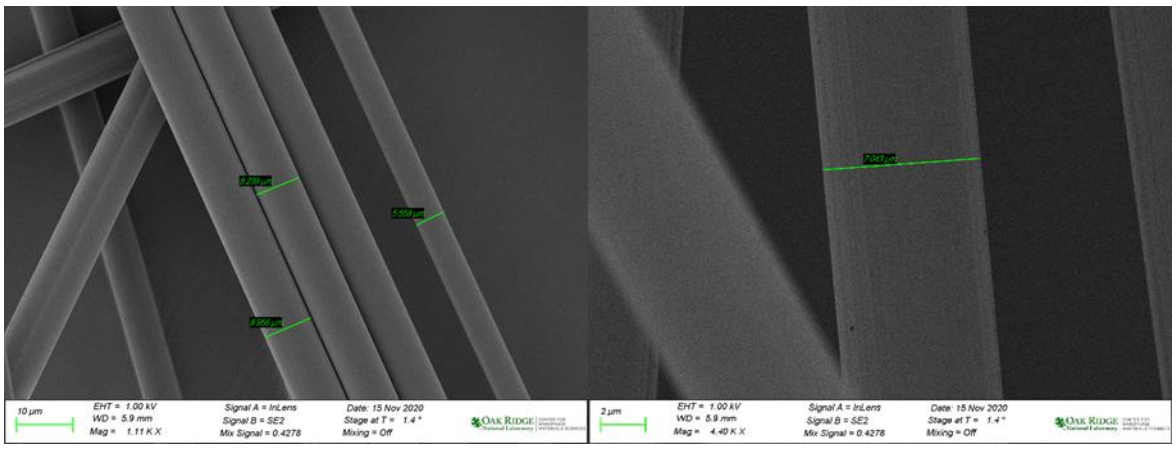

Figure 263: Scanning electron micrographs of PPM from filtered isotropic pitch in the as spun (left) and carbonized (right) form.

Additional studies were performed to control the effect of diameter in the filtered and unfiltered systems. Contrasts in the apparent spinnability were found, exhibited by differences in the minimum achievable diameter. Filtered PPM was spun to a diameter of approximately 13 µm and was able to reach a peak strength and percent elongation of 285 ksi and 1.17, respectively. In comparison, the unfiltered material at a similar diameter produced a peak elongation of 0.6 %. This contrast clearly illustrates the effect of isotropic filtration to remove the few percent of primary QI initially present in the PP on the final CF properties, potentially attributed to the reduction of coke or semi-coke inclusions within the microstructure.

Pitch-based Feedstock and Precursor Analyses

In January 2020 Koppers joined this project as an industrial advisor and provided some samples of PP mesophase, isotropic pitch and some corresponding slurry oil. These samples were analyzed so that the data can be used for the modeling and ML efforts. A mesophase sample produced at the end of 2019, KP-PM-19, had a SP of 298 (KPPM SP298) and the visual texture of the melted sample was homogenous and continuous as shown in Figure 264. This sample was processed at ORNL which qualified to produce CF than met DOE strength and modulus requirements but was shy of the elongation requirements. It is believed by ORNL that with

additional refinement of the spinning conditions, that the material can meet the elongation requirements.

Figure 264: Photograph of the KPPM SP298 after SP determination.

Cross-polarized light optical microscopy of the KPPM SP298 showed a large amount of continuous mesophase but also a significant amount of large isotropic domains with mesophase spheres, this is shown in Figure 265.

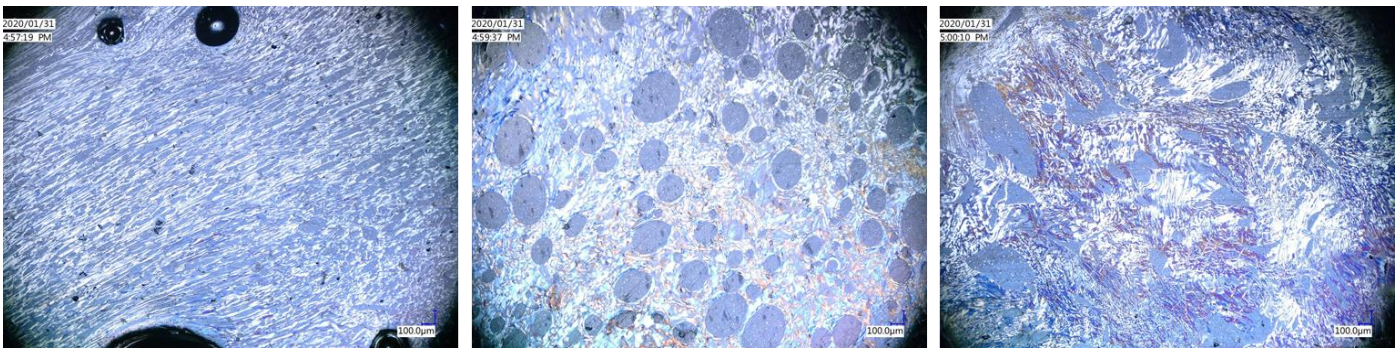

Figure 265: Cross-polarized light optical microscopy of KPPM SP298 showing different types of morphology from different sample of the mesophase.

Additional batches of PPM were supplied by Koppers which contained samples with a SP 299.7 and SP 361.1. Figure 266 shows some cross-polarized light microscopy images for the SP 299.7.1 material. From the samples that were evaluated, the SP 299.7 material did appear to have less, larger isotropic domains than the previous SP 298 material. For the SP 361.1 PPM material, it appeared to be nearly all mesophase with very little to no isotropic pitch remaining in the samples. The SP 361.1 material was highly porous which is likely due to its high viscosity at processing conditions which doesn't allow the pitch to readily release entrained gas which evolves during the reaction or the purge gas. During the SP testing, the two new materials produced smooth teardrop formation and dropped smoothly and uniformly from the SP cups. This suggests that these materials are suitable for continuous spinning.

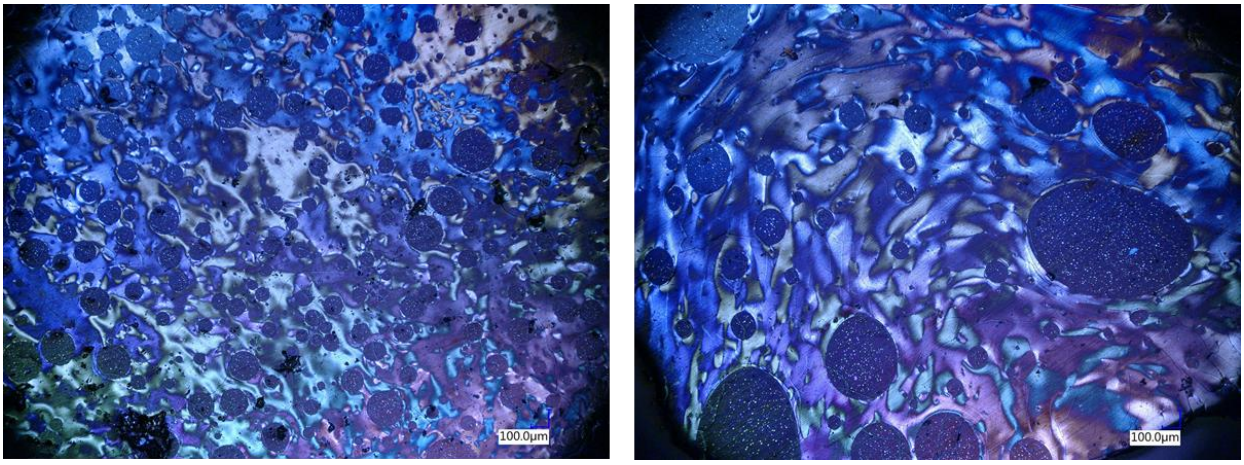

Figure 266: Cross-polarized light optical microscopy of KPPM SP299.7 showing different types of morphology from different samples of the mesophase. Small mesophase spheres are present within the larger isotropic spheres.

PP that was used to prepare larger batches (~1Kg) for multifilament CF during BP2 easily met DOE targets for strength and modulus, however it did not meet DOE requirements for elongation. The DOE goal is 1% elongation, and 0.62% was achieved. One possible reason for the lower than expected elongation is the presence of primary QI initially present in the Koppers PP (KP-PP-19). Filtration studies showed that KP-PP-19 contained about 2.3% of primary-QI that was not soluble in N-methyl-2-pyrrolidone (NMP). During BP1it is was found the primary QI levels filtered from quinoline and NMP were very similar. Figure 267 shows the primary-QI filtered from KP-PP-19. The black color of the filtered primary-QI shows that this material is carbonaceous and not typical of catalyst fines which are usually grey. TGA also shows that the samples are 98+% carbonaceous.

Figure 267: Dried primary-QI (2.3 %) from initial Koppers PP (500 g) that was insoluble in NMP and collected by filtration.

It is expected that the primary-QI physical impurities present in KP-PP-19 lead to point defects within the CF. These particles introduce heterogeneous boundaries at the particle interfaces where stresses accumulate ultimately leading to failure in the CF. The low amount of primary-QI, compared to most traditional North American CTP, doesn't appear to significantly affect the evolution in the mesophase morphology. This is inferred from cross-polarized light optical microscopy which shows continuous mesophase domains with smaller isotropic pitch inclusions. When high primary-QI is present, as is the case for most CTP, the QI accumulates at mesophase sphere surfaces and prevents coalescence of the mesophase into continuous flow domains. Although the mesophase morphology is not significantly affected, these point defects may become more significant during mesophase production since about half of the pitch is lost during the mesophase conversion process meaning that the amount of defects are significantly higher in the PPM (~4-5 %) than in the KP-PP-19 (2.3 %).

To determine the impact of the bulk carbonacous primary-QI on the final CF strength and elongation properties, samples of KP-PP-19 filtered (0% primary-QI) and unfiltered (2.3% primary-QI) were converted into mesophase pitch. These PPM samples were sent to ORNL for small-scale single filament melt spinning and CF production. The goal was to produce mesophase from the filtered and unfiltered samples with about the same SP, have them spun to about the same fiber diameter, and processed identically to produce CF. The difference in the elongation properties of the resulting CFs did help to quantify the effect of primary QI (explained previously). Table 91 shows the KP-PP-19 mesophase experiments that were

performed and the samples that were sent to ORNL. The yields for the PPM averaged to 48% with 42% effluent collected, 2% infusible material from the reactor and 7% mass loss.

Table 91: PPM experiments performed with filtered and unfiltered KP-PP-19. Lines highlighted in green were sent to ORNL.

Treatment	Date	Feed Material (SP, °C)	Feed, g	SP, °C	Yield, g	Effluent, g	Infusible, g	Total, g	Loss, g
Unfiltered	9/23/2020	KP-MP-19 (116.2)	65.02	307.9	26.86	32.40	1.75	61.01	4.01
	9/28/2020	KP-MP-19 (116.2)	65.00	298.6	27.99	30.80	0.71	59.50	5.50
	10/6/2020	KP-MP-19 (116.2)	65.03	303.0	27.47	30.93	1.71	60.11	4.92
	10/20/2020	KP-MP-20 (121.6)	65.00	307.2	29.05	31.17	1.22	61.44	3.56
Filtered	10/8/2020	KP-MP-19A (122.4)	65.00	308.1	35.20	24.26	1.50	60.96	4.04
	10/15/2020	KP-MP-19A (122.4)	65.03	303.2	37.17	22.09	1.24	60.50	4.53

Cross-polarized light optical microscopy was used to evaluate the mesophase content and morphology. Samples with a SP above around 305 °C showed very high mesophase content with generally small amounts of small isotropic domains, while samples with a lower SP showed more and larger isotropic domains containing some dispersed mesophase spheres. Figure 268 shows examples of the filtered and unfiltered PPM, both with about a 308 SP.

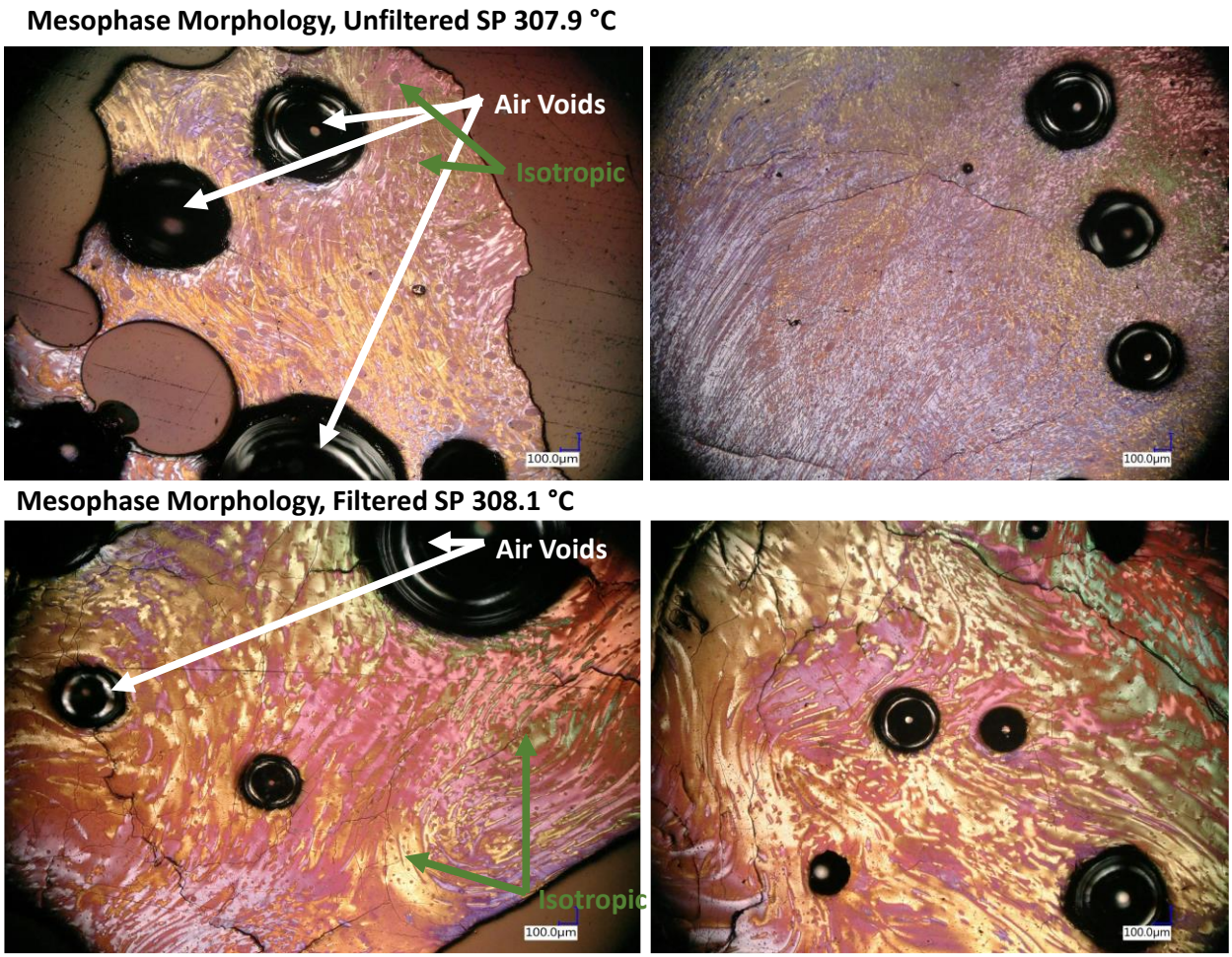

Figure 268: Cross-polarized light optical microscopy of KP-PP-19 filtered and unfiltered that was used to produce PPM a SP of about 308 °C. Top shows images from SP 307.9 °C PPM and the bottom shows images from SP 308.1 °C PPM.

WRI prepared 2.5 Kg of filtered PP and sent this to Koppers to prepare mesophase pitch. WRI received 1.5 Kg of mesophase pitch produced by Koppers (KP-MP-21-0480) and characterized the sample before sending it to ORNL for spinning. Cross-polarized light optical microscopy showed that the bulk of the sample had a high mesophase content of around 90% and it did contain some larger isotropic pitch domains with mesophase spheres (Figure 269).

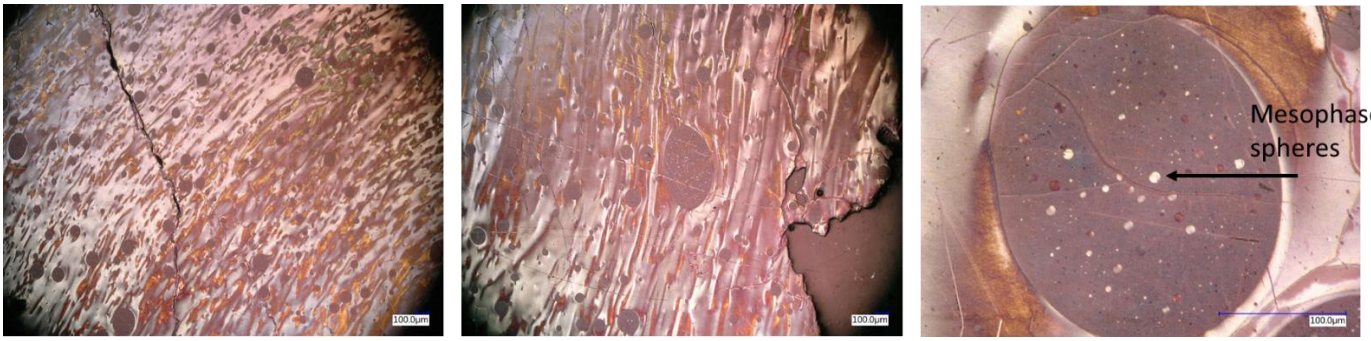

Figure 269: Cross-polarized light optical microscopy for KP-MP-21-0480.

The SP was determined to be 317.7 °C and SP sample showed that the pitch had uniform melt behavior with a smooth surface and did not phase separate, however there was a significant amount of buildup on the walls of the glass tube used for the SP test from volatiles. A photograph of the SP test sample is shown in Figure 270.

Figure 270: Photograph of the SP sample for KP-MP-21-0480. Yellow haze on the glass of the SP test vials indicates the presence of volatiles.

TGA analysis of the sample showed that it did contain significant volatiles below about 395 °C. A portion of the sample was crushed and devolatilized at 220 °C overnight under vacuum. However this led to only a small reduction in the volatiles. The sample was then loaded into a 1L reactor and heated to 395 °C for 2 hrs using a sparge of nitrogen through the stirred and heated sample (a smaller volume trial run was completed using a 100 mL reactor). The resulting sample had about 3% less volatiles (< 395 °C) and a SP of 331.5 °C (KP-MP-21-0480DV). The lower

amount of volatiles can be shown in the overlays of the derivative curves for the TGA in Figure 271. This devolatilized sample was sent to ORNL for evaluation for CF spinning. However, due to limitations on budget and time the CF spinning evaluation of this material was not completed.

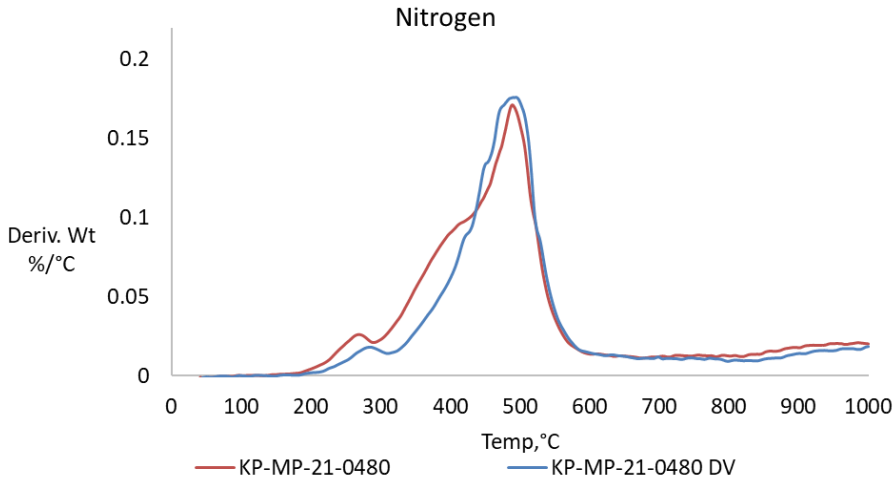

Figure 271: Derivative of the TGA weight loss curve for KP-MP-21-0480 and KP-MP-21-0480DV.

To fulfil the PPM scale up requirements of BP3, Koppers provided about 5 Kg of PPM to the program in three separate batches. These samples are 20-1079 (SP = 316.8 °C), 20-1133 (SP = 317.8), and 20-1222 (316.3). These materials were characterized by their SP to determine suitability of CF spinning. During analysis it was discovered that the fines in two of the samples were significantly different in consistency from the larger chunks. Fines from two of the samples exhibited heterogeneous melt behavior. It is recommended that the fines be removed and only the large chunks be used for further study. Figure 272 shows the SP samples after the analysis of the three different Koppers PM.

Figure 272: Photograph of scaled up Koppers PPM SP samples after analysis. SP samples of the fines are shown at the top and SP samples from the bulk chunks are shown at the bottom. Fines from the two samples on the left were heterogeneous and significantly different from the bulk (coarse chunks). The SP in °C is listed at the bottom of the bottom row of SP samples.

Further TGA analysis was obtained of the bulk chunks with homogenous melt properties and the fines exhibiting heterogeneous melt properties during SP testing. From the TGA data, it is clear the fines contained significantly more volatiles than the bulk coarse chunks. Figure 273 shows the derivative of the weight loss profile showing that the fines in two samples contained significantly more volatiles than the bulk chunks, and the imbedded table shows the carbon residue, or coking index, for the various samples. Volatiles can be detrimental to the melt spinning process because the off gassing can potentially cause defects during the spinning leading to breakage and short sections of fibers and they can potentially lead to defects in the final CF. As a result it recommended that fines from the scaled up batches of PPM from Koppers be removed and discarded prior to further characterization and spinning.

Sample Name	Carbon Residue Wt%
KP-MP-20-1079 (fines)	60.02
KP-MP-20-1133 (fines)	60.65
KP-MP-20-1222 (fines)	73.36
KP-MP 20-1079 (chunks)	72.50
KP-MP 20-1133 (chunks)	72.83
KP-MP 20-1222 (chunks)	72.38

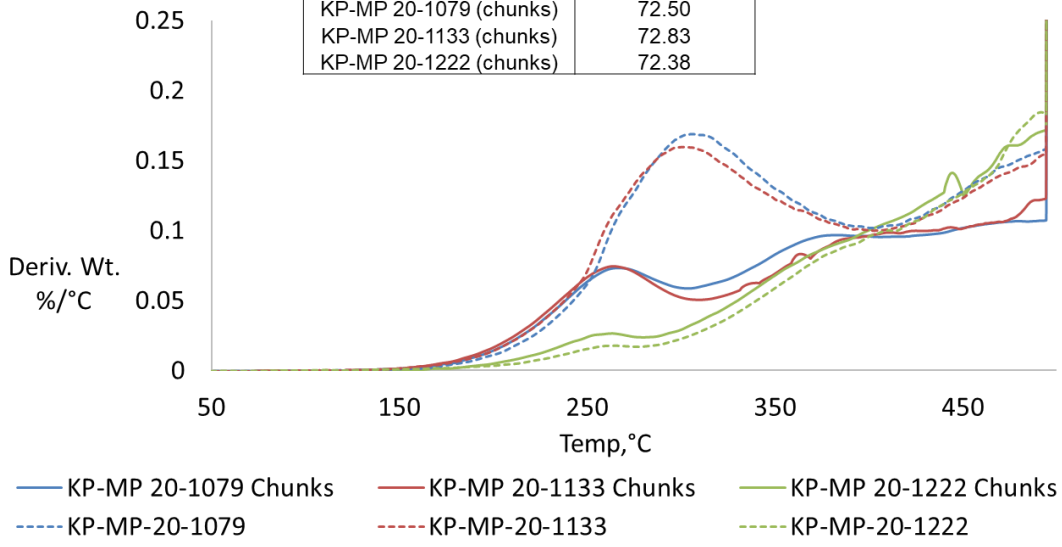

Figure 273: Derivative of the TGA weight loss profile for the fines and bulk chunks of various Koppers mesophase samples and the imbedded table shows the coking index (carbon residue) values for the fines and chunks.

All PP and PPM materials were characterized by their SP. As previously mentioned, the behavior of the samples during SP determination can immediately rule out samples that are not appropriate for spinning continuous fibers, as well as insight into appropriateness for melt spinning conditions and an indication of mesophase content, yield, and spinning and stabilization. Since each pitch material is slightly different, the SP is a quick and indispensable method to judge the materials, and obtaining this data is useful also for ML purposes. Table 92 shows the SP of the mesophase samples prepared by WRI as well as samples of mesophase that were received from Koppers.

Table 92: Softening point for PP and PPM for samples received or prepared. Samples marked with an * indicate samples which underwent phase separation.

	Sample	Label	Cup 1	Cup 2	Mean	Difference
Koppers/ WRI Prepared	Koppers Petroleum Pitch 2019-1261	KP-PP-19	116.2	116.3	116.3	0.1
	Koppers Petroleum Pitch 2019-1261 (Filtered)	KP-PP-19A	122.3	122.5	122.4	0.2
	Koppers Petroleum Pitch 2020-0784	KP-PP-20	121.6	121.6	121.6	0.0
	Koppers Petroleum Pitch 2020-0784 (Filtered)	KP-PP-20A	122.6	122.6	122.6	0.0
	Koppers Petroleum Pitch 2020-0784 (Filtered)	KP-PP-20B	122.3	122.4	122.3	0.1
Koppers Prepared	Koppers Mesophase 2019-1741	KP-MP-19	297.2	296.1	296.7	1.1
	Koppers Mesophase 2020-0289*	KP-MP-20	294.4	288.2	291.3	6.2
	Koppers Mesophase 2020-0655	KP-MP-20-0655	299.6	299.8	299.7	0.2
	Koppers Mesophase 2020-0508	KP-MP-20-0508	361.4	360.8	361.1	0.6
	Koppers Mesophase 20-1079 (fines)*	KP-MP-20-1079	298.5	293.5	296.0	5.0
	Koppers Mesophase 20-1133 (fines)*	KP-MP-20-1133	294.3	286.2	290.3	8.1
	Koppers Mesophase 20-1222 (fines)	KP-MP-20-1222	317.2	316.5	316.8	0.7
	Koppers Mesophase 20-1222 (fines)	KP-MP-20-1222	315.7	316.9	316.3	1.2
	Koppers Mesophase 20-1133 (chunks)	KP-MP-20-1133	318.0	317.7	317.8	0.3
	Koppers Mesophase 20-1079 (fines)	KP-MP-20-1079	316.5	317.1	316.8	0.6
WRI Prepared	Koppers Mesophase Reaction date: 9/23	KP-MP-9/23	308.0	307.9	308.0	0.1
	Koppers Mesophase Reaction date: 9/28	KP-MP-9/28	298.9	298.3	298.6	0.6
	Koppers Mesophase Reaction date: 10/1	KP-MP-10/1	302.9	302.0	302.5	0.9
	Koppers Mesophase Reaction date: 10/6	KP-MP-10/6	302.9	303.1	303.0	0.2
	Koppers Mesophase Reaction date: 10/8	KP-MP-10/8	308.0	308.3	308.1	0.3
	Koppers Mesophase Reaction date: 10/15	KP-MP-10/15	303.0	303.5	303.2	0.5
	Koppers Mesophase Reaction date: 10/20	KP-MP-10/20	307.7	306.8	307.2	0.9
	Koppers Mesophase Reaction date: 10/23	KP-MP-10/23	304.9	305.5	305.2	0.6
	Koppers Mesophase Reaction date: 10/28	KP-MP-10/28	304.0	303.8	303.9	0.2
	Koppers Mesophase Reaction date: 11/18	KP-MP-11/18	302.9	302.6	302.7	0.3
Other Commercial Source	Commercial Petroleum Pitch	Com-PP-20	113.4	112.8	113.1	0.6
	Commercial Petroleum Pitch (Filtered)	Com-PP-20A	114.9	115	115.0	0.1
	Commercial Mesophase	Com-MP-20	297.3	296.7	297.0	0.6

Elemental composition (Table 93) data for PP and PPM samples were obtained to help understand the chemical composition of the PP and PPM samples and as an input for ML. As expected the samples were quite high in carbon content and very low in nitrogen and oxygen with some variation in sulfur content, depending on the source of the pitch. As seen in the previous BPs, PP has lower aromaticity than derived PPM samples as expected to occur during dealkylation and dehydrogenation to produce the mesophase.

Table 93: CHNOS data for PP and PPM samples in BP3.

	Sample ID	Carbon % w/w	Hydrogen % w/w	Nitrogen % w/w	Oxygen % w/w	Sulfur % w/w	Total	H/C
PP	M-50	94.43	5.50	0.19	0.61	0.55	101.28	0.70
	ACP 10	93.85	5.69	0.07	1.43	0.28	101.32	0.73
	KP-PP-19	94.61	5.44	0.15	0.25	0.30	100.75	0.69
	KP-PP-20	95.41	5.64	0.08	0.20	0.12	101.45	0.71
PPM	ACP-M1	95.08	4.27	0.27	0.29	0.55	100.46	0.54
	ACP 20	95.64	4.39	0.09	0.50	0.52	101.14	0.55
	KP-MP-19	95.63	4.34	0.11	0.18	0.23	100.49	0.54
	KP-MP-20-0289	96.20	4.53	0.09	0.31	0.25	101.38	0.57
	KP-MP-20	96.27	4.41	0.08	0.34	0.23	101.33	0.55
	KP-MP-20-0508	96.62	4.07	0.09	0.33	0.23	101.34	0.51
	KP-MP-20-1222c	96.80	4.28	0.08	0.28	0.10	101.54	0.53
	KP-MP-20-1133c	96.71	4.26	0.09	0.25	0.10	101.41	0.53
	KP-MP-20-1079c	96.55	4.32	0.08	0.22	0.09	101.26	0.54
	KP-MP-9/23	95.41	5.64	0.08	0.20	0.12	101.45	0.71
	KP-MP-9/28	96.33	4.46	0.06	0.20	0.24	101.29	0.56
	KP-MP-10/1	96.44	4.40	0.06	0.21	0.25	101.36	0.55
	KP-MP-10/6	96.48	4.47	0.06	0.23	0.25	101.49	0.56
	KP-MP-10/8	96.49	4.50	0.06	0.24	0.24	101.53	0.56
	KP-MP-10/15	96.36	4.47	0.07	0.23	0.23	101.36	0.56
	KP-MP-10/20	96.33	4.49	0.07	0.23	0.23	101.35	0.56
	KP-MP-10/23	96.42	4.49	0.06	0.21	0.09	101.27	0.56
	KP-MP-10/28	96.81	4.47	0.06	0.20	0.10	101.64	0.55
	KP-MP-11/18	95.96	4.53	0.06	0.21	0.09	100.85	0.57
Effluent	KP-MP-Effluent	93.22	6.24	0.16	0.57	0.43	100.62	0.80

The various PP samples receive in this program were analyzed by the WRI saturates, aromatics, resins-Asphaltene Determinator (SAR-AD^{TM}) separation. SAR-AD data (Table 94) showed that there was a general correlation between the SP and the asphaltene content of the pitch (Figure 274). The ACP 10 sample does not fit the general trend. The total area for the evaporative light scattering detector did not indicate that this material is softer because it contains more light ends than the other samples. The relatively high asphaltene content, coupled with the lower SP, may be an indicator of ACP's unique process. In any case, SAR-AD data shows that PP is largely dominated by Aro 3 which contains 4+ ring aromatic structures and also asphaltenes which are assumed to be ring structures which are greater than about 8-10 rings. The data also shows that that decant oil (FCC slurry oil with most catalyst fines removed), which is used to produce PP, contains Saturates and more Aro 2 (2-3 ring aromatics) than the PP. This is consistent with the thermal soaking process which is used to convert the smaller aromatic units in the decant oil into PP. SAR-AD data also shows that the effluent from PPM contains mainly Aro 2 and Aro 3 material and lacks heavier asphaltenes. The lack of asphaltenes is expected since asphaltenes are very large molecules and typically not volatile.

Table 94: SAR-AD data for various isotropic pitch samples as well as feed decant oils and reactor effluent after thermal processing to produce the mesophase pitch.

Sample ID	Maltenes					Asphaltenes			
	Sat	Aro 1	Aro 2	Aro 3	Resins	CyC_6	Toluene	CH_2Cl_2:	Total
KP-PP-20 Mesopahse Effluent (WRI)	1.05	0.07	26.53	72.20	0.13	0.00	0.03	0.00	0.03
KP-PP-20	0.22	0.02	14.85	68.21	0.15	0.04	14.34	2.17	16.55
KP-PP-19	0.15	0.00	16.51	66.71	0.24	0.03	14.06	2.30	16.39
Com-PP-20	0.53	0.04	11.27	77.42	0.63	0.04	9.28	0.79	10.12
ACP-10	0.19	0.03	20.42	61.25	0.92	0.05	14.86	2.27	17.19
M-50	0.03	0.00	12.18	68.99	0.85	0.05	15.88	2.02	17.95
MC Pitch	0.63	0.04	14.03	67.38	0.38	0.06	14.93	2.55	17.53
Slurry/Decant Oil 1	18.34	0.37	41.45	38.01	0.51	0.00	1.31	0.00	1.31
Slurry/Decant Oil 2	17.12	0.31	49.93	31.95	0.34	0.00	0.35	0.00	0.35

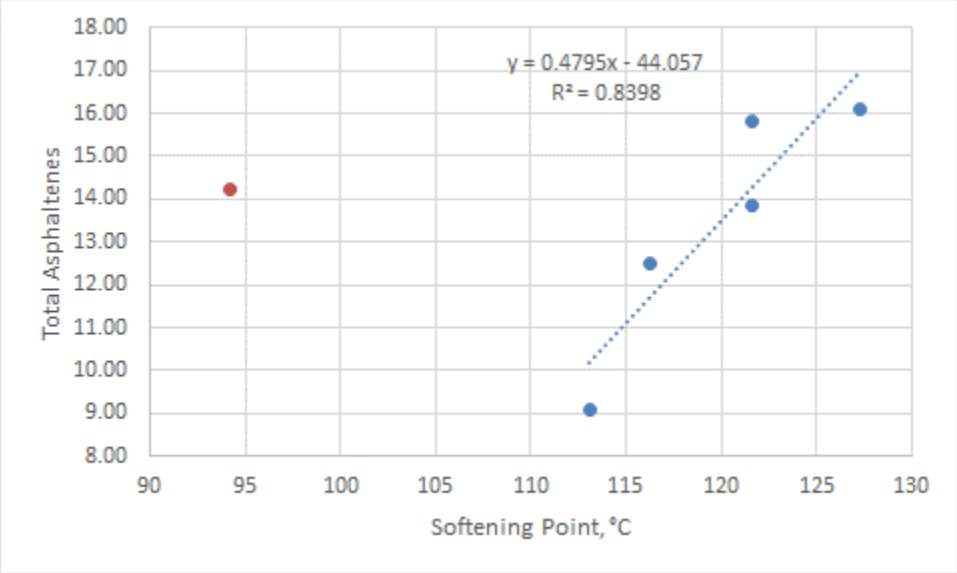

Figure 274: Correlation between asphaltene content and SP for the various PP samples.

PP and PPM samples were characterized for the chemical functional groups by FTIR using the KBr pellet method. The data was worked up according to procedures in BP1 and BP2. Figure 275 shows selected FTIR spectra for PP, Figure 276 shows select FTIR spectra for PPM, and Figure 277 shows the comparison between PP and PPM. Overall, from Figure 275 there is not a significant difference between the different PP samples with the largest variations occurring in the aromatic and alkyl C-H stretch region (3100-2750 cm^{-1}) and some small differences in the out-of-plane bands (900-675 cm^{-1}). In Figure 276 small differences between the Koppers PPM samples and a commercial mesophase was observed in the aromatic and alkyl C-H stretch region. When comparing PP to PPM, in Figure 277, there are significant differences such as PPM having a decrease in the alkyl C-H stretch region (2950-2855 cm^{-1}) and alky C-H bending (1437 cm^{-1}) with and an increase in the aromatic C-H stretch (3035 cm^{-1}) and aromatic C=C ring

stretch (1600 cm^{-1}). These changes are consistent with dealkylation and increased aromatic condensation upon mesophase formation.

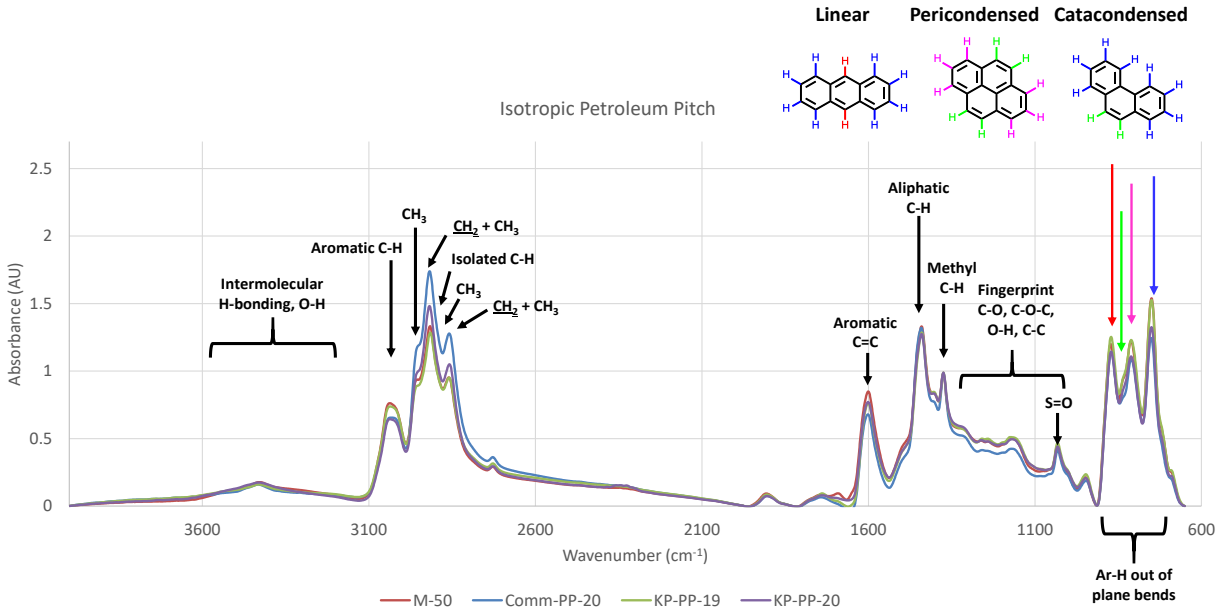

Figure 275: FTIR spectra of select PP materials with some assignments.

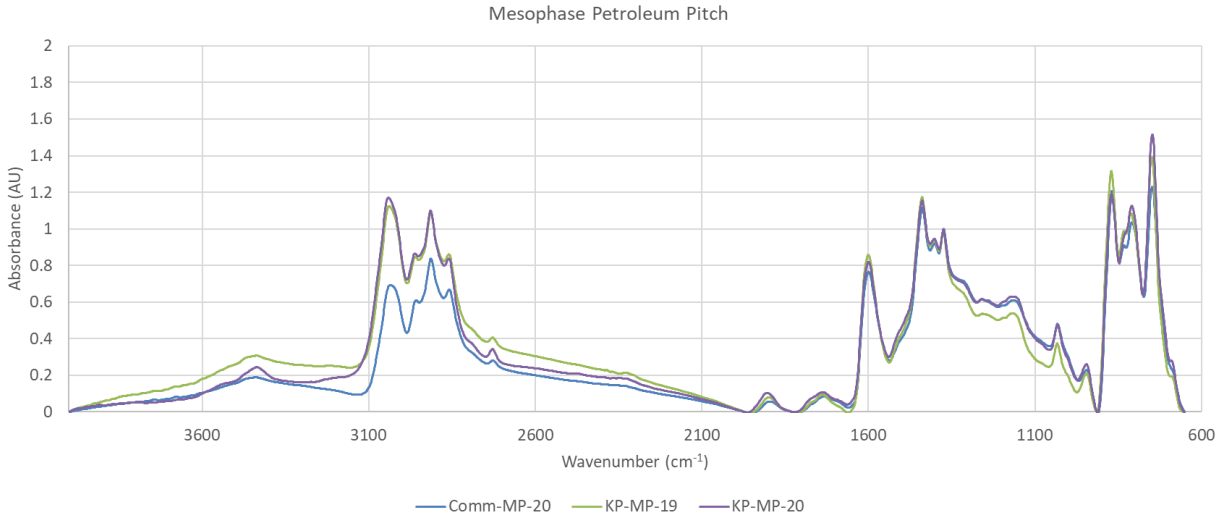

Figure 276: FTIR spectra of select PPM materials.

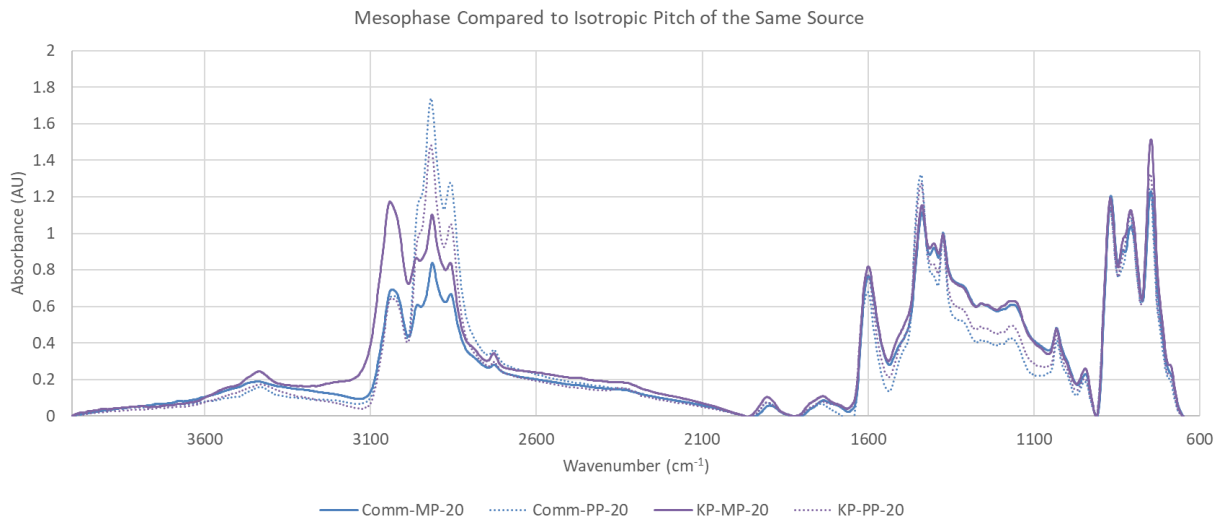

Figure 277: FTIR spectra of select PP and PPM materials.

As with BP1 and BP2, various metrics from the FTIR spectra were calculated and used to characterize the materials and to provide inputs for ML. Table 95 shows the calculated FTIR values for the PP and PPM samples.

Table 95: Various FTIR indices calculated using parameters from BP1 and BP2.

	Sample ID	Chain Index 1	Chain Index 2A	Chain Index 2B	Aromatic Index 1	Aromatic Index 2	ortho-substitution index
		ICH3(2956)/ICH2(2921)	CH2(1452)/CH3(1376)	1437/1376	C=C(1601)/(C=C(1601)+CH2(1437)+CH3(1376)	ArC-H(3044)/(ArC-H(3044)+CH2(2921))	746/(876+839+813+746)
PP	M-50	0.710	1.346	1.425	0.280	0.359	0.311
	ACP 10	0.707	0.972	1.118	0.271	0.343	0.305
	KP-PP-19	0.677	1.104	1.271	0.251	0.351	0.310
	KP-PP-19A	0.716	1.042	1.210	0.259	0.373	0.309
	KP-PP-20	0.671	1.130	1.250	0.255	0.296	0.298
	KP-PP-20A	0.682	1.200	1.270	0.239	0.267	0.290
	KP-PP-20B	0.802	1.164	1.281	0.265	0.399	0.301
PPM	ACP-MP	0.726	1.017	1.192	0.293	0.500	0.299
	ACP 20	0.708	1.040	1.210	0.288	0.482	0.283
	KOP MP 1	-	-	-	-	-	-
	KP-MP-19	0.699	1.107	1.264	0.298	0.496	0.280
	KP-MP-20-0289	0.657	1.024	1.234	0.276	0.490	0.314
	KP-MP-20	0.685	1.011	1.195	0.288	0.485	0.287
	KP-MP-20-0508	0.702	0.962	1.156	0.290	0.546	0.292
	KP-MP-20-1222c	0.681	1.061	1.242	0.299	0.516	0.285
	KP-MP-20-1133c	0.667	1.072	1.249	0.301	0.531	0.294
	KP-MP-20-1079c	0.666	1.062	1.240	0.299	0.531	0.294
	KP-MP-21-0480	-	-	-	-	-	-
	KP-MP-21-0480 (DV)	-	-	-	-	-	-
	KP-MP-9/23	0.681	1.077	1.244	0.293	0.492	0.275
	KP-MP-9/28	0.677	1.010	1.207	0.282	0.478	0.283
	KP-MP-10/1	0.675	1.050	1.234	0.289	0.485	0.282
	KP-MP-10/6	0.675	1.034	1.218	0.287	0.482	0.280
	KP-MP-10/8	0.687	1.033	1.215	0.288	0.486	0.280
	KP-MP-10/15	0.689	0.987	1.176	0.276	0.476	0.284
	KP-MP-10/20	0.690	0.994	1.191	0.278	0.469	0.278
	KP-MP-10/23	0.688	0.984	1.176	0.278	0.464	0.278
	KP-MP-10/28	0.687	0.994	1.193	0.279	0.464	0.277
	KP-MP-11/18	0.696	0.957	1.166	0.274	0.460	0.280

Fluorescence spectra were obtained for the various PP samples used in this program under different excitation wavelengths. Qualitatively, it appears that at 360 nm excitation the emission spectra show some correlations with the compositional SAR-AD data. In the emission spectra lower wavelengths correspond to conjugated ring systems with less fused aromatic rings and higher wavelengths correspond to ring systems with more fused aromatic rings. Figure 4 shows that the sample with the most Aromatics 3 has the highest intensity at lower emission wavelengths and that increasing asphaltene content manifests as an increasing intensity at higher wavelengths. Differences in the degree of peri-condsensed and cata-condesned can also have an effect on the shift, however since these are all petroleum pitch samples it can be assumed that the distribution of condensation is similar. Heteroatoms can also be responsible for a red shift, however there are very few heteroatoms present in PP.

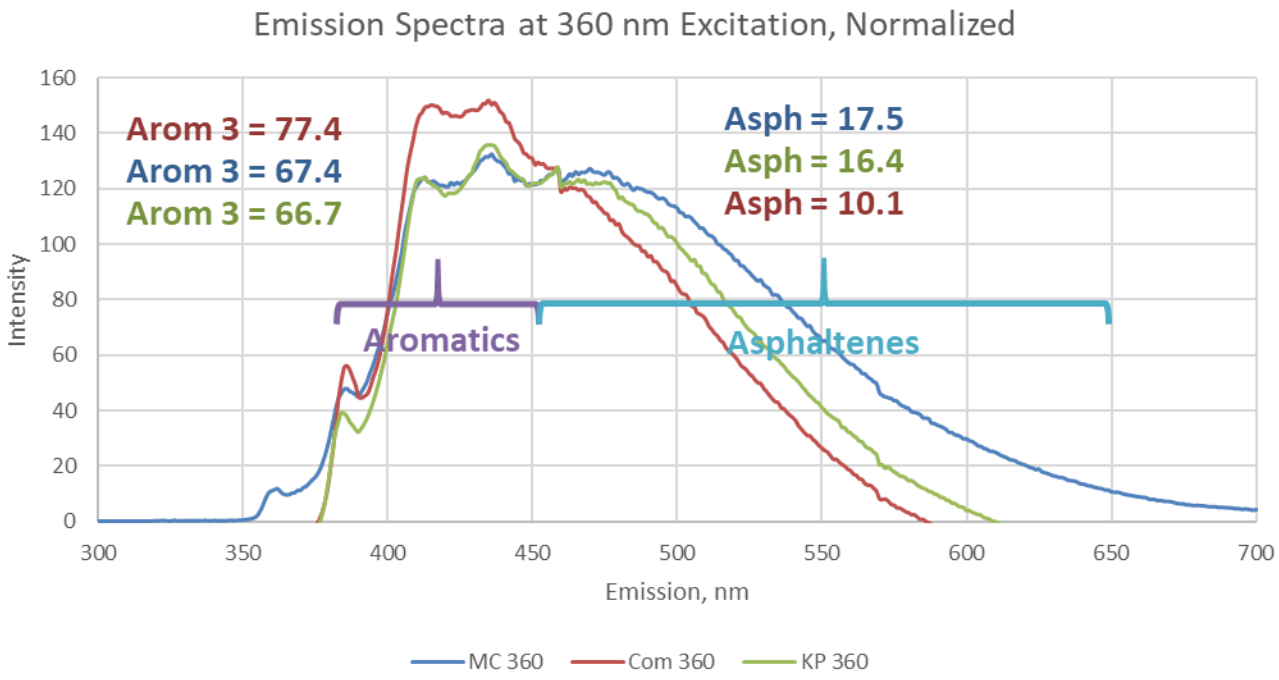

Figure 278: Emission spectra collected using 360 nm excitation for three different pitch samples with varying SAR-AD composition. Imbedded values come from SAR-AD data in Table 94.

During the production of PPM, about half of the material is lost as an effluent, which is easily collected. This material can be recycled back into the isotropic PP production process and used to make additional mesophase. It was determined by GCMS that this material contains mainly 3-6 (mostly 4-5) ring aromatics with 1 or more methyl groups. These compounds are similar to aromatic species already found in PP, which was also verified by GCMS. Moreover, these results are also consistent with SAR-AD results.

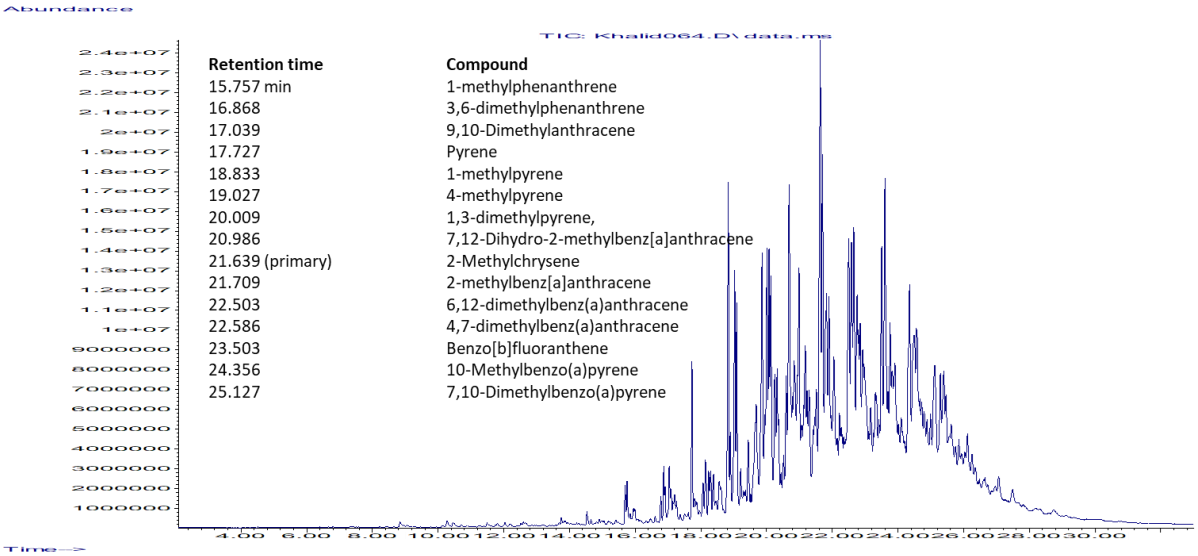

Figure 279: GCMS chromatogram of the reactor effluent from production of KP-PP-19 into mesophase. Select identified compounds are listed in the embedded table.

Quantification of common small PAH molecules were further determined using GCMS. Table 96 shows PAH values for CTP, CTPM and effluent produced from mesophase production and Table 97 shows values for slurry oil PP, PPM and effluent. Results show that CTP is very high in small PAH compounds, up to 26 wt%, and that the effluent is also heavily enriched in these PAH compounds. Mesophase pitch, on the other hand, has relatively very little small PAH content. Slurry oil and PP have significantly less PAH than CTP due to their high degree of mainly methyl and other alkyl substitutions. As with CTP, mesophase produced from PP has significantly less smaller PAH molecules, but the effluent contains a higher amount of PAH molecules due to pyrolysis which cleave aromatic-aliphatic bonds and due to smaller aromatic fragments being liberated during bond rearrangements.

Table 96: PAH quantification of CTP, CTPM and effluent produced during mesophase production.

	Coal Tar Pitch							
PAH	CTP3	CTP4	CTP5	CTP6	CTP7	CTP6M SP 314	CTP6M SP 320	Effluent CTP6
Naphthalene	-	-	-	-	-	0.69	1.6	-
Acenaphthylene	-	5	7.9	3.5	2.2	-	-	-
Acenaphthene	1.8	200	470	180	100	9.3	10	1700
Fluorene	8.4	300	880	120	82	0.22	0.54	60
Phenanthrene	120	7000	16000	5700	3200	1.1	2.0	1900
Anthracene	82	2200	4000	2400	1400	0.81	0.94	900
Carbazole	28	1700	2400	1300	780	0.10	0.24	1100
Fluoanthrene	330	19000	28000	26000	19000	2.0	2.3	22000
Pyrene	500	16000	24000	23000	17000	5.9	8.3	19000
Chrysene	830	15000	20000	26000	18000	3.1	7.4	27000
Benz(a)anthracene	740	16000	22000	25000	17000	1.2	5.5	27000
Benzo(b)fluoranthene	1200	21000	29000	38000	26000	6.8	18	43000
Benzo(k)fluoranthene	1000	13000	17000	21000	13000	5.4	15	28000
Benzo(a)pyrene	1400	20000	22000	35000	23000	26	49	43000
Indeno(1,2,3-C,D)pyrene	2100	15000	15000	23000	15000	73	250	25000
Dibenz(a,h)anthracene	1700	4400	4200	6800	4600	26	26	6500
Benzo(ghi)perylene	2100	15000	16000	20000	15000	130	450	20000
Total ppm	12140	165805	220958	253504	173164	292	847	266160
% of Sample	1.2	16.6	22.1	25.4	17.3	0.0	0.1	26.6

Table 97: PAH quantification of slurry oil, PP, PPM and effluent produced during mesophase production. For the last 3 samples the benzo(b)fluoranthene and benzo(K)fluoranthene are added together.

	Slurry Oil	Petroleum Pitch						
PAH	Koppers	KP-PP-19	KP-MP-19	M50	ACP20	Com-PP-20	Com-MP-20	Effluent KP-PP-20
Naphthalene	15	-	-	-	1.3	-	-	32
Acenaphthylene	-	-	-	-	-	-	-	-
Acenaphthene	18	-	-	-	1.1	6.1	-	31
Fluorene	36	-	0.50	-	1.2	12	-	8.3
Phenanthrene	410	-	9.0	51	17	4.6	3.9	85
Anthracene	100	-	11	36	8.5	3.1	-	44
Carbazole	-	-	-	-	0.69	-	-	6.7
Fluoanthrene	40	23	3.4	51	13	20	2.0	61
Pyrene	550	280	17	860	150	79	2.2	380
Chrysene	1300	640	19	960	87	180	6.0	560
Benz(a)anthracene	2400	1500	24	1600	74	180	3.2	700
Benzo(b)fluoranthene	230	490	36	610	33	250	4.9	1800
Benzo(k)fluoranthene	79	180	17	480	16			
Benzo(a)pyrene	800	2700	350	2400	240	1200	7.6	9800
Indeno(1,2,3-C,D)pyrene	-	230	170	160	29	430	14	3200
Dibenz(a,h)anthracene	120	420	130	320	27	870	6.8	3500
Benzo(ghi)perylene	380	1600	1200	1300	220	2200	85	17000
Total ppm	6478	5363	1987	8828	919	5435	136	37208
% of Sample	0.6	0.5	0.2	0.9	0.1	0.5	0.0	3.7

TGA was also performed on the PP and PPM samples according to procedures developed in BP1 and BP2. Accordingly TGA was performed under three different methods: #1) under nitrogen from ambient to 1000 °C then switching to air for a carbon burn off, #2) under air from ambient to 1000 °C and #3) under nitrogen up to 500 °C to provide the carbon residue, or coking index value. Table 98 shows the data for method #1, Table 99 shows the data for method #2 and Table 100 shows the data for method #3. General trends show that higher SP materials, with higher mesophase and with increasing mesophase content, produce materials with a higher amount of combustible carbon (e.g. carbon reside) and higher coking index. Interestingly, for the air atmosphere experiments with high mesophase content the oxygen uptake can be observed leading to a volatiles and combustible carbon values that were greater than 100%. This is somewhat expected since oxidative stabilization does increase the PPM CF weights.

Table 98: TGA data collected under a nitrogen atmosphere to 1000°C before switching to air for PPM samples produced at WRI (9/23-11/18) from Koppers PP, a commercial PPM, and Koppers produced PPM.

		Nitrogen	Nitrogen	Air	Air	
		Volatiles Range	**Pyrolysis Range**	**Combustion**	**Residue**	**Closure**
	Name	Room Temp to 395°C (%)	395°C to 1000°C (%)	15 minutes (%)	(%)	(Weight%)
PP	MCE-PP	43.76	26.22	29.73	0.2463	99.96
	M-50	45.74	29.97	23.44	0.8722	100.02
	ACP 10	51.27	20.47	26.62	1.662	100.02
	KP-PP-19	47.64	23.87	26.92	1.831	100.26
	KP-PP-19A	45.27	23.68	30.05	0.9826	99.98
	KP-PP-20	47.50	24.96	26.99	0.6078	100.06
	KP-PP-20A	47.27	25.15	27.02	0.4843	99.92
	KP-PP-20B	47.65	25.38	26.74	0.4031	100.17
PPM	ACP-MP	1.70	24.86	73.64	-0.20	100.00
	ACP 20	3.35	25.47	70.91	0.26	99.99
	KOP MP 1	7.67	27.81	63.47	1.06	100.01
	KP-MP-19	6.76	37.22	56.18	-0.20	99.96
	KP-MP-20-0289	18.01	20.24	61.06	0.68	99.99
	KP-MP-20	19.07	25.29	55.04	0.65	100.05
	KP-MP-20-0508	3.38	18.57	76.98	1.11	100.04
	KP-MP-20-1079f	22.01	22.40	54.82	0.79	100.02
	KP-MP-20-1133f	23.20	24.45	51.87	0.51	100.03
	KP-MP-20-1222f	7.11	23.85	68.63	0.44	100.03
	KP-MP-20-1222c	8.05	23.8	67.2	0.74	99.80
	KP-MP-20-1133c	11.85	19.42	67.59	1.09	99.95
	KP-MP-20-1079c	13.32	19.92	68.83	-2.12	99.95
	KP-MP-21-0480	6.83	24.26	68.11	0.75	99.96
	KP-MP-21-0480 (DV)	3.87	24.38	71.35	0.39	99.99
	KP-MP-9/23	4.31	30.42	65.22	0.08	100.03
	KP-MP-9/28	5.63	28.03	64.81	1.51	99.98
	KP-MP-10/1	5.39	28.56	65.59	0.42	99.96
	KP-MP-10/6	4.23	28.63	66.52	0.56	99.95
	KP-MP-10/8	3.46	28.69	67.15	0.79	100.09
	KP-MP-10/15	5.92	29.14	63.17	1.70	99.93
	KP-MP-10/20	4.16	28.48	66.20	1.09	99.93
	KP-MP-10/23	4.19	28.17	67.05	0.54	99.95
	KP-MP-10/28	5.40	28.17	64.75	1.69	100.01
	KP-MP-11/18	4.24	29.04	66.22	0.53	100.02

Table 99: TGA data collected under an air atmosphere to 1000°C for PPM samples produced at WRI (9/23-11/18) from Koppers PP, a commercial PPM, and Koppers produced PPM.

		Air	Air	Air	
		Volatiles Range	**Combustion**	**Residue**	**Closure**
	Name	Room Temp to 395°C (%)	395°C to 1000°C (%)	(%)	(Weight %)
PP	MCE-PP	27.08	72.27	1.21	100.56
	M-50	29.95	69.36	1.86	101.17
	ACP 10	37.04	62.03	1.75	100.81
	KP-PP-19	31.03	68.32	1.64	100.99
	KP-PP-19A	-	-	-	-
	KP-PP-20	30.44	69.02	1.23	100.69
	KP-PP-20A	-	-	-	-
	KP-PP-20B	-	-	-	-
PPM	ACP-MP	2.095	101.05	1.93	105.07
	ACP 20	1.122	100.96	0.73	102.81
	KOP MP 1	0.131	99.13	1.72	100.98
	KP-MP-19	0.517	99.11	0.87	100.50
	KP-MP-20-0289	8.924	90.47	1.54	100.94
	KP-MP-20	11.67	87.88	0.41	99.96
	KP-MP-20-0508	1.248	100.31	1.63	103.18
	KP-MP-20-1079f	12.30	87.75	-0.03	100.02
	KP-MP-20-1133f	12.33	87.61	0.03	99.97
	KP-MP-20-1222f	0.157	99.81	0.32	100.29
	KP-MP-20-1222c	0.054	98.98	1.91	100.94
	KP-MP-20-1133c	4.382	95.49	0.67	100.54
	KP-MP-20-1079c	4.895	94.52	1.29	100.71
	KP-MP-21-0480	0.293	100.34	0.42	101.06
	KP-MP-21-0480 (DV)	1.149	100.29	1.52	102.95
	KP-MP-9/23	1.048	100.87	0.20	102.12
	KP-MP-9/28	0.228	100.29	0.00	100.52
	KP-MP-10/1	1.128	100.57	0.55	102.25
	KP-MP-10/6	0.985	100.61	0.37	101.96
	KP-MP-10/8	0.972	100.56	0.51	102.05
	KP-MP-10/15	0.686	101.48	-0.01	102.16
	KP-MP-10/20	1.250	101.40	-0.11	102.54
	KP-MP-10/23	1.016	100.55	0.46	102.02
	KP-MP-10/28	0.873	101.04	0.00	101.91
	KP-MP-11/18	1.347	103.80	-2.42	102.73

Table 100: TGA data collected under a nitrogen atmosphere to 500°C to produce the carbon residue yield/coking index for PPM samples produced at WRI (9/23-11/18) from Koppers PP, a commercial PPM, Koppers produced PPM, and PP. PP samples designated by A and B are samples that were filtered to remove QI. PP. PP samples design

	Sample ID	Coking Index
PP	MCE-PP	31.89
	M-50	35.39
	ACP 10	27.28
	KP-PP-19	31.46
	KP-PP-19A	32.18
	KP-PP-20	31.19
	KP-PP-20A	31.61
	KP-PP-20B	31.23
PPM	ACP-MP	93.55
	ACP 20	-
	KOP MP 1	-
	KP-MP-19	73.07
	KP-MP-20-0289	-
	KP-MP-20	65.57
	KP-MP-20-0508	-
	KP-MP-20-1079f	60.02
	KP-MP-20-1133f	60.65
	KP-MP-20-1222f	73.36
	KP-MP-20-1222c	72.50
	KP-MP-20-1133c	72.83
	KP-MP-20-1079c	72.38
	KP-MP-21-0480	-
	KP-MP-21-0480 (DV)	-
	KP-MP-9/23	72.10
	KP-MP-9/28	69.90
	KP-MP-10/1	70.63
	KP-MP-10/6	71.47
	KP-MP-10/8	72.42
	KP-MP-10/15	70.64
	KP-MP-10/20	72.78
	KP-MP-10/23	71.80
	KP-MP-10/28	72.08
	KP-MP-11/18	71.29

TGA is useful as a screening and diagnostic tool that can be related to poor melt flow properties in some pitch materials due to excessive volatiles. As was previously shown, significant entrained volatiles which lead to heterogeneous melt properties are easily diagnosed with this method. Figure 280 shows the differential TGA thermograms for PPM samples produced at WRI from filtered and unfiltered PP using Koppers PP, and also thermograms for a commercial PPM and PPM fines from the Koppers samples. Samples with excess volatiles in the region of 200-350 °C are evident. This is consistent with data in Table 100 which shows that the fines from two of the Koppers samples with excess volatiles, that produced heterogeneous melt properties, had a coking index of about 60 wt% while the chunks had coking index values that were around 72 wt%. The higher coking index of the chunks is consistent with the mesophase PPM samples produced at WRI (70-73 wt%).

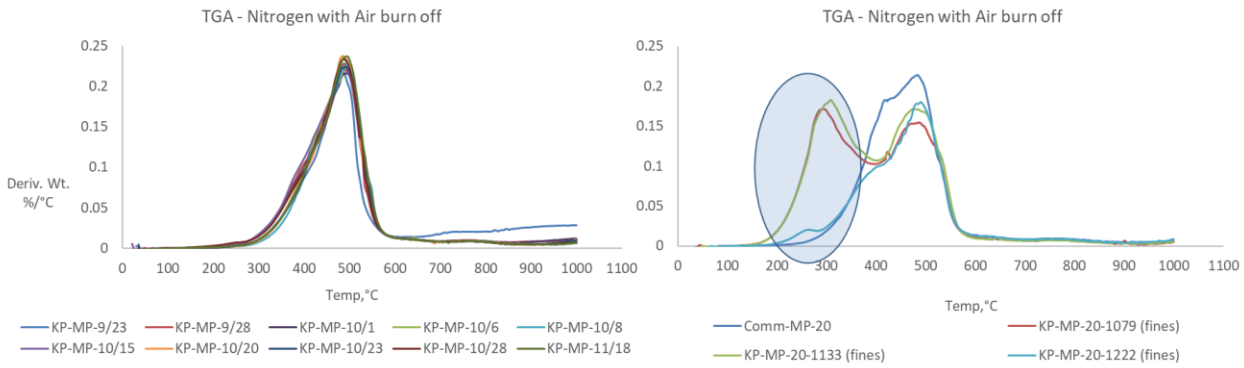

Figure 280: Derivative thermograms at the left of PPM samples produced at WRI using Koppers PP. Thermograms at the right are fines from PPM samples produced by Koppers and a commercial PPM. Blue circle highlights samples -1079 and -1133 which contained a significant amount of lighter volatile components which are likely responsible for the heterogeneous melt flow properties of the fines relative to the chunks.

A common way to characterize carbonaceous materials is from the amount of carbon residue left in the material after pyrolyzing under and inert atmosphere. As the amount of carbon residue increases it generally infers that the material has a higher amount of connected carbon atoms that do not undergo volatilization or pyrolysis to yield liquid or gas. For highly aromatic materials, a higher carbon residue value indicates a greater amount of connected (usually conjugated) larger aromatic rings that are unable to become volatilized prior to cross linking. With respect to pitch and CF yield, it is desirable to have a higher amount of carbon residue because this increases the resulting yield of CF—and ensures high utilization of carbon from the pitch feed. As was done in BP1 and BP2, carbon residue values were obtained for PP and PPM using the microcarbon residue test (MCRT) according to ASTM D4530. In general, CTP (~50 wt%) has a similar carbon residue value as PP (~50 wt%). For PPM samples, the carbon residue values are significantly higher than PP, but again there is not a large difference between PP and CTP mesophase for successfully spun CF. CTPM with a higher SP (around 320 °C) had a carbon residue around 92 wt%, while lower SP (around 300 °C) PPM had a similar carbon residue around 91 wt%. This difference in SP between the two materials may be related to the slight differences in aromaticity between the materials. However, this is inconsistent with the fact that PP and CTP mesophase of SP around 330 both had a carbon residue around 94 wt%. MCRT values for the PP samples are reported in Table 101.

Table 101: Carbon residue values from MCRT (ASTM D4530) for many of the samples produced during the program.

	Sample ID	MCRT
PP	MCE-PP	55.7
	M-50	50.8
	ACP 10	46.6
	KP-PP-19	53.1
	KP-PP-19A	53.4
	KP-PP-20	53.3
	KP-PP-20A	53.4
	KP-PP-20B	-
PPM	ACP-MP	94.0
	ACP 20	91.7
	KOP MP 1	-
	KP-MP-19	-
	KP-MP-20-0289	-
	KP-MP-20	88.3
	KP-MP-20-0508	93.7
	KP-MP-20-1079f	77.5
	KP-MP-20-1133f	77.6
	KP-MP-20-1222f	88.1
	KP-MP-20-1222c	-
	KP-MP-20-1133c	-
	KP-MP-20-1079c	-
	KP-MP-21-0480	-
	KP-MP-21-0480 (DV)	-
	KP-MP-9/23	92.1
	KP-MP-9/28	89.8
	KP-MP-10/1	90.5
	KP-MP-10/6	91.1
	KP-MP-10/8	91.8
	KP-MP-10/15	91.2
	KP-MP-10/20	91.0
	KP-MP-10/23	91.9
	KP-MP-10/28	91.9
	KP-MP-11/18	92.3

Other spectra and characterization data for the pitch based data were collected and input into a master spreadsheets and uploaded to the MIT database and they are also available on through the LightMAT Consortium.

Bio-PAN Scaled-up Processing and Analyses

To improve the properties of the biogenic bio-PAN CF produced in prior budget periods, ORNL developed a ter-polymer system to more closely replicate specialty acrylic formulation for CF. Small ~ 10 mL amounts of ACN monomer—from the 1 L batches sent by SRI—were combined with methyl acrylate [MA] and itaconic acid [IA] co-monomers. Re-crystallized AIBN was used as the radical initiator at a nominal mol ratio of 2500:1 that was added to the DMSO – monomer mixture. The reaction flask (~ 100 mL) was heated to a temperature of 70 °C for 2-10 hours based on targeted monomer conversion. Final AN:MA:IA ratio ranges of [96-98]:[2-4]:[0.5-2] were targeted in the final polymer. The differences in chain transfer for each monomer need to be properly predicted and accounted for via the stoichiometric monomer ratios to ensure the

propagating chain has the correct composition. A terpolymer sample characterized via ^{1}H NMR following purification resulted in a composition of 98:1.8:0.2. Based on the compositional data from NMR, coupled with thermal characterization, an optimal composition was targeted for scale-up using a multi-liter reactor.

Scale up to multi-liter quantities of the small scale ter-polymer synthesis was performed. After checking each delivered batch of monomer from SRI for uniform activity, the reaction mixture was charged and heated to 70 °C under inert atmosphere. The reaction mixture was quenched and precipitated in methanol followed by DI water. The white product is allowed to dry to constant weight. ^{1}H NMR was used to resolve the composition of the terpolymer and revealed an acid co-monomer content of approximately 0.4% (Figure 281). Two large scale batches have been synthesized and purified for spinning. Rheology of the bio-PAN terpolymer suggests a spinnable processing window between 12 - 18 wt % (Figure 282). Conversion of the terpolymer will be adapted from the bio-PAN fibers from the previous budget period as the onset of oxidation is expected to occur lower in this system containing catalytic amounts of acid co-monomer.

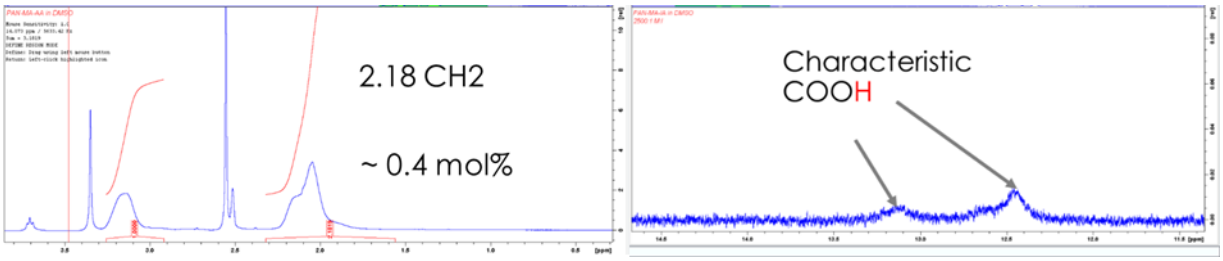

Figure 281: ^{1}H NMR of the bio-PAN terpolymer developed in this project. Itaconic acid mol % is calculated at 0.4 based on peak integration.

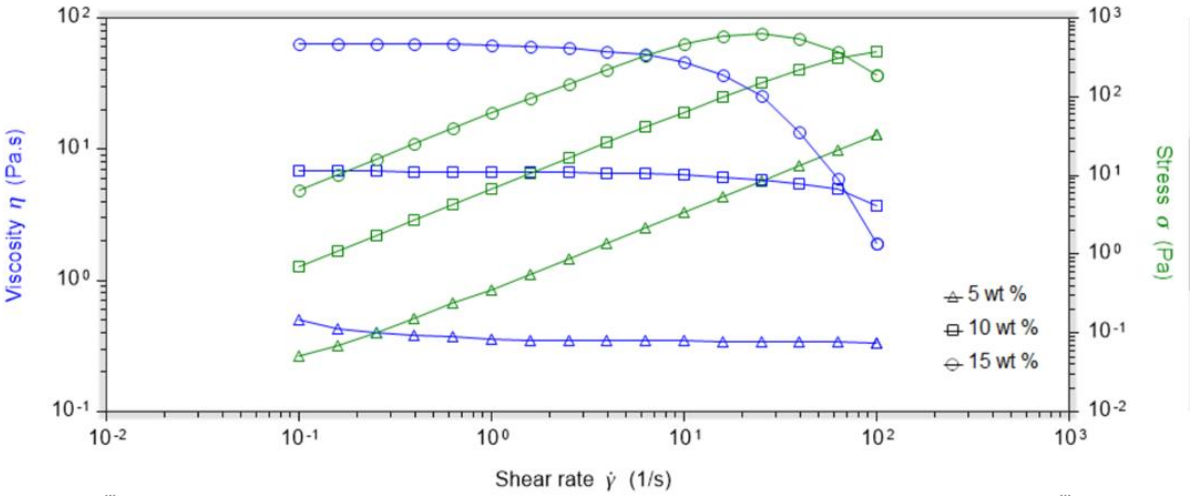

Figure 282: Flow rheology of the scaled-up bio-PAN terpolymer showing the onset of shear thinning at polymer loadings >10 wt%

Using the concentration dependent rheological properties a dope was prepared and spun into precursor fibers exhibiting 91 ksi break strength and 15 % elongation at break with a diameter of 13.6 µm. The resultant fiber properties is consistent with highly drawn specialty acrylic formulations. Due to the presence of acid containing moieties the exothermic behavior of the system is significantly altered. Relative to an unaccelerated formulation, the onset temperature is shifted lower as well as a reduction in the peak magnitude of the exotherm (Figure 283a). This enables a reduction in the energy required to achieve sufficient fiber density as well as retention of the polymer chain orientation during oxidation.

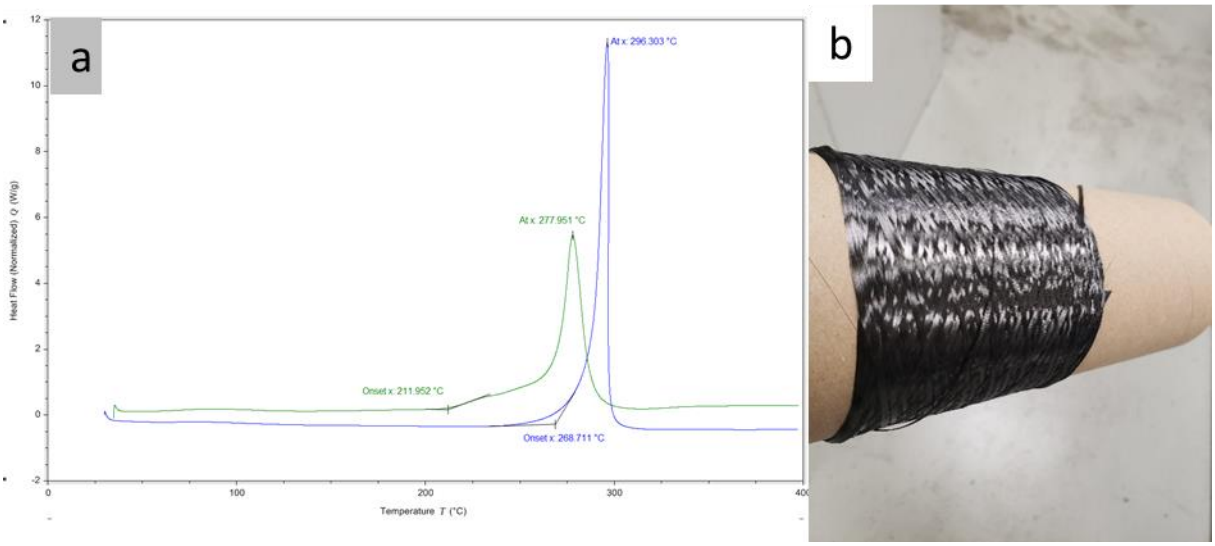

Figure 283: (a)Differential scanning thermogram showing the heat release as a function of temperature for the two Bio-PAN polymer systems. BP3 terpolymer formulation (green) is plotted alongside the copolymer composition from BP2 (blue). (b) Bio-PAN terpolymer CF tow, delivered to UW for testing..

Utilizing the exothermic responses of the materials as a starting point, a new oxidative protocol was developed by tracking the oxidized fiber density after each progressive step. If the oxidation is not fully complete or overly applied, the thermoset fiber will not achieve good CF properties. A moderate carbonization was then performed on the oxidized fibers which exhibited a final carbonized density of approximately 1.35 g/cm^3 to achieve final CF properties of 289 ksi strength, 27 Msi modulus and 1.06 % elongation at break. The 1500 filament tow was approximately 240 feet long and was delivered to UW for composite level testing. A photograph of the bundle of tow CF is shown in Figure 283b.

Additional pitch based and bio-PAN CF processing and characterization data that were used to develop the integrated models are given in Appendix A.

Cost Estimation

Techno-economic analysis (TEA) was prepared for each identified raw material and processing route under consideration. These CF precursors are:

- Bio-ACN: Produced from sugars and biomass, SRI is the investigating subrecipient. The process uses the traditional PAN fiber solution spinning process.
- PAN: This is the baseline cost of production.
- Petroleum Decant Oil: Typically used for production of carbon black or petroleum coke, this is the use of petroleum pitch to make isotropic or mesophase pitch for melt spun fibers. ACP was the original industry partner in BP1 and BP2. They have since been replaced by Koppers Inc.
- Upgraded Petroleum Decant Oil (this is PP): This is decant oil that has been thermally treated to increase its pitch yield.

Prior TEA updates included CTP and isotropic pitch from direct coal liquefaction. These were not included in the following discussion as CTP was omitted during BP3 after BP2 down-selection.

TEA was performed in order to verify <$5/lb cost. At this stage analysis it is assumed that the first and second goal will be met through specifically designed trials. From Mitsubishi, the following chart shows the quality of a fiber that achieves the project goals in comparison to existing products on the market (Figure 284). This performance competitive landscape can be used as a basis for pricing the fiber product on a market-basis.

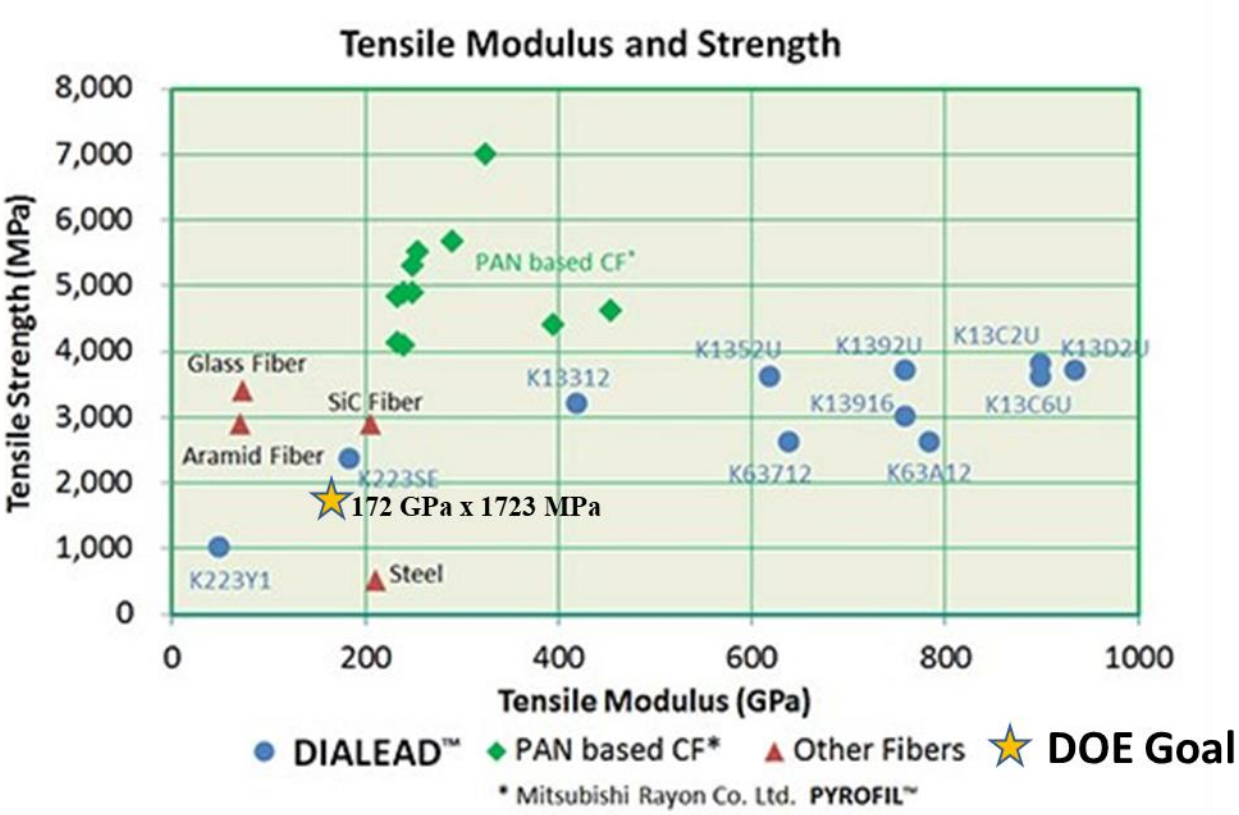

Figure 284: Profile for strength vs modulus for various products. https://www.m-chemical.co.jp/en/products/departments/mcc/cfcm/product/1201229_7502.html

The following are key parameters that effect the economics of any new technology.

Annual Production Capacity

Following the CF Conference in late 2019, in an interview with composites expert Tony Roberts of AJR Consulting, Composites World published the following Table 102 and Table 103 on global supply and demand of CFs.

Table 102: CF suppliers, nameplate capacity, annual metric tons.

Manufacturer	Headquarters	2019
Toray	Japan	57,000
Hexcel	U.S.	16,000
Mitsubishi Chemical CF & Composites	U.S.	16,000
Teijin	Japan	14,000

Manufacturer	Headquarters	2019
SGL Carbon	Germany	13,000
Formosa Plastics	Taiwan	9,000
Solvay Composite Materials	U.S.	4,400
DowAksa	U.S.	3,000
Hyosung	South Korea	2,000
Various	China	21,800
Various	Rest of World	5,000
Total		161,200

Table 103: CF demand, annual metric tons.

End market	2017	2020 (est.)	2025 (est.)
Aerospace	18,000	24,500	30,000
Industrial	68,000	85,000	142,350
Sports/Leisure	12,000	13,800	19,000
Total	98,000	123,300	191,350

It was considered the existing pitch-based fibers market will grow from its current global demand of less than 2,000 metric tons per year with the new availability of lower priced fibers rather than the current market price of $25-$50+ per pound. Further, the existing 161,200 metric tons of PAN-based fiber annual capacity (Sloan, 2021) may permit partial substitution by pitch-based fibers. Based on a market report purchased by Ramaco there is in recent years a CF industry compound annual growth rate (CAGR) of 10+% (Romand & Sandrine, 2018). Ramaco considers that it would not be a large commercial challenge for pitch-based CFs to displace PAN fibers provided that those fibers were of the same or better quality and at a lower price. Ramaco expects their business plan to support the production of 10,000 metric tons per year of CFs and this figure has been used across the board for comparing raw materials and production routes as it is reasonable commercial scale for a new facility.

Capital Investment

Capital investment is largely based on the annual production capacity. In addition, the location of a site and whether it is greenfield or brownfield with some infrastructure is an important aspect of the overall process economics. Furthermore, the investment source likely requires a balance of debt and equity as neither private investors nor banks would want to bear the combined technical and commercial risk alone.

For the raw materials reviewed there is a distinct difference in investment. PAN substitutes like bio-ACN, or lignin, can reuse existing PAN solution spinning equipment with perhaps minor changes. Petroleum, coal tar or coal-based pitches, either isotropic or mesophase, require new, but perhaps less expensive melt spinning production equipment.

In order to deploy the comparative analysis of investment requirements there are several underlying assumptions that can be considered:

In order to compare operating expenses of two different processes, the capital investment is converted into an annual and unit capital charge. The term capital charge refers to the rate of return required to attract investors. Investors often require a 20% internal rate of return (the return to them). Large investments in new technologies are often funded by both equity and debt. The lower rate of secured borrowing lowers the overall capital charge. Referred to as the weighted-average cost of capital (WACC), if investor return expectations are 20% and the rate of borrowing is 4-8% then for an investment that is funded 50% with equity and 50% with debt then the WACC is 12-14%. Given the current borrowing rate environment, the applied WACC will be 12%.

Note that some sources consider the application of depreciation of fixed assets as an operating expense. While depreciation and amortization are used to reduce the effective remaining value of a facility over a prescribed period, they are not considered part of the capital charge.

The facility specified and costed out is in a facility with existing infrastructure and using incremental investment in the equipment needed to produce the precursor as well as the CF.

The investment level of facilities of different capacities in publicly available information is scaled by the ratios of the facility capacity. This is known as the cost-to-capacity method of estimating at the conceptual design level. In an article by Clayton T. Baumann, PE in the Quarter 1 2014 issue of The Journal of the International Machinery & Technical Specialties of the Appraisal Society of America, the cost-to-capacity concept was originally applied in 1947 by Roger Williams Jr. to develop equipment cost estimates; later, in 1950, C.H. Chilton expanded the concept’s application to estimate total chemical plant costs.

Typically given for chemical plants as the ratio of two plant capacities to the 0.6 power times the investment in the capacity in the denominator, in the case of multiple parallel production lines as in fiber spinning, this will be higher. Facilities such as power plants have been extensively studied and with multiple boilers and turbines, use an exponential factor of 0.64-0.85 (Phung,

1987). Given the multiple of fiber spinning lines wherein most processing unit are in parallel, an economy of scale factor of 0.75 is considered.

The investment charges do not include financing interest during the planning and construction of the facility. This is otherwise known as “overnight capital” deployment, a common basis of investment comparison.

There is no consideration of varying needs of infrastructure between two facilities. Storage facilities and warehousing needs are considered to be the same.

PAN-based fibers are produced from acrylonitrile polymerization that is spun, stabilized in an oxidizing environment, carbonized, surface treated or, alternatively graphitized. Alternatively, pitch-based fibers are made from an isotropic pitch that is thermally polymerized to a high melting point mesophase pitch, typically above 275-325 °C, and then spun from a melt. This graphic (Figure 285) shows both systems with their common components:

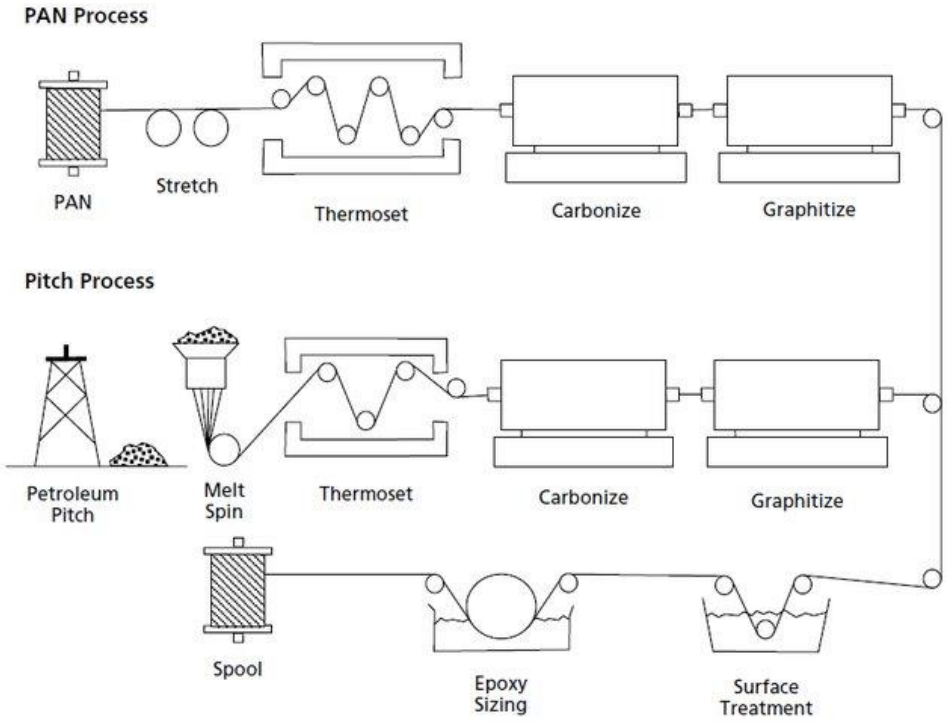

Figure 285: Schematic showing basic steps for CF production from PAN-based and pitch-based CF.

There are several references in the public domain for the investment for PAN-based fibers. One study with a full breakout of capital costs was performed in 2012 by Omnia LLC (Omnia, LLC, 2012) for the Invest in Iceland organization for foreign investment. This report provides a total capital investment for a 4,000 metric ton of 12k tow facility of US$ 75.5 million with a direct installed equipment cost of US$ 53.5 million. This facility would be based on about 25 acres and include a manufacturing building of approximately 50,000 square meters.

Another reference for a capital investment by Teijin CFs on an existing site was developed and submitted to the U.S Department of Commerce for Foreign Trade Zone qualification (U.S. Department of Comerce, 2020). The facility to be based in Greenwood, SC would produce 15,000 metric tons of 24k tow fiber to offset Teijin's import from Japan and Germany. In a letter to respond to public comments, Teijin quoted Commerce Secretary Wilbur Ross that the greenfield development would cost US$ 643 million. This may include the costs of land and the basic infrastructure existing at an incremental production site that might add as much as $50-100 million netting the incremental production investment to be $593-543 million.

The direct investment of the petroleum pitch upgrade and conversion for spinning is given by the example of ConocoPhillips construction of an 8 million pound (3,629 metric ton) CF facility in their Ponca City, OK refinery. This was commissioned in 2002 at a construction cost of US $125 million but was shut down after six months of production (Taylor, 2003). Conoco's process to produce their Cevolution product employed a solvent to reduce the melt's viscosity, this would have required additional investment for solvent mixing and recovery as compared to undiluted processes.

Another reference to isotropic pitch melt spinning capital investment is given in a presentation by Sujit Das during the 2019 Pittsburgh Coal Conference (Das). The investment provided to melt spin mesophase pitch is US $44 million in processing equipment to produce 7,500 metric tons of 50k tow fiber. Dave Warren presented an estimate of US $28 million for a 12,000,000 lb (5,443 metric ton) pitch precursor facility (Warren). Assuming a 75% CF yield from pitch precursor, Warren's precursor plant would produce 4,082 metric tons of CF. This additional investment is included in the capital estimates presented herein.

Table 104 shows a comparison of these technologies with the economy of scale factor of 0.75 to 10,000 metric tons per year.

Table 104: Comparisons of PAN-based technologies for 10,000 MT CapEX and capital charge.

10,000 MT CapEx Estimate and Capital Charge

Process/ Source	PAN - Omnia	PAN - Teijin	Pitch - Das/ Warren	Pitch - Conoco
Capacity, metric tons/ year	4,000	15,000	7,500	3,629
Source Spinning Investment, 1000s USD	$75,500	$543,000	$88,187	$125,000
0.75 Economy of Scale Factor	1.988	0.738	1.241	2.139
Estimated 10,000 MT Facility	$150,107	$400,619	$109,424	$267,356
Annual 12% Capital Charge, 1000s USD	$18,013	$48,074	$13,131	$32,083
12% Capital Charge/ kg carbon fiber	$1.80	$4.81	$1.31	$3.21
12% Capital Charge/ lb carbon fiber	$0.82	$2.18	$0.60	$1.46

There is a large disparity between the two PAN-based CF sources for the investment amount but it is hard to tell how much if any Teijin would have spent on site purchase and infrastructure development. The Omnia study for Invest in Iceland did not include land and infrastructure however the authors may have been attempting to keep the economics competitive for the region.

The combination of DOE investigators Das and Warren agree significantly with the level of Conoco's investment, albeit at about one-third of the production scale. In any case, the production of pitch-based fibers is likely less capital intensive than the production of PAN-based fibers which may be attributable to the conversion of acrylonitrile monomer into PAN at the front end of the process. For purposes of this study, the lesser of each capital recovery rate will be used.

The opportunity to lower capital investment in the fiber oxidation step has been presented by 4M CF of Oak Ridge, TN. They claim the use of plasma heating in the oxidation step will save 50% of the estimated US$ 40 million per 2,000 ton production line.

Processing Yields and Raw Material Cost

Yield of CF from PAN or bio-PAN is about 40-50% by weight from acrylonitrile (Das & Mao, 2018). For this analysis, an average of 45% will be used for both petroleum-based acrylonitrile and that from the Bio-ACN process.

From the same source Das and Mao report petroleum-based ACN prices range from $1.98 to $2.58 per pound when petroleum prices range from $65-115 per barrel. At about 300 lbs/ barrel, this drives an ACN price range ratio between 9.1 on the low end and 6.7 on the high end of the price of oil. Since recent oil pricing has rebounded to around $65 per barrel then the comparable ACN price will be $1.98 per pound, or $4.37/ kg.

The Bio-ACN route developed by Dr. Amit Goyal when he was with Southern Research Institute produce a CF precursor at a dramatically net lower price. For a facility to produce enough ACN for a 10,000 metric tons per year of CF the manufacturing cost breakdown is given in Table 105 (Goyle, 2020).

Table 105: Updated cost analysis for bio-ACN for 25,547 mt/year acrylonitrile, 33,740 mt/year propylene glycol and 6,828 mt/year ammonium sulfate. Total permanent investment (TPI) $43,253,812.75 and Total capital investment, TCI (including working capital) $49,152,060.

Type of cost	$/year	$/lb ACN
Sugar	$39,690,000	$0.705
Hydrogen	$4,536,000	$0.081
Ammonia	$4,628,359	$0.082
Oxygen	$336,051	$0.006
Sulfuric acid	$407,207	$0.007
Process water	$862,467	$0.015
Total raw materials	$50,460,085	$0.896
Utility cost	$12,558,675	$0.223
General expense	$12,546,882	$0.223
Fixed cost	$1,906,433	$0.034
Catalyst cost	$2,155,941	$0.038
Total operating cost excluding raw materials	$29,167,931	$0.518
Capital cost (TPI ÷ 10 year)	$4,325,381	$0.077
By-product sale	($61,879,774)	($1.099)
Cost of ACN production		$0.392

Note that while the capital charge of 10% and adjusting for this study's assumed 12%, the bio-ACN cost is $1.51/ lb, or $3.33/ kg before the co-products of propylene glycol and ammonium sulfate. This is 23.7% lower than the expected current petroleum ACN cost.

Petroleum pitch is made from "decant" oil, or that heavy fraction left behind after catalytic cracking. Produced by filtering the spent catalyst from "slurry" oil, it is used primarily to produce carbon black or blending into fuel oils. Isotropic pitch produced by straight vacuum distillation often has yields lower than 30% by weight. Advanced Carbon Products (ACP) has developed a process called ACP-10 to produce isotropic pitch. When coupled with their ACP-20

process to convert isotropic to mesophase pitch, yields as high as 85% are possible although neither of their patents claim minimum yields (Boyer, Holocombe, & Malone, 2016). There is no information on how much of the balance is recovered distillate versus a low-valued pyrolysis gas. ACP further claims that their process can produce mesophase pitch for less than $1.50/ lb without an allocation for raw material costs. This analysis will take this claim as fact and that it is net of all by-product credits.

The yield of CF from mesophase pitch is also much higher than that from PAN. Addressed solely as carbon yield from mesophase pitch, Table 3 in the DE-E0008203 Q4 2020 quarterly report lists carbon residues of >90% for mesophase pitches. While this does not include yield lost to mechanical breakage, an overall yield of 75% will be used for comparison.

Coproduct Revenue

There is an inherent danger in using co or by-product credits as they have often been used to justify otherwise uneconomical processes. However, they are also a basic element of most petrochemical economic analyses. Chemicals, distillates and solid carbon by-products require some further market development, however there are existing target product quantities and market prices. Bio-ACN produces propylene glycol and ammonium sulfate coproducts. Organic distillates have many uses as solvents and aromatic oils.

As shown above, the bio-ACN route produces significant amounts of propylene glycol and ammonium sulfate. Both commodity chemicals, they are used in the food and pharmaceutical and fertilizer industries. Those credits were presented by A. Goyal above and are included in the Table 15 below. The production of petroleum mesophase pitch produces co-product aromatic oil depending on the degree that its distillates are recycled. The credits for the ACP process are included in the mesophase pitch raw material production costs.

Table 106: Net Raw Material Cost Contribution.

Raw Material Cost Contribution

Raw Material/ Source	ACN, petro-based	Bio-ACN, SRI	Petro Pitch - ACP
Raw Material Cost, $/ kg	$4.37	$3.32	$3.31
Co-product Credit, $/ kg Raw Material	-	($2.42)	-
Net Raw Material Cost, $/ kg	$4.37	$0.90	$3.31
Yield to Carbon Fiber	45%	45%	75%
Raw Material Charge/ kg carbon fiber	$9.70	$1.99	$4.41
Raw Material Charge/ lb carbon fiber	$4.40	$0.90	$2.00

Operating Expense

As in most scenarios for new process economics, raw material cost and operating costs can greatly impact the process economics. Expected yields of precursor from raw material as well as the projected CF yield from the precursor has been factored into the analysis. . In addition to Omnia and Das references, the introduction of a CEMAC publication by Cook and Booth (Cook & Booth, 2019) provides operating expenses for 50k tow fibers.

Other operating expenses include the cost of utilities (energy), maintenance and repair, labor and supervision (direct labor), and site management (site overheads) which is assumed to be 50% of the direct labor. Corporate overheads, insurance and technology license royalties are not included in this economic review as 1) existing companies are expected to enter the business as a growth opportunity, 2) insurance on additional assets and product liability vary greatly based on location and carrier and 3) technology license fees may not apply such as the case for internal development or may be included in equipment purchase. Table 107 outlines the comparison of operating expenses by process.

Table 107: Comparison of operating expenses by different processes.

	Operating Expense		
OpEx Item/ Source	PAN, 12K - Omnia[1]	PAN, 50K - CEMAC[2]	Petro Pitch - Das[3]
Energy, kWh/ kg carbon fiber	31.08	22.76	22.0
Assumed Industrial Power Rate, $/ MWh	$60.00	$60.00	$60.00
Energy, $/ kg	$1.87	$1.37	$1.32
M&R Expense (8% of Inv.), $/ kg	$1.20	$1.19	$0.88
Direct Labor Expense @$30/hr), $/ kg	$1.52	$1.74	$1.74
Site Overheads (50% of Directs), $/ kg	$0.76	$0.87	$0.87
Total OpEx/ kg carbon fiber	$5.35	$5.17	$2.00
Total OpEx/ lb carbon fiber	$2.42	$2.34	$0.91

[1] Average of USA East and West Coast energy costs as presented by Omnia.

[2] Cook, J. & Booth, S., “Carbon Fiber Manufacturing, Facility Siting & Policy Considerations: International Comparison”. CEMAC, Technical Report. NREL/TP-6A20-66875, June 2017

[3] Das, Sujit, “Opportunities and Challenges for Domestic High-Value Coal Products”, presented September 4, 2019, 36th Annual International Pittsburgh Coal Conference.

Production Cost of CF

The Table 108 below outlines the overall CF production costs presented above including the net raw material and operating expense, including capital charges to produce CFs from each respective precursor. Figure 286, Figure 287, Figure 288 represent the data in Table 108 as cost per pound of CF in pie charts for each different material, traditional PAN, bio-PAN and PP, respectively.

Table 108: Data showing the production costs including net raw material, operating expense and capital charges.

Consolidated Production Costs

OpEx Item/ Source	ACN, petro-based	Bio-ACN, SRI	Petro Pitch - ACP
Raw Material Charge/ kg carbon fiber	$9.70	$1.99	$4.41
Energy, $/ kg	$1.62	$1.62	$1.32
M&R Expense (8% of Inv.), $/ kg	$1.20	$1.19	$0.88
Direct Labor Expense @$30/hr), $/ kg	$1.74	$1.74	$1.74
Site Overheads (50% of Directs), $/ kg	$0.87	$0.87	$0.87
12% Capital Charge, $/ kg	$0.82	$0.82	$0.60
Total OpEx/ kg carbon fiber	$15.94	$8.23	$9.81
Total OpEx/ lb carbon fiber	$7.23	$3.73	$4.45

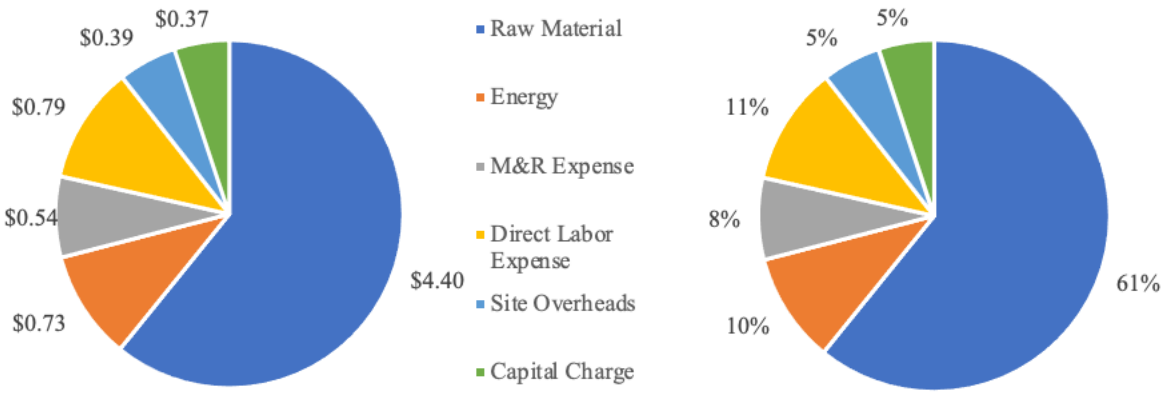

Figure 286: Costs per pound for traditional PAN CF – total $7.23/ lb.

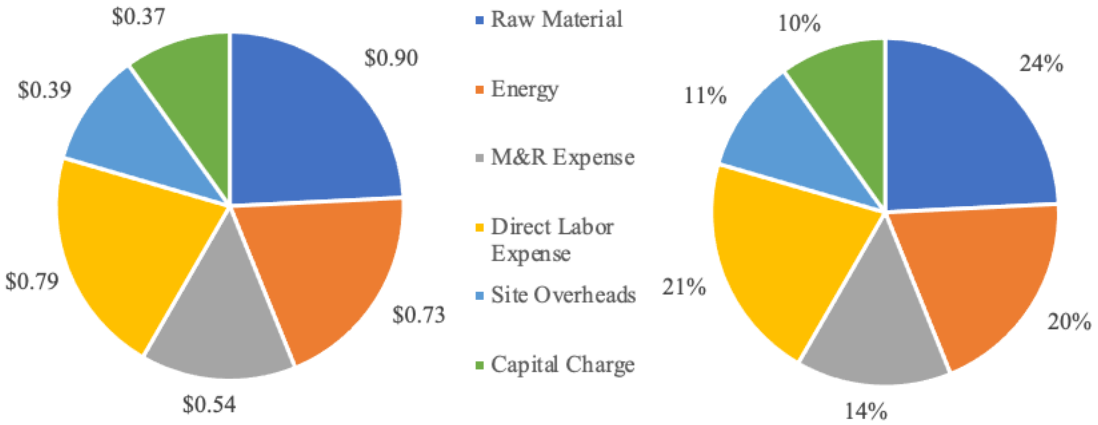

Figure 287: Costs per pound for bio-PAN CF – total $3.73/ lb.

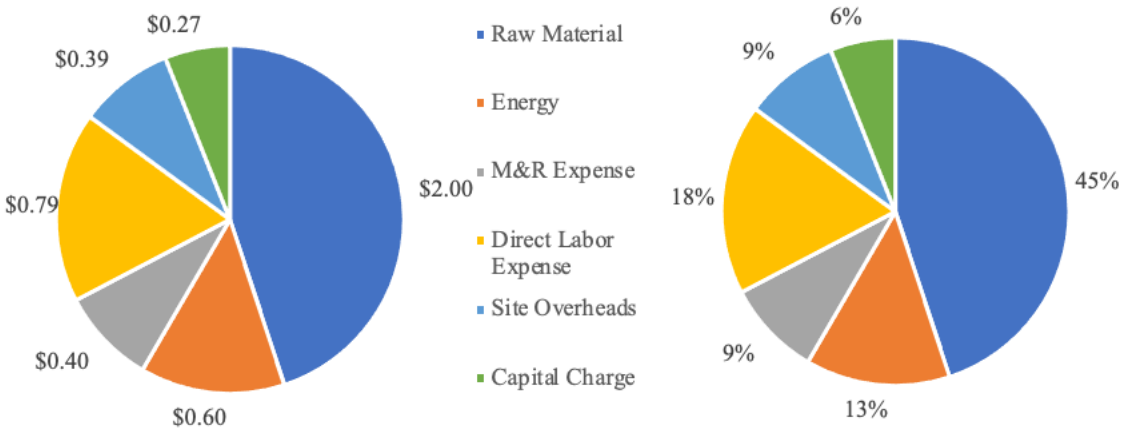

Figure 288: Costs per pound PP CF – total $4.45/ lb.

As can be seen, based on acceptable fiber performance, the development of bio-ACN can greatly reduce PAN fiber production costs. Additionally, this may offer an opportunity to convert existing petroleum-based PAN production capital over to bio-ACN raw material but it is not clear to the author that this is not without additional investment. In any case, should additional investment be required there is certainly margin in the $3.73/ lb CF cost to add further cost of capital without exceeding the project goal of $5.00/ lb. Also, the overall economics of bio-ACN are heavily dependent upon the price and sale of significant amounts of the processes by-products propylene glycol and ammonium sulfate. This may suggest that the most likely producers of bio-ACN may be companies that currently produce those commodity materials.

PP-based fibers are still very competitive provided that they too have acceptable performance. Furthermore, while transportation costs are not addressed by this study, the ability to add a

petroleum pitch and CF facility either in or near an existing refinery and its infrastructure, would provide an opportunity to minimize capital investment and logistics expense.

Sensitivity Analysis of Input Costs

The following charts in Figure 289 represent the sensitivity to the cost structure of the inputs for each of the bio-ACN and petroleum pitch routes to produce CF. Examined factors were the cost of precursor production, co-product credit, yield of CF from precursor, energy, maintenance and repair expense and the capital charge of either investment level, the debt-to-equity ratio in funding or investor expectations. Each input was varied by plus/minus 20%.

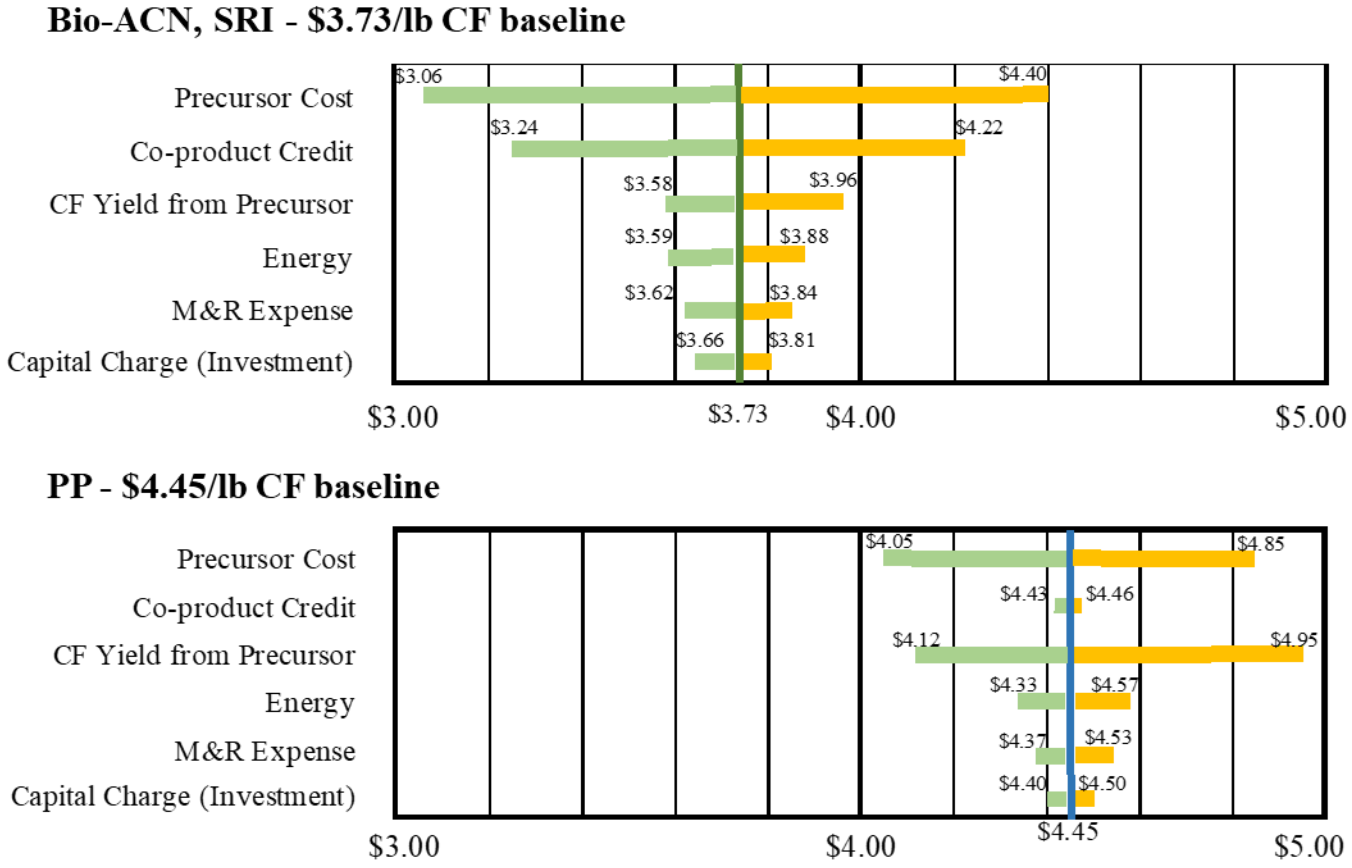

Figure 289: +/-20% cost sensitivity analysis for bio-ACN (top) and PP (bottom).

One can observe that there is no single input that up to 20% in a negative impact that causes the cost of CF to exceed $5.00/ pound. As may be expected, precursor cost are the most sensitive to product costing. The bio-ACN route relies heavily on the value of its co-product propylene glycol and ammonium sulfate. Still, it has a sufficiently low cost basis to bear significant resilience to reduced co-product prices. With petroleum pitch, the yield of CF from its mesophase pitch precursor is higher than bio-ACN and has a higher sensitivity to variations in yield.

Supply Chain Risks

The production of bio-ACN requires sugar obtained from biomass, hydrogen, ammonia, oxygen, sulfuric acid and water. Location near a biomass sugar producer to reduce the supply chain risk would be an advantage. Most all sugar cane processing in the U.S. is based in Florida and Louisiana (Statista, 2020). Being a solid product it is easily stored so supply concerns can be protected by inventory. There would be more of a risk that a key supplier or logistics provider would have equipment failures or other hardship. Hydrogen and oxygen can be produced via electrolysis, opening an opportunity for green production. Ammonia is a common commodity although storing in large quantities can lead to consideration of off-site leakage impacts to nearby communities.

Rather than raw materials, of significant risk to the production of bio-ACN is the ability to ensure commercially practical off-take of the propylene glycol and ammonium sulfate coproducts. There would be a need to have multiple customers that can be accessed within a practical distance for a given mode of transportation. However, like any commodities there will be fluctuation in demand and therefore pricing. Ammonium sulfate is a low-cost fertilizer, so the offtake risk is reduced. For propylene glycol, one approach would be to partner with someone who needs it as a raw material. This is used often in the case where supply agreements can be based on a known price index.

Petroleum decant oil is currently plentiful although subject to fluctuations in crude oil pricing. Figure 290 shows a graph from the U.S. Energy Information Administration (EIA) showing recent wholesale petroleum pricing. It shows that residual fuel prices are about $0.20 per gallon over crude oil refinery acquisition cost (RAC) under current production and economic conditions (note: these are heavily affected by COVID-19).

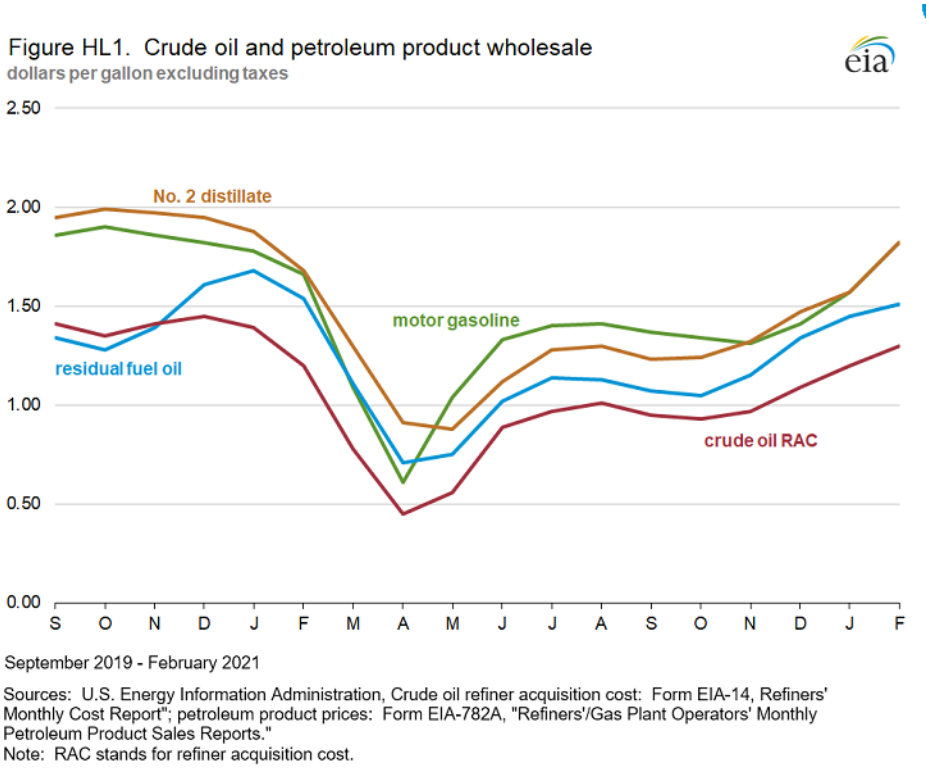

Figure 290: Graph from the U.S. Energy Information Administration (EIA) showing recent wholesale petroleum pricing.

Prediction of future energy prices build risk into any business however in the case of PP, raw material is 45% of the overall costs structure. Price increases would have to passed onto the CF customer which may be difficult under some long-term contracts, particularly those used to secure the investment in production equipment. One factor to consider is the future demand for petroleum as a transportation fuel. According to the EIA at the end of 2019 there were 44.2 billion barrels of proven U.S. oil reserve and in 2020 there was 17.7 million barrels per day of refining capacity with cat cracking ability (Energy Information Administration, Refinery Capacity Report). However, the drive towards electric vehicles could make some of those refineries operating at low levels of capacity obsolete.

One raw material that has not been selected for further consideration in this study is the conversion of coal into CFs through low-severity direct coal liquefaction or supercritical CO_2 extraction. Ramaco Carbon is currently under two DOE award contracts and has produced isotropic and mesophase pitch and CFs. Current cost projections are also well below $5.00 per pound of CF. The U.S. demonstrated reserve base, that which is known to be recoverable is 473 billion short tons (Energy Information Administration, Coal Explained). This is enough to make CFs for a CF demand of 500,000 metric tons per year (twice as much as the 2026 projection) for 80,000+ years.

Price versus Cost

The cost of production of CFs through different route are compared in this report. While investors are rewarded with a 20% rate in the cost of capital, this does not assure that they will be adequately compensated for their risk. One can assume that the sales of CF would not be at the production cost even with a cost of capital component but rather at commercial market prices. Such prices may be higher in order to provide higher business returns in order to attract investors.

TEA Summary

As can be seen at this time, the project goal of producing CF for less than $5.00 per pounds has been met. It is this Ramaco's opinion that further work in the area of product performance and its integration into markets seeking to benefit from its lower cost of production is needed to advance these new technologies.

Conclusions

By taking experimental molecular information from feedstock CTP, PP and bio-ACN, it is possible to design models from the molecular-level that are capable of predicting CF properties such as elastic modulus, compressive modulus, shear modulus, Poisson's ratio and density, well within ±15%. The models are unique in that they are built up from the chemistry and reactivity producing excellent fits to experimental CF data without applying corrections, scaling factors and fitting methods. Building CF models from the atomistic level (this is at the nano-level but falls within the micro-level modeling) is dependent upon the "sheet" (nano-scale molecules and their properties) and fiber morphology which buildup the micro-structure of the resulting CF. This is different from the macro-scale models which were produced using FEA modeling of the tow-level epoxy composites and macro-scale modeling was already shown to meet DOE targets ±15% in BP2. However, the unique challenge of integrating between the different scales is not something commonly practiced. This challenge was overcome using NN to relate the sheet properties to CF elastic modulus components to the tow-level CF composite properties with significantly less than the ±15% error for scaled up PPM and bio-PAN CF. The models need to be further tested with other CF morphologies and with other chemistries for further validation and to understand the boundaries of the developed models.

Other properties such as strength and elongation, which are not inherently a material properties, are more closely related to impurities or flaws in the precursor chemistry, flaws during CF spinning or flaws introduced during tow-level composite production. This last point is especially important when handling un-sized CF. The combination of these flaws contribute to increase the defect density thus reducing strength and elongation. With respect to this, one aspect that was studied was the role of carbonaceous insolubles in PP. These insolubles were shown to decrease the strength, elongation and CF diameter for PPM CF. It was also demonstrated that the presence of excess volatiles in pitch-based materials affects CF spinnability and properties. Proper

modeling of strength and elongation CF properties requires more information than was able to be collected within the constraints of this project.

During the pitch-based atomistic modeling efforts, it was shown that density is a key property which takes into account the packing of the various aromatic molecules during CF synthesis. As the density increases, due to the formation of more carbon-carbon bonds, the modulus also increases and this was found to be more influence by the orientation of the molecules than other molecular parameters such as molecular shape and size. By pushing the boundaries of the computational models to densities greater than the theoretical maximum of a fully sp2 graphite system (>2.27 g/cm^3), it was discovered that forcing additional linkages, by increasing sp3 bonding (towards diamond-like connectivity), resulted in ultrahigh density CF to produce a theoretical CF with both a high tensile modulus and compressive modulus. This is unique because traditional sp2 CF has a low compressive modulus. Although experimental methods to produce this type of bonding in CF are currently unknown, this result opens the door to new possible types of materials with new applications, and experimental methods should be developed to explore this new carbon material space.

PAN-based modeling was further refined to more accurately predict density and elastic properties by taking the optimized CG-MD structures and adding back in all the hydrogen atoms. This method converts CG-MD back into a fully atomistic model so that it is possible for all the atoms to relax. This improved the models accuracy to predict properties at much less than ±15%. This development created a novel framework that is able to predict PAN CF properties relative to processing parameters such as stretching force, stabilization time and stabilization temperature. The model is also capable of predicting where failure will occur when pushing the processing boundaries. From this model, it is possible to tune PAN-based CF synthesis without trial an error approaches. Admittedly, the model needs to be improved by testing and optimizing for various co-monomer formulations typically used in PAN CF formulations.

ML was successfully implemented at the different scales (micro- and macro-level) to predict properties for pitch, CF, and tow-level elastic properties. These models were developed into user-friendly web-based platforms. Another key challenge in this study was how to account for CF processing conditions in a way that was compliant with export control regulations. CF processing is just as critical to CF properties and performance as proper molecule selection and precursor formulation. This was achieved by applying encryption to the various processing (spinning conditions, stretching, stabilization, carbonization, etc.) and then using ML to find relationships between the processing conditions and CF properties.

Scaled up PPM and bio-PAN CF were able to be produced that meet DOE physical properties as well as the cost coals of less than $5/lb. Various assumptions and aspects between the different materials were considered, as well as sensitivity analyses for the most costly aspects of CF production for the different materials. From the analysis bio-PAN was shown to be significantly cheaper than petroleum-based PAN due to co-product credits for propylene glycol and

ammonium sulfate. However, bio-PAN may be more attractive in the future as a way to reduce the carbon footprint as it is produced from bio-based and renewable sugar feedstocks. This may become more important especially as carbon credits become more widely accepted and enforced.

Deliverable: Table Demonstrating that Integrated Model Results are within 15% of Experimental Results for All Relevant Outputs.

The micro-scale modeling framework is evaluated within a few nm (essentially a nano-scale), and can capture properties like elastic modulus, compressive modulus, shear modulus, and Poisson's ratio (Table 109). These properties were found to up-scale well from nm to larger scales, as evidenced by good agreement with experiments well within the required 15%. However, to represent other mechanical properties like yield strength, fracture strength, and elongation, micro-scale and macroscale features like grain boundaries, surface fracture, voids, morphological inhomogeneities, etc. need to be considered, or predefined models for fraction propagation in these materials are required and need to be validated against actual experimental evidence (Evans & Adler, 1978; Chand, 2000; Wangxi, Jie, & Gang, 2003; Langston, 2016).

Table 109: Table demonstrating that integrated model results are within ±15% of experimental results for fiber level predictions. Reference 1 taken from www.matweb.com.

Name	Alignment	Density (g/cm^3)	Elastic Modulus (GPa)			Reference /Source
			Predicted	Experimental	% error	
PP	Mesophase	1.9	181	159	12	Solvay[1]
PP	Mesophase	1.92	187	172	8	Solvay[1]
PP	Mesophase	2	212	207	2	Solvay[1]
CTP	Mesophase	1.845	189	163.5±34.1	13	ORNL
PAN – T300	-	1.76	259	231	12	Solvay[1]
PAN – T650/42	-	1.78	271	290	7	Solvay[1]
PAN – IM5	-	1.79	277	279	1	Solvay[1]

A suite of high-speed tools capable of linking micro-scale to macro-scale composite properties were developed. The models utilize a complex web of connections between neurons of multiple NNs to provide near instantaneous and accurate predictions. The neural networks were trained using data generated from the FEA Abaqus micromechanics plugin and an in-house volume-

averaging software package. However, no FEA modeling experience is required to generate the predicted properties. These tools can be used to help guide manufacturing decisions, because embedded within the nanoscale sheets are details unique to the manufacturing processes of the fibers. Ultimately, the predicted properties were in good agreement with experimental values and well within the required 15% error (Table 110 for bio-PAN fibers and Table 111 for pitch-based fibers).

Table 110: Table demonstrating that integrated model results are within ±15% of experimental results for composite tow-level predictions for bio-PAN CF.

Component	Model	Property	Predicted	Experimental	% error
Fiber	Nano-Macro	E_{11} [GPa]	169.3	169.2	0.06
Fiber	Macro-Micro	E_{11} [GPa]	165.29	169.2	4.61
Composite	Nano-Macro	E_{11} [GPa]	81.94	80.99	1.17
Composite	Nano-Macro	E_{22} [GPa]	4.45	4.86	8.44
Composite	Nano-Macro	ν_{12}	0.33	0.33	0.00

Table 111: Table demonstrating that integrated model results are within ±15% of experimental results for composite tow-level predictions for pitch-based CF.

Component	Model	Property	Predicted	Experimental	% error
Fiber	Macro-Micro	E_{11} [GPa]	300.73	298.58	0.72
Composite	Nano-Macro	E_{11} [GPa]	144.26	143.41	0.59

Deliverable: Models Available to the Automotive Materials Community and Public.

Table 112 shows the various models used in this study and their documentation and references that are available to the automotive materials community and the public.

Table 112: The various models used in this study and their documentation and references that are available to the automotive materials community and the public.

Modeling Tool	**Information Developed by the Tool in this Program**	**Source/reference for the Tool**

MD	Modeling molecular evolution from pitch precursor to CFs and testing CF properties. Implemented using ReaxFF.	LAMMPS: https://www.lammps.org/ S. Plimpton, Fast Parallel Algorithms for Short-Range Molecular Dynamics, J Comp Phys, 117, 1-19 (1995). PACKMOL: http://leandro.iqm.unicamp.br/m3g/packmol/home.shtml L. Martínez, R. Andrade, E. G. Birgin, J. M. Martínez. Packmol: A package for building initial configurations for molecular dynamics simulations. *Journal of Computational Chemistry*, 30(13):2157-2164, 2009. VMD: https://www.ks.uiuc.edu/Research/vmd/ Humphrey, W., Dalke, A. and Schulten, K., "VMD - Visual Molecular Dynamics", J. Molec. Graphics, 1996, vol. 14, pp. 33-38. Python 3: https://www.python.org/
ReaxFF	Hydrogen abstraction of aromatic molecules to build larger cross-linked aromatic structure present in mesophase and the CF structures. This allowed to model the density and modulus of CF.	ReaxFF 2021.1, SCM, Theoretical Chemistry, Vrije Universiteit, Amsterdam, The Netherlands, http://www.scm.com A.C.T. van Duin, S. Dasgupta, F. Lorant, and W. A. Goddard, *ReaxFF: A reactive force field for hydrocarbons*, Journal of Physical Chemistry A 105, 9396-9409 (2001) K. Chenoweth, A.C.T. van Duin, and W.A. Goddard, *ReaxFF reactive force field for molecular dynamics simulations of hydrocarbon oxidation*, Journal of Physical Chemistry A 112, 1040-1053 (2008)

TensorFlow	General purpose Machine Learning framework for implementing custom scripts for Neural Network Scripts	Google Tensorflow https://www.tensorflow.org/ Abadi et al. "large-Scale Machine Learning on Heterogeneous Distributed Systems" https://static.googleusercontent.com/media/research.google.com/en//pubs/archive/45166.pdf
DataML	Neural network Machine Learning Regression and classification models using Neural Networks for predicting CF elastic properties from fabrication processes Correlation maps to identify Pearson and Spearman correlations and cross-correlations between properties to determine and reduce the number of variables in ML models.	DataML: Software and documentation https://github.com/feranick/DataML Python 3: https://www.python.org/ With Python Modules: Numpy: https://numpy.org/ Harris, C.R., Millman, K.J., van der Walt, S.J. et al. *Array programming with NumPy*. Nature 585, 357–362 (2020). DOI: 10.1038/s41586-020-2649-2. (Publisher link). Pandas: https://pandas.pydata.org/ Data structures for statistical computing in python, McKinney, Proceedings of the 9th Python in Science Conference, Volume 445, 2010. Scikit-learn: https://scikit-learn.org/stable/ Scikit-learn: Machine Learning in Python, Pedregosa *et al.*, JMLR 12, pp. 2825-2830, 2011.

		TensorFlow: https://www.tensorflow.org/ Abadi et al. “large-Scale Machine Learning on Heterogeneous Distributed Systems” https://static.googleusercontent.com/media/research.google.com/en//pubs/archive/45166.pdf
FEA	Model fiber and composite properties via hex-pack representative volume element.	Abaqus 2018: https://www.3ds.com/products-services/simulia/products/abaqus/ Micromechanics Plugin For Abaqus/CAE Version 1.15

References

Al - Muhareb, E., Morgan, T. J., Herod, A. A., & Kandiyoti, R. (2007). Characterization of Petroleum Asphaltenes by Size Exclusion Chromatography, UV - Fluorescence and Mass Spectrometr. *Petroleum Science and Technology, 25*, 81 - 91.

ASTMD7337. (2019). *Test Method for Tensile Creep Rupture of Fiber Reinforced Polymer Matrix Composite Bars.* West Conshohocken: ASTM International. doi:DOI: 10.1520/D7337_D7337M-12R19

Azemani, M., & Rabbani, A. R. (2016). Oil - oil Correlation by FTIR Spectroscopy of Asphaltene Samples. *Geosciences Journal, 20*, 273 - 283.

Barckholtz, C., Fadden, M. J., & Hadad, C. M. (1999). Computational Study of the Mechanisms for the Reaction of O2 with Aromatic Radicals. *Phys. Chem., 103*, 8108-8117.

Bermudez, V., Lukubira, S., & Ogale, A. A. (2018). 1.3 Pitch Precurosr - Based Carbon Fibers. In P. W. Beaumont, & C. Zwebe (Eds.), *Comprehensive Composite Materials II* (pp. 41-65).

Boyer, C., Holocombe, T., & Malone, D. (2016). New Process for Making Mesophase Pitch. *The Carbon Fiber Conference.*

Burgess, W. A., Pittman, J. J., Marcus, R. K., & Thies, M. C. (2010). Structural Identification of the Monomeric Constituents of Petroleum Pitch. *Energy Fuels*, 4301-4311.

Chand, S. (2000). Review carbon fibers for composites. *Journal of materials science, 35*(6), 1303-1313.

Chen, P., Metz, J. N., Merchant, S., Smith, S. E., Siskin, M., Rucker, S. P., . . . Zhang, Y. (2020). Petroleum Pitch: Exploring a 50-year Structure Puzzle with Real-Space Molecular Imaging. *Carbon*, 456-465.

Chung, D. D. (1994). Chapter 4 Properties of Carbon Fibers. In *Carbon Fiber Components.*

Clark, E. R., Darwent, J. R., Demirici, B., Flunder, K., Gaines, A. F., & Jones, A. C. (1987). . Fluorescence of Pyridine Ex tracts of Coals. *Energy Fuels, 1*, 392 - 397.

Cook, J., & Booth, S. (2019). *Carbon Fiber Manufacturing, Facility Siting & Policy Considerations: International Comparison.* CEMAC.

D4530-15, A. (2020). *Standard Test Method for Determination of Carbon Residue (Micro Method).* Retrieved from ASTM International: www.astm.org

Das, S. (n.d.). Opportunities and Challenges for Domestic High-Value Coal Products.

Das, S., & Mao, E. (2018). Techno-Economic and Market Pricing for Coal Products from Coal. *2019 Ramaco Research Rodeo.*

Das, S., Warren, J., & West, D. (2016). *Carbon Fiber Composites Supply Chain Competitiveness.* Analysis Clean Energy Manufacturing Analysis Center.

Delfosse, F., Drouadaine, I., Faucon-Dumont, S., Largeaud, S., Eckmann, B., Planche, J. P., & Turner, F. (2016, July 18-21). In Impact of Bitumen Quality on Asphalt Mixes Performances. Jackson Hole: International Society of Asphalt Pavements.

Delfosse, F., I. Drouadaine, S. F.-D., Largeaud, S., Eckmann, B., Planche, J. P., Turner, F., & Glaser, R. (2016). In Impact of the Bitumen Quality on the Asphalt Mixes Performance. *6th Eurasphalt and Eurobitume Congress.* Prague.

Diefendorf, R. J. (2000). 1.02 Pitch Precursor Carbon Fibers. In A. Kelly, & C. Zweben (Eds.), *Comprehensive Composite Materials* (pp. 35-83).

Diez, N., Alvarez, P., Santamaria, R., Blamco, C., Menendez, R., & Granda Ferreira, M. (2012, January). Optimisation of the melt-spinning of anthracene oil-based pitch for isotropic carbon fibre preparation. *Fuel Processing Technology, 93,* 99-104.

Dordevic, D. M., Stankovic, M. N., Dordevic, M. G., Krstic, N. S., Pavlovic, M. A., & Radivojevic, A. R. (2012). FTIR Spectroscopic Characterization of Bituminous Limestone: Maganik Mounta in (Montenegro). *Studia UBB Chemia, 4*, 39-54.

Energy Information Administration. (n.d.). *Coal Explained*. Retrieved 2021, from https://www.eia.gov/energyexplained/coal/how-much-coal-is-left.php

Energy Information Administration. (n.d.). *Refinery Capacity Report*. Retrieved 2021, from https://www.eia.gov/petroleum/refinerycapacity/

Esguerra, D. F., Hoffman, W. P., & Thies, M. C. (2014). Liquid Crystallinity in Trimer Oligomers Isolated from Petroleum and Pyrene Pitches. *Carbon*, 265-273.

Evans, A. G., & Adler, W. F. (1978). Kinking as a mode of structural degredation in carbon fiber composites. *Acta Metallurgica, 26*(5), 725-738.

Everaers, R., & Ejtehadi, M. R. (2003). Interaction potentials for soft and hard ellipsoids. *Physical Review*.

Fan, X., Fei, Y., Chen, L., & Li, W. (2017). Distribution and Structural Analysis of Polycyclic Aromatic Hydrocarbons Abundant in Coal Tar Pitch. *Energy Fuels*, 4694-4704.

Fetzer, J. C. (2007). The Chemistry and Analysis of Large PAHs. Polycyclic Aromatic Compounds. *Polycyclic Aromatic Compounds*, 143-162.

Fitzer, E., Frohs, W., & Heine, M. (1986). Optimization of stabilization and carbonization treatment of PAN fibres and structural characterization of the r esulting carbon fibres. *Carbon, 24*(4), 387 - 395.

García, R., Crespo, J. L., Snape, C. E., & Moinelo, S. R. (2003, January 28). Development of Mesophase from a Low-Temperature Coal Tar Pitch. *Energy Fuels, 17*(2), 291-301.

George, A., Morgan, T. J., Alvarez, P., Millan, M., Herod, A. A., & Kandiyoti, R. (2010). Fractionation of Coal Tar Pitch by Ultra - filtration, and Characterization by Size Exlucsion Chromatography, UV - fluoresence and Laser Desorption - mass Spectroscopy. *Fuel, 89*(10), 2953-2970.

Glaser, R., Planche, J. P., Turner, F., Boysen, R., Schabron, J. F., Delfosse, F., . . . Eckman, B. (2016). In Relationship between Solubility and Chromatographically Defined Bitumen Fractions and Physical Properties. *6th Eurasphalt and Eurobitume Congress.* Pragu.

Goyle, A. (2020, June 9). *Email*.

Grotschel, M., Lovasz, L., & Schrijver, A. (1988). Geometric Algorithms and Combinatorial Optimization. *Springer*.

Guillen, M. D., Iglesias, M. J., Dominguez, A., & Blanco, C. G. (1992). Figure X. Correlation between the SP and the FTIR C - H alkyl bend at 1442 cm - 1 for HTCTP and CTPM (l eft) and correlation between HTCTP and CTPM with the same IR band. Figure X. Correlations between various aromatic out - of - plane C - H bends and the. *Energy Fuels, 6*, 518 - 525.

Hawthorne, H. M., Baker, C., Bentall, R. H., & Linger, K. R. (1970). High Strength, High Modulus Graphite Fibers from Pitch. *Nature*, 946-947.

Herod, A. A., & Kandiyoti, R. (1995). Fractionation by Planar Chromatography of Coal Tar Pitch for Characterization by Size - exclusion Chromatography, UV - fluorescence and Direct - probe Mass Spectrometr. *Journal of Chromatography A, 708*, 143-160.

Hortal, A. R., Hurtado, P., Martinez - Haya, B., & Mullins, O. C. (2007). Molecular - Weight Distributions of Coal and Petroleum Asphaltenes from Laser Desorption/Ionization Experiments. *Energy Fuels, 21*, 2863 - 2868.

Hortal, A. R., Martinez - Haya, B., Lobato, M. D., Pedrosa, J. M., & Lago, S. (2006). On the Determination of Molecular Weight Distributions of Asphaltenes and Their Aggregates in Laser Desorption Ionization Experiments. *Journal of Mass Spectrometr, 41*, 960 - 968.

Huang, D. M., Geissler, P. L., & Chandler, D. (n.d.). Scaling of Hydrophobic Solvation Free Energies. *J. Phys. Chem., B*(105), 6704-6709.

Huang, X. (2008). Fabrication and Properties of Carbon Fibers. *Materials*, 2369-2403.

Huang, X. (2009). Fabrication and Properties of Carbon Fibers. *Materials*, 2369-2403.

Inagaki, M., & Kang, F. (2014). Chapter 3 Engineering and Applications of Carbon Materials. In M. Inagaki, & F. Kang, *Materials Science and Engineering of Carbon: Fundamentals* (pp. 219-252).

Ingaki, M. (2000). Chapter 4 - Carbon Fibers. In M. Ingaki, *New Carbons - Control of Structure and Functions* (pp. 82-123). Elsevier Science.

Islas, C. A., Suelves, I., Li, W., Morgani, T. J., Herod, A. A., & Kandiyoti, R. (2003). The Unusual Properties of High Mass Materials from Coal - derived Liquids. *Fuel, 82*, 1813 - 182.

Jensen, E. M. (2014). Creep and creep rupture of fiber reinforced polymers. *Long term variability*.

Jian, C., Zhu, T., Adams, J. J., Grossman, J. C., & Ferralis, N. (2021). Naphthalene-based carbon fibers: Correlating atomistic models with elastic properties via Ractive force fields. *Carbon, 176*(Molecular Dynamics), 569-579.

Kershaw, J. R. (1995). Fluorescence Spectroscopic Studies of Mesophase Formation. *Fuel, 74*, 1104 - 1107.

Kershaw, J. R., & Black, K. J. (1993). Structural Characterization of Coal-Tar and Petroleum Pitches. *Energy Fuels, 7*, 420-425.

Korai, Y., Yoon, S. H., Oka, H., Mochida, I., Nakamura, T., Kato, I., & Sakai, Y. (1998). The properties of Co-oligomerized mesophase pitch from methylnaphthalene and naphthalene catalyzed by HF/BF3. *Carbon, 36*(4), 369-375.

Kraca, F., Morgan, T. J., George, A., Bull, I. D., Herod, A. A., Mill an, M., & Kandiyoti, R. (2009). Molecular Mass Ranges for Coal Tar Pitch Fractions by Mass Spectrometry and Size - exclusion Chromatography. *Rapid Communications in Mass Spectrometry, 23*, 2087 - 2098.

Langston, T. (2016). The tensile behavior of high=strength carbon fibers. *Microscopy and Microanalysis, 22*(4), 841-844.

Lavin, J. G. (1992). *Chemical Reactions in the Stabilization of Mesophase Pitch - Based Carbon Fiber* (Vol. 30).

Li, C. -Z., Wu, F., Cai, H. -Y., & Kandiyoti, R. (1994). UV - Fluorescence Spectroscopy of coal Pyrolysis Tar. *Energy Fuels, 8*(5), 1039–1048.

Li, M. L., Du, H., Li, Q., Hou, X., & Ye, J. (2015). Preparation of Mesophase Pitch by Aromatics - rich Distillate of Naphthenic Vacuum Gas Oil. *Applied Petrochemical Research, 5*, 339 - 346.

Li, X. -Y., Li, N., Luo, H. -D., Lin, L. -R., Zo u, Z. -X., Jia, Y. -Z., & Li, Y. -Q. (2011). A novel Synchronous Fluorescence Spectroscopic Approach for the Rapid Determination of Three Polycyclic Aromatic Hydrocarbons in Tea with Simple Microwave - Assisted Pretreatment of Sample. *Journal of Agricultural and Fo od Chemistry, 59*, 5899 - 5905.

Lischka, H., Ventura, E., & Dallos, M. (2004). The Diels-Alder Reaction of Ethene and 1, 3-Butadiene: An Extended Multireference ab initio Investigation. *ChemPhysChem, 5*, 1365-1371.

Lloyd, J. B. (1971, October 11). The nature and evidential value of the luminescence of automobile engine oils and related materials. 3. Separated luminescence. *J Forensic Sci Soc, 4*, 235-253.

Manocha, L. M. (2007). Concise Encyclopedia of Composite Materials. In A. Mortensen (Ed.), *Concise Encyclopedia of Composite Materials* (pp. 85-96).

McHenry, E. R. (1977). *U.S. Patent No. 4,026,788.*

Menendez, R., Bermejo, J., & Figueiras, A. (2000). Chapter 5 - Tar and Pitch: Composition and Application. In H. Marsh, & F. Rodriquez-Reinoso (Eds.), *In Sciences of Carbon Material* (pp. 173 - 204).

Menendez, R., Blanco, C., Santamaria, R., Bermeo, J., Suelves, I., Herod, A. A., & Kandiyoti, R. (2001). On the Chemical Composition of Thermally Treated Coal - tar Pitches. *Energy Fuels, 15*, 214 - 223.

Menendez, R., Blanco, C., Santamaria, R., Dominquez, A., & Blanco, C. G. (2002). Effects of Air - blowing on the Molecular Size and Structure of Coal - Tar Pitch Components. *Energy Fuels, 16*, 1540 - 1549.

Mochida, I., Korai, Y., & Hieida, T. A. (1991). Detailed Analyses of FCC Decant Oil as a Starting Feedstock for Mesophase Pitch. *Fuel Science and Technology International., 9*, 485-504.

Morgan, P. (2005). *Carbon Fibers and Their Composites* (1st ed.).

Mullins, O. C. (1998). Chapter 2: Optical Interrogation of Aromatic Moieties in Crude Oils and Asphaltenes. In O. C. Mullins, & E. Y. Sheu (Eds.), *In Structures and Dynamics of Asphaltenes* (pp. 21 - 77).

Noda, T., & Kato, H. (1965). Heat Treatment of Carbon Under High Pressure. *Carbon, 3*, 291-297.

Omnia, LLC. (2012). *Assessment of Carbon Fiber Manufacturing Cost.* Iceland.

Ozcan, S., Vautard, F., & Naskar, A. K. (2014). Chapter 10: Designing the Structure of Carbon Fibers for Optimal Mechanical Properties. In *Polymer Precursor-Derived Carbon* (Vol. 1173, pp. 215-232). ACS Symposium Series.

Phung. (1987, May). Theory and Evidence for Using the Economy-of-Scale Law in Power Plant Economics. *Oak Ridge National Laboratory Subcontract 12X-79356V*.

Pomerantz, A. E., Hammond, M. R., Marrow, A. L., Mullins, O. C., & Zare, R. N. (2009). . Asphaltene Molecular - Mass Distribution Determined by Two - Step Laser Mass Spectrometry. *Energy Fuels, 23*, 1162 - 1168.

Rebouillat, S., Donnet, J.-B., & Wang, T. K. (1998). *Carbon Fiber* (3rd ed.). CRC Press Taylor & Francis Group.

Roenzin, H., & Mullins, O. C. (2000). Molecular Size and Structure of Asphaltenes from Variou s Sources. *Energy Fuels, 14*, 667 - 684.

Rogel, E., & Moir, M. W. (2015). Atm ospheric Pressure Photoionization and Laser Desorption Ionization Coupled to Fourier Transform Ion Cyclotron Resonance Mass Spectrometry to Characterize Asphaltene Solubility Fractions: Studying the Link between Molecular Composition and Physical Beha. *Energy Fuels, 29*, 4201 - 4209.

Romand, & Sandrine. (2018, October). Publication TECH 2018S8. *Technoeconomics Energy and Chemicals - Carbon Fiber*, 125.

Rosenblatt, F. (1961). *Principles of Neurodynamics: Perceptrons and the Theory of Brain Mechanisms.* Washington, DC: Spartan Books.

Rumelhart, D. E., Hinton, G. E., & Williams, R. J. (1985, September 01). *Learning internal representations by error propagation*. Retrieved from Defense Technical Information Center: https://apps.dtic.mil/sti/citations/ADA164453

Sabbah, H., Marrow, A. K., Pomerantz, A. E., Mullins, O. C., Tan, X., Gray, M. R., . . . Zare, R. N. (2010). Comparing Laser Desorption/Laser Ionization Mass Spectra of Asphaltenes and Model Compounds. *Energy Fuels, 24*, 3589 - 3594.

Sanei, S. H., Barsotti, E. J., Leonhardt, D., & Fertig, R. S. (2017). Characterization, synthetic generation, and statistical equivalence of composite microstructures. *Journal of Composite Materials*, 1817-1829.

Scotti, R., & Montanari, L. (1998). Chapter 3: Molecular Struct ure and Inermolecular Interaction of Asphaltenes by FT - IR, NMR, EP. In M. O. C., & E. Y. Sheu (Eds.), *In Structures and Dynamics of Asphaltenes* (pp. 93 - 9).

Senda, T., Yamada, Y., Morimoto, M., Momo, N., Sogabe, T., Kubo, S., & Sato, S. (2019). Analyses of Oxidation Process for Isotropic Pitch-based Carbon Fibers using Model Compounds. *Carbon, 142*, 311-326.

Sherigara, B. S., & Yashoda, M. P. (1999). *Journal of Physical Organic Chemistry*, 605-611.

Sloan, J. (2021). Carbon fiber suppliers gear up for next-gen growth. Knoxville: Composites World. Retrieved from https://www.compositesworld.com/articles/carbon-fiber-suppliers-gear-up-for-next-gen-growth

Songasasen, A., Bangkedphol, S., & Pornsinlapatip, P. (2002). Synchronous Fluorescence Spectrscopic Technique: The Tool for Rapid Identification of Polycyclic Aromatic Hydrocarbon (PAHs) at Sub - ppm Level in Liquid Samples. *Nat. Sci., 36*, 301 - 311.

Statista. (2020). Retrieved from U.S. sugar cane production by state, 2020: https://www.statista.com/statistics/191975/sugarcane-production-in-the-us-by-state/

Sun, Q., Zhou, G., Meng, Z., Guo, H., Chen, Z., Liu, H., & al., e. (2019). . Failure criteria of unidirectional carbon fiber reinforced pol ymer composites informed by a computational micromechanics model. *Composites Science and Technology*.

Tagawa, T., & Miyata, T. (1997, November 15). Size effect on tensile strength of carbon fibers. *Materials Science and Engineering, 238*(2), 336-342.

Taylor, G. (2003). *Conoco to Close Carbon Fibre Facility 6 Months After Start.* Independent Commodity Intelligence Sercices. Retrieved from https://www.icis.com/explore/resources/news/2003/02/13/190123/conoco-to-close-carbon-fibre-plant-6-months-after-start/

Thies, M. C. (2014). Chapter 5: . Fractionation and Characterization of Carbonaceous Pitch Oligomers: Unders tanding the Building Blocks for Carbon Material. In *Polymer Precursor - Derived Carbon* (Vol. 1173, pp. 85 - 136). ACS Symposium Series.

Thies, M. C. (2014). Fractionation and Characterization of Carbonaceous Pitch Oligomers: Understanding the Building Blocks for Carbon Materials. . In *In Polymer Precursor-Derived Carbon* (pp. 85-136).

U.S. Department of Comerce. (2020). *Teijin Carbon Fibers, Inc. Response to Public Comments.*

U.S. Drive. (2021, October 9). Retrieved from Energy.gov: https://www.energy.gov/eere/vehicles/us-drive

Unterreiner, B. V., Sierka, M., & Ahlrichs, R. (2004). Reaction Pathways for Growth of Polycyclic Aromatic hydrocarbons under Combustion Conditions, a DFT Study. *Phys. Chem. Chem. Phys., 6*, 4377-4384.

Wakeham, S. G. (1977). Synchronous Fluorescence Spectroscopy and It s Application to Indigenous and Petroleum - Derived Hydrocarbon in Lacustrine Sediments. *Environmental Science and Technology, 11*, 272-276.

Wangxi, Z., Jie, L., & Gang, W. (2003). Evolution of structure and properties of PAN precursers during their conversion to carbon fibers. *Carbon, 41*(14), 2805-2812.

Warren, D. C. (n.d.). *Carbon Fibers Precurser and Conversion.* DOE Oak Ridge National Labs.

Xie, T., & Grossman, J. C. (2018). Crystal Graph Convolutional Neural Networks for an Accurate and Interpretable Prediction of Material Properties. *Phys. Rev. Lett., 120*(14), 145301.

Zander, M. (2000). Chapter 6: Chemistry and properties of Coal - tar and Petroleum Pitch. In *The Science of Carbon Materials* (pp. 205 - 258).

Zander, M., & Haenel, W. (1990). Regularities in the Fluorescence Spectra of Coal - tar Pitch Fractions. *Fuel,* 1206-1207.

Zhang, T., & Yan, Y. (2015). Failure Locus Analysis of Fibre-Reinforced Composites Under Combined Transverse Stresses Through Computational Micromechanics. *International Conference on Composite Materials.* Copenhagen.

Zheng, S. M., Maeda, T., Tokumitsu, K., & Mondori, J. (1993). Preparation of isotropic pitch precursors for general purpose carbon fibers (GPCF) by air blowing—II. Air blowing of coal tar, hydrogenated coal tar, and petroleum pitches. *Carbon, 31*, 413 - 419.

Appendix A

CTPM pitch experimental conditions

Table 113 provides the experimental conditions, observations and SP for CTPM produced using a 100 mL stirred reactor. Table 114 provides the experimental conditions and SP for CTPM produced using a 1000 mL stirred reactor.

Table 113: 100 mL reactor CTPM experimental conditions and SP.

Feed Material (NMPI-removed)	Feed SP, °C	Feed, g	Reaction Conditions:			Approx. MP %	Mesophase SP, °C	Yield, g	Comments
			Temp., °C	Time, hr	Flowrate, L/min				
CTP 6C	111.5	65.00	390	1.5	0.5	5		-	
CTP 6C	111.5	65.00	400	2.5	0.5	15	219.6	35.18	
CTP 6C	111.5	65.00	410	2	0.5	35	236.9	32.54	
CTP 6C	111.5	65.00	410	4	0.5	70	318.9	30	Combined
CTP 6C	111.5	65.00	410	4	0.5	70	320.8	30.86	
CTP 6D	125.7	65.00	410	5	0.5	90	294.5	41.17	Globule, included top infusible
CTP 6D	125.7	65.00	410	5	0.5	80	320.2	34.40	Looks similar to 4 hrs
CTP 7B	128.7	65.00	410	5	0.75	90	340.2	27.86	
CTP 6E	147.5	65.00	410	4	0.5	50	304.8	36.78	Large globules, not coalesced
CTP 6E	147.5	65.00	410	6	0.5	95	333.5	32.78	
CTP 6E	147.5	65.00	410	6	0.5	99	331.9	32.27	

Table 114: 1000 mL reactor CTPM experimental conditions and SP.

Feed Material	Feed SP, °C	Feed, g	Reaction Conditions			Approx. MP %	Meophase SP, °C	Yield, g	Effluent, g	Loss, g
			Temp., °C	Time, hr	Flowrate, L/min					
CTP 7	116	650	410	5	3	90	339.4	311.64	-	-
CTP 7	116	650	410	4	3	80	330.2	311.90	-	-
CTP 7	116	650	410	4	3	90	340.2	310.80	-	-
CTP 7	116	650	400	4	3	80	328.0	316.01	-	-
CTP 6	112	650	400	4	3	75	320.9	322.53	-	-
CTP 7	116	650	400	4	3	50	318.5	326.10	-	-
CTP 7	116	650	400	4	3	50	317.5	322.63	-	-
CTP 6	112	650	400	4	3	40	305.6	330.49	-	-
CTP 7	116	650	400	5	3	-	340.0	321.58	-	-
CTP 7	116	650	400	4	3	-	335.8	341.17	-	-
CTP 7	116	650	400	3	3	-	313.8	342.32	-	-
CTP 6	112	650	400	4	3	50	320.4	316.12	252.06	81.82
CTP 6	112	650	400	4	3	40	308.9	319.55	101.86	228.59
CTP 6	112	650	400	4	3	50	313.8	301.39	188.40	160.21
CTP 6	112	650	400	4	3	50	316.1	312.66	195.91	141.43
CTP 6	112	650	400	4	3	50	314.0	305.67	205.92	138.41
CTP 6	112	650	400	4	3	-	300.1	336.61	188.77	124.62
CTP 6	112	650	400	4	3	-	302.2	325.78	107.55	216.67
CTP 6	112	650	400	5	3	-	305.2	326.78	172.71	150.51
CTP 6	112	650	400	6	3	-	310.4	320.56	185.68	143.76
CTP 6	112	650	400	6.25	3	60	315.6	317.61	176.00	156.39
CTP 6	112	650	400	6.25	3	60	314.7	314.72	188.53	146.75
CTP 6	112	650	400	6.5	3	80	317.6	316.25	187.46	146.29
CTP 6	112	650	400	6.5	3	80	317.1	318.70	177.06	154.24
CTP 6	112	650	400	6.5	3	80	314.5	316.66	174.98	158.36

Encrypted Processing and CF Characterization Data Used to Build the Integrated Predictive Models.

BP3_KOP MP 297													Testable Fiber
Specimen	C1	C2	C3	C4	C5	C6	C7	C8	C9	P1	P2	P3	(1= Y, 0 =N)
2194	0.03	0.29	0.25	0.10	1.00	0.33	0.10	0.10	20.32 (1.02)	127.18 (34.76)	20.86 (1.10)	0.64 (0.14)	1
2201	0.03	0.29	0.25	0.10	1.00	0.33	0.10	0.10	19.88 (1.74)	96.48 (35.71)	20.22 (1.50)	0.50 (0.15)	1
2221	0.03	0.29	0.25	0.40	1.00	0.33	0.10	0.40	24.16 (1.58)	103.20 (43.23)	22.02 (1.18)	0.49 (0.19)	1
2246	0.03	0.29	0.25	1.00	1.00	0.33	0.10	1.00	23.46 (0.99)	159.81 (26.44)	22.17 (1.06)	0.74 (0.10)	1
2247	0.03	0.29	0.25	1.00	1.00	0.33	0.10	1.00	24.00 (1.52)	149.00 (24.00)	23.12 (1.00)	0.67 (0.09)	1
2282	0.14	0.29	0.25	0.10	1.00	0.33	0.10	0.00	20.20 (0.67)	177.98 (22.24)	21.65 (1.49)	0.83 (0.09)	1
2202	0.03	0.43	0.25	0.10	1.00	0.33	0.10	0.10	23.65 (0.48)	146.05 (28.28)	24.77 (2.19)	0.61 (0.12)	1
2223	0.03	0.43	0.25	0.40	1.00	0.33	0.10	0.40	23.81 (0.88)	145.58 (29.40)	22.37 (1.55)	0.67 (0.12)	1
2250	0.03	0.43	0.25	1.00	1.00	0.33	0.10	1.00	21.92 (0.79)	86.65 (26.67)	16.78 (0.00)	0.47 (0.15)	1
2307	0.43	0.43	0.25	0.10	1.00	0.33	0.10	0.10	19.99 (0.69)	197.57 (30.04)	20.72 (0.61)	0.95 (0.13)	1
2206	0.03	0.57	0.25	0.10	1.00	0.33	0.10	0.10	23.13 (1.45)	91.30 (24.90)	21.43 (0.00)	0.46 (0.12)	1
2225	0.03	0.57	0.25	0.40	1.00	0.33	0.10	0.40	22.58 (1.08)	63.58 (27.42)		0.34 (0.13)	1
2268	0.03	0.57	0.25	0.10	1.00	0.33	0.10	1.00	20.54 (0.66)	151.83 (31.59)	20.96 (0.95)	0.75 (0.14)	1

2292	**0.14**	**0.57**	**0.25**	**0.10**	**1.00**	**0.33**	**0.10**	**0.10**	**19.26 (0.27)**	**175.16 (31.01)**	**20.26 (0.35)**	**0.87 (0.15)**	**1**
2219	**0.03**	**0.71**	**0.25**	**0.10**	**1.00**	**0.33**	**0.10**	**0.10**	**21.90 (1.74)**	**85.06 (31.75)**	**18.38 (0.00)**	**0.50 (0.14)**	**1**
2295	**0.14**	**0.71**	**0.25**	**0.10**	**1.00**	**0.33**	**0.10**	**0.10**	**18.54 (0.62)**	**136.95 (21.20)**	**19.38 (0.61)**	**0.72 (0.10)**	**1**
2711	**0.43**	**0.43**	**0.03**	**0.10**	**0.00**	**0.44**	**0.05**	**0.20**	**17.46 (0.79)**	**225.66 (42.62)**	**24.69 (3.17)**	**0.92 (0.13)**	**1**
2280	**0.14**	**0.29**	**0.05**	**0.05**	**1.00**	**0.33**	**0.00**	**0.00**	**20.50 (0.79)**	**197.29 (22.41)**	**21.06 (0.46)**	**0.94 (0.10)**	**1**
BP3_CTP6M SP316+													**Testable Fiber**
Specimen	**C1**	**C2**	**C3**	**C4**	**C5**	**C6**	**C7**	**C8**	**C9**	**P1**	**P2**	**P3**	**(1= Y, 0 =N)**
2222	**0.03**	**0.29**	**0.25**	**0.40**	**1.00**	**0.33**	**0.10**	**0.40**	**18.95 (0.72)**	**218.52 (56.12)**	**18.78 (0.62)**	**1.14 (0.24)**	**1**
2248	**0.03**	**0.29**	**0.25**	**1.00**	**1.00**	**0.33**	**0.10**	**1.00**	**20.47 (2.42)**	**202.14 (67.06)**	**19.79 (2.25)**	**1.00 (0.28)**	**1**
2249	**0.03**	**0.29**	**0.25**	**1.00**	**1.00**	**0.33**	**0.10**	**1.00**	**20.88 (2.05)**	**213.80 (63.13)**	**18.05 (1.34)**	**1.16 (0.30)**	**1**
2280	**0.14**	**0.29**	**0.25**	**0.05**	**1.00**	**0.33**	**0.10**	**0.05**	**20.50 (0.79)**	**197.29 (22.41)**	**21.06 (0.46)**	**0.94 (0.10)**	**1**
2282	**0.14**	**0.29**	**0.25**	**0.05**	**1.00**	**0.33**	**0.10**	**0.05**	**20.20 (0.67)**	**177.98 (22.24)**	**21.65 (1.49)**	**0.83 (0.09)**	**1**
2203	**0.03**	**0.43**	**0.25**	**0.10**	**1.00**	**0.33**	**0.10**	**0.10**	**20.10 (3.41)**	**142.99 (34.84)**	**18.02 (1.58)**	**0.81 (0.20)**	**1**
2224	**0.03**	**0.43**	**0.25**	**0.40**	**1.00**	**0.33**	**0.10**	**0.40**	**19.23 (0.55)**	**236.70 (51.20)**	**17.53 (0.78)**	**1.31 (0.24)**	**1**
2251	**0.03**	**0.43**	**0.25**	**1.00**	**1.00**	**0.33**	**0.10**	**1.00**	**18.01 (0.56)**	**203.78 (28.47)**	**16.58 (0.49)**	**1.19 (0.14)**	**1**
2307	**0.43**	**0.43**	**0.25**	**0.10**	**1.00**	**0.33**	**0.10**	**0.10**	**19.99 (0.69)**	**197.57 (30.04)**	**20.72 (0.61)**	**0.95 (0.13)**	**1**

2268	**0.43**	**0.57**	**0.05**	**0.10**	**1.00**	**0.33**	**0.10**	**0.10**	**20.54 (0.66)**	**151.83 (31.59)**	**20.96 (0.95)**	**0.75 (0.14)**	**1**
2207	**0.03**	**0.57**	**0.25**	**0.10**	**1.00**	**0.33**	**0.10**	**0.10**	**20.51 (3.83)**	**197.91 (47.80)**	**17.86 (2.14)**	**1.10 (0.26)**	**1**
2226	**0.03**	**0.57**	**0.25**	**0.40**	**1.00**	**0.33**	**0.10**	**0.40**	**18.94 (1.38)**	**228.31 (49.18)**	**17.89 (1.06)**	**1.24 (0.24)**	**1**
2269	**0.03**	**0.57**	**0.25**	**1.00**	**1.00**	**0.33**	**0.10**	**1.00**	**18.43 (0.31)**	**262.93 (62.44)**	**18.24 (0.78)**	**1.42 (0.38)**	**1**
2220	**0.03**	**0.71**	**0.25**	**0.10**	**1.00**	**0.33**	**0.10**	**0.10**	**19.74 (2.51)**	**148.50 (47.66)**	**17.22 (1.40)**	**0.86 (0.26)**	**1**
2468	**0.03**	**0.14**	**0.50**	**0.10**	**0.00**	**0.44**	**0.20**	**0.20**	**18.40 (0.62)**	**264.31 (43.97)**	**21.44 (0.96)**	**1.19 (0.17)**	**1**
2469	**0.14**	**0.14**	**0.50**	**0.10**	**0.00**	**0.44**	**0.20**	**0.20**	**18.43 (0.58)**	**210.70 (55.91)**	**22.99 (0.92)**	**0.90 (0.21)**	**1**
2585	**0.43**	**0.71**	**0.03**	**0.10**	**1.00**	**0.44**	**0.20**	**0.20**	**18.94 (1.58)**	**295.75 (61.29)**	**19.37 (1.14)**	**1.43 (0.25)**	**1**
2697	**0.03**	**0.29**	**1.00**	**0.10**	**1.00**	**0.44**	**0.05**	**0.10**	**13.02 (1.52)**	**209.39 (53.13)**	**21.63 (1.47)**	**0.94 (0.22)**	**1**
BP3_SSKOP Unfiltered													**Testable Fiber**
Specimen	**C1**	**C2**	**C3**	**C4**	**C5**	**C6**	**C7**	**C8**	**C9**	**P1**	**P2**	**P3**	**(1= Y, 0 =N)**
2270	**0.71**	**0.29**	**0.25**	**0.10**	**1.00**	**0.33**	**0.10**	**0.10**	**17.23 (0.48)**	**111.44 (33.86)**	**23.98 (0.42)**	**0.51 (0.14)**	**1**
2301	**0.14**	**0.43**	**0.25**	**0.10**	**1.00**	**0.44**	**0.20**	**0.10**	**17.04 (0.98)**	**118.89 (23.13)**	**24.23 (0.43)**	**0.53 (0.08)**	**1**
2265	**0.43**	**0.57**	**0.05**	**0.10**	**1.00**	**0.33**	**0.10**	**0.10**	**16.17 (0.57)**	**73.92 (29.98)**	**15.64 (0.00)**	**0.36 (0.16)**	**1**
2261	**0.03**	**0.57**	**0.25**	**0.40**	**1.00**	**0.33**	**0.10**	**0.40**	**15.73 (1.07)**	**28.82 (13.75)**	**n/a**	**0.23 (0.09)**	**1**
2476	**0.43**	**0.57**	**0.03**	**0.10**	**1.00**	**0.44**	**0.20**	**0.20**	**14.01 (0.27)**	**167.88 (47.66)**	**22.54 (1.74)**	**0.74 (0.21)**	**1**

2472	**0.43**	**0.43**	**0.03**	**0.50**	**1.00**	**0.44**	**0.20**	**0.20**	**17.26 (0.35)**	**124.23 (36.59)**	**24.83 (0.88)**	**0.55 (0.13)**	**1**
2475	**0.43**	**0.71**	**0.03**	**0.10**	**1.00**	**0.44**	**0.20**	**0.20**	**16.91 (1.25)**	**121.40 (55.51)**	**24.94 (2.17)**	**0.54 (0.19)**	**1**
2473	**0.43**	**0.43**	**0.03**	**0.50**	**1.00**	**0.44**	**0.20**	**0.20**	**15.93 (0.88)**	**131.22 (46.01)**	**22.85 (0.77)**	**0.64 (0.15)**	**1**
2488	**0.03**	**0.00**	**0.03**	**0.10**	**0.00**	**0.44**	**0.20**	**0.20**	**20.96 (0.64)**	**136.87 (25.00)**	**22.93 (0.94)**	**0.65 (0.08)**	**1**
2489	**0.14**	**0.14**	**0.90**	**0.00**	**1.00**	**0.44**	**0.20**	**0.20**	**15.84 (1.14)**	**141.46(27.51)**	**23.45(1.41)**	**0.64 (0.12)**	**1**
2563	**0.03**	**0.14**	**0.30**	**0.10**	**1.00**	**0.44**	**0.20**	**0.20**	**16.92 (1.03)**	**172.80 (25.89)**	**24.91 (1.28)**	**0.73 (0.10)**	**1**
2583	**0.14**	**0.14**	**0.90**	**0.10**	**1.00**	**0.44**	**0.20**	**0.20**	**17.57 (1.36)**	**134.18 (43.84)**	**26.13 (1.22)**	**0.55 (0.15)**	**1**
BP3_SSKOP Filtered													**Testable Fiber**
Specimen	**C1**	**C2**	**C3**	**C4**	**C5**	**C6**	**C7**	**C8**	**C9**	**P1**	**P2**	**P3**	**(1= Y, 0 =N)**
2279	**0.14**	**0.29**	**0.25**	**0.10**	**1.00**	**0.33**	**0.10**	**0.10**	**7.16 (0.54)**	**209.25 (70.37)**	**15.59 (1.22)**	**1.25 (0.34)**	**1**
2421	**0.43**	**0.43**	**0.03**	**0.10**	**0.00**	**0.44**	**0.20**	**0.20**	**7.40 (0.56**	**299.56 (123.28)**	**18.74 (2.97)**	**1.43 (0.45)**	**1**
2309	**0.43**	**0.43**	**0.13**	**0.10**	**0.38**	**0.44**	**0.20**	**0.40**	**6.57 (0.58)**	**214.84 (78.55)**	**16.84 (1.39)**	**1.20 (0.39)**	**1**
2300	**0.14**	**0.43**	**0.25**	**0.10**	**1.00**	**0.44**	**0.20**	**0.10**	**6.90 (0.58)**	**186.43 (45.84)**	**15.48 (1.28)**	**1.16 (0.29)**	**1**
2298	**0.14**	**0.43**	**0.25**	**0.10**	**1.00**	**0.33**	**0.10**	**0.10**	**7.46 (0.65)**	**264.94 (58.10)**	**16.82 (0.72)**	**1.45 (0.28)**	**1**
2420	**0.43**	**0.57**	**0.03**	**0.10**	**1.00**	**0.44**	**0.20**	**0.20**	**7.02 (0.94)**	**285.87 (72.32)**	**15.99 (1.20)**	**1.62 (0.39)**	**1**
2305	**0.43**	**0.57**	**0.25**	**0.10**	**0.00**	**0.44**	**0.20**	**0.10**	**6.90 (0.54)**	**265.97 (46.45)**	**15.84 (0.46)**	**1.51 (0.22)**	**1**

2419	**0.43**	**0.71**	**0.03**	**0.00**	**1.00**	**0.44**	**0.20**	**0.20**	**6.41 (0.48)**	**183.05 (61.03)**	**15.28 (1.46)**	**1.14 (0.32)**	**1**
2422	**0.43**	**0.71**	**0.03**	**0.10**	**1.00**	**0.44**	**0.20**	**0.20**	**6.79 (0.52)**	**185.81 (58.62)**	**17.12 (1.37)**	**1.05 (0.30)**	**1**
2312	**0.43**	**0.43**	**0.13**	**0.10**	**0.00**	**0.44**	**0.20**	**0.10**	**6.96 (1.08)**	**224.54 (48.10)**	**15.70 (0.72)**	**1.33 (0.22)**	**1**
2492	**0.03**	**0.14**	**0.30**	**0.10**	**1.00**	**0.44**	**0.20**	**0.20**	**21.47 (0.32)**	**231.42 (75.47)**	**17.69 (5.81)**	**0.98 (0.29)**	**1**
2690	**0.03**	**0.43**	**1.00**	**0.10**	**1.00**	**0.44**	**1.50**	**0.20**	**12.08 (0.50)**	**231.60 (22.81)**	**19.76 (0.74)**	**1.11 (0.10)**	**1**
2699	**0.43**	**0.43**	**0.03**	**0.10**	**1.00**	**0.44**	**2.00**	**0.20**	**13.02 (0.25)**	**263.84 (77.92)**	**22.27 (1.19)**	**1.12 (0.28)**	**1**
2698	**0.03**	**0.29**	**1.00**	**0.10**	**1.00**	**0.44**	**0.05**	**0.20**	**19.12 (0.76)**	**174.86 (32.59)**	**19.95 (1.89)**	**0.87 (0.12)**	**1**
2707	**0.43**	**0.43**	**0.03**	**0.10**	**0.25**	**0.44**	**0.75**	**0.20**	**9.84 (1.61)**	**385.84 (56.65)**	**21.79 (1.20)**	**1.56 (0.21)**	**1**
2709	**0.03**	**0.57**	**0.03**	**0.10**	**0.25**	**0.44**	**0.75**	**0.20**	**12.53 (1.50)**	**199.86 (45.40)**	**22.11 (1.14)**	**0.90 (0.17)**	**1**
2800	**0.43**	**0.43**	**0.01**	**0.10**	**0.00**	**0.44**	**0.05**	**0.20**	**11.75 (2.35)**	**187.59 (78.91)**	**21.29 (2.90)**	**0.88 (0.34)**	**1**
2801	**0.43**	**0.43**	**0.01**	**0.10**	**1.00**	**0.44**	**0.55**	**0.20**	**12.96 (2.66)**	**284.70 (76.78)**	**23.11 (1.45)**	**1.17 (0.27)**	**1**
2813	**0.43**	**0.43**	**0.05**	**0.10**	**1.00**	**0.44**	**0.05**	**0.20**	**12.23 (1.96)**	**264.74 (89.50)**	**21.47 (0.94)**	**1.17 (0.34)**	**1**
2826	**0.43**	**0.43**	**0.10**	**0.10**	**0.25**	**0.44**	**0.75**	**0.20**	**9.83 (1.67)**	**240.19 (74.51)**	**22.99 (2.85)**	**1.02 (0.30)**	**1**
BP3_SSKOP Unfilter 307.2													**Testable Fiber**
Specimen	**C1**	**C2**	**C3**	**C4**	**C5**	**C6**	**C7**	**C8**	**C9**	**P1**	**P2**	**P3**	**(1= Y, 0 =N)**
2304	**0.14**	**0.29**	**0.25**	**0.10**	**0.00**	**0.44**	**0.20**	**0.10**	**12.71 (0.45)**	**144.36 (54.49)**	**23.62 (1.93)**	**0.61 (0.23)**	**1**

2302	**0.43**	**0.43**	**0.13**	**0.10**	**0.38**	**0.44**	**0.20**	**0.10**	**13.97 (0.58)**	**125.38 (25.49)**	**20.76 (0.47)**	**0.61 (0.12)**	**1**
2311	**0.43**	**0.43**	**0.13**	**0.10**	**0.38**	**0.44**	**0.20**	**0.40**	**6.75 (0.92)**	**217.37 (45.47)**	**15.57 (0.88)**	**1.31 (0.22)**	**1**
2299	**0.14**	**0.43**	**0.25**	**0.10**	**1.00**	**0.33**	**0.10**	**0.10**	**13.24 (0.38)**	**132.46 (28.67)**	**20.90 (0.29)**	**0.64 (0.13)**	**1**
2306	**0.14**	**0.57**	**0.25**	**0.10**	**0.00**	**0.44**	**0.20**	**0.10**	**10.59 (0.83)**	**129.18 (17.68)**	**19.84 (0.48)**	**0.67 (0.08)**	**1**
2310	**0.14**	**0.57**	**0.25**	**0.10**	**0.00**	**0.44**	**0.20**	**0.10**	**12.88 (0.35)**	**129.25 (23.98)**	**21.09 (0.92)**	**0.62 (0.12)**	**1**
2313	**0.43**	**0.43**	**0.13**	**0.10**	**0.00**	**0.44**	**0.20**	**0.10**	**13.81 (0.95)**	**167.30 (40.51)**	**21.87 (1.13)**	**0.77 (0.17)**	**1**
2314	**0.43**	**0.43**	**0.13**	**0.10**	**0.38**	**0.44**	**0.20**	**0.10**	**13.53 (0.35)**	**182.24 (42.22)**	**21.86 (1.24)**	**0.83 (0.19)**	**1**
BP3_KOP MP 300													**Testable Fiber**
Specimen	**C1**	**C2**	**C3**	**C4**	**C5**	**C6**	**C7**	**C8**	**C9**	**P1**	**P2**	**P3**	**(1= Y, 0 =N)**
2804	**0.43**	**0.43**	**0.01**	**0.10**	**0.00**	**0.44**	**0.05**	**0.20**	**24.55 (1.98)**	**150.12 (50.22)**	**17.32 (1.03)**	**0.89 (0.28)**	**1**
2805	**0.43**	**0.43**	**0.01**	**0.10**	**1.00**	**0.44**	**0.05**	**0.20**	**25.19 (0.95)**	**138.03 (34.03)**	**15.83 (0.38)**	**0.90 (0.20)**	**1**
2813	**0.43**	**0.43**	**0.05**	**0.10**	**1.00**	**0.44**	**0.05**	**0.20**	**21.83 (2.19)**	**202.86 (53.51)**	**19.06 (0.71)**	**1.08 (0.24)**	**1**
2824	**0.43**	**0.43**	**0.03**	**0.10**	**0.00**	**0.44**	**0.05**	**0.20**	**23.35 (1.27)**	**258.84 (39.63)**	**22.07 (3.56)**	**1.21 (0.14)**	**1**
2825	**0.43**	**0.43**	**0.10**	**0.10**	**0.25**	**0.44**	**0.75**	**0.20**	**25.90 (0.74)**	**239.93 (52.11)**	**20.04 (1.20)**	**1.21 (0.26)**	**1**
2839	**0.43**	**0.43**	**0.05**	**0.10**	**0.00**	**0.44**	**1.00**	**0.20**	**27.34 (1.38)**	**185.63 (37.12)**	**17.57 (1.52)**	**1.09 (0.15)**	**1**
2890	**0.43**	**0.43**	**0.03**	**0.00**	**0.00**	**0.44**	**0.10**	**0.20**	**27.72 (1.20)**	**203.87 (27.55)**	**16.54 (0.85)**	**1.26 (0.14)**	**1**

2912	**0.09**	**0.51**	**0.15**	**0.10**	**0.38**	**0.33**	**0.30**	**0.20**	**26.10 (1.87)**	**173.69 (26.95)**	**16.46 (1.13)**	**1.09 (0.13)**	**1**
2893	**0.71**	**0.71**	**0.10**	**0.10**	**1.00**	**0.06**	**0.50**	**0.20**	**25.86 (2.53)**	**170.96 (21.98)**	**15.25 (1.06)**	**1.16 (0.12)**	**1**
2988	**0.43**	**0.43**	**0.05**	**0.10**	**0.00**	**0.33**	**0.03**	**0.20**	**25.56 (2.35)**	**173.41 (31.24)**	**18.88 (1.86)**	**0.98 (0.13)**	**1**
BP3_REfMP													**Testable Fiber**
Specimen	**C1**	**C2**	**C3**	**C4**	**C5**	**C6**	**C7**	**C8**	**C9**	**P1**	**P2**	**P3**	**(1= Y, 0 =N)**
2881	**0.43**	**0.43**	**0.03**	**0.10**	**0.00**	**0.44**	**1.00**	**0.20**	**23.26 (2.16)**	**236.86 (49.11)**	**19.28 (0.92)**	**1.05 (0.35)**	**1**
2889	**0.43**	**0.43**	**0.03**	**0.00**	**0.00**	**0.44**	**0.10**	**0.20**	**23.46 (2.58)**	**226.42 (37.80)**	**20.24 (1.10)**	**1.13 (0.18)**	**1**
2894	**0.71**	**0.71**	**0.10**	**0.10**	**1.00**	**0.06**	**0.50**	**0.20**	**23.12 (3.46)**	**203.92 (53.09)**	**16.68 (1.72)**	**1.23 (0.30)**	**1**
2913	**0.09**	**0.51**	**0.15**	**0.10**	**0.38**	**0.33**	**0.30**	**0.20**	**23.35 (2.47)**	**256.92 (78.32)**	**21.2 (2.81)**	**1.22 (0.31)**	**1**
2941	**0.14**	**0.57**	**0.00**	**0.10**	**0.38**	**0.33**	**0.20**	**0.20**	**27.54 (0.96)**	**139.90 (35.74)**	**16.48 (0.53)**	**0.91 (0.23)**	**1**
2999	**0.03**	**0.29**	**0.00**	**0.10**	**0.38**	**0.11**	**0.50**	**0.20**	**23.64 (2.16)**	**138.61 (36.10)**	**17.71 (0.88)**	**0.81 (0.21)**	**1**
BP3_bPANCF													**Testable Fiber**
Specimen	**C1**	**C2**	**C3**	**C4**	**C5**	**C6**	**C7**	**C8**	**C9**	**P1**	**P2**	**P3**	**(1= Y, 0 =N)**
2942	**0.43**	**0.46**	**0.03**	**0.10**	**0.38**	**0.11**	**0.05**	**0.20**	**10.03 (0.77)**	**143.26 (41.40)**	**19.22 (0.47)**	**0.78 (0.21)**	**1**
2988	**0.03**	**0.29**	**0.00**	**0.10**	**0.38**	**0.11**	**0.50**	**0.10**	**8.83 (1.15)**	**257.36 (147.23)**	**27.15 (2.54(**	**0.95 (0.45)**	**1**

2922	**0.43**	**0.29**	**0.03**	**0.10**	**1.00**	**0.44**	**0.20**	**0.10**	**8.00 (0.74)**	**206.6 (72.71)**	**29.9 (0.85)**	**0.71 (0.23)**	**1**